

2023

The Development of Microdosimetric Instrumentation for Quality Assurance in Heavy Ion Therapy, Boron Neutron Capture Therapy and Fast Neutron Therapy

James Vohradsky

Follow this and additional works at: <https://ro.uow.edu.au/theses1>

University of Wollongong

Copyright Warning

You may print or download ONE copy of this document for the purpose of your own research or study. The University does not authorise you to copy, communicate or otherwise make available electronically to any other person any copyright material contained on this site.

You are reminded of the following: This work is copyright. Apart from any use permitted under the Copyright Act 1968, no part of this work may be reproduced by any process, nor may any other exclusive right be exercised, without the permission of the author. Copyright owners are entitled to take legal action against persons who infringe their copyright. A reproduction of material that is protected by copyright may be a copyright infringement. A court may impose penalties and award damages in relation to offences and infringements relating to copyright material.

Higher penalties may apply, and higher damages may be awarded, for offences and infringements involving the conversion of material into digital or electronic form.

Unless otherwise indicated, the views expressed in this thesis are those of the author and do not necessarily represent the views of the University of Wollongong.

Research Online is the open access institutional repository for the University of Wollongong. For further information contact the UOW Library: research-pubs@uow.edu.au

The Development of Microdosimetric Instrumentation for Quality Assurance in Heavy Ion Therapy, Boron Neutron Capture Therapy and Fast Neutron Therapy

James Vohradsky

This thesis is presented as part of the requirements for the conferral of the degree:

Doctor of Philosophy

Supervisors:

Distinguished Professor Anatoly B. Rosenfeld & Dr. Linh T. Tran

The University of Wollongong

Centre for Medical Radiation Physics

School of Physics, Faculty of Engineering and Information Sciences

May 17, 2023

This work © copyright by James Vohradsky, 2023. All Rights Reserved.

No part of this work may be reproduced, stored in a retrieval system, transmitted, in any form or by any means, electronic, mechanical, photocopying, recording, or otherwise, without the prior permission of the author or the University of Wollongong.

This research has been conducted with the support of an Australian Government Research Training Program Scholarship.

Declaration

I, *James Vohradsky*, declare that this thesis is submitted in fulfilment of the requirements for the conferral of the degree *Doctor of Philosophy*, from the University of Wollongong, is wholly my own work unless otherwise referenced or acknowledged. This document has not been submitted for qualifications at any other academic institution.

All of the experiments, simulations and work presented in this thesis were performed by myself, unless explicitly acknowledged otherwise. Throughout this thesis, where there is mention of experimental work, simulation codes, software development, designs, etc with no attribution, I have performed this work. All processing and analysis of experimental and simulation data in this thesis was performed by me. All simulations and their code were written and performed by me. Assistance from others is specified below:

- The experimental data from beamlines and radiotherapy facilities presented in chapter 7 was obtained as a team consisting of myself and Dr. Linh Tran (CMRP, UOW), and other collaborators for various experiments.
- The experimental data obtained from iThemba LABS, as presented in chapter 5 was acquired by the CMRP team without me present. I assisted with planning the experiment and procuring the required samples. However, I carried out processing and analysis of the data obtained.
- The Geant4 geometry of the HIMAC beamline used in chapter 7 was provided by Dr. David Bolst (CMRP, UOW), with the simulations performed by me.
- The original basis for the Radiodosimeter software in Qt C++ was provided by Dr. Lachlan Chartier (CMRP, UOW), which was further developed by me in the work presented in chapter 7.
- The design and hardware development of the Radiodosimeter electronics board was performed by Dr. Alex Pogosso (CMRP, UOW) in 2018. Hardware testing, software development and experimental validation was performed by me, as presented in chapter 7.
- The CAD model of the Motion Stage system that was adapted by me for use in Geant4 (presented in chapter 5, 6 and 7) was provided by Dr. Lachlan Chartier (CMRP, UOW).
- The original design of the Radiodosimeter enclosure was designed by Jason Paino (CMRP, UOW), which was modified by me and presented in chapter 7.

James Vohradsky

May 17, 2023

Abstract

This thesis presents research for the development of new microdosimetric instrumentation for use with solid-state microdosimeters in order to improve their portability for radioprotection purposes and for QA in various hadron therapy modalities. Monte Carlo simulation applications are developed and benchmarked, pertaining to the context of the relevant therapies considered. The simulation and experimental findings provide optimisation recommendations relating to microdosimeter performance and possible radioprotection risks by activated materials.

The first part of this thesis is continuing research into the development of novel Silicon-on-Insulator (SOI) microdosimeters in the application of hadron therapy QA. This relates specifically to the optimisation of current microdosimeters, development of Monte Carlo applications for experimental validation, assessment of radioprotection risks during experiments and advanced Monte Carlo modelling of various accelerator beamlines.

Geant4 and MCNP6 Monte Carlo codes are used extensively in this thesis, with rigorous benchmarking completed in the context of experimental verification, and evaluation of the similarities and differences when simulating relevant hadron therapy facilities.

The second part of this thesis focuses on the development of a novel wireless microdosimetry system - the *Radiodosimeter*, to improve the operation efficiency and minimise any radioprotection risks. The successful implementation of the wireless Radiodosimeter is considered as an important milestone in the development of a microdosimetry system that can be operated by an end-user with no prior knowledge.

Acknowledgements

Firstly, I would like to express my sincere appreciation to my supervisor, Distinguished Professor **Anatoly Rosenfeld**, and co-supervisor, Dr **Linh T. Tran** for their tireless support, encouragement and guidance throughout my PhD studies. They are both truly the best supervisors anyone could have, and the completion of this thesis would not have been possible without them. They have always gone above and beyond to inspire me to do the very best work that I am capable of. The opportunities they provided me over the years exceeded all expectations. The knowledge and wisdom gained from working with them has been invaluable.

Secondly, I would like to thank Dr **Jeremy Davis**, who was my previous co-supervisor when I completed my Masters by Research. I thank Jeremy, who was the first to teach me Geant4 back in 2016 and for encouraging me continue academic research in a PhD. I also thank Associate Professor **Susanna Guatelli**, who was my supervisor when I completed my Masters by Research.

Those credited for their work that was used in some of the results or formed a basis for further development in this thesis:

- Dr **David Bolst** for all the discussions and for providing the Geant4 geometry of the HIMAC beamline, that was used for to simulate the HIMAC heavy ion beam presented in the work of this thesis.
- The **entire CMRP team** that travelled to South Africa in 2018 to collect the experimental data used in the Fast Neutron Therapy chapter (note: that the data was analysed by myself).
- **Lachlan Chartier** for providing the basis of the software used to develop the Radiodosimeter. Also for the ‘CMRP Microdosimetry Suite’ software used to control the motion stage system at HIMAC. I also thank Lachlan for all the detailed CAD files describing the Motion

Stage system that was used in the Tokai activation study.

- **Jason Paino** for providing the original design of the Radiodosimeter case, with CAD files and 3D printed model. I also thank Jason for teaching me how to use the 3D printer at the CMRP lab.

My appreciation is also extended to the following people for their help and support during my PhD studies:

- **Karyn and Tamsyn Vohradsky** for proof reading chapters of my thesis (when they were very rough drafts) and for providing valuable, if not self-evident, recommendations such as: ‘multiple shades of brown, orange, and yellow lines should not be used together in the same figure’.
- **John and Elise Vohradsky** for their ongoing support throughout my PhD studies.
- **Mat Niksic** for his overwhelming support and for providing me with the necessary motivation to complete my thesis.
- **Ange Everts** for helping me through the past year.
- **Dr Dean Cutajar** for providing assistance with Geant4 and technical support of the CMRP computing cluster.
- **Željko Pastuović** for his assistance with the accelerators at ANSTO.
- **Karen Ford** for all the administrative assistance and kind help.
- Thanks to CMRP PhD students: **Klaudiusz Jakubowski, Vladimir Pan, Benjamin James, Owen Brace, Albert Le** and **Fang-Yi Su**.
- Also thanks to the support of my friends: Kirsten, Jonno, Nikolina, Tallulla, Buss, Stefania and Melek.

I would especially like to thank my family for their support and encouragement throughout all of my studies.

This research was supported through the Australian Government Research Training Program (RTP) Scholarship and UOW EIS Faculty Scholarship.

Publications

1. James Vohradsky, Linh T. Tran, Susanna Guatelli, Lachlan Chartier, Charlot Vandevoorde, Evan Alexander de Kock, Jaime Nieto-Camero, David Bolst, Stefania Peracchi, Carina Hoglund, and Anatoly B. Rosenfeld (2021). *Response of SOI microdosimeter in fast neutron beams: experiment and Monte Carlo simulations*, Physica Medica, 90. DOI: 10.1016/j.ejmp.2021.09.008
2. James Vohradsky, Susanna Guatelli, Jeremy A. Davis, Linh T. Tran, and Anatoly B. Rosenfeld (2019). *Evaluation of silicon based microdosimetry for Boron Neutron Capture Therapy Quality Assurance*, Physica Medica, 66. DOI: 10.1016/j.ejmp.2019.09.072
3. James Vohradsky, Lachlan Chartier, Alex Pogosso, Saree Alnaghy, Jason Paino, Stefania Peracchi, Vladimir Pan, Marco Povoli, Angela Kok, Linh T. Tran, and Anatoly B. Rosenfeld (2022). *Introduction and implementation of the CMRP radiodosimeter — a novel wireless microdosimetry system*, Journal of Instrumentation, 17. DOI: 10.1088/1748-0221/17/03/p03006
4. James Vohradsky, Linh T. Tran, Lachlan Chartier, Stefania Peracchi, Susanna Guatelli, Hiroaki Kumada, and Anatoly B. Rosenfeld (2022). *Activation study of experimental setup at Tokai accelerator based iBNCT*, submitted to Applied Radiation and Isotopes (under review).
5. Vladimir A. Pan, James Vohradsky, Benjamin James, Federico Pagani, Lachlan Chartier, Emily Debrot, Željko Pastuović, Dean Cutajar, Joel Poder, Mitchell Nancarrow, Elena Pereloma, David Bolst, Sung H. Lee, Taku Inaniwa, Mitra

- Safavi-Naeini, Dale Prokopovich, Susanna Guatelli, Marco Petasecca, Michael Lerch, Marco Povoli, Angela Kok, Linh T. Tran, and Anatoly B. Rosenfeld (2022). *Application of an SOI Microdosimeter for Monitoring of Neutrons in Various Mixed Radiation Field Environments*, IEEE Transactions on Nuclear Science, 69(3). DOI: 10.1109/TNS.2021.3125999
6. Stefania Peracchi, James Vohradsky, Susanna Guatelli, David Bolst, Linh T. Tran, Dale A. Prokopovich, and Anatoly B. Rosenfeld (2019). *Modelling of the Silicon-On-Insulator microdosimeter response within the International Space Station for astronauts' radiation protection*, Radiation Measurements, 128. DOI: 10.1016/j.radmeas.2019.106182
 7. Jeremy A. Davis, Peter Lazarakis, James Vohradsky, Michael L.F. Lerch, Marco Petasecca, Susanna Guatelli, and Anatoly B. Rosenfeld (2019). *Tissue equivalence of diamond for heavy charged particles*, Radiation Measurements, 122. DOI: 10.1016/j.radmeas.2019.01.002
 8. Benjamin James, Linh T. Tran, James Vohradsky, David Bolst, Vladimir Pan, Madeline Carr, Susanna Guatelli, Alex Pogosso, Marco Petasecca, Michael Lerch, Dale A. Prokopovich, Mark I. Reinhard, Marco Povoli, Angela Kok, David Hinde, Mahananda Dasgupta, Andrew Stuchbery, Vladimir Perevertaylo, and Anatoly B. Rosenfeld (2019). *SOI Thin Microdosimeter Detectors for Low-Energy Ions and Radiation Damage Studies*, IEEE Transactions on Nuclear Science, 66(1). DOI: 10.1109/TNS.2018.2885996
 9. Linh T. Tran, David Bolst, Benjamin James, Vladimir Pan, James Vohradsky, Stefania Peracchi, Lachlan Chartier, Emily Debrot, Susana Guatelli, Marco Petasecca, Michael Lerch, Dale Prokopovich, Željko Pastuović, Marco Povoli, Angela Kok, Taku Inaniwa, Sung Hyun Lee, Naruhiro Matsufuji, and Anatoly B. Rosenfeld (2022). *Silicon 3D Microdosimeters for Advanced Quality Assurance in Particle Therapy*, Applied Sciences, 12(1), 238. DOI: 10.3390/app12010328

10. Stefania Peracchi, Benjamin James, Federico Pagani, Vladimir Pan, James Vohradsky, David Bolst, Dale A. Prokopovich, Susanna Guatelli, Marco Petasecca, Michael L. F. Lerch, Sung Hyun Lee, Taku Inaniwa, Naruhiro Matsufuji, Marco Povoli, Angela Kok, Michael Jackson, Timothy Squire, Anatoly B. Rosenfeld, and Linh T. Tran (2021). *Radiation Shielding Evaluation of Spacecraft Walls Against Heavy Ions Using Microdosimetry*, IEEE Transactions on Nuclear Science, 68(5). DOI: 10.1109/TNS.2020.3032946

11. Vladimir A. Pan, Federico Pagani, Benjamin James, David Bolst, Stefania Peracchi, James Vohradsky, Alex Pogosso, Susanna Guatelli, Marco Petasecca, Michael L.F. Lerch, Dale A. Prokopovich, David Boardman, Vladimir L. Perevertaylo, Scott D. Chambers, Alastair G. Williams, Sylvester Werczynski, Taku Inaniwa, Naruhiro Matsufuji, Michael Jackson, Linh T. Tran, and Anatoly B. Rosenfeld (2021). *Characterization of a novel large area microdosimeter system for low dose rate radiation environments*, Nuclear Instruments and Methods in Physics Research Section A: Accelerators, Spectrometers, Detectors and Associated Equipment, 1002. DOI: 10.1016/j.nima.2021.165238

12. Stefania Peracchi, Benjamin James, Serena Psoroulas, Martin Grossmann, David Meer, David Bolst, Željko Pastuović, James Vohradsky, Susanna Guatelli, Dale A. Prokopovich, Marco Petasecca, Michael L. F. Lerch, Marco Povoli, Angela Kok, Michael Jackson, Anatoly B. Rosenfeld, and Linh T. Tran (2021). *Modelling of protons spectra encountered in space using medical accelerator and its microdosimetric characterization*, Advances in Space Research, 67(8). DOI: 10.1016/j.asr.2021.01.041

Conferences

1. James Vohradsky, Susanna Guatelli, Jeremy A. Davis, Linh T. Tran, and Anatoly B. Rosenfeld (2017). *Evaluation of silicon based microdosimetry for Boron Neutron Capture Therapy Quality Assurance*. Presented at the 2017 Geant4 User Workshop and Collaboration Meeting, 19th-22nd September 2017, Wollongong, Australia.
2. James Vohradsky, Susanna Guatelli, Jeremy A. Davis, Linh T. Tran, and Anatoly B. Rosenfeld (2017). *Evaluation of silicon and diamond based microdosimetry for boron neutron capture therapy quality assurance*. Presented at the International Conference on Monte Carlo Techniques for Medical Applications (MCMA2017), 15th-17th October 2017, Naples, Italy.
3. James Vohradsky, Susanna Guatelli, Jeremy A. Davis, Linh T. Tran, and Anatoly B. Rosenfeld (2017). *Design optimisation of Silicon Bridge Microdosimeter for use in Boron Neutron Capture Therapy*. Presented at the 9th Young Researchers BNCT Meeting (YBNCT9) Conference, 13th-15th November 2017, Kyoto, Japan.
4. James Vohradsky, Susanna Guatelli, Jeremy A. Davis, Linh T. Tran, and Anatoly B. Rosenfeld (2017). *Design optimisation of Silicon Bridge Microdosimeter for use in Boron Neutron Capture Therapy*. Presented at ACPSEM MedPhys17 Conference, 7th December 2017, Sydney, NSW, Australia.
5. James Vohradsky, (2018). *Design optimisation of Silicon and Diamond Based Microdosimeters for use in Boron Neutron Capture Therapy*. Presented at the Mini-Micro- Nano- Dosimetry, and Innovative Technologies in Radiation Oncology (MMND/ITRO 2018) Conference, 6th-11th February 2018, Mooloolaba, QLD,

Australia.

6. James Vohradsky, Susanna Guatelli, Linh T. Tran, Jeremy A. Davis, Charlot Vandevoorde, Evan Alexander de Kock, Jaime Nieto-Camero, Carina Hoglund, and Anatoly B. Rosenfeld (2018). *Evaluation of silicon based microdosimetry for Boron Neutron Capture Therapy Quality Assurance using fast neutron beams*. Presented at the 18th International Congress on Neutron Capture Therapy (ICNCT18), 28th October - 2nd November 2018, Taipei, Taiwan.
7. James Vohradsky, Susanna Guatelli, Linh T. Tran, Jeremy A. Davis, Charlot Vandevoorde, Evan Alexander de Kock, Jaime Nieto-Camero, Carina Hoglund, and Anatoly B. Rosenfeld (2018). *Evaluation of silicon based microdosimetry for Boron Neutron Capture Therapy Quality Assurance using fast neutron beams*. Presented at the 2018 IEEE Symposium on Nuclear Science (NSS/MIC) Conference, 10th-17th November 2018, Sydney, Australia.
8. James Vohradsky, Susanna Guatelli, Linh T. Tran, Jeremy A. Davis, Charlot Vandevoorde, Evan Alexander de Kock, Jaime Nieto-Camero, Carina Hoglund, and Anatoly B. Rosenfeld (2018). *Evaluation of silicon based microdosimetry for Boron Neutron Capture Therapy Quality Assurance using fast neutron beams*. Presented at the ACPSEM MedPhys18 Conference, 4th December 2018, Sydney, Australia.
9. James Vohradsky, Susanna Guatelli, Linh T. Tran, Jeremy A. Davis, Charlot Vandevoorde, Evan Alexander de Kock, Jaime Nieto-Camero, Carina Hoglund, and Anatoly B. Rosenfeld (2019). *Optimisation of physics options required to appropriately simulate BNCT microdosimetry using Geant4*. Presented at the 4th Geant4 School & Monte Carlo Workshop for Radiotherapy, Imaging and Radiation Protection, 2nd-8th December 2019, Wollongong, Australia.

10. James Vohradsky, Susanna Guatelli, Linh T. Tran, Jeremy A. Davis, Hiroaki Kumada, and Anatoly B. Rosenfeld (2019). *Geant4 simulations for microdosimetry in BNCT*. Presented at the 4th Geant4 School & Monte Carlo Workshop for Radiotherapy, Imaging and Radiation Protection, 2nd-8th December 2019, Wollongong, Australia.
11. James Vohradsky, Lachlan Chartier, Alex Pogossoff, Saree Alnaghy, Jason Paino, Stefania Peracchi, Vladimir Pan, Marco Povoli, Angela Kok, Linh T. Tran, and Anatoly B. Rosenfeld (2020). *Introduction and implementation of the CMRP radiodosimeter - a novel wireless microdosimetry system*. Presented at 2020 Mini- Micro- Nano- Dosimetry, and Innovative Technologies in Radiation Oncology (MMND/ITRO 2020) Conference, 10th-13th February 2020, Wollongong, Australia.
12. James Vohradsky, Linh T. Tran, Lachlan Chartier, Alex Pogossoff, and Anatoly B. Rosenfeld (2020). *Introduction and implementation of the CMRP radiodosimeter - a novel wireless microdosimetry system*. Presented at the 27th IEEE Symposium on Nuclear Science (NSS/MIC) Conference, 31st October - 7th November 2020, Boston, USA.
13. James Vohradsky, Lachlan Chartier, Linh T. Tran, Alex Pogossoff, and Anatoly B. Rosenfeld (2020). *Introduction and implementation of the CMRP radiodosimeter - a novel wireless microdosimetry system*. Presented at the ACPSEM MedPhys20 Conference, 15th December 2020, Sydney, Australia.

Awards

1. The ***Kent Riley Award*** for the ‘*best oral presentation of original scientific work*’ at the 9th Young Researchers BNCT Meeting (YBNCT9) Conference in Kyoto, Japan.
2. The ***Fairchild Award*** for ‘*excellent academic performance of all required duties, researches and enthusiastic devotion to BNCT*’ at the 18th International Congress on Neutron Capture Therapy (ICNCT18) in Taipei, Taiwan.
3. The ***IEEE Trainee Grant*** at the 2018 IEEE Symposium on Nuclear Science (NSS/MIC) Conference in Sydney, Australia.

Contents

Abstract	iv
Acknowledgments	v
Publications	vii
Conferences	x
Awards	xiii
List of Tables	xviii
List of Figures	xxi
1 Introduction	1
1.1 Thesis Outline	3
2 Literature Review	4
2.1 Microdosimetry	4
2.1.1 Microdosimetric Quantities	5
2.1.2 Microdosimetry Theory	14
2.1.3 Microdosimetric Methods	15
2.1.4 CMRP Experimental Microdosimetry Peripherals	31
2.2 Boron Neutron Capture Therapy (BNCT)	33
2.2.1 Physics of Neutron Interactions	33
2.2.2 How BNCT Works	44
2.2.3 Treatment Protocols and Techniques	45
2.2.4 Reactor-Based BNCT	47
2.2.5 Accelerator-Based BNCT	50
2.2.6 Open Issues with BNCT	57
2.2.7 Detectors used for BNCT	58

2.3	Hadrons in Charged Particle Therapy	65
2.4	Fast Neutron Therapy	71
2.5	Geant4 Simulation Toolkit	78
2.6	MCNP: Monte Carlo N-Particle Transport Code	83
3	The Geant4 and MCNP Simulation Applications	88
3.1	Overview of the Geant4 Simulations	89
3.1.1	Physics Options and Definitions	89
3.1.2	Simulation Flow	93
3.2	Overview of MCNP Simulations	95
3.2.1	Physics Options and Definitions	95
3.2.2	Advanced Particle Tracking in MCNP for microdosimetry	100
3.3	Computing Systems used	101
4	Optimisation of the SOI Bridge microdosimeter for BNCT QA	104
4.1	Method	105
4.2	Depth Dose Calculation in Water	108
4.3	Geometry optimisation of the SOI Bridge microdosimeter	109
4.4	Activation and Fragmentation in Experimental Setup	117
4.5	Discussion	121
5	Model of the South Africa iThemba Fast Neutron Beamline	123
5.1	Method	124
5.2	Neutrons generated in ^9Be target by physics options	128
5.3	Simulation to model the neutron gantry of the iThemba facility	130
5.3.1	Characterisation of Neutron Fluence in Gantry and Treatment Room	130
5.4	Comparison of the experimental and simulation microdosimetric response of the Bridge	135
5.5	Discussion	146
6	Model of the Tokai iBNCT Epithermal Neutron Beamline	152
6.1	Introduction	153
6.2	Method	154
6.2.1	Simulation to model the BSA of the iBNCT facility	154
6.2.2	Neutron Activation of Sample Materials	155
6.2.3	Neutron Activation of the Realistic Experimental Setup	157
6.2.4	Dose equivalent from the activated materials	161
6.3	Simulation to model the BSA of the iBNCT facility	164
6.3.1	Model of the Tokai facility from ^9Be target into treatment room	164

6.4	Neutron Activation of Sample Materials	166
6.5	Neutron Activation of the Realistic Experimental Setup	186
6.6	Dose equivalent from the activated materials	194
6.6.1	H*(10) at 1 m distance - μ^+ probe in water phantom	194
6.6.2	H*(10) at 0.4 m distance - μ^+ probe in water phantom	197
6.6.3	H*(10) at 0.4 m distance - μ^+ probe including sheath and shaper in free air	199
6.6.4	H*(10) at 0.4 m distance - μ^+ probe only in free air	200
6.7	Discussion	202
7	Development of a Wireless Microdosimetry System	206
7.1	Introduction	207
7.1.1	Description of the Radiodosimeter	207
7.1.2	Design of the Radiodosimeter GUI Software	211
7.1.3	Web interface for managing Wi-Fi settings	214
7.2	Materials and Methods	217
7.2.1	Benchmark calibration using radioactive sources	217
7.2.2	Hardware capability testing	218
7.2.3	Benchmark experiment with heavy ion therapy	219
7.3	Results	223
7.3.1	Calibration of the Radiodosimeter	223
7.3.2	Hardware capability testing	227
7.3.3	Comparison with conventional microdosimetric measurements at HIMAC	230
7.4	Discussion and Future Improvements	232
8	Validation of different physics models in Geant4 and MCNP6 for QA in FNT and BNCT	240
8.1	Method	241
8.2	Monoenergetic neutrons in water phantom	244
8.2.1	Comparison of BICHP with neutron thermal treatment on/off . . .	244
8.2.2	Comparison of different physics options in water phantom	252
8.2.3	Neutron fluence in water phantom - BICHP and MCNP	257
8.3	Monoenergetic neutrons in 50ppm B10 water phantom	261
8.3.1	Comparison of BICHP with thermal treatment on/off	262
8.3.2	Comparison of different physics options in 50ppm B10 water phantom	267
8.4	Discussion	272

<i>CONTENTS</i>	xvii
9 Conclusions and Future Work	274
Bibliography	279
A Statistics test data for different physics options	300
A.1 Comparison of different physics options in water phantom	301
A.2 Comparison of different physics options in 50ppm ^{10}B water phantom . .	302

List of Tables

2.1	Mean chord length for various convex shapes using the Cauchy formula.	6
2.2	Description of ray interaction definitions.	14
2.3	Examples of (n,x) neutron reactions.	40
2.4	Cross-sections of important isotopes relating to this work. Data sourced from ENDF/B-VII.1 [54].	41
2.5	Comparison between the reactor-based system (KUR-HWNIF) and the accelerator-based system (C-BENS) at KURNS [64].	53
2.6	Neutron Flux and Energies for iBNCT output [71].	56
2.7	Typical LET of low-LET radiation types in tissue [89].	66
2.8	Typical range and LET of high-LET radiation types in tissue [47].	69
2.9	Current fast neutron facilities worldwide. Number of patients treated was collected in 2013 [114].	73
2.10	Inter-comparison of biological effectiveness and key considerations for treatment optimisation in BNCT, FNT, and Carbon Ion Therapy.	77
2.11	ENDF/B-VII.1 $S(\alpha, \beta)$ scattering matrix datasets for neutron energies less than 4 eV available in Geant4 with the G4NDL4.5 data files. Data has been evaluated as a function of temperature [54].	82
2.12	ENDF/B-VII.1 $S(\alpha, \beta)$ scattering matrix datasets for neutron energies less than 4 eV available in MCNP 6.2 to be used with the MT card [144]. Data has been evaluated as a function of temperature [54].	86
3.1	Summary of the main differences in some hadronic physics lists in Geant4.	90
3.2	Details of the computing systems used for the simulations in this work.	102
4.1	Ratio of crosser or stopper by particle type for different detector designs and 3 μm thick B_4C film.	111
4.2	Ratio of crosser or stopper by particle type for different detector designs and 0.5 μm thick B_4C film.	112
4.3	Interactions within the SOI Bridge microdosimeter and detector probe materials (see Figure 4.2) resulting from neutron irradiation.	117
5.1	Various physics options used in Geant4 and MCNP simulation for the preliminary assessment, which is only considering the ^9Be target in vacuum world.	128

5.2	Experimental microdosimetric quantities derived from microdosimetric spectra at varying depths within the water phantom using the Bridge microdosimeter. The values have been scaled to be tissue equivalent. In the case of $^{10}\text{B}_4\text{C}$ converter, they are “apparent” mean average lineal energies.	136
5.3	Simulated microdosimetric quantities and count rate from reactions with proton products at 5 cm depth within the water phantom using the bare Bridge microdosimeter. \overline{y}_F and \overline{y}_D values have been scaled to be tissue equivalent.	144
5.4	Simulated microdosimetric quantities and count rate from reactions with deuteron products at 5 cm depth within the water phantom using the bare Bridge microdosimeter. \overline{y}_F and \overline{y}_D values have been scaled to be tissue equivalent.	144
5.5	Simulated microdosimetric quantities and count rate from reactions with alpha products at 5 cm depth within the water phantom using the bare Bridge microdosimeter. \overline{y}_F and \overline{y}_D values have been scaled to be tissue equivalent.	145
5.6	Simulated microdosimetric quantities and count rate from reactions with heavy ion products at 5 cm depth within the water phantom using the bare Bridge microdosimeter. \overline{y}_F and \overline{y}_D values have been scaled to be tissue equivalent.	146
6.1	Components of the motion and MicroPlus probe microdosimetry systems and their material compositions, which has been labelled in figures 6.5 and 6.6.	157
6.2	Components of the NEMA17 stepper motor and its material compositions, which has been labelled in figure 6.7.	159
6.3	Integral neutron flux ($\text{n}/\text{cm}^2/\text{s}$) values for different energy ranges, calculated using PHITS [164] and Geant4 (this work). Calculated based on the data also presented in figure 6.15. .	165
6.4	Interactions within Aluminium target resulting from neutron irradiation. Decay energy and short-lived half-life referenced from [72].	167
6.5	Interactions within Silicon target resulting from neutron irradiation. Decay energy and short-lived half-life referenced from [72].	168
6.6	Interactions within Diamond target resulting from neutron irradiation. Decay energy and short-lived half-life referenced from [72].	170
6.7	Interactions within SiO_2 target resulting from neutron irradiation. Decay energy and short-lived half-life referenced from [72].	171
6.8	Interactions within PMMA target resulting from neutron irradiation. Decay energy and short-lived half-life referenced from [72].	173
6.9	Interactions within Water target resulting from neutron irradiation. Decay energy and short-lived half-life referenced from [72].	175
6.10	Interactions within AlO target resulting from neutron irradiation. Decay energy and short-lived half-life referenced from [72].	177
6.11	Interactions within Gold target resulting from neutron irradiation. Decay energy and short-lived half-life referenced from [72].	179
6.12	Interactions within Copper target resulting from neutron irradiation. Decay energy and short-lived half-life referenced from [72].	180
6.13	Interactions within Borosilicate Glass target resulting from neutron irradiation. Decay energy and short-lived half-life referenced from [72].	183
6.14	Interactions within $^{10}\text{B}_4\text{C}$ target resulting from neutron irradiation. Decay energy and short-lived half-life referenced from [72].	185

6.15	Radioactivations within the experiment materials resulting after 30 minutes of neutron irradiation. Half-life values and effective decay emission energies (E_γ and E_β) referenced from [72]. Abbreviations used in this table: ‘Tank’ (PMMA Tank), ‘XMot.’ (X-axis NEMA17 stepper motor), and ‘YMot.’ (Y-axis NEMA17 stepper motor).	187
7.1	Expected quality for different wireless RSSI values.	219
7.2	Specifics of the Radiodosimeter battery usage.	227
7.3	Received signal strength by client computer for personal/ad hoc methods at HIMAC at different positions.	229
7.4	$\overline{y_D}$ percentage difference of standard and wireless measurements compared to Geant4 as a function of depth in the water phantom.	232
8.1	Fourteen selected physics options for the Geant4 and MCNP6 simulations performed in this chapter. Seven different hadronic physics lists for Geant4, with thermal neutron treatment disabled (no /T labelled) and enabled (labelled with /T). MCNP uses the Bertini INC hadronic physics model with with thermal neutron treatment disabled (no /T labelled) and enabled (labelled with /T).	241
8.2	Eighteen different neutron monoenergies simulated in this chapter.	243
8.3	Statistics tests for depth dose distribution of monoenergetic neutrons in water phantom, comparing BICHP against BICHP/T.	244
8.4	Statistics tests for depth dose distribution of monoenergetic neutrons in 50ppm ^{10}B water phantom, comparing BICHP against BICHP/T.	262
A.1	Statistics tests for depth dose distribution of monoenergetic neutrons in water phantom for the different physics lists compared against BICHP. All physics with thermal on (T) are compared against BICHP/T, and physics with thermal off (no T) are compared against BICHP.301	
A.2	Statistics tests for depth dose distribution of monoenergetic neutrons in 50ppm ^{10}B water phantom for the different physics lists compared against BICHP. All physics with thermal on (T) are compared against BICHP/T, and physics with thermal off (no T) are compared against BICHP.	302

List of Figures

2.1	Quality factor Q defined as a function of LET (ICRP 60) and lineal energy (ICRU40) [7]. .	8
2.2	The quality relation between lineal energy and LET. Dashed line shows 1:1 relation. [7]. .	8
2.3	Definition of rays interacting with a sensitive volume, adapted from [4].	14
2.4	Rossi Tissue Equivalent Proportional Counter [18].	16
2.5	First generation silicon microdosimeter: a) Basic SOI diode array schematic b) IBICC median energy map of the diode array in response to 2 MeV He^{2+} [23].	18
2.6	Second generation silicon microdosimeter: a) Schematic of a single SV region with guard ring, top down (i) and cross-section (ii) [27]. b) Scanning electron microscope (SEM) image zoomed on an SOI diode array section, c) IBICC median energy map of the diode array in response to 3 MeV He^{2+} [23].	19
2.7	Third generation n-SOI microdosimeter: a) Cross-section schematic of a single cell, b) Top-down schematic of a single SV, c) IBICC median energy map of n-SOI array in response to 2 MeV H ions (zoomed out), d) IBICC median energy map of n-SOI array in response to 5.5 MeV He^{2+} ions (zoomed in) [23] [28].	20
2.8	Schematic diagram of Bridge microdosimeter V1 (left) and V2 (right). (a) Section of six cells with adjoining silicon bridge regions [29], (b) cross-section view [29], (c) V2 device with n^+ stop layer surrounding top edges and sides of the SV [21].	21
2.9	SEM Images of Bridge SV arrays. (a) Bridge V1 (partially etched), (b) Bridge V2 (fully etched) [21].	22
2.10	Images of the 2- μm -thick Mushroom microdosimeter. a) Surface SEM image showing a number of SVs, b) zoomed-in SEM image of a single SV, c) cross-sectional SEM image of a single SV, d) cross-sectional and top-view schematic of the planar structure [32].	23
2.11	a) Schematic of a single SV in the trench 3D Mushroom microdosimeter with planar n^+ core and p^+ doped trench filled with polysilicon [33], b) SEM image of a trench 3D Mushroom with planar core SV array [32].	24
2.12	a) Schematic of trench 3D Mushroom microdosimeter with voided p^+ trench and voided n^+ trench [32], b) SEM image of a single SV of the trench 3D Mushroom microdosimeter [33], c) SEM image of an array of SVs in the trench 3D Mushroom microdosimeter with odd and even aluminium tracks highlighted [34]	25
2.13	a) Schematic of the free-standing 3D SV embedded in tissue-equivalent material [33], b) SEM image of the 3D Mushroom microdosimeter with free-standing SV and surrounding silicon removed by etching [32].	26
2.14	(Left) Top view of 3d-LES before wire bonding showing A, B electrodes, T isolation trench, D contact separation distance. (Right) Cross section of simulated electric field due to 20V potential between contact electrodes [36].	27

2.15	Cross-section of the U3DTHIN detector (not to scale) [39].	28
2.16	Cross-section of the thin silicon device by Guardiola et. al. [42].	29
2.17	Side-Brazed Dual In-Line Ceramic Package - 20 pin, used for SOI microdosimeter mounting [48].	31
2.18	The μ^+ probe connected to the microdosimeter chip [49]. Zoomed lens shows the array of the SOI Mushroom mounted on the DIL package.	32
2.19	a) Initial motion stage design [51], b) rendering of the rebuild version.	33
2.20	Basic process of neutron elastic scattering interactions.	34
2.21	Basic process of neutron inelastic scattering interactions.	35
2.22	Basic process of neutron capture interactions, two paths are presented, whether the isotope is stable (path 1) or activated (radioactive) (path 2).	36
2.23	ENDF/B-VII.1 cross-sections for ^{10}B , adapted from [54].	37
2.24	ENDF/B-VII.1 cross-sections for ^1H , adapted from [54].	38
2.25	ENDF/B-VII.1 cross-sections for ^{14}N , adapted from [54].	39
2.26	Basic process of nuclear fission interactions.	40
2.27	ENDF/B-VII.1 cross-sections for ^{12}C , adapted from [54].	42
2.28	ENDF/B-VII.1 cross-sections for ^{16}O , adapted from [54].	42
2.29	ENDF/B-VII.1 cross-sections for ^{27}Al , adapted from [54].	43
2.30	ENDF/B-VII.1 cross-sections for ^{197}Au , adapted from [54].	43
2.31	Nuclear reaction occurring in BNCT [55].	44
2.32	Top-down view of the Kyoto University Research Reactor, with main KUR-HWNIF system and other various beam ports shown [65].	48
2.33	Outline of the KUR-HWNIF system installed in KUR for BNCT [64].	49
2.34	Finnish BNCT Fir 1, BNCT facility treatment setup [59].	49
2.35	BNCT at INFN, Italy utilising thermal neutrons for shallow tumours [56].	51
2.36	Beam shaping assembly and treatment room of C-BENS [69].	52
2.37	Neutron flux comparison between KUR-HWNIF and C-BENS at KURNS [70].	53
2.38	Schematic of Tokai LINAC-based BNCT Device [61].	54
2.39	Layout of facility: accelerator room and irradiation room [61].	54
2.40	Basic Configuration of Tokai iBNCT proton LINAC [71].	54
2.41	Three layer neutron generator target at Tokai iBNCT [71].	55
2.42	Neutron Generator at iBNCT, showing moderator components for neutron energy selection [68].	55
2.43	Simulated depth-dose curve; iBNCT (accelerator) and JRR-4 (reactor) [73].	56
2.44	Neutron flux ($\text{n/cm}^2/\text{s}/\text{lethargy}$) as a function of energy (MeV) comparing JRR-4 to iBNCT [68].	57
2.45	Microdosimetric spectra comparing boron coated devices irradiated by BMRR epithermal source [2].	62
2.46	Diagram illustrating the process of neutron capture by a target nucleus followed by the emission of gamma rays [88].	64
2.47	Simplified biological differences between photons, protons, and carbon ions. Photons have mostly single strand DNA breaks by indirect damage, where protons and carbon ions have direct damage to DNA by DSB. [90]	66
2.48	Dose dose distributions for various therapy beams. Protons and carbon ions exhibit the Bragg peak at the end of their range, compared with the almost exponential dose distribution of X-rays and fast neutrons. Adapted from [91].	67

2.49	Depth dose plots of pristine proton Bragg peaks (red) and their summation to form the SOBP (blue). Photons (green) are shown for comparison [92].	68
2.50	Comparison of 2 Gy dose contour maps from one port irradiation by low-LET photons versus high-LET carbon ions [93].	68
2.51	Model of the HIMAC facility (left) adapted from [100]. View of the biological experimental irradiation room (right) adapted from [51].	70
2.52	Diagram of the Separated-Sector Cyclotron Facility, with beam line leading into the isocentric neutron therapy room, adapted from: [113].	74
2.53	Scale diagram of the p(66) + Be isocentric neutron therapy gantry, from accelerated protons to treatment room [115].	74
2.54	a) Isocentric neutron gantry with patient on bed [113], b) Multi-blade trimmer variable collimator [113].	75
2.55	Neutron fluence (relative) at iThemba for p(66)+Be. Measured using NE-213 liquid scintillator [116], MCNP4 + LAHET [119] and MCNP4 only [122]. Figure adapted from: [122].	76
2.56	Partial inventory of Geant4 hadronic physics models for version 10 [132].	79
3.1	Steps required in Geant4 to enable the thermal neutron treatment, which describes the new elastic scatter process for neutrons below 4 eV, based on the G4NeutronHPThermalScattering model.	92
3.2	Geant4 output confirming thermal neutron treatment is enabled (after following the steps outlined in figure 3.1).	93
3.3	The Geant4 application developed for this work - simplified flow chart.	94
3.4	Example of defining ‘water’ in MCNP, based on isotopic mass fraction. Thermal neutron treatment is included by definition of the ‘MT’ card.	96
3.5	Options to use Bertini INC Model.	96
3.6	Neutron specific physics options selected for the MCNP simulations.	97
3.7	Proton specific physics options selected for the MCNP simulations.	98
3.8	Photon specific physics options selected for the MCNP simulations.	99
3.9	Other particle specific physics options selected for the MCNP simulations.	99
3.10	Configuration required to use PTRAC in MCNP with full-analog neutron simulation. Example shown is for scoring energy deposition in ‘cell 1’ relating to interactions by various particle types.	100
3.11	Images of the Fenrisúlfr Computational Node. a) Original mounting in modified side table ‘rack’, b) Current mounting in more appropriate server rack - lid has been opened to show interior components.	103
4.1	KUR epithermal neutron energy spectrum used as the primary source in all simulations [153], courtesy of Baba et al.	105
4.2	Detail of the geometry of the detector and its packaging, in the direction of incidence of the neutron beam (incident from left). The neutron beam has a diameter exceeding the lateral sizes of the microdosimeter device. The microdosimeter is set at 2.7 cm depth in the water phantom.	106
4.3	Bridge SOI Microdosimeter. The SVs shown in green have dimensions of $30 \times 30 \mu\text{m}^2$ with $10 \mu\text{m}$ thickness along the direction of incidence of the neutron beam.	107

4.4	Depth dose curve in the water phantom, with 25ppm ^{10}B uniformly distributed in water. The total energy deposition is depicted in black. The contribution deriving from each secondary particle under investigation is indicated as well, together with the process originating the secondary particle (see the legend).	109
4.5	Microdosimetric spectra of $30\times30\times10\text{ }\mu\text{m}^3$ SOI Bridge SVs with $3\text{ }\mu\text{m}$ thick $^{10}\text{B}_4\text{C}$ film (mostly stoppers).	110
4.6	Microdosimetric spectra of $30\times30\times2\text{ }\mu\text{m}^3$ SOI Bridge SVs with $3\text{ }\mu\text{m}$ thick $^{10}\text{B}_4\text{C}$ film (increased crossers).	110
4.7	Microdosimetric spectra of $30\times30\times1\text{ }\mu\text{m}^3$ SOI Bridge SVs with $3\text{ }\mu\text{m}$ thick $^{10}\text{B}_4\text{C}$ film (mostly crossers).	110
4.8	Relative ratio of alpha particle crossers and total number of alpha particle crossers and stoppers in the microdosimeter SVs obtained using the $3\text{ }\mu\text{m}$ B_4C thick film (blue) and $0.5\text{ }\mu\text{m}$ B_4C thick film (green). The ratio of crossers/total in the bare detector is obtained using only the boron doped p^+ region implanted in the SVs is depicted in red.	112
4.9	Microdosimetric spectra of $30\times30\times2\text{ }\mu\text{m}^3$ SOI Bridge SVs with $0.5\text{ }\mu\text{m}$ thick $^{10}\text{B}_4\text{C}$ conversion film.	113
4.10	Microdosimetric spectra of $10\times10\times2\text{ }\mu\text{m}^3$ SOI Bridge SVs with $0.5\text{ }\mu\text{m}$ $^{10}\text{B}_4\text{C}$ conversion film.	113
4.11	Microdosimetric spectra of bare $30\times30\times10\text{ }\mu\text{m}^3$ SOI Bridge SVs - alpha particles and ^7Li nuclei originating only from p^+ region (mostly stoppers).	115
4.12	Microdosimetric spectra of bare $30\times30\times2\text{ }\mu\text{m}^3$ SOI Bridge SVs - alpha particles and ^7Li nuclei originating only from p^+ region (increased crossers).	115
4.13	Microdosimetric spectra of bare $30\times30\times1\text{ }\mu\text{m}^3$ SOI Bridge SVs - alpha particles and ^7Li nuclei originating only from p^+ region (mostly crossers).	115
4.14	Secondary radiation field produced by the KUR epithermal neutron field in the materials of the SOI microdosimeter device.	118
4.15	Activity of radioisotopes produced within the materials of the SOI Bridge detector device for 30 minute irradiation period with cool-down.	118
4.16	Gamma ray spectrum produced in SOI detector probe materials by the KUR epithermal neutron source.	120
5.1	Basic details of the treatment head and variable collimator of the neutron gantry, cut through the centre. This figure was obtained from the visualisation output of the MCNP simulation developed, based on the CAD model provided by iThemba LABS.	125
5.2	Detail of the geometry of the detector and its packaging, in the direction of incidence of the neutron beam (incident from left). The width of the neutron beam exceeds the lateral sizes of the microdosimeter device. The microdosimeter is set at 5 cm depth in the water phantom.	126
5.3	Details of the MicroPlus probe inserted in the PMMA sheath positioned in the water tank at 5 cm depth.	127
5.4	Bridge SOI Microdosimeter. The device consists of an array of 4248 SVs, representing cells. The SVs shown in green have dimensions of $30\times30\text{ }\mu\text{m}^2$ with $10\text{ }\mu\text{m}$ thickness along the direction of incidence of the neutron beam. The mean chord length of an SV in the array is $12\text{ }\mu\text{m}$.	127
5.5	Bridge SOI Microdosimeter mounted in DIL package on the MicroPlus Probe (adapted from [21] and [33]). The probe has been removed from the PMMA sheath (see figure 5.3).	127

5.6	Initial neutron energy spectra produced from the $^9\text{Be}(p,n)$ reaction for various Geant4 and MCNP6 physics models. a) Geant4 physics options also including MCNP6 Bertini (+TENDL), b) MCNP6 non-TENDL physics options also including Geant4 QGSP_BIC_AllHP and MCNP6 Bertini (+TENDL), c) MCNP +TENDL physics options also including Geant4 QGSP_BIC_AllHP.	129
5.7	Radial neutron fluence maps calculated using Geant4 (a) and MCNP (b) within the neutron gantry and treatment room. Percentage difference map (c) between the distributions of Geant4 (negative) and MCNP (positive).	131
5.8	Relative neutron energy fluence calculated at 150 cm from the ^9Be target in the treatment room air. Previous publications using measured [116] (black) and MCNP4 [122] (blue) data. This work; calculated using Geant4 (blue) and MCNP6.2 (red).	132
5.9	Relative neutron energy fluence calculated at 150 cm from the ^9Be target in the treatment room air for additional physics models of Geant4. Data for Geant4 (BIC_All_HP) and MCNP6.2 (BERT INC (+TENDL)) are also shown in figure 5.8. Previous publications using measured [116] (black).	133
5.10	Neutron fluence plane profile map taken on the incident surface of the water phantom located at $z=150$ cm using a) Geant4, and b) MCNP.	134
5.11	Line profiles of neutron fluence taken on the incident surface of the water phantom located at $z=150$ cm, sampled across X-axis at $y=0$ from figures 5.10a and 5.10b.	134
5.12	Neutron fluence as a function of depth in the water phantom calculated using Geant4 and MCNP. The energies are separated by fast (>10 keV), epithermal (<10 keV) and thermal (<0.5 eV).	135
5.13	Absorbed dose per monitor unit measured using the Bridge microdosimeter for experimental and simulation methods. Comparing bare (solid lines) and $^{10}\text{B}_4\text{C}$ converter (dotted lines) sources.	137
5.14	Dose equivalent derived from measurements with the Bridge microdosimeter for experimental and simulation methods in lateral field measurements from the central axis taken at 5 cm depth in the water phantom. Field size is 10×10 cm ² . Comparing bare (solid lines) and Boron Carbide converter (dotted lines) sources.	138
5.15	Microdosimetric spectra measured experimentally at 5 cm depth. Bare (red), Al film (green), $^{10}\text{B}_4\text{C}$ converter (black), subtracted (blue).	139
5.16	Microdosimetric spectra for Bridge with $^{10}\text{B}_4\text{C}$ converter calculated using MCNP at 5 cm depth with secondary components contributing to the total dose shown.	140
5.17	Microdosimetric spectra for Bridge with $^{10}\text{B}_4\text{C}$ converter calculated using Geant4 at 5 cm depth with secondary components contributing to the total dose shown.	140
5.18	Microdosimetric spectra for bare Bridge calculated using MCNP at 5 cm depth with secondary components contributing to the total dose shown.	142
5.19	Microdosimetric spectra for bare Bridge calculated using Geant4 at 5 cm depth with secondary components contributing to the total dose shown.	142
6.1	Model of the Tokai BSA implemented in the Geant4 simulation, production of neutrons from the proton + ^9Be reaction.	155
6.2	Strawman diagram of the Tokai BSA (courtesy of iBNCT [164]).	155

6.3	Simulation geometry setup to study the activation of unit samples, shown from bird's-eye view (a) and side view (b). The target (red cube) is located at the centre of an air world volume (blue frame). The Tokai neutron source originates at one side of the air world and irradiates the face of the target volume.	156
6.4	Experiment setup of motion stage system featuring water phantom with MicroPlus on couch. Shaper is inserted on top with grey output cable.	157
6.5	Bird's-eye view of the motion stage system (figure 6.4) modelled in the Geant4 simulation. Zoomed-in section (right) of the lower end of the MicroPlus probe, shown with DIL package containing SOI microdosimeter (blue) inserted.	158
6.6	Top-down view of the motion stage system (figure 6.4) modelled in the Geant4 simulation. The direction of neutrons from the BSA nozzle is indicated (i.e. this side faces the BSA). .	158
6.7	The NEMA17 stepper motor (figures 6.5 and 6.6 labelled 'A') modelled in the Geant4 simulation; a) Normal view, b) face on view, c) face on view with exterior casing removed to show internal components.	159
6.8	Simulation geometry used for irradiation of the realistic experiment setup. The motion stage is placed as close as possible to the beam nozzle, with microdosimeter aligned at the beam central axis. Note that the phase space recorded previously at the beam nozzle is used (blue dashed line), the BSA is only shown here for reference of relative positions. Also note that the behaviour of neutrons in this figure (straight line trajectory) was been simplified and is not realistic.	160
6.9	ICRU sphere showing the geometry used for $H^*(10)/\phi$ simulations (not to scale). The trajectory of the particles form a uniform fluence on sphere cross section with largest diameter.	161
6.10	Configuration 1 - spherical scoring shell (purple) with 1 metre radius encapsulating all of the equipment. Particles are scored when they cross the surface of the shell.	161
6.11	Configuration 2; spherical scoring shell with 0.4 metre radius encapsulating all of the equipment.	163
6.12	Configuration 3; spherical scoring shell with 0.4 metre radius encapsulating MicroPlus probe (including sheath and shaper) in free air.	163
6.13	Configuration 4; spherical scoring shell with 0.4 metre radius encapsulating only MicroPlus probe in free air.	163
6.14	Neutron fluence map per incident proton, describing the distribution throughout the BSA and treatment room. Black wireframe of the BSA has been overlaid. The treatment room is from $z > 0$ cm.	164
6.15	Neutron flux recorded at the beam exit nozzle, normalised to the number of primary protons generated per second corresponding to 2mA current. PHITS simulation was performed by iBNCT, reported in [164].	165
6.16	Activity of radioisotopes produced within 1 cm ³ sample of Aluminium target material. Simulated for 30 min irradiation period with following cool-down.	168
6.17	Activity of radioisotopes produced within 1 cm ³ sample of Silicon target material. Simulated for 30 min irradiation period with following cool-down.	169
6.18	Activity of radioisotopes produced within 1 cm ³ sample of Diamond target material. Simulated for 30 min irradiation period with following cool-down.	170
6.19	Activity of radioisotopes produced within 1 cm ³ sample of SiO ₂ target material. Simulated for 30 min irradiation period with following cool-down.	171
6.20	Activity of radioisotopes produced within 1 cm ³ sample of PMMA target material. Simulated for 30 min irradiation period with following cool-down.	174

6.21	Activity of radioisotopes produced within 1 cm ³ sample of Water target material. Simulated for 30 min irradiation period with following cool-down.	176
6.22	Activity of radioisotopes produced within 1 cm ³ sample of AlO target material. Simulated for 30 min irradiation period with following cool-down.	178
6.23	ENDF/B-VII.1 neutron cross-section for the ¹⁹⁷ Au neutron interactions observed in the Geant4 simulation [54].	179
6.24	Activity of radioisotopes produced within 1 cm ³ sample of Gold target material. Simulated for 30 min irradiation period with following cool-down.	180
6.25	Activity of radioisotopes produced within 1 cm ³ sample of Copper target material. Simulated for 30 min irradiation period with following cool-down.	181
6.26	Activity of radioisotopes produced within 1 cm ³ sample of Borosilicate Glass target material. Simulated for 30 min irradiation period with following cool-down.	182
6.27	The decay scheme of ¹² B. This is a simple decay, which most of the time goes to the ground state of ¹² C.	184
6.28	Activity of radioisotopes produced within 1 cm ³ sample of ¹⁰ B ₄ C target material. Simulated for 30 min irradiation period with following cool-down.	186
6.29	Microdosimetric spectra of the SOI Bridge during a 30 minute irradiation, with ¹⁰ B ₄ C Film covering the DIL package. Zoomed in y-axis range shown in b).	190
6.30	Microdosimetric spectra of the SOI Bridge during a 30 minute irradiation, with no film covering the DIL package (bare). Zoomed in y-axis range shown in b).	191
6.31	Dose equivalent H*(10) at 100 cm distance from the centre of the motion stage system, facing the side of the water tank that was irradiated by neutrons (0 deg).	194
6.32	Gamma ray spectra from the activated radioisotopes decay, recorded at 0 degrees azimuthal angle position, 1 m distance from the Experimental System. Gamma ray spectra for time after beam off: a) 0 minutes (initial), b) 1 minute, and c) 30 minutes.	196
6.33	Dose equivalent H*(10) at 0.4 m distance from the centre of the motion stage system, facing the side of the water tank that was irradiated by neutrons (0 deg).	197
6.34	Isodose equivalent H*(10) at 0.4 m distance for all azimuthal angles around the system following beam off. Radial axis (mSv/hr) is in log scale.	198
6.35	Dose equivalent H*(10) at 0.4 m distance from the MicroPlus probe including sheath and shaper in free air, facing the side that was previously irradiated by neutrons.	199
6.36	Dose equivalent H*(10) at 0.4 m distance from the MicroPlus probe only, facing the side that was previously irradiated by neutrons.	200
7.1	Front view of the Radiodosimeter inside its housing box	208
7.2	Back view of the Radiodosimeter inside its housing box	209
7.3	Interior of the Radiodosimeter. All components except the MCA are mounted on the main PCB board.	210
7.4	Representation of MicroPlus probe (with SOI microdosimeter on DIL package plugged in) inserted into the Radiodosimeter via DB9 connector.	210
7.5	Main screen of the Radiodosimeter software suite application.	212
7.6	Dialog that pops-up when the new measurement button is pressed.	213
7.7	Radiodosimeter software during a calibration showing the output pulses.	214
7.8	Web page interface for the RPi network management.	215
7.9	List of available networks on the web interface. The icons next to the network name indicates the signal strength and security type.	215

7.10	Example of the new network form, adding a WPA2 Enterprise security type (such as eduroam).	216
7.11	Wireless setup for radioactive source measurements using the Radiodosimeter.	217
7.12	a) Standard experiment setup with wires, b) Wireless experiment setup (note: Radiodosimeter is mounted in a different 3D printed enclosure), c) Standard experiment setup shown from top-down view, d) motorised door at biological beam line at HIMAC, where cable is normally drawn through the doorway (open).	220
7.13	Communication methods with the treatment room with door closed: a) standard method with cables (not wireless), b) connected to personal Wi-Fi router inside treatment room, c) connected to enterprise Wi-Fi network inside treatment room, d) direct connection to Radiodosimeter's ad hoc Wi-Fi network inside treatment room.	221
7.14	Three locations at HIMAC that the Wi-Fi signal strength was tested for personal and ad hoc methods with motorised door open or closed.	222
7.15	Calibrated MCA spectrum acquired with standard setup using Si PIN diode and spectrum of ^{241}Am alpha source.	223
7.16	Un-calibrated MCA spectra for the six discrete pulse energies (labelled 1-6) and ^{241}Am alpha source, acquired with Radiodosimeter using Si PIN diode.	224
7.17	Calibrated MCA spectrum acquired with Radiodosimeter using Si PIN diode and spectrum of ^{241}Am alpha source.	225
7.18	Calibrated MCA spectrum acquired with Radiodosimeter using SOI Mushroom microdosimeter and ^{241}Am alpha source.	226
7.19	Voltage monitoring of the Radiodosimeter batteries in different scenarios for an infinite acquisition.	227
7.20	Received Wi-Fi signal strength from the Radiodosimeter operating in ad hoc mode to client computer in free air.	228
7.21	Microdosimetric spectra measured at different depths in water with SOI Mushroom microdosimeter on ^{28}Si ion 230 MeV/u beam with standard method and Radiodosimeter.	230
7.22	Dose-mean lineal energy ($\overline{y_D}$) as a function of depth in water for Mushroom and ^{28}Si 230 MeV/u. Secondary y-axis represents relative dose to Bragg peak for the PTW IC.	231
7.23	Traditional Wi-Fi Network Architecture. The single access point (router) has finite range. Radiodosimeters which travel too far away result in disconnection.	235
7.24	Decentralised Wi-Fi Mesh Network Architecture. The single access point (router) has finite range. Radiodosimeters within range connect to the access point by default. Radiodosimeters out of range are permitted to connect to the closest neighbouring Radiodosimeter, extending the network mesh.	235
7.25	OLED display for Raspberry Pi Zero [180].	236
7.26	e-Ink display [181].	236
7.27	Summary of wireless data transmission modes [182]. RFID, BLE, 802.11 (Wi-Fi), 2G/3G/4G/5G (mobile phone networks) and LPWAN.	238
7.28	LoRa node module for Raspberry Pi Zero [185]. Note the module is as small as the RPi so its presence is negligible.	238
7.29	Cisco LoRa gateway host module [186]. This is a high end model used for industrial purposes.	238
7.30	Simple LoRa network diagram showing the data transfer between nodes (Radiodosimeters) and gateways (LoRa host modules to receive and send data between the Radiodosimeter and management server). Adapted from [187].	239

8.1	Geometry visualisation of the segmented water phantom inside the air world used in Geant4 from bird's-eye view. The water phantom has been segmented in z axis by 0.5 cm increments (shown with red lines in the phantom).	242
8.2	Absorbed dose per incident neutron as a function of depth in water phantom for monoenergetic neutrons using BICHP with thermal treatment on (a) and off (b).	244
8.3	Absorbed dose per incident neutron as a function of depth in water phantom for monoenergetic neutrons using BICHP with thermal treatment on (a) and off (b). Same as Figure 8.2 but zoomed in to show lower energies.	245
8.4	Absorbed dose per incident neutron as a function of depth in water phantom represented in terms of individual components calculated using BICHP and MCNP with T and noT; 0.0253 eV, 0.1 eV and 1 eV neutrons.	246
8.5	Absorbed dose per incident neutron as a function of depth in water phantom represented in terms of individual components calculated using BICHP and MCNP with T and noT; 10 eV, 100 eV and 1 keV neutrons.	247
8.6	Absorbed dose per incident neutron as a function of depth in water phantom represented in terms of individual components calculated using BICHP and MCNP with T and noT; 10 keV and 100 keV. With only T; 1 MeV neutrons.	248
8.7	Absorbed dose per incident neutron as a function of depth in water phantom represented in terms of individual components calculated using BICHP and MCNP with only T; 2 MeV, 5 MeV and 10 MeV neutrons.	249
8.8	Absorbed dose per incident neutron as a function of depth in water phantom represented in terms of individual components calculated using BICHP and MCNP with only T; 20 MeV, 30 MeV and 40 MeV neutrons.	250
8.9	Absorbed dose per incident neutron as a function of depth in water phantom represented in terms of individual components calculated using BICHP and MCNP with only T; 50 MeV, 60 MeV and 70 MeV neutrons.	251
8.10	Absorbed dose per incident neutron as a function of depth in water phantom; 0.0253 eV to 100 keV.	253
8.11	Absorbed dose per incident neutron as a function of depth in water phantom; 1 MeV to 30 MeV.	254
8.12	Absorbed dose per incident neutron as a function of depth in water phantom; 40 MeV to 70 MeV.	255
8.13	Statistics tests for depth dose distribution of monoenergetic neutrons in water phantom for the different physics lists compared against BICHP. All physics with thermal on (T) are compared against BICHP/T. Data shown in table A.1 of Appendix A.1.	256
8.14	Statistics tests for depth dose distribution of monoenergetic neutrons in water phantom for the different physics lists compared against BICHP. All physics with thermal off (noT) are compared against BICHP. Data shown in table A.1 of Appendix A.1.	256
8.15	Neutron fluence per incident neutron as a function of depth in water phantom represented in terms of neutron energy: total, epithermal and thermal, calculated using BICHP and MCNP with T and noT; 0.0253 eV to 0.1 eV.	257
8.16	Neutron fluence per incident neutron as a function of depth in water phantom represented in terms of neutron energy: total, epithermal and thermal, calculated using BICHP and MCNP with T and noT; 10 eV to 100 keV.	258

8.17	Neutron fluence per incident neutron as a function of depth in water phantom represented in terms of neutron energy: total, epithermal and thermal, calculated using BICHP and MCNP with T and noT; 1 MeV to 20 MeV.	259
8.18	Neutron fluence per incident neutron as a function of depth in water phantom represented in terms of neutron energy: total, epithermal and thermal, calculated using BICHP and MCNP with T and noT; 30 MeV to 70 MeV.	260
8.19	Absorbed dose per incident neutron as a function of depth in 50ppm ^{10}B water phantom for monoenergetic neutrons using BICHP with thermal treatment on (a) and off (b).	262
8.20	Absorbed dose per incident neutron as a function of depth in 50ppm ^{10}B water phantom for monoenergetic neutrons using BICHP with thermal treatment on (a) and off (b). Same as Figure 8.19 but zoomed in to show lower energies.	263
8.21	Absorbed dose per incident neutron as a function of depth in 50ppm ^{10}B water phantom represented in terms of individual components calculated using BICHP and MCNP with T and noT; 0.0253 eV and 0.1 eV.	264
8.22	Absorbed dose per incident neutron as a function of depth in 50ppm ^{10}B water phantom represented in terms of individual components calculated using BICHP and MCNP with T and noT; 1 eV, 1 keV and 1 MeV.	265
8.23	Absorbed dose per incident neutron as a function of depth in 50ppm ^{10}B water phantom represented in terms of individual components calculated using BICHP and MCNP with T and noT; 10 MeV, 20 MeV and 50 MeV.	266
8.24	Absorbed dose per incident neutron as a function of depth in 50ppm ^{10}B water phantom; 0.0253 eV to 100 keV.	268
8.25	Absorbed dose per incident neutron as a function of depth in 50ppm ^{10}B water phantom; 1 MeV to 70 MeV.	269
8.26	Statistics tests for depth dose distribution of monoenergetic neutrons in 50ppm ^{10}B water phantom for the different physics lists compared against BICHP. All physics with thermal on (T) are compared against BICHP/T. Data shown in table A.2 of Appendix A.2.	271
8.27	Statistics tests for depth dose distribution of monoenergetic neutrons in 50ppm ^{10}B water phantom for the different physics lists compared against BICHP. All physics with thermal off (noT) are compared against BICHP. Data shown in table A.2 of Appendix A.2.	271

Chapter 1

Introduction

Microdosimetry is a useful method to evaluate the relative biological effectiveness (RBE) as well as dose equivalent of any mixed radiation field without prior knowledge of type of charged particles and their spectra. Some practical applications of microdosimetry include; therapeutic beam Quality Assurance (QA) in hadron therapy facilities, real-time radiation protection assessment for nuclear accidents and space environment, and for homeland security purposes.

The purpose of this thesis relates to the research and development of new microdosimetric instrumentation for use with solid-state microdosimeters for radioprotection purposes and QA of various hadron therapy modalities. The main work presented in this thesis relates to four components, which include; the design optimisation of the existing Silicon-on-Insulator (SOI) Bridge V2 microdosimeter for BNCT QA, the characterisation of iThemba LABS Fast Neutron Therapy facility using experimental and Monte Carlo simulation verification, the characterisation of Tokai iBNCT epithermal neutron facility as well as an assessment of possible radioprotection risks during microdosimetry experiments, and finally, the development of a novel wireless microdosimeter.

In this thesis, Geant4 and MCNP6 Monte Carlo codes are employed extensively. Thorough benchmarking of the two codes are performed in the context of experimental verification, whilst comparing the similarities and differences in their simulation of the relevant hadron therapy facilities. Advanced methods for processing and analysing the data output by MCNP and Geant4, allowing a detailed description of nuclear interactions and all associated particles deriving from them. The final chapter of presented work in this thesis applies a methodical and rigorous approach to benchmark fourteen different physics models available in Geant4 and MCNP6 based on various neutron monoenergies.

Relating back to an experimental focus; the need for portable, user friendly devices for microdosimetric QA measurements are necessary to avoid sophisticated setup and time-consuming data analysis. These considerations are crucial when developing out-of-the-box microdosimetric instrumentation, intended for operation by users with limited technical experience. These factors are the major motivations for the work completed in this thesis, which have lead to successful advancements regarding the optimisation and implementation of new microdosimetric instrumentation.

1.1 Thesis Outline

- Chapter 2: Presents a literature review, introducing the history and concepts of microdosimetry. This is followed by the physics of neutron interactions and specifics of BNCT. Charged particle hadron therapy and fast neutron therapy are then described. The last sections describe the two Monte Carlo codes Geant4 and MCNP6.
- Chapter 3: Describes the general methodology adopted for the Monte Carlo simulation work performed in the study. This chapter provides the basic setup in the simulations, consolidating the information that would have been repeated in chapters that use similar settings.
- Chapter 4: Presents the simulation-based study relating to the optimisation of the SOI Bridge V2 microdosimeter geometry for BNCT QA. Geant4 simulations are used, considering the Kyoto University Research Reactor beam characteristics. The contribution of BNC products from the p^+ dopant region in the Bridge V2 is also simulated and discussed.
- Chapter 5: Presents an experiment and simulation-based characterisation of the fast neutron therapeutic beam produced at iThemba LABS in South Africa. Geant4 and MCNP6 were used to model the beam characteristics. Experimental and simulation results are compared using the SOI Bridge V2 microdosimeter.
- Chapter 6: Presents a simulation-based characterisation of the epithermal neutron therapeutic beam produced at the iBNCT facility in Tokai, Japan. Geant4 simulations were used to model the beamline and investigate any radioprotection risks associated with the current experiment setup for taking microdosimetric measurements.
- Chapter 7: Presents a novel Wireless Microdosimetry System developed by CMRP. The focus of this chapter is mainly relating to software development. Calibration of the system is performed with an ^{241}Am alpha sealed source. The finalised product is tested experimentally with ^{28}Si heavy ions using the SOI Mushroom microdosimeter. Geant4 simulations are used to validate the experimental measurements.
- Chapter 8: Presents a satellite chapter that applies an intensive methodical approach to benchmark fourteen different physics models in Geant4 and MCNP6 for QA in Fast Neutron Therapy and BNCT. The results found inferred the physics options that were selected for the various simulation applications developed in this thesis.
- Chapter 9: Presents the conclusions of the thesis and suggestions for future work.

Chapter 2

Literature Review

2.1 Microdosimetry

Microdosimetry is a technique for measuring the biological effects of radiation. Microdosimetry is based on the measurement of the frequency distribution of lineal energy or specific energy deposited in an actual or similar microscopic volume. Since the energy deposition is stochastic, the distribution of radiation properties may be quantified, which is useful for radioprotection and radiation treatment.

Microdosimetry has made a substantial contribution to our understanding of radiation effects in tissue and other materials [1]. Microdosimetry is very important for Boron Neutron Capture Therapy (BNCT), Fast Neutron Therapy (FNT), Proton Therapy, heavy ion treatment, and radiation protection, as it enables for a cellular level measurement of the effects from a mixed radiation field.

In a radiation environment where the particle species or their energy distribution are unknown or time variable, such as in space and other mixed radiation fields, the microdosimetric technique is compelling [1]. Microdosimetry can be utilised in space applications to provide real-time radiation exposure evaluations, taking into account biological impacts on astronauts and electronic damage [1]. In this project, innovative silicon microdosime-

ters created at the University of Wollongong's Centre for Medical Radiation Physics are characterised for Hadron Therapy and Heavy Ion Therapy Quality Assurance.

2.1.1 Microdosimetric Quantities

Microdosimetry [2] can be used to investigate radiological interactions in intricate mixed radiation fields, such as those associated with BNCT. The measurement of energy deposited in micron-sized sensitivity volumes (SV) with dimensions equivalent to biological cells is the basis of regional microdosimetry. According to ICRU report 36 [3], these microdosimetric quantities are defined. Lineal energy is a quantity used to describe the energy imparted to matter in a volume of interest by a single energy deposition event (ϵ) divided by the mean chord length of the volume dimensions (\bar{l}). The mean chord length is the average length of randomly oriented chords in a volume exposed to a uniform isotropic field of infinite straight lines. Lineal energy is commonly expressed in keV/ μm and defined as:

$$y = \frac{\epsilon}{\bar{l}} \quad (2.1)$$

The Cauchy formula can be used to determine the mean chord length of isotropic radiation fields in most convex volume types such as rectangular-parallelepiped (RPP), spherical, and cylindrical [4]. For convex volumes, the Cauchy formula for mean chord length is given by;

$$\bar{l} = \frac{4V}{S} \quad (2.2)$$

Examples of various convex shapes that the Cauchy formula can be used to define the mean chord length are shown in table 2.1.

Note that the use of the Cauchy formula to determine the mean chord length is only applicable for isotropic radiation fields. For highly directional radiation fields, such as those typical of heavy ion therapy, the mean path length $\langle l_{Path} \rangle$ should be used, which

Shape	Mean Chord Length (\bar{l})
Cube	$\bar{l} = \frac{2a}{3}$; a = side length
RPP	$\bar{l} = \frac{2abh}{bh+ab+ah}$; h = height, a & b = side lengths
Sphere	$\bar{l} = \frac{4r}{3}$; r = radius
Cylindrical	$\bar{l} = \frac{2rh}{h+r}$; r = radius, h = height

Table 2.1: Mean chord length for various convex shapes using the Cauchy formula.

is equal to the thickness of the SV [5]. The radiation field of heavy ion therapy is very directional, which is normally incident on the detector and produces a secondary radiation field that has varying degrees of directionality based on the type of nuclear recoil.

The spectrum of stochastic events for all primary and secondary particles is described by the lineal energy distribution:

$$f(y) = \frac{dF(y)}{dy} \quad (2.3)$$

where $F(y)$ is the probability that the lineal energy is equal to or less than y .

In order to analyse the dose in mixed radiation fields, the microdosimetric technique allows the separation of Linear Energy Transfer (LET) components. The energy loss of a particle while traversing a distance through a substance is described by LET. During its passage, it loses energy due to ionisations and excitations. LET is the average energy loss for a given path length travelled.

Alpha particles and protons are examples of high-LET particles, while electrons, positrons, and electromagnetic radiation such as gamma-rays and X-rays are examples of low-LET particles.

During the transit through the material, restricted LET accounts for the creation of secondary electrons, also known as delta electrons, through ionisation. Unrestricted LET refers to no production of delta electrons, and represents the linear stopping power of that radiation type.

LET is usually indicated in the units of keV/ μm ;

$$\text{LET} = \frac{dE}{dx} \quad (2.4)$$

The frequency-weighted mean lineal energy, \overline{y}_F is a non-stochastic quantity defined as;

$$\overline{y}_F = \int_0^{\infty} y f(y) dy \quad (2.5)$$

If $D(y)$ is the fraction of an absorbed dose with lineal energy equal to, or less than y , the dose probability density, $d(y)$ can be defined as;

$$d(y) = \frac{dD(y)}{dy} = \frac{1}{\overline{y}_F} y f(y) \quad (2.6)$$

The dose-weighted mean lineal energy \overline{y}_D , is given as;

$$\overline{y}_D = \int_0^{\infty} y d(y) dy = \frac{1}{\overline{y}_F} \int_0^{\infty} y^2 f(y) dy \quad (2.7)$$

The microdosimetric spectra are commonly shown in a log scale due to the large range that the lineal energy y and its distribution $f(y)$ can span. In order to graphically display spectra of the fraction of events having lineal energy ranges in a given range of interest, $y f(y)$ vs $\log(y)$ is used and given as;

$$\int_{y_1}^{y_2} f(y) dy = \int_{y_1}^{y_2} [y f(y)] d\log(y) \quad (2.8)$$

The Dose Equivalent, H , used in radiation protection can be derived by using the microdosimetric spectra of a radiation field ($y^2 f(y)$ vs $\log(y)$);

$$H = D \int Q(y) y^2 f(y) d(\log(y)) \quad (2.9)$$

where $Q(y)$ is a Quality Factor obtained from experimental data for biological weighting of this radiation type, and D is the absorbed dose [6].

The weighted dependency on the energy transfer qualities of radiation, i.e. linear energy transfer, is represented by this quality factor. Unlike lineal energy measurements, which represent microdosimetric energy deposition events, LET is not an easily measured quantity.

ICRU Publication 40 recommends a Q factor based on lineal energy;

$$Q(y) = \frac{a_1}{y} [1 - \exp(-a_1 y^2 - a_3 y^3)] \quad (2.10)$$

where $a_1 = 5510 \text{ keV}/\mu\text{m}$, $a_2 = 5 \times 10^{-5} \mu\text{m}^2/\text{keV}^2$, $a_3 = 2 \times 10^{-7} \mu\text{m}^3/\text{keV}^3$.

Comparison between the lineal energy and LET based quality factor is shown in figure 2.1. At values above a few $\text{keV}/\mu\text{m}$, there is a nice linear trend for the quality relationship between lineal energy and LET, which can be seen in figure 2.2.

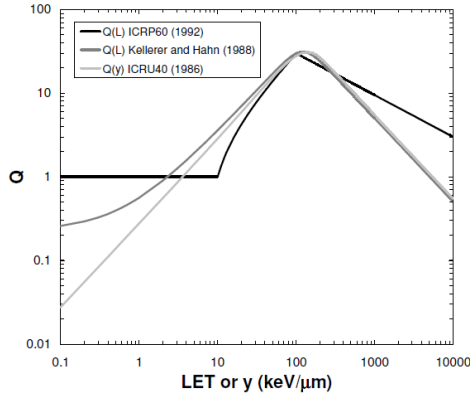


Figure 2.1: Quality factor Q defined as a function of LET (ICRP 60) and lineal energy (ICRU40) [7].

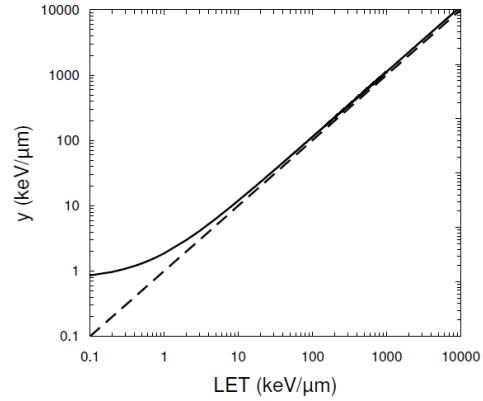


Figure 2.2: The quality relation between lineal energy and LET. Dashed line shows 1:1 relation. [7].

The Relative Biological Effectiveness (RBE) is used to describe the dose delivered by a particular radiation (H) relative to different type of radiation (L) [8].

$$RBE = \frac{D_L}{D_H} \quad (2.11)$$

where D_L and D_H are the absorbed doses of the two radiations causing an equal effect.

Modelling Radiobiological Effects based on Microdosimetry

Linear-Quadratic Model (LQM)

The Linear-Quadratic Model (LQM) is a mathematical model used to predict the survival of cells after exposure to ionizing radiation. This model is based on the effect of radiation to the DNA structure and their repair. The LQM equation is typically expressed as:

$$S = e^{-\alpha D - \beta D^2} \quad (2.12)$$

where S is the surviving fraction of cells, D is dose delivered to cell, and α and β are constants that depend on the type of radiation and the type of tissue being irradiated.

The LQM is commonly used to predict the biological effects of ionizing radiation and determine the optimal radiation doses in Treatment Planning Systems. The LQM can be derived using either experimental or mechanistic methods. The experimental method involves conducting radiobiological experiments to study cell survival after irradiation. The mechanistic method involves using theoretical models, such as:

- Theory of Dual Radiation Action (TDRA) model,
- Microdosimetric-Kinetic (MK) model,
- Local Effect Model (LEM).

Theory of Dual Radiation Action (TRDA) model

The Theory of Dual Radiation Action (TDRA) was proposed in 1972 [8] to help understand the relative biological effectiveness (RBE) values of high-LET radiation (such as neutrons with energies around 100 keV to a few MeV), compared to low-LET radiation (such as X-rays or gamma rays).

The main concept behind the theory is that biological effects, such as mutation or inactivation of cells, only happen when two sub-lethal events are produced simultaneously. This assumption is used to calculate the biological effect by measuring the specific energy deposited in the SV and considering the probability of two lesions occurring in the same SV. Based on equation (2.11), the RBE of higher LET to lower LET radiation can be defined by:

$$RBE = \frac{\alpha_L}{2\beta_L D_H} \left[\sqrt{1 + \frac{4\beta_L(\alpha_H D_H + \beta_H D_H^2)}{\alpha_L^2}} - 1 \right] \quad (2.13)$$

where D is the absorbed dose and α and β are coefficients depending on the quality of radiation.

TDRA has developed through three stages: the site model, the distance model, and compound dual radiation action (CDRA). These models were based on fundamental concepts such as the geometrical distribution of sub-lesions. However, TDRA does not consider the possibility of cell repair after irradiation, which is why the Microdosimetric Kinetic (MK) model was developed to include repair kinetics in estimating the biological effects.

Microdosimetric-Kinetic (MK) model

The Microdosimetric-Kinetic (MK) model is an extension of the TDRA theory. It combines the principles of repair kinetics and TDRA to calculate cell survival. The biological effect in the MK model is determined by the probability of three types of damage: non-repairable double strand breaks, one-track single strand breaks, and two-track double strand breaks.

The model uses two types of parameters: tissue-specific parameters and the dose-mean lineal energy derived from measurements made with a Tissue Equivalent Proportional Counter (TEPC). Hawkins presented a derivation of RBE according to the MK model [9][10][11]. In this model, the cell nucleus is divided into spherical domains, which are

used to define the restricted region where a pair of sub-lethal lesions created by a single event can produce a lethal lesion. The MK model presents a mathematical expression for the mean number of lethal lesions in a domain using an LQM of specific energy z :

$$L(z) = Az + Bz^2 \quad (2.14)$$

From equation (2.14) the dose-effect relationship for this model can be described as:

$$L(D) = aD + bD + cD^2 = (a + b)D + cD^2 \quad (2.15)$$

where a , b , and c are the probabilities of a non-repairable 1 track-single strand break (track-ssb), 1 track-double strand break (track-dsb), and 2 track-double strand breaks occurring, respectively.

The microdosimetric quantity of measured radiation fields is represented by $d(y)$, which is the distribution of an absorbed dose in lineal energy. The \bar{y}_D value represents the biological effectiveness of the microdosimetric spectrum when RBE is proportional to \bar{y}_D , which only applies at low absorbed doses. At very high doses, a saturated biological effect occurs, so the empirical quantity y^* was introduced [8]. y^* is the saturation-corrected dose-mean lineal energy, which is used when the deposition of excessive local energy leads to an over-kill effect, defined by:

$$y^* = \frac{y_0^2 \int_0^\infty (1 - \exp(-y^2/y_0^2)) f(y) dy}{\int_0^\infty y f(y) dy} \quad (2.16)$$

where y_0 is typically chosen to be 125 keV/ μm [8].

The modified MK model allows the RBE for a given kind of mammalian cell irradiated by ions to be determined. The α term used to describe the surviving fraction (S) of human salivary gland (HSG) tumour cells was derived in terms of particular cell characteristics

and microdosimetric quantities by:

$$\alpha = \alpha_0 + \frac{\beta}{\rho \pi r_d^2} y^* \quad (2.17)$$

where $\alpha_0 = 0.13 \text{ Gy}^{-1}$ (a constant that represents the initial slope of the survival fraction curve in the limit of zero LET), $\beta = 0.05 \text{ Gy}^{-2}$ (a constant independent of LET), $\rho = 1 \text{ g/cm}^3$ (density of tissue), and $r_d = 0.42 \text{ }\mu\text{m}$ (radius of a sub-cellular domain in the MK model).

The RBE_{10} for HSG cells that corresponds to 10% cell survival is defined by the formula [12]:

$$RBE_{10} = \frac{2\beta D_{10,R}}{\sqrt{\alpha^2 - 4\beta \ln(0.1)} - \alpha} \quad (2.18)$$

where $D_{10,R} = 5.0 \text{ Gy}$ (10% survival dose of 200 kVp X-rays for HSG cells) [13].

Local Effect Model (LEM)

The Local Effect Model (LEM) was introduced to describe the biological effects of radiation within cells in terms of the local energy deposition. LEM was introduced by Scholz and Kraft in 1996 [14]. It assumes that the lethal events that cause cell inactivation are not dependent of the type of radiation but rather on the track structure produced in the molecule of these lethal events. The LEM was proposed as an alternative to previous models from Katz and Kiefer, which described the biological effect only in terms of integral dose within a volume of interest without regard for the track structure that was produced at the cellular level [15].

With the assumption that the lethal events are randomly distributed, and the number of these events (N) is determined by the dose (D) deposited within, the survival probability (S) can be obtained by the equation:

$$S(D) = e^{-N(D)}, \quad N(D) = -\ln(S(D)) = \alpha D + \beta D^2 \quad (2.19)$$

Since the distribution of sites is assumed to be homogeneous within the cell, the number of lethal events per volume of the nucleus within the cell V is constant and dependent on dose, expressed as:

$$v(D) = \frac{N(D)}{V} = \frac{-\ln(S(D))}{V} = \frac{\alpha D + \beta D^2}{V} \quad (2.20)$$

As the event density is constant with the cell, the average number of lethal events \bar{N} produced by any local dose distribution $D(x, y, z)$ can then be expressed in the form of a volume integral:

$$\bar{N} = \frac{1}{V} \int_x \int_y \int_z -\ln(SD(x, y, z)) \, dx \, dy \, dz \quad (2.21)$$

Finally, the survival probability can be expressed using:

$$S = e^{-\bar{N}} \quad (2.22)$$

Using LEM, the radiobiological effect produced by heavy ion particles can be obtained using X-ray survival curves. This assumes that an equal number of lethal events will be produced by heavy charged particles and X-rays at a point where the same dose is absorbed, regardless of the method of dose deposition. However, it has limitations, such as the assumption that the radio-sensitivity of the cell and size of the nucleus remain unchanged during different phases of the cell cycle. Additionally, the effect of dose rate is not considered in LEM.

The validity of the LEM model can only be confirmed through radiobiological experiments, whereas the MK approach is based on experimental measurements of microdosimetric spectra for RBE derivation.

When highly energized charged particles interact with matter, delta electrons are produced by knocking orbital electrons out of atoms. The dense track of delta electrons along the trajectories of the charged particles can affect the biological effects and therefore, the

determination of RBE.

The interaction of radiation and its generated secondary particles with a sensitive volume have different definitions, namely: stopper, crosser, starter and insider. The definitions are illustrated in figure 2.3 and described in table 2.2. In the application of microdosimetry, the ideal case is that all particles interacting with the SV are crossers. Large uncertainties and misrepresentations in the microdosimetric spectra arise if there is a high proportion of stoppers, crossers and starters, as the lineal energy deposition in the SV is not continuous.

Type	Description	Ideal for Microdosimetry
Stopper	Particle originates outside the SV and does not have sufficient range to pass through.	No
Crosser	Particle originates outside the SV and has sufficient range to pass through.	Yes
Starter	Particle originates inside the SV and has sufficient range to leave the SV.	No
Insider	Particle originates inside the SV and does not have sufficient range to leave the SV.	No

Table 2.2: Description of ray interaction definitions.

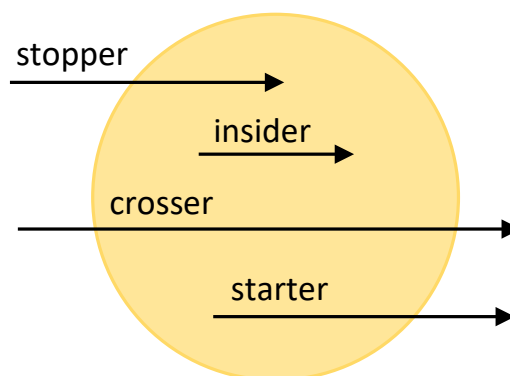


Figure 2.3: Definition of rays interacting with a sensitive volume, adapted from [4].

2.1.2 Microdosimetry Theory

Microdosimetry is a method for measuring the dose equivalent and RBE of mixed radiation fields based on a measure of stochastic energy deposition events that occur on a

cellular level [16].

The RBE must be considered in charged particle, neutron, and binary therapies [16]. The differences in cell or tumour response to various types of particle beams are described by this quantity. The RBE is <1 in most of these therapies, but it is changing along the Bragg Peak (BP) in charged particle therapy due to a change in LET and the formation of high-LET products due to inelastic reactions [16].

The initial formulation of microdosimetry, known as regional microdosimetry, was based on the concept of sites, that are regions of specified dimensions, in which the energy absorbed by ionising radiations is calculated without respect to the microscopic distribution within the site [6]. Structural microdosimetry, an alternate and more exact representation, allows for a more complete description of the microscopic pattern of energy absorption based on the average length of a series of chords taken through the volume of interest [6].

A. B. Rosenfeld, at the Centre for Medical Radiation Physics (CMRP), University of Wollongong (UOW), pioneered the representation of biological cells using an array of micron-sized semiconductor sensitive volumes, which now serves as the foundation for semiconductor microdosimetry [16]. The microscopic size of the semiconductor volumes is comparable to that of biological cells, so they can be utilised to approximate the dose equivalent delivered to tissue.

2.1.3 Microdosimetric Methods

Tissue Equivalent Proportional Counter

Rossi [17] pioneered the Tissue Equivalent Proportional Counter (TEPC), which is considered the gold-standard for measuring microdosimetry spectra. The TEPC is made up of a detector with a gas-filled cavity, which serves as the sensitive volume, and which experiences electrical changes in its gas as a result of ionising radiation. The energy absorbed in the gas and the surrounding medium is connected to the charge collected within

a gas-filled cavity by TEPC measurements, which provide the absorbed dose and dose equivalent quantities.

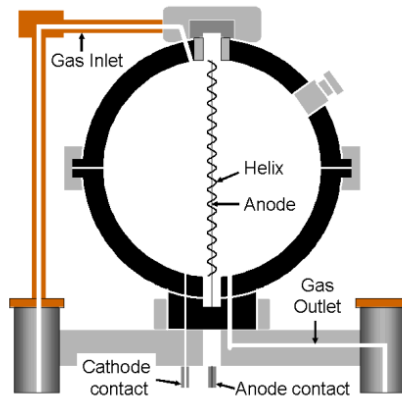


Figure 2.4: Rossi Tissue Equivalent Proportional Counter [18].

Although currently considered the best available microdosimeter, the TEPC has several shortcomings. These constraints include; wall effects, high operating voltage (up to 1000 V), relatively large physical size, phase effects due to measurement in the gaseous phase, and most critically, the inability to mimic an array of cells [2]. Conte et. al. of Laboratori Nazionali di Legnaro (INFN) recently developed miniaturised TEPCs with a physical cylindrical SV of about 2 mm, which partially addressed these mentioned problems [19].

Solid-state silicon microdosimeters

The solid-state silicon microdosimeter (SSM), which has been reported on by numerous groups, as an alternative to the TEPC. The SSM substitutes a solid-state volume for the gas volume, but works comparably. The p-n junction generated at the interface between p-doped and n-doped semiconductors is the basis for the SSM [1]. Electrons from the n-doped region diffuse into the p-doped region, causing a depletion region at the junction and generating an intrinsic electric field in the n-doped to p-doped direction [1]. The microdosimetric spectra that result are caused by charged particle energy deposition in the irradiated medium [2].

The CMRP at UOW demonstrated the possibility of a solid state microdosimeter on

a single SV in 1996, using a small area reverse biased p–n junction of the source diode in the MOSFET transistor [20]. A MOSFET die covered with PMMA material was irradiated with a mixed gamma-neutron field produced by d(48.5)+Be cyclotron source in a water phantom at the fast neutron therapy (FNT) facility at the Gershenson Cancer Institute, Detroit [20]. The resulting microdosimetric spectra of the neutron field obtained at different depths. This method enabled the total gamma-neutron dose to be measured simultaneously with fast neutron microdosimetry, however the SV of the MOSFET was poorly defined due to charge diffusion from the bulk of the diode to the depleted region [20].

The later development of Silicon-on-Insulator (SOI) solid-state microdosimeters by CMRP aimed to eliminate some of the drawbacks of the TEPC, such as huge size, high operating voltage, phase effects, and wall effects. Unwanted diffusion effects and charge sharing through the device have been greatly decreased thanks to advancements in SOI microdosimeter fabrication techniques and design [21]. While SOI microdosimeters address some of the problems associated with TEPC, they still have two major drawbacks: difficulties in tissue equivalent silicon scaling and well-defined sensitive volumes due to diffusion effects and complex charge collection mechanisms [2]. The CMRP has created and manufactured numerous generations of SOI microdosimeters to overcome these drawbacks, which are discussed in detail below.

Early generations of SOI microdosimeters

The first generation silicon microdosimeter consisting of an SOI diode array structure was developed at CMRP by Rosenfeld, Bradley et. al. in 1998 [22]. The prototype device was fabricated by Fujitsu Research Laboratories [4], with small p-n junction diode test structures created on 2, 5, and 10 μm thick bonded SOI wafers. The first generation microdosimeter, as shown in figure 2.5a, was a planar SOI design with an array of 2D 30 μm by 30 μm parallelepiped sensitive volumes adjacent to each other.

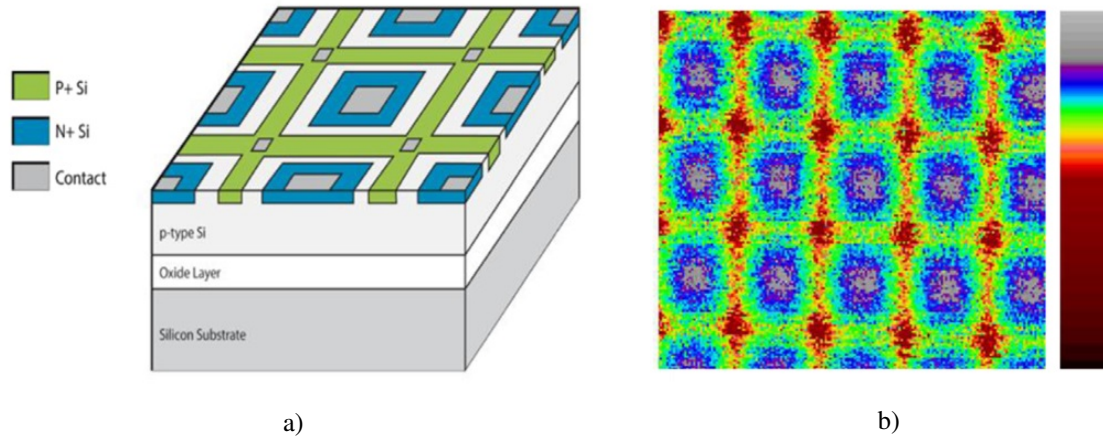


Figure 2.5: First generation silicon microdosimeter: a) Basic SOI diode array schematic b) IBICC median energy map of the diode array in response to 2 MeV He^{2+} [23].

The microdosimeter was first developed for research into space radiation effects, but it was later utilised to hadron therapy Quality Assurance [24]. It was tested extensively in Proton Therapy (PT), Boron Neutron Capture Therapy, and Fast Neutron Therapy [2] [2]. Monte Carlo simulations have been utilised to characterise the performance of the SOI microdosimeters in mixed field applications [24] [25]. It has been demonstrated that the SOI microdosimeter is capable of mixed gamma-neutron measurements, such that the contribution of lineal energy events in the microdosimetric spectrum can be distinguished and verified using Monte Carlo simulations [25]. The ability to read events in real time, demonstrated by the SOI microdosimeter operation, is extremely beneficial for abrupt changes in radiation, particularly in the space environment [26].

The microdosimeter was studied using the Induced Ion Beam Charge Collection (IBICC) technique, as shown in figure 2.5b. Due to the planar design, the device suffered from additional lateral charge collection via diffusion from outside the depletion region, with cross-talk causing the ill-defined sensitive volume regions. Although the device had relatively poor performance in terms of its charge distribution, this proved the feasibility of the silicon microdosimeter concept.

Following these successes, the design was improved to produce the second generation silicon microdosimeter in 2008, designed by CMRP [27] and fabricated in collaboration with the Australian National Fabrication Facility (ANFF), University of New South Wales

(UNSW).

The second generation featured an array of 2500 individual cylindrical planar SVs, fabricated on high resistivity p-SOI with 2, 5, and 10 μm thick layers of active silicon. To avoid cross talk, the cylindrical SVs were placed 40 μm apart. A guard ring was included around each SV to prevent charge collection outside the depletion region, as shown in figure 2.6a. All the SVs were connected in two parallel odd and even arrays (figure 2.6b), which has the advantage of a dual-channel read out for improved RBE identification of different high energy ions. The second generation microdosimeter was tested using the IBICC technique, with vastly improved charge distribution observed over the previous generation that conforms mostly within the SV region, as shown in figure 2.6c.

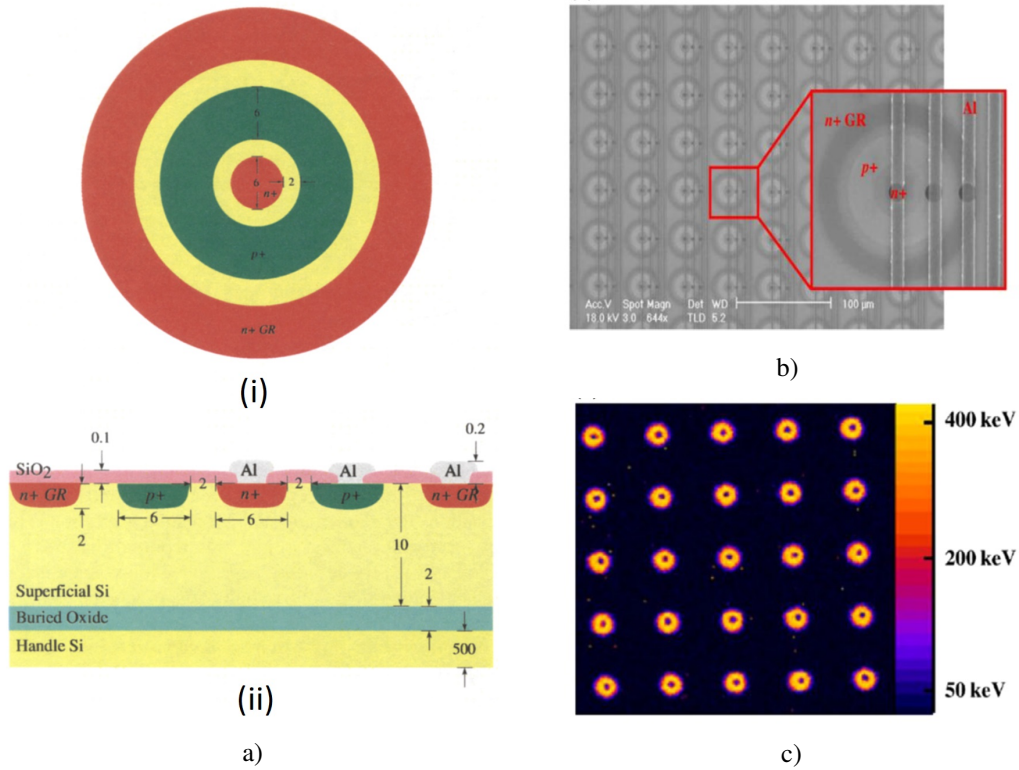


Figure 2.6: Second generation silicon microdosimeter: a) Schematic of a single SV region with guard ring, top down (i) and cross-section (ii) [27]. b) Scanning electron microscope (SEM) image zoomed on an SOI diode array section, c) IBICC median energy map of the diode array in response to 3 MeV He^{2+} [23].

The third generation silicon microdosimeter was designed in 2012 by CMRP, with its fabrication performed by the SPA-BIT Micro-Electronics Foundry in Kyiv, Ukraine. This device featured a large area chip (4.52 mm \times 3.60 mm) and was based on an array of

planar 6 μm and 10 μm diameter cylindrical sensitive volumes, fabricated on a 10 μm thick, high resistivity n-type SOI wafer [28].

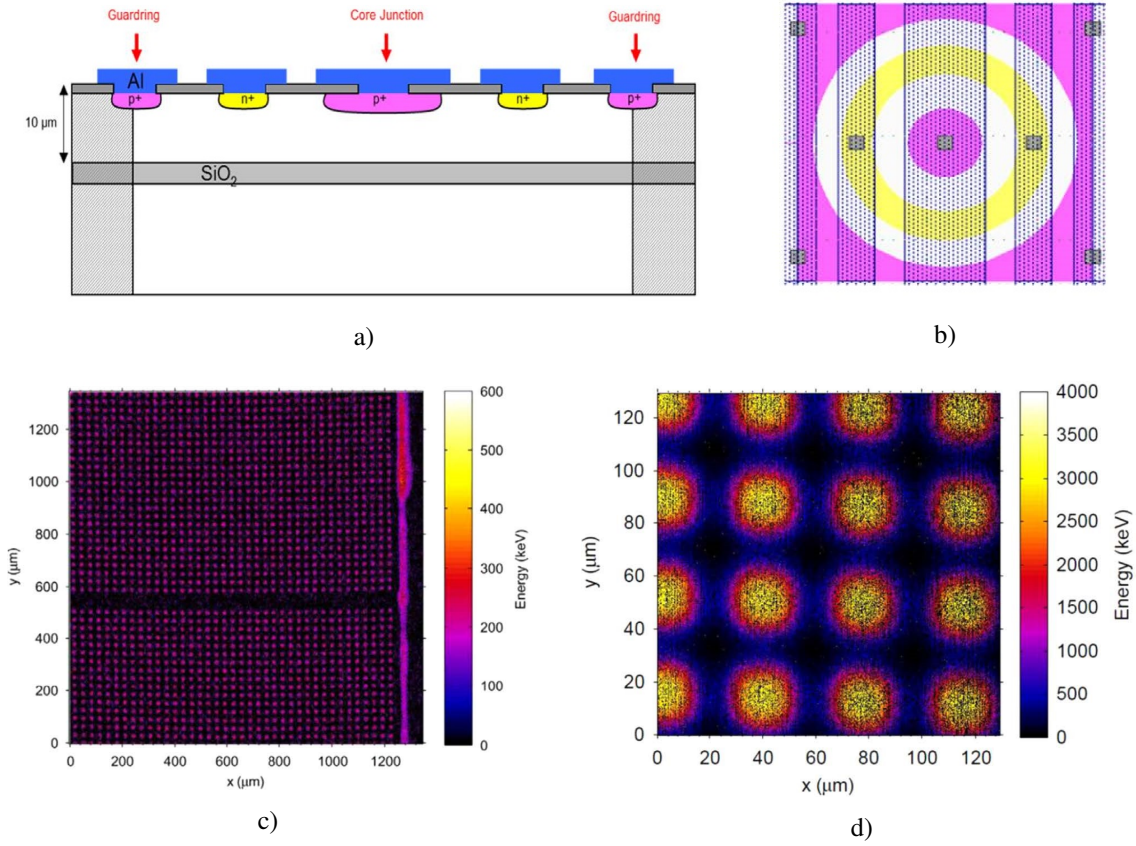


Figure 2.7: Third generation n-SOI microdosimeter: a) Cross-section schematic of a single cell, b) Top-down schematic of a single SV, c) IBICC median energy map of n-SOI array in response to 2 MeV H ions (zoomed out), d) IBICC median energy map of n-SOI array in response to 5.5 MeV He^{2+} ions (zoomed in) [23] [28].

To achieve well-defined sensitive volumes in the n-SOI planar silicon wafer, a veto p^+ electrode was incorporated, so events associated with the lateral diffusion of charge into the SV were avoided. This veto p^+ electrode allowed coincidence techniques to be utilised, to reject any events registered in both the p^+ core and veto p^+ electrode. Figures 2.7a and 2.7b show a simplified schematic of a single cell in the third generation n-SOI microdosimeter. IBICC median energy maps (figures 2.7c and 2.7d) present a significant improvement over the previous generations, with 100% CCE yield and minimal charge diffusion outside the core of the SVs [28].

SOI Bridge Microdosimeter

The SOI Bridge V2 microdosimeter is recent development of SOI technology by CMRP. The SOI Bridge microdosimeter is presented as the fourth generation of this technology. The microdosimeter consists of fully etched silicon volumes, producing a 3D description of the silicon SV, providing enhanced performance. The development of the first generation SOI Bridge microdosimeter was reported in 2015 [30]. The Bridge microdosimeter consists of a silicon substrate with etched silicon around the SVs and thin silicon bridges between them to support the aluminium conductive tracks. These thin silicon bridges connect the sensitive chambers and eliminate the poor yield concerns that plagued prior generations of microdosimeters [30]. It has been demonstrated that implanting an n^+ stop layer reduces lateral charge propagation across the device [21].

An array of roughly 4248 cells, each containing a $30 \times 30 \times 10 \mu\text{m}^3$ cubic SV, provides a large sensitive area of $4.1 \times 3.6 \text{ mm}^2$ on the V2 device. The structure and SEM image of the Bridge V2 microdosimeter are shown in figures 2.8c and 2.9b, respectively. Ion implantation-produced square p-i-n diodes sit atop the SVs, beneath a deposited layer of phosphorus silicate glass (PSG) and silicon dioxide (SiO_2). The active layer is composed of a $3 \text{ k}\Omega\cdot\text{cm}$ n-SOI active layer with a thickness of $10 \mu\text{m}$ and a low resistivity supporting

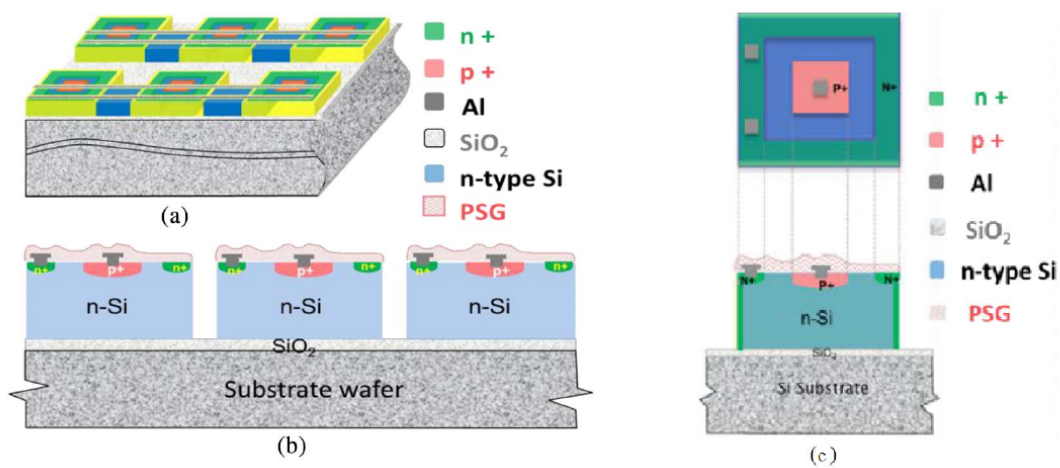


Figure 2.8: Schematic diagram of Bridge microdosimeter V1 (left) and V2 (right). (a) Section of six cells with adjoining silicon bridge regions [29], (b) cross-section view [29], (c) V2 device with n^+ stop layer surrounding top edges and sides of the SV [21].

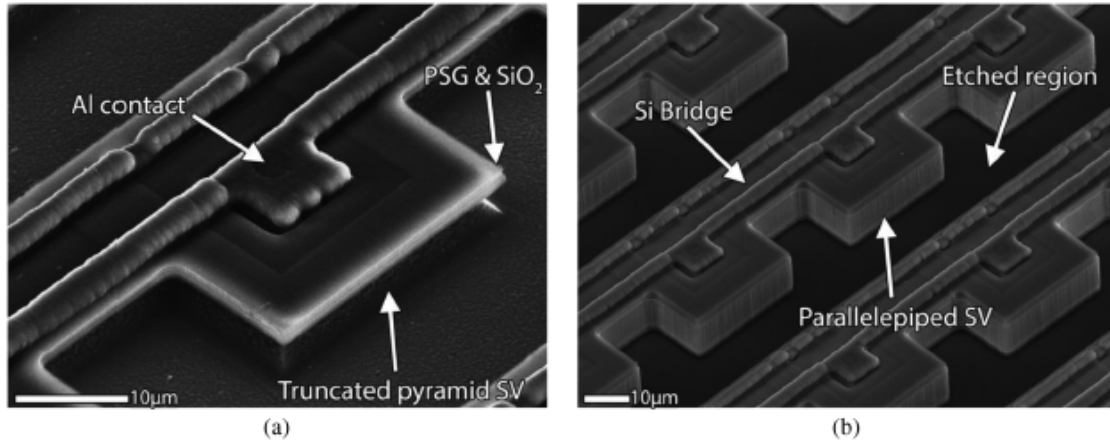


Figure 2.9: SEM Images of Bridge SV arrays. (a) Bridge V1 (partially etched), (b) Bridge V2 (fully etched) [21].

wafer [30]. The well-defined SV that separates the SOI from the low-resistivity silicon substrate wafer base is ensured by this insulating layer. Laterally nearby portions of silicon were entirely etched away for each array row of SVs, leaving thin 15 μm-long bridges to support charge-carrying aluminium tracks. Single events can be isolated from neighbouring interactions by reading SVs in odd and even rows independently [30]. This reduces cross talk and allows single events to be isolated from nearby interactions.

SOI Mushroom Microdosimeter

The SOI “Mushroom” microdosimeter was developed by CMRP [23] [29] in collaboration with SINTEF MiNalab (Oslo, Norway), for microdosimetry of mixed radiation fields. The original SOI Mushroom microdosimeter was developed with initial modelling and proof of concept in 2014 [31]. The latest generation (2021) of four different SOI Mushroom microdosimeter designs [32] are discussed below.

2-μm-Thick Mushroom Microdosimeter Fabricated by Planar Technology

The 2-μm-thick Mushroom microdosimeter was fabricated using planar technology due to its thin active layer. This device consists of well-defined cylindrical SVs with 20 μm diameter and 2 μm height [32]. The planar design consists of a n^+ doped core (phosphorus ion implantation) and p^+ doped (boron ion implantation) circular outer ring region of the

SV. An additional p-stop layer was created outside the SV that connects to the p^+ outer electrode to reduce positive charge build-up. In this design, linear arrays of SVs are connected by aluminium buses. Figure 2.10 shows SEM images and schematic of the 2- μm -thick Mushroom microdosimeter design.

The small thickness of the SVs reduces the number of stopper events, providing more precise microdosimetric spectra of the mixed radiation field. This is important for high-LET particles such as in BNCT, as well as for separation of radiation components in mixed gamma-neutron fields [32].

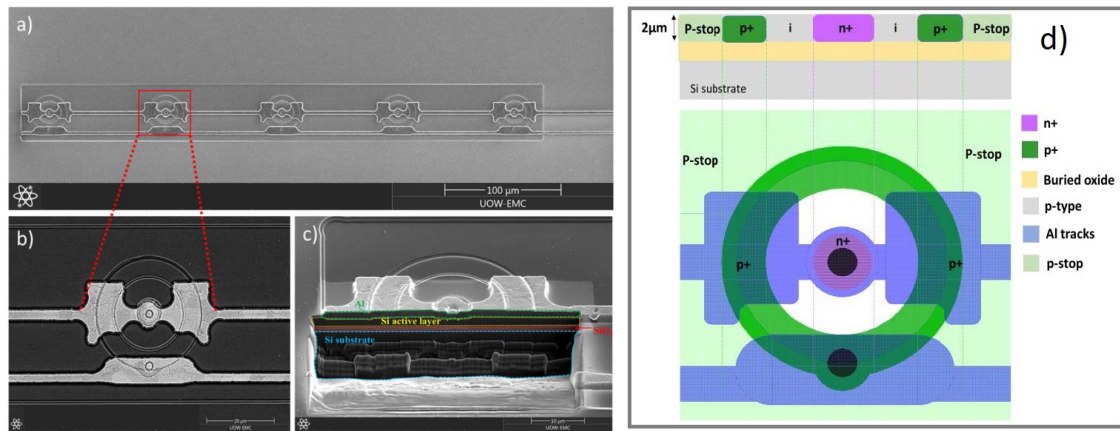


Figure 2.10: Images of the 2- μm -thick Mushroom microdosimeter. a) Surface SEM image showing a number of SVs, b) zoomed-in SEM image of a single SV, c) cross-sectional SEM image of a single SV, d) cross-sectional and top-view schematic of the planar structure [32].

Trenched-3D Mushroom Microdosimeter with a Planar Core Electrode

The trenched-planar Mushroom microdosimeter consists of 3D SVs with a cylindrical shape and a planar n^+ core. The silicon surrounding the cylindrical volumes has been etched away to form the 3D structure. The design consists of a 3D cylindrical SV with planar n^+ inner core produced by ion implantation, surrounded by a outer trench with p^+ doped walls around the SV, which has been filled with polysilicon. Similarly to the $2\mu\text{m}$ thick SV design, a p-stop layer was added connected to the p^+ electrode to avoid charge build-up.

Each SV is 20, 30 or 50 μm diameter and 5 or 10 μm height. The linear arrays of SVs are connected with aluminium buses, one across the n^+ core and the other to the p^+ electrode on the outer edge of the SV. The schematic and SEM image of the trenched-planar design is shown in figure 2.11.

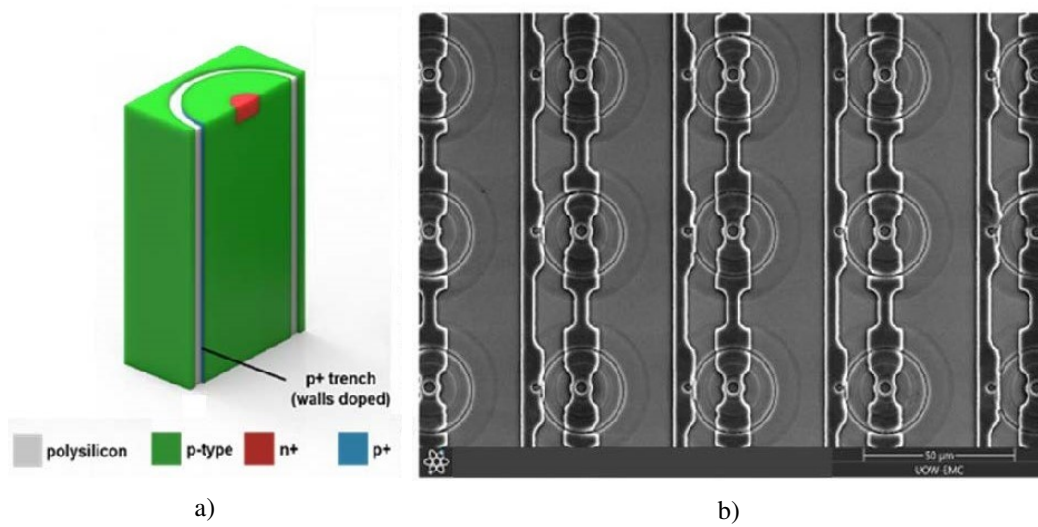


Figure 2.11: a) Schematic of a single SV in the trenched 3D Mushroom microdosimeter with planar n^+ core and p^+ doped trench filled with polysilicon [33], b) SEM image of a trenched-3D Mushroom with planar core SV array [32].

Trenched-3D Mushroom Microdosimeter fabricated by 3D Detector Technology

The design of the trenched-3D Mushroom microdosimeter is similar to the trenched-planar Mushroom, except the SV centre has been trenched, leaving a voided column of air and n^+ doping applied to the inner walls to form the inner core [32]. The outer trench is also voided (air), instead of a polysilicon fill, forming the fully 3D structure of the SVs. The outer air trench in the second design aims to avoid the possibility of charge generated outside the SV from being collected. The schematic and SEM images of the trenched-3D Mushroom design is shown in figure 2.12

To electrically connect the SVs in an array, aluminium tracks run laterally across the SVs, along unetched silicon. The n^+ track runs across the SV centres, connecting n^+ electrodes and two tracks along each outer edge of the SVs, connecting p^+ electrodes, as shown in figure 2.12b. The trenched-3D design has SVs with diameters of 20 μm or 30 μm , fabricated on high resistivity p-type SOI wafer with a 10 μm thick active layer, bonded to low resistivity supporting silicon wafer. Between the SOI wafer and supporting silicon wafer is a 2 μm thick silicon dioxide passivation layer. The Mushroom microdosimeter with 20 μm diameter, 10 μm thick SVs has approximately 2500 fully 3D free-standing cylindrical SVs.

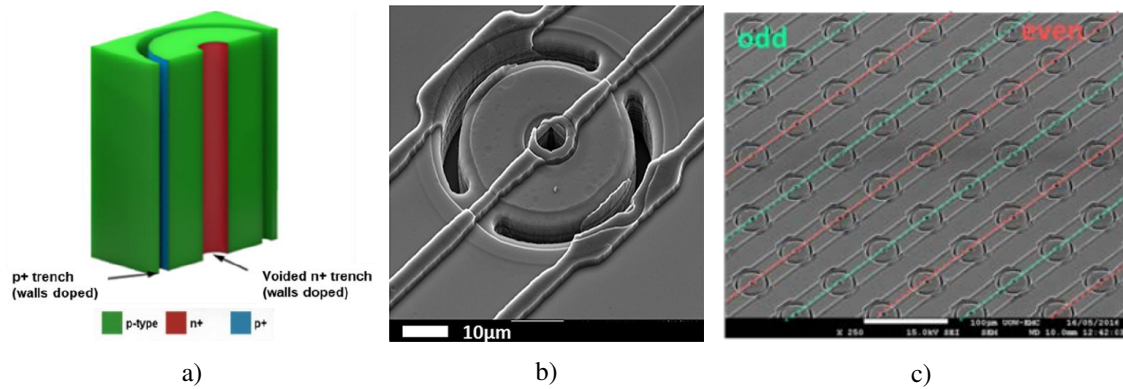


Figure 2.12: a) Schematic of trenched-3D Mushroom microdosimeter with voided p^+ trench and voided n^+ trench [32], b) SEM image of a single SV of the trenched-3D Mushroom microdosimeter [33], c) SEM image of an array of SVs in the trenched-3D Mushroom microdosimeter with odd and even aluminium tracks highlighted [34]

Fully Free-Standing 3D Mushroom Microdosimeter

Figure 2.13 show the design schematic and SEM image of a free-standing 3D SV array of microdosimetric SVs, later named the 3D Mushroom microdosimeter. The silicon surrounding the SV has been fully etched with cylindrical shape to form the fully free-standing 3D SV design. The SVs have diameter of 20 to 50 μm and thickness of 5 or 10 μm . An array of SVs can either be surrounded by air or embedded in polyimide (a tissue equivalent material), that extends 12 μm above SVs.

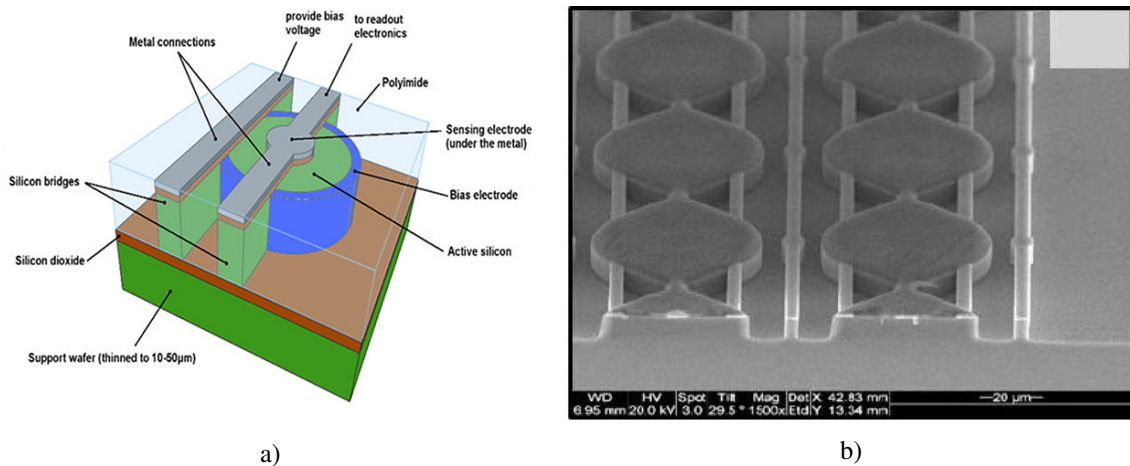


Figure 2.13: a) Schematic of the free-standing 3D SV embedded in tissue-equivalent material [33], b) SEM image of the 3D Mushroom microdosimeter with free-standing SV and surrounding silicon removed by etching [32].

Diamond-based Microdosimeters

Other recent work at CMRP has concentrated on the fabrication of diamond-based microdosimeters in conjunction with the University of Melbourne [35] [36] [37]. Diamond-based radiation detectors are distinguished by their comparatively simple design, which allows for greater flexibility in the structures that may be constructed without the need of p-n junctions [36]. CMRP Diamond-based devices have been constructed to generate 3D vertical wall-less sensitive volumes embedded in a diamond matrix. These detectors are most suitable for applications where radiation hardness is more important than sensitivity [35]. The first generation detectors were the first known attempts in diamond to produce buried cylindrical sensitive volume structures.

CMRP's latest diamond-based microdosimeter development is the 3D Lateral Electrode Structure (3D-LES) device [36]. On a high purity diamond, laser ablation milling and active brazing silver alloys are employed to create a lateral electric field in the sensitive volume between electrodes. To reduce charge collection from remote regions, isolation trenches are built around the contact electrodes. The conducting walls operate as a virtual electrode, resulting in a greater leakage current and an extra electric field component. Figure 2.14 depicts a device with a 20 μm contact spacing and its simulated electric field distribution derived using TCAD.

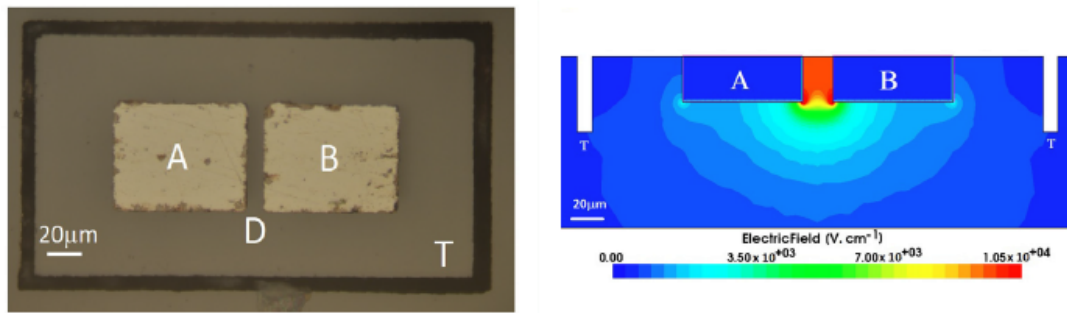


Figure 2.14: (Left) Top view of 3d-LES before wire bonding showing A, B electrodes, T isolation trench, D contact separation distance. (Right) Cross section of simulated electric field due to 20V potential between contact electrodes [36].

Diamond-based detectors have been well studied and are appealing due to their radiation hardness, high breakdown voltage, and temperature independence. Low dark current and high carrier mobility are also advantages. Diamond-based devices have a low capacitance due to their low dielectric constant (5.6), allowing for fast signal collection and low noise operation [37]. The wide band gap of diamond (5.5 eV) means that thermally excited charge carriers have a limited likelihood of crossing the band gap.

Other silicon-based microdosimeter developments

U3DTHIN detector

The U3DTHIN detector was developed in 2009 at Centro Nacional de Microelectrónica in Barcelona for high flux neutron detection [38]. It was designed to address the low sen-

sitivity, poor energy resolution and low signal-to-noise characteristics of PMT scintillator systems. The U3DTHIN detector, shown in figure 2.15, features vertical $5\ \mu\text{m}$ diameter p^+ and n^+ electrodes, placed in $10\ \mu\text{m}$ deep etched holes from the top of the substrate down to the extremely thin oxide layer below.

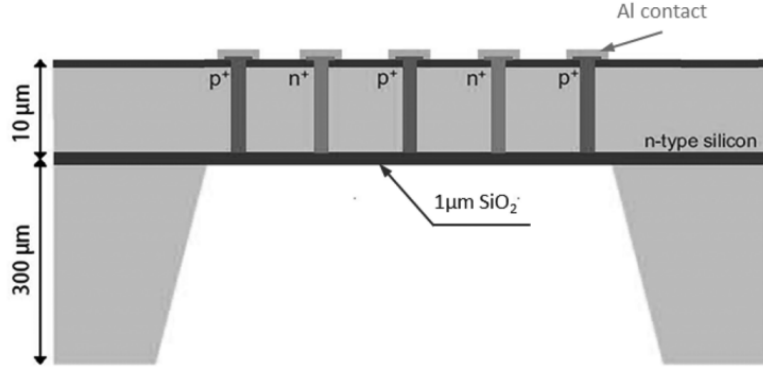


Figure 2.15: Cross-section of the U3DTHIN detector (not to scale) [39].

The distance between electrodes is smaller than that of planar devices, allowing shorter charge collection time and reduced trapped potential. In addition, this results in less applied bias to reach full depletion. The U3DTHIN detector can operate under high fluence conditions due to the vertical junctions, allowing depletion to occur laterally, which is desirable for microdosimetric devices. The U3DTHIN detector has been characterised for microdosimetric applications by CMRP [39] [40].

Adaptations based on the U3DTHIN design

A similar design was built by Guardiola et. al. in 2012 [41] for applications in neutron detection and gamma rejection, as shown in figure 2.16. Whilst the device was not intended for microdosimetry, the silicon wafer sensitive volume thickness is on the microscopic scale ($10\ \mu\text{m}$ thick). A thin ^{10}B -based acrylic converter layer was deposited on top of the detector to capture low energy neutrons and convert them to detectable charged particles in the silicon sensitive volume.

The concept of a device with thin, lateral depletion has the advantage of decreased capacitance (leading to an increased signal-to-noise ratio compared with planar devices), though there are considerations associated with this design. Although reducing the space

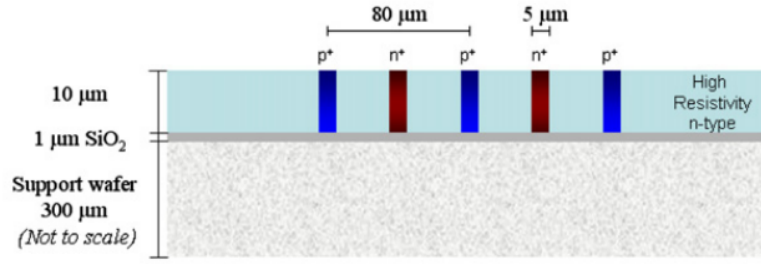


Figure 2.16: Cross-section of the thin silicon device by Guardiola et. al. [42].

between electrodes will decrease the required depletion voltage, the capacitance will increase, which results in a higher noise in the signal. Furthermore, it is desirable to minimise the electrode size (as they are sensitive to radiation), which may result in material and etching issues [43].

Due to the thin detection layer in this design, this renders the detector relatively insensitive to gamma radiation, which will have a low probability of interaction with the silicon sensitive volume. Additionally, as the bulk volume of this detector is monolithic (i.e. does not possess individual SVs), oblique ion tracks can deposit large amounts of energy in the bulk silicon, making it unsuitable for microdosimetry [39].

The same group further developed on this concept and successfully built a microdosimeter with cylindrical SVs [44]. Planar techniques were used to create the p⁺ electrodes of each SV, which were fabricated on a high resistivity n-type silicon substrate. After removing a cylindrical portion of silicon with deep reactive ion etching (DRIE), n⁺ polysilicon was deposited along the depth of the wafer to create the n⁺ electrode. Charge collection studies [45] demonstrated 100% yield and successful charge collection, however well-defined geometry was not observed. Additionally, the device suffered from high noise in the low energy region (< 0.5 MeV) during ion beam induced charge collection studies using 5 MeV and 2 MeV alpha particles [45].

Tissue Equivalent Scaling Factors

One of the key challenges with solid-state microdosimetry, as previously indicated, is the difficulty in converting microdosimetric energy deposition to tissue equivalent deposited dose. Through the use appropriate geometric scaling factors, microdosimetric spectra can be converted to water or tissue equivalents. Combining the spectra with the established ICRP quality factor $Q(y)$ [16] yields the dosage equivalent. Rosenfeld and Bradley [22], Davis [46], and Guatelli [26] demonstrated the scaling of microdosimetric spectra for varied sensitivity volume thickness and material types, with results verified using Monte Carlo simulations.

Guatelli [26] demonstrated that in a proton radiation field with an energy range between few MeV and 250 MeV, a simple geometrical scaling factor, $\bar{C} = (0.56 \pm 0.03)$, of linear dimensions of the SV is sufficient to convert experimentally obtained microdosimetric energy deposition spectra in silicon to equivalent microdosimetric energy deposition spectra in water. The scaling factor is equal to the ratio of stopping power of protons in water to silicon.

Diamond-based detectors have the advantage that the atomic number (Z) of diamond is 6, which is approximately identical to the Z of muscle (7.2), resulting in excellent tissue equivalency of these types of detectors [16]. For photons and charged particles above a specific energy threshold, diamond can be called tissue comparable material [46]. Davis [46] used a similar method based on the ratio of stopping powers for protons and alpha particles to convert diamond energy deposition to tissue equivalent microdosimetric energy deposition. $\bar{C}=0.32$, which is only stable over the MeV to GeV range [46], has been identified as an acceptable scaling factor for diamond. A dynamic low energy scaling factor is necessary for sub-MeV energies.

Rosenfeld and Bradley determined that a geometric scaling factor of roughly $\bar{C}=0.63$ is applicable for converting the microdosimetric energy deposition measurements of incident ions observed in silicon to energy deposition in tissue. The range-energy relation-

ships were acquired using SRIM software [47], and the conversion factor was calculated using:

$$\bar{C}(ion) = \frac{1}{E_{max}} \int_0^{E_{max}} \frac{R(E, ion, Si)}{R(E, ion, tissue)} dE \quad (2.23)$$

where $R(E, ion, target)$ is the range as a function of energy (E) for the required ion and target.

2.1.4 CMRP Experimental Microdosimetry Peripherals

MicroPlus Probe

The CMRP SOI microdosimeters (such as the SOI Mushroom and SOI Bridge) are mounted on a 20 pin dual in-line (DIL) package. The terminal pads on the microdosimeter, which are electrically connected to each array of SVs by the aluminium tracks, are wirebonded to the leads of the DIL package.

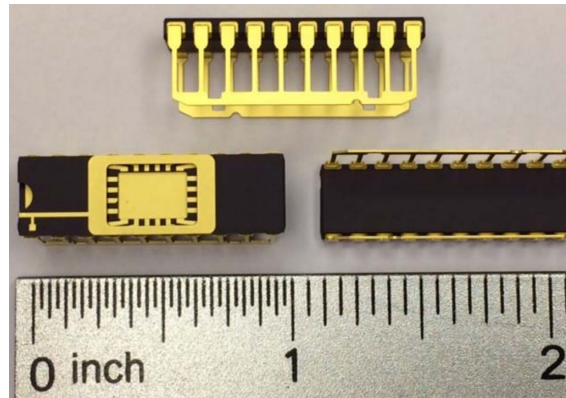


Figure 2.17: Side-Brazed Dual In-Line Ceramic Package - 20 pin, used for SOI microdosimeter mounting [48].

The DIL package, with SOI microdosimeter mounted is plugged at the end of a printed circuit board (PCB), called the MicroPlus probe (μ^+ probe), as shown in figure 2.18. The μ^+ probe was developed at CMRP, which connects the arrays of the SOI microdosimeter to a low noise spectroscopy-based circuit charge sensitive amplifier (CSA) [49], allowing readout and electrical bias. Jumper pins on the μ^+ probe allow different arrays on the

microdosimeter to be connected (or disconnected). The CSA electronics are located 10 cm away from the microdosimeter on the PCB to prevent radiation damage to the electronics. The probe is usually then connected to a shaping amplifier, that sends the signal to a Multi Channel Analyser (MCA) to process the signal through acquisition software on a computer. The μ^+ probe can be encapsulated in a PMMA sheath, which allows the microdosimeter to be operated in water.

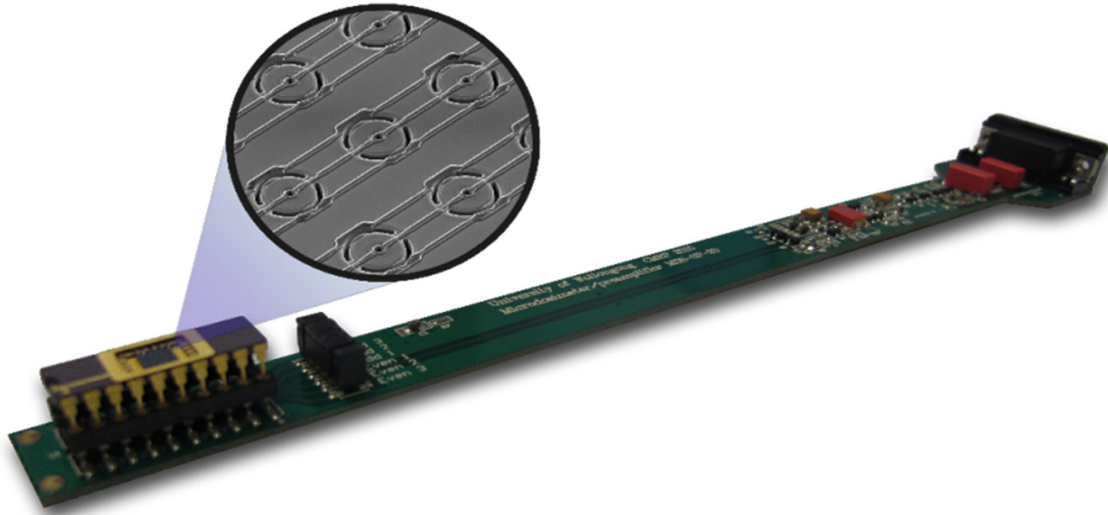
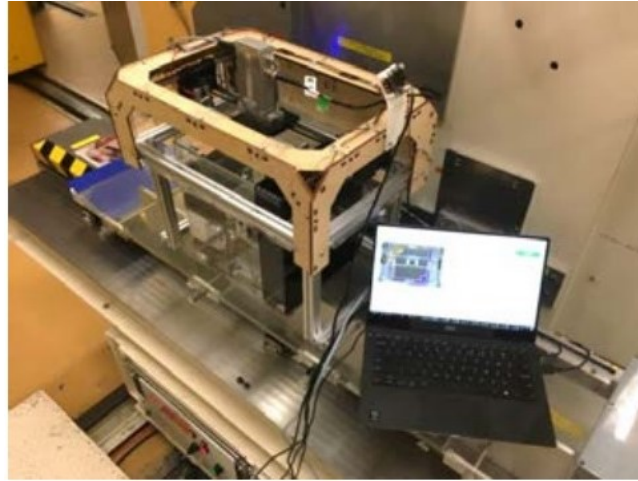


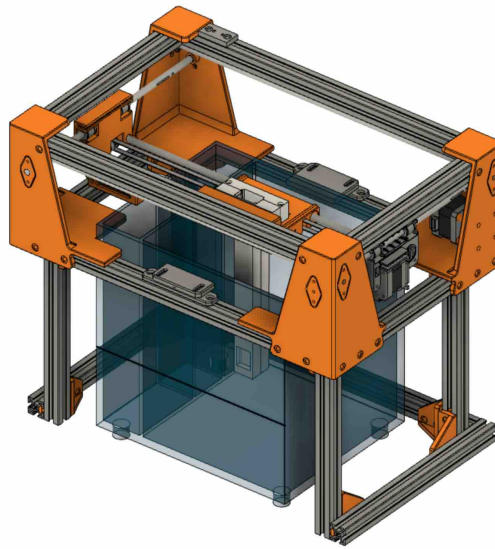
Figure 2.18: The μ^+ probe connected to the microdosimeter chip [49]. Zoomed lens shows the array of the SOI Mushroom mounted on the DIL package.

Motion Stage Positional System

The CMRP motion stage system was developed by Chartier [50] to remotely control the X-Y positioning of the μ^+ probe in a water phantom PMMA tank. The position is controlled using Arduino driven stepper motors to allow different depths and lateral measurements to be adjusted without needing to enter the treatment rooms. The motion stage is shown in figure 2.19, as its initial build and subsequent rebuild to improve stability and ruggedness during transport.



a)



b)

Figure 2.19: a) Initial motion stage design [51], b) rendering of the rebuild version.

2.2 Boron Neutron Capture Therapy (BNCT)

2.2.1 Physics of Neutron Interactions

Neutrons are sub-atomic particles with no charge. Neutrons are classified into three energy levels: thermal (~ 0.5 eV), epithermal (0.5 eV - 10 keV) and fast (> 10 keV) [52].

Several interactions can occur between incident neutrons and their target nucleus with the most common interactions being scatter (elastic and inelastic), capture and fission.

The nuclear cross-section of the target nucleus is used to determine the probability of these interactions. The cross-section is dependent on the characteristics of the target nucleus and the energy of the incident neutron. A scattering interaction can be elastic or inelastic, depending on whether the neutron transfers some of its energy to the target nucleus.

Neutron Elastic Scatter

In elastic scatter, the neutron and nuclide share some of their kinetic energy during collision. The total kinetic energy before and after the collision remains the same. The basic process of elastic scatter is outlined in figure 2.20.

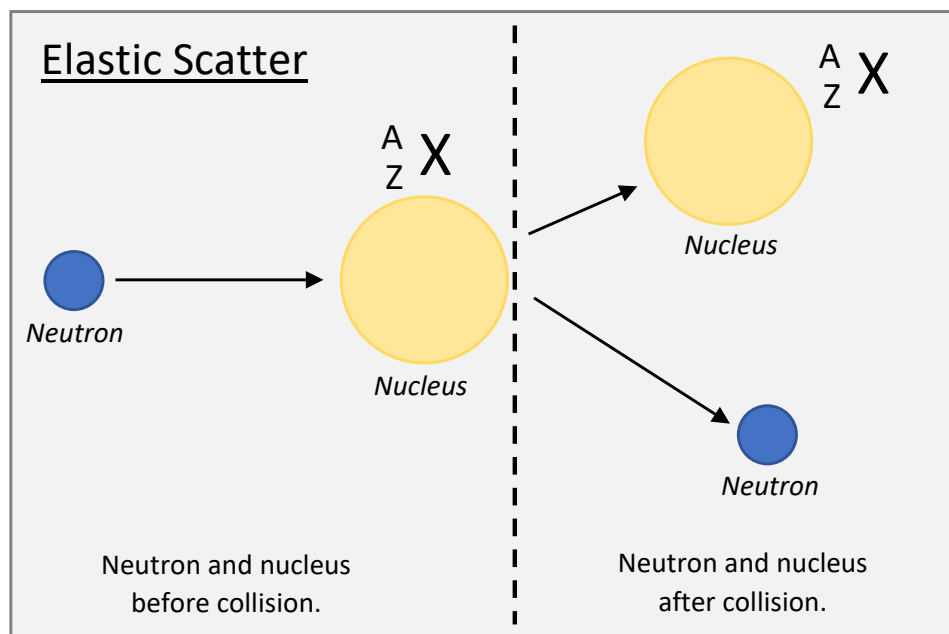


Figure 2.20: Basic process of neutron elastic scattering interactions.

When a neutron collides with a stationary nucleus, the nucleus will receive energy from the neutron and begin to move, while the neutron is slowed down by the loss of kinetic energy. The residual nucleus is in its ground state (not excited). Elastic scattering is used to slow down fast neutrons to lower energies. However, the neutron can gain energy if the nucleus has higher kinetic energy than the neutron.

Neutron Inelastic Scatter

Neutron inelastic scattering involves a transfer of kinetic energy to the nucleus causing it to enter an excited state where radiation is released before it returns to its ground state [53]. As a result, the total kinetic energy after the collision is less than before the collision. The excited nucleus de-excites by gamma emission. The basic process of inelastic scatter is outlined in figure 2.21.

If the nucleus is stationary before collision, the neutron must have kinetic energy greater than the excitation energy for such a reaction to occur. The threshold of heavy nuclides are lower than those of light nuclides.

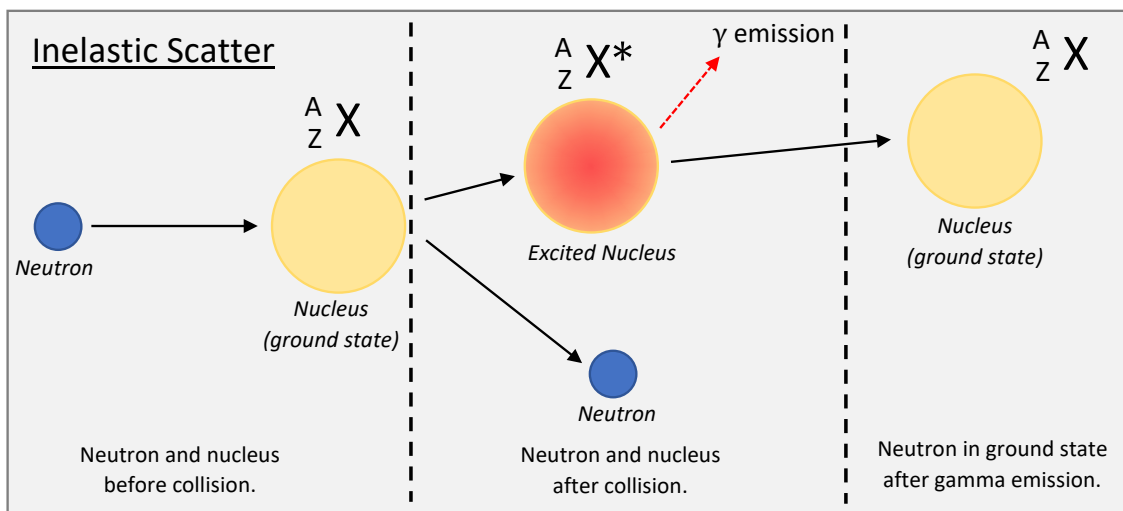


Figure 2.21: Basic process of neutron inelastic scattering interactions.

Neutron Capture

In an absorption interaction, also known as neutron capture, the neutron is absorbed by the target nucleus to form an isotope with atomic mass number, $A+1$, in an excited state. This new isotope de-excites by gamma emission. This reaction rearranges the internal structure of the nucleus, resulting in a variety of emissions such as gamma rays, protons, deuterons and alpha particles. The neutron is lost in this reaction as it is absorbed by the nucleus. The basic process of neutron capture is shown in figure 2.22.

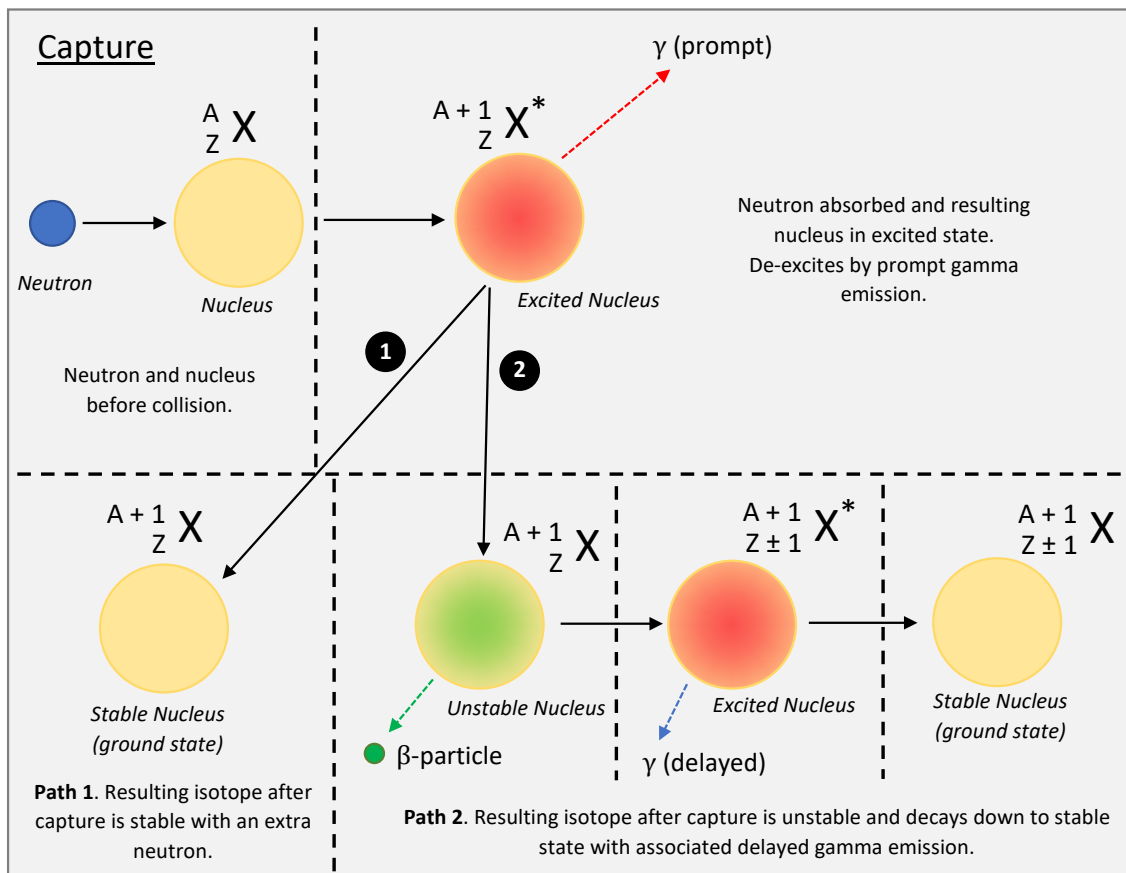


Figure 2.22: Basic process of neutron capture interactions, two paths are presented, whether the isotope is stable (path 1) or activated (radioactive) (path 2).

In the application of Boron Neutron Capture Therapy (BNCT), there are three types of neutron capture reactions that occur to form the total dose in the treatment region and surrounding healthy tissue: thermal capture of ^{10}B ; radiative capture of hydrogen; and (n,p) reaction by ^{14}N [53].

(i) Thermal Capture of ^{10}B .

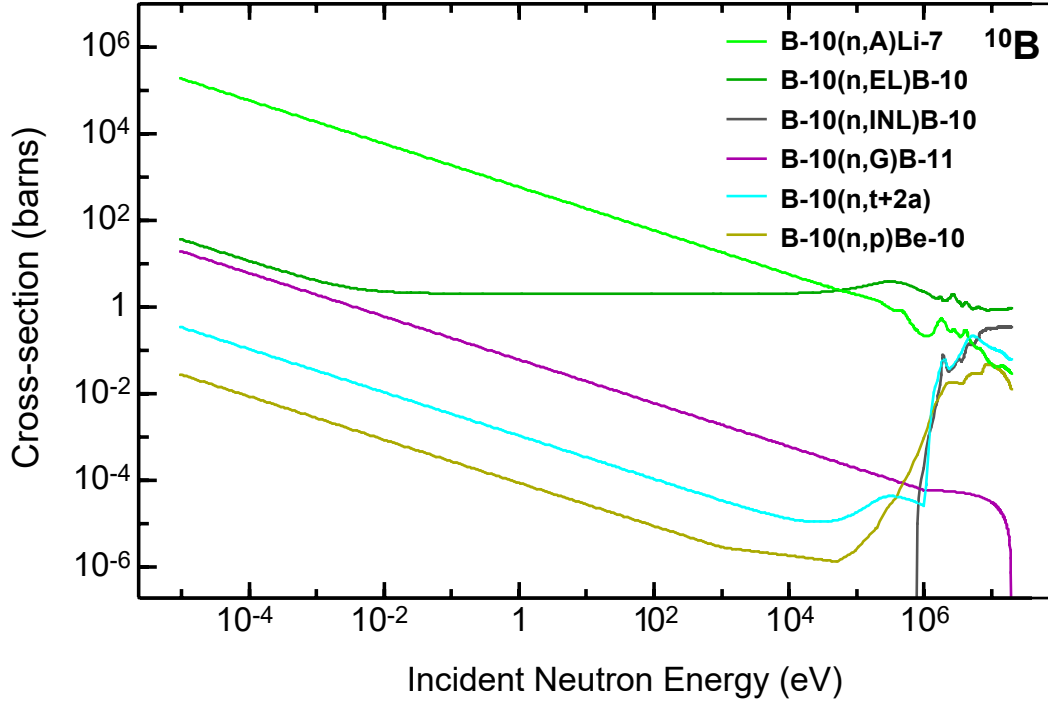
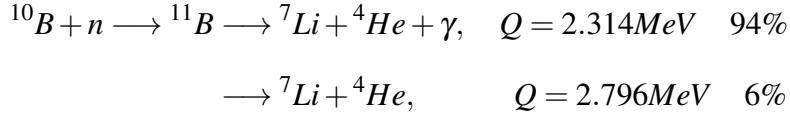


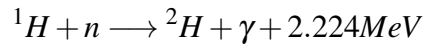
Figure 2.23: ENDF/B-VII.1 cross-sections for ^{10}B , adapted from [54].

Thermal neutron capture in ^{10}B has a high cross section, and thus high probability of interaction, making it an effective choice for therapy. When the ^{10}B target nucleus captures low energy neutrons an alpha particle and lithium nucleus are emitted. These emissions have very high LET, resulting in localised energy deposition within 10 micrometers - roughly the size of a human cell. The 94% reaction produces 0.48 MeV gamma, 0.84 MeV ^7Li and 1.47 MeV alpha. The 6% reaction produces 1.01 MeV ^7Li and 1.77 MeV alpha.

^{10}B has several other neutron interactions such as $^{10}\text{B}(n,\gamma)^{11}\text{B}$ capture and $^{10}\text{B}(n,t+2\alpha)$ total disintegration. In the total disintegration reaction, the ^{10}B absorbs the incident neutron and produces triton and two alpha particles. This reaction is sensitive to thermal

neutrons and fast neutrons, with a high cross section above 1 MeV. This is also the case for $^{10}\text{B}(\text{n},\text{p})^{10}\text{Be}$, producing radioactive ^{10}Be , outlining the importance of moderating neutrons by elastic scatter to lower energies in BNCT applications.

(ii) $^1\text{H}(\text{n},\text{G})^2\text{H}$ - Radiative capture of hydrogen.



An incident neutron binds to the proton, forming deuterium, ^2H . In this reaction, energy is released with a single gamma photon of 2.23 MeV.

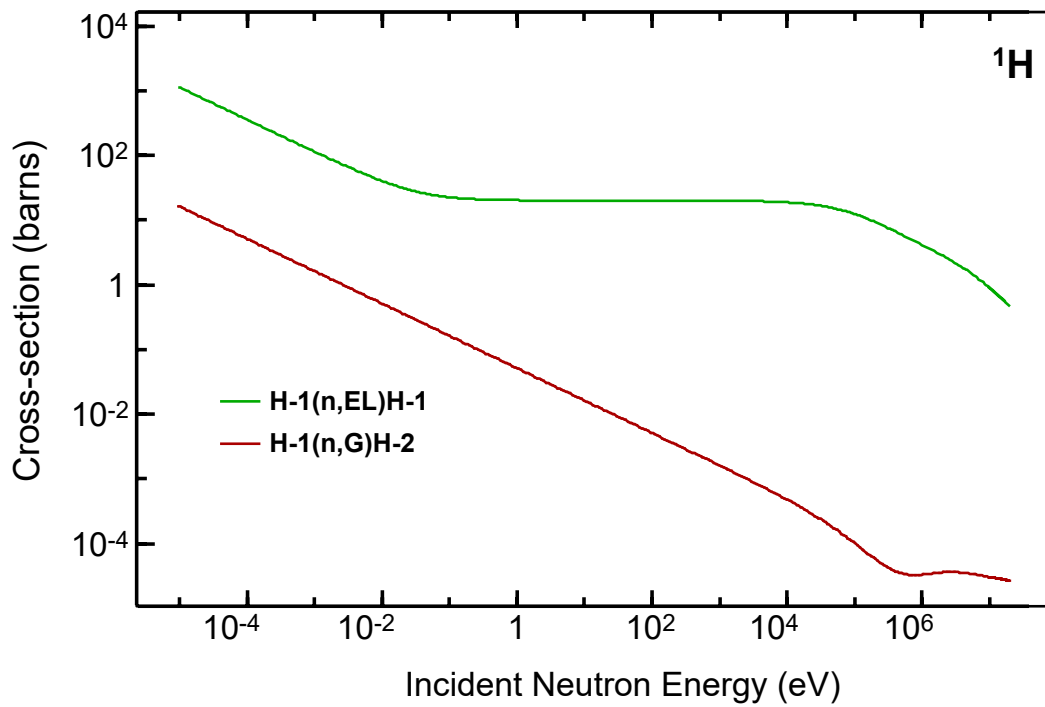
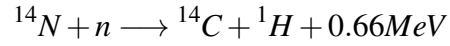


Figure 2.24: ENDF/B-VII.1 cross-sections for ^1H , adapted from [54].

(iii) $^{14}\text{N}(n,p)^{14}\text{C}$ - (n,p) reaction by ^{14}N .



Nitrogen-14 captures low energy thermal neutrons and releases a proton with energy 0.58 MeV. This reaction results in a ^{14}C nucleus, which is a beta emitter with a half-life of 5730 years.

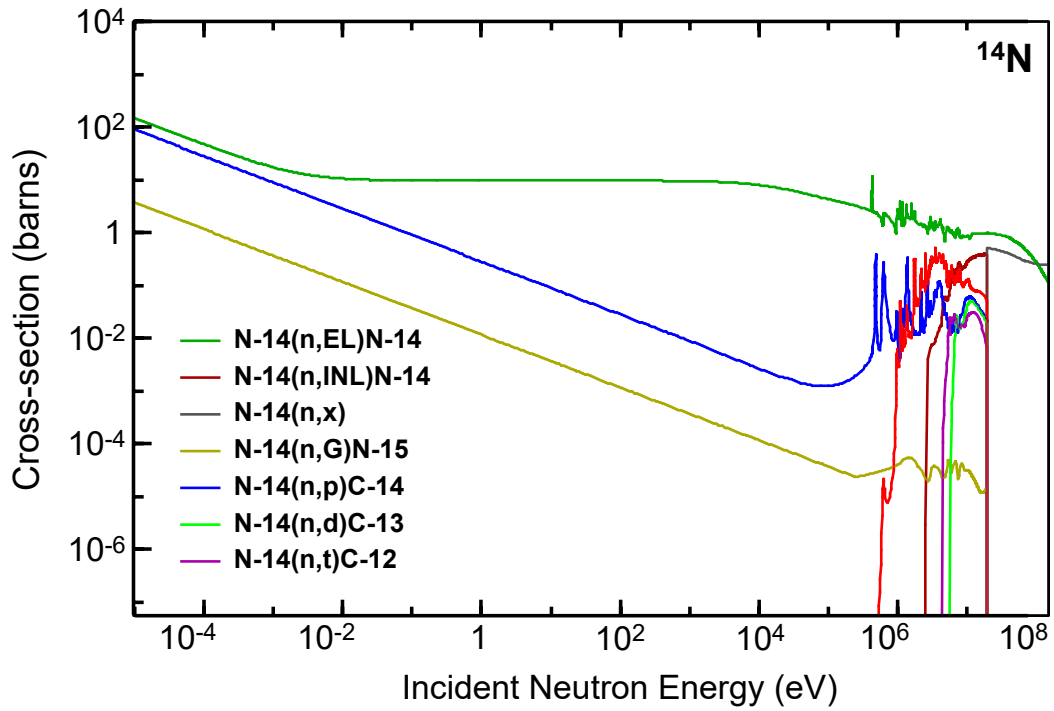


Figure 2.25: ENDF/B-VII.1 cross-sections for ^{14}N , adapted from [54].

(n,x) Neutron Reactions

In this type of neutron interaction, the neutron (n) collides with the nucleus, resulting in the emission of any particle (x) such as neutron, proton, deuteron, alpha, etc - or a combination of such particles. Such examples are:

(n,x)	Comment	New Isotope	Reaction Example
(n, α)	emitted particle is alpha	$\begin{smallmatrix} A-3 \\ Z-2 \end{smallmatrix} X$	$^{16}\text{O}(n,\alpha)^{13}\text{C}$
(n,p)	emitted particle is proton	$\begin{smallmatrix} A-0 \\ Z-1 \end{smallmatrix} X$	$^{27}\text{Al}(n,p)^{27}\text{Mg}$
(n,d)	emitted particle is deuteron	$\begin{smallmatrix} A-1 \\ Z-1 \end{smallmatrix} X$	$^{28}\text{Si}(n,d)^{27}\text{Al}$
(n,n+p)	emitted particles are neutron and proton	$\begin{smallmatrix} A-1 \\ Z-1 \end{smallmatrix} X$	$^{16}\text{O}(n,n+p)^{15}\text{N}$
(n,2n)	emitted particles are two neutrons	$\begin{smallmatrix} A-1 \\ Z-0 \end{smallmatrix} X$	$^{59}\text{Co}(n,2n)^{58}\text{Co}$

Table 2.3: Examples of (n,x) neutron reactions.

Nuclear Fission

Nuclear fission occurs when a neutron interacts with a heavy nucleus, splitting it into lighter nuclei, called the fission fragments. If the absorbed neutron in the heavy nucleus results in a new energy state sufficient for it to split, fission will occur. This reaction gives off a large amount of energy and emits two or more high energy neutrons, and gamma rays. The most commonly referred to heavy nuclide in fission is ^{235}U . The basic process of neutron fission is shown in figure 2.26.

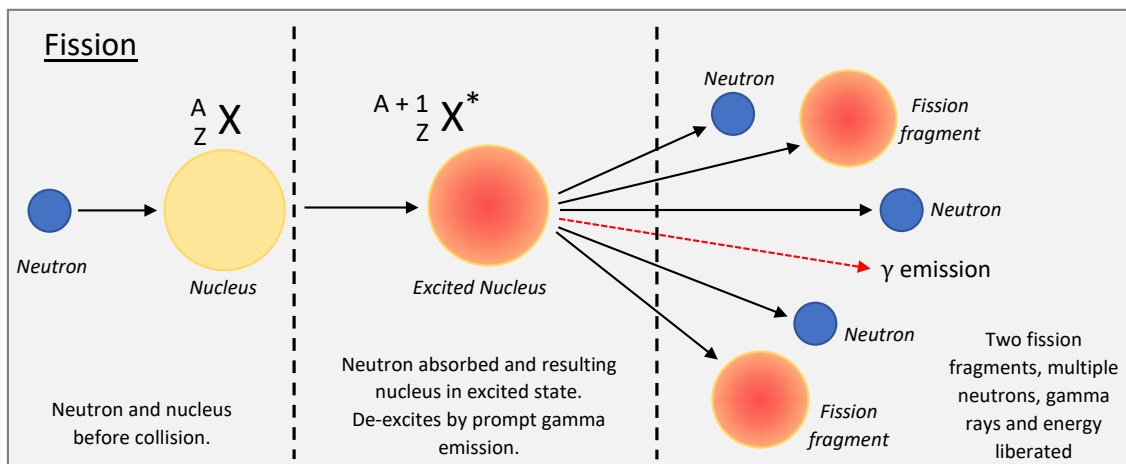


Figure 2.26: Basic process of nuclear fission interactions.

Nuclear cross-section

The probability of an interaction occurring is defined by the nuclear cross-section for the target nucleus, which is dependent on the energy of the incident particle and characteristics of the target. The cross section has units of area, called *barns*, where 1 barn = 10^{-28} m² and is defined by:

$$\sigma = \frac{R}{I} \quad (2.24)$$

where R is the number of reactions per unit time per nucleus, and I is the number of incident particles per unit time per unit area. Important examples of isotopic cross-sections are listed in table 2.4.

Isotope	Cross-section (barns)			
	Thermal (0.0253 eV)		Fast (10 keV)	
	Elastic	Capture	Elastic	Capture
¹ H	30.1	0.3	19.1	0.0005
¹⁰ B	2.2	3844.2	2.1	5.9
¹² C	4.9	0.004	4.4	0.00002
¹⁴ N	10.3	1.8	8.1	0.003
¹⁶ O	3.9	0.0002	3.6	0.00001
²⁷ Al	1.5	0.2	21.3	0.3
¹⁹⁷ Au	8.3	98.8	15.5	1.1

Table 2.4: Cross-sections of important isotopes relating to this work. Data sourced from ENDF/B-VII.1 [54].

The cross-section plots of these neutrons interactions are presented for ¹²C, ¹⁶O, ²⁷Al and ¹⁹⁷Au in figures 2.27, 2.28, 2.29 and 2.30, respectively.

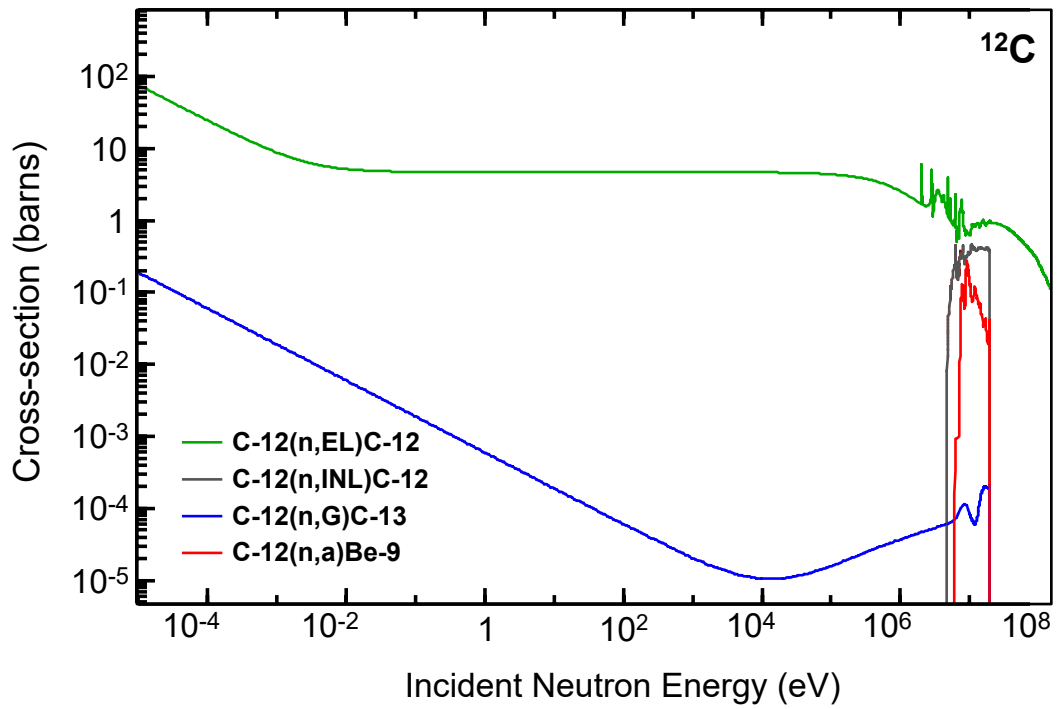


Figure 2.27: ENDF/B-VII.1 cross-sections for ^{12}C , adapted from [54].

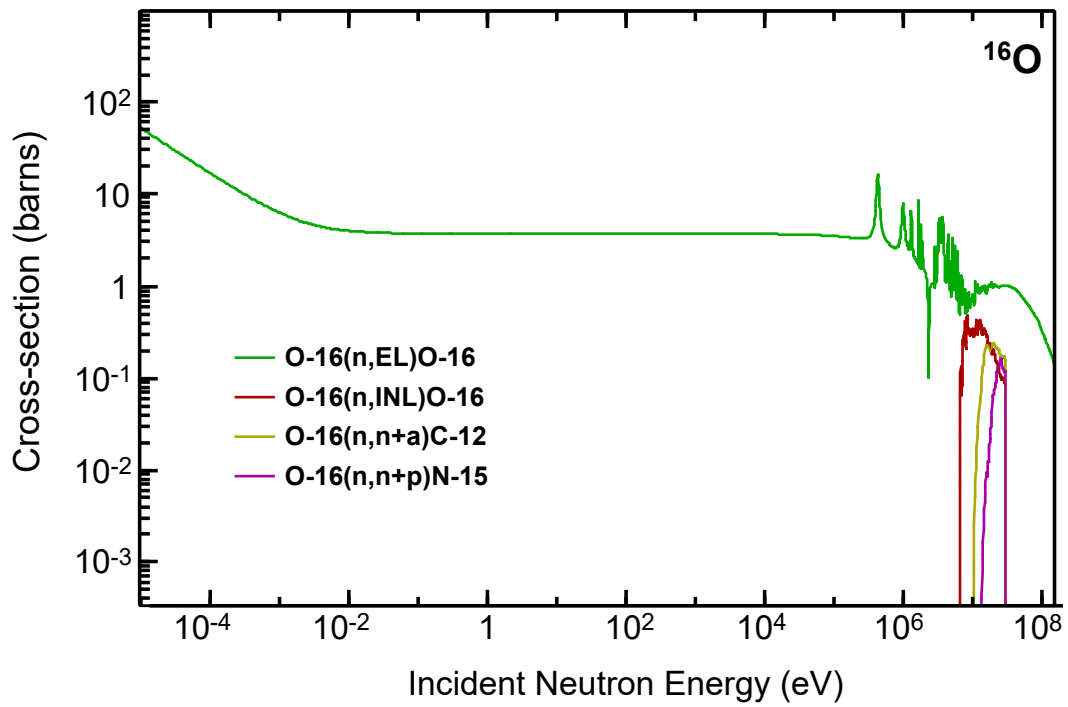


Figure 2.28: ENDF/B-VII.1 cross-sections for ^{16}O , adapted from [54].

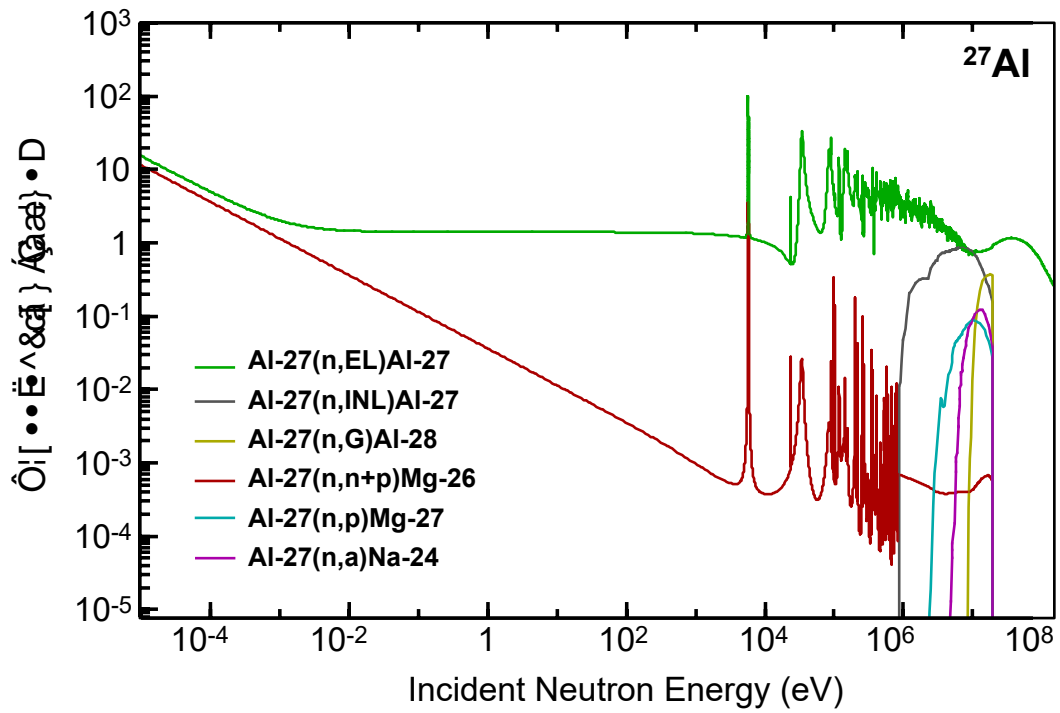


Figure 2.29: ENDF/B-VII.1 cross-sections for ^{27}Al , adapted from [54].

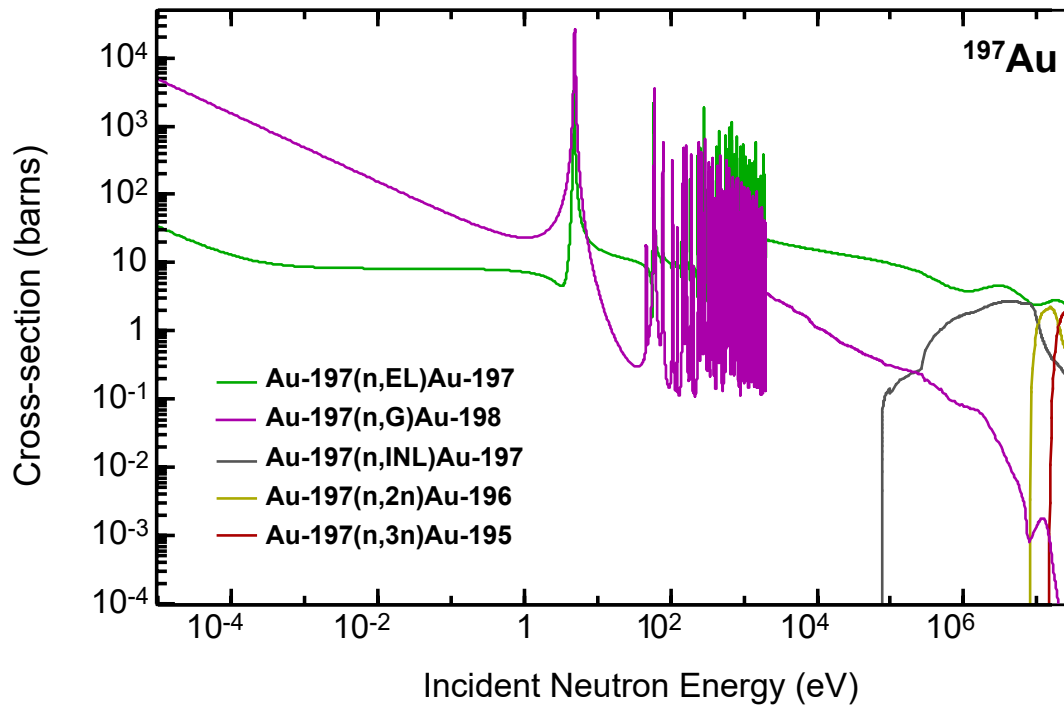


Figure 2.30: ENDF/B-VII.1 cross-sections for ^{197}Au , adapted from [54].

2.2.2 How BNCT Works

Boron Neutron Capture Therapy (BNCT) is a type of radiotherapy that treats cancer using epithermal neutrons, interacting with a boron biodistribution within the body. Because it selectively uptakes incident neutrons to the area of boron concentration, BNCT is referred to as a binary modality. As previously mentioned, there is interest in using BNCT to treat high-grade astrocytomas. This is especially true in Japan, which continues to invest in this type of treatment while other countries look for alternatives to BNCT.

Irradiating a patient who has received a boron delivery drug will result in epithermal neutrons generating a short-term exothermal nuclear reaction within the boron-loaded tumour cells. Due to their high LET and short range, alpha and ^7Li nuclei produced by this reaction are highly toxic; killing the cells from which they originated.

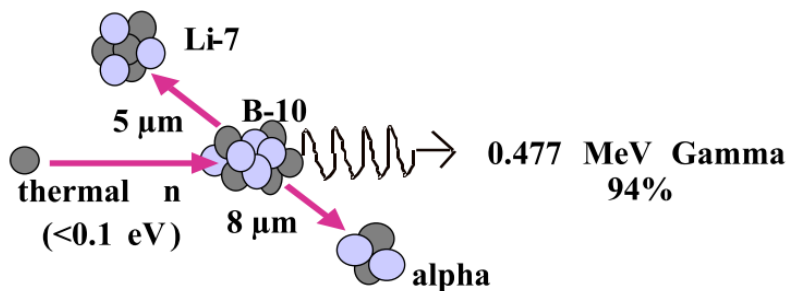


Figure 2.31: Nuclear reaction occurring in BNCT [55].

The success of BNCT is dependent on the tumour cells absorbing a high amount of ^{10}B , as well as a sufficient number of thermal neutrons reaching the boron atoms and inducing boron neutron capture [56]. The nuclear reaction used in BNCT is seen in Figure 2.31. A ^{10}B nucleus absorbs a thermal neutron and promptly generates a ^7Li ion and an alpha particle. The path length of these high-LET products in tissue is between $5\text{--}9\ \mu\text{m}$, offering a method to selectively target malignant cells while sparing neighbouring normal cells, assuming adequate uptake of ^{10}B by tumour cells [57].

A nuclear reactor or linear accelerator is used to generate epithermal neutrons for BNCT. Research in BNCT has been going on for more than 60 years, and it was first

developed utilising nuclear research reactors. The earliest clinical trials with BNCT for malignant brain tumours were conducted in the 1950s and 1960s at Brookhaven National Laboratory (BNL) and Massachusetts Institute of Technology (MIT). As neutron sources were not yet perfected, low-energy thermal neutron beams were used for irradiation in these early trials. However, because neutrons penetrate tissue so shallowly, a craniotomy was required to allow neutrons to reach deeper areas of the brain [58]. BNCT with higher-energy epithermal neutrons (0.5 eV - 10 keV) was not initiated until the 1990s. These clinical trials were carried out at BNL, MIT, and the High Flux Reactor (HFR) in Petten, the Netherlands [57]. Low energy, high intensity particle accelerators have been developed for BNCT as an alternative to nuclear reactors since the 1980s [56].

2.2.3 Treatment Protocols and Techniques

For the past 50 years, researchers have been investigating a wide variety of low molecular weight boron compounds to produce boron-containing delivery agents for BNCT, from which the first generation agents emerged.

The following are the most critical requirements for a BNCT delivery agent[57]:

1. Low toxicity with normal tissue absorption in the context of tumour uptake, with a tumour:normal tissue and tumour:blood (T:Bl) boron concentration ratios of ~ 3 .
2. Tumor boron concentration is $\sim 20 \mu\text{g}^{10}\text{B/g}$ tumour.
3. Relatively quick clearance from blood and normal tissues, but persistence in tumour during the neutron irradiation treatment period.

Sodium borocaptate (BSH) and the boron-containing amino acid boronophenylalanine (BPA) are the only two BNCT delivery methods currently being tested in clinical trials [57]. Unfortunately, neither of these agents meets the above-mentioned criteria, so third generation agents have been studied [57].

BNCT is conducted by first injecting the patient with an intravenous, non-toxic, high-tumour cell specific ^{10}B carrier compound. The carrier compound is distributed to various

tissues in the body which, after a period of time, concentrate in the tumour cells due to their low clearance rate, resulting in lower concentration in healthy cells and a more targeted therapy approach [59]. To be successful, a sufficient amount of the ^{10}B compound must be selectively delivered to all tumour cells to approximately $20\text{ }\mu\text{g/g}$ weight or 10^9 atoms/cell. The diameter of a typical human cell is about $10\text{ }\mu\text{m}$, making the range of alpha particles ($7.8\text{ }\mu\text{m}$) and Li-7 nuclei ($4.1\text{ }\mu\text{m}$) suitable for this application. To cause tumour cell death, enough thermal neutrons must be available for absorption from the $^{10}\text{B}(\text{n},\alpha)^7\text{Li}$ reaction [57].

When epithermal neutrons are irradiated onto the scalp surface, thermal neutrons reach their maximum dose value at the brain surface. When treating deep seated malignancies, intra-operative surgery is no longer required as epithermal energy neutrons have a greater range in tissue allowing them to reach the therapeutic depth of 8cm [57] [58].

The beam requirements for BNCT treatments are provided by the International Atomic Energy Agency (IAEA) [52]. These requirements detail the required neutron flux and dose contamination limits used when designing suitable sources. As epithermal intensity increases, the required irradiation times become shorter. However, proper beam quality must be provided by minimising gamma and fast neutron dose contamination. The epithermal beam intensity has a desired minimum of 10^9 epithermal neutrons/ cm^2/s , with 5×10^8 n/ cm^2/s usable, but results in long irradiation times [52]. Better treatment quality can be achieved by higher intensity beams with adequate boron concentration within tumour cells, reducing reported issues associated with drug clearance from the tumour [52].

The incident beam quality is determined by four parameters [52]:

1. The fast neutron component ($>10\text{ keV}$) has undesirable characteristics, such as the production of high-LET protons, therefore the dose contamination should be kept under $2 \times 10^{-13}\text{ Gy/cm}^2$ per epithermal neutron.
2. The gamma component produced with the incident beam should be kept under $2 \times$

10^{-13} Gy/cm² per epithermal neutron.

3. The ratio between thermal flux and epithermal flux should be below 0.05 to reduce damage to the scalp by neutrons with thermal energies.
4. The ratio between total neutron current and total neutron flux provides a measure of neutrons moving in the forward beam direction. The ratio should be above 0.7 to limit the divergence of the neutron beam and permit flexibility in patient positioning along the beam central axis.

Monte Carlo-based simulations have been demonstrated as a useful investigation tool for BNCT, with many facilities adopting Monte Carlo based software tools for use in BNCT Treatment Planning Systems [60] [61] [62].

2.2.4 Reactor-Based BNCT

Neutrons for therapeutic use, particularly epithermal neutrons for BNCT, can be produced in nuclear fission reactors. The two methods for production include a) direct use of core neutrons as source or b) conversion of reactor's thermal neutrons to high energy fission neutrons by use of a fission converter [63]. Nuclear reactors have been modified to generate neutron sources usable for BNCT [57]. When a neutron is captured by a heavy nucleus such as ²³⁵U, nuclear fission occurs. This forms a new compound which can decay into lighter nuclides, causing a release of energy, gamma radiation and free neutrons. This process is used in nuclear reactors, triggering a chain reaction, producing further fission events and neutrons. Control rods of boron or cadmium can absorb neutrons without undergoing fission and thus are used to control the reaction [63].

One concern with current setups is that treatment reactors for BNCT have one irradiation port which is fixed to the side wall of the irradiation room, limiting the ability to achieve desirable dose distributions compared to using multiple field irradiation [58]. Another concern is that required size and suitable location of research reactors means that patients must be transferred from the hospital to the facility, resulting in delays of a few

weeks post-surgery [58].

KUR - Kyoto University Research Reactor

At the Kyoto University Research Reactor (KUR) in Japan, various mixtures of thermal and epithermal neutron spectra are able to be produced, suitable for head and neck cancers where deep beam penetration may not be required [57]. Epithermal neutrons beams are now standard in all clinical trials of brain tumours [55]. By 2014, KUR had carried out 510 clinical irradiations using the KUR-Heavy Water Irradiation Facility (KUR-HWNIF) reactor-based system [64]. The treatment of brain tumours has been carried out since 1990, and since 2002 no craniotomy is required, solving the issue of delay in needing to transport post-surgical patients.

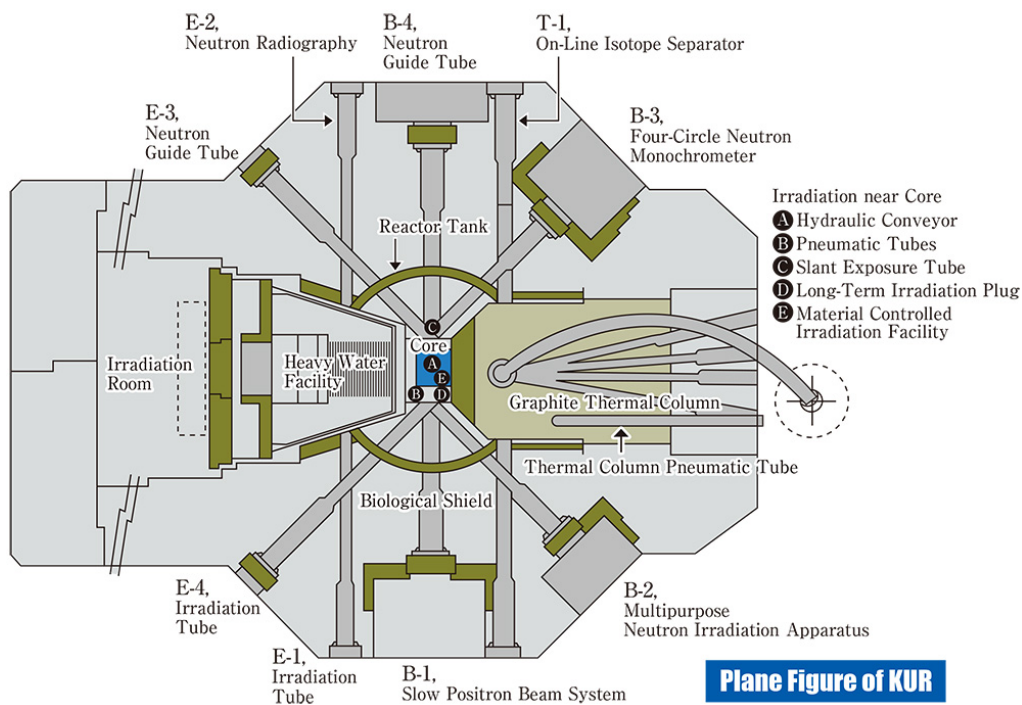


Figure 2.32: Top-down view of the Kyoto University Research Reactor, with main KUR-HWNIF system and other various beam ports shown [65].

Relating to irradiation ports, the clinical potential of neutron beam sources in nuclear reactors is enhanced by reducing fast neutron and photon contamination through particular geometry. Scattering media such as light water, heavy water or graphite can be used to moderate fast neutrons, allowing them to lose energy and thermalise [66].

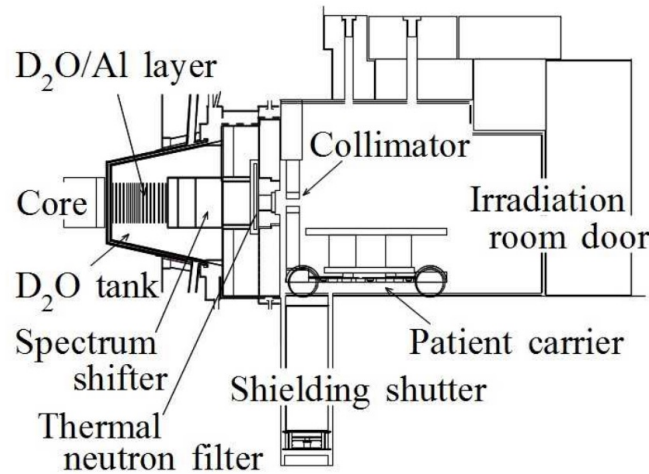


Figure 2.33: Outline of the KUR-HWNIF system installed in KUR for BNCT [64].

The moderated epithermal beam is then collimated to achieve optimal beam geometry for patient irradiation. The shield collimator reflects neutrons back in the direction of the beam, where the outer collimator thermalises the neutron beam and captures the epithermal neutrons hitting it, producing the specific beam shape. Excess gamma emission can be reduced by using appropriate absorbers in collimator material type [59].

FiR 1 - Finland Reactor 1

For example, a Finnish BNCT facility uses a shield of Bi is used to block gamma radiation that is produced by the core and neutron activated parts, but allows neutrons to pass after the moderator. The reactor, FiR 1 (Finland Reactor 1) in Espoo shown in figure 2.34, is a light-water moderated 250kW ^{235}U fueled nuclear reactor [59].

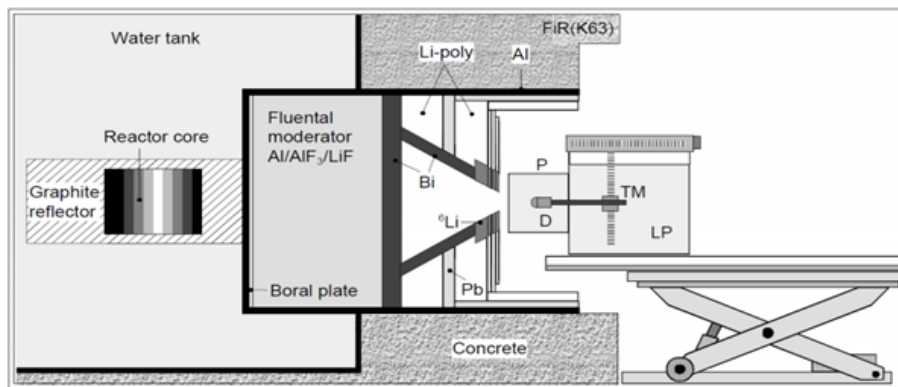


Figure 2.34: Finnish BNCT Fir 1, BNCT facility treatment setup [59].

The FiR 1 core is situated within a water tank with a graphite reflector that is used to maximise neutron flux. The neutron field is moderated by a 63 cm thick block consisting of AlF_3 (69%), Al (30%) and LiF (1%). Natural lithiated polyethylene, ^6Li -PE, is situated at the beam port, at the base of the beam collimator discs, to define the beam outline and produce an optional beam diameter for treatment [59]. The output before collimation produces a high quality, isotropic neutron field with a total free-in-air flux of 1.4×10^9 n/cm²/s [59].

The distance between the patient and the neutron source should be minimised to maximise the flux-to-power ratio of the output beam and produce optimal beam intensity. Gamma radiation is detected by ionisation chambers. Beam position and symmetry are determined by each pair of detectors around the beam axis, maintaining quality control through the beam calibration and dosimetry [59].

2.2.5 Accelerator-Based BNCT

Accelerator-based neutron sources are gaining attention over reactor-based sources due to their reduced safety concerns (minimal exposure to radioactive materials) allowing them to be better suited for use within a hospital [64].

In-hospital accelerator-based neutron sources have been developed and are now providing neutron beams for clinical studies using BNCT [56]. Accelerator-based systems usually consist of a proton accelerator, target, moderator, and collimator. Nuclear interactions with the proton beam within the target material (Be, Li, etc.) will produce neutrons. For neutron therapy, a variety of accelerators types can be employed, including ones that regulate the beam from high-energy proton accelerators to produce the necessary energy range [67]. High energy neutron and proton therapy sources, which are approximately 3-4 times more expensive than a high energy linear accelerator (LINAC) are comparable in cost to particle accelerators appropriate for BNCT [67].

The design of a thermal neutron proton-moderated accelerator source for BNCT from Pavia, Italy is shown in Figure 2.35. A high-intensity proton beam is injected into the

radio-frequency quadrupole (RFQ) by the Trasco Intense Proton Source (TRIPS), which is accelerated and has its trajectory altered by a 90-degree magnet. When a proton beam strikes a beryllium target in the BSA centre, a fully thermalised neutron beam is produced, which can be utilised to treat superficial tumours such skin melanomas [56].

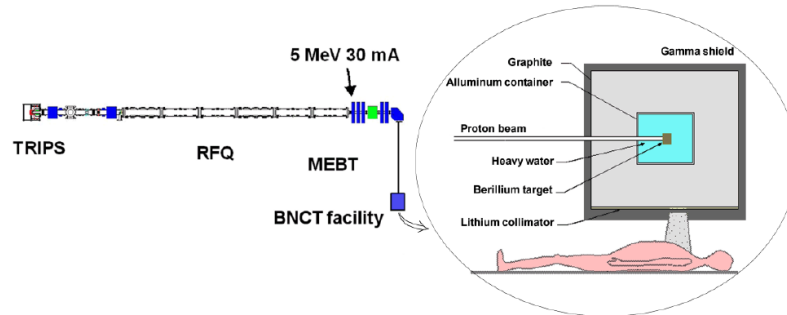


Figure 2.35: BNCT at INFN, Italy utilising thermal neutrons for shallow tumours [56].

For fast neutron and proton treatment, high-energy accelerators like as cyclotrons are used. Studies at PSI have shown that epithermal beams can be created using cyclotrons with the application of appropriate moderators [67]. Low-energy proton accelerator systems with neutron conversion targets are the most popular for BNCT because they can produce neutrons with energies up to 1.5 MeV and are relatively inexpensive. Varied designs can be used to generate different neutron beam energies, allowing for more thermal components in both the surface and deeper areas [67]. When 1.89 MeV protons are bombarded into a target material such as lithium, epithermal neutron emission occurs in a narrow forwards directed cone. However, the quality of the neutron beam produced by these systems is highly dependent on the proton source's voltage stability [67].

In most BNCT proton accelerators, the target material is ^9Be or ^7Li [68]. Lithium is promising because it has a low energy threshold for neutron production, which means that the neutron loss during moderation is lessened. The primary neutron producing reaction with a lithium target is $^7\text{Li}(p,n)^7\text{Be}$. Some neutrons, however, will collide with and react with the ^6Li isotope, which will unavoidably remain in the target [68].

For BNCT applications, fast neutrons produced by (p,n) reactions must be thermalised.

The beam shaping assembly (BSA), which is a stack of several types of materials that shape the beam in terms of both energy and geometry [56], shifts their energy. Due to the greater neutron energy arising from $\text{Be}(p,n)$ reactions, the BSA size and weight is less in a facility that uses a lithium target rather than beryllium [56].

C-BENS - Cyclotron-Based Epithermal Neutron Source

The focus at the Institute for Integrated Radiation and Nuclear Science, Kyoto University (KURNS), Japan, has switched to accelerator-based therapy, including the Cyclotron-Based Epithermal Neutron Source (C-BENS) - the first accelerator-based device for BNCT clinical irradiations, which was completed in 2009. C-BENS beryllium target accelerator clinical trials began in late 2012 [64]. C-BENS utilises the reaction of ${}^9\text{Be}(p,n){}^9\text{B}$ with 30 MeV incident protons. Pb, Fe, Al, and CaF_2 are used to reduce the high-energy neutrons produced by the reaction to the thermal and epithermal range. Cd and Pb filters minimise the production of thermal neutrons and gamma rays, resulting in an epithermal neutron beam suitable for BNCT [64].

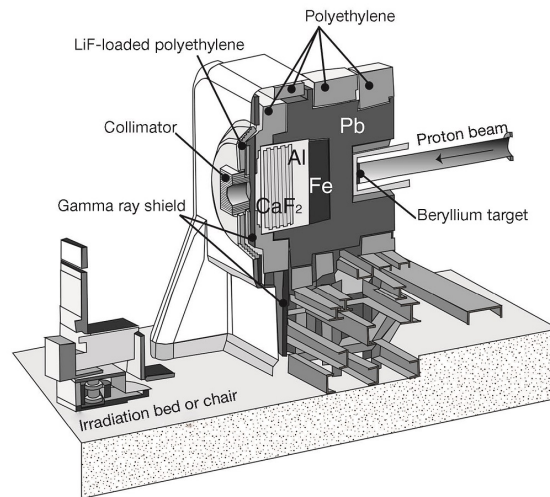


Figure 2.36: Beam shaping assembly and treatment room of C-BENS [69].

The information in Table 2.5 can be used to compare the reactor-based KUR-HWNIF with the accelerator-based C-BENS at the KURNS facilities. Figure 2.37 depicts the neutron flux of C-BENS and KUR-HWNIF. The beam quality of C-BENS is slightly better than KUR-HWNIF due to smaller contamination of fast neutrons and gamma rays [64].

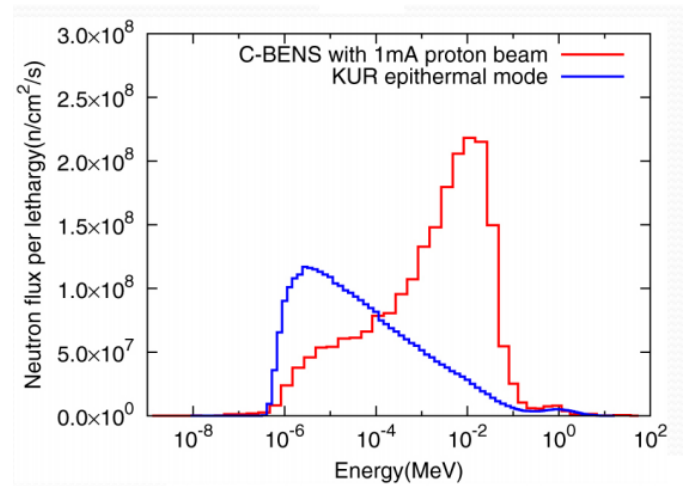


Figure 2.37: Neutron flux comparison between KUR-HWNIF and C-BENS at KURNS [70].

Facility	Type	Epi-thermal neutron flux ($\text{cm}^{-2}\text{s}^{-1}$)	Fast neutron dose / epi-thermal flux (Gy/cm^{-2})	Gamma-ray dose / epi-thermal flux (Gy/cm^{-2})	Purpose	BNCT application
KUR-HWNIF (epi-thermal mode)	Reactor- based	9.1×10^8	6.1×10^{-13}	2.4×10^{-13}	Research and study	New challenge and wider application
C-BENS	Accelerator -based	1.9×10^9	5.8×10^{-13}	7.8×10^{-14}	Clinical use only	For tumors with sufficient experiments and achievements at KUR-HWNIF

Table 2.5: Comparison between the reactor-based system (KUR-HWNIF) and the accelerator-based system (C-BENS) at KURNS [64].

C-BENS has more than twice the neutron flux in the epithermal region compared to KUR-HWNIF.

iBNCT - Ibaraki Tokai BNCT Facility

The Ibaraki Neutron Medical Research Center (iNMRC) in Tokai Village, Japan, has made recent advances in neutron production using accelerators for BNCT [61]. The iNMRC facility at the University of Tsukuba is also known as Ibaraki-BNCT (iBNCT). In recent years, the development of accelerators for BNCT facilities has become more common in Japan, owing in part to the negative stigma associated with nuclear reactors. Tokai Village's team is working to enhance accelerator technology as a safe and reliable neutron source for BNCT operations both in Japan and around the world.

The accelerator-based neutron beam was built with the accelerating tubes in one room

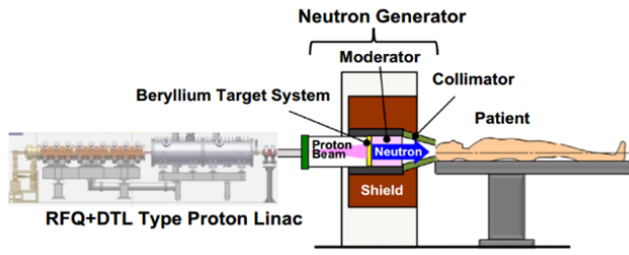


Figure 2.38: Schematic of Tokai LINAC-based BNCT Device [61].

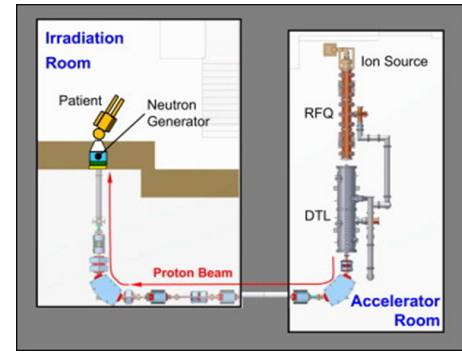


Figure 2.39: Layout of facility: accelerator room and irradiation room [61].

and the proton beam delivered to the irradiation room via a separation wall. This incident beam is directed towards the neutron generator, resulting in the production of neutrons, before being delivered into the patient [61]. The LINAC utilised in Tokai is approximately 8 metres long and has a diameter of around 1.5 metres [61].

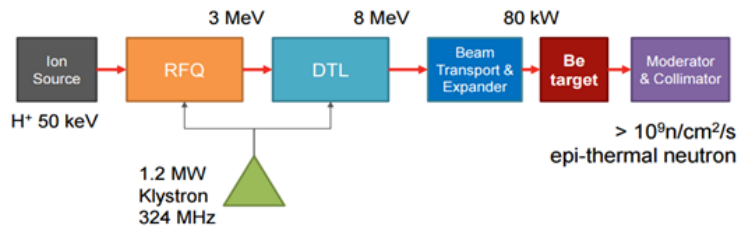


Figure 2.40: Basic Configuration of Tokai iBNCT proton LINAC [71].

To produce neutrons, Radio-Frequency Quadrupole (RFQ) and Drift Tube LINAC (DTL) linear proton accelerators are used with moderators. An incident proton energy of 8 MeV with power 80 kW is generated from the LINAC at 50 mA peak current. Beryllium-9, which is also employed at C-BENS, is used as the neutron generator target material, creating high-intensity neutrons from ${}^9\text{Be}(p,n){}^9\text{B}$ processes [61]. The neutron flux produced by interacting with ${}^9\text{Be}$ is epithermal neutrons of high intensity, which are suited for BNCT [61]. As shown in figure 2.38, the neutron generator comprises of a moderator, collimator, and shielding that are designed together with the beryllium target system. The Radio-Frequency Quadrupole (RFQ) produces 3 MeV of output energy, with a 5 MeV gain from the Drift Tube LINAC (DTL). Both completed construction in 2012 [61].

The target materials ^9Be and ^7Li were explored for the generation of neutrons with a proton accelerator [68]. Beryllium has a greater energy threshold than lithium, requiring a more powerful accelerator, yet it is inactive in water [68]. Another factor to consider was the target's radioactivity after neutron generation, with ^9B having a half-life of 8×10^{-10} ns and ^7Be having a half-life of 53.22 days [72]. As a result, when choosing the target material for the iBNCT facility, neutron generation through the $^9\text{Be}(p,n)^9\text{B}$ reaction was optimal [68]. The fundamental goal of accelerator-based BNCT development is to enable hospital-based facilities with very little residual radioactivity. One of the main reasons for not using ^7Li is that the resulting ^7Be compounds have a long half-life and high radioactivity [68].

A beryllium plate with a copper backing plate served as a heat sink in the first neutron target device. An intermediate material was required to avoid scorching due to the high current proton incidence [61]. The removal of heat generated by the 80 kW proton power incident on the thin beryllium plate was a key concern, leading to the creation of a three-layered target. The first layer is 0.5 mm thick beryllium, which generates neutrons, and the second layer is 0.5 mm thick palladium, which absorbs hydrogen and stops protons. The third layer is made up of oxygen-free copper, which allows for better heat conduction when the system is cooled with water [71].

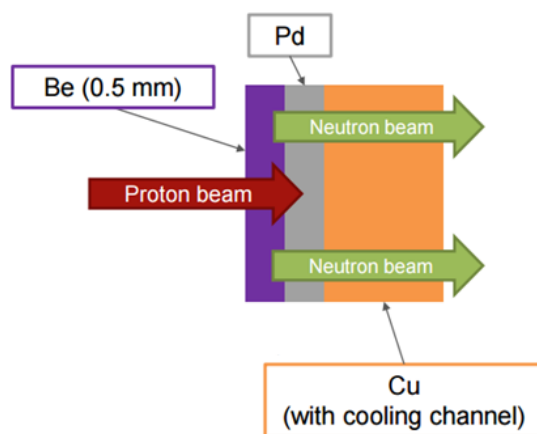


Figure 2.41: Three layer neutron generator target at Tokai iBNCT [71].

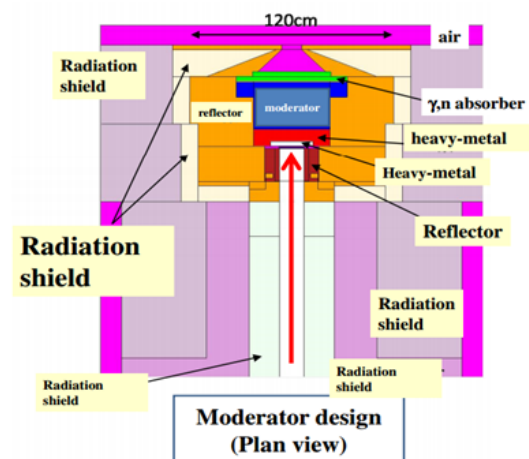


Figure 2.42: Neutron Generator at iBNCT, showing moderator components for neutron energy selection [68].

The maximum energy of neutrons produced by a proton beam is typically lower than the energy of the incident protons by about 2 MeV [68]. This implies that 6 MeV neutrons can be yielded from 8 MeV incident protons. The Bragg peak position of 8 MeV protons is less than 1 mm, which allows the incident proton beam to stop in the target. Therefore such energy for the incident beam was selected to overcome limitations such as heat removal and residual radiation [68].

Table 2.6 shows the beam characteristics achieved with a 10 mA average beam current and an 8 MeV incident proton beam. The contamination rate of fast neutrons and gamma rays is less than the IAEA's recommended maximum level of 2×10^{-13} Gy/cm² per epithermal neutron [52]. The ratio of thermal to epithermal flux is found to be less than 0.05, with a ratio of 0.043. The simulated beam characteristics reveal that the iBNCT facility is capable of producing epithermal neutron beams that meet the IAEA's guidelines.

Neutron Flux	Thermal (~ 0.5 eV)	1.85×10^8 n/cm ² /s
	Epi-thermal (0.5 eV \sim 10 keV)	4.34×10^9 n/cm²/s
	Fast (10 keV \sim)	4.70×10^8 n/cm ² /s
Gamma ray dose		0.74 Gy/h
Contamination ratio	Fast neutron	5.28×10^{-13} Gy \cdot cm ²
	Gamma ray	4.75×10^{-14} Gy \cdot cm ²

Table 2.6: Neutron Flux and Energies for iBNCT output [71].

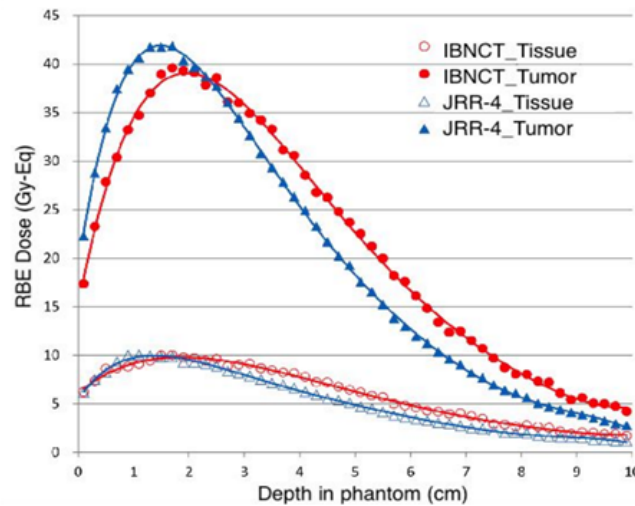


Figure 2.43: Simulated depth-dose curve; iBNCT (accelerator) and JRR-4 (reactor) [73].

Monte Carlo simulations of the most recent facility design have shown that an epither-

mal neutron flux of 4.34×10^9 n/cm²/sec can be generated [71]. The beam quality is sufficient for usage in BNCT, according to a simulated depth-dose utilising BPA agent of 30 parts-per-million (ppm) in tumour and 10 ppm in tissue [52]. Figure 2.43 depicts the depth-dose curve comparing accelerator-based iBNCT with reactor-based JRR-4. This demonstrates that the iBNCT facility can provide an RBE that is comparable to reactor-based treatment [68].

Figure 2.44 depicts the iBNCT neutron flux as well as a comparison with the JRR-4 reactor. The overall neutron flux in simulated iBNCT beam quality is 4.66×10^9 n/cm²/sec, which is more than four times higher than that of JRR-4 [68].

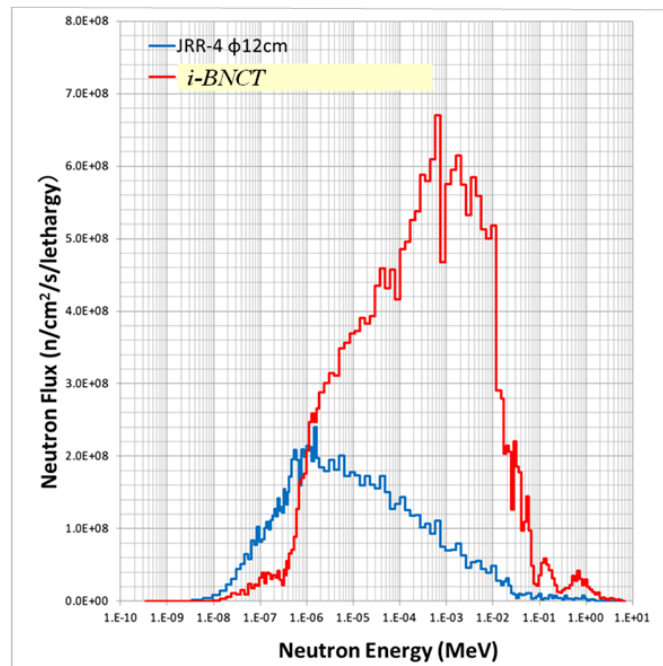


Figure 2.44: Neutron flux (n/cm²/s/lethargy) as a function of energy (MeV) comparing JRR-4 to iBNCT [68].

2.2.6 Open Issues with BNCT

The neutron sources, boron compounds, and therapeutic uses are all key concerns with BNCT. The necessity for more effective boron delivery agents, as well as a quantitative estimation of boron content in tumour volume before therapy, are both critical challenges that must be addressed.

The optimisation of agent delivery to tumour cells is required to increase the dose delivered whilst reducing unwanted dose to normal tissue. Another factor to consider is the ratio of boron agent concentration in tumour to normal tissue, which limits the quantity of boron concentration that can be used. In an ideal world, all of the boron agent would reach the tumour cells, resulting in localised double-strand breaks. Since the concentration must be kept low, the overall treatment time is increased, with BNCT taking between 20 and 90 minutes, compared to less than 15 minutes for other radiation modalities [66].

Aside from boron delivery agents, enhancing the neutron source is another major issue in BNCT. These problems necessitate increasing the epithermal component while reducing dose contamination from fast neutrons and gamma sources [52].

Pre and post BNCT imaging is being used to determine whether the tumour size has reduced after therapy. The detection of prompt-gamma rays has been limited to proper real-time treatment measures, which is still in its early phases [61]. The goal of the research presented here is to improve BNCT treatment dosimetry using epithermal neutron beam characteristics and known ^{10}B concentrations.

2.2.7 Detectors used for BNCT

The capacity to accurately measure the absorbed dose to the patient and anticipate the RBE associated with it is one of the most difficult parts of BNCT. The relative contribution of the absorbed dosage components in BNCT varies with depth, making their determination problematic. Because neutrons are moderated within the body, the RBE of neutrons can vary dramatically with depth. Treatment planning in BNCT requires an accurate assessment of each component in the treatment field as well as a grasp of the overall RBE [74].

Dual-dosimeter methods are typically employed to calculate the absorbed dose because the radiation field created during BNCT contains both neutrons and photons, utilising an approach designed for mixed fields dosimetry [17]. This method, which uses activation

foils to monitor the thermal neutron flux and calculate the BNC dosage, cannot directly quantify the absorbed dose owing to BNC reactions. A second foil measurement is required for energy separation because epithermal neutrons in the beam induce some of the activation in the foil. To acquire the photon, neutron, and BNC absorbed dose components, this must be done four times, resulting in high uncertainties when using this method for BNCT dosimetry [74]. This outlines the importance of such a device that can measure all absorbed components of the mixed radiation field simultaneously.

The dose components associated with BNCT can be detected and characterised using a variety of ways. Chemical analysis, such as mass spectrometry, or physical measurements of the ^{10}B capture are examples of this. Physical measurement approaches include the use of TEPCs to detect alpha particles and prompt-gamma detectors.

Neutron Converters

Accurate neutron detection requires a low-weight device that is compact, robust and produces a fast response. As neutrons do not interact with matter by direct ionisation and produce free carriers, it is necessary to convert them into detectable charged particles using appropriate materials [75].

The most common elements with a high thermal cross section that can be used as a converter to detect thermal neutrons are Boron-10, Lithium-6 and Helium-3 [75]. Helium-3 is typically applied in gas-proportional counters for neutron detection. However due to its shortage, the development of solid-state thermal neutron detectors is required. The neutron detection efficiency in lithium-6 targets are limited due to self-absorption, making boron-10 the suitable candidate for solid-state neutron detectors.

Most neutron conversion layers are fabricated directly onto the detector surface or onto a substrate such as copper, aluminium or silicon oxide. These methods are mostly described by PVD [76] and sputtering techniques [77]. Alternative sources for neutron converters include boronated polymers [78][4][79] and boronated glass [80]. A novel design for neutron detectors based on the isotope ^{10}B instead of ^3He has been suggested by the

European Spallation Source (ESS) to overcome the very limited availability of ^3He . In the detector design, very large area aluminum blades are coated with a thin film containing high amounts of ^{10}B by DC magnetron sputtering [77]. The prototype boron-layer detector has been developed at the Linköping University. It has a detection surface of $8\text{cm} \times 200\text{cm}$ with 30 layers of $^{10}\text{B}_4\text{C}$, each a micron thick. Enriched boron-10 carbide ($^{10}\text{B}_4\text{C}$) was chosen as the thin film material instead of pure ^{10}B , since it is easier to handle in a deposition process and due to its high resistance towards oxidation and wear.

The ESS detector coatings workshop is equipped with 4 magnetron sputtering machines, able to coat large ($50 \times 10\text{ cm}^2$) targets [81]. 27000 blades were coated with $^{10}\text{B}_4\text{C}$ in 45 days, proving the mass production capabilities of the ESS coatings workshop. $^{10}\text{B}_4\text{C}$ can be properly transferred to several substrates like aluminium, stainless steel, alumina, silicon, copper and Kapton. Difficult substrates, where the adhesion is not optimal are glass, Teflon, nickel and MgO.

Piscitelli et al. (2016) have acquired $^{10}\text{B}_4\text{C}$ thin films from Linköping University and characterised them using X-ray spectroscopy and neutron reflectometry techniques [82], confirming the effectiveness of the thin films as a neutron conversion material.

Commercially available thin films comprised of enriched ^{10}B are difficult to find. The Linköping University Thin Films Division have made advanced developments in producing boron carbide films, but they are not commercially available yet. However, a small number of prototype samples for testing have been acquired for the work completed in this project.

Many groups utilise physical or chemical vapour deposition techniques to fabricate a neutron conversion layer onto the surface of the detector. This requires the fabrication of dedicated detectors with the addition of a neutron converting layer. The development of a neutron detector composed of a plasma CVD-grown ^{10}B enriched film on c-Si substrate has been shown [76]. This method produces a thin layer of ^{10}B directly onto the silicon diode surface, allowing them to be electrically connected.

Borosilicate glass (BSG) is used as a surface passivation layer which provides protection of a chip surface. Arita et al. (2001) have demonstrated that ^{10}B in a BSG passivation layer is responsible for sensitising a circuit to neutron radiation [80]. A patent (2005) has been taken out which outlines the use of a BSG passivation substrate as a neutron conversion device near an active semiconductor to produce a solid state thermal neutron detector [83]. Thus, the number of papers providing characterisation of a neutron converting BSG passivation layer in a solid-state detector are limited and difficult to find.

Kaplan (2001) produced boronated polymethyl methacrylate (PMMA) for coating the surface of a MOSFET chip [79]. Decaborane ($\text{B}_{10}\text{H}_{14}$) and PMMA were selected as they are soluble in dichloroethane. For the preparation of 1% weight ^{10}B PMMA cover, 10 g of PMMA was dissolved in 300 mL of dichloroethane to which 0.625 g of decaborane was added. The solution was then deposited drop by drop onto the surface of the MOSFET chip and left to dry. The thickness of the cover on detector was estimated between 50 μm and 100 μm [79]. Bradley (1999) has utilised a similar methodology to produce a detachable PMMA-based neutron converter without the need for sacrificing the device for boron-specific measurements [4]. A detachable boron coated PMMA lid was coated with the same 1% ^{10}B solution used by Kaplan.

As fast neutrons are moderated and thermalised in PMMA, the use of a removable ^{10}B coated PMMA layer above the surface of the detector could provide an effective solution as a fast neutron converter. As this method of producing a conversion layer does not require further detector fabrication and is simple to perform, this may be the most suitable option.

Tissue Equivalent Proportional Counters

TEPCs are most commonly used for measuring the individual dose components of the radiation fields associated with BNC [57]. A tissue equivalent mixture of methane, propane, or other gases is commonly used [1] for BNCT. Dosimetry using TEPCs allows the direct measurement of the BNC dose, with smaller uncertainties in the neutron absorbed dose.

Most importantly, lineal energy spectra measured with TEPCs can be used to predict the RBE through the use of biological weighting functions [74].

SOI Microdosimeters

Bradley and Rosenfeld [2] demonstrated the first application of solid-state silicon p-n junction SOI arrays for microdosimetric measurements in BNCT. The use of boron coated silicon diode arrays as microdosimetric detectors for BNCT was demonstrated. Bradley analyzed the effects of several boron-coating options on microdosimetric spectra as well as device orientation. The boron coating simulates a biological circumstance in which boron accumulates on the cell surface, such as when boron binds to monoclonal antibodies, and allows researchers to study the microdosimetric spectra within cell nuclei using a two-dimensional array of cells [2].

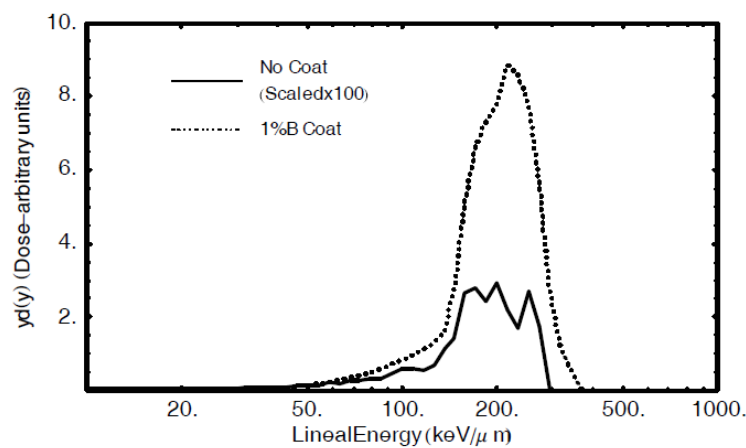


Figure 2.45: Microdosimetric spectra comparing boron coated devices irradiated by BMRR epithermal source [2].

Between 1-1.35 μm , the device overlayer made of SiO_2 and Al closely represents the cytoplasm gap between the cell nucleus and the surface [2]. The device was made with a Lucite coating containing 1% ^{10}B and a minimum coating thickness of 7.4 μm , which corresponds to the range of a 1.78 MeV alpha produced by boron neutron capture. If the lucite coating is excessively thick, thermal neutron fluence may be reduced. Figure 2.45 shows Bradley's results employing a BMRR epithermal source with a 300 kW reactor output. In figure 2.45, the lineal spectrum of the device produced with no boron coating

has been scaled up by 100, revealing the minor contribution from boron fission events within the device's p^+ doped area.

The fact that boron implantation directly into the SV resulted in relatively few fission events in a non-coated device demonstrates the validity of boron implantation directly onto the SV. This system would be able to replicate boron deposition in multiple parts of a cell, something that a proportional gas counter cannot do.

Bradley [4] has discussed the effect of ^{10}B present in the microdosimeter's p^+ area and substrate. The number of boron thermal neutron events in the substrate was four orders of magnitude lower than in the p^+ region of the detector, according to Bradley. Additionally, the number of boron thermal events on the top of the detector's 1% ^{10}B impregnated Lucite cover was up to 1300 times higher than in the p^+ region.

When employed in epithermal neutron fields for BNCT, the contribution of events coming from the p^+ boron implanted in the silicon SV of these devices is minimal [2]. It has been proposed that specialised BNCT SOI devices with boron implanted regions on the chip might be used to model boron cellular dispersion. A proportional gas counter, which cannot represent an array of individual cells, would not be able to do this.

Prompt Gamma Ray Imaging

With recent developments in the building of high-resolution instrumentation for this application, the use of prompt-gamma detection for computing the ^{10}B concentration in the treatment area has been theorised [84]. Drug kinetics, such as clearance rates from various organ and tissue types, are currently used to compute the ^{10}B within the tumour in the treatment area.

The ultimate goal for all BNCT facilities is to adopt prompt-gamma detection by Single-Photon Emission Computed Tomography (SPECT), which would allow them to reproduce 3D images of boron-rich areas without the need for extra ionising radiation, such as that delivered by CT. Kobayashi [85] proposed using SPECT in BNCT to mea-

sure the 478 keV prompt-gamma ray released during boron capture. Tokai iBNCT is now developing a treatment planning system that includes prompt-gamma SPECT imaging of boron removal from tumour cells in real time [61].

Yoon et. al. [86] demonstrated that image reconstruction of a prompt-gamma ray identified during BNCT simulation may be analysed and used to create a picture relative to ^{10}B concentration within phantom zones. For detection, LYSO scintillation crystals were employed, which are extensively used in SPECT and PET imaging. The compactness and longevity of CdTe semiconductor detectors make them ideal for prompt-gamma SPECT experiments [84]. CdTe also has the advantage of being able to operate at room temperature, making it better suited for combining many detectors into an array [87].

Neutron Activation Analysis

Neutron Activation Analysis (NAA) provides risk evaluation and quantification of isotopes produced from interactions. The analysis includes half-life decay measurements and interpretation of the characteristic gamma ray spectrum. NAA can also be useful for determining which nuclear reactions have taken place within the sample and the composition of the non-radioactive original material. NAA is often used in practice for detection of semiconductor impurities and lunar and planetary surface composition. Figure 2.46 shows the use of NAA to identify the reactions in the process of neutron capture.

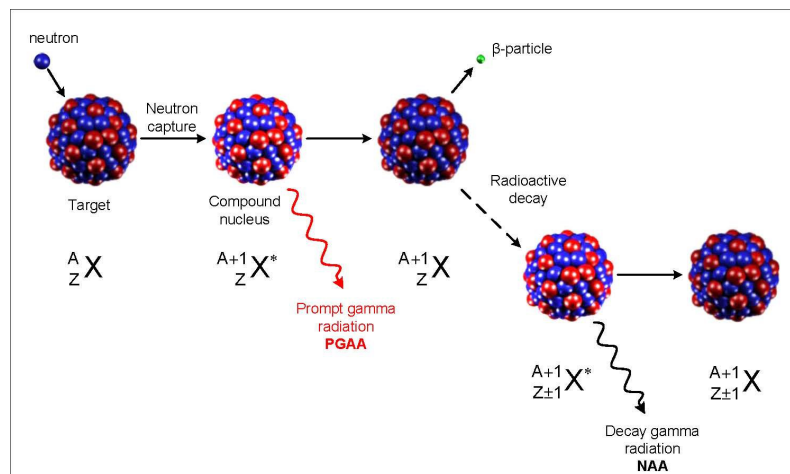


Figure 2.46: Diagram illustrating the process of neutron capture by a target nucleus followed by the emission of gamma rays [88].

The production of radioactive nuclei is described by:

$$\frac{dN}{dt} = \phi \sigma N_0 - \lambda N = RN_0 - \lambda N \quad (2.25)$$

Where ϕ is neutron flux in neutrons/cm²/sec, σ is reaction cross section in cm², N_0 is the number of target nuclei per cm³, R is the reaction rate per second, N is number of radioactive nuclei per cm³, λ is the decay constant in sec⁻¹. The disintegration rate of the produced radionuclide after a set irradiation time is:

$$D(t_d) = N(1 - e^{-\lambda t_d}) \quad (2.26)$$

Where $D(t_d)$ is disintegration rate in Bq of produced radionuclide at time t_d after irradiation time has finished [88].

2.3 Hadrons in Charged Particle Therapy

The treatment of cancer using highly energised charged particles, such as protons and heavy ions, is a type of hadron therapy. Hadron therapy modalities that utilise charged particles have several advantages, making them superior to conventional radiotherapy treatments with X-rays. The key feature is that charged particles have maximum dose deposition at the end of their range, inverse to photons, which have maximum dose deposition at the surface. Additionally, charged particles penetrate tissue with minimal lateral dispersion, therefore, much better dose conformity than photons. Heavy ions have clustered ionisation tracks when passing through a cell volume, which results in more complex damage within the cell, thus a higher radiobiological effectiveness [11].

Photons are considered as low-LET radiation. They deposit energy within cells by exciting or liberating the tissue's electrons. These electrons can scatter at large angles in the irradiated region, damaging DNA directly, or indirectly by producing free radicals. These highly reactive molecules diffuse and damage DNA, even at a greater distance. The

resulting energy deposition pattern is spread over a relatively large volume. The overall effect by photons is referred to as sparsely ionising radiation, which has lower damage effect in the cells. As photons induce mostly single-strand breaks in the DNA, the cell is able to repair, either correctly or incorrectly, with the latter leading to cell mutations or secondary tumours [11]. The typical LET of several low-LET radiation types are shown in table 2.7.

Radiation Type	LET in tissue (keV/ μm)
11 MeV electrons	0.2
Cobalt-60 gamma-rays (~ 1.25 MeV)	0.24
250 kVp X-rays	2.0

Table 2.7: Typical LET of low-LET radiation types in tissue [89].

Charged particles (protons and heavy ions) are high-LET radiation, primarily damaging the DNA through direct interaction. The ionisation is clustered in close proximity to the particle trajectory as delta electrons. As such, charged particles are referred to as densely ionising radiation, with higher probability of double-strand breaks (DSB) in the DNA. When DNA is damaged by DSB, there is a higher cell death probability as it is damaged beyond repair and will undergo apoptosis (programmed cell death) [11].

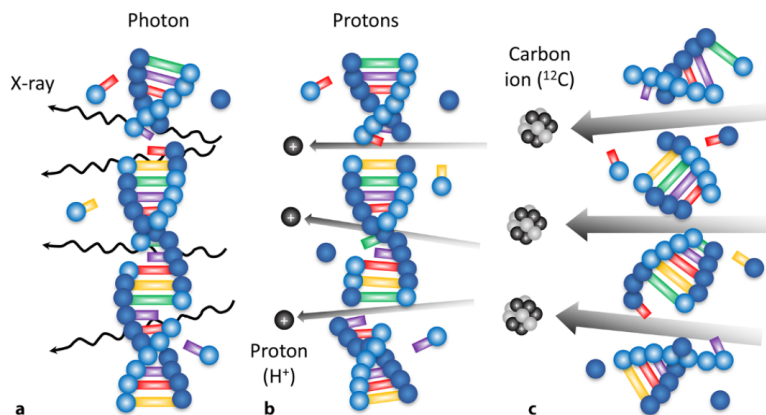


Figure 2.47: Simplified biological differences between photons, protons, and carbon ions. Photons have mostly single strand DNA breaks by indirect damage, where protons and carbon ions have direct damage to DNA by DSB. [90]

The relative depth dose of 8 MV X-rays, 60 MeV fast neutrons, 148 MeV/u protons and 270 MeV/u ^{12}C ions in tissue is shown in figure 2.48. The range of 8 MV X-rays is comparable to 60 MeV neutrons, depositing most of its dose at the surface. In contrast to proton and ^{12}C therapy, the maximum dose is deposited within several centimeters of tissue penetration and distal tissues receive a gradually decreasing dose. The characteristic pronounced peak on the depth dose curves of heavy ions is known as the Bragg Peak (BP). The BP of individual heavy ion beam energies are referred to as “pristine” peaks. The carbon ion BP is sharper due to less multiple scattering and has a longer tail due to lighter fragments produced.

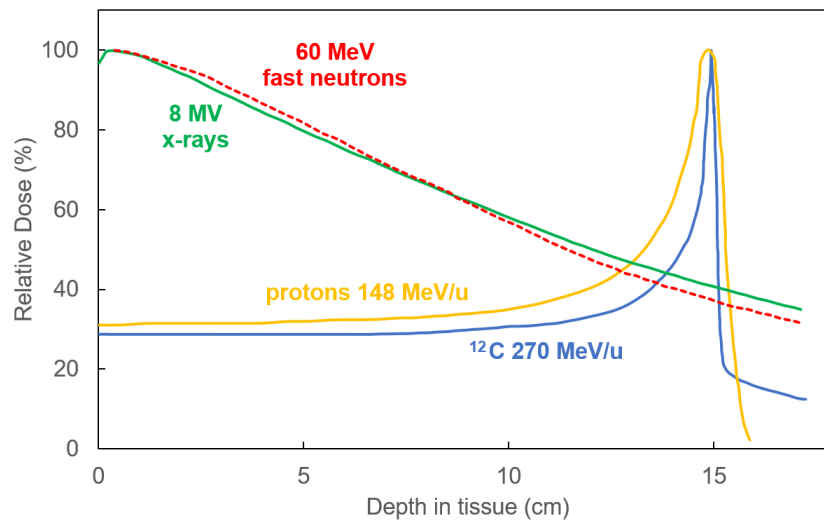


Figure 2.48: Dose dose distributions for various therapy beams. Protons and carbon ions exhibit the Bragg peak at the end of their range, compared with the almost exponential dose distribution of X-rays and fast neutrons. Adapted from [91].

The summation of multiple pristine peaks from individual heavy ion beam energies and intensities can be used to produce the Spread-out Bragg Peak (SOBP). This SOBP is calculated through treatment planning and delivered such that the desired depth in the target receives the maximum radiation dose, as shown in figure 2.49. The sharp dose drop-off following the Bragg peak allows tissues distal to the target to be spared.

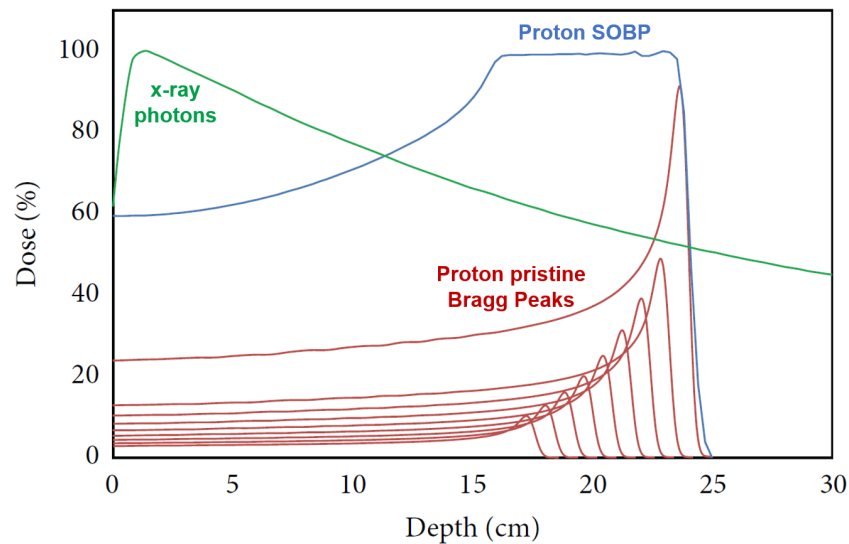


Figure 2.49: Depth dose plots of pristine proton Bragg peaks (red) and their summation to form the SOBP (blue). Photons (green) are shown for comparison [92].

Figure 2.50 compares the dose contour maps of a one port (fixed single position) irradiation by X-rays and SOBP carbon ion beam. The sparing of normal tissue at the surface and distal to the desired target can be seen, demonstrating the advantage of heavy ion beams versus traditional radiotherapy.

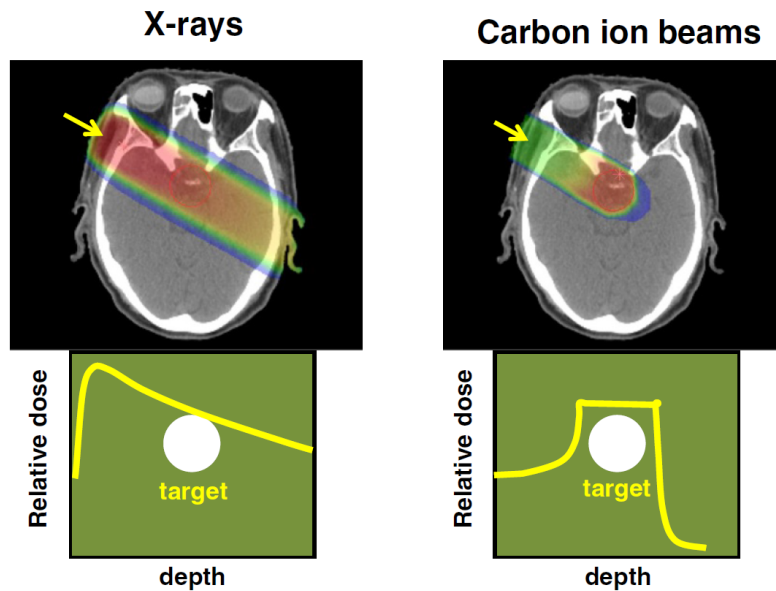


Figure 2.50: Comparison of 2 Gy dose contour maps from one port irradiation by low-LET photons versus high-LET carbon ions [93].

The typical LET of several high-LET radiation types are shown in table 2.8. The importance of the Bragg Peak is emphasised here through the significant difference in LET at the entrance and BP locations.

Radiation Type	Range in tissue	Entrance LET in tissue (keV/ μ m)	LET in tissue at BP (keV/ μ m)
148 MeV/u protons	147.55 mm	0.6	93
5.5 MeV alpha particles	40.89 μ m	88.1	240
260 MeV/u carbon ions	141.74 mm	13.6	937

Table 2.8: Typical range and LET of high-LET radiation types in tissue [47].

The first proposal to use charged particles for therapeutic purposes was by R. Wilson in 1946 [94]. This led to increased investigations of accelerated proton beams and their radiobiological effects at Lawrence Berkeley Laboratory (LBL) in 1948. By 1954, the first patients were being treated with protons at LBL [95].

Treatment with heavier ions began at LBL in 1975 with helium and neon ions [96]. This eventuated into treatments with a wider range of heavy ions such as carbon, nitrogen, oxygen, silicon, and argon [97]. However, due to complications with ions such as neon and argon, treatments were limited only to carbon ions, based on a sufficient compromise between the treatment of radio-resistant tumours and the sparing of healthy tissue [98].

HIMAC - Heavy Ion Medical Accelerator in Chiba

Due to the successes in particle therapy at LBL, the Japanese government began construction of the National Institute of Radiological Sciences (NIRS) in 1984. The Heavy Ion Medical Accelerator in Chiba (HIMAC) was built in 1993, which was the first heavy ion medical accelerator system specifically dedicated for clinical research and patient treatment. NIRS began carbon ion radiotherapy treatments in 1994, and to the present day have treated over 8000 patients using carbon ions [99].

A model of the HIMAC facility is shown in figure 2.51. The facility houses a 41 m

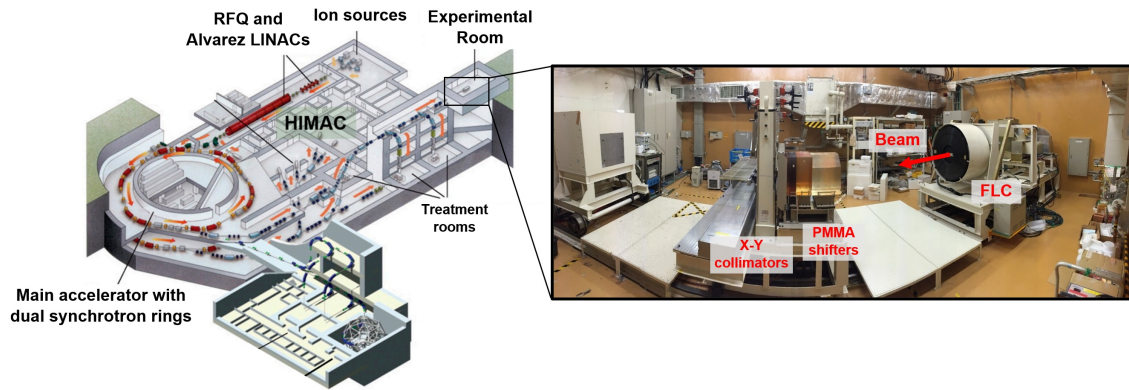


Figure 2.51: Model of the HIMAC facility (left) adapted from [100]. View of the biological experimental irradiation room (right) adapted from [51].

diameter synchrotron to accelerate ions ranging from helium to argon. ^{12}C ion beams are typically used for patient radiotherapy treatments, however heavier ions such as ^{28}Si are available for research purposes. These heavier ions are studied for investigation of multi-ion therapies and modelling environmental conditions similar to space for radiation detector research [101].

The HIMAC accelerator features a 7.3 m long radio frequency quadrupole (RFQ) LINAC for low speed ions (up to 6 MeV/u) and a 24 m long Alvarez LINAC, which injects medium speed ions into the dual ring synchrotron, producing ion energies up to 400 MeV/u. The ion beam transport system delivers the accelerated ions through vertical and horizontal beam lines to different treatment rooms and the experimental biological irradiation room [99]. The biological irradiation room is used for clinical research at the facility, which is the only beam line used in this study.

The biological irradiation room beam line has a bar ridge filter to obtain fixed modulation depth, wobbler system to laterally spread the spot beam, and four-leaf collimator (FLC) to shape the beam [99]. After the beam exits the nozzle, PMMA range shifters in the biological room are used to reduce the output beam energy without changing the accelerator conditions.

2.4 Fast Neutron Therapy

Fast neutrons offer therapeutic advantages in treating certain types of locally advanced or radioresistant tumours [102]. Radioresistant tumours tend to be hypoxic, which inhibits the creation of reactive oxygen species. Conventional radiation therapy using photons relies on the creation of oxygen free-radicals to provide the lethal effect. Neutrons do not interact with atomic electrons like photons do, but instead the uncharged fast neutrons interact with hydrogen nuclei, producing recoil protons that ionise.

The advantage of using neutrons is due to the high linear energy transfer (LET) of the secondary particles, such as protons, alpha particles and heavy ion recoils, created by neutron interactions. These locally produced secondary particles inflict a significant number of DNA double strand breaks, leading to irreparable damage of tumour cells.

Unlike photon radiation, neutrons depend less on the presence of oxygen in the tumour to act as a mediator, and have a greater tendency to cause cell death through direct interaction [103]. Therefore, the hypoxic component of the tumours is spared to a lesser extent by neutron irradiation than by low-LET particle therapies (such as photons or electrons), leading to a higher RBE. Additionally for neutron irradiation, the KERMA (kinetic energy released per unit mass) in lipid-containing tissues that contain a relatively high proportion of hydrogen can exceed that in water, which results in increased local dose. These tissues include lipids and lipoproteins such as myelin and sphingomyelin in white matter of the brain and spinal cord, and body fat. Thus, neutrons can be more effective for certain types of cancer, such as head and neck tumours with large hypoxic areas which reoxygenate slowly [104].

The depth-dose distribution for fast neutrons in water follows a similar profile to gamma photons [105] and therefore provide no benefit in terms of improved depth-dose, as shown in figure 2.48.

The application of fast neutrons for human cancer treatment began in 1938 by Stone at Lawrence Berkeley Laboratory (LBL), with neutrons produced using a cyclotron accel-

erating 8 MeV deuteron onto beryllium [106]. This was 7 years after the first cyclotron was developed by Lawrence in 1931 [107], and even more remarkably, only 6 years after the discovery of the neutron by Chadwick in 1932 [108]. The 1938-1939 fast neutron trials treated 24 patients using a cyclotron that featured an 80-ton magnet, producing 8 MeV deuterons. From 1939-1943, 226 patients were treated using neutrons generated by a larger cyclotron with 190-ton magnet, that produced 16 MeV deuterons [106].

The result of the trials by Stone were initially encouraging, with some tumours regressing and disappearing completely (not found in post mortem specimens) [106]. However, almost all of the long-term survivors had severe radiation damage in the normal tissue surrounding the tumour sites, especially radio-necrotic ulcerations on the skin which failed to heal [106]. One patient with laryngeal squamous cell carcinoma was treated with 19 treatments over 48 days with Stone stating the total dose to the skin surface was 12.5 Gy [106], though later estimated to be over 20 Gy [109]. Cross-section dose treatment plans were not carried out, with Stone reporting that: *no treatment was considered complete unless a good erythema was produced and in the majority of cases some degree of epidemolysis was produced* [106].

The work by Stone ceased in 1943, as both the cyclotron and Stone were required for other purposes. The severe late skin and subcutaneous damage in this trial deterred any other further clinical investigation in fast neutron therapy for approximately 20 years. It was later argued that the poor results obtained by Stone was due to the poor understanding of radiation biology at the time [110], because with less recovery between fast-neutron fractions, the doses are more additive than for X-rays, resulting in higher total dose delivered [110].

Following extensive studies by Gray in 1953 on the influence of oxygen on the radiation sensitivity of different biological materials [111], the interest in fast neutrons was renewed. This started with the clinical work in 1970 at Hammersmith Hospital by Catterall [112], which resulted in the subsequent opening of over 40 fast neutron therapy facilities worldwide for patient treatment [113]. At the present date, over 30,000 patients

have been treated using fast neutrons [114], however most of these facilities have been decommissioned due to poor clinical results and lack of funding support. There are only four fast neutron therapy facilities remaining worldwide [114], located in Germany, South Africa, USA, and Russia, as summarised in table 2.9.

Location	Source	Mean energy (MeV)	50% depth	Beam direction	Collimator type	First patient	Patients treated
University of Washington Medical Center, Seattle, USA.	Cyclotron, p(50.5)+Be	20	14 cm	Isocentric	Multi leaf	1984	2960
iThemba LABS, Cape Town, South Africa.	Cyclotron, p(66)+Be	25	16 cm	Isocentric	Multi blade trimmer	1988	1788
Tomsk Polytechnic University, Tomsk, Russia.	Cyclotron, d(13.6)+Be	6.3	6 cm	Horizontal	Inserts	1983	1500
FRM II, Technische Universität München, Garching, Germany.	Uranium converter	1.9	5 cm	Horizontal	Multi leaf	2007	124

Table 2.9: Current fast neutron facilities worldwide. Number of patients treated was collected in 2013 [114].

iThemba Laboratories for Accelerator Based Sciences (LABS)

iThemba LABS is one of the last remaining fast neutron facilities in the world, located in Cape Town, South Africa. The fast neutron therapy facility opened in 1988 [115]. The layout of the accelerator facilities is shown in figure 2.52. The variable-energy separated-sector cyclotron (SSC) is capable of accelerating protons up to a maximum energy of 200 MeV. For fast neutron therapy, 66 MeV protons are accelerated using the SSC and injected into the beam line directing to the isocentric neutron therapy room.

The diagram of the isocentric neutron therapy gantry is shown in figure 2.53. The 66 MeV protons travel through the gantry, with trajectory directed by a quadrupole magnetic system. Once the protons are in the upper head of the gantry, they are bombarded onto a copper-backed 19.6 mm thick ^9Be target, dissipating 40 MeV and producing a spectrum of high energy neutrons [116]. The neutron beam is modified by 0.8 cm thick iron flattening

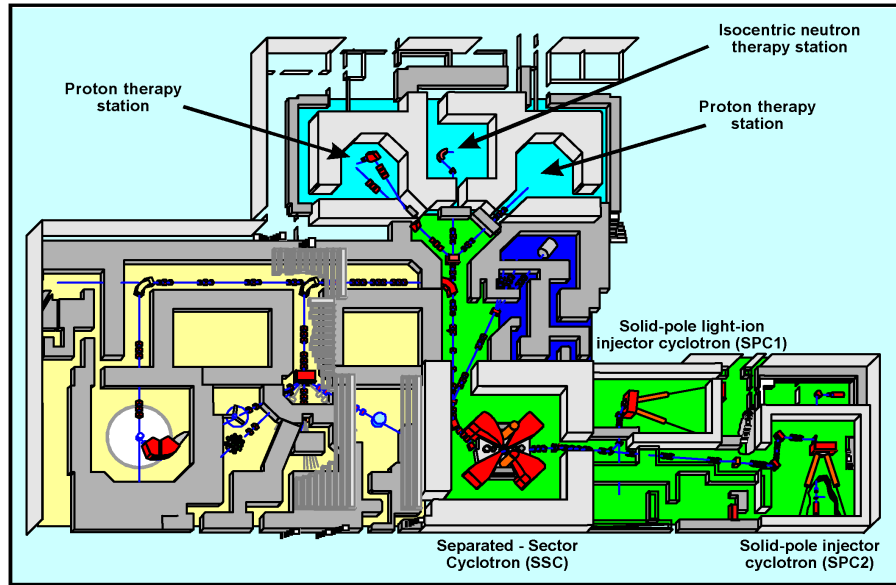


Figure 2.52: Diagram of the Separated-Sector Cyclotron Facility, with beam line leading into the isocentric neutron therapy room, adapted from: [113].

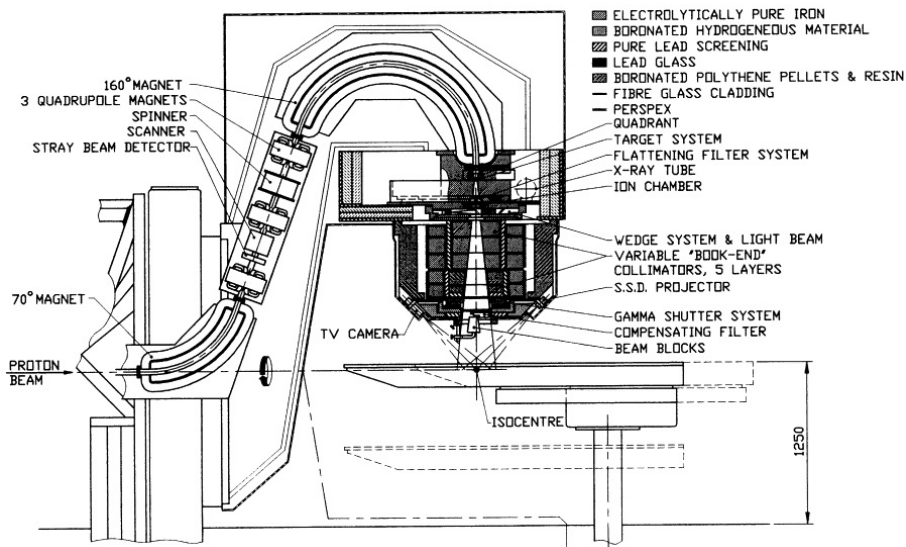


Figure 2.53: Scale diagram of the p(66) + Be isocentric neutron therapy gantry, from accelerated protons to treatment room [115].

filters, three tungsten wedge filters and a 2.5 cm thick polyethylene hardening filter [116] [115]. Blocks of 12 cm thick tungsten can be inserted in the beam downstream of the collimator for shielding purposes. The physical characteristics of the fast neutron beam is similar to that of an 8 MV X-ray beam [115].

The isocentric gantry, also shown in figure 2.54a, is capable of ± 185 degree rotation around the patient bed. The beam is collimated using five variable jaws in the lower head

and a multi-blade trimmer at nozzle for target specific beam shaping [117]. The multi-blade trimmer, shown in figure 2.54b, can rotate 360 degrees with a continuously variable leaves, providing field sizes between $5 \times 5 \text{ cm}^2$ to $30 \times 30 \text{ cm}^2$ at source-to-axis distance of 150 cm [118]. The adjustable patient couch (bed) is constructed mainly of wood to reduce neutron activation.

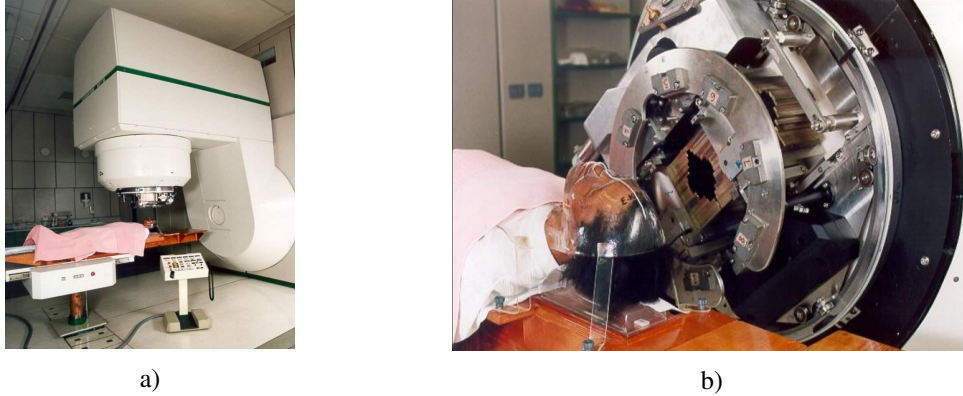


Figure 2.54: a) Isocentric neutron gantry with patient on bed [113], b) Multi-blade trimmer variable collimator [113].

The measured and calculated neutron energy fluence for the iThemba facility is shown in figure 2.55. The measured spectrum by Jones [116] was performed using a cylindrical 5 cm long by 5 cm diameter NE-213 liquid scintillator, coupled to a photomultiplier tube. The collimators were set to produce a $10 \times 10 \text{ cm}^2$ field at isocenter [116]. An important note in the measurements is that the neutron detection threshold was 3.5 MeV, and data below this was exponentially extrapolated to 0 MeV. This means that the data in the first two bins of the measured data (figure 2.55) is not reliable for effective comparison with simulation results.

The calculation by Ross [119] modelled the same setup as Jones, utilising MCNP version 4A [120] and LAHET [121] for the simulations. This was such that LAHET transported neutrons above 20 MeV, and then using MCNP4 for neutrons below 20 MeV. This was argued by Bohm [122] to be an inaccurate method, who repeated the simulations using MCNP4 with evaluated nuclear data libraries (ENDF/B) up to 100 MeV.

Though Bohm had applied evaluated nuclear datasets, the only available isotope data was for ^1H , ^9Be , ^{12}C , ^{16}O , ^{27}Al , $^{\text{nat}}\text{Si}$, ^{40}Ca , $^{\text{nat}}\text{Fe}$, $^{\text{nat}}\text{W}$, and ^{238}U [122]. For materials

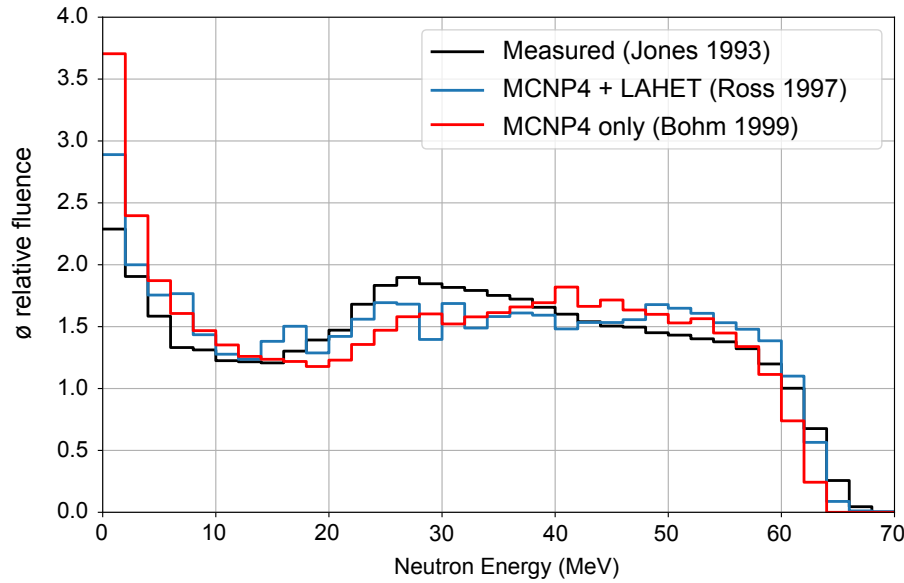


Figure 2.55: Neutron fluence (relative) at iThemba for p(66)+Be. Measured using NE-213 liquid scintillator [116], MCNP4 + LAHET [119] and MCNP4 only [122]. Figure adapted from: [122].

not available in the library, these were substituted with available isotopes with similar atomic mass, and adjusted the atomic density to match the actual material [122]. For example;

- Air was modelled as ^{16}O ,
- Stainless steel was modelled as $^{\text{nat}}\text{Fe}$,
- Copper (in the target backing) was modelled as $^{\text{nat}}\text{Fe}$,
- Lead in the collimator was modelled as $^{\text{nat}}\text{W}$, using the atomic density of lead,
- Boron (in the polyethylene collimators) was neglected.

Bohm expected that the results would not be affected by more than a few percent, as neutron inelastic scattering was the dominant interaction in the simulations [122]. Bohm noted that the specific effects of these substitutions should be assessed as more isotopes are made available in the evaluated nuclear data libraries [122].

The various substitutions made due to the lack of evaluated nuclear datasets has some concerns. The copper in the target backing (substituted with $^{\text{nat}}\text{Fe}$) is directly in the primary proton beam. Neglecting the high composition of nitrogen in air also ignores the

important $^{14}\text{N}(\text{n},\text{p})^{14}\text{C}$ reaction [4]. The substitution of lead with tungsten in the collimator will affect the rate of neutron reflection and absorption, as these properties do not relate solely back to the atomic density. These are intrinsic properties that rely on nuclear interactions. Most importantly, the lack of boron in the collimators will greatly affect the results in the epithermal/thermal neutron energy range.

Summary of key differences between BNCT, FNT, and Carbon Ion Therapy

Table 2.10 summarises the biological effectiveness and key considerations for treatment optimisation in BNCT, FNT, and Carbon Ion Therapy.

Modality	Typical RBE_{10}	Most effective for cancer types	Treatment optimisation and comparisons
BNCT	3.6 [123]	<ul style="list-style-type: none"> glioblastoma (brain), melanoma (skin), squamous cell carcinoma (head and neck), salivary gland carcinoma (head and neck), malignant mesothelioma [124]. 	<ul style="list-style-type: none"> RBE is dependent on uptake of ^{10}B compounds. Specificity of dose delivered to ^{10}B would allow greatest sparing of normal tissue. Epithermal beam is required for deeper tumours. Fractionation typically not required, can be treated in a single treatment. Patient must be positioned on beam port. Consideration required with tumour:tissue ^{10}B ratio (BPA is 3:1 ratio in best case). Current ^{10}B compounds can be biologically toxic at high concentrations.
FNT	3.0 [113]	<ul style="list-style-type: none"> salivary gland carcinoma (head and neck), adenoid cystic carcinoma (head and neck), prostate cancer [125]. 	<ul style="list-style-type: none"> Higher penetration depth than photons, effective for treating deep-seated tumours. Does not selectively spare tissue due to no Bragg peak or compound dose localisation. Multiple fractions are required to minimise damage to normal tissue. Highest RBE to hydrogen-lipids such as central nervous system white matter. Oxygen enhancement ratio is higher in FNT compared to BNCT and carbon ion therapy.
Carbon Ion Therapy	3.0 [12]	<ul style="list-style-type: none"> prostate cancer, bone and soft tissue sarcomas, adenoid cystic carcinoma (head and neck), NSC lung cancer, HCC (liver), pancreatic cancers [126]. 	<ul style="list-style-type: none"> Superior dose conformity due to high-LET, important for sparing critical areas of body (ie. brain/spinal cord). Suitable for all cancers that are localised without metastasis. Multiple fractions are required. Most expensive type of treatment compared with FNT and BNCT.

Table 2.10: Inter-comparison of biological effectiveness and key considerations for treatment optimisation in BNCT, FNT, and Carbon Ion Therapy.

2.5 Geant4 Simulation Toolkit

General Overview

The Monte Carlo toolkit, Geant4 (GEometry ANd Tracking) [127] simulates the transport of radiation through matter. From high energies (TeV) to sub-eV scales, Geant4 can describe electromagnetic and hadronic interactions. Geant4 also has interfaces for visualisation and analysis of the data it generates.

Users can create a Geant4 application by providing information such as particle types, detector properties, tracking management parameters, and physics packages. Geant4 has been used by CMRP in a number of prior and continuing innovative microdosimeter research [101][128] [129], and has been used in this work to characterise the mixed radiation field created during various radiotherapy modalities.

Geant4 uses a random number generator to select between a series of probable outcomes during particle transport. Particle transport occurs in discrete steps, with the random number generated at each step being used to either apply a process to the particle (i.e. ionisation, scattering, decay, nuclear processes, etc.) or not apply any process and allow the particle to go to the next step. A statistical description of particle behaviour can be determined once a significant number of particle tracks have been built up [7].

Several categories, packages, classes, and processes facilitate this procedure in Geant4. The run package (G4Run) defines the events with the same beam and detector implementation, while the event category (G4Event) manages the events from primary and secondary particles in the simulation settings. The General Particle Source (GPS) or G4ParticleGun are components that allow user-defined properties to be defined such as beam shape, energy, and type of particles to be generated, in order to model the specific radiation field [130].

Particles are not considered self-moving in Geant4, but rather as being transported by the tracking package, which controls the transportation process. The tracking process is carried out independently of the particle type or physics processes involved. The

G4SteppingManager class [127] manages the updating of tracks at each step.

Geometrical volumes are defined by a hierarchical tree structure of volumes created to accommodate the approximate an experimental or theoretical set-up. These geometries are described by solid, logical and physical volumes built from materials using the G4Material class, where material characteristics such as atomic number, mass, density and elemental composition are user defined. Logical volumes can be set as sensitive materials, allowing event information such as track length and energy deposition within a specified geometry to be retrieved [130].

Geant4 Physics Lists

Geant4 defines seven types of physics processes; Electromagnetic, hadronic, transportation, optical, decay, photolepton hadron, and parametrization. These describe the interaction of particles travelling through geometry material. The photoelectric effect, Rayleigh scattering, Compton scattering, pair production, particle ionisation, and Bremsstrahlung are all managed by the electromagnetic physics process model, which includes both discrete and continuous interactions. All electromagnetic models in Geant4 have been validated to be in good agreement with the National Institute of Standards and Technology (NIST) database, indicating that they fulfil the objectives of this study [131].

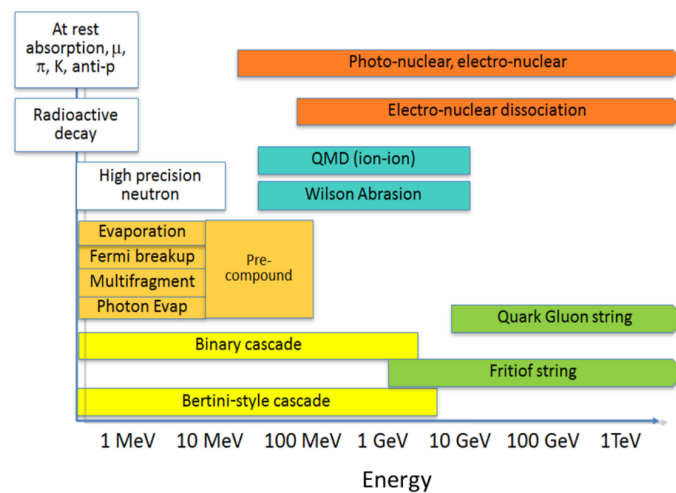


Figure 2.56: Partial inventory of Geant4 hadronic physics models for version 10 [132].

Depending on the radiation field under investigation, there are a variety of alternative hadronic physics models that can be utilised. Figure 2.56 depicts the energy limits for which some hadronic physics models are applicable for, which includes elastic and inelastic scattering, neutron fission, and neutron capture.

The Binary Ion Cascade All High Precision (BIC-AllHP) Physics List

The Binary Ion Cascade All High Precision (BIC-AllHP) physics list (QGSP_BIC_AllHP) was introduced in Geant4.10.2, which is a data-driven, high precision physics model that uses TALYS-based Evaluated Nuclear Data Library (TENDL) [133]. TENDL provides datasets to describe the interactions of charged particles such as proton, deuteron, triton, ^3He , and alpha particles below 200 MeV [133]. Users need to download the G4TENDL data set from the Geant4 site and add to the PATH to use it. The HP package in this model describes neutron interactions at energies below 20 MeV using evaluated neutron data, named G4NDL4.5, which is largely sourced from the ENDF/B-VII.1 libraries [54].

$S(\alpha,\beta)$ Thermal Neutron Scattering Model

The G4NDL data set provides high precision evaluated data libraries for neutrons in Geant4. This defines the neutron physics behind elastic scatter, inelastic scatter, capture and fission processes.

Neutrons lose energy in a medium via inelastic and elastic collisions. The probability of these interactions are dependent on the neutron energy. Therefore, it is necessary to simulate a wide energy range, from tens of MeV (or larger) down to thermal energies.

At low energies close to thermal, the collisions of the neutron with atoms or molecules can result in a gain or loss of energy, by reducing/increasing the velocity of the molecule (translational modes), making the molecule reduce/increase the speed of its rotations (rotational modes) or vibrations (vibrational modes).

Thermal neutron treatment is necessary, in order to accurately account for the low energy neutron interactions with matter, with consideration depending on the structure of

the material (crystalline, liquid, etc).

Since the release of Geant4.10.0, the thermal neutron scattering model has been included, which defines the elastic scatter of very low energy neutrons below 4 eV in specific materials. These very low-energy processes take into account the binding effects for molecularly bound nuclei. Before the thermal neutron scattering models were included, significant discrepancies were reported in Geant4 results [75] [134] for low energy regions when compared to experimental data and MCNP software [135]. Since its addition in Geant4.10.0, comparison with experimental results have reported better agreements [136] [137] [138] [139]

The double-differential cross section for thermal neutron scattering is parameterised in terms of the thermal scattering law, $S(\alpha, \beta)$,

$$\frac{d\sigma}{d\Omega dE'}(E \rightarrow E', \mu, T) = \frac{\sigma_b}{4\pi kT} \sqrt{\frac{E'}{E}} e^{-\beta/2} S(\alpha, \beta, T)$$

where Ω is the solid scattering angle, μ is the cosine of the neutron scattering angle, σ_b is the bound total scattering cross section of the scattering nucleus, k is the Boltzmann constant, T is the temperature, E is incident neutron energy, and E' is the scattered neutron energy [140]. α and β are dimensionless coefficients that parameterise the momentum and energy transfers, respectively:

$$\alpha = \frac{m_n}{MkT}(E + E' - 2\sqrt{EE'}\mu), \quad \text{and} \quad \beta = \frac{E' - E}{kT}$$

where m_n is the neutron mass and M is the mass of the principal scattering nucleus. Fortunately, these calculations are performed internally by the G4NeutronHPThermalScattering physics model. In ENDF-6 format, $S(\alpha, \beta)$ is explicitly tabulated for certain materials as a function of temperature. The available $S(\alpha, \beta)$ scattering datasets in G4NDL4.5 are listed in table 2.11.

Evaluation Name	Secondary Scatterer	Available Temperatures (K)
H in H ₂ O	Free O	293.6, 350, 400, 450, 500, 550, 600, 650, 800
H in CH ₂	Free C	293.6, 350
Benzine	None	293.6, 350, 400, 450, 500, 600, 800, 1000
H in ZrH	None	293.6, 400, 500, 600, 700, 800, 1000, 1200
D in D ₂ O	Free O	293.6, 350, 400, 450, 500, 550, 600, 650
Be in metal	None	296, 400, 500, 600, 700, 800, 1000, 1200
Be in BeO	None	293.6, 400, 500, 600, 700, 800, 1000, 1200
Graphite	None	293.6, 400, 500, 600, 700, 1000, 1200, 1600, 2000
O in BeO	None	293.6, 400, 500, 600, 700, 800, 1000, 1200
O in UO ₂	None	293.6, 400, 500, 600, 700, 800, 1000, 1200
Al in metal	None	20, 80, 293.6, 400, 600, 800
Fe in metal	None	20, 80, 293.6, 400, 600, 800
Zr in ZrH	None	293.6, 400, 500, 600, 700, 800, 1000, 1200
U in UO ₂	None	293.6, 400, 500, 600, 700, 800, 1000, 1200
Para H ₂	None	20
Ortho H ₂	None	20
Para D ₂	None	19
Ortho D ₂	None	19
Liquid CH ₄	None	100
Solid CH ₄	None	22

Table 2.11: ENDF/B-VII.1 $S(\alpha, \beta)$ scattering matrix datasets for neutron energies less than 4 eV available in Geant4 with the G4NDL4.5 data files. Data has been evaluated as a function of temperature [54].

The $S(\alpha, \beta)$ datasets have been evaluated as a function of temperature, so it is important for the user to specify it in the material definition. Otherwise, the default temperature of Geant4 will be set of 273.15 K. The process for setting up the thermal neutron treatment in Geant4 is outlined in section 3.1.1.

2.6 MCNP: Monte Carlo N-Particle Transport Code

The Monte Carlo method of calculating radiation particle transport originated at the Los Alamos National Laboratory (LANL), dating back to 1946. This was theorised and created by S. Ulam, J. von Neumann, R. Richtmyer and N. Metropolis [141]. The Monte Carlo method originates with S. Ulam, whilst recovering from illness and playing Solitaire, trying to find a method to determine the statistical outcome of the card game; with motivation to beat the casinos in the city of Monte Carlo.

The first version of Monte Carlo for radiation particle transport was developed at LANL in 1948 and run on the ENIAC (Electronic Numerical Integrator and Computer), taking 5 hours to process 100 primary neutrons. The ENIAC computer fit into a room with area $6 \times 12 \text{ m}^2$, weighed 30 tons and featured over 18000 vacuum tubes with a computing clock speed of 0.1 MHz [141].

In following decades, various versions of special-purpose Monte Carlo codes were developed (individual codes specifically for neutrons, protons, or photons), with their unification in 1977 to create the LANL Monte Carlo N-Particle (MCNP) radiation particle transport code. In 1983, MCNP version 3 was released, which was the first public distribution of MCNP [141].

MCNP version 6.2 was released in 2018 [135], which is a general purpose three-dimensional simulation tool that transports 37 different particle types and arbitrary heavy ions [142]. The traditional domain of the MCNP code package is the simulation of low energy neutron propagation and their interactions.

For neutrons, all reactions given in a particular cross-section evaluation (sourced from ENDF/B-VII.1 data sources) are accounted for. Thermal neutrons are described by both the free gas and $S(\alpha, \beta)$ models. For photons, the code accounts for incoherent and coherent scattering, fluorescent emission after photoelectric absorption, pair production (absorption and annihilation secondary radiation), and bremsstrahlung. For electrons, a continuous-slowing-down model is used for transport which includes positrons, k x-rays,

and bremsstrahlung.

Specific areas of application include (but are not limited to): radiation protection and dosimetry, radiation shielding, radiography, medical physics, detector design and analysis, accelerator target design, fission and fusion reactor design, decontamination and decommissioning [135].

MCNP is written in Fortran computing language [143], which allows for faster execution times. However, this does limit the user ease of access and requires much different coding style to Geant4, which is written in C++. MCNP is also very heavily regulated and requires a screening process to obtain a copy of the software. The source code version of MCNP is much more difficult to obtain than the executable version. The executable version of MCNP 6.2 has been used for the work in this project.

MCNP6 Physics Options

In MCNP6, the ‘LCA’ card can be used to select which physics models are implemented in the energy range where data is available. For the intranuclear cascade (INC), there are several models available, including the Cascade-Exciton Model (CEM3.03), Bertini, ISABEL and INCL4 models [135]. The CEM is the default option if the user does not specify the LCA card parameters. The Bertini INC model for reactions induced by nucleons and pions is valid up to 3.5 GeV [135].

When setting up the geometry of the MCNP simulation, the Material card (‘M’ card) is used to define the nuclides associated with a material based on its fractional composition. If ENDF/B-VII.1 data is available for that nuclide, it is automatically applied with the high-precision physics that defines the nuclear processes of all particles included in the simulation. The energy limit for the high-precision physics model associated with a particular nuclide is based on what is available in the ENDF dataset, which is typically 20 MeV. However, if TENDL data is available in the ENDF dataset, it can be much higher (up to 200 MeV high-precision) for protons, deuterons, alpha and ^3He nuclei.

All charged particles have the option of enabling lower energy delta-ray production, which is disabled by default. For this work, delta-rays were enabled for all charged particles.

The ‘PHYS:<pl>’ card can be used to set the specific physics options of particles; e.g. ‘PHYS:N’ (for neutrons), ‘PHYS:H’ (for protons), ‘PHYS:P’ (for photons), etc.

The ‘CUT:<pl>’ card allows the user to select time, energy and weight cutoffs for various particles. For example, the ‘CUT:N’ card must be set so analog capture is used, otherwise a biasing technique will be applied (non-analog capture).

The specific physics options selected in this work is discussed in chapter 3, however in short; only analog capture with applied evaluated datasets were used for neutrons (i.e. no memory reduction biasing).

$S(\alpha, \beta)$ Thermal Neutron Scattering Model

Similarly to Geant4, MCNP has thermal neutron scattering data-based models, sourced from the ENDF/B-VII.1 libraries [144] [145]. By defining materials with the ‘MT’ card included, a particular isotope (or isotopes) in that material can be treated in the thermal energy region as a molecular compound with an $S(\alpha, \beta)$ data set (if that data set exists) [135]. The available scattering matrix datasets in MCNP version 6.2 with ENDF/B-VII.1 libraries is shown in table 2.12.

The ENDF $S(\alpha, \beta)$ scattering matrix datasets available in Geant4 and MCNP 6.2 is the same, as shown in tables 2.11 and 2.12, respectively. This is with the exception of ^{16}O , ^{28}Si & ^{29}Si in *Silicon Dioxide*, which is only available in MCNP 6.2.

Evaluation Name	Available Temperatures (K)
²⁷ Al in metal	20, 80, 293.6, 400, 600, 800
⁹ Be in metal	293.6, 400, 500, 600, 700, 800, 1000, 1200
⁹ Be in Beryllium Oxide	293.6, 400, 500, 600, 700, 800, 1000, 1200
¹ H, ¹² C & ¹³ C in Benzene	293.6, 350, 400, 450, 500, 600, 800, 1000
² H in Ortho Deuterium	19
² H in Para Deuterium	19
⁵⁶ Fe in metal	20, 80, 293.6, 400, 600, 800
¹² C & ¹³ C in Graphite	293.6, 400, 500, 600, 700, 1000, 1200, 1600, 2000
¹ H in Zirconium Hydride	293.6, 400, 500, 600, 700, 800, 1000, 1200
¹ H in Ortho Hydrogen	20
¹ H in Para Hydrogen	20
² H in Heavy Water	293.6, 350, 400, 450, 500, 550, 600, 650
¹ H in Liquid Methane	100
¹ H in Light Water	293.6, 350, 400, 450, 500, 550, 600, 650, 800
¹⁶ O in Beryllium Oxide	293.6, 400, 500, 600, 700, 800, 1000, 1200
¹⁶ O in Uranium Oxide	293.6, 400, 500, 600, 700, 800, 1000, 1200
¹ H in Polyethylene	293.6, 350
¹ H in Solid Methane	22
²³⁸ U in Uranium Oxide	293.6, 400, 500, 600, 700, 800, 1000, 1200
⁹⁰ Zr, ⁹¹ Zr, ⁹² Zr, ⁹⁴ Zr & ⁹⁶ Zr in Zirconium Hydride	293.6, 400, 500, 600, 700, 800, 1000, 1200
¹⁶ O, ²⁸ Si & ²⁹ Si in Silicon Dioxide	293.6, 350, 400, 500, 800, 1000, 1200

Table 2.12: ENDF/B-VII.1 $S(\alpha, \beta)$ scattering matrix datasets for neutron energies less than 4 eV available in MCNP 6.2 to be used with the MT card [144]. Data has been evaluated as a function of temperature [54].

PTRAC

MCNP contains numerous flexible tally cards, such as: surface & volume flux, point detectors and pulse height tally for energy deposition [135]. These pre-set tally cards allow the user to easily record the quantities of interest in a simulation, but lack the level of detail required for microdosimetry purposes (i.e. particle-by-particle delta-ray analysis).

The ‘PTRAC’ card (Particle Track output card) allows the user to export a detailed list of particle events to an output file. The data that is stored in the output file is based on a

set of conditions. After the simulation has completed, the PTRAC file can be processed and analysed. The level of detail provided by PTRAC for particle tracking in an event is sufficient for performing microdosimetric analysis in MCNP. The use of the PTRAC card to perform microdosimetry in MCNP is discussed in more detail in chapter 3.

Chapter 3

The Geant4 and MCNP Simulation Applications

The Monte Carlo simulation codes; Geant4 and MCNP6 are used extensively throughout all chapters for the work completed in this thesis. To avoid repetition, the configuration of each of these codes is listed in this chapter. This includes physics options, material definitions and the basic methods of recording information. Any variations to these settings will be noted in the ‘Method’ section of the relevant chapters.

The justification and reasoning for the selected physics options configured for Geant4 and MCNP are described extensively in the benchmarking work completed in chapter 8. Due to the extensive systematic approach to benchmark Geant4 and MCNP, that chapter is at the end of the thesis (as it may not be of interest to all readers).

3.1 Overview of the Geant4 Simulations

3.1.1 Physics Options and Definitions

Geant4 Versions

For all work completed using Geant4 [127], version 10.5.p01 was utilised. ROOT version 6.16 [146] was adopted as the analysis tool for exported data by Geant4. Note that this is with the exception of chapter 4, which uses Geant4 version 10.1 and ROOT version 5.34. Geant4.10.1 was used as the newer version of Geant4.10.5 was not released when the work was completed. Both of these versions use the same G4NDL4.5 neutron datasets, so the results from the older Geant4 are still acceptable.

Material Definitions

The materials used in all the Geant4 simulations were obtained from the *G4NistManager*, which provides material definitions derived from the NIST data reference [147].

Electromagnetic Processes

The Geant4 Standard Electromagnetic Option 4 (referred to as Opt4, or EMZ) physics list was selected to describe all the electromagnetic interactions of particles, down to 100 eV [148].

Particle Cut Values

A default cut value of 0.01 μm was set due to the short path length of secondary particles associated with the mixed radiation fields studied. This is particularly important when studying microdosimetry, as the consideration of sub-micron interactions within the SVs and overlays are crucial.

Hadronic Processes

The Binary Ion Cascade All High Precision (BIC_AllHP) data libraries were adopted, which is a data-driven, high precision physics model that uses TALYs-based Evaluated Nuclear Data Library (TENDL) [133]. The ‘HP’ (high-precision) package in this model

describes neutron interactions at energies below 20 MeV using evaluated neutron data, named G4NDL4.5, which is largely sourced from the ENDF/B-VII.1 libraries [54]. G4TENDL (‘AllHP’ package, referring to TENDL data) provides datasets to describe the interactions of charged particles such as proton, deuteron, triton and alpha particles [133].

QGSP_BIC_AllHP was used for all simulations performed using Geant4.10.5.p01. For the work performed in chapter 4 using Geant4.10.1, QGSP_BIC_HP was used. G4TENDL was introduced in Geant4.10.2 and was not available for Geant4.10.1, though its use was outside the scope of the study in chapter 4. Both QGSP_BIC_AllHP and QGSP_BIC_HP use the same G4NDL4.5 data to describe high-precision nuclear interactions.

Table 3.1 presents the differences of hadronic inelastic physics for neutrons and protons in some physics lists in Geant4. The information in this table is important for chapters 5 and 8, where different physics lists are benchmarked.

Physics List Package	Main differences in hadronic physics models
QGSP_BIC_HP	Neutron: < 20 MeV; High Precision Neutron Model, > 20 MeV; Binary Cascade. Proton: < 9.9 GeV; Binary Cascade.
QGSP_BERT_HP	Neutron: < 20 MeV; High Precision Neutron Model, > 20 MeV; Bertini Cascade. Proton: < 9.9 GeV; Bertini Cascade.
QGSP_INCLXX_HP	Neutron: < 20 MeV; High Precision Neutron Model, > 20 MeV; INCL++. Proton: < 2 MeV; PRECO, > 1 MeV; INCL++.
Shielding	Neutron: < 20 MeV; High Precision Neutron Model, > 20 MeV; Bertini Cascade (using JENDL data). Proton: < 9.9 GeV; Bertini Cascade.
QGSP_BIC_AllHP	Neutron: < 20 MeV; High Precision Neutron Model, > 20 MeV; Binary Cascade. Proton: < 200 MeV; ParticleHP (G4TENDL HP datasets), < 9.9 GeV; Binary Cascade.
G4LEND	Neutron: < 20 MeV; LEND Model using GND1.3 ENDF/B-VII.1, > 20 MeV; Bertini Cascade (using JENDL data). Proton: < 9.9 GeV; Bertini Cascade.

Table 3.1: Summary of the main differences in some hadronic physics lists in Geant4.

The advantage of QGSP_BIC_AllHP is indicated in table 3.1 for protons, where TENDL data provides evaluated data describing their nuclear interactions < 200 MeV.

The ‘LEND’ physics list is based on the ‘Shielding’ physics list, but uses the GND1.3 ENDF/B-VII.1 neutron dataset for its high precision model. All other high-precision neutron models use G4NDL4.5. It is very important to note that there is a bug in the code for the LEND model, which has been reported to the Geant4 developers by this author, and is expected to be corrected in the public source code in a later update. The bug specifically relates to the mass definitions of specific particles, leading to incorrect energy balancing in certain reactions.

Radioactive Decay

The radioactive decay was modelled, provided by the Geant4 RadioactiveDecay 5.3 data package, which is derived from the ENSDF database [72]. Its use is crucial to investigate the neutron activation and decay for the relevant radioprotection purposes.

Thermal Neutron Scattering Physics Model

The HP thermal neutron physics model (G4NeutronHPThermalScattering) was activated, as outlined in [149], to describe elastic scatter interactions below 4 eV for available materials listed in the ‘G4NeutronHPThermalScatteringNames’ definitions.

The steps for enabling the neutron thermal treatment are shown in figure 3.1. The regular ‘NeutronHPElastic’ model for high-precision data sourced the selected physics list describing the neutron elastic scatter process is overridden for neutrons with energy below 4 eV.

Changes required to activate the thermal neutron treatment -
based on the PhysicsList class of radioprotection example in Geant4.10.5.p01

Step 1) Thermal Neutron Libraries to include at start of PhysicsList.cc

```
#include "G4HadronicInteractionRegistry.hh"
#include "G4HadronicProcess.hh"
#include "G4HadronicProcessStore.hh"
#include "G4HadronicProcessType.hh"
#include "G4Neutron.hh"
#include "G4NeutronHPThermalScattering.hh"
#include "G4NeutronHPThermalScatteringData.hh"
#include <assert.h>
```

Step 2) Add the new physics for neutron elastic scatter below 4eV to the end of ConstructProcess function in PhysicsList.cc

```
void PhysicsList::ConstructProcess()
{
    // .....

    // Thermal Scattering Treatment
    // Get the elastic scattering process for neutrons
    G4ParticleDefinition* nPD = G4Neutron::Definition();
    G4ProcessVector* pvec = nPD->GetProcessManager()->GetProcessList();
    G4HadronicProcess* nElastic = 0;
    for (G4int i=0; i<pvec->size(); i++) {
        if ((*pvec)[i]->GetProcessSubType() != fHadronElastic) continue;
        nElastic = dynamic_cast<G4HadronicProcess*>((*pvec)[i]);
        break;
    }
    assert(nElastic != 0);

    // Get the "regular" HP elastic scattering model, exclude thermal scattering region
    G4HadronicInteraction* nElasticHP = G4HadronicInteractionRegistry::Instance()->FindModel("NeutronHPElastic");
    assert(nElasticHP != 0);
    nElasticHP->SetMinEnergy(4.*eV);

    // Attach HP thermal scattering model and data files to process
    nElastic->RegisterMe(new G4NeutronHPThermalScattering);
    nElastic->AddDataSet(new G4NeutronHPThermalScatteringData);

    // .....
}
```

Step 3) Define the materials in DetectorConstruction to what is available in G4NeutronHPThermalScatteringNames.

```
// In this example, we show the definition of water.
// Other popular options are H in polyethylene, C in graphite, D in heavy water.

// Normal definition using NIST dataset for G4_WATER, this is the reference to use S(a,B) data set, but temperature will be 273.15K.
G4Material* water = G4NistManager::Instance()->FindOrBuildMaterial("G4_WATER");

OR

// Correct definition of water to use the thermal scattering data. The real temperature of the moderator material must be specified.
// By default, materials are defined in GEANT4 at a temperature STP_temperature which is a CLHEP constant equal to 273.15 K.

// In this case, we use room temperature for the water (293.6 K), which is available in the S(a,B) data set for G4_WATER.
G4Material* water = G4NistManager::Instance()->FindOrBuildMaterial("G4_WATER", 293.6*kelvin);
```

Figure 3.1: Steps required in Geant4 to enable the thermal neutron treatment, which describes the new elastic scatter process for neutrons below 4 eV, based on the G4NeutronHPThermalScattering model.

The output from Geant4 to confirm that the thermal neutron treatment has been correctly enabled is shown in figure 3.2.

```
Neutron HP Thermal Scattering: Following material-element pairs or elements are registered.
Material G4_WATER - Element H, internal thermal scattering id 0

=====
HADRONIC PROCESSES SUMMARY (verbose level 1)
=====

Hadronic Processes for neutron

Process: hadElastic
  Model: hElasticCHIPS: 19.5 MeV ---> 100 TeV
  Model: NeutronHPElastic: 4 eV ---> 20 MeV
  Model: NeutronHPThermalScattering: 0 eV ---> 4 eV
Cr_sctns: NeutronHPThermalScatteringData: 0 eV ---> 4 eV
Cr_sctns: NeutronHPElasticXS: 0 eV ---> 20 MeV
Cr_sctns: G4NeutronElasticXS: 0 eV ---> 100 TeV
```

Figure 3.2: Geant4 output confirming thermal neutron treatment is enabled (after following the steps outlined in figure 3.1).

3.1.2 Simulation Flow

The Geant4 simulation application was developed based on the examples provided in the Geant4 source code. The examples that formed the basis of this simulation were from ‘Hadr02’, ‘Hadr03’ and ‘Hadr04’ (extended/hadronic), ‘rdecay02’ (extended/ radioactiveDecay), and ‘hadrontherapy’ (advanced/hadrontherapy). The motivation on the development of this Geant4 application was to improve the information available about the track history. This enabled a better relation of the processes induced by parent particles, allowing a full description of the reactions, which is required for accurate microdosimetric measurements.

A simplified flow chart describing the execution steps in the Geant4 application is shown in figure 3.3. The Sensitive Detector class is used to calculate specific quantities in the regions of interest, such as energy deposition, fluence, phase space details, etc. The Geant4 General Particle Source (GPS) is used to generate primary particles in the Primary Generator Class, which is defined simply by macro-based commands, or in more advanced cases, from a phase space file (depending on the simulation). The Analysis Manager class referred to in many steps, as it contains the vector map of parent particles

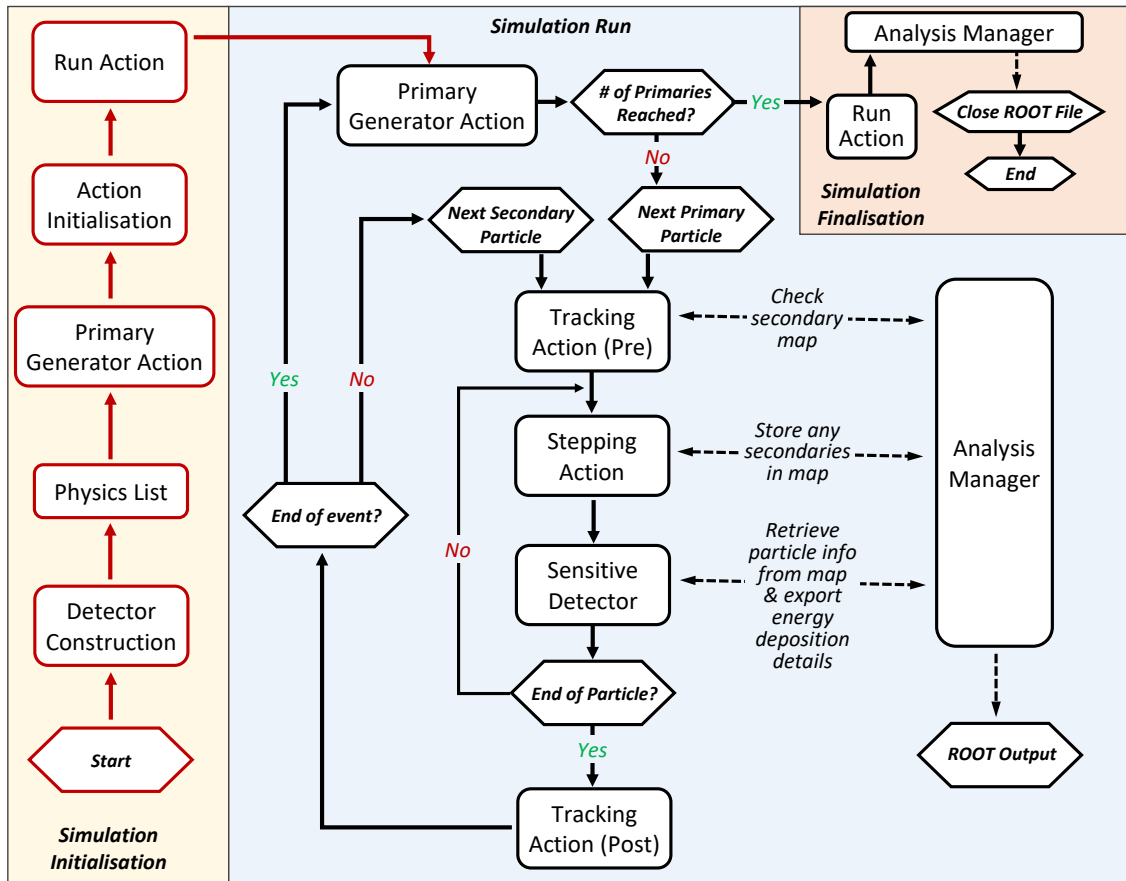


Figure 3.3: The Geant4 application developed for this work - simplified flow chart.

and their associated secondaries. When a particular process interaction occurs, the details of the interaction and any secondary particle information is stored in the vector map of Analysis Manager. Once the secondary particles are simulated, the information in the vector map is referred to, using this stored data to correctly connect this particle to the relevant reaction chain. This additional routine is important as the regular function calls in Geant4 regarding creator information lacks such detail. This is emphasised for neutron processes, as the details of which reaction and parent particle produced the secondaries is normally ambiguous, and would reduce to guess-work interpretation when identifying them.

The track history of each particle was recorded, such as information regarding the parent particle and the physics process which produced it. For each interaction, the kinetic energy, the point where the secondary particle is generated, its final location and when it comes to rest, is also stored. This information allows the identification of reactions

that occurred in the materials and calculation of the microdosimetric quantities during irradiation.

3.2 Overview of MCNP Simulations

3.2.1 Physics Options and Definitions

MCNP version 6.2 [135] code was used for all work completed using MCNP. ROOT v6.16 was adopted as analysis tool [146] when processing the output data files. ROOT was utilised for post-simulation analysis to maintain continuity between that obtained using Geant4.

A general overview of the MCNP input options is described. Basic details such as defining cell volumes and surface geometry can be found in the MCNP6.2 user manual [135]. As examples of the MCNP code utilised for microdosimetric purposes cannot be found easily, such extended introduction is outlined.

Material Definitions

When setting up the material definitions of the MCNP simulation, the Material card ('M' card) is used to define the nuclides associated with a material based on its fractional composition. Materials must be defined in the format *ZZZAAA* (use the default ENDF dataset for this nuclide) or *ZZZAAA.abx* (use a specific ENDF dataset for this nuclide). The energy limit for the high-precision physics model associated with a particular nuclide is based on what is available in the ENDF dataset. This is typically 20 MeV, though it is much higher (up to 200 MeV high-precision) for protons, deuterons, and alpha and ^3He nuclei that have TALYS data available.

In the example below (figure 3.4), water is defined by the isotopic mass fraction, which must be entered accurately by the user. For ^1H , the ENDF data set associated with continuous neutron data from a particular evaluation has been set.

M1	1001.90c	-0.1118732	\$ H-1
	1002	-0.0000257	\$ H-2
	8016	-0.8856944	\$ O-16
	8017	-0.0003586	\$ O-17
	8018	-0.0020482	\$ O-18
MT1	LWTR.20t	\$ Include H-1 in light water thermal scatter data	

Figure 3.4: Example of defining ‘water’ in MCNP, based on isotopic mass fraction. Thermal neutron treatment is included by definition of the ‘MT’ card.

Thermal Neutron Scattering Physics Model

As seen in the above example for water (figure 3.4), the ‘MT’ card has been defined for material 1 (M1). This sets the material to use the $S(\alpha, \beta)$ scattering matrix data associated with it. In this case, LWTR.20t data has been linked to water, which is the neutron thermal elastic scattering treatment for ‘H-1 in Light Water’. It is important that the user is familiar with which scattering matrix is available and defines it to the appropriate material it was intended for.

Hadronic Physics

The ‘LCA’ card is used to select which physics models are implemented in the energy range where data is available. For the intranuclear cascade (INC), available models are CEM3.03, Bertini, ISABEL and INCL4. The Bertini INC model for reactions induced by nucleons and pions is valid up to 3.5 GeV. For the MCNP simulations performed in this work, the Bertini INC model was used by default, with the options selected:

LCA	2	1	1	0023	1	1	0	1	0	0	66
-----	---	---	---	------	---	---	---	---	---	---	----

Figure 3.5: Options to use Bertini INC Model.

The ‘PHYS:<pl>’ card can be used to set the specific physics options of particles. ENDF datasets have been enabled for all particles such that evaluated data is used in the physics model where available. For energies above the upper limit of the ENDF datasets, the Bertini INC model is used to describe these nuclear reactions.

All charged particles have the option of enabling lower energy delta-ray production, which is disabled by default. For this work, delta-rays were enabled for all charged par-

ticles. Delta-ray production was enabled to describe the microdosimetric processes in the SVs [150]. The ‘CUT:<pl>’ card allows the user to select time, energy and weight cutoffs for various particles.

Neutron Specific Physics

The ‘PHYS:N’ card allows the user to select the neutron physics parameters. The ability to reduce memory requirements and perform non-analog (implicit) capture is available, however all neutron interactions in the MCNP simulations were set so full analog capture was performed. The settings for neutron physics are:

PHYS:N	70	70	0	3J	4.0	-1	2	2J	0	0
	emax	emcnf	iunr	-	coilf	cutn	ngam	-	i.int	i.els

Figure 3.6: Neutron specific physics options selected for the MCNP simulations.

- **emax** (70): Upper energy limit (MeV) of neutron tracking,
- **emcnf** (70): Upper energy limit (MeV) to apply analog capture,
- **iunr** (0): Allows table treatment of unresolved resonances,
- **coilf** (4.0): light-ion recoil ions from elastic scatter, NCIA ions from neutron capture,
- **cutn** (-1): Use ENDF data tables up to their upper limit for each nuclide, then use the physics models above that limit,
- **ngam** (2): secondary photons are produced using CGM,
- **i.int** (0): process all nuclear interactions,
- **i.els** (0): control elastic scattering by Prael/Liu/Striganov model.

Neutron tracking and capture processes were set to be in full analog mode with no variance reduction. Specifically, neutron upper tracking limit (emax) and upper analog limit (emcnf) were set to 70 MeV. Neutron interactions were described using continuous energy datasets, largely sourced from the ENDF/B-VII.1 libraries [145]. The Neutron Capture Ion Algorithm (NCIA) describes the production of light and heavy ions from neutron capture and was only used when the production of these ions were not modelled with available nuclear data tables. To allow prompt gamma correlation with captures, secondary photon production by neutron interactions was controlled using the Cascading

Gamma-ray Multiplicity (CGM) code.

The ‘CUT:N’ card was set so analog capture is used (CUT:N 2J 0 0), otherwise a biasing technique will be applied (non-analog capture).

Proton Specific Physics

The physics options set for protons using the ‘PHYS:H’ card are shown in figure 3.7:

PHYS:H	100	100	-1	J	1	J	1	3J	0	0	0	0.917	J	0	-1
	E_{max}	E_{an}	Tabl	-	Istrg	-	Recl	-	i_{mcs}	i_{int}	i_{els}	efrac	-	ckv	drp

Figure 3.7: Proton specific physics options selected for the MCNP simulations.

- **E_{max}** (100): Upper energy limit (MeV) of proton tracking,
- **E_{an}** (100): Upper energy limit (MeV) to apply analog capture when interacting with neutrons,
- **Tabl** (-1): Use ENDF data tables up to their upper limit for each nuclide, then use the physics models above that limit,
- **Istrg** (1): use continuous slowing-down approximation for charged-particle straggling,
- **Recl** (1): light ions to be created at each proton elastic scatter event with light nuclei,
- **i_{mcs}** (0): use FermiLab angular deflection model with Vavilov straggling for Coloumb scattering,
- **i_{int}** (0): process all nuclear interactions,
- **i_{els}** (0): control elastic scattering by Prael/Liu/Striganov model,
- **efrac** (0.917): stopping power energy spacing of 0.917,
- **ckv** (0): Cerenkov emission turned off,
- **drp** (-1): delta-ray production *enabled* with default energy cutoff (0.020 MeV).

The ‘CUT:H’ card was set for protons (CUT:H J 0 0 0) so the lower energy cutoff is forced to set as close to 0 MeV as permitted.

Photon Specific Physics

The physics options set for photons using the ‘PHYS:P’ card are shown in figure 3.7:

PHYS:P	100	0	0	-1	0	J	1
	emcpf	ides	nocoh	ispn	nodop	-	fism

Figure 3.8: Photon specific physics options selected for the MCNP simulations.

- **emcpf** (100): Upper energy limit (MeV) for detailed photon physics treatment,
- **ides** (0): Generation of electrons via Bremsstrahlung is enabled,
- **nocoh** (0): Coherent scattering is turned on,
- **ispn** (-1): Photonuclear particle production enabled and is analog,
- **nodop** (0): Doppler energy broadening is turned on,
- **fism** (1): Photofission is enabled and uses the LLNL fission model.

Other Particle Specific Physics

PHYS:A	100	3J	1	5J	0	0	0	0.917	J	0	-1
PHYS:D	100	3J	1	5J	0	0	0	0.917	J	0	-1
PHYS:#	100	3J	1	5J	0	0	0	0.917	J	0	-1
PHYS:T	100	3J	1	5J	0	0	0	0.917	J	0	-1
	emax	-	istr	-	i_mcs	i_int	i_els	Efrac	-	Ckv	Drp

Figure 3.9: Other particle specific physics options selected for the MCNP simulations.

These parameters share the same definition as protons (PHYS:H), which can be referred to as above. The particles referred to as ‘#’ represents all heavy ions. The CUT:<pl> for all these particles were set as (CUT:<pl> J 0 0 0), to force the lowest possible energy cutoff permitted.

General Source Definition

The primary particles that are generated in the simulation are defined using the ‘SDEF’ card. This card allows the user to define the source type (plane circular, plane rectangular, volume, point), direction, energy, and particle type. All of these values can be based on a distribution. Multiple sources can be defined and given weighting values, when representing mixed radiation fields.

3.2.2 Advanced Particle Tracking in MCNP for microdosimetry

MCNP contains numerous flexible tally cards, such as: surface & volume flux, point detectors and pulse height tally for energy deposition. These pre-set tally cards allow the user to easily record the quantities of interest in a simulation, but lack the level of detail required for microdosimetry purposes (i.e. particle-by-particle delta-ray analysis).

The microdosimetric method was applied using the ‘PTRAC’ card, which produces an output “tape” containing relevant tracking details of the current event.

The ‘PTRAC’ card allows the user to export a list of particle events to an output file. The data that is stored in the output file is based on a set of conditions. The output variables include: x, y, z location of the particle, cell number, material number, u, v, w direction cosines, particle energy, particle type, event type and current time. The PTRAC card must be linked to an MCNP tally, such that when the quantity is recorded by that tally, the detailed track information is output to PTRAC.

An example of the configuration required to use PTRAC in MCNP is shown in figure 3.10. In this example, the ‘*F8’ energy deposition tally card is linked to PTRAC such that any of the listed particle types scoring this quantity in ‘cell 1’ will trigger PTRAC output. The ‘*F18’ energy deposition tally card with associated ‘F18 CAP’ card acts as a dummy to force full-analog neutron simulation.

```
*F8:N,H,P,A,D,#,E,T 1
E8 0 70i 70
*F18:N,H,P,A,D,#,E,T 1
E18 0 70i 70
FT18 CAP
PTRAC FILE=BIN WRITE=ALL TYPE=N,H,P,A,D,#,E,T
      CELL=1 TALLY=8 MAX=1000000
```

Figure 3.10: Configuration required to use PTRAC in MCNP with full-analog neutron simulation. Example shown is for scoring energy deposition in ‘cell 1’ relating to interactions by various particle types.

The amount of information set to be stored in the output file will considerably increase

the I/O and size of the file, ultimately slowing down the simulation time. For example, a simulation set to store every interaction in the complete simulation world will reach several GB within a few minutes. To overcome this, the conditions should be set to only store the events of interest. These conditions include: event type (source/banked/surface crossing/collision/termination), particle type, energy range, and cell number.

The PTRAC output file is processed using Python scripting [151] with the *MCNPTools* [152] library add-on. The information stored in the file is very compact and uses mostly integer indexes when referring to particle type and interaction type. As such, lookup tables are essential to define the reactions and particles associated with them. Unfortunately, there is no complete application available publicly with this data included. These must be obtained from the MCNP reference documentation. As such, the post-simulation analysis application was developed entirely from the ground up, requiring extensive coding to process the PTRAC data with all the necessary lookup information.

As part of this thesis, the method for microdosimetry scoring in MCNP was developed entirely from scratch, utilizing the specified PTRAC output and associated analysis application discussed in this section.

The analysis application was written in Python; the *MCNPTools* base for exporting PTRAC, and C++; the ROOT base for analysing the data extracted using Python. The use of ROOT for the analysis was essential to maintain continuity with the data obtained using Geant4. The application is capable of performing detailed microdosimetric analysis from MCNP output. A full description of reaction chains is possible, with the ability to discriminate between crossers/stoppers, and account for delta-rays as demonstrated in chapter 5 and [129].

3.3 Computing Systems used

Various computing systems were used for the simulations performed in this work. The locations and details of these systems are outlined in table 3.2. The two servers from

the National Computational Infrastructure (NCI) are Gadi, and Raijin (now decommissioned), which are located at the Australian National University (ANU), Canberra, Australia.

Name	Location	Computation per Node	Operating System
NCI Gadi	NCI - ANU, Canberra, Australia	Two 24-core Intel® Xeon® ‘Cascade Lake’ CPUs @ 2.9 GHz & 192 GB of RAM	CentOS 8
UOW Hadron	CMRP - UOW, Wollongong, Australia	18-core Intel® Xeon® E5-2695v4 CPU @ 2.10 GHz	CentOS 7
UOW HPC	IMTS - UOW, Wollongong, Australia (now decommissioned)	16-Core AMD® Opteron® @ 2.3 GHz & 256 GB of RAM	CentOS 6
UOW Centaur	CMRP - UOW, Wollongong, Australia (now decommissioned)	10-core Intel® Xeon® E5-2650v3 CPU @ 2.30 GHz	CentOS 6
NCI Raijin	NCI - ANU, Canberra, Australia (now decommissioned)	Two 14-core Intel® Xeon® E5-2690 v4 CPUs @ 2.6 GHz & 128 GB of RAM	CentOS 6
Fenrisúlfr	Owned and managed by J. Vohradsky, Wollongong, Australia	Four 10-Core Intel® Xeon® E7-4870 CPUs @ 2.4 GHz & 96 GB of RAM	CentOS 7

Table 3.2: Details of the computing systems used for the simulations in this work.

The Fenrisúlfr Computational Node

To compensate for the amount of computing power required to complete the vast number of simulations in this work, a personal CentOS 7 server was acquired and set up. The *Fenrisúlfr Computational Node*, (named after the wolf of Norse mythology) was configured to provide a dependable personal computer that could be fully utilised solely for this work. The server is a single-node Dell® PowerEdge® R810, with 4×10 -Core Intel® Xeon® E7-4870 CPUs and 96 GB of NVRAM. Each of the 40 cores have 2 threads,

meaning that 80 separate simulations could be run simultaneously.



Figure 3.11: Images of the Fenrisúlf Computational Node. a) Original mounting in modified side table ‘rack’, b) Current mounting in more appropriate server rack - lid has been opened to show interior components.

Emphasis was placed on ensuring the operating system and software versions (e.g. compilers) were the same as the ‘UOW Hadron’ server, for continuity of specific simulation output.

Due to the large amount of RAM available, a virtual RAM drive could be configured in the operating system to act as a ‘scratch’ directory when running multiple simulations. This reduces the I/O ‘bottleneck’ of the storage devices, as both Geant4 and MCNP6 are constantly reading (such as when referring to ENDF data) and writing (when outputting to ROOT and/or PTRAC files) to the HDD/SSD.

The successful implementation of the personal computational node allowed many simulations to be completed quickly, which was highly beneficial for checking the results of numerous configurations before running longer to reduce the statistical uncertainty.

Chapter 4

Optimisation of the SOI Bridge microdosimeter for BNCT QA ¹

In this chapter, Geant4 was used to model and optimise the geometry and packaging of Silicon on Insulator (SOI) microdosimeters for BNCT Quality Assurance purposes in view of experimental measurements at the KUR research reactor, in Japan.

In this context, design optimisation pertains to the sensitive volume size and probability of neutron activation. This study has shown conclusively that whilst the materials currently used in the fabrication of silicon based microdosimeters are appropriate, there are changes with respect to the sensitive volume thickness that should be addressed to reduce the number of ‘stoppers’ in the microdosimeter.

The Geant4 simulation was developed to characterise the detector response of SOI microdosimeters in a BNCT radiation field in order to optimise their design. The probability of neutron activation was studied to investigate any potential radioprotection hazards.

The research performed in this study was conducted using the latest generation V2

¹Part of this chapter has been published in the European Journal of Medical Physics: James Vohradsky, Susanna Guatelli, Jeremy A. Davis, Linh T. Tran, Anatoly B. Rosenfeld (2019). *Evaluation of silicon based microdosimetry for Boron Neutron Capture Therapy Quality Assurance*. Physica Medica. DOI: 10.1016/j.ejmp.2019.09.072. (Accepted, 6 September 2019)

silicon Bridge microdosimeter design [21].

4.1 Method

Geant4 version 10.01 [127] [131] was used to model the BNCT radiation field produced by an incident epithermal neutron source in a water phantom. ROOT v5.34 was adopted as analysis tool [146]. The simulation was based on the experimental setup adopted in Onizuka et al. (2003) at the Kyoto University Research Reactor (KUR) [153] [154]. The phantom consisted of a $30 \times 30 \times 15 \text{ cm}^3$ water box and is surrounded by air.

Geometrical scaling factors can be used in solid-state microdosimetry to convert energy deposition in silicon to a tissue equivalent response. For BNCT microdosimetry, a suitable scaling factor of approximately 0.63 has been determined [22], which has been applied to all results presented in this study. The 1.47 MeV alpha particle produced in BNCT has a range of 5 μm and 8 μm in silicon and tissue, respectively.

The modelled incident radiation field consisted of a 5 cm diameter cylindrical beam of epithermal neutrons which originate on one side of the water phantom. The neutron energy fluence was based on the KUR reactor operating in epithermal mode, as shown in Figure 4.1.

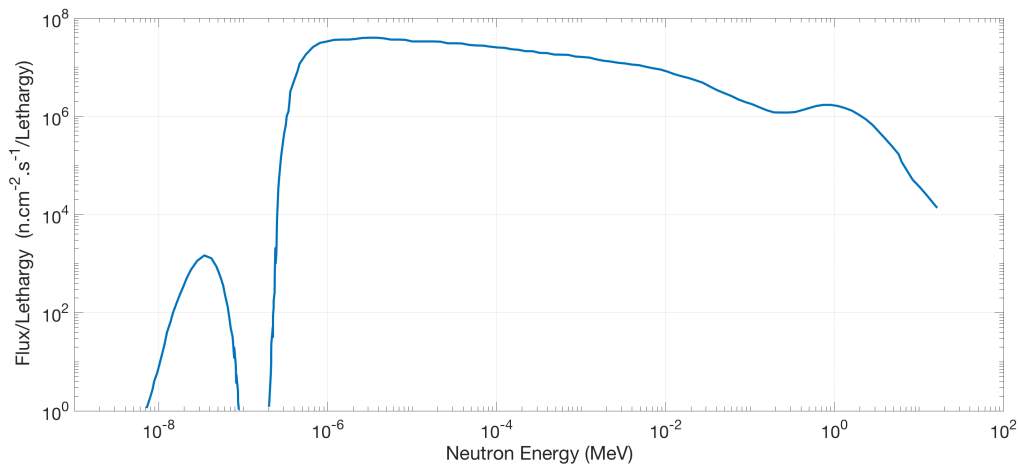


Figure 4.1: KUR epithermal neutron energy spectrum used as the primary source in all simulations [153], courtesy of Baba et al.

The first simulation was designed to calculate the optimal depth in the water phantom to place the detector to maximize BNCT reactions. For this simulation, 25 parts-per-million ^{10}B was distributed uniformly in the water, which is the typical concentration of ^{10}B in the tumour for BNCT. The optimal depth is located at the depth of 27 mm in the water phantom to maximise the number of recorded BNCT reactions. Section 4.2 shows the results deriving from this study. The detector probe used by CMRP, which houses the Bridge microdosimeter, was modelled and positioned at the optimal depth within the water phantom, facing the incident beam direction as shown in Figure 4.2.



Figure 4.2: Detail of the geometry of the detector and its packaging, in the direction of incidence of the neutron beam (incident from left). The neutron beam has a diameter exceeding the lateral sizes of the microdosimeter device. The microdosimeter is set at 2.7 cm depth in the water phantom.

A PMMA layer with thickness equal to 500 μm in the direction of incidence of the neutron beam, 100 μm thick polyethylene (PE), the boron conversion layer with varying thickness, the 100 μm air gap and Bridge microdosimeter follow. The PMMA layer represents the waterproof outer casing which houses the detector components. The removable neutron converter in the setup consists of a 3 μm thin film of enriched boron carbide ($^{10}\text{B}_4\text{C}$) deposited on a 170 μm aluminium substrate. PE tape is used to attach the converter layer onto the top of the detector package. This leaves a thin air gap between the microdosimeter and the converter film. The Bridge microdosimeter is shown from bird's eye view in Figure 4.3.

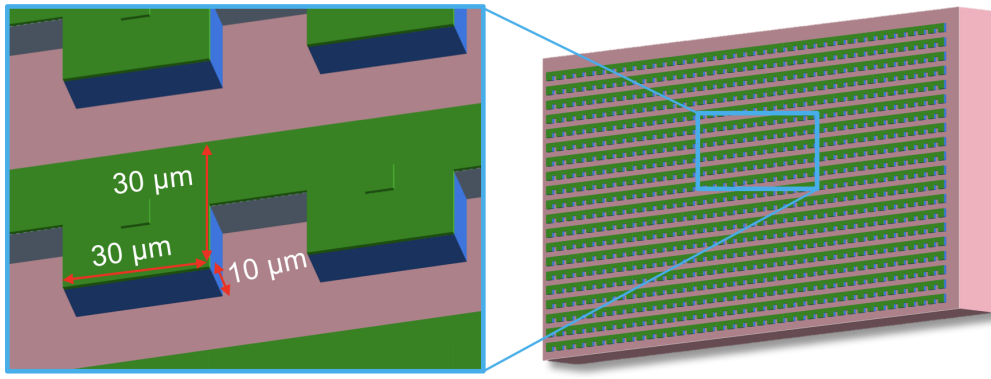


Figure 4.3: Bridge SOI Microdosimeter. The SVs shown in green have dimensions of $30 \times 30 \mu\text{m}^2$ with $10 \mu\text{m}$ thickness along the direction of incidence of the neutron beam.

The second simulation focused on the optimisation of detector geometry for the CMRP SOI Bridge microdosimeter in terms of its SV geometry. Microdosimetry is only appropriate in radiation environments where the particles incident on the detector have a range that exceeds the mean chord length of the SV [3]. That is, most events within the SVs must pass through the device (crossers). Those which have shorter range than the mean chord length range and come to rest within the SV are undesired (stoppers). Therefore it is essential to increase the relative number of crossers versus stoppers interacting with the SVs. This work investigates the proportion of stoppers and crossers in the microdosimetric spectra with respect to three key variables: SV thickness, SV lateral area and thickness of the $^{10}\text{B}_4\text{C}$ converter film. Reduction in the SV thickness and SV area will reduce the mean chord length of the SVs, which should increase the number of crossers. Unfortunately, a compromise has to be reached as smaller SV sizes, which favour crossers against stoppers, reduce the sensitivity of the detector and may require a larger array of SVs, translating into an overall bigger device. For the simulated microdosimetric response of each microdosimeter configuration described, 10^{11} primary events were generated to achieve a statistical uncertainty lower than 1%.

The use of boron conversion films which have a thickness close to the range of the products originated in it is problematic. This is because the BNCT products lose more energy within the converter leading to a higher probability of stoppers in the SV. As a means of verifying the most optimal experimental set-up, the $^{10}\text{B}_4\text{C}$ film thickness is

investigated with respect to the ratio of crossers/stoppers within the target SV. Another site of BNC reactions is the built-in boron doped p^+ region of the SVs [22]. It is expected that particles produced in this region will have greater range than those in the converter film, allowing for more crossers in the SVs. The relative number of BNC particles reaching the SVs and type of interaction will be compared for the $^{10}\text{B}_4\text{C}$ film and p^+ region of the SVs.

The secondary radiation field produced in the microdosimeter by the incident BNCT neutron field was studied as well. This mainly relates to the radioprotection of experiment operators and the investigation of background noise that could be produced in the detector. The flux of the KUR epithermal neutron beam was used to calculate the relative number of incident particles required in the simulation for a 5 cm diameter cylindrical beam. The detector was simulated to be irradiated for the typical BNCT treatment time of 30 minutes. In the simulation, the track history of each particle was recorded, such as information regarding the parent particle and which physics process produced it. For each interaction, the kinetic energy, the point where the secondary particle is generated and its final location, when it comes to rest, is also stored. The rate at which materials produced dangerous levels of ionising radiation and the required cool-down of the detector time was investigated. This was achieved by modelling the rate of neutron activation during irradiation and the time required for radioactivity to fall below 1 μBq . This lower activity threshold was chosen as it is well below the limit of concern given by the IAEA for the materials tested [155].

4.2 Depth Dose Calculation in Water

The simulated depth-dose response is depicted in Figure 4.4. The maximum response for alpha particles, lithium nuclei and protons was 22, 23 and 31 mm, respectively. Using this result, the optimal depth was chosen to be 27 mm. This placement is consistent with experimental measurements obtained by Onizuka et al. (2003) [154].

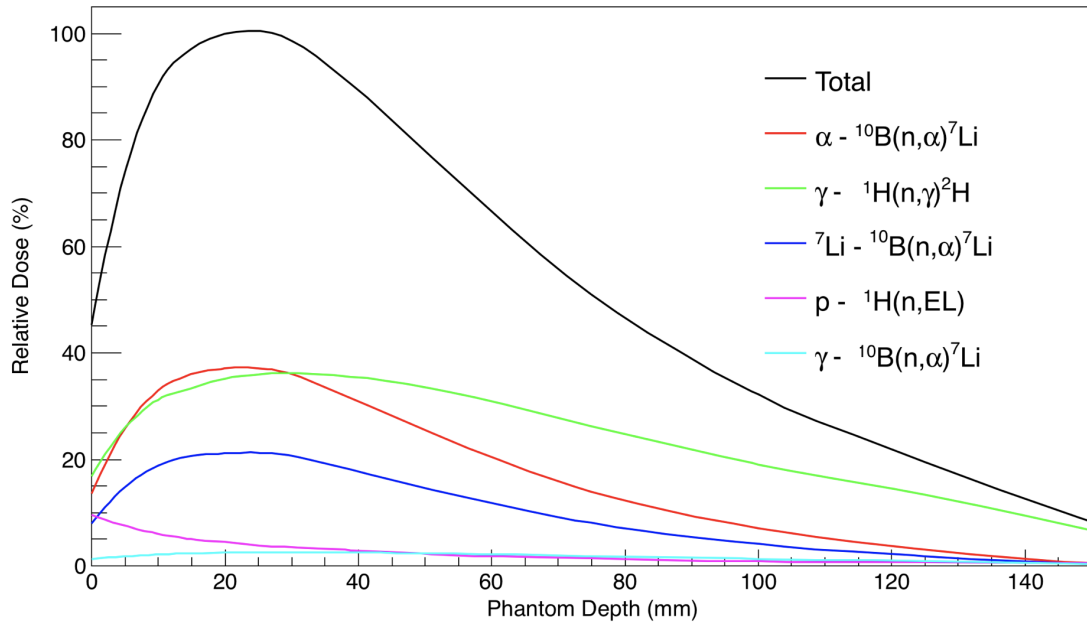


Figure 4.4: Depth dose curve in the water phantom, with 25ppm ^{10}B uniformly distributed in water. The total energy deposition is depicted in black. The contribution deriving from each secondary particle under investigation is indicated as well, together with the process originating the secondary particle (see the legend).

4.3 Geometry optimisation of the SOI Bridge microdosimeter

Sensitive Volume thickness reduction

In order to increase the number of crossers in the microdosimeter, the thickness of the SVs was reduced in the direction of incidence to the neutron beam. Three different thicknesses were considered in this study: 10, 2 and 1 μm , with their microdosimetric responses shown in Figures 4.5, 4.6 and 4.7, respectively.

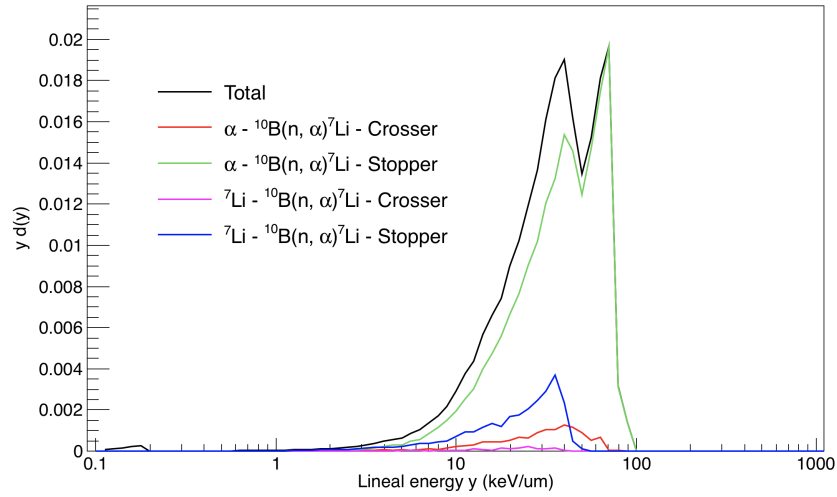


Figure 4.5: Microdosimetric spectra of $30 \times 30 \times 10 \mu\text{m}^3$ SOI Bridge SVs with $3 \mu\text{m}$ thick $^{10}\text{B}_4\text{C}$ film (mostly stoppers).

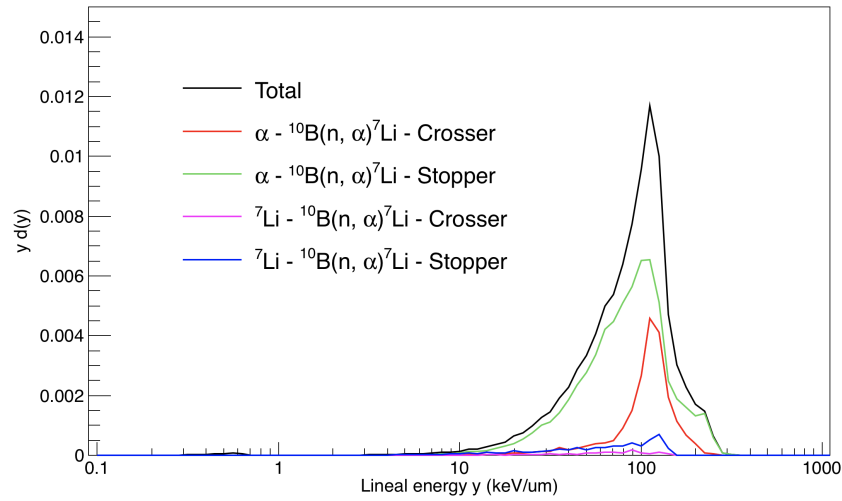


Figure 4.6: Microdosimetric spectra of $30 \times 30 \times 2 \mu\text{m}^3$ SOI Bridge SVs with $3 \mu\text{m}$ thick $^{10}\text{B}_4\text{C}$ film (increased crossers).

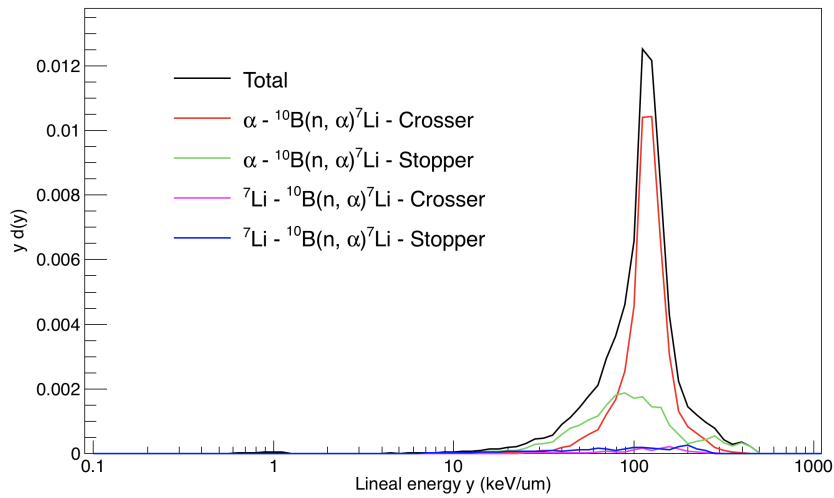


Figure 4.7: Microdosimetric spectra of $30 \times 30 \times 1 \mu\text{m}^3$ SOI Bridge SVs with $3 \mu\text{m}$ thick $^{10}\text{B}_4\text{C}$ film (mostly crossers).

The range of the 1.47 MeV alpha particles and 0.84 MeV ^7Li nuclei produced by BNC in silicon are 5.26 μm and 2.46 μm , respectively [47]. A-priori knowledge of the range of these particles provides a means of optimising the detector geometry. It is obvious that the current SOI microdosimeter would be unsuitable for BNCT given the thickness (10 μm) is greater than the maximum range of the BNCT products.

Detector Design	B_4C	α		^7Li	
		Crossers	Stoppers	Crossers	Stoppers
$30 \times 30 \times 10 \mu\text{m}^3$ SV	3 μm	0.050	0.950	0.039	0.961
$30 \times 30 \times 2 \mu\text{m}^3$ SV	3 μm	0.283	0.717	0.185	0.815
$30 \times 30 \times 1 \mu\text{m}^3$ SV	3 μm	0.694	0.306	0.373	0.627

Table 4.1: Ratio of crosser or stopper by particle type for different detector designs and 3 μm thick B_4C film.

Table 4.1 shows the proportion of crossers and stoppers by particle type for different SV thicknesses. The current Bridge design with 10 μm thick SVs (Figure 4.5) yielded a response which mostly consisted of stoppers. The double peak for alpha stoppers seen in this figure is due to energy loss variations in the 3 μm thick B_4C film (causing variations in arrival kinetic energies), which result in ‘apparent’ lineal energy differences in the microdosimeter SVs. With the SV thickness design reduced to 2 μm , as shown in Figure 4.6, the fraction of crossers is about 40%, which is approximately 7.6 times higher. For the conceptual design which uses 1 μm thick SVs, as shown in Figure 4.7, the number of crossers were further increased. However, due to limitations with the current technology used for detector fabrication, only the 2 μm thick SV design is feasible.

Reduced boron carbide film thickness

The current design of the boron converter is based upon what will be used experimentally. Figure 4.8 shows the fraction of alpha particles crossing the SV, for two different $^{10}\text{B}_4\text{C}$ thicknesses (3 μm , 0.5 μm) and for bare detector with doped p^+ region.

For the 3 μm thick $^{10}\text{B}_4\text{C}$ film, the alpha particles and ^7Li nuclei emerging from the film had an overall lower kinetic energy due to ionisation. As such, larger angles of incidence are prevented, which shaped the field to increase propagation in one direction

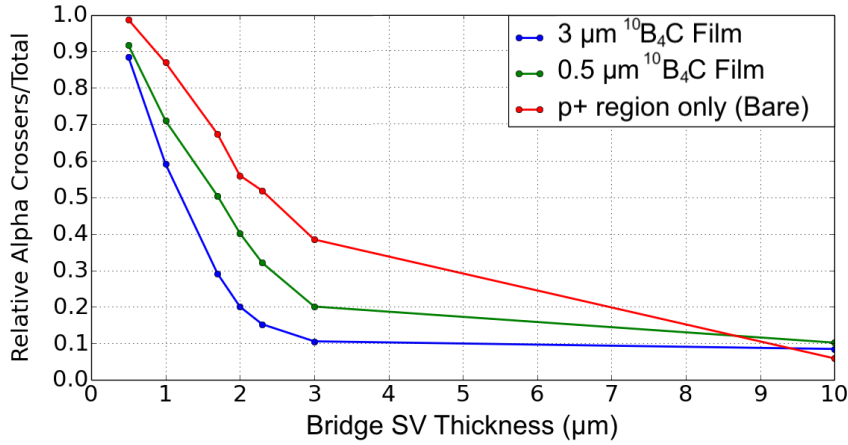


Figure 4.8: Relative ratio of alpha particle crossers and total number of alpha particle crossers and stoppers in the microdosimeter SVs obtained using the 3 μm B₄C thick film (blue) and 0.5 μm B₄C thick film (green). The ratio of crossers/total in the bare detector is obtained using only the boron doped p⁺ region implanted in the SVs is depicted in red.

towards the SVs. The range of the 1.47 MeV alpha particle produced by BNC in ¹⁰B₄C is approximately 3.43 μm [146].

The proportion of alpha particles and ⁷Li nuclei in terms of crosser and stoppers are shown in table 4.2 for the 0.5 μm thick ¹⁰B₄C layer. The count collected by the device with 30×30×2 μm³ SVs compared with that of 30×30×10 μm³ SVs is 105 counts/sec and 78 counts/sec, respectively, which is approximately 26% less. This should be taken into consideration, as an increase in the number of SV in the array may be required. Unlike the results shown in table 4.1 with the 3 μm thick ¹⁰B₄C film, the relative number of alpha and ⁷Li particles are much closer in value for the 30×30×10 μm³ SV device.

Detector Design	B ₄ C	α		⁷ Li	
		Crossers	Stoppers	Crossers	Stoppers
30×30×10 μm ³ SV	0.5 μm	0.193	0.807	0.081	0.919
30×30×2 μm ³ SV	0.5 μm	0.762	0.238	0.301	0.699
10×10×2 μm ³ SV	0.5 μm	0.950	0.050	0.777	0.223
10×10×1 μm ³ SV	0.5 μm	0.983	0.017	0.894	0.106

Table 4.2: Ratio of crosser or stopper by particle type for different detector designs and 0.5 μm thick B₄C film.

For the 0.5 μm thick ¹⁰B₄C layer, the distribution of the radiation field that emerges from the film is more isotropic with higher kinetic energy. This provides an advantage of more crossers in the SVs. The number of alpha particles and ⁷Li nuclei that reach the SVs

is twice as much. The microdosimetric spectra obtained with $30 \times 30 \times 2 \mu\text{m}^3$ SVs using this film thickness is shown in Figure 4.9. The lower energy alpha stoppers have been minimised with this configuration, but a shoulder between 120 and 250 keV/ μm is now present due to larger angles of incidence of emission from the film.

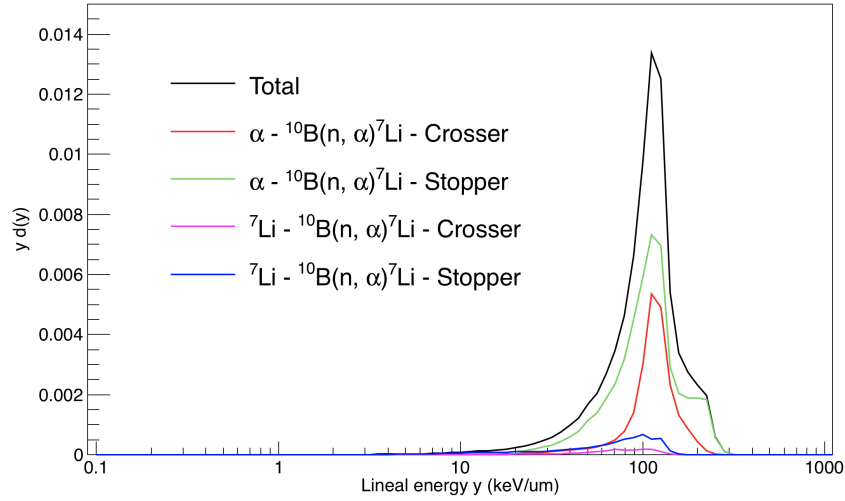


Figure 4.9: Microdosimetric spectra of $30 \times 30 \times 2 \mu\text{m}^3$ SOI Bridge SVs with $0.5 \mu\text{m}$ thick $^{10}\text{B}_4\text{C}$ conversion film.

Sensitive Volume lateral width reduction

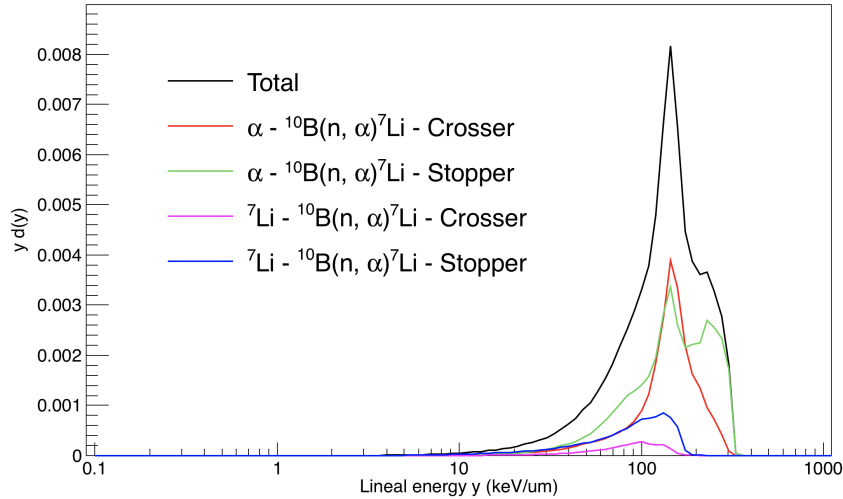


Figure 4.10: Microdosimetric spectra of $10 \times 10 \times 2 \mu\text{m}^3$ SOI Bridge SVs with $0.5 \mu\text{m}$ $^{10}\text{B}_4\text{C}$ conversion film.

The changes to the microdosimetric spectra relative to the lateral area of the device is presented in Figure 4.10. The lateral area was reduced from $30 \times 30 \mu\text{m}^2$ to 10×10

μm^2 . The decreasing volume size should lead to lower mean chord lengths and higher probability of crossers. However, as the lateral area is smaller, interactions with the SV by normally incident particles is lower. As such, the proportion of stoppers in this case are mostly high energy alpha particles, which enter the SV at extreme angles.

Table 4.2 also describes the ratio of interaction types between alpha particles and ^7Li nuclei in terms of the lateral width of the SVs. The equivalent mean chord length of SVs with smaller lateral area allow for a much higher probability of crossers. However, the total count of these smaller SVs is significantly reduced. The count rate for the $10 \times 10 \times 2 \mu\text{m}^3$ and $10 \times 10 \times 1 \mu\text{m}^3$ SVs is 8.1 counts/sec and 7.6 counts/sec, respectively. Compared with the $30 \times 30 \times 10 \mu\text{m}^3$ SV device, the count rate is approximately 92% lower.

Provided the current technology using a detector with $2 \mu\text{m}$ thick SVs, the worst case scenario would require the number of counts deriving from the BNCT reactions to be higher than 1000, to be well above the noise threshold. This poses a potential issue when using thinner SVs and only using products from the p^+ region. The theoretical designs using $0.5 \mu\text{m}$ film plus $30 \times 30 \times 2 \mu\text{m}^3$, $10 \times 10 \times 2 \mu\text{m}^3$ and p^+ region only would need to be exposed for 15, 123 and 104 seconds, respectively, to have sufficient counts. Given the typical treatment time of 30 minutes for BNCT, this should not cause major concern.

Investigating the p^+ region as neutron converter

Another site of BNC reactions is the boron doped p^+ region of the SVs. For the alpha particles produced in this built-in neutron converter, the rate of crossers are much higher than the $^{10}\text{B}_4\text{C}$ film. This was due to a lower energy loss of alpha particles as they did not have to pass through overlayers to reach the SV. The microdosimetric spectra of the bare Bridge (no $^{10}\text{B}_4\text{C}$ film) shows the deposition type from products arising only from the p^+ region of the SVs. The microdosimetric spectra are shown with decreasing SV thickness in figures 4.11, 4.12 and 4.13 for $10 \mu\text{m}$, $2 \mu\text{m}$ and $1 \mu\text{m}$ SVs, respectively.

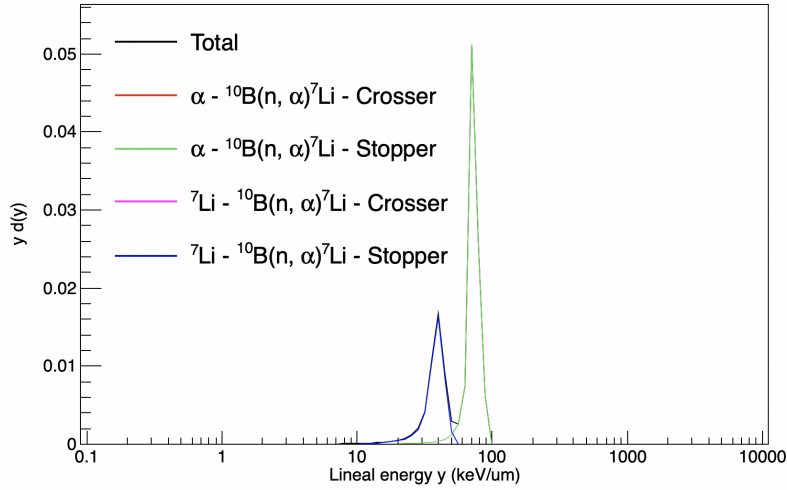


Figure 4.11: Microdosimetric spectra of bare $30 \times 30 \times 10 \mu\text{m}^3$ SOI Bridge SVs - alpha particles and ^7Li nuclei originating only from p^+ region (mostly stoppers).

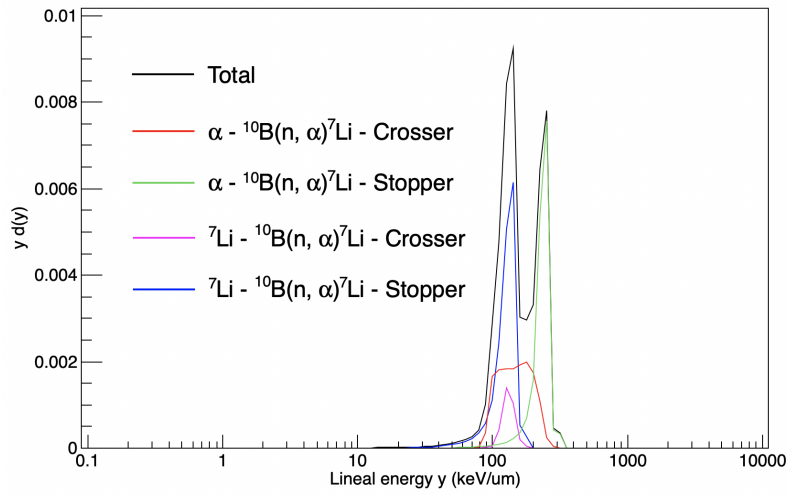


Figure 4.12: Microdosimetric spectra of bare $30 \times 30 \times 2 \mu\text{m}^3$ SOI Bridge SVs - alpha particles and ^7Li nuclei originating only from p^+ region (increased crossers).

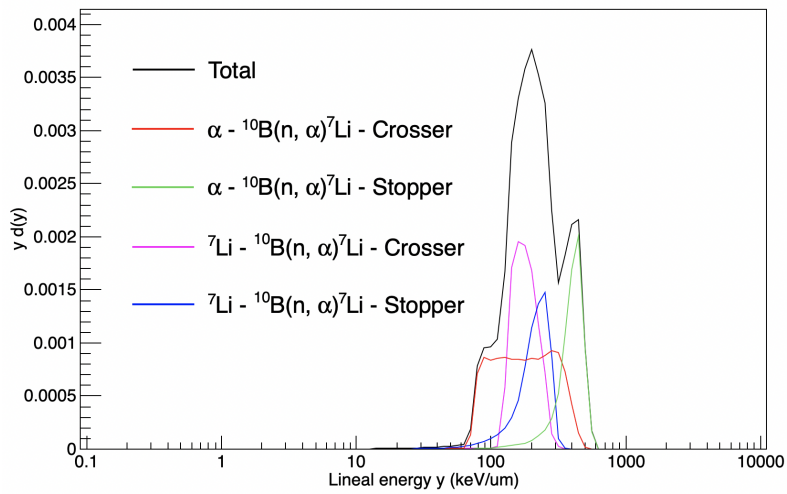


Figure 4.13: Microdosimetric spectra of bare $30 \times 30 \times 1 \mu\text{m}^3$ SOI Bridge SVs - alpha particles and ^7Li nuclei originating only from p^+ region (mostly crossers).

As shown in the microdosimetric spectra for the bare Bridge, as the SV thickness is decreased, the rate of crosser alpha particles and ^7Li nuclei increases. The 10 μm SV spectra has a single peak for both alpha and ^7Li stoppers as there is a lower angular distribution through the SV and no products reaching neighbouring SVs.

As the SV thickness is reduced to 2 μm , the rate of crosser products arising from the p^+ region increases. This results in two distinct peaks in the microdosimetric spectra, however the lower peak is mostly consisting of ^7Li stoppers. Finally, as the SV thickness is reduced to 1 μm , this results in the lower peak (around 200 $\text{keV}/\mu\text{m}$) consisting mainly of alpha and ^7Li crossers.

For a summary of the difference in the fraction of alpha particles crossing the SVs which originated only from the doped p^+ region versus those from $^{10}\text{B}_4\text{C}$ film, refer to Figure 4.8.

This result validates the feasibility of applying the boron doped p^+ region in SOI microdosimeters for dedicated BNCT microdosimetry. However, the rate of $^{10}\text{B}(\text{n},\alpha)^7\text{Li}$ reactions in the p^+ region is approximately 500 times lower than with the $^{10}\text{B}_4\text{C}$ film. The detection rate of these products from the p^+ region by the SVs is 9.6 counts/sec.

4.4 Activation and Fragmentation in Experimental Setup

The reaction rate that occurred in the SOI Bridge and detector probe materials during neutron irradiation by the KUR epithermal source is shown in table 4.3. The detector configuration consists of $30 \times 30 \times 2 \mu\text{m}^3$ SVs and a $0.5 \mu\text{m}$ thick B_4C film. Figure 4.14 shows the radiation field of secondary particles produced in the detector materials. For the SOI Bridge microdosimeter, most activations are associated with silicon and aluminium, which have high nuclear cross sections in this neutron energy range. Interactions in silicon occur mainly in the substrate of the microdosimeter.

Reaction	Count/sec	Material
$^{10}\text{B}(\text{n},\alpha)^7\text{Li}$	5.35×10^3	$^{10}\text{B}_4\text{C}$ Film (99.82%), p^+ region (0.18%)
$^1\text{H}(\text{n},\text{G})^2\text{H}$	3.19×10^2	PMMA (77.96%), PE (22.04%)
$^{28}\text{Si}(\text{n},\text{G})^{29}\text{Si}$	5.96×10^1	Si Substrate (99.57%), SV (0.63%), SiO_2 (0.2%)
$^{27}\text{Al}(\text{n},\text{G})^{28}\text{Al}$	5.91×10^1	Al Film (100%)
$^{12}\text{C}(\text{n},\text{G})^{13}\text{C}$	3.51×10^0	PMMA (82.37%), PE (17.63%)
$^{29}\text{Si}(\text{n},\text{G})^{30}\text{Si}$	1.90×10^0	Si Substrate (98.31%), SV (1.13%), SiO_2 (0.56%)
$^{30}\text{Si}(\text{n},\text{G})^{31}\text{Si}$	1.58×10^0	Si Substrate (99.32%), SiO_2 (0.68%)
$^{10}\text{B}(\text{n},\text{G})^{11}\text{B}$	5.33×10^{-1}	$^{10}\text{B}_4\text{C}$ Film (100%)
$^{28}\text{Al} \rightarrow ^{28}\text{Si}$ Decay	3.05×10^{-1}	Al Film (96.61%), Si Substrate (3.39%)
$^{14}\text{N}(\text{n},\text{p})^{14}\text{C}$	2.35×10^{-1}	Air Gap (100%)
$^{18}\text{O}(\text{n},\alpha)^{15}\text{C}$	9.60×10^{-2}	PMMA (100%)
$^{13}\text{C}(\text{n},\text{G})^{14}\text{C}$	7.46×10^{-2}	PMMA (85.71%), PE (14.29%)
$^{10}\text{B}(\text{n},2\alpha+\text{t})$	3.20×10^{-2}	$^{10}\text{B}_4\text{C}$ Film (100%)
$^{28}\text{Si}(\text{n},\alpha)^{25}\text{Mg}$	3.20×10^{-2}	Si Substrate (100%)
$^{15}\text{C} \rightarrow ^{15}\text{N}$ Decay	2.72×10^{-2}	PMMA (100%)
$^{16}\text{O}(\text{n},\alpha)^{13}\text{C}$	2.13×10^{-2}	PMMA (100%)
$^{14}\text{N}(\text{n},\text{G})^{15}\text{N}$	2.13×10^{-2}	Air Gap (100%)
$^{29}\text{Si}(\text{n},\alpha)^{26}\text{Mg}$	1.07×10^{-2}	Si Substrate (100%)
$^{28}\text{Si}(\text{n},\text{p})^{28}\text{Al}$	1.07×10^{-2}	Si Substrate (100%)
$^{18}\text{O}(\text{n},\text{G})^{19}\text{O}$	1.07×10^{-2}	PMMA (100%)
$^{19}\text{O} \rightarrow ^{19}\text{F}$ Decay	2.74×10^{-4}	PMMA (100%)
$^{31}\text{Si} \rightarrow ^{31}\text{P}$ Decay	1.16×10^{-4}	Si Substrate (99.32%), SiO_2 (0.68%)

Table 4.3: Interactions within the SOI Bridge microdosimeter and detector probe materials (see Figure 4.2) resulting from neutron irradiation.

There are minimal recoils in the same energy range as BNCT products. Scattered protons arising from neutron moderation have kinetic energy mainly lower than 1.5 MeV. The significant production of deuteron by ^1H thermal capture had very low kinetic energy and range of only a few micron in water [47], so it does not pose a particular concern.

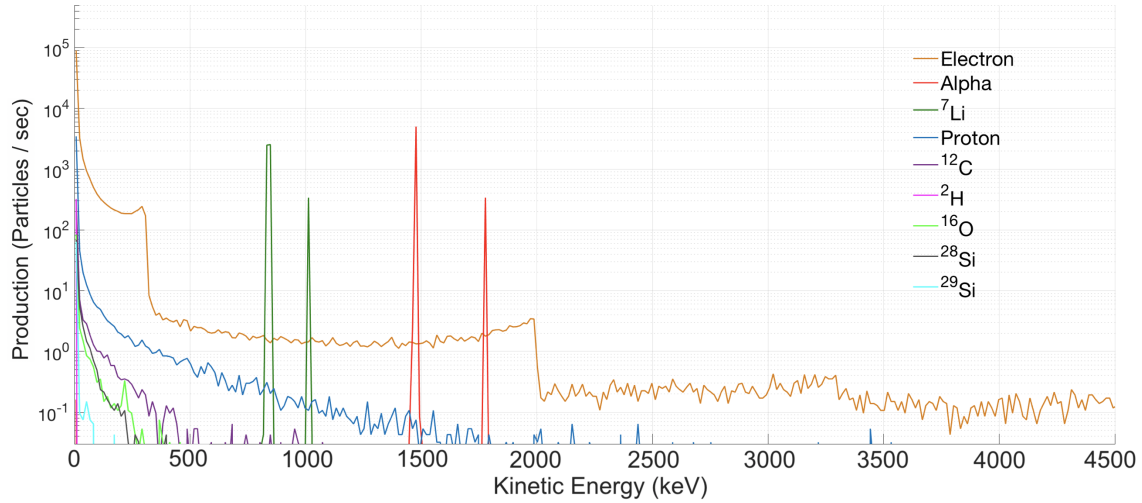


Figure 4.14: Secondary radiation field produced by the KUR epithermal neutron field in the materials of the SOI microdosimeter device.

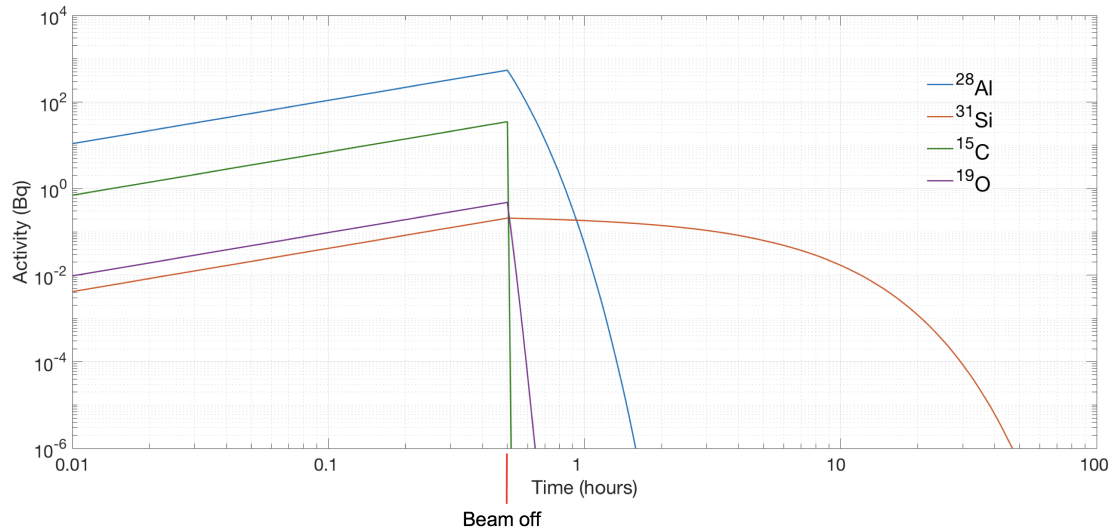


Figure 4.15: Activity of radioisotopes produced within the materials of the SOI Bridge detector device for 30 minute irradiation period with cool-down.

Figure 4.15 shows the activity curve of secondary particles produced in the detector materials. In terms of radioprotection, ^{28}Al and ^{31}Si have a high activation rate. Following the beam shut-off, ^{28}Al takes less than 2 hours to reach 1 μBq . For ^{31}Si , it would take over 376 years of constant irradiation to reach the IAEA activity limit of 10^6 Bq [155].

It is important to note that all activations of ^{28}Al occurred in the aluminium film of the neutron converter, with a negligible count in the aluminium tracks of the detector.

The gamma ray spectrum produced in the detector materials is shown in Figure 4.16. The major gamma ray energy peak at 478 keV is due to BNC reactions, which occurs with 94% of the captures. Due to the high abundance of hydrogenous materials, the thermal capture of ^1H with prompt gamma emission is observed at 2.23 MeV. Prompt gamma lines associated with ^{27}Al captures occur with a high rate due to its high nuclear cross section. Aluminium may pose a potential concern if larger quantities are used, such as the addition of a frame for the water phantom, due to its high activation rate. However, it is not an issue for the current design, with only a few hours of cooldown required following a 30 minute irradiation period.

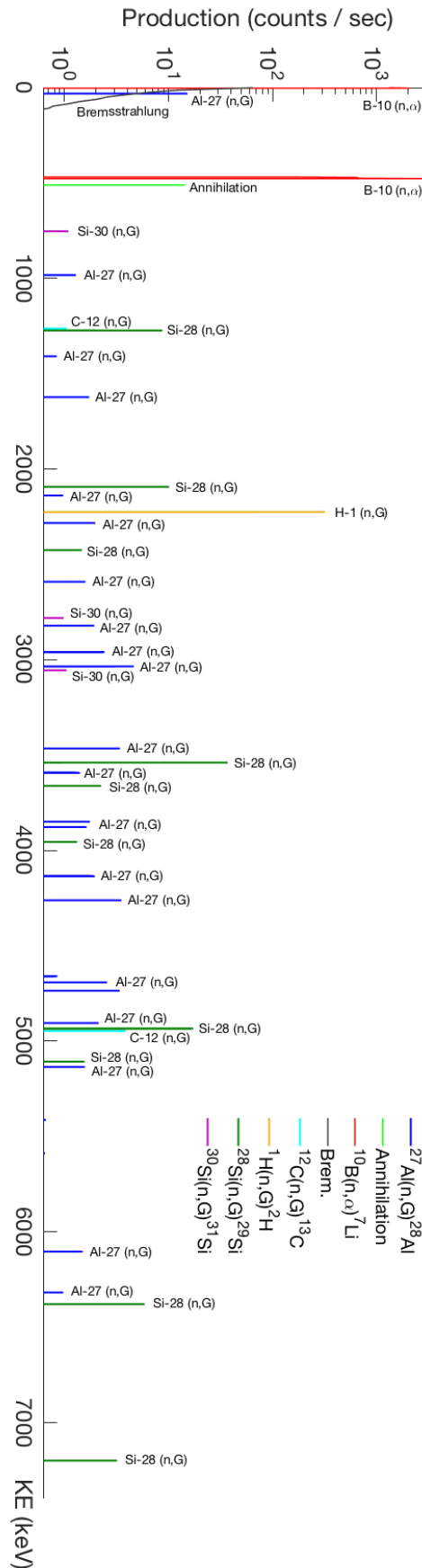


Figure 4.16: Gamma ray spectrum produced in SOI detector probe materials by the KUR epithermal neutron source.

4.5 Discussion

This study has shown conclusively that whilst the materials currently used in the fabrication of SOI microdosimeters are appropriate in terms of radioprotection, there are changes with respect to the sensitive volume size that should be addressed for the application of SOI microdosimetry to BNCT. The 3D Bridge microdosimeter with 2 μm SV thickness and $30 \times 30 \mu\text{m}^2$ SV lateral area is the most feasible design for BNCT QA using the current fabrication technology. SVs with thickness of 1 μm or less have been shown to be more suitable for microdosimetry but are currently unable to be manufactured. The current fabrication process may have difficulty creating p-n junctions in 3D sensitive volumes defined in a 1 μm thick silicon active layer. n^+ and p^+ electrode regions are typically implanted with a depth of 1 μm in the active layer silicon. However, if the total active layer is approximately 1 μm thick, the electrodes would need to be deposited with a depth less than 1 μm , which could impact the depletion region. While this microdosimeter design may be viable in theory, it is uncertain how the electrical characteristics of a device made with these methods would perform in practice. The reduction in sensitivity must also be taken into account when considering smaller SVs. Compared with the 10 μm thick SV, the total reduction in counts for the 2 μm and 1 μm SVs are approximately 26% and 30% less, respectively.

Thinner $^{10}\text{B}_4\text{C}$ films are required to decrease the energy loss of BNC products, in order to enhance the number of SV crossers. This also has the advantage of shaping the field emerging from the film to be more isotropic. The boron implanted p^+ region in the SVs provided an adequate source of BNC products, which were mostly crossers. However, it has a much lower count rate than the $^{10}\text{B}_4\text{C}$.

The activation study has shown that the device does not pose any significant concern in terms of radiation protection for use in epithermal mode BNCT. However, the production of secondary nuclear recoils can contribute to the background noise in the detector, which must be taken into account. Alternative substrates for the neutron conversion film will be investigated in future work.

Future work will involve the modelling of the electrical and charge collection characteristics of the ideal SOI microdosimeter in Synopsys TCAD for BNCT applications. These results will be compared with experimental measurements. This study supports the characterisation of the response of the SOI Bridge microdosimeter, for when it will be irradiated at the KUR reactor.

Chapter 5

Model of the South Africa iThemba Fast Neutron Beamline ²

In this chapter, Monte Carlo codes, Geant4 and MCNP6, were used to characterize the fast neutron therapeutic beam produced at iThemba LABS in South Africa. Experimental and simulation results were compared using the latest generation of Silicon on Insulator (SOI) microdosimeters from the Centre for Medical Radiation Physics (CMRP).

Geant4 and MCNP6 were able to successfully model the neutron gantry and simulate the expected neutron energy spectrum produced from the reaction by protons bombarding a ^9Be target. The neutron beam was simulated in a water phantom and its characteristics recorded by the silicon microdosimeters; bare and covered by a ^{10}B enriched boron carbide converter, at different positions. The microdosimetric response is considered for a bare microdosimeter and with ^{10}B converter, which is used to make the detector more sensitive to the low energy neutron component. The Monte Carlo codes were benchmarked against experimental measurements made using the SOI Bridge microdosimeter, comparing their simulated microdosimetric response to the experimental measurements.

²Part of this chapter has been published in the European Journal of Medical Physics: James Vohradsky, Linh T. Tran, Susanna Guatelli, Lachlan Chartier, Charlot Vandevorode, Evan Alexander de Kock, Jaime Nieto-Camero, David Bolst, Stefania Peracchi, Carina Høglund, Anatoly B. Rosenfeld (2021). *Response of SOI microdosimeter in fast neutron beams: experiment and Monte Carlo simulations*. Physica Medica. DOI: 10.1016/j.ejmp.2021.09.008. (Available online [129], 20 October 2021)

The thermal neutron sensitivity and production of ^{10}B capture products in the p^+ boron-implanted dopant regions of the Bridge microdosimeter is investigated. The obtained results are useful for the future development of dedicated SOI microdosimeters for Boron Neutron Capture Therapy (BNCT). This work provides a benchmark comparison of Geant4 and MCNP6 capabilities in the context of further applications of these codes for neutron microdosimetry.

5.1 Method

Two Monte Carlo based simulation applications were developed using Geant4 version 10.5.p01 [127, 131] and MCNP version 6.2 [135] codes. ROOT v6.16 was adopted as analysis tool [146]. These simulations were used to characterise the fast neutron therapy beam line at iThemba LABS, South Africa. Characterisation, in this context, pertains to the neutron field distribution within the gantry, treatment room and water phantom. In experiments performed at iThemba LABS, the Bridge microdosimeter was positioned at various depths within the water phantom, and its response was characterised in the incident neutron field. This work attempts to characterise the interactions of the fast neutron beam with the modelled experimental setup using the two simulation codes. The experimental results will then be compared to simulations and used to benchmark the validity of the two Monte Carlo codes.

The beam line blue prints for the gantry treatment head and collimator were digitised into a CAD model and implemented in the geometry of the Geant4 and MCNP simulations as shown in figure 5.1. The beamline was simulated, tracking all secondary particles produced from the ^9Be proton collision passing through the collimation system and into the treatment room. The resulting phase space from the characterisation of the neutron beam emerging from the treatment head was taken at a distance 150 cm from the ^9Be target in the treatment room and used as the primary source in all following simulations.

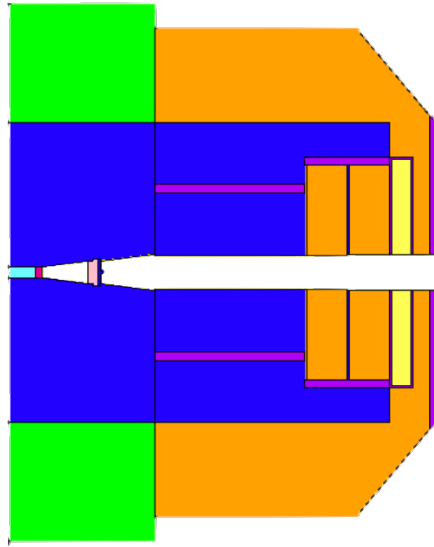


Figure 5.1: Basic details of the treatment head and variable collimator of the neutron gantry, cut through the centre. This figure was obtained from the visualisation output of the MCNP simulation developed, based on the CAD model provided by iThemba LABS.

Geant4 and MCNP were used to model the radiation field produced by the incident fast neutron beam in a water phantom. The simulations are based on the experimental setup performed at iThemba LABS. The phantom consisted of a $30 \times 30 \times 30 \text{ cm}^3$ water box. Surrounding the water phantom is a $31 \times 31 \times 31 \text{ cm}^3$ air box (called *World*). The MicroPlus probe [49], which houses the Bridge microdosimeter, was modelled and positioned at varying depths within the water phantom, facing the incident beam direction as shown in figure 5.2. The MicroPlus probe modelled here consists of a thin PCB stick with the microdosimeter attached to the lower end, which is inserted into a PMMA sheath. In front of the microdosimeter is a $500 \text{ }\mu\text{m}$ thin window in the PMMA sheath that allows closer proximity to the water. The primary radiation field emerging from the exit nozzle of the simulated neutron gantry consists of a $10 \times 10 \text{ cm}^2$ rectangular beam of mostly fast neutrons which are incident on one side of the water phantom.

Figure 5.1 presents the CAD model implemented in the simulations. The proton collision with the ^9Be target occurs in vacuum region located at left-centre. A forward peaked source of neutrons is produced from the ^9Be target, which is shielded by iron and passes down the beamline. The neutrons pass through the flattening and hardening filters in the treatment head and into the variable collimator that shapes the beam. The polyethylene

beam hardening filter removes low energy neutrons from the beam. The variable collimator consists of iron and borated polyethylene layers (or blocks). The end of the neutron collimation channel and treatment room are filled with air.

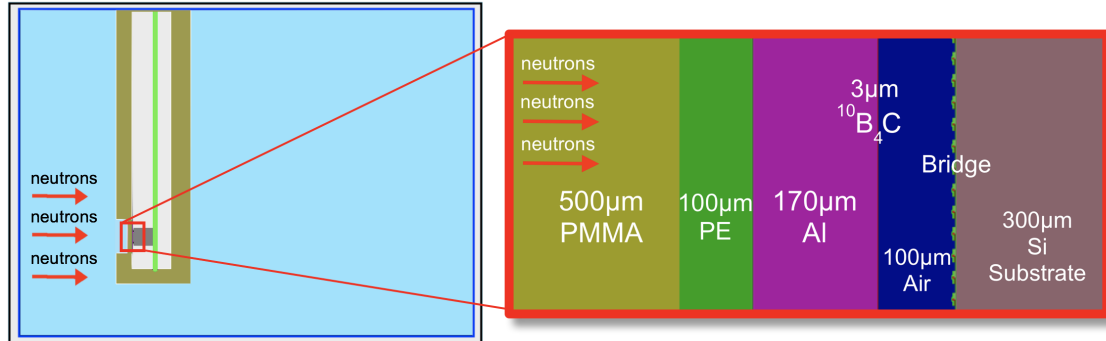


Figure 5.2: Detail of the geometry of the detector and its packaging, in the direction of incidence of the neutron beam (incident from left). The width of the neutron beam exceeds the lateral sizes of the microdosimeter device. The microdosimeter is set at 5 cm depth in the water phantom.

Figure 5.2 shows the MicroPlus probe positioned at an arbitrary depth within the water phantom. A region of interest has been expanded in the figure to show a cross section of the materials present at the entrance window of the MicroPlus probe PMMA sheath cover. In this region, there is the 500 μm thin window of the PMMA sheath in the direction of incidence of the neutron beam, 100 μm thick polyethylene (PE), the boron conversion layer, a 100 μm air gap and then the Bridge microdosimeter. The PMMA layer is part of the waterproof outer casing which houses the detector components. The removable neutron converter in the setup consists of a 3 μm thin layer of $>96\%$ enriched boron carbide ($^{10}\text{B}_4\text{C}$, $\rho = 2.52 \text{ g/cm}^3$), deposited on a 170 μm aluminium substrate, which was sourced from the European Spallation Source (ESS) [77]. Polyethylene film is used to attach the converter onto the top of the detector package and also to protect the microdosimeter from light in the case when there is no converter (bare). This leaves a thin air gap between the device and the converter. Refer to figure 5.2 to see all layers. A different perspective of the setup is shown in figure 5.3 for further understanding. The Bridge microdosimeter is shown from bird's-eye view in figure 5.4.

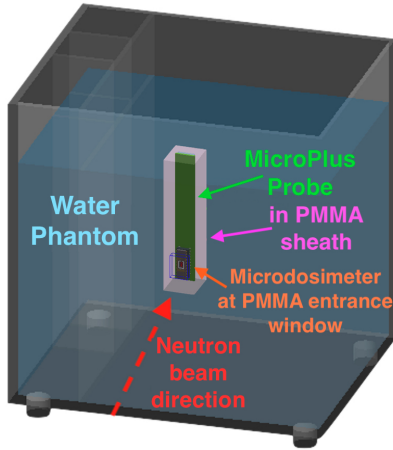


Figure 5.3: Details of the MicroPlus probe inserted in the PMMA sheath positioned in the water tank at 5 cm depth.

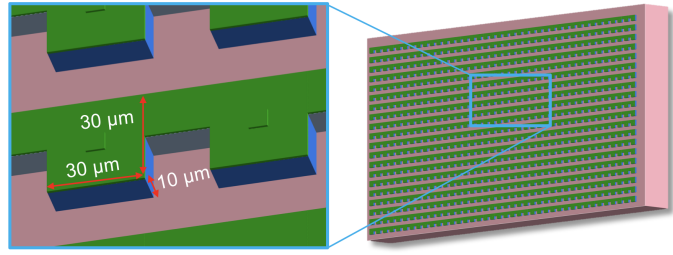


Figure 5.4: Bridge SOI Microdosimeter. The device consists of an array of 4248 SVs, representing cells. The SVs shown in green have dimensions of $30 \times 30 \mu\text{m}^2$ with $10 \mu\text{m}$ thickness along the direction of incidence of the neutron beam. The mean chord length of an SV in the array is $12 \mu\text{m}$.

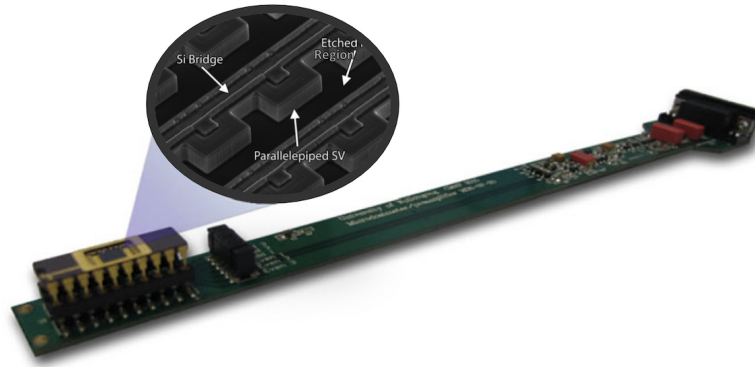


Figure 5.5: Bridge SOI Microdosimeter mounted in DIL package on the MicroPlus Probe (adapted from [21] and [33]). The probe has been removed from the PMMA sheath (see figure 5.3).

The Bridge V2 microdosimeter was modelled in the simulations and used experimentally at iThemba LABS. The ^{10}B concentration inside the $0.6 \mu\text{m}$ thick p^+ region layer on top of the SV is about $10^{18} \text{ atoms/cm}^3$ or 7 ppm, relating to the Si in this region. The experimental setup with the Bridge microdosimeter mounted in its DIL package and inserted in the MicroPlus probe is shown in figure 5.5. The waterproof PMMA sheath featured in figure 5.3 is not shown here.

Previous publications attempting to characterise the neutron field were restricted by limited nuclear cross section data and neutron upper energy limits [119, 122, 156]. This

work attempts to model all materials used in the neutron gantry in greater detail by including the latest versions of ENDF nuclear datasets available to MCNP6 and Geant4.

5.2 Neutrons generated in ^9Be target by physics options

This first section of results compares different physics options available in the Geant4 and MCNP6 simulations, considering a simple simulation geometry consisting of only the ^9Be target in a vacuum world. This was simulated to observe the difference in neutron yields generated from the $^9\text{Be}(p,n)$ inelastic collision for various physics lists available in Geant4 and MCNP6. The different physics options used in the two simulation codes are shown in table 5.1. A rigorous assessment on the specific processes of the different physics lists is outlined in chapter 3.

Geant4	MCNP6
1. QGSP_BERT_HP	1. Bertini INC
2. QGSP_INCLXX_HP	2. INCL INC
3. QGSP_BIC_HP	3. CEM INC
4. QGSP_BIC_AllHP (TENDL)	4. Isabel INC
	5. Bertini INC (+TENDL)
	6. INCL INC (+TENDL)
	7. CEM INC (+TENDL)
	8. Isabel INC (+TENDL)

Table 5.1: Various physics options used in Geant4 and MCNP simulation for the preliminary assessment, which is only considering the ^9Be target in vacuum world.

The simple geometry in the simulations for this preliminary assessment is emphasised. The simulations in this section only consider the ^9Be target (not the entire BSA in this case) in a vacuum world. 66 MeV protons are fired at the ^9Be target with normal incidence and the energy spectrum of neutrons is recorded. To score the neutron characteristics, the sensitive detector class and PTRAC card was used in Geant4 and MCNP, respectively. The neutron energy spectra generated from the $^9\text{Be}(p,n)$ reaction are shown in figures 5.6a, 5.6b, and 5.6c, which have been normalised per incident proton. The energy spectra for this set of results has been separated into relevant figures to assist comparison.

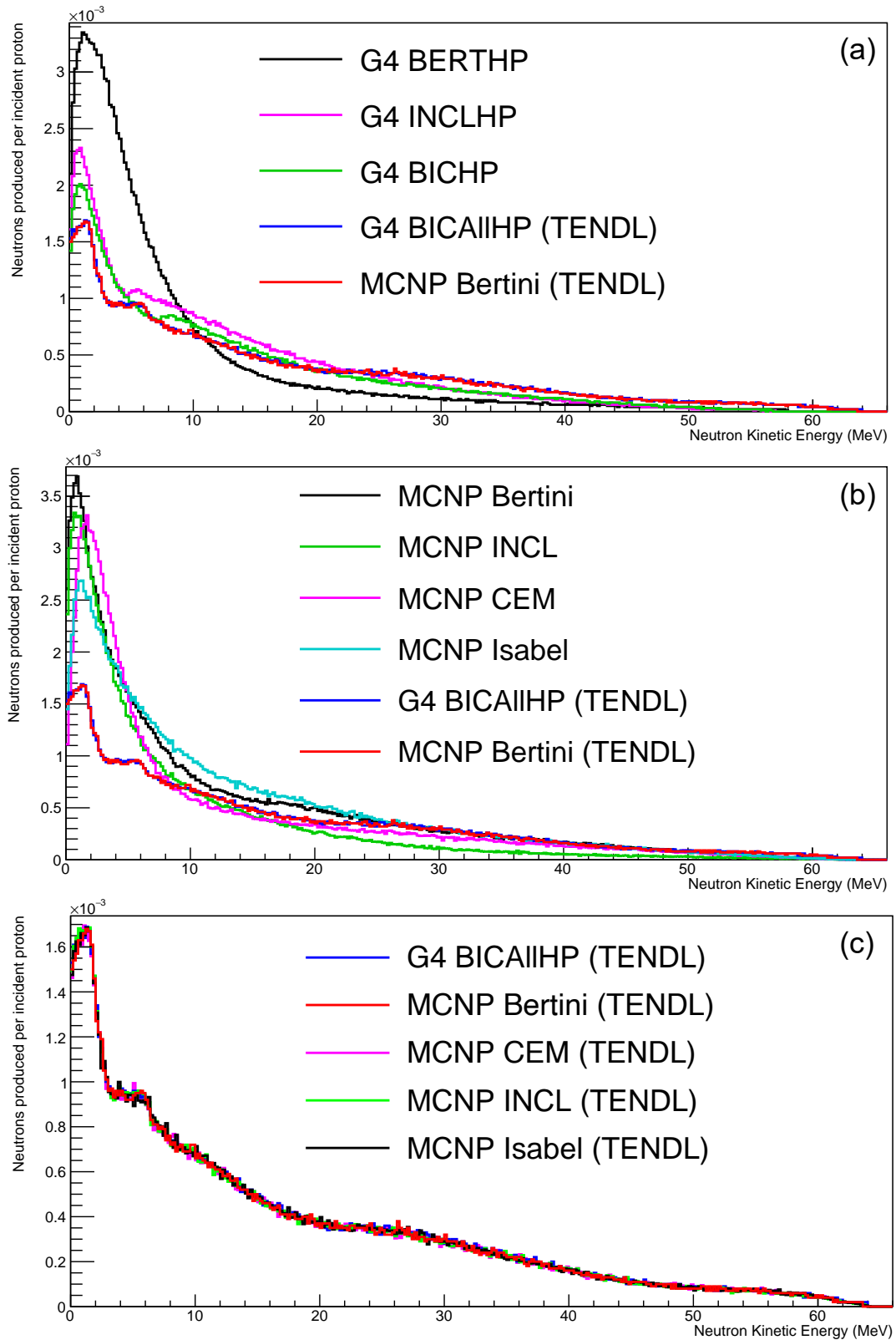


Figure 5.6: Initial neutron energy spectra produced from the $^9\text{Be}(p,n)$ reaction for various Geant4 and MCNP6 physics models. **a)** Geant4 physics options also including MCNP6 Bertini (+TENDL), **b)** MCNP6 non-TENDL physics options also including Geant4 QGSP_BIC_AllHP and MCNP6 Bertini (+TENDL), **c)** MCNP +TENDL physics options also including Geant4 QGSP_BIC_AllHP.

Figure 5.6a directly compares the various proton inelastic models of Geant4. BERT_HP, BIC_HP, and INCLXX_HP all use different models, which are not based on any evaluated dataset, and as such have unequal neutron energy yields. The same is also true for the proton inelastic process result of MCNP6 in figure 5.6b for Bertini/INCL/CEM/Isabel INC, which use their own respective model.

From the results made clear in figure 5.6c, all proton inelastic physics models deriving from evaluated datasets in Geant4 and MCNP6 yield the exact same neutron energy spectrum. The BIC_All_HP physics list of Geant4 and Bertini/INCL/CEM/Isabel INC (+TENDL) models of MCNP6 use the same TENDL [133] evaluated dataset to describe the proton inelastic process.

This observation in the preliminary assessment results is valuable, as it demonstrates that Geant4 and MCNP6 is capable of producing the same neutron energy yield via the $^9\text{Be}(p,n)$ reaction. This affirms that for the simulation work performed in the rest of this chapter, BIC_All_HP and Bertini INC (+TENDL) will be used for Geant4 and MCNP6, respectively.

5.3 Simulation to model the neutron gantry of the iThemba facility

The following set of results in this section considers the full geometry of the neutron gantry used in the iThemba facility.

5.3.1 Characterisation of Neutron Fluence in Gantry and Treatment Room

Neutron fluence map

Figure 5.7 presents the radial neutron fluence maps within the treatment head and collimator and in the treatment room. The percentage difference map between the fluence

calculated by the two codes is shown in figure 5.7c. Greater fluence for MCNP is represented by a positive value (red) and greater for Geant4 by a negative value (blue).

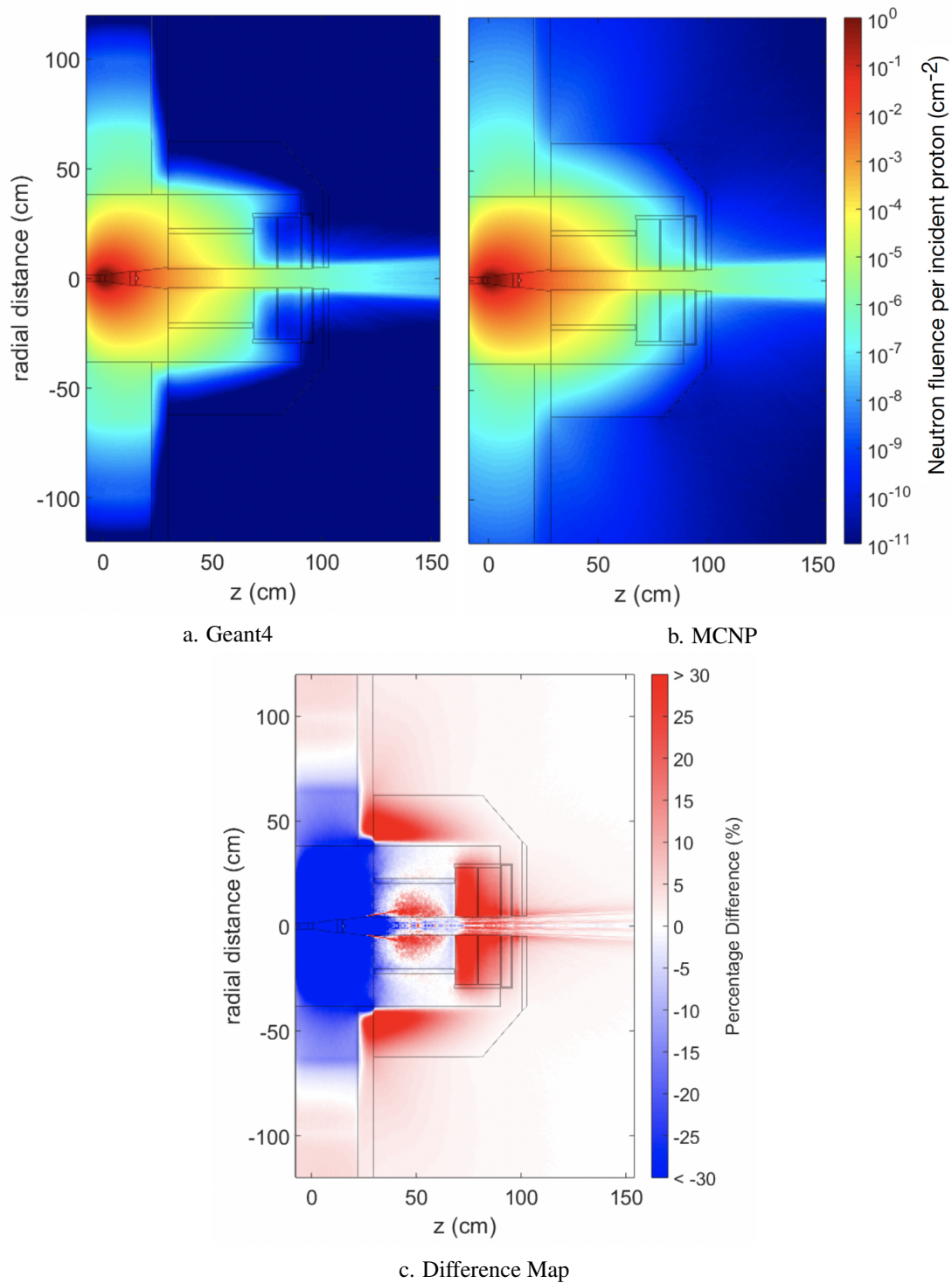


Figure 5.7: Radial neutron fluence maps calculated using Geant4 (a) and MCNP (b) within the neutron gantry and treatment room. Percentage difference map (c) between the distributions of Geant4 (negative) and MCNP (positive).

The ^9Be target is positioned at $z=0$ cm, which can be identified as the spot with the

highest neutron fluence per incident proton. The number of neutrons at $z=150$ cm from the target is in the same order for Geant4 and MCNP. The neutron fluence is similar for the two simulations, but with differences in some regions, as shown in figure 5.7c. The neutron fluence in the iron upper head is much higher for Geant4. Interactions with lead based materials are at parity. The most distinctive difference is seen in the boronated polyethylene outer shielding, with more neutrons propagating through this material in MCNP. This is also seen in the last two layers (or blocks) of the variable collimator, which consist of a boronated plastic. As such, compared with Geant4, there is a slightly higher neutron fluence in the treatment room air. The therapeutic primary beam emerging from the beam exit nozzle into the treatment room is very similar for both codes, with MCNP having a slightly wider spread to Geant4.

Neutron energy fluence at 150cm SSD

The relative neutron energy fluence spectra were calculated with the variable collimator set to produce a $10 \text{ cm} \times 10 \text{ cm}$ field size at 150 cm from the ^9Be target source, as shown in figure 5.8.

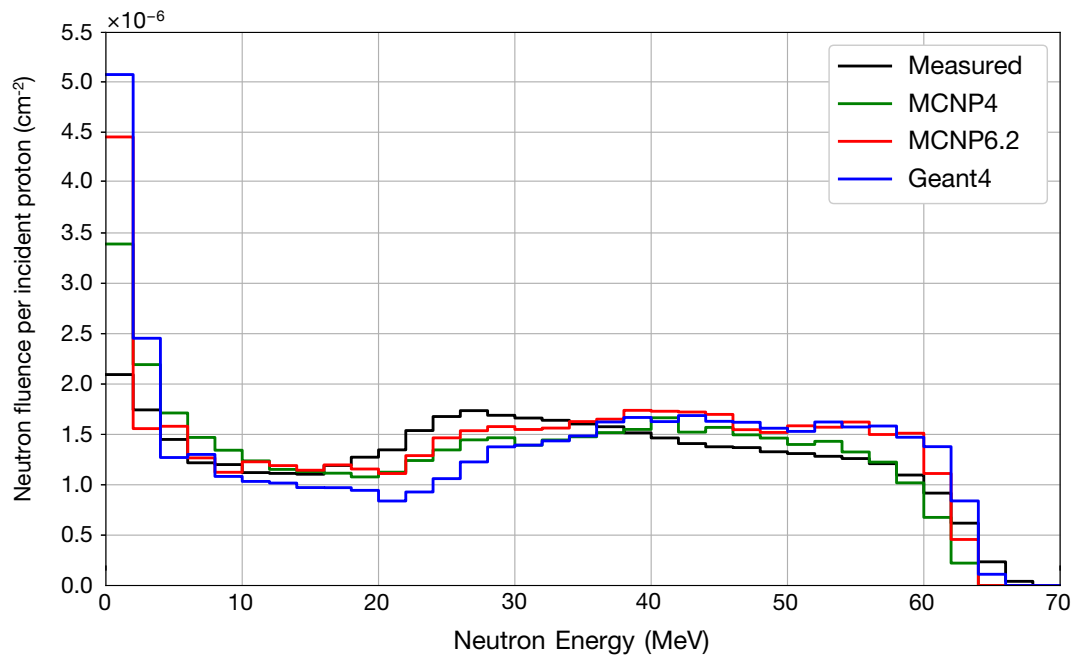


Figure 5.8: Relative neutron energy fluence calculated at 150 cm from the ^9Be target in the treatment room air. Previous publications using measured [116] (black) and MCNP4 [122] (blue) data. This work; calculated using Geant4 (blue) and MCNP6.2 (red).

The MCNP6 results agree well with previous publications using older versions of MCNP, but with higher proportion of fast neutrons. Geant4 also matches well to the other data, following the same trend as MCNP6.2 for higher energies (above 35 MeV). Both codes have a higher proportion of epithermal neutrons compared to MCNP4 and the measured data.

This confirms that Geant4 using BIC_All_HP and MCNP6 using BERT INC (+TENDL) achieves a satisfactory result compared to previous experimental measurements [116]. Figure 5.9 presents the neutron energy fluence obtained using additional physics lists of Geant4. As seen in figure 5.9, the additional BERT_HP, INCLXX_HP, and BIC_HP physics lists do not correctly represent what is obtained by experimental measurements. The lack of high energy neutrons produced by these physics models results in a significant disagreement, especially above 20 MeV. This result is presented solely to reaffirm that evaluated datasets from TENDL are required to accurately simulate the $^9\text{Be}(p,n)$ inelastic reaction.

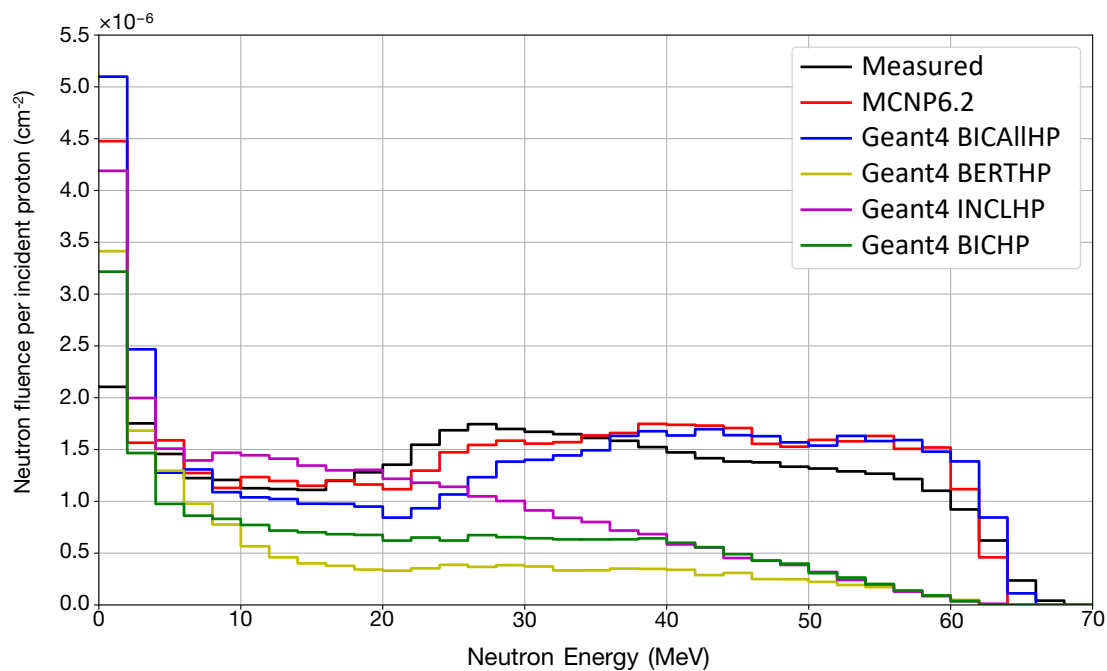


Figure 5.9: Relative neutron energy fluence calculated at 150 cm from the ^9Be target in the treatment room air for additional physics models of Geant4. Data for Geant4 (BIC_All_HP) and MCNP6.2 (BERT INC (+TENDL)) are also shown in figure 5.8. Previous publications using measured [116] (black).

Simulated neutron fluence in water phantom using phase space file

The following sections of results use the neutron phase space recorded at the beam exit nozzle as the primary source. The incident surface of the water phantom is positioned at 150 cm from the ^9Be target. The beam characteristics at this position are shown in figures 5.10 and 5.11.

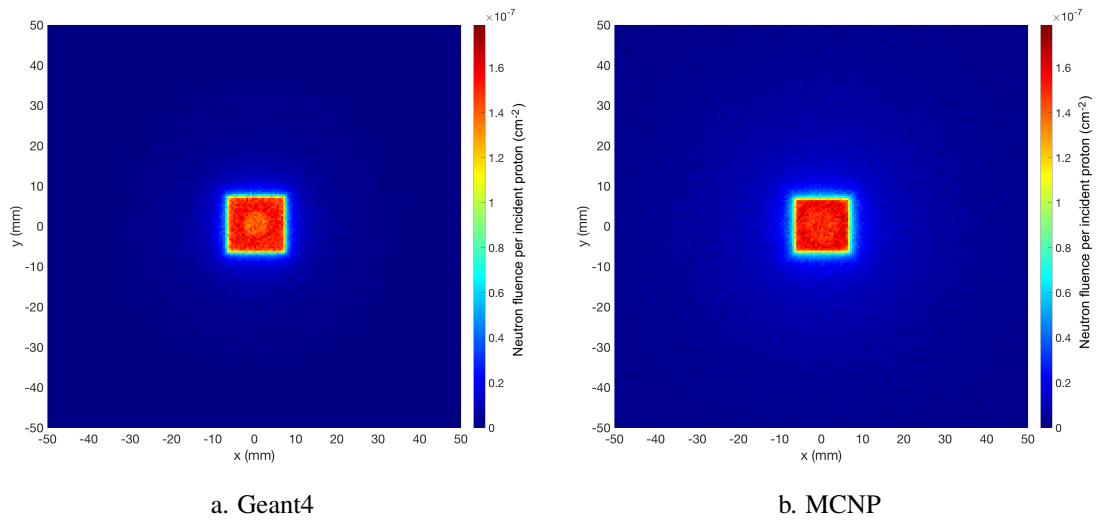


Figure 5.10: Neutron fluence plane profile map taken on the incident surface of the water phantom located at $z=150$ cm using a) Geant4, and b) MCNP.

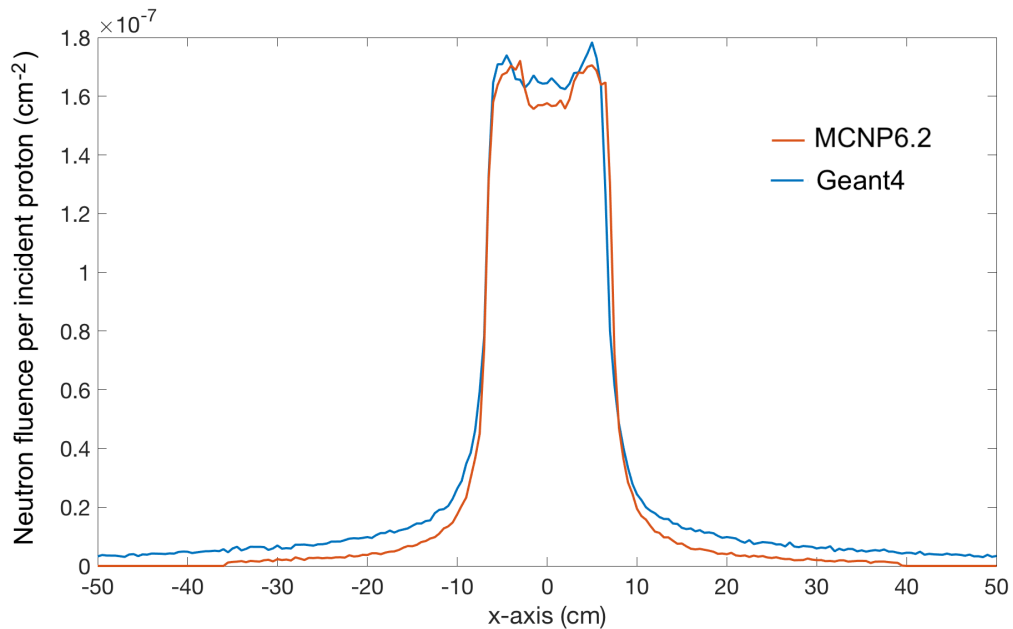


Figure 5.11: Line profiles of neutron fluence taken on the incident surface of the water phantom located at $z=150$ cm, sampled across X-axis at $y=0$ from figures 5.10a and 5.10b.

Figure 5.12 shows the neutron fluence of the primary beam as a function of depth in the water phantom calculated using Geant4 and MCNP.

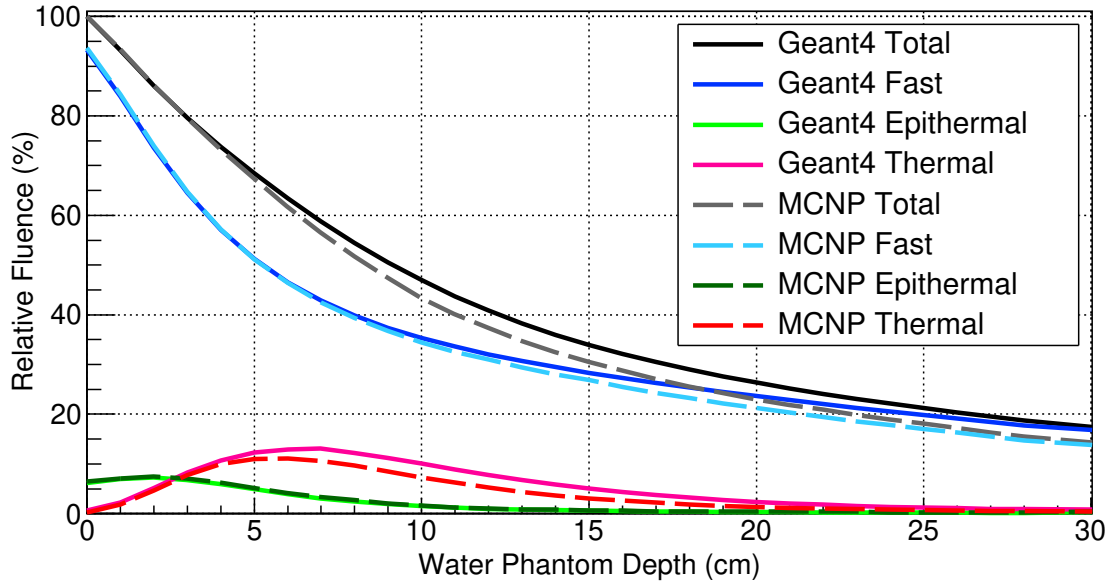


Figure 5.12: Neutron fluence as a function of depth in the water phantom calculated using Geant4 and MCNP. The energies are separated by fast (>10 keV), epithermal (<10 keV) and thermal (<0.5 eV).

As the higher energy neutrons propagate through the water phantom, they are moderated through scatter interactions with hydrogen nuclei, producing recoil protons and also secondaries through inelastic reactions with ^{16}O . The proportion of epithermal and thermal neutrons increases, which gives rise to lower energy specific interactions such as $^1\text{H}(n,\gamma)^2\text{H}$ capture in water and $^{10}\text{B}(n,\alpha)^7\text{Li}$ reactions in the boron carbide converter. The behaviour of the neutrons propagating through the water phantom is similar for Geant4 and MCNP, until at the end of the water phantom (30 cm), where Geant4 has a slightly higher neutron fluence compared with MCNP.

5.4 Comparison of the experimental and simulation microdosimetric response of the Bridge

The response of the Bridge microdosimeter was studied theoretically at different positions in the phantom as described in the method. This section uses the calculated phase space as

primary source incident on the water phantom. Experimental results obtained at iThemba LABS for the same positions are also presented.

Table 5.2 presents the microdosimetric quantities of the experimental in-field measurements obtained using the Bridge microdosimeter. With increasing depth in the water phantom, there is a slight decrease in \bar{y}_F and \bar{y}_D due to the proportional change in neutron energies.

Converter	Depth	\bar{y}_F (keV/ μm)	\bar{y}_D (keV/ μm)	D (Gy/MU)
Bare	1.0 cm	5.54 ± 0.10	32.17 ± 0.40	0.38 ± 0.02
Bare	3.0 cm	5.53 ± 0.10	31.76 ± 0.31	0.37 ± 0.02
Bare	5.0 cm	5.51 ± 0.10	31.72 ± 0.46	0.34 ± 0.02
Bare	7.0 cm	5.41 ± 0.10	31.23 ± 0.54	0.33 ± 0.02
Bare	9.0 cm	5.36 ± 0.10	30.86 ± 0.34	0.29 ± 0.02
Bare	11.0 cm	5.26 ± 0.10	30.58 ± 0.14	0.27 ± 0.01
Bare	13.0 cm	5.14 ± 0.10	30.20 ± 0.14	0.24 ± 0.01
Al film only	5.0 cm	4.99 ± 0.15	27.17 ± 0.51	0.30 ± 0.02
Al film only	11.0 cm	4.88 ± 0.16	27.46 ± 0.65	0.23 ± 0.02
$^{10}\text{B}_4\text{C}$	5.0 cm	7.59 ± 0.21	26.05 ± 0.32	0.72 ± 0.03
$^{10}\text{B}_4\text{C}$	11.0 cm	7.50 ± 0.24	26.94 ± 0.39	0.54 ± 0.03
$^{10}\text{B}_4\text{C}$ minus Al Film	5.0 cm	12.71 ± 0.36	32.79 ± 0.58	0.45 ± 0.04
$^{10}\text{B}_4\text{C}$ minus Al Film	11.0 cm	13.02 ± 0.44	34.77 ± 0.64	0.34 ± 0.04

Table 5.2: Experimental microdosimetric quantities derived from microdosimetric spectra at varying depths within the water phantom using the Bridge microdosimeter. The values have been scaled to be tissue equivalent. In the case of $^{10}\text{B}_4\text{C}$ converter, they are “apparent” mean average lineal energies.

The absorbed dose (D) has been normalised to 1 monitor unit (MU), which is equal to the reference measurement of 1 Gy at 2 cm depth in water (d_{max}) using an ionization chamber (IC) [118, 157] under the same beam delivery conditions. The reduction of the dose with depth follows the expected behaviour equivalent to that of 8 MV X-rays in water [117]. The average quality factor (\bar{Q}) derived from microdosimetric spectra measured at 5 cm depth by bare Bridge microdosimeter and with $^{10}\text{B}_4\text{C}$ converter attached are approximately $\bar{Q}=6.7$ and $\bar{Q}=7.3$, respectively. Additionally, measurements were carried out with 170 μm Al foil in front of the Bridge microdosimeter to understand its effect on microdosimetric parameters.

The microdosimetric quantities derived from the spectra obtained using the 3 μm $^{10}\text{B}_4\text{C}$

converter is shown in table 5.2 in terms of total ($^{10}\text{B}_4\text{C}$) and subtraction ($^{10}\text{B}_4\text{C}$ minus Al film). The subtracted data was determined from the difference in the normalised per MU MCA spectra for $^{10}\text{B}_4\text{C}$ and Al film at the corresponding depths. It should be mentioned that the microdosimetric spectra obtained in the case of $^{10}\text{B}_4\text{C}$ converter is not a classical representation where ideally all particles are crossers; for this result, all alpha and ^7Li secondaries are all stoppers, which essentially leads to reduced derived lineal energies of such events. For the results derived in this case, \overline{y}_F and \overline{y}_D should be referred to as “apparent” mean lineal energies, which is suitable for benchmarking of Monte Carlo codes simulating the same scenario.

Figure 5.13 shows the depth dose measured with the Bridge microdosimeter taken at increasing depths within the water phantom. The simulation results for bare microdosimeter are shown with solid lines and for attached $^{10}\text{B}_4\text{C}$ converter with dotted lines. The simulation results were normalised to the absorbed dose measured experimentally using the bare microdosimeter at d_{max} . For each simulated position of the microdosimeter in the water phantom, 10^{10} primary events were simulated to achieve a statistical uncertainty lower than 1%.

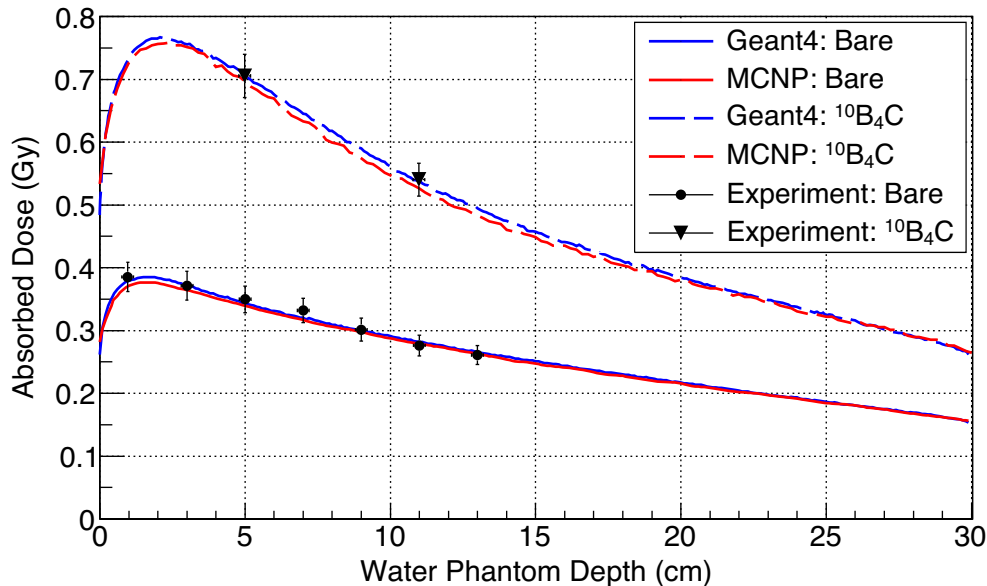


Figure 5.13: Absorbed dose per monitor unit measured using the Bridge microdosimeter for experimental and simulation methods. Comparing bare (solid lines) and $^{10}\text{B}_4\text{C}$ converter (dotted lines) sources.

The dose equivalent (H) as a function of displacement from the central axis of the primary beam in the phantom at 5 cm depth is shown in figure 5.14. The dose equivalent is normalised based on the IC reference of 1 Gy/MU at d_{\max} (2 cm), the same as figure 5.13. The modeled microdosimetric response of the Bridge was simulated using the two MC codes and then compared to experimental results. The primary beam field size is $10 \times 10 \text{ cm}^2$. The dose equivalent measured at 6 cm from the central axis, which is 1 cm from the field edge, in the case of a bare Bridge microdosimeter is 0.68 Sv/Gy. As expected, the dose equivalent rapidly falls off with increased distance out-of-field, converging to approximately 0.04 Sv/Gy at 15 cm from the central axis, based on the simulation results.

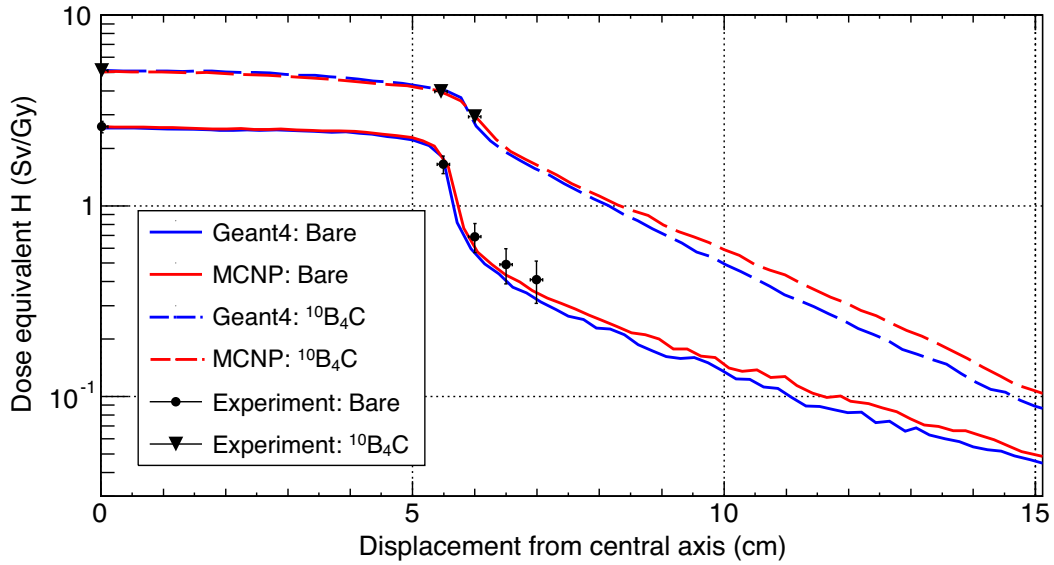


Figure 5.14: Dose equivalent derived from measurements with the Bridge microdosimeter for experimental and simulation methods in lateral field measurements from the central axis taken at 5 cm depth in the water phantom. Field size is $10 \times 10 \text{ cm}^2$. Comparing bare (solid lines) and Boron Carbide converter (dotted lines) sources.

The simulations match well for both cases of bare microdosimeter and with $^{10}\text{B}_4\text{C}$ converter. The lateral dose profile calculated using MCNP is slightly wider. In the case of microdosimeter with $^{10}\text{B}_4\text{C}$ converter, the dose equivalent is higher than derived from measurements with bare microdosimeter and not so steep on the field edge. This is due to a higher proportion of the thermal neutron component distributed outside the beam dimensions. Boron agents may be used in the body to provide a dose boost in FNT and

can be useful for killing the cancer cells infiltrated outside the tumour region [158, 159]. However, this requires a precise differentiation in ^{10}B compound uptake between normal tissue and tumour cells. This remains a challenge pertaining to the chemistry of the boron labelled drugs.

Microdosimetric spectra - $^{10}\text{B}_4\text{C}$ result

Figure 5.15 shows the microdosimetric spectra obtained experimentally at 5 cm depth in the water phantom. The $^{10}\text{B}_4\text{C}$ spectrum (black) has been normalised so the area under the curve is equal to 1. The other spectra, bare (red) and Al film (green), have been scaled based on their fractional dose contribution relating to the $^{10}\text{B}_4\text{C}$ measurements per monitor unit delivered (based on IC reference of 1 Gy at d_{max} , as described earlier). The subtraction of $^{10}\text{B}_4\text{C}$ from Al film (blue) represents the dose weighted microdosimetric spectra associated only with interactions in the $^{10}\text{B}_4\text{C}$ converter. The difference in the microdosimetric responses obtained with a bare microdosimeter versus one covered with 170 μm Al film is negligible (red and green, respectively).

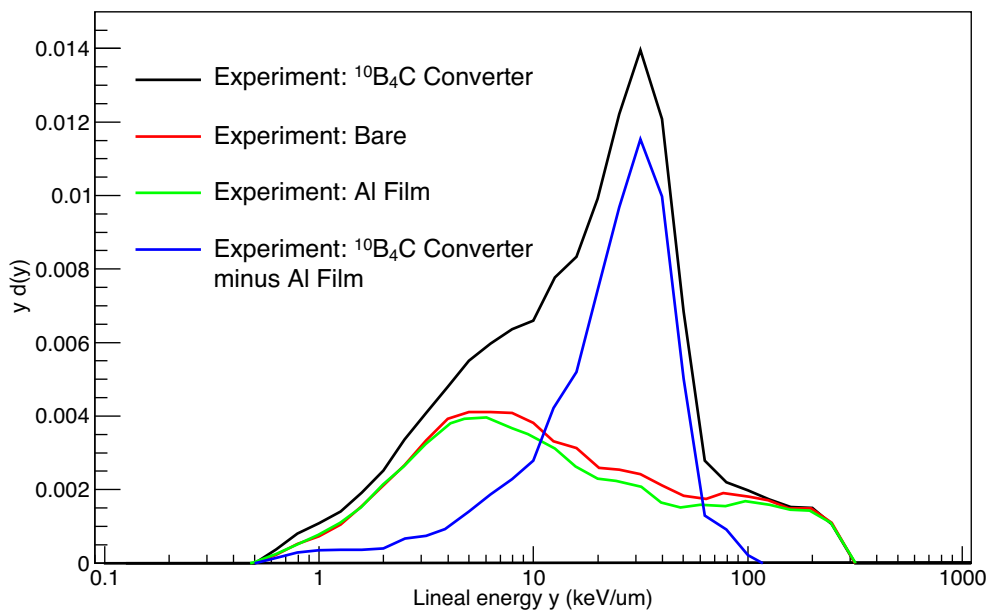


Figure 5.15: Microdosimetric spectra measured experimentally at 5 cm depth. Bare (red), Al film (green), $^{10}\text{B}_4\text{C}$ converter (black), subtracted (blue).

Figures 5.16 and 5.17 show the microdosimetric spectra calculated using MCNP and

Geant4 simulations at 5 cm depth in the water phantom. The individual particle components of the respective dose weighted microdosimetric spectra have been normalised based on their dose ratio contribution to the total response. Both codes were able to describe the individual components of the mixed radiation field, which are in agreement with each other. The total microdosimetric spectra of MCNP and Geant4 matches well to the experimental data measured at this depth in water.

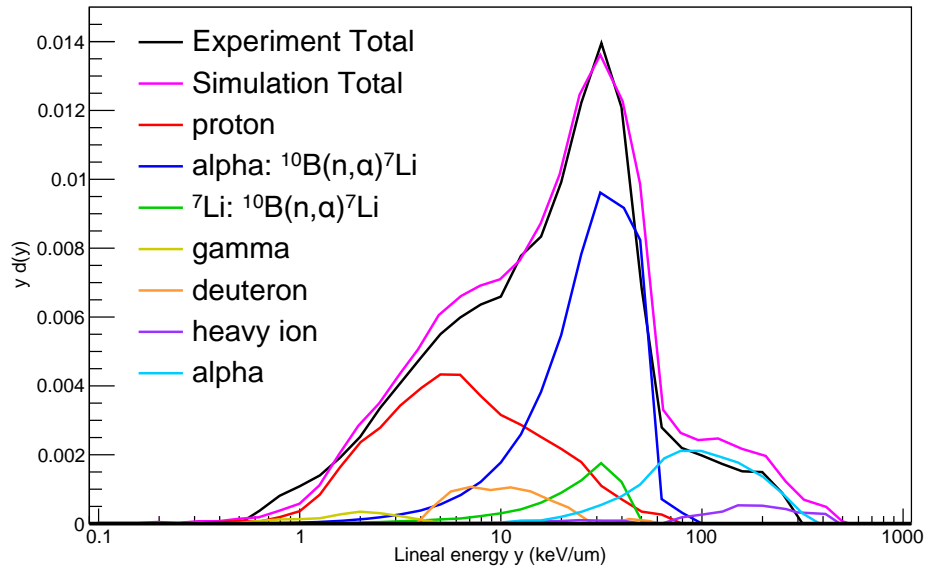


Figure 5.16: Microdosimetric spectra for Bridge with $^{10}\text{B}_4\text{C}$ converter calculated using MCNP at 5 cm depth with secondary components contributing to the total dose shown.

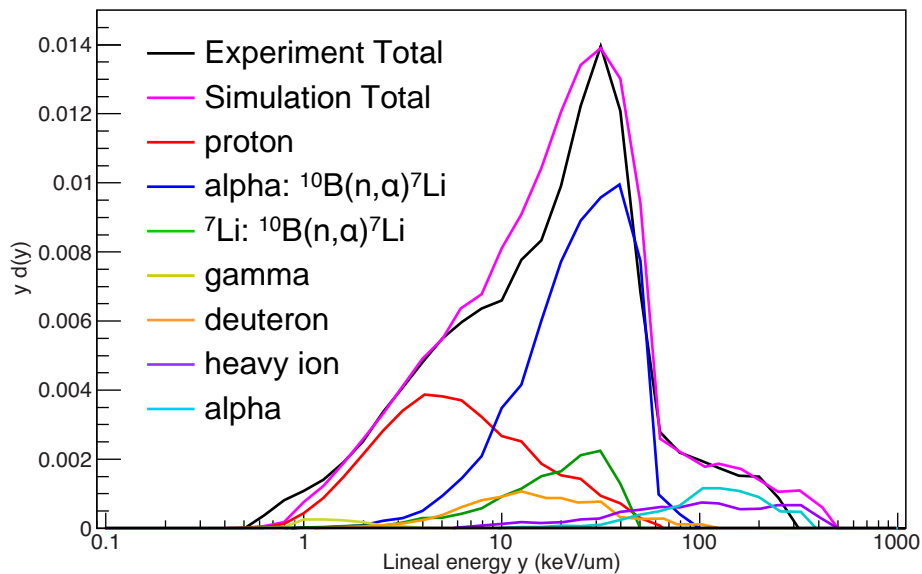


Figure 5.17: Microdosimetric spectra for Bridge with $^{10}\text{B}_4\text{C}$ converter calculated using Geant4 at 5 cm depth with secondary components contributing to the total dose shown.

The simulation results illustrate the partial contribution of the different components in the mixed radiation fields to microdosimetric spectra. Four distinct components can be identified, namely:

- (i) 0.5 to 5 keV/ μm , (olive colour) associated with secondary Compton electrons produced in the silicon SVs by the 478 keV and 2.23 MeV prompt gamma rays emitted during capture reactions; $^{10}\text{B}(\text{n},\alpha)^7\text{Li}$ and $^1\text{H}(\text{n},\gamma)^2\text{H}$, respectively. There is also contribution of gamma radiation from the accelerator. ^1H neutron capture is occurring in the water phantom and PMMA sheath.
- (ii) 0.5 to 80 keV/ μm , (red) due to elastically scattered protons produced in the water phantom and PMMA sheath during fast neutron moderation.
- (iii) 2 to 100 keV/ μm , (blue and green) from α particles and ^7Li nuclei produced by $^{10}\text{B}(\text{n},\alpha)^7\text{Li}$ capture.
- (iv) Above 80 keV/ μm , (cyan and purple) which originate from neutron interactions due to recoils. These are mostly due to recoil Si atoms, resulting from the elastic scattering of neutrons within the silicon SVs. There is a very small amount of recoiled O atoms, which are originating from the silicon dioxide passivation layers in the microdosimeter. This lineal energy range also includes alpha particles produced within the silicon SVs arising from $^{28}\text{Si}(\text{n},\alpha)^{25}\text{Mg}$ reactions, however the relative contribution for 10 μm thick SOI microdosimeters is low [24].

Both Geant4 and MCNP have responded well to simulating the experimental setup with $^{10}\text{B}_4\text{C}$ converter, with the total of their the dose components matching closely. The dose weighted microdosimetric spectrum due to alpha particles emitted from $^{10}\text{B}_4\text{C}$ converter simulated with MCNP is sharper than in Geant4, but is approximately in the same central position. There is a larger proportion of alpha particles and heavy ion recoils arising from fast neutron inelastic interactions in MCNP.

Microdosimetric spectra - Bare result

The following results in this section present the microdosimetric spectra and microdosimetric quantities for bare Bridge microdosimeter at 5 cm depth in the water phantom calculated using MCNP and Geant4 in figures 5.18 and 5.19, respectively.

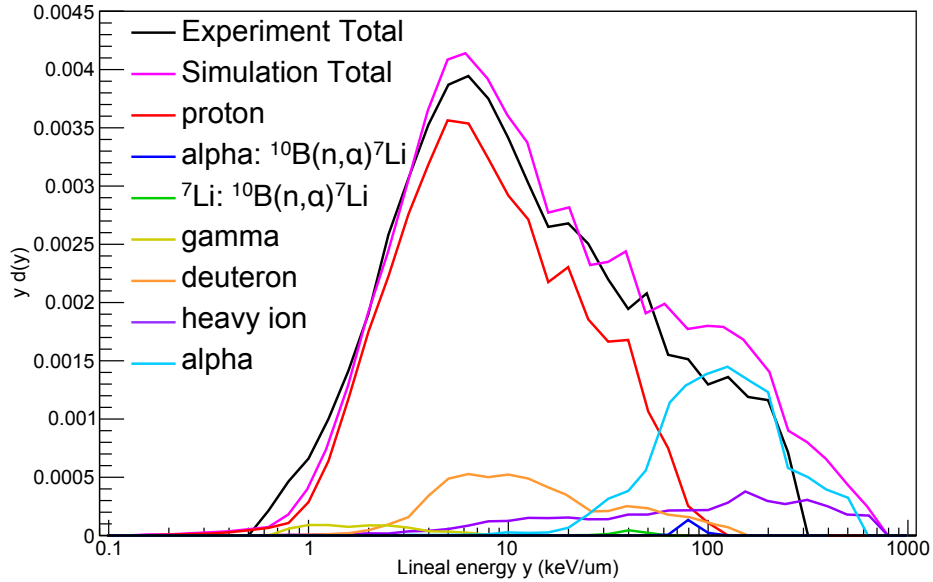


Figure 5.18: Microdosimetric spectra for bare Bridge calculated using MCNP at 5 cm depth with secondary components contributing to the total dose shown.

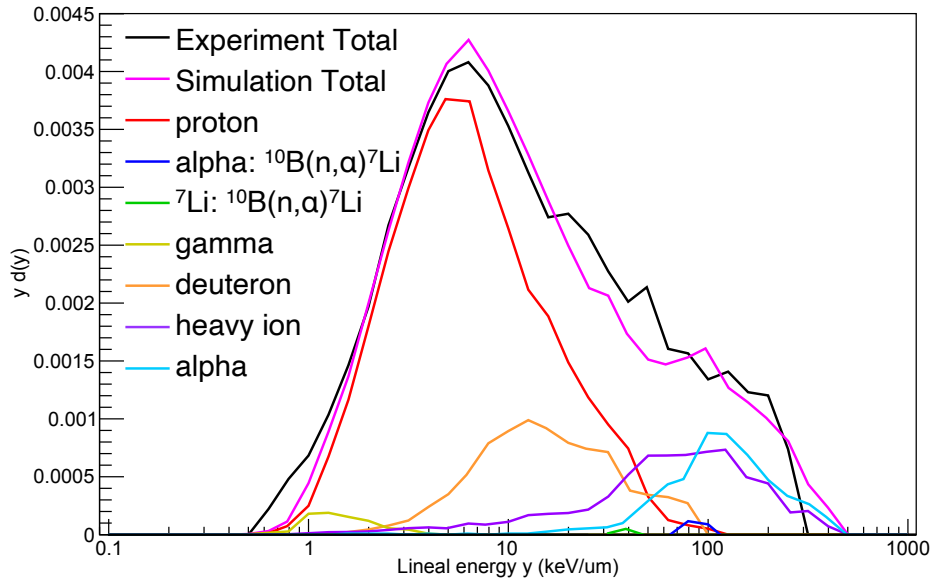


Figure 5.19: Microdosimetric spectra for bare Bridge calculated using Geant4 at 5 cm depth with secondary components contributing to the total dose shown.

As seen in the case of the Bridge microdosimeter with $^{10}\text{B}_4\text{C}$ converter, the dose com-

ponents match closely, though with some small differences. Compared to Geant4, there is a larger proton edge in MCNP, leading broadly past 50 keV/ μm . However, the simulation total still matches the experiment total microdosimetric spectra in this range well. This is due to an increased contribution from deuteron for Geant4 in this region, compensating for its shorter proton edge. Another small difference is the increased number of alpha particles contributing to the total in MCNP compared to Geant4. The inverse is true for heavy ions, with a much higher contribution in Geant4. Interestingly, there is a small amount of alpha particles and ^7Li nuclei seen in the microdosimetric spectra for both MCNP and Geant4. These boron neutron capture products are arising from the p^+ boron dopant region of the Bridge SVs. The proportion of these components are almost the same for the two codes. As the neutron spectrum at 5 cm depth consists mostly of fast neutrons, the dose weighted fractional contribution is low, which makes it difficult to distinguish in the experimental results.

To compare in more detail, the specifics of the particle interactions for the two codes using the bare Bridge microdosimeter, outlining which reaction they arise from, is described in the four proceeding tables. Reactions with significant contributions from protons, deuterons, alpha particles and heavy ions in its output channel are described in tables 5.3, 5.4, 5.5 and 5.6, respectively. The count rate of each product has been normalised to the neutron fluence for the $10 \times 10 \text{ cm}^2$ beam, which has the unit of counts per incident proton (fired into the ^9Be target in the accelerator). Microdosimetric quantities such as $\overline{y_F}$, $\overline{y_D}$, average energy deposition in the SV ($\overline{\text{edep}}$) and average kinetic energy when entering the SV (Enter $\overline{\text{KE}}$) are shown in the columns for the product particles from each reaction listed.

Proton product reactions are described in table 5.3. Protons have the highest count contributing to the microdosimetric spectra. MCNP has a higher proton count to Geant4 for most reactions, though with similar microdosimetric quantities for most reactions. The origin of the reactions are in the same materials for both codes. The count rate for elastically scattered protons in $^1\text{H}(n,n)p$ is higher for MCNP.

Reaction: Proton		Count/incident proton, (E-12)	$\overline{\text{edep}}$ (keV)	Enter $\overline{\text{KE}}$ (keV)	$\overline{y_F}$ (keV/ μm)	$\overline{y_D}$ (keV/ μm)	Origin
$^1\text{H}(n,n)p$	MCNP	1429.78	72.80	10916.10	4.22	8.03	Water, μ^+ sheath
	Geant4	1036.30	60.02	11171.80	3.48	7.11	Water, μ^+ sheath
$^{16}\text{O}(n,n+p)^{15}\text{N}$	MCNP	269.20	85.67	11196.10	4.97	15.13	Water, μ^+ sheath
	Geant4	189.91	82.26	10900.60	4.77	12.49	Water, μ^+ sheath
$^{16}\text{O}(n,n+p+\alpha)^{11}\text{B}$	MCNP	74.11	90.82	11212.40	5.27	16.43	Water, μ^+ sheath
	Geant4	24.53	98.45	10224.10	5.71	10.88	Water, μ^+ sheath
$^{28}\text{Si}(n,n+p)^{27}\text{Al}$	MCNP	51.38	279.56	5243.10	16.21	34.86	Si sub, SiSV, SiO ₂
	Geant4	116.48	129.61	8438.38	7.52	18.03	Si sub, SiSV, SiO ₂

Table 5.3: Simulated microdosimetric quantities and count rate from reactions with proton products at 5 cm depth within the water phantom using the bare Bridge microdosimeter. $\overline{y_F}$ and $\overline{y_D}$ values have been scaled to be tissue equivalent.

The major deuteron product reactions are described in table 5.3, with similar quantities for all values recorded by Geant4 and MCNP. The difference between the two codes is the count rate, with Geant4 having significantly more deuterons from $^{28}\text{Si}(n,d)^{27}\text{Al}$. It is worth noting that in terms of fractional dose deposition, the major neutron inelastic interactions with proton and deuteron production contributing to the microdosimetric spectra are from similar reactions. For example, $^{16}\text{O}(n,n+p)^{15}\text{N}$ and $^{16}\text{O}(n,d)^{15}\text{N}$, or $^{16}\text{O}(n,n+p+\alpha)^{11}\text{B}$ and $^{16}\text{O}(n,d+\alpha)^{11}\text{B}$.

Reaction: Deuteron		Count/incident proton, (E-12)	$\overline{\text{edep}}$ (keV)	Enter $\overline{\text{KE}}$ (keV)	$\overline{y_F}$ (keV/ μm)	$\overline{y_D}$ (keV/ μm)	Origin
$^{16}\text{O}(n,d)^{15}\text{N}$	MCNP	85.41	121.88	11283.50	7.07	14.01	Water, μ^+ sheath
	Geant4	69.77	136.11	11453.00	7.90	13.73	Water, μ^+ sheath
$^{16}\text{O}(n,d+\alpha)^{11}\text{B}$	MCNP	25.09	119.51	10831.90	6.93	12.33	Water, μ^+ sheath
	Geant4	6.43	166.06	9787.91	9.63	12.29	Water, μ^+ sheath
$^{28}\text{Si}(n,d)^{27}\text{Al}$	MCNP	2.63	172.71	11299.30	10.02	16.32	Si sub, SiSV, SiO ₂
	Geant4	35.33	146.90	11430.00	8.52	18.43	Si sub, SiSV, SiO ₂

Table 5.4: Simulated microdosimetric quantities and count rate from reactions with deuteron products at 5 cm depth within the water phantom using the bare Bridge microdosimeter. $\overline{y_F}$ and $\overline{y_D}$ values have been scaled to be tissue equivalent.

The major alpha product reactions are described in table 5.5. As seen in the microdosimetric spectra of figures 5.18 and 5.19, MCNP has a higher contribution from alpha particles. This is mainly due to MCNP having a lot more $^{12}\text{C}(\text{n},\text{n}+3\alpha)$ reactions occurring in the PMMA μ^+ sheath. $^{12}\text{C}(\text{n},\text{n}+3\alpha)$ can also be described as $^{12}\text{C}(\text{n},\text{n}+\alpha)^8\text{Be}$, which then very quickly decays, producing an additional two α particles. However, despite the difference in count rate, the microdosimetric quantities are similar for alpha particles produced from MCNP and Geant4. Significantly, alpha particles produced from $^{10}\text{B}(\text{n},\alpha)^7\text{Li}$ reactions in the p^+ boron dopant region are recorded in both MCNP and Geant4 with similar count and other microdosimetric quantities. This indicates that the proportion of thermal neutrons at 5 cm depth in the water phantom and the track structure based recording method is similar for the two codes. The initial kinetic energy of the alpha is usually 1470 keV, with kinetic energy of alpha particle when entering the SVs for MCNP and Geant4 of 1367.99 keV and 1255.26 keV, representing an energy loss of only 7% and 15% when travelling from 0.6 μm p^+ region to SV, respectively.

Reaction: Alpha		Count/incident proton, (E-12)	$\overline{\text{edep}}$ (keV)	Enter $\overline{\text{KE}}$ (keV)	$\overline{y_F}$ (keV/ μm)	$\overline{y_D}$ (keV/ μm)	Origin
$^{28}\text{Si}(\text{n},\text{n}+\alpha)^{24}\text{Mg}$	MCNP	5.12	1379.18	6558.75	79.99	119.21	SiSV, Si sub, SiO ₂
	Geant4	3.49	1322.06	4556.66	76.68	110.65	Si sub, SiSV, SiO ₂
$^{28}\text{Si}(\text{n},\alpha)^{25}\text{Mg}$	MCNP	0.53	1411.91	3823.59	81.90	92.59	SiSV, Si sub, SiO ₂
	Geant4	2.92	1357.54	4083.38	78.73	99.36	Si sub, SiSV, SiO ₂
$^{12}\text{C}(\text{n},\text{n}+3\alpha)$	MCNP	14.46	1379.18	6558.75	79.99	119.21	μ^+ sheath
	Geant4	2.34	1216.22	5034.79	70.54	118.77	μ^+ sheath
$^{10}\text{B}(\text{n},\alpha)^7\text{Li}$	MCNP	0.68	1354.70	1367.99	78.57	82.50	p^+ boron dopant
	Geant4	0.65	1199.64	1255.26	69.57	77.04	p^+ boron dopant
$^{16}\text{O}(\text{n},\text{n}+\alpha)^{12}\text{C}$	MCNP	6.58	1500.96	1968.89	87.05	132.75	SiO ₂
	Geant4	0.43	1637.86	1637.86	94.98	133.14	SiO ₂
$^{28}\text{Si}(\text{n},\text{d}+\alpha)^{23}\text{Na}$	MCNP	1.83	1676.26	5297.84	97.22	166.86	SiSV, Si sub, SiO ₂
	Geant4	1.33	964.29	5261.11	55.93	112.93	Si sub, SiSV, SiO ₂

Table 5.5: Simulated microdosimetric quantities and count rate from reactions with alpha products at 5 cm depth within the water phantom using the bare Bridge microdosimeter. $\overline{y_F}$ and $\overline{y_D}$ values have been scaled to be tissue equivalent.

Finally, heavy ion products are shown in table 5.6, with large differences seen between the two codes. Most heavy ion products recorded by the SVs are produced through elastic scatter within the Bridge microdosimeter due to short path length. As seen for the alpha products, there are the related ^7Li nuclei produced through ^{10}B neutron capture. The count rate is similar to its related alpha particles. Again, the energy loss while travelling from the $0.6\text{ }\mu\text{m}$ thick p^+ region to the SVs is approximately 30% and 20% for MCNP and Geant4, respectively.

Reaction: Heavy ion		Count/incident proton, (E-12)	$\overline{\text{edep}}$ (keV)	Enter $\overline{\text{KE}}$ (keV)	$\overline{y_F}$ (keV/ μm)	$\overline{y_D}$ (keV/ μm)	Origin
$^{28}\text{Si}(\text{n},\text{n})^{28}\text{Si}$	MCNP	25.88	129.97	133.19	7.54	26.99	SiSV
	Geant4	48.61	250.72	254.17	14.54	51.20	SiSV
$^{28}\text{Si}(\text{n},\text{n}+\text{p})^{27}\text{Al}$	MCNP	2.58	158.55	158.55	9.20	29.72	SiSV
	Geant4	3.21	595.4	688.1	63.11	108.18	SiSV
$^{16}\text{O}(\text{n},\text{n})^{16}\text{O}$	MCNP	0.27	566.00	566.00	27.08	49.61	SiO_2
	Geant4	0.87	627.76	627.76	36.41	57.68	SiO_2
$^{10}\text{B}(\text{n},\alpha)^7\text{Li}$	MCNP	0.68	581.663	591.238	33.74	39.06	p^+ boron dopant
	Geant4	0.67	669.276	679.47	38.81	41.15	p^+ boron dopant

Table 5.6: Simulated microdosimetric quantities and count rate from reactions with heavy ion products at 5 cm depth within the water phantom using the bare Bridge microdosimeter. $\overline{y_F}$ and $\overline{y_D}$ values have been scaled to be tissue equivalent.

5.5 Discussion

This study has shown conclusively that Geant4 and MCNP can be used to simulate the mixed field associated with fast neutrons, with agreement between the two simulation codes on a micro and nano-scale. The agreement has been shown in this work in terms of neutron production from a ^9Be target, neutron dose distribution and spectra as a function of depth in water and the calculation of microdosimetric spectra. This refers to the microdosimetric spectra from bare Bridge microdosimeter and “apparent” microdosimetric spectra from Bridge microdosimeter with $^{10}\text{B}_4\text{C}$ converter. The experimental work presented in this work has demonstrated that the Bridge V2 microdosimeter is capable of measuring the microdosimetric spectra comprised by individual components of the mixed field associated with fast neutrons. Specifically, the clear separation of the contribution

by fast and thermal neutrons using the Bridge with and without $^{10}\text{B}_4\text{C}$ converter, respectively.

In the case of the Bridge covered with $^{10}\text{B}_4\text{C}$ converter; alpha particles and ^7Li ions emitted from converter are not crossers in the $10\text{ }\mu\text{m}$ thick SVs of the Bridge but stoppers, while microdosimetric spectra were simulated with the same mean average path length of $12\text{ }\mu\text{m}$. Contribution of alpha and ^7Li ions is reflected in the differential microdosimetric spectra in figure 5.15, which shifted to lower lineal energies than expected for the alpha and ^7Li edge around $150\text{--}200\text{ keV}/\mu\text{m}$ (in tissue) and a lower “apparent” $\overline{y_D}$ than expected in the case of crossers. This is why these microdosimetric spectra are named “apparent”. However for the aim of this work, the comparison of the two MC codes with experimental measurements in FNT is not essential. The obtained results, in addition to benchmarking of the two codes, suggests that SOI microdosimeters with thin ^{10}B converter can be used in hadron therapy for dose and RBE enhancement modeling due to neutron capture reactions. Future work will be carried out with SOI microdosimeters with $2\text{ }\mu\text{m}$ thick SVs that was modeled by Vohradsky et al [128].

The distribution of neutrons throughout the gantry and treatment room was calculated for Geant4 and MCNP6. There were some differences seen in the population of neutrons in different materials such as iron and boronated plastics. However, the final therapeutic beam characteristics was similar for the two codes in terms of neutron spectrum, depth dose distribution and lateral penumbrae in water for the $10 \times 10\text{ cm}^2$ beam.

The neutron energy fluence was compared between Geant4, MCNP6, MCNP4 [122] and experimental data [116]. MCNP6 agreed well with the previous publications using older versions of MCNP. Geant4 also agreed well with the results of MCNP6, especially for higher neutron energies. Both codes used in this study had a higher epithermal neutron component compared to previous publications, possibly due to the improvements in low energy neutron datasets available. The physics models chosen for Geant4 and MCNP6 produce similar simulation results, as the neutron datasets are sourced from the same ENDF/B-VII/1 libraries [54]. The cross sections for the proton + ^9Be reaction is

also derived from ENDF/B-VII/1 for both codes, providing the same neutron yield from the ^9Be target. Some discrepancies are present in the neutron fluence for higher energy neutrons, which is mainly attributed to the difference in neutron physics of Geant4 and MCNP above 20 MeV, where neutron interactions are described with models rather than datasets. As seen in figure 5.8, there is a higher neutron fluence in the 10 to 35 MeV energy range for MCNP, which may explain the higher amount of alpha neutron inelastic interactions occurring at 5 cm depth.

The low neutron energy component described in the neutron energy fluence of the beamline is essential when simulating BNC reactions in FNT and other hadron therapies such as NCEPT [158]. This was the primary motivation of this work, as preliminary simulations sampling the neutron energy data [116, 122] had insufficient BNC reactions compared with the experimental data. There are several considerations that are required such as the thermal neutron treatment (scattering matrix data) [149] for the materials and full TENDL libraries that include proton datasets [133]. A rigorous assessment of the different physics models was undertaken in order to find the appropriate models for Geant4 and MCNP6, which will be shown in future work.

Radiation damage affects the performance of the silicon microdosimeter by reducing charge collection efficiency. To monitor any possible radiation damage occurred in the silicon microdosimeter during the experiment, the leakage current was measured before and after each neutron irradiation. The same microdosimeter and readout electronics was used for all measurements. Throughout the measurements, no significant change in terms of the charge collection was observed for this device.

The microdosimetric quantities measured with the Bridge microdosimeter at different positions in the water tank showed a favourable result. The values of $\overline{y_F}$ and $\overline{y_D}$ derived from microdosimetric spectra measured by bare Bridge microdosimeter decreased slightly with increasing depth, which is in agreement with TEPC data [118]. The absorbed depth dose matched well for both simulations to experimental data. The dose reduction is negligible for the Al film on top of the microdosimeter, however the $\overline{y_D}$ is reduced by 15% in

comparison to the bare microdosimeter. This is due to stopping recoil protons for energies below 4.8 MeV in 170 μm of Al, which would normally provide the higher LET end of the proton spectrum. When the $^{10}\text{B}_4\text{C}$ converter is present, the absorbed dose at 5 cm depth is doubled for the same beam MU. For the subtracted $^{10}\text{B}_4\text{C}$ from Al film spectra, \overline{y}_F and \overline{y}_D also increase by 2.31 and 1.03 times, compared to bare spectra, respectively. However, this is just an indication of increasing dose due to neutron capture reactions as an accurate evaluation requires alpha particles and ^7Li nuclei to be crossers in the SVs.

The lateral dose equivalent distribution at depth 5 cm in water derived from simulated response of the Bridge microdosimeter with and without $^{10}\text{B}_4\text{C}$ converter are in a good agreement between two codes. The penumbra of the “apparent” dose equivalent is wider than dose equivalent derived with bare Bridge microdosimeter as expected due to scattering and moderation of neutrons. Both penumbras have a good agreement with the experimental measurements, suggesting that both codes are correctly modelling the transport of fast neutrons and their moderation in water.

The “apparent” microdosimetric spectra derived from experimental measurements and those simulated with Geant4 and MCNP are in good agreement. It is not surprising as the neutron interaction physics selected in this study for Geant4 and MCNP are both largely sourced from the same ENDF/B-VII.1 dataset libraries. The proportion of high LET alpha and heavy ions associated with fast neutron interactions in the results calculated using MCNP is higher than Geant4 as shown in figures 5.16 and 5.17, respectively. This difference may be explained by the discrepancy in the neutron energy spectra shown in figure 5.8 for energies between 10 and 35 MeV for the two MC codes. This energy range has a high neutron cross section for inelastic interactions with ^{28}Si and ^{16}O [54].

The enriched boron carbide converter provided by the ESS [77] produced a suitable source of BNC reactions which were measured experimentally by the Bridge microdosimeter and can be used for evaluation of the thermal component of the neutron field. The rate of BNC products contributing to the total apparent microdosimetric spectra was in agreement with both experiment and simulation data. This indicates the validity of the

referenced elemental properties, such as the amount of impurities and ^{10}B enrichment in the converter [77] and identity of the physics process cross sections leading to $^{10}\text{B}(\text{n},\alpha)^7\text{Li}$ reactions in Geant4 and MCNP.

The concentration of ^{10}B in the p^+ region is about 10^{18} atoms/ cm^3 or 7 ppm in silicon, which is equivalent to the typical clinical values used in BNCT. The distribution is on the upper surface of the SV, which is analogous to a boron biodistribution accumulated on the surface of a biological cell (ie. BSH). Measurement of the spectra generated from the ^{10}B deposited within the device p^+ regions demonstrates that typical clinical concentrations of ^{10}B used in BNCT may be introduced in the device via ion implantation. As the p^+ region is directly on the surface of the SVs, the entrance energy loss of alpha and ^7Li is minimised as they do not need to pass through SiO_2 and aluminium overlayers. This result indicates the validity of using the p^+ regions as a source of ^{10}B capture products, albeit observed in this work using a fast neutron source. The rate of reactions in the p^+ region is around 10^5 times lower than that from the $^{10}\text{B}_4\text{C}$ converter, which is determined not only by concentration of ^{10}B but also geometrical location of ^{10}B relative to SV in both cases. For a better evaluation, the experiments should be repeated with an epithermal/thermal neutron source. Overall, the observation of small peaks from the p^+ regions with 7 ppm indicates how sensitive Geant4 and MCNP are for ^{10}B neutron capture in microdosimetric spectra simulations. Additionally, increased implantation of B in the p^+ region by 10 times is possible, which can provide realistic modeling of uptake in tissue and in a particular location in a cell.

Both simulation codes had higher lineal energy events leading up to 500 keV/ μm compared with the experimental data, observed up to about 300 keV/ μm , that is possibly due to a cut off associated with the dynamic range of readout electronics used in this particular experiment. To avoid this, the recommendation is to reduce the thickness of SOI SVs and additionally increase the dynamic range of electronics.

A new iteration of the Bridge microdosimeter is currently being developed with 2 μm thin SVs, which will allow more crossers for classic BNC microdosimetry measure-

ments.

While experimental microdosimetry for BNCT is challenging due to different possible localizations of ^{10}B compound in a cell, the obtained results shown in this work using the Bridge microdosimeter with ^{10}B converter modelling ^{10}B uptake on a cell surface is encouraging. Future work will be directed in the placement of ^{10}B in the core of the 3D SVs to model ^{10}B uptake by a cell nucleus.

Chapter 6

Model of the Tokai iBNCT Epithermal Neutron Beamline³

The chapter investigates the rate of unwanted neutron activation in the equipment used by the Centre for Medical Radiation Physics for BNCT QA measurements in view of experiments at the iBNCT neutron accelerator in Tokai, Japan.

The beamline was simulated in Geant4, successfully modelling the beam shaping assembly (BSA) and production of epithermal neutrons with close agreement with PHITS. This information was used in further simulations to model and optimise the geometry of materials which would be used in the experimental setup. The ambient dose equivalent $H^*(10)$ as a function of time was calculated for different positions in the treatment room, indicating that a short cool-down period is required before interacting with the equipment.

The Geant4 simulation results indicate that whilst the majority of materials used in our experimental measurement system is appropriate in terms of radioprotection, there is need for changes with respect to some material choices. The use of aluminium in the structural frame needs to be minimised to reduce the activation of ^{28}Al . Components of

³Part of this chapter has been submitted to Applied Radiation and Isotopes: James Vohradsky, Linh T. Tran, Lachlan Chartier, Stefania Peracchi, Susanna Guatelli, Hiroaki Kumada, Anatoly B. Rosenfeld (2022). *Activation study of experimental setup at Tokai accelerator based iBNCT*.

the MicroPlus measurement system were activated with long half-lives; including ^{198}Au and ^{66}Cu , mostly in the dual-inline (DIL) package, and ^{24}Na in the PCB board. Alternative materials have been identified and will be evaluated in terms of neutron activation and signal quality degradation in a future work.

6.1 Introduction

This work investigates the neutron activation of materials used in microdosimetry experiments with a SOI microdosimeter and the possible radioprotection risks involved, which is important due to growing interest in semiconductor microdosimetry applications for neutron radiation fields [160–163]. The Ibaraki Boron Neutron Capture Therapy Centre (iBNCT) located at Tokai in the Ibaraki Prefecture of Japan was considered for the neutron source [164]. At iBNCT, 8 MeV protons are accelerated into a ^9Be target by a LINAC and shaped by the BSA to produce clinical epithermal neutrons.

Microdosimetry experiments with developed solid state microdosimeters are planned to take place at the iBNCT facility in late 2023. The planned experimental setup involves the microdosimetric characterisation of the neutron beam using a water phantom. The microdosimeter is suspended in the water phantom using the CMRP motion stage system, which allows remote controlled positioning in the X-Y planes, eliminating the need for re-entry into the treatment room to manually adjust the position. This planned experimental setup involving the motion stage system has been used for many other microdosimetric studies as reported by [33, 101, 165] for particle therapy modalities, such as proton and heavy ion. In these cases, activation of the equipment was not important as the production of secondary neutrons was minimal. However, for the case of BNCT, when considering the application with epithermal neutrons, it is important to assess activation and possible risks. Although the motion stage system allows autonomous positioning of the microdosimeter, it may be necessary to enter the treatment room to change the setup configuration, such as changing detectors, neutron converter films or readout electronics.

This work investigates whether the planned experimental setup will become radioactive, and if so, the time frame required until it is safe for the operators to enter the room and interact with the equipment before starting the next acquisition. The current packaging of the solid state microdosimeter contains gold and copper plating in the dual inline (DIL) package, which may lead to long lived radioisotopes. The results inform the future design of experiments and microdosimetry instruments in order to reduce the rate of induced radioactivity.

6.2 Method

Geant4 version 10.5.p01 [127, 131] was used to simulate the beamline from the beryllium target to beam aperture leading into the treatment room. ROOT v6.16 was adopted as analysis tool [146]. The beam shaping assembly (BSA) was modelled to scale with correct materials as indicated by iBNCT.

This study consists of four separate simulations: modelling the neutron fluence through the BSA, activation of cubic material samples, activation of the experimental materials and the ambient dose equivalent following beam off.

6.2.1 Simulation to model the BSA of the iBNCT facility

At the iBNCT facility, neutrons are produced by accelerating 8 MeV protons onto a ^9Be target, which pass through a BSA, providing an epithermal neutron output from the nozzle. The BSA was modelled using Geant4, as shown in figure 6.1, to simulate the proton interaction and resulting epithermal neutron beam. This model was based on the Tokai reference, shown in figure 6.2.

The primary 8 MeV proton beam originates in the vacuum region, which has a $13 \times 13 \text{ cm}^2$ rectangular surface distribution that is normally incident on the Be target. The Be target system is a three-layered structure comprised of 0.5 mm thick ^9Be , 0.5 mm Ta and backed by a copper heat sink block [164]. The neutrons produced by the $p + ^9\text{Be}$ reaction

are shaped by the various materials of the BSA, with resulting epithermal neutrons exiting the beam nozzle.

To calculate the neutron fluence map of the BSA and treatment room in Geant4, these volumes were enclosed in a $900 \times 900 \times 1800 \text{ mm}^3$ voxelised scoring mesh, aligned on the y-axis with $5 \times 5 \times 5 \text{ mm}^3$ size voxel size. The phase space file was recorded across the beam exit nozzle, storing the position, momentum, and energy of all particles crossing this plane. The particles stored in the phase space were mainly neutrons, but also includes gamma rays, protons, etc.

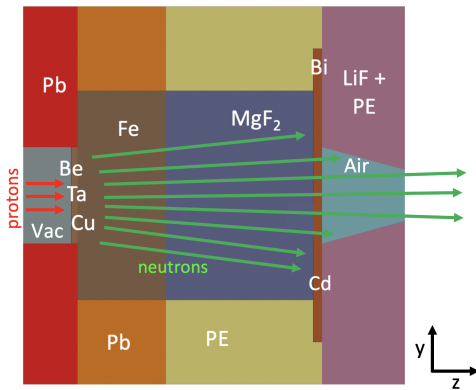


Figure 6.1: Model of the Tokai BSA implemented in the Geant4 simulation, production of neutrons from the proton + ^9Be reaction.

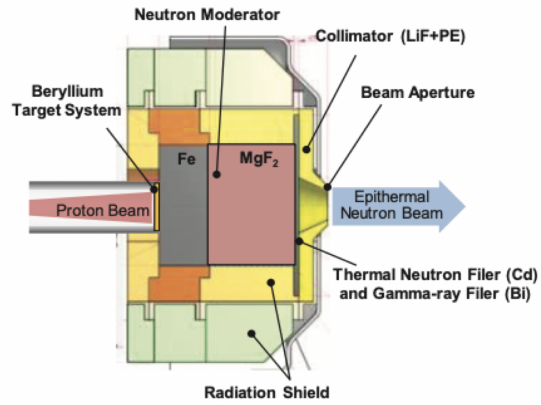


Figure 6.2: Strawman diagram of the Tokai BSA (courtesy of iBNCT [164]).

6.2.2 Neutron Activation of Sample Materials

The next set of simulations focuses on the investigation of activated nuclei fragments within cubic samples of various materials during a typical 30 minute neutron irradiation period. The results presented from the unit sample irradiation indicates the typical materials used in our experiments which may be activated at the Tokai facility.

The simulation setup consists of a $1 \times 1 \times 1 \text{ cm}^3$ target volume within a $50 \times 50 \times 50 \text{ cm}^3$ air box (called World). The target material is irradiated on one entire side with the Tokai neutron phase space, which was calculated in the previous section simulation using Geant4. The simulation is repeated for eleven different materials to investigate their

activation: Aluminium, Silicon, Diamond, Silicon Dioxide, PMMA, Water, Aluminium Oxide, Gold, Copper, Borosilicate glass and Enriched Boron Carbide.

These materials were selected as they have a potential use or are currently used in CMRP microdosimeters and the experiment apparatus. Based on the calculated neutron fluence in the phase space, the simulation results were normalised per incident neutron and then multiplied to provide the equivalent number of incident neutrons per second. The activation rate was normalised to this fluence, providing the rate of activated nuclei per second in the material.

The activated radioisotope rate of decay is presented as a function of time for a typical 30 minute irradiation period. This includes the cool-down time required for activity to drop below 1 microBecquerel (μBq). This lower activity threshold was chosen as it is well below the natural background variability of the materials tested.

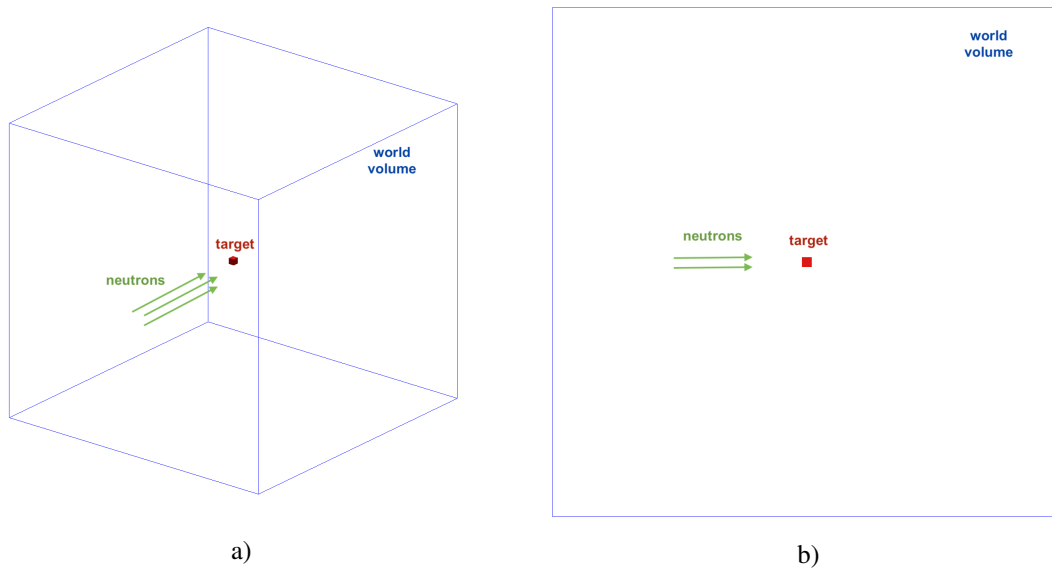


Figure 6.3: Simulation geometry setup to study the activation of unit samples, shown from bird's-eye view (a) and side view (b). The target (red cube) is located at the centre of an air world volume (blue frame). The Tokai neutron source originates at one side of the air world and irradiates the face of the target volume.

6.2.3 Neutron Activation of the Realistic Experimental Setup

The experimental setup used by CMRP for microdosimetric measurements as shown in figure 6.4 was modelled in Geant4. The setup includes a motion stage system which allows autonomous positioning of the microdosimeter inside a water phantom as shown in figures 6.5 and 6.6. The MicroPlus (μ^+) probe [49] is suspended in the water phantom by the carriage, which can be moved to different X and Y coordinates using stepper motors. All components including shafts, supports, screws and belts were modelled with the indicated material deriving from the NIST reference [147] as described in table 6.1. The dimensions of the water tank is $27 \times 27 \times 22 \text{ cm}^3$. The overall dimensions of the supporting frame is $45 \times 31 \times 27 \text{ cm}^3$.

The entire experimental apparatus was modeled as detailed as possible considering any trace elements inside a material that may become radioactive and potentially dangerous when irradiated by neutrons.



Figure 6.4: Experiment setup of motion stage system featuring water phantom with MicroPlus on couch. Shaper is inserted on top with grey output cable.

	Component	Composition
A	Stepper Motor (NEMA17)	See table 6.2
B	PMMA Tank	PMMA
C	Water in tank	Water
D	3D Printed Parts	ABS Plastic
E	Roller Bearings	Stainless Steel
F	Rubber Belts	Synthetic Butyl Rubber
G	Rotating Shafts	Stainless Steel
H	Pulse Shaper Box	Aluminium Diecast Steel
I	Metal Screws	Stainless Steel
J	Aluminium Extrusion Bars	Aluminium
K	MicroPlus Sheath	PMMA & Aluminium Foil
L	MicroPlus PCB	Copper foil & Dielectric Glass
M	Dual Inline (DIL) Substrate	Aluminium Oxide
N	DIL Package Leads	Gold plated Nickel
O	Integrated Circuit (IC) Sockets	BeCu alloy & Brass
P	Boron Carbide Converter	$^{10}\text{B}_4\text{C}$ & Al substrate

Table 6.1: Components of the motion and MicroPlus probe microdosimetry systems and their material compositions, which has been labelled in figures 6.5 and 6.6.

Most importantly, the MicroPlus (μ^+) probe and sheath were described in the simulation including all contacts and connections of the microdosimeter, as shown in detail in figure 6.5. The removable neutron converter in this setup consists of a $3 \mu\text{m}$ thin film

of enriched boron carbide ($^{10}\text{B}_4\text{C}$) deposited on a $170\text{ }\mu\text{m}$ aluminium substrate, provided by the European Spallation Source (ESS) [77]. Polyethylene tape is used to attach the converter film onto the top of the detector package.

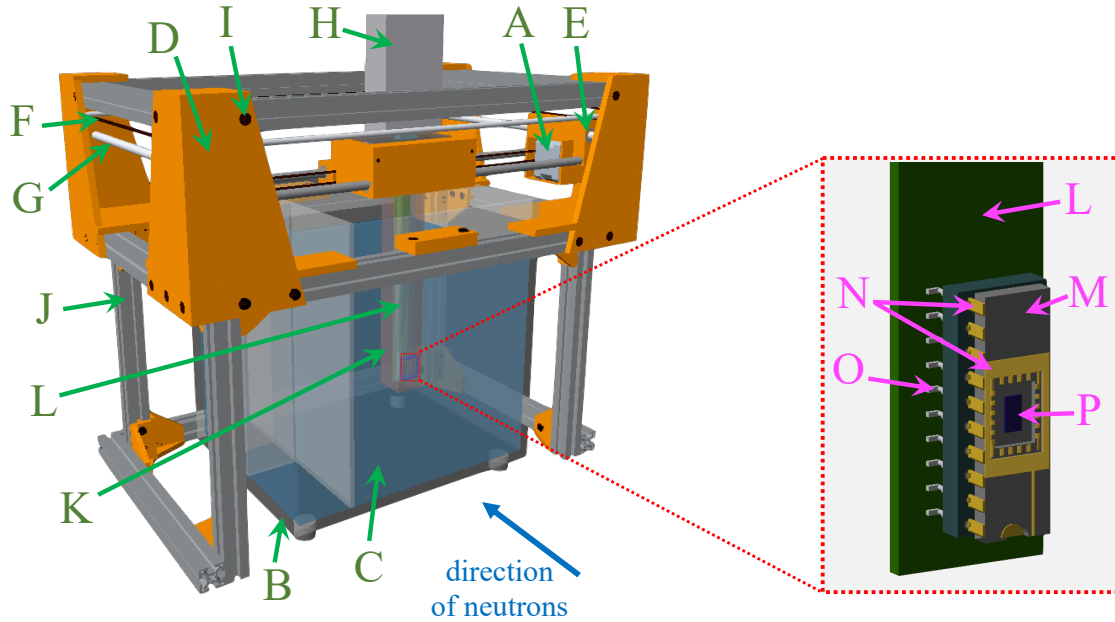


Figure 6.5: Bird's-eye view of the motion stage system (figure 6.4) modelled in the Geant4 simulation. Zoomed-in section (right) of the lower end of the MicroPlus probe, shown with DIL package containing SOI microdosimeter (blue) inserted.

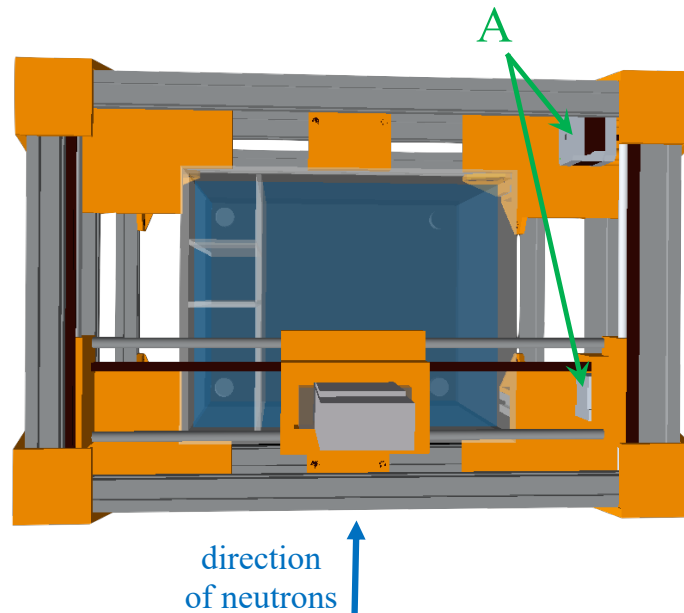


Figure 6.6: Top-down view of the motion stage system (figure 6.4) modelled in the Geant4 simulation. The direction of neutrons from the BSA nozzle is indicated (i.e. this side faces the BSA).

The motion system includes two NEMA17 stepper motors, which are shown in figures 6.5 and 6.6, labelled ‘A’. The stepper motor is shown with more detail in figure 6.7, which was modelled to include all moving components such as the stator, rotor, copper coils, insulation and more. Accurate modelling of the motor is crucial, as high Z materials such as Nd and Fe are present, which may have a long half-life [72].

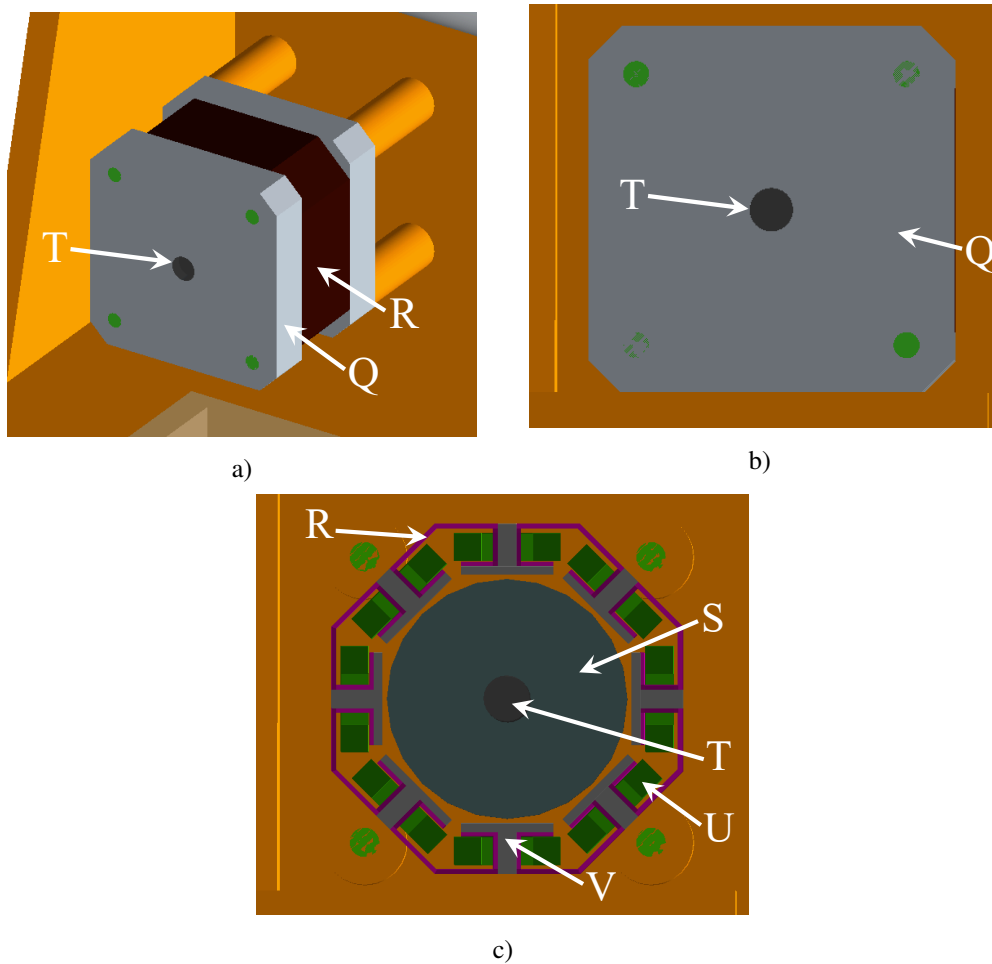


Figure 6.7: The NEMA17 stepper motor (figures 6.5 and 6.6 labelled ‘A’) modelled in the Geant4 simulation; a) Normal view, b) face on view, c) face on view with exterior casing removed to show internal components.

	Component	Composition
Q	NEMA17 Exterior	Aluminium & Silicon Steel
R	NEMA17 Stator	Silicon Steel
S	NEMA17 Rotor	NdFeB Magnet & Silicon Steel
T	NEMA17 Shaft	Stainless Steel
U	NEMA17 Coils	Copper Wire
V	NEMA17 Insulator	Polycarbonate

Table 6.2: Components of the NEMA17 stepper motor and its material compositions, which has been labelled in figure 6.7.

For this simulation, the Tokai phase space calculated with the Geant4 simulation described in previous section (6.2.1) was used as the primary particle source with the motion stage apparatus placed in front of it, as shown in figure 6.8. Note that in this figure, the phase space is used as was recorded along the blue dashed line in the previous simulation (section 6.2.1); i.e. the BSA is not considered in this simulation, only the phase space recorded earlier.

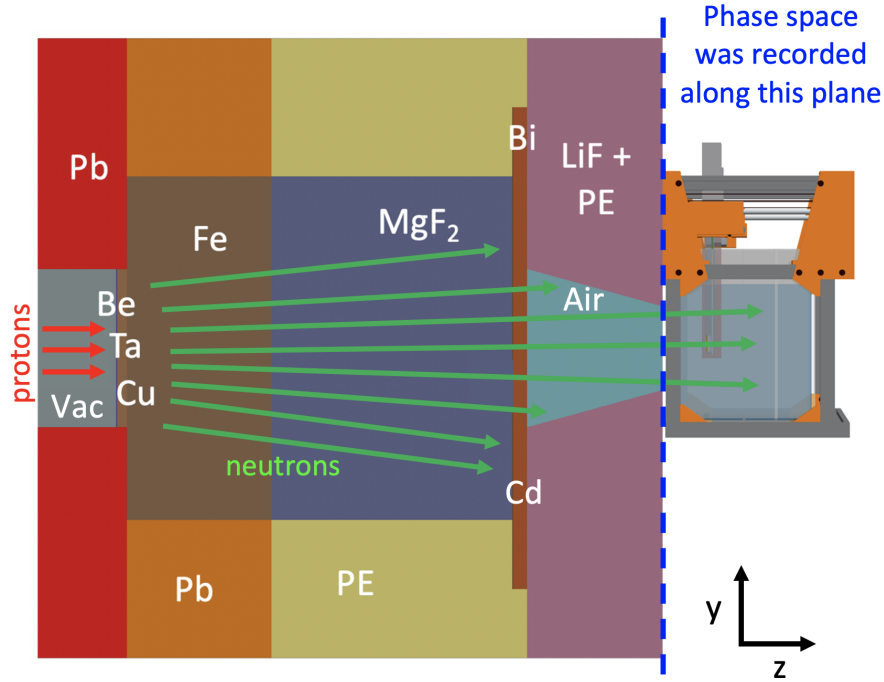


Figure 6.8: Simulation geometry used for irradiation of the realistic experiment setup. The motion stage is placed as close as possible to the beam nozzle, with microdosimeter aligned at the beam central axis. Note that the phase space recorded previously at the beam nozzle is used (blue dashed line), the BSA is only shown here for reference of relative positions. Also note that the behaviour of neutrons in this figure (straight line trajectory) was been simplified and is not realistic.

The experimental setup considers the case when the water phantom tank is positioned directly in front of the beam nozzle aperture so that it is almost touching, mimicking a patient being treated using BNCT for the brain [166]. The MicroPlus probe is inserted into the PMMA sheath and is positioned at a depth 50 mm in the water tank. The neutrons irradiate the same spot for 30 minutes; a typical treatment time for BNCT [164]. The fluence of the iBNCT epithermal neutron beam was used to calculate the relative number of incident particles required in the simulation. The secondary radiation field produced in the

equipment by the incident BNCT neutron field was studied. This primarily relates to the radioprotection of experiment operators. The track history of each particle was recorded, such as information regarding the parent particle and the physics process which produced it. For each interaction, the kinetic energy, the point where the secondary particle is generated, its final location and when it comes to rest, is also stored. This information allows the identification of reactions that occurred in the materials and calculation of the specific activity proceeding the neutron irradiation.

6.2.4 Dose equivalent from the activated materials

The Geant4 simulation described in the previous section (6.2.3) was amended to include a 1 metre radius spherical shell, which encapsulated all of the experimental equipment, as shown in figure 6.10. The rate at which materials produced dangerous levels of ionising radiation and the required cool-down time of the detector was investigated. This was achieved by modelling the rate of neutron activation during irradiation and the time required for radioactivity to fall below an acceptable limit. The radioactive decay was simulated based on the regions in the materials that were activated from the results of the previous simulation.

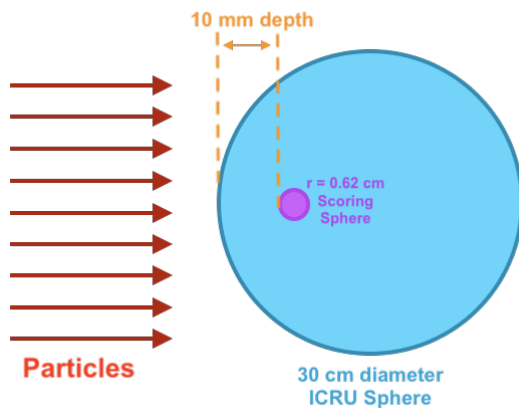


Figure 6.9: ICRU sphere showing the geometry used for $H^*(10)/\phi$ simulations (not to scale). The trajectory of the particles form a uniform fluence on sphere cross section with largest diameter.

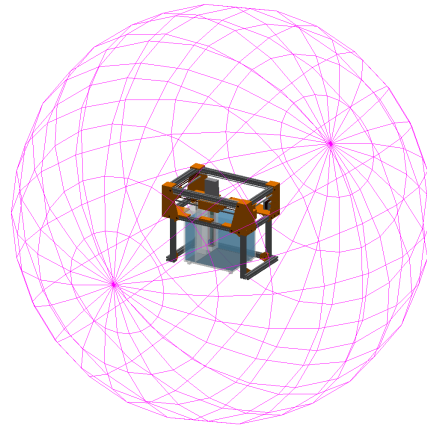


Figure 6.10: Configuration 1 - spherical scoring shell (purple) with 1 metre radius encapsulating all of the equipment. Particles are scored when they cross the surface of the shell.

The emitted decay products from the materials are detected when they reach the spherical shell (purple wireframe in figure 6.10) with their kinetic energy and spherical coordinates recorded. Using the particle information at this position, the ambient dose equivalent $H^*(10)$ at 1 m and 0.4 m was simulated, based on the methodology outlined by the ICRP [167]. The trajectory of the particles are aligned and expanded, producing a uniform distribution on a disc surface with diameter of 30 cm, the same as that of the ICRU A150 spherical phantom [167]. In order to score the ambient dose equivalent, a spherical scoring volume (0.62 cm radius) was placed 10 mm deep inside the ICRU sphere, recording energy deposition. The scoring sphere has the same TE A150 material as the ICRU sphere, see figure 6.9. The dose is normalised based on the Tokai fluence to provide the dose equivalent rate.

Four different configurations of the experimental setup were considered for the dose equivalent $H^*(10)$ calculations, by means of the Geant4 simulation;

1. MicroPlus probe including sheath and shaper in water tank with motion system, at 1 m distance (figure 6.10),
2. MicroPlus probe including sheath and shaper in water tank with motion system, at 0.4 m distance (figure 6.11),
3. MicroPlus probe including sheath and shaper in free air, at 0.4 m distance (figure 6.12),
4. MicroPlus probe only in free air, at 0.4 m distance (figure 6.13).

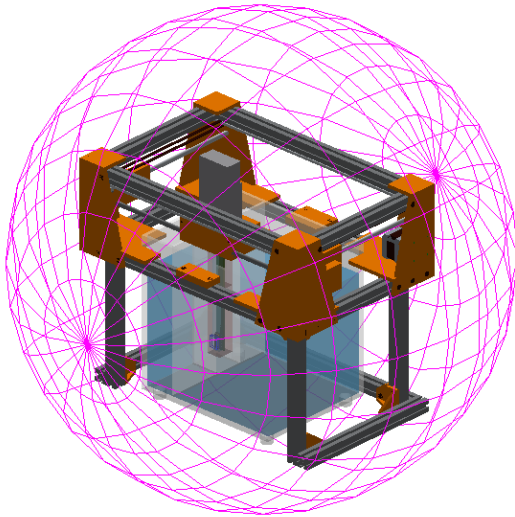


Figure 6.11: Configuration 2; spherical scoring shell with 0.4 metre radius encapsulating all of the equipment.

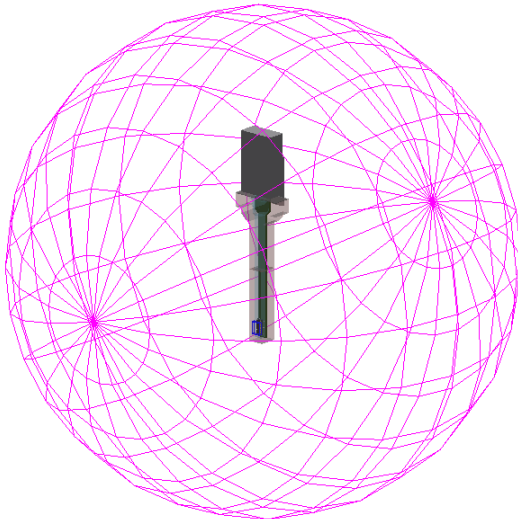


Figure 6.12: Configuration 3; spherical scoring shell with 0.4 metre radius encapsulating MicroPlus probe (including sheath and shaper) in free air.

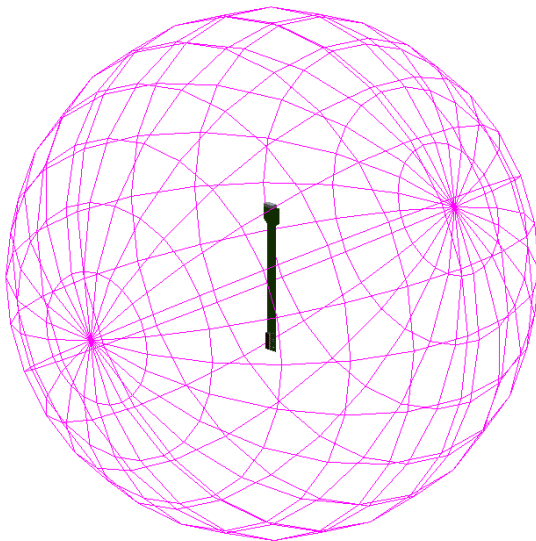


Figure 6.13: Configuration 4; spherical scoring shell with 0.4 metre radius encapsulating only MicroPlus probe in free air.

6.3 Simulation to model the BSA of the iBNCT facility

6.3.1 Model of the Tokai facility from ^9Be target into treatment room

The proton interaction with the ^9Be target produces a forward peaked emission of neutrons, which are shielded and shaped by the BSA as shown in figure 6.14. This results in a 12 cm diameter circular beam exiting the nozzle, which is in agreement with that reported by the iBNCT facility [164]. The lithiated polyethylene collimator positioned from approximately -20 cm to 0 cm absorbs a large population of neutrons, providing high quality shielding for low energy neutrons.

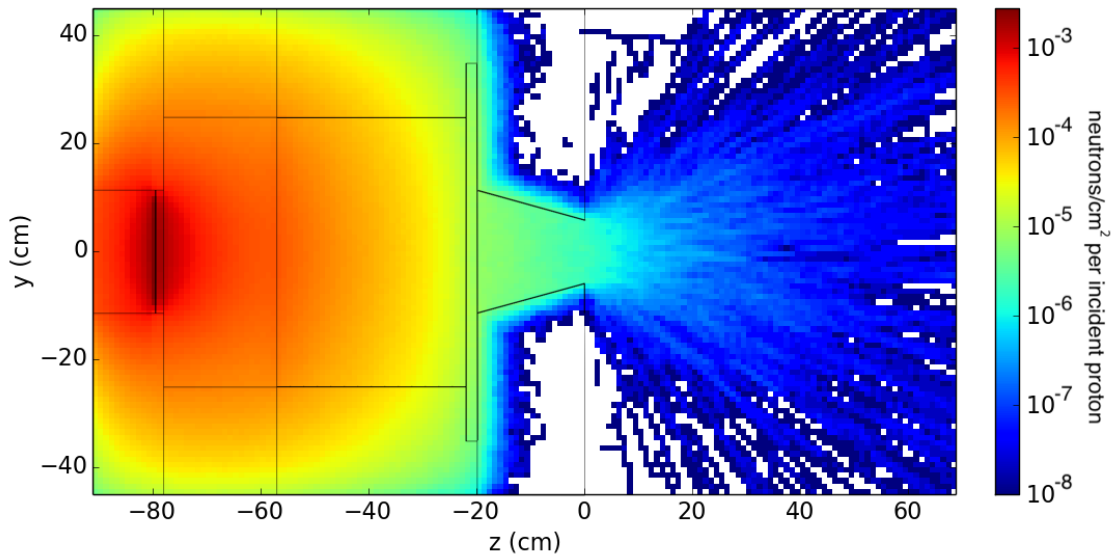


Figure 6.14: Neutron fluence map per incident proton, describing the distribution throughout the BSA and treatment room. Black wireframe of the BSA has been overlaid. The treatment room is from $z > 0$ cm.

Figure 6.15 shows the neutron spectrum at the beam aperture, with comparison to a PHITS [168] study performed by iBNCT [164]. The neutron intensity has been normalized to an average proton current of 2 mA. The integral neutron flux values for different energy ranges were calculated using this data, shown in table 6.3.

The neutron energy spectra obtained in this work using Geant4 is similar to that of PHITS [164]. The difference of neutron flux in terms of the total and epithermal for Geant4 compared with PHITS is -2.89% and -0.85%, respectively.

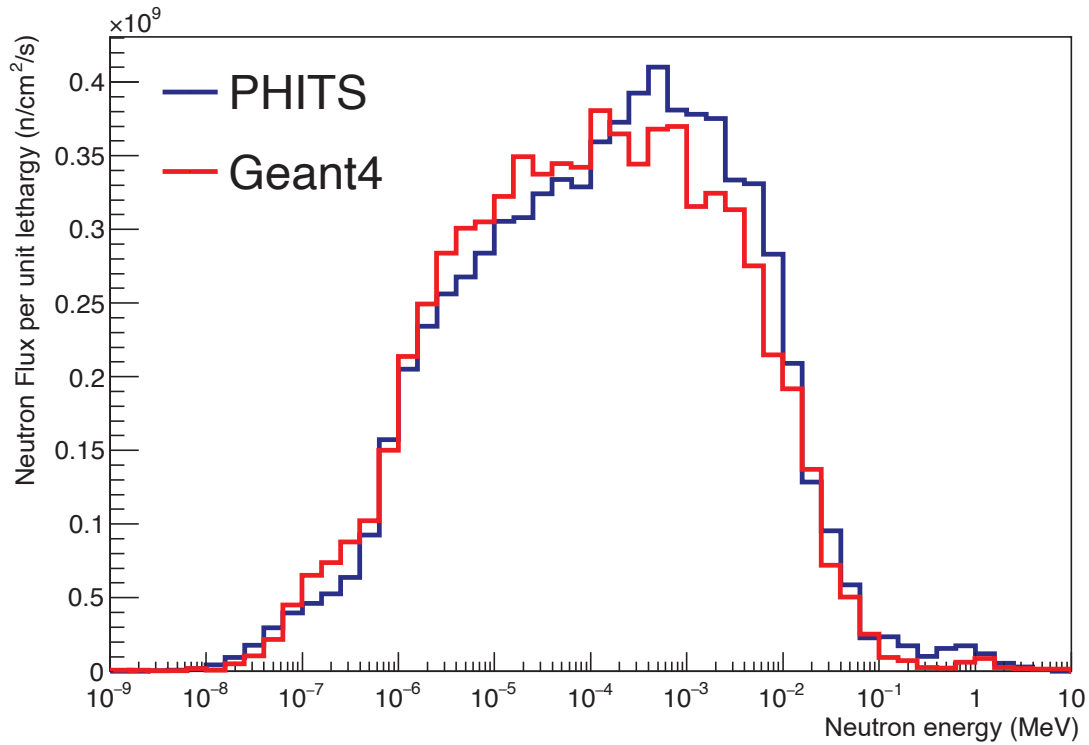


Figure 6.15: Neutron flux recorded at the beam exit nozzle, normalised to the number of primary protons generated per second corresponding to 2mA current. PHITS simulation was performed by iBNCT, reported in [164].

Energy Range	PHITS neutron flux (Kumada, 2019) [164]	Geant4 neutron flux (this work)
Total	2.81×10^9 n/cm ² /s	2.73×10^9 n/cm ² /s
Thermal (< 0.5 eV)	9.87×10^7 n/cm ² /s	11.6×10^7 n/cm ² /s
Epithermal (0.5 eV - 10 keV)	2.37×10^9 n/cm ² /s	2.35×10^9 n/cm ² /s
Fast (> 10 keV)	3.33×10^8 n/cm ² /s	2.71×10^8 n/cm ² /s

Table 6.3: Integral neutron flux (n/cm²/s) values for different energy ranges, calculated using PHITS [164] and Geant4 (this work). Calculated based on the data also presented in figure 6.15.

As seen in figure 6.15, there is a lower proportion of fast neutrons in the Geant4 result, with the neutron flux spectra appearing to be shifted/moderated to lower energies. Possible explanations may include differences in the cross section libraries, physics models, and BSA geometry used between the two codes, which are discussed below.

Cross section libraries: As Geant4 and PHITS use evaluated neutron data libraries sourced from both ENDF/B-VII.1 [54] and JENDL-4.0 [169], it is unlikely that this is the

cause of fast neutron disagreement.

Physics models: Differences in the elastic and inelastic scatter models (that are not based on cross section data) may explain the variance in the fast neutron component. Another possibility is whether the $p + {}^9\text{Be}$ interactions were described using the proprietary physics model of each simulation code, rather than evaluated data. This could result in different initial neutron energies produced in this reaction from the Be target.

BSA geometry: The most probable explanation is a difference in the definition of some BSA components, as the geometry used in the Geant4 simulation for this work was based on the simplified model, shown in figure 6.2. As the Fe and MgF_2 layers in the BSA both act as fast neutron filters, a slightly excessive thickness would explain the increased neutron moderation observed in the Geant4 result.

This will be investigated in future studies in more detail but has minimal impact in the context of this work. The neutron energy fluence in the primary region is mainly epithermal and the neutrons scattered out-of-field are mostly thermal. This may induce different reactions in the out-of-field region for materials which favour thermal neutrons.

6.4 Neutron Activation of Sample Materials

This set of results shows the neutron activation in cubic samples of various materials after they have been irradiated by the Tokai neutron phase space. The neutron phase space was calculated in the previous section, with the accelerator proton current operating at 2 mA, corresponding to $1 \times 10^9 \text{ n/cm}^2/\text{sec}$ total neutron flux. The tested elements/compounds can be either microdosimeter or phantom materials that are typically used in our experimental measurements. For each target material, the activation rate of nuclei/sec is presented in tabular form. The results presented in these tables report the production directly from neutron irradiation or indirectly by radioactive decay, taken at the 30 minute mark after irradiation, when the beam is turned off.

Aluminium Activation

Aluminium is utilised as a conductive coating in microdosimeters to connect circuit elements. In the apparatus of the experiment setup, aluminium is used in the extrusion bars (the supporting frame of the motion stage system), pulse shaper box (aluminium Diecast steel), shielding foil of the μ^+ sheath, substrate of the $^{10}\text{B}_4\text{C}$ converter film and exterior of the NEMA17 motor.

Aluminum does not produce many radioactive byproducts when irradiated, with the exception of ^{28}Al , which was formed by ^{27}Al thermal neutron capture at a rate of $1.39\text{E}+5$ nuclei/sec. Table 6.4 shows the reactions that occurred within the target during irradiation.

Elem.	Radioactive Product	Reaction	Nuclei/sec	Decay Type & Average KE [72]	Half-life
Al	^{28}Al	$^{27}\text{Al}(\text{n},\gamma)^{28}\text{Al}$	$1.39\text{E}+5$	β^- : 4642.36 keV	134.55 s
Al	—	$^{28}\text{Al} \rightarrow ^{28}\text{Si}[1779.03]$	$7.18\text{E}+2$	γ : 1778.70 keV	475 fs
Al	—	$^{28}\text{Si}[1779.03] \rightarrow ^{28}\text{Si}$	$7.18\text{E}+2$	—	—
Al	^{27}Mg	$^{27}\text{Al}(\text{n},\text{p})^{27}\text{Mg}$	$7.30\text{E}-2$	β^- : 2610.00 keV	564.72 s
Al	—	$^{27}\text{Mg} \rightarrow ^{27}\text{Al}[843.76]$	$6.32\text{E}-5$	γ : 843.76 keV	35 ps
Al	—	$^{27}\text{Al}[843.76] \rightarrow ^{27}\text{Al}$	$6.32\text{E}-5$	—	—
Al	—	$^{27}\text{Mg} \rightarrow ^{27}\text{Al}[1014.56]$	$2.62\text{E}-5$	γ : 1014.52 keV	1.49 ps
Al	—	$^{27}\text{Al}[1014.56] \rightarrow ^{27}\text{Al}$	$2.62\text{E}-5$	—	—

Table 6.4: Interactions within Aluminium target resulting from neutron irradiation. Decay energy and short-lived half-life referenced from [72].

There are two radioactive isotopes produced as shown in table 6.4; ^{28}Al and ^{27}Mg . Figure 6.16 shows the activity of these radioactive compounds during irradiation and decay over time. The time it takes for activity to drop below $1\text{ }\mu\text{Bq}$ is simulated throughout a 30 minute irradiation session. As ^{28}Al has a short half-life, it is not a major concern. It takes less than 1.5 hours for the concentration of ^{28}Al to decrease below $1\text{ }\mu\text{Bq}$ after a 30 minute irradiation period.

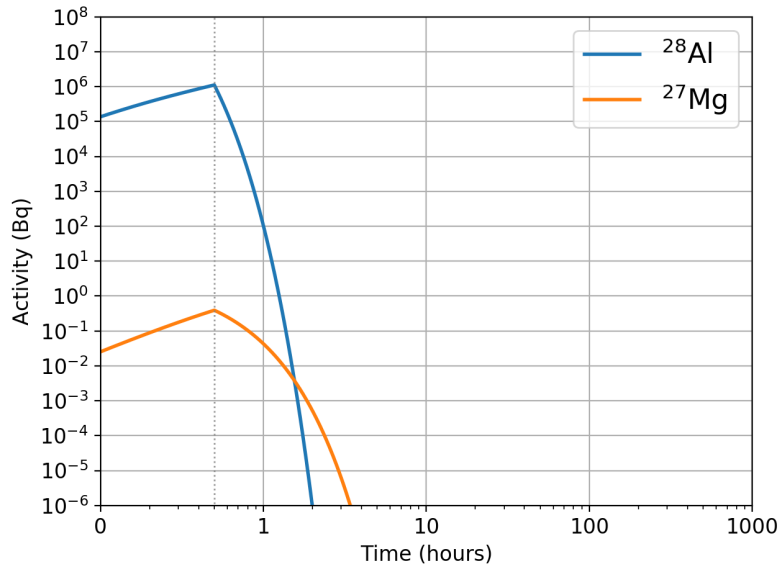


Figure 6.16: Activity of radioisotopes produced within 1 cm³ sample of Aluminium target material. Simulated for 30 min irradiation period with following cool-down.

Silicon Activation

Silicon is generally utilized as an insulating substrate and the sensitive volume inside microdosimeters. The NEMA17 motors of the experimental setup contain silicon as silicon steel in the exterior, stator and rotor. Table 6.5 presents the reactions that take place inside the silicon sample when it is irradiated by the Tokai neutron source.

Elem.	Radioactive Product	Reaction	Nuclei/sec	Decay Type & Average KE [72]	Half-life
Si	—	$^{28}\text{Si}(n,\gamma)^{29}\text{Si}$	7.42E+4	—	—
Si	^{31}Si	$^{30}\text{Si}(n,\gamma)^{31}\text{Si}$	2.92E+3	β^- : 1491.51 keV	157.09 m
Si	—	$^{29}\text{Si}(n,\gamma)^{30}\text{Si}$	2.62E+3	—	—
Si	—	$^{31}\text{Si} \rightarrow ^{31}\text{P}$	1.91E-1	—	—
Si	—	$^{31}\text{Si} \rightarrow ^{31}\text{P}[1226.15]$	1.02E-4	γ : 1266.1 keV	0.52 ps
Si	—	$^{31}\text{P}[1226.15] \rightarrow ^{31}\text{P}$	1.02E-4	—	—

Table 6.5: Interactions within Silicon target resulting from neutron irradiation. Decay energy and short-lived half-life referenced from [72].

Figure 6.17 depicts the simulated production of radioactive products in the silicon target. ^{31}Si has a high production rate by neutron capture, resulting in just above 10^3 Bq activity after 30 minutes of constant neutron irradiation. ^{31}Si activity concentrations exceeding 10^6 Bq or 10^3 Bq/g is the limit as to which the presence of this isotope activity

would be of ‘moderate’ concern [155]. To reach this limit, the silicon target would have to be exposed to constant irradiation for more than 15 hours. The cool-down of ^{31}Si after 30 minutes of irradiation takes roughly 82 hours to decay below $1\ \mu\text{Bq}$.

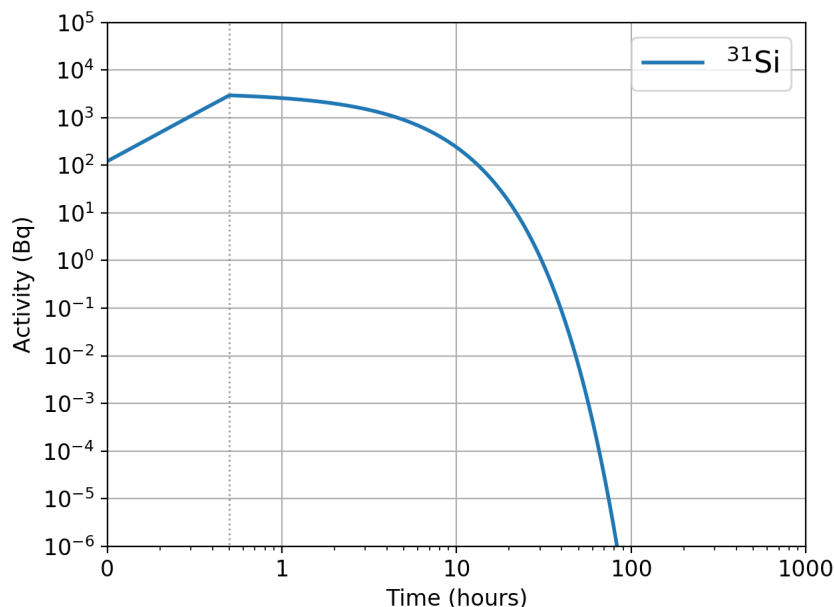


Figure 6.17: Activity of radioisotopes produced within $1\ \text{cm}^3$ sample of Silicon target material. Simulated for 30 min irradiation period with following cool-down.

Diamond Activation

Carbon was used to represent diamond, with density set to $3.515\ \text{g/cm}^3$. Diamond is commonly employed as a sensitive material or as the detector substrate in some microdosimeters. As a microdosimeter, diamond has the highest atomic density of any material, allowing for high neutron efficiency per unit volume. Due to its high intrinsic efficiency, diamond is especially well suited for sub-MeV neutron detection. The processes that occur within diamond during epithermal neutron irradiation are shown in Table 6.6. ^{14}C is the sole radioisotope generated, with a production rate of $7.70\text{E}+1$ nuclei per sec.

Figure 6.18 depicts the simulated generation of radioactive isotopes in diamond over time. The half-life of ^{14}C is extremely long and is not a cause for concern as it is below the IAEA’s recommended activity level [155]. Diamond is very stable with an epithermal neutron source, making it an appealing material option in this energy range. However,

Elem.	Radioactive Product	Reaction	Nuclei/sec	Decay Type & Average KE [72]	Half-life
C	–	$^{12}\text{C}(\text{n},\gamma)^{13}\text{C}$	6.56E+3	–	–
C	^{14}C	$^{13}\text{C}(\text{n},\gamma)^{14}\text{C}$	7.70E+1	β^- : 156.48 keV	5805.13 yr
C	–	$^{14}\text{C} \rightarrow ^{14}\text{N}$	2.92E-8	–	–

Table 6.6: Interactions within Diamond target resulting from neutron irradiation. Decay energy and short-lived half-life referenced from [72].

for higher neutron energies above 6 MeV, the generation of ^9Be from the fast-neutron reaction, $^{12}\text{C}(\text{n},\alpha)^9\text{Be}$, becomes too high.

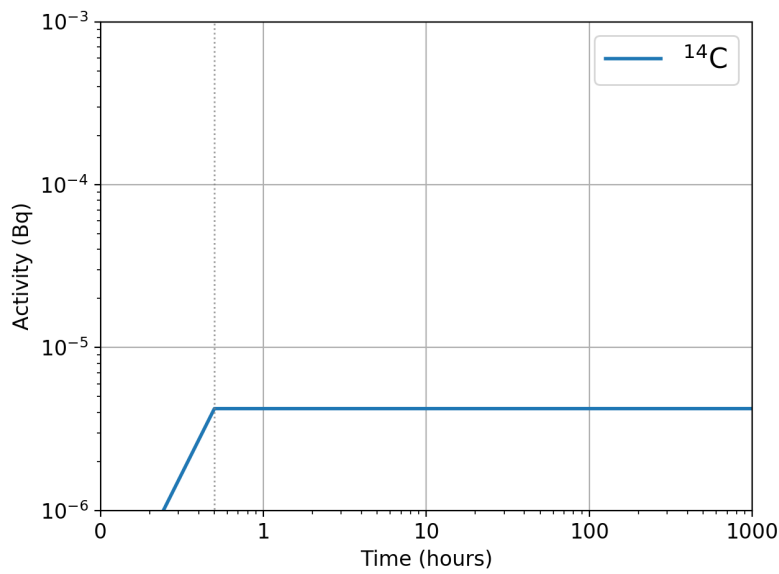


Figure 6.18: Activity of radioisotopes produced within 1 cm³ sample of Diamond target material. Simulated for 30 min irradiation period with following cool-down.

Silicon Dioxide (SiO₂) Activation

Silicon Dioxide (SiO₂) is utilised as an electronic insulator for passivation in silicon microdosimetry. Table 6.7 shows the reactions which occur within the SiO₂ sample. Figure 6.19 depicts the simulated decay of radioactive products in SiO₂ over time.

Elem.	Radioactive Product	Reaction	Nuclei/sec	Decay Type & Average KE [72]	Half-life
Si	–	$^{28}\text{Si}(n,\gamma)^{29}\text{Si}$	3.46E+4	–	–
Si	^{31}Si	$^{30}\text{Si}(n,\gamma)^{31}\text{Si}$	1.53E+3	β^- : 1491.51 keV	157.09 m
Si	–	$^{29}\text{Si}(n,\gamma)^{30}\text{Si}$	1.32E+3	–	–
O	^{15}C	$^{18}\text{O}(n,\alpha)^{15}\text{C}$	2.30E+2	β^- : 9771.71 keV	2.47 s
O	–	$^{16}\text{O}(n,\gamma)^{17}\text{O}$	1.09E+2	–	–
O	^{14}C	$^{17}\text{O}(n,\alpha)^{14}\text{C}$	4.52E+1	β^- : 156.48 keV	5805.13 yr
O	–	$^{15}\text{C} \rightarrow ^{15}\text{N}[5298.82]$	4.12E+1	γ : 5297.82 keV	17 fs
O	–	$^{15}\text{N}[5298.82] \rightarrow ^{15}\text{N}$	4.12E+1	–	–
O	–	$^{15}\text{C} \rightarrow ^{15}\text{N}$	2.32E+1	–	–
Si	–	$^{31}\text{Si} \rightarrow ^{31}\text{P}$	1.12E-1	–	–
O	–	$^{15}\text{C} \rightarrow ^{15}\text{N}[8312.62]$	2.52E-2	γ : 8310.15 keV	1.2 fs
O	–	$^{15}\text{N}[8312.62] \rightarrow ^{15}\text{N}$	2.52E-2	–	–
O	–	$^{15}\text{C} \rightarrow ^{15}\text{N}[9049.71]$	2.24E-2	γ : 9046.78 keV	0.35 fs
O	–	$^{15}\text{N}[9049.71] \rightarrow ^{15}\text{N}$	2.24E-2	–	–
O	–	$^{15}\text{C} \rightarrow ^{15}\text{N}[8571.40]$	1.04E-2	γ : 8568.77 keV	0.5 fs
O	–	$^{15}\text{N}[8571.40] \rightarrow ^{15}\text{N}$	1.04E-2	–	–
Si	–	$^{31}\text{Si} \rightarrow ^{31}\text{P}[1226.15]$	5.98E-5	γ : 1266.1 keV	0.52 ps
Si	–	$^{31}\text{P}[1226.15] \rightarrow ^{31}\text{P}$	5.98E-5	–	–
O	–	$^{14}\text{C} \rightarrow ^{14}\text{N}$	1.72E-8	–	–

Table 6.7: Interactions within SiO_2 target resulting from neutron irradiation. Decay energy and short-lived half-life referenced from [72].

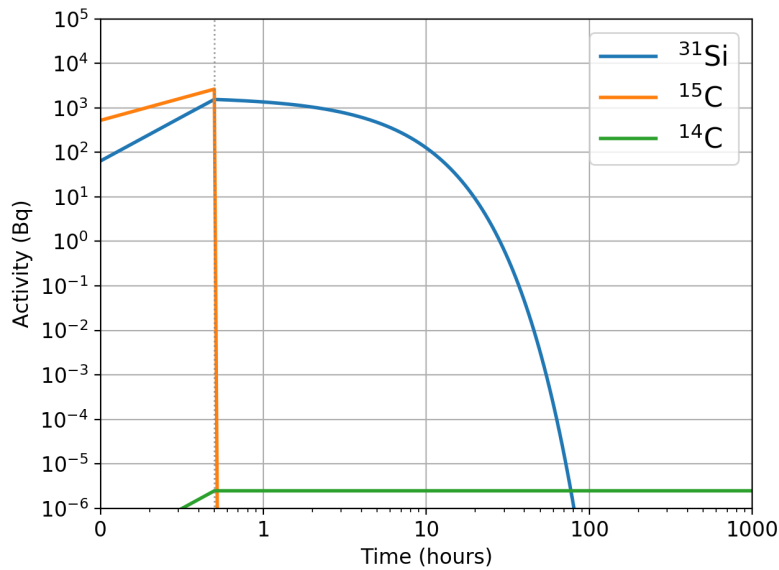


Figure 6.19: Activity of radioisotopes produced within 1 cm^3 sample of SiO_2 target material. Simulated for 30 min irradiation period with following cool-down.

In SiO_2 , three radioisotopes are produced: ^{14}C , ^{15}C , and ^{31}Si . Although ^{15}C is produced at a high rate, it decays below $1\ \mu\text{Bq}$ within a few minutes following irradiation. As observed previously in the silicon target material, ^{31}Si is created at a high rate, progressively approaching the IAEA's 'moderate' activity concentration limit of $10^6\ \text{Bq}$ or $10^3\ \text{Bq/g}$ [155]. Due to the reduced amount of silicon present, reaching this limit will take over 250 hours. The cool-down of ^{31}Si after 30 minutes of irradiation takes less than 80 hours to fall below $1\ \mu\text{Bq}$.

PMMA Activation

PMMA, commonly known as Lucite or Perspex, is a translucent thermoplastic. In microdosimetry experiments, PMMA is employed as a water equivalent material surrounding the detection device (i.e. MicroPlus sheath) because of its density of $1.18\ \text{g/cm}^3$. It is also used in the walls of the water phantom tank. PMMA was characterised as having a composition by weight of 8.05% hydrogen, 59.99% carbon, and 31.96% oxygen.

The reactions that occur inside the PMMA target are shown in Table 6.8. Due to the high neutron cross-section of hydrogen in the epithermal energy range, the $^1\text{H}(\text{n},\gamma)^2\text{H}$ reaction is the most frequent neutron interaction. The radioactive decay of ^{15}C , which is created by the $^{18}\text{O}(\text{n},\alpha)^{15}\text{C}$ reaction, is the principal source of delayed gamma rays. ^{15}C decays into its daughter isotope, ^{15}N , with a short half-life and wide range of energy levels, resulting in various gamma radiation emissions.

Elem.	Radioactive Product	Reaction	Nuclei/sec	Decay Type & Average KE [72]	Half-life
H	–	$^1\text{H}(n,\gamma)^2\text{H}$	2.74E+5	–	–
C	–	$^{12}\text{C}(n,\gamma)^{13}\text{C}$	2.38E+3	–	–
O	^{15}C	$^{18}\text{O}(n,\alpha)^{15}\text{C}$	6.34E+1	β^- : 9771.71 keV	2.47 s
O	–	$^{16}\text{O}(n,\gamma)^{17}\text{O}$	4.98E+1	–	–
C	^{14}C	$^{13}\text{C}(n,\gamma)^{14}\text{C}$	3.16E+1	β^- : 156.48 keV	5805.13 yr
O	^{14}C	$^{17}\text{O}(n,\alpha)^{14}\text{C}$	3.12E+1	β^- : 156.48 keV	5805.13 yr
O	–	$^{15}\text{C} \rightarrow ^{15}\text{N}[5298.82]$	1.13E+1	γ : 5297.82 keV	17 fs
O	–	$^{15}\text{N}[5298.82] \rightarrow ^{15}\text{N}$	1.13E+1	–	–
O	–	$^{15}\text{C} \rightarrow ^{15}\text{N}$	6.40E+0	–	–
O	–	$^{17}\text{O}(n,\gamma)^{18}\text{O}$	4.52E+0	–	–
O	^{19}O	$^{18}\text{O}(n,\gamma)^{19}\text{O}$	4.40E+0	β^- : 4822.26 keV	24.90 s
O	–	$^{19}\text{O} \rightarrow ^{19}\text{F}[1554.04]$	7.04E-2	γ : 1554.0 keV	3.5 fs
O	–	$^{19}\text{F}[1554.04] \rightarrow ^{19}\text{F}$	7.04E-2	–	–
O	–	$^{19}\text{F} \rightarrow ^{19}\text{F}[197.14]$	4.84E-2	γ : 197.1 keV	89.3 ns
O	–	$^{19}\text{F}[197.14] \rightarrow ^{19}\text{F}$	4.84E-2	–	–
O	–	$^{19}\text{O} \rightarrow ^{19}\text{F}$	5.44E-3	–	–
O	–	$^{15}\text{C} \rightarrow ^{15}\text{N}[8312.62]$	6.98E-3	γ : 8310.15 keV	1.2 fs
O	–	$^{15}\text{N}[8312.62] \rightarrow ^{15}\text{N}$	6.98E-3	–	–
O	–	$^{15}\text{C} \rightarrow ^{15}\text{N}[9049.71]$	6.14E-3	γ : 9046.78 keV	0.35 fs
O	–	$^{15}\text{N}[9049.71] \rightarrow ^{15}\text{N}$	6.14E-3	–	–
O	–	$^{15}\text{C} \rightarrow ^{15}\text{N}[8571.40]$	2.86E-3	γ : 8568.77 keV	0.5 fs
O	–	$^{15}\text{N}[8571.40] \rightarrow ^{15}\text{N}$	2.86E-3	–	–
O	–	$^{14}\text{C} \rightarrow ^{14}\text{N}$	1.19E-8	–	–
C	–	$^{14}\text{C} \rightarrow ^{14}\text{N}$	1.20E-8	–	–

Table 6.8: Interactions within PMMA target resulting from neutron irradiation. Decay energy and short-lived half-life referenced from [72].

Figure 6.20 depicts the simulated production of radioactive products in PMMA over time. The only radioisotopes created are ^{14}C , ^{15}C and ^{19}O . ^{15}C and ^{19}O decay quickly after 30 minutes of irradiation. The half-life of ^{14}C is long, but it is not of concern as it does not exceed the IAEA's activity recommendations of 10^7 Bq or 10^4 Bq/g activity concentration [155].

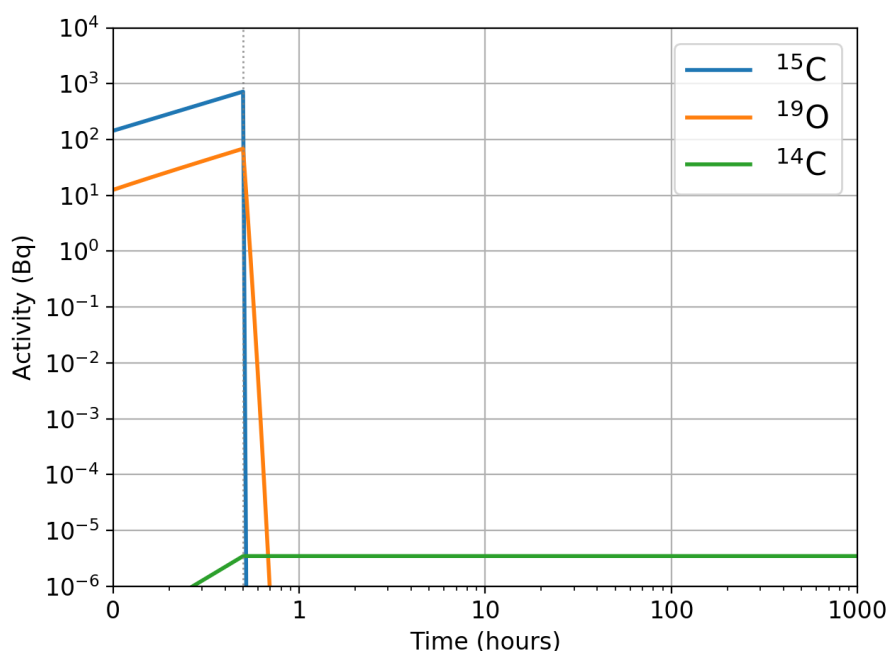


Figure 6.20: Activity of radioisotopes produced within 1 cm^3 sample of PMMA target material. Simulated for 30 min irradiation period with following cool-down.

Water Activation

In microdosimetry experiments, a large volume of water is used for the water phantom, where the MicroPlus probe is suspended inside of. Table 6.9 depicts the processes that occur within the water target when irradiated by epithermal neutrons. The most common activation type is $^1\text{H}(n,\gamma)^2\text{H}$ thermal neutron capture, due to the large neutron cross-section of ^1H for this reaction. The neutron irradiation of water does not produce many radioactive compounds, as shown in the activity production models in figure 6.21.

Elem.	Radioactive Product	Reaction	Nuclei/sec	Decay Type & Average KE [72]	Half-life
H	–	$^1\text{H}(n,\gamma)^2\text{H}$	3.36E+5	–	–
O	^{15}C	$^{18}\text{O}(n,\alpha)^{15}\text{C}$	2.54E+2	β^- : 9771.71 keV	2.47 s
O	–	$^{16}\text{O}(n,\gamma)^{17}\text{O}$	9.50E+1	–	–
O	–	$^{15}\text{C} \rightarrow ^{15}\text{N}[5298.82]$	4.54E+1	γ : 5297.82 keV	17 fs
O	–	$^{15}\text{N}[5298.82] \rightarrow ^{15}\text{N}$	4.54E+1	–	–
O	^{14}C	$^{17}\text{O}(n,\alpha)^{14}\text{C}$	3.16E+1	β^- : 156.48 keV	5805.13 yr
O	–	$^{15}\text{C} \rightarrow ^{15}\text{N}$	2.56E+1	–	–
O	–	$^{17}\text{O}(n,\gamma)^{18}\text{O}$	4.56E+0	–	–
O	^{19}O	$^{18}\text{O}(n,\gamma)^{19}\text{O}$	4.48E+0	β^- : 4822.26 keV	24.90 s
O	–	$^{19}\text{O} \rightarrow ^{19}\text{F}[1554.04]$	7.16E-2	γ : 1554.0 keV	3.5 fs
O	–	$^{19}\text{F}[1554.04] \rightarrow ^{19}\text{F}$	7.16E-2	–	–
O	–	$^{19}\text{F} \rightarrow ^{19}\text{F}[197.14]$	4.92E-2	γ : 197.1 keV	89.3 ns
O	–	$^{19}\text{F}[197.14] \rightarrow ^{19}\text{F}$	4.92E-2	–	–
O	–	$^{15}\text{C} \rightarrow ^{15}\text{N}[8312.62]$	2.78E-2	γ : 8310.15 keV	1.2 fs
O	–	$^{15}\text{N}[8312.62] \rightarrow ^{15}\text{N}$	2.78E-2	–	–
O	–	$^{15}\text{C} \rightarrow ^{15}\text{N}[9049.71]$	2.46E-2	γ : 9046.78 keV	0.35 fs
O	–	$^{15}\text{N}[9049.71] \rightarrow ^{15}\text{N}$	2.46E-2	–	–
O	–	$^{15}\text{C} \rightarrow ^{15}\text{N}[8571.40]$	1.14E-2	γ : 8568.77 keV	0.5 fs
O	–	$^{19}\text{O} \rightarrow ^{19}\text{F}$	5.64E-2	–	–
O	–	$^{15}\text{N}[8571.40] \rightarrow ^{15}\text{N}$	1.14E-2	–	–
O	–	$^{14}\text{C} \rightarrow ^{14}\text{N}$	1.20E-8	–	–

Table 6.9: Interactions within Water target resulting from neutron irradiation. Decay energy and short-lived half-life referenced from [72].

Figure 6.21 depicts the simulated production of radioactive isotopes in water during irradiation, with respect to time. ^{14}C , ^{15}C and ^{19}O are the three radioisotopes produced. Except for ^{14}C , all of these decay below 1 μBq after 30 minutes of irradiation, making their high rate of production not an issue.

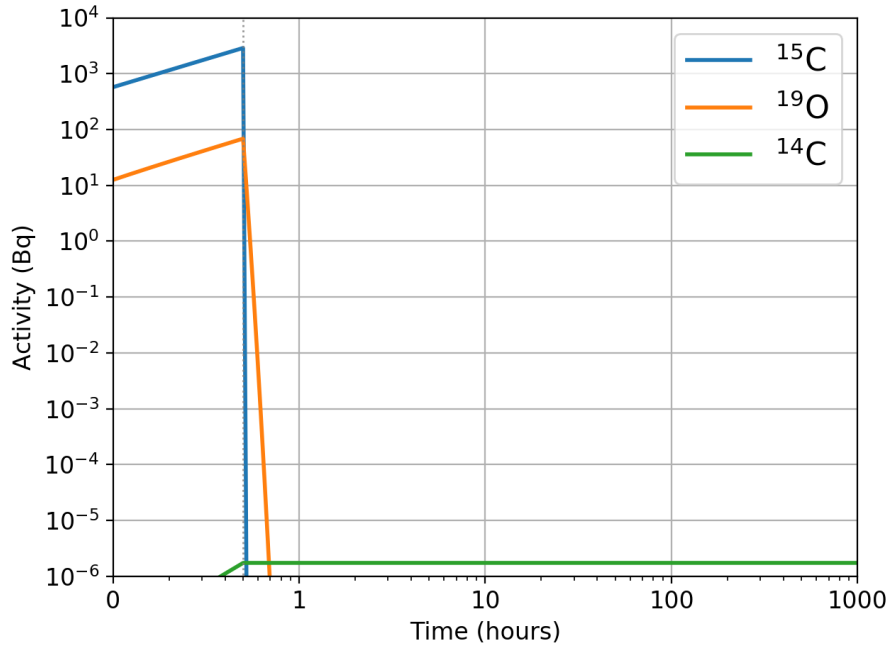


Figure 6.21: Activity of radioisotopes produced within 1 cm³ sample of Water target material. Simulated for 30 min irradiation period with following cool-down.

Aluminium Oxide (AlO) Activation

Aluminium Oxide (AlO) is a ceramic commonly utilised in electronics for its great electrical insulation properties. In the experimental setup, it is used in DIL package substrate, in which is microdosimeter is embedded onto. Table 6.10 presents the processes which occur in the AlO sample when it is irradiated by the Tokai neutron source. There are four radioisotopes produced; ^{28}Al , ^{15}C , ^{14}C and ^{19}O . Radioactive ^{28}Al is produced by neutron capture at a rate of $1.11\text{E}+5$ nuclei/second. ^{15}C radionuclides are produced by the $^{18}\text{O}(n,\alpha)^{15}\text{C}$ reaction at a rate of $3.04\text{E}+2$ nuclei/second.

The simulated decay of produced radioisotopes in the AlO sample are shown in figure 6.16. As seen for other activated oxides, ^{15}C and ^{19}O decay quickly after the beam has been turned off. Following irradiation, the activated ^{28}Al radioisotopes take less than 1 hour to decay below 1 μBq .

Elem.	Radioactive Product	Reaction	Nuclei/sec	Decay Type & Average KE [72]	Half-life
Al	^{28}Al	$^{27}\text{Al}(\text{n},\gamma)^{28}\text{Al}$	1.11E+5	β^- : 4642.36 keV	134.55 s
O	^{15}C	$^{18}\text{O}(\text{n},\alpha)^{15}\text{C}$	3.04E+2	β^- : 9771.71 keV	2.47 s
O	–	$^{16}\text{O}(\text{n},\gamma)^{17}\text{O}$	1.67E+2	–	–
O	–	$^{15}\text{C} \rightarrow ^{15}\text{N}[5298.82]$	5.44+1	γ : 5297.82 keV	17 fs
O	–	$^{15}\text{N}[5298.82] \rightarrow ^{15}\text{N}$	5.44+1	–	–
O	^{14}C	$^{17}\text{O}(\text{n},\alpha)^{14}\text{C}$	3.62E+1	β^- : 156.48 keV	5805.13 yr
O	–	$^{15}\text{C} \rightarrow ^{15}\text{N}$	3.08E+1	–	–
O	–	$^{17}\text{O}(\text{n},\gamma)^{18}\text{O}$	4.54E+0	–	–
O	^{19}O	$^{18}\text{O}(\text{n},\gamma)^{19}\text{O}$	4.50E+0	β^- : 4822.26 keV	24.90 s
O	–	$^{19}\text{O} \rightarrow ^{19}\text{F}[1554.04]$	7.20E-2	γ : 1554.0 keV	3.5 fs
O	–	$^{19}\text{F}[1554.04] \rightarrow ^{19}\text{F}$	7.20E-2	–	–
O	–	$^{19}\text{F} \rightarrow ^{19}\text{F}[197.14]$	4.96E-2	γ : 197.1 keV	89.3 ns
O	–	$^{19}\text{F}[197.14] \rightarrow ^{19}\text{F}$	4.96E-2	–	–
O	–	$^{15}\text{C} \rightarrow ^{15}\text{N}[8312.62]$	3.34E-2	γ : 8310.15 keV	1.2 fs
O	–	$^{15}\text{N}[8312.62] \rightarrow ^{15}\text{N}$	3.34E-2	–	–
O	–	$^{15}\text{C} \rightarrow ^{15}\text{N}[9049.71]$	2.94E-2	γ : 9046.78 keV	0.35 fs
O	–	$^{15}\text{N}[9049.71] \rightarrow ^{15}\text{N}$	2.94E-2	–	–
O	–	$^{15}\text{C} \rightarrow ^{15}\text{N}[8571.40]$	1.37E-2	γ : 8568.77 keV	0.5 fs
O	–	$^{15}\text{N}[8571.40] \rightarrow ^{15}\text{N}$	1.37E-2	–	–
Al	–	$^{28}\text{Al} \rightarrow ^{28}\text{Si}[1779.03]$	4.32E-3	γ : 1778.70 keV	475 fs
Al	–	$^{28}\text{Si}[1779.03] \rightarrow ^{28}\text{Si}$	4.32E-3	–	–
O	–	$^{19}\text{O} \rightarrow ^{19}\text{F}$	5.68E-3	–	–
O	–	$^{14}\text{C} \rightarrow ^{14}\text{N}$	1.38E-8	–	–

Table 6.10: Interactions within AlO target resulting from neutron irradiation. Decay energy and short-lived half-life referenced from [72].

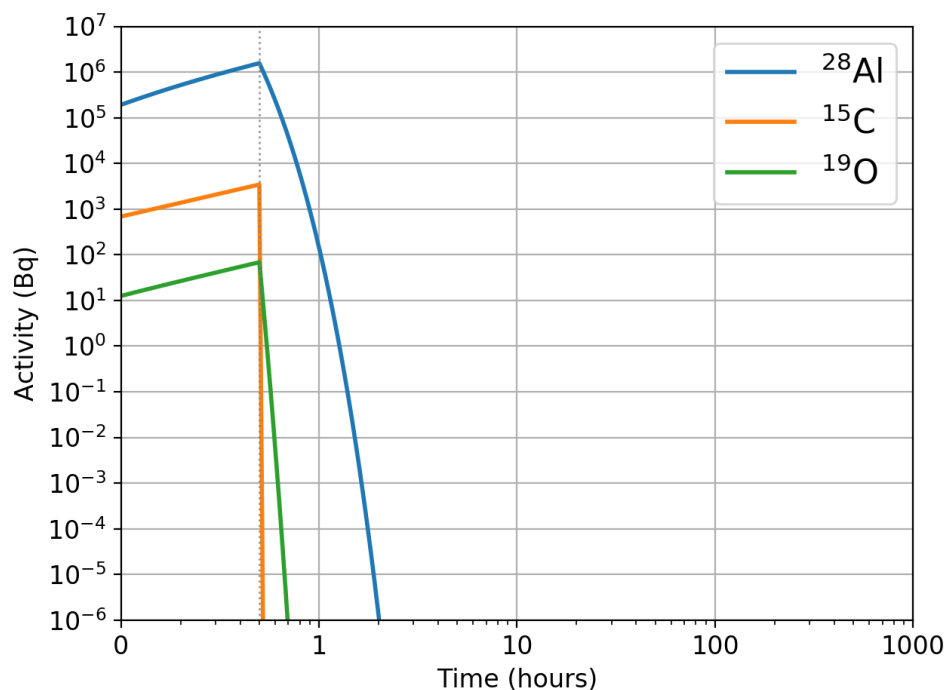


Figure 6.22: Activity of radioisotopes produced within 1 cm^3 sample of AlO target material. Simulated for 30 min irradiation period with following cool-down.

Gold Activation

Gold is used in the DIL20 package readout leads, providing the contacts that carry signal to the IC plugs of the MicroPlus probe. The microdosimeter is embedded onto the surface of the DIL package. The pads of the microdosimeter arrays are wire-bonded to each of the DIL readout leads, allowing electronic interaction. Table 6.11 presents the activated radioisotopes when the unit sample of gold is irradiated by the neutron source. The main activation is $^{197}\text{Au}(n,\gamma)^{198}\text{Au}$ epithermal neutron capture, yielding radioactive ^{198}Au isotopes. The other main reaction is the $^{197}\text{Au}(n,n')^{197}\text{Au}^*$ fast neutron inelastic interaction, though it is less frequent given the lower amount of higher energy neutrons in the source. The ENDF/B-VII.1 neutron cross-sections for the ^{197}Au neutron interactions observed is shown in figure 6.23.

Elem.	Radioactive Product	Reaction	Nuclei/sec	Decay Type & Average KE [72]	Half-life
Au	^{198}Au	$^{197}\text{Au}(n,\gamma)^{198}\text{Au}$	$6.46\text{E}+7$	β^- : 1.37 MeV	2.69 d
Au	—	$^{197}\text{Au}(n,n')^{197}\text{Au}^*$	$1.42\text{E}+4$	—	—
Au	—	$^{198}\text{Au} \rightarrow ^{198}\text{Hg}$	$4.62\text{E}+2$	—	—

Table 6.11: Interactions within Gold target resulting from neutron irradiation. Decay energy and short-lived half-life referenced from [72].

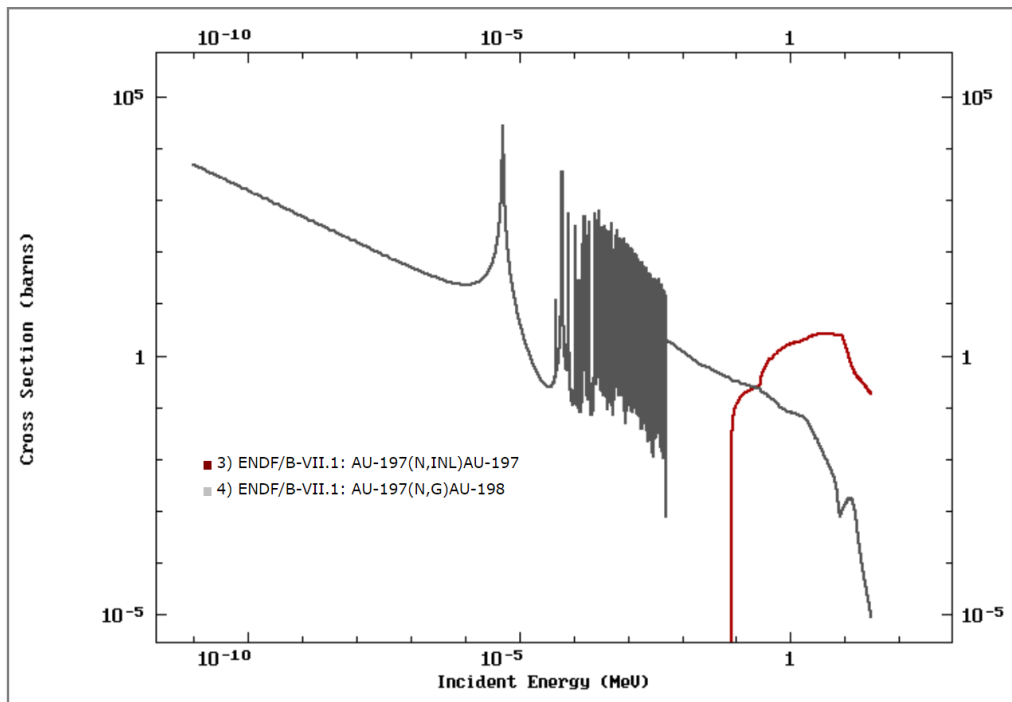


Figure 6.23: ENDF/B-VII.1 neutron cross-section for the ^{197}Au neutron interactions observed in the Geant4 simulation [54].

The simulated decay of activated ^{198}Au isotopes over time is depicted in figure 6.24. The rate of ^{198}Au production during irradiation is high and takes a long time to decay, with a half-life of 2.69 days [72]. This activation may be of concern, given the beta decay energy of 1.37 MeV [72] and its proximal location in the experiment (the microdosimeter is positioned at beam central axis). However, the typical volume of gold used in the DIL package is around 0.065 cm^3 , which is much less than the unit cubic sample considered here. Thus, it is expected to be much lower when considering the activation of the realistic experiment (which is shown in the proceeding section).

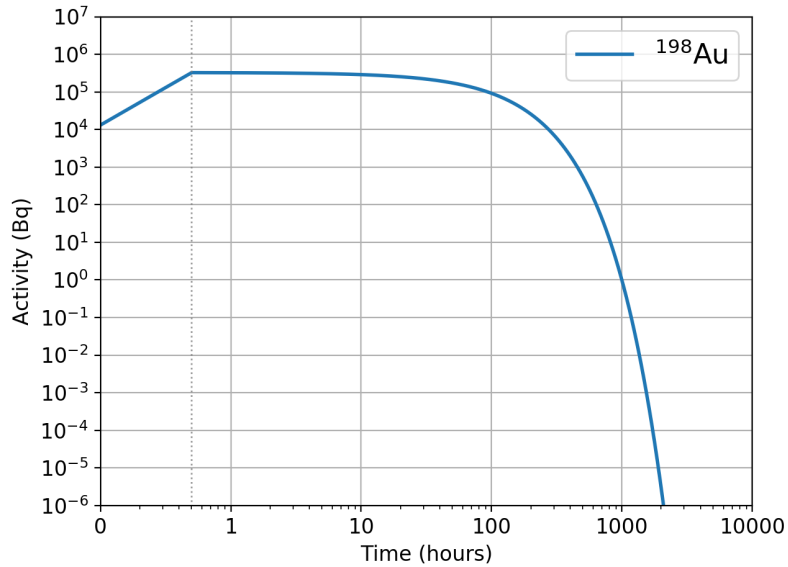


Figure 6.24: Activity of radioisotopes produced within 1 cm³ sample of Gold target material. Simulated for 30 min irradiation period with following cool-down.

Copper Activation

Copper is a commonly used material in the experimental setup, located in the MicroPlus (PCB and IC sockets), coils of the NEMA17 stepper motors and the aluminium diecast steel (steel alloy contains 3.5% Cu) of the shaper box. The reactions that occur in the unit sample of copper during neutron irradiation are shown in table 6.12. The simulated decay over time of radioactive isotopes produced in the copper sample target are shown in figure 6.25. The main activated radioisotopes are ⁶⁴Cu and ⁶⁶Cu from neutron capture.

Elem.	Radioactive Product	Reaction	Nuclei/sec	Decay Type & Average KE [72]	Half-life
Cu	⁶⁴ Cu	⁶³ Cu(n,γ) ⁶⁴ Cu	2.78E+6	β^+ : 652.8 keV, β^- : 579.4 keV	12.7 hr
Cu	⁶⁶ Cu	⁶⁵ Cu(n,γ) ⁶⁶ Cu	5.76E+5	β^- : 2.64 MeV	5.12 m
Cu	—	⁶⁶ Cu→ ⁶⁶ Zn	1.26E+3	—	—
Cu	—	⁶⁴ Cu→ ⁶⁴ Ni	2.60E+1	—	—
Cu	—	⁶⁴ Cu→ ⁶⁴ Zn	1.64E+1	—	—

Table 6.12: Interactions within Copper target resulting from neutron irradiation. Decay energy and short-lived half-life referenced from [72].

As discussed previously for the gold target; the amount of copper present in the realistic experiment is much less, with 0.43 cm³ in the MicroPlus (Cu foil in the PCB and BeCu

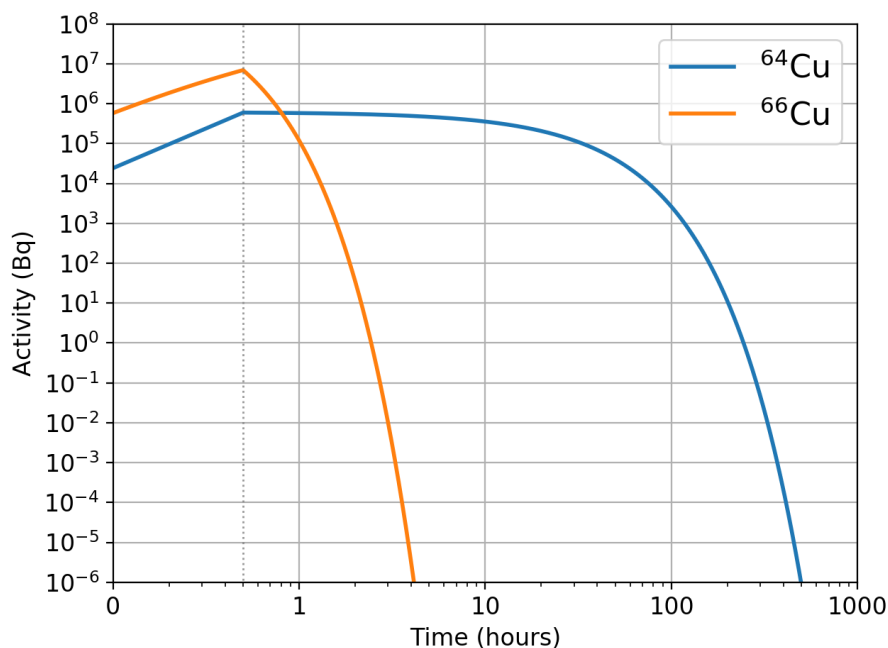


Figure 6.25: Activity of radioisotopes produced within 1 cm³ sample of Copper target material. Simulated for 30 min irradiation period with following cool-down.

alloy in IC sockets) and 0.56 cm³ for the Cu coils of each NEMA17 stepper motor. The shaper box contains 1.72 cm³ of Cu in its diecast steel alloy.

However, for the case of copper, only the MicroPlus IC sockets are located entirely in the primary beam. Only the lower end MicroPlus PCB is in the primary beam. The NEMA17 motors are located out-of-field, thus only scattered neutrons will be to reach them. Additionally, the NEMA17 coils in the electric motors are located beneath the exterior casing (aluminium and silicon steel), which may shield many neutrons from reaching it. The activation of a unit sample of material indicates potential radioprotection risks, though the reasons mentioned here highlights the importance of considering the realistic setup when making a full assessment.

Borosilicate Glass Activation

Borosilicate glass is used in electronics fabrication due to its high chemical durability, low thermal expansion and high electrical insulation. The main glass-forming constituents of borosilicate glass are boron trioxide and silicon dioxide (SiO₂). The MicroPlus PCB

used in our microdosimetry experiments contains wafers of borosilicate glass, which serve mainly as an insulating passivation layer. The borosilicate glass material considered in the simulations was defined using *G4_Pyrex_Glass*, which was obtained from the G4NistManager [147]. The composition by weight of this material consists of 53.96% oxygen, 37.72% silicon, 4.01% boron, 2.82% sodium, 1.16% aluminium and 0.33% potassium.

Due to the presence of ^{10}B in this material, the study of neutron activation in this material is important. The reactions that occur in the borosilicate glass when irradiated by the neutron source is shown in table 6.13. The simulated decay of the activated radioisotopes in borosilicate over time is presented in figure 6.26.

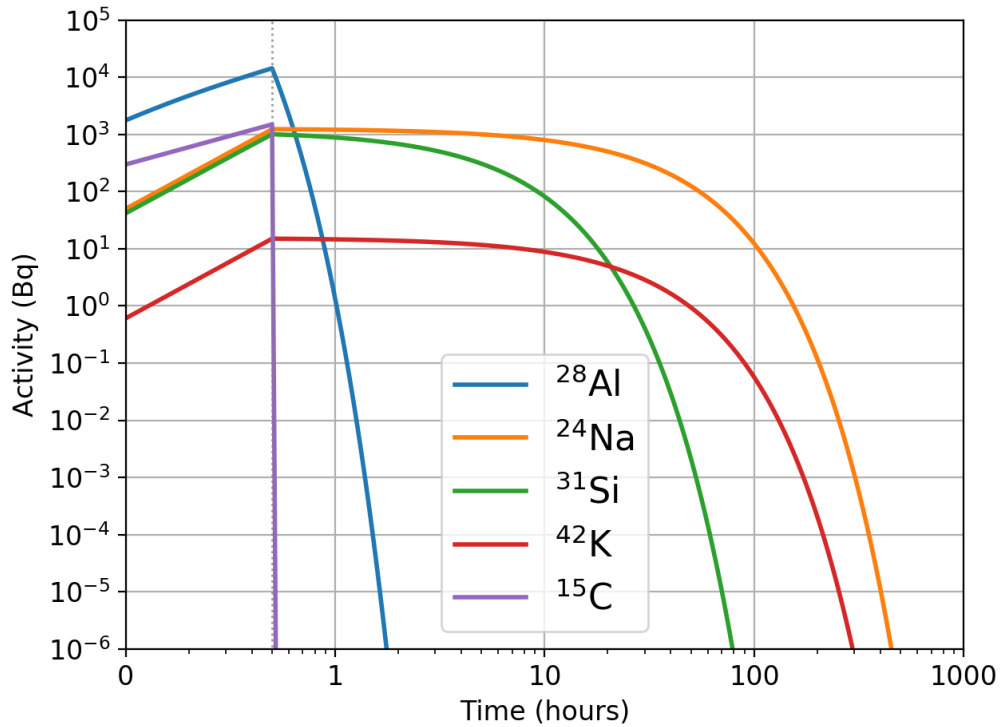


Figure 6.26: Activity of radioisotopes produced within 1 cm³ sample of Borosilicate Glass target material. Simulated for 30 min irradiation period with following cool-down.

The main activation in this material is $^{10}\text{B}(n,\gamma)^7\text{Li}$, due to its high cross section for thermal neutrons. The other major radioisotope activations by neutron capture are ^{24}Na , ^{12}B , ^{28}Al , ^{31}Si and ^{42}K . Radioactive ^{15}C is produced by fast neutrons (> 5 MeV [170]) in the $^{18}\text{O}(n,\alpha)^{15}\text{C}$ reaction, which decays quickly.

Elem.	Radioactive Product	Reaction	Nuclei/sec	Decay Type & Average KE [72]	Half-life
B	—	$^{10}\text{B}(\text{n},\gamma)^7\text{Li}$	2.66E+7	γ : 478 keV	—
Si	—	$^{28}\text{Si}(\text{n},\gamma)^{29}\text{Si}$	2.02E+4	—	—
Na	^{24}Na	$^{23}\text{Na}(\text{n},\gamma)^{24}\text{Na}$	6.74E+3	β^- : 5515.45 keV	17.04 d
B	—	$^{10}\text{B}(\text{n},\gamma)^{11}\text{B}$	3.36E+3	—	—
B	^{12}B	$^{11}\text{B}(\text{n},\gamma)^{12}\text{B}$	3.36E+3	β^- : 13.37 MeV, $\beta^- \alpha$: 6.0 MeV	20.2 ms
B	—	$^{12}\text{B} \rightarrow ^{12}\text{C}$	3.36E+3	—	—
K	—	$^{39}\text{K}(\text{n},\gamma)^{40}\text{K}$	1.49E+3	—	—
Al	^{28}Al	$^{27}\text{Al}(\text{n},\gamma)^{28}\text{Al}$	1.01E+3	β^- : 4642.36 keV	134.55 s
Si	^{31}Si	$^{30}\text{Si}(\text{n},\gamma)^{31}\text{Si}$	1.00E+3	β^- : 1491.51 keV	157.09 m
Si	—	$^{29}\text{Si}(\text{n},\gamma)^{30}\text{Si}$	7.14E+2	—	—
O	^{15}C	$^{18}\text{O}(\text{n},\alpha)^{15}\text{C}$	1.31E+2	β^- : 9771.71 keV	2.47 s
K	^{42}K	$^{41}\text{K}(\text{n},\gamma)^{42}\text{K}$	6.78E+1	β^- : 3.53 MeV	12.32 hr
O	—	$^{16}\text{O}(\text{n},\gamma)^{17}\text{O}$	6.76E+1	—	—
B	—	$^{10}\text{B}(\text{n},\text{t}+2\alpha)$	5.88E+1	—	—
O	^{14}C	$^{17}\text{O}(\text{n},\alpha)^{14}\text{C}$	3.02E+1	β^- : 156.48 keV	5805.13 yr
O	—	$^{15}\text{C} \rightarrow ^{15}\text{N}[5298.82]$	2.42E+1	γ : 5297.82 keV	17 fs
O	—	$^{15}\text{N}[5298.82] \rightarrow ^{15}\text{N}$	2.42E+1	—	—
O	—	$^{15}\text{C} \rightarrow ^{15}\text{N}$	1.32E+1	—	—
K	^{36}Cl	$^{39}\text{K}(\text{n},\alpha)^{36}\text{Cl}$	9.04E+0	β^- : 0.71 MeV, β^+ : 1.14 MeV	3E+5 yr
B	^8Be	$^{12}\text{B} \rightarrow ^8\text{Be}$	2.68E+0	2α : 91.84 keV	0.08 fs
Si	—	$^{31}\text{Si} \rightarrow ^{31}\text{P}$	7.40E-2	—	—
O	—	$^{15}\text{C} \rightarrow ^{15}\text{N}[8312.62]$	1.45E-2	γ : 8310.15 keV	1.2 fs
O	—	$^{15}\text{N}[8312.62] \rightarrow ^{15}\text{N}$	1.45E-2	—	—
O	—	$^{15}\text{C} \rightarrow ^{15}\text{N}[9049.71]$	1.28E-2	γ : 9046.78 keV	0.35 fs
O	—	$^{15}\text{N}[9049.71] \rightarrow ^{15}\text{N}$	1.28E-2	—	—
O	—	$^{15}\text{C} \rightarrow ^{15}\text{N}[8571.40]$	6.86E-3	γ : 8568.77 keV	0.5 fs
O	—	$^{15}\text{N}[8571.40] \rightarrow ^{15}\text{N}$	6.86E-3	—	—
Al	—	$^{28}\text{Al} \rightarrow ^{28}\text{Si}[1779.03]$	5.20E-4	γ : 1778.70 keV	475 fs
Na	—	$^{24}\text{Na} \rightarrow ^{24}\text{Mg}[4122.89]$	3.18E-3	γ : 2745.0 keV	22 fs
Na	—	$^{24}\text{Mg}[4122.89] \rightarrow ^{24}\text{Mg}$	3.18E-3	—	—
K	—	$^{42}\text{K} \rightarrow ^{42}\text{Ca}$	1.06E-3	—	—
Al	—	$^{28}\text{Si}[1779.03] \rightarrow ^{28}\text{Si}$	5.20E-4	—	—
Si	—	$^{31}\text{Si} \rightarrow ^{31}\text{P}[1226.15]$	4.08E-5	γ : 1266.1 keV	0.52 ps
Si	—	$^{31}\text{P}[1226.15] \rightarrow ^{31}\text{P}$	4.08E-5	—	—
O	—	$^{14}\text{C} \rightarrow ^{14}\text{N}$	1.16E-8	—	—

Table 6.13: Interactions within Borosilicate Glass target resulting from neutron irradiation. Decay energy and short-lived half-life referenced from [72].

^{12}B is produced by $^{11}\text{B}(n,\gamma)^{12}\text{B}$ neutron capture, with its decay scheme shown in figure 6.27. 97% of the time, ^{12}B decays directly via β^- into the ground state of a stable ^{12}C nucleus with no associated photons. In the second and third decay branches, it decays into the excited states of ^{12}C and de-excites, emitting photons. In the fourth decay branch (0.008%), ^{12}B decays into the very excited state of $^{12}\text{C}[10300]$, which de-excites by emitting a 6 MeV alpha particle, producing ^8Be in its ground state. The ^8Be nucleus is unstable and quickly decays, leading to its exotic double-alpha disintegration.

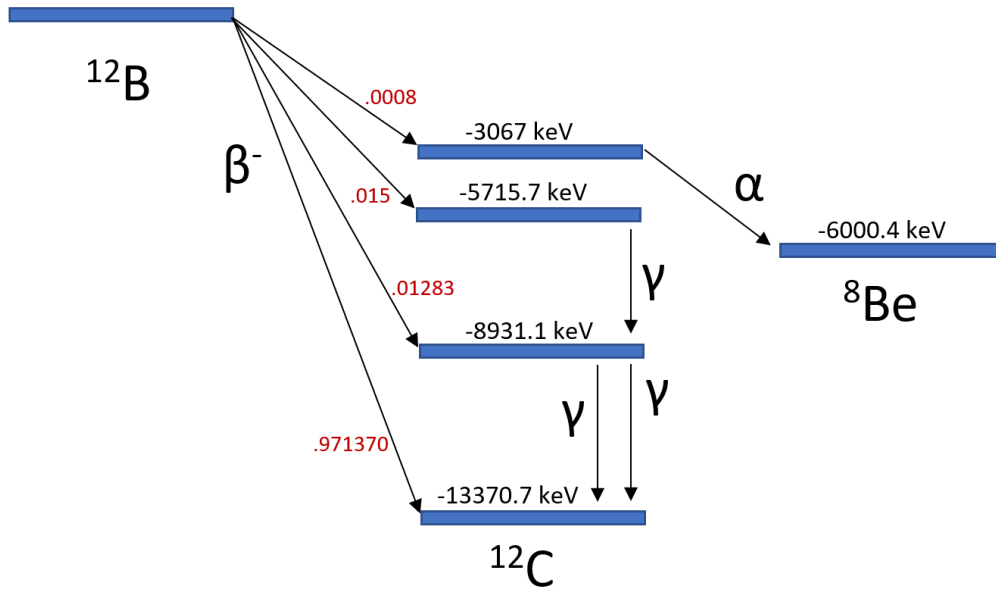


Figure 6.27: The decay scheme of ^{12}B . This is a simple decay, which most of the time goes to the ground state of ^{12}C .

Due to the relatively long half lives of ^{24}Na , ^{31}Si and ^{42}K with high energy β^- decay, their radioprotection risk will need to be evaluated in the activation study of the realistic setup.

If the 478 keV prompt-gamma ray emitted by the $^{10}\text{B}(n,\gamma)^7\text{Li}$ reaction is of interest, for example in single photon emission spectroscopy (SPECT), the presence of boron in the MicroPlus PCB may be problematic. Due their short range in the MicroPlus PCB materials, the alpha particle and ^7Li nuclei produced in this reaction will not reach the detector. Therefore it is not an issue in terms of microdosimetry measurements.

Enriched Boron Carbide ($^{10}\text{B}_4\text{C}$) Activation

The final material considered in the unit sample activation study was enriched Boron Carbide ($^{10}\text{B}_4\text{C}$), defined by composition reported by the ESS in their $^{10}\text{B}_4\text{C}$ films [77]. The purpose of this study is to see if the $^{10}\text{B}_4\text{C}$ neutron converter film, which is placed on top of the microdosimeter will become radioactive when irradiated by the Tokai neutron source. The reactions that occur in the $^{10}\text{B}_4\text{C}$ unit sample during irradiation is presented in table 6.14. The radioactive products are ^{12}B , ^{10}Be and ^{27}Mg . The half life of ^{10}Be is extremely long, however its level of activity is not of concern as defined by the IAEA limits [155]. The only radioactive product produced in $^{10}\text{B}_4\text{C}$ that needs to be considered is ^{27}Mg , with its simulated decay and cool-down required to fall below 1 μBq shown in figure 6.28.

Elem.	Radioactive Product	Reaction	Nuclei/sec	Decay Type & Average KE [72]	Half-life
B	—	$^{10}\text{B}(\text{n},\gamma)^7\text{Li}$	1.87E+9	γ : 478 keV	—
B	—	$^{10}\text{B}(\text{n},\gamma)^{11}\text{B}$	2.52E+4	—	—
H	—	$^1\text{H}(\text{n},\gamma)^2\text{H}$	5.42E+2	—	—
B	—	$^{10}\text{B}(\text{n},\text{t}+2\alpha)$	3.12E+2	—	—
B	^{12}B	$^{11}\text{B}(\text{n},\gamma)^{12}\text{B}$	9.96E+1	β^- : 13.37 MeV, $\beta^- \alpha$: 6.00 MeV	20.2 ms
B	—	$^{12}\text{B} \rightarrow ^{12}\text{C}$	9.96E+1	—	—
Mg	—	$^{24}\text{Mg}(\text{n},\gamma)^{25}\text{Mg}$	4.52E+1	—	—
B	^{10}Be	$^{10}\text{B}(\text{n},\text{p})^{10}\text{Be}$	3.62E+1	β^- : 555.9 keV	1.5E+6 yr
C	—	$^{12}\text{C}(\text{n},\gamma)^{13}\text{C}$	3.46E+1	—	—
Mg	—	$^{25}\text{Mg}(\text{n},\gamma)^{26}\text{Mg}$	1.36E+1	—	—
Mg	^{27}Mg	$^{26}\text{Mg}(\text{n},\gamma)^{27}\text{Mg}$	9.04E+0	β^- : 2610.00 keV	564.72 s
B	^8Be	$^{12}\text{B} \rightarrow ^8\text{Be}$	7.96E-2	2α : 91.84 keV	0.08 fs
Mg	—	$^{27}\text{Mg} \rightarrow ^{27}\text{Al}[843.76]$	7.82E-3	γ : 843.76 keV	35 ps
Mg	—	$^{27}\text{Al}[843.76] \rightarrow ^{27}\text{Al}$	7.82E-3	—	—
Mg	—	$^{27}\text{Mg} \rightarrow ^{27}\text{Al}[1014.56]$	3.26E-3	γ : 1014.52 keV	1.49 ps
Mg	—	$^{27}\text{Al}[1014.56] \rightarrow ^{27}\text{Al}$	3.26E-3	—	—
B	—	$^{10}\text{Be} \rightarrow ^{10}\text{Be}$	5.30E-13	—	—

Table 6.14: Interactions within $^{10}\text{B}_4\text{C}$ target resulting from neutron irradiation. Decay energy and short-lived half-life referenced from [72].

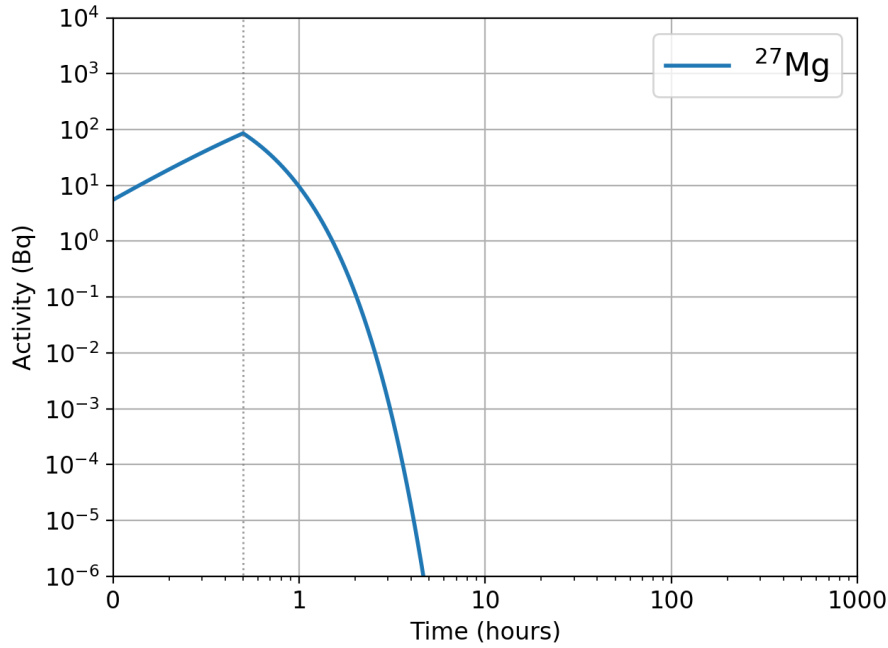


Figure 6.28: Activity of radioisotopes produced within 1 cm³ sample of ¹⁰B₄C target material. Simulated for 30 min irradiation period with following cool-down.

The main activation observed in the simulation for this material is associated with ¹⁰B(n,γ)⁷Li neutron capture, which is the only reaction of interest for our microdosimetry measurements. The result is favourable and indicates the suitability of this material when studying the rate of boron neutron capture interactions in an experimental setting.

6.5 Neutron Activation of the Realistic Experimental Setup

This section reports on the activation of the experimental setup materials, as described in section 6.2.3. The motion stage system is positioned against the BSA beam nozzle (as shown in figure 6.8), with the MicroPlus probe set at 50 mm depth in the water phantom. The neutron flux at 50 mm depth in the water phantom on beam central axis is 3.35×10^8 n/cm²/s (total), 7.70×10^7 n/cm²/s (epithermal), and 2.47×10^8 n/cm²/s (thermal).

Activated radioisotopes in all components

The activity of radioisotopes produced in the materials of the apparatus following a 30 minute irradiation period is shown in table 6.15.

Reaction	Activity (Bq)	Half-life $t_{1/2}$	E_γ (MeV)	E_β (MeV)	Components
$^{27}\text{Al}(n,\gamma)^{28}\text{Al}$	4.98E+8	2.24 m	1.78E+0	1.24E+0	Al Extrusions (81.3%), Shafts (9.9%), Shaper (3.1%), DIL (2.5%), Sheath (1.7%)
$^{18}\text{O}(n,\alpha)^{15}\text{C}$	9.72E+7	2.45 s	3.36E+0	3.00E+0	Water (94.9%), Tank (3.9%), Sheath (1.1%)
$^{65}\text{Cu}(n,\gamma)^{66}\text{Cu}$	6.98E+6	5.10 m	8.47E-2	1.07E+0	μ^+ probe (87.1%), XMot. (6.0%), Shaper (5.2%), YMot. (1.7%)
$^{18}\text{O}(n,\gamma)^{19}\text{O}$	3.75E+6	26.88 s	9.40E-1	1.51E+0	Water (95.5%), Tank (3.4%), μ^+ probe (1.0%)
$^{63}\text{Cu}(n,\gamma)^{64}\text{Cu}$	5.79E+5	12.70 h	1.90E-1	1.23E-1	μ^+ probe (87.2%), XMot. (6.0%), Shaper (5.2%), YMot. (1.7%)
$^{197}\text{Au}(n,\gamma)^{198}\text{Au}$	3.06E+5	2.70 d	4.04E-1	3.26E-1	DIL (100%)
$^{54}\text{Cr}(n,\gamma)^{55}\text{Cr}$	2.79E+5	3.497 m	6.72E-4	1.10E+0	Bearings (49.7%), Screws (45.3%), XMot. (3.8%), YMot. (1.2%)
$^{68}\text{Zn}(n,\gamma)^{69}\text{Zn}$	2.18E+5	56.33 m	6.00E-6	3.21E-1	μ^+ probe (91.5%), Shaper (8.5%)
$^{55}\text{Mn}(n,\gamma)^{56}\text{Mn}$	1.05E+5	2.58 h	1.69E+0	8.29E-1	Shaper (100%)
$^{27}\text{Al}(n,p)^{27}\text{Mg}$	5.81E+4	9.46 m	8.91E-1	7.02E-1	Shafts (59.5%), DIL (36.3%), Al Extrusions (2.0%), Shaper (1.0%), $^{10}\text{B}_4\text{C}$ Film (1.0%)
$^{23}\text{Na}(n,\gamma)^{24}\text{Na}$	5.59E+4	14.99 h	4.12E+0	5.53E-1	PCB (100%)
$^{30}\text{Si}(n,\gamma)^{31}\text{Si}$	2.58E+4	2.62 h	8.86E-4	5.95E-1	PCB (94.2%), Shaper (4.1%), XMot. (1.4%), YMot. (0.2%)
$^{65}\text{Cu}(n,p)^{65}\text{Ni}$	2.05E+4	2.52 h	5.49E-1	6.32E-1	Bearings (36.3%), DIL (35.3%), Screws (21.8%), XMot. (5.0%), YMot. (1.3%)
$^{37}\text{Cl}(n,\gamma)^{38}\text{Cl}$	7.59E+3	37.21 m	1.49E+0	1.53E+0	μ^+ probe (100%)
$^{70}\text{Zn}(n,\gamma)^{71}\text{Zn}$	6.05E+3	2.45 m	3.14E-1	1.04E+0	μ^+ probe (100%)
$^{50}\text{Cr}(n,\gamma)^{51}\text{Cr}$	5.57E+3	27.70 d	3.26E-2	3.86E-3	Bearings (53.5%), Screws (41.2%), XMot. (4.0%), YMot. (1.3%)
$^{16}\text{O}(n,\gamma)^{17}\text{F}$	4.62E+3	64.49 s	—	7.38E-1	Water (100%)
$^{150}\text{Nd}(n,\gamma)^{151}\text{Nd}$	3.54E+3	12.44 m	8.82E-1	6.35E-1	XMot. (57.1%), YMot. (42.9%)
$^{41}\text{K}(n,\gamma)^{42}\text{K}$	8.89E+2	12.36 h	2.76E-1	1.43E+0	PCB (100%)
$^{37}\text{Cl}(n,p)^{37}\text{S}$	7.48E+2	5.05 m	2.93E+0	8.00E-1	μ^+ probe (100%)
$^{148}\text{Nd}(n,\gamma)^{149}\text{Nd}$	7.40E+2	1.73 h	3.77E-1	4.94E-1	XMot. (74.9%), YMot. (25.1%)
$^{23}\text{Na}(n,p)^{23}\text{Ne}$	1.83E+2	37.24 s	1.65E-1	1.90E-0	PCB (100%)
$^{54}\text{Fe}(n,\gamma)^{55}\text{Fe}$	1.68E+2	2.70 y	1.69E-3	4.20E-3	Bearings (40.1%), Screws (34.4%), XMot. (19.5%), YMot. (5.9%)
$^{58}\text{Fe}(n,\gamma)^{59}\text{Fe}$	9.41E+1	44.53 d	1.19E+0	1.17E-1	Screws (36.5%), Bearings (35.8%), XMot. (21.9%), YMot. (5.8%)
$^{64}\text{Zn}(n,\gamma)^{65}\text{Zn}$	7.07E+1	243.66 d	5.84E-1	6.87E-3	μ^+ probe (90.5%), Shaper (9.5%)
$^{151}\text{Nd} \rightarrow ^{151}\text{Pm}$	4.19E+1	28.40 h	3.06E-1	2.97E-1	XMot. (57.1%), YMot. (42.9%)
$^{149}\text{Nd} \rightarrow ^{149}\text{Pm}$	2.57E+1	53.08 h	1.06E-2	3.65E-1	XMot. (74.9%), YMot. (25.2%)
$^{35}\text{Cl}(n,p)^{35}\text{S}$	2.46E+1	87.44 d	—	4.88E-2	μ^+ probe (100%)
$^{120}\text{Sn}(n,\gamma)^{121}\text{Sn}$	1.26E+1	27.06 h	—	1.14E-1	Shaper (100%)
$^{146}\text{Nd}(n,\gamma)^{147}\text{Nd}$	5.76E-2	10.97 d	1.42E-1	2.34E-1	XMot. (67.3%), YMot. (32.7%)
$^{62}\text{Ni}(n,\gamma)^{63}\text{Ni}$	2.68E-2	101.29 y	—	1.74E-2	DIL (34.9%), Bearings (33.3%), Screws (28.1%), XMot. (2.3%), YMot. (0.9%), Shaper (0.5%)
$^{32}\text{S}(n,p)^{32}\text{P}$	1.66E-2	14.27 d	—	6.95E-1	μ^+ probe (100%)
$^{17}\text{O}(n,\alpha)^{14}\text{C}$	1.36E-2	5.7E+3 y	—	4.95E-2	Tank (82.1%), ABS Plastic (17.6%), XMot. (0.2%), YMot. (0.1%)
$^{124}\text{Sn}(n,\gamma)^{125}\text{Sn}$	8.19E-3	9.64 d	3.34E-1	8.02E-1	Shaper (100%)
$^{58}\text{Ni}(n,p)^{58}\text{Co}$	1.11E-3	70.86 d	9.75E-1	3.00E-2	DIL (100%)
$^{58}\text{Ni}(n,\gamma)^{59}\text{Ni}$	1.91E-4	7.6E+4 y	2.42E-3	9.00E-9	DIL (35.5%), Bearings (32.5%), Screws (28.3%), XMot. (2.3%), YMot. (0.9%), Shaper (0.5%)
$^{151}\text{Pm} \rightarrow ^{151}\text{Sm}$	1.68E-5	90.08 y	1.45E-5	1.96E-2	XMot. (57.1%), YMot. (42.9%)
$^{35}\text{Cl}(n,\gamma)^{36}\text{Cl}$	7.29E-6	3.0E+5 y	—	2.47E-1	Shaper (100%)
$^{10}\text{B}(n,p)^{10}\text{Be}$	8.56E-10	1.5E+6 y	—	2.03E-1	$^{10}\text{B}_4\text{C}$ Film (100%)
$^{147}\text{Nd} \rightarrow ^{147}\text{Pm}$	4.82E-10	2.63 y	4.36E-6	6.18E-2	XMot. (67.3%), YMot. (32.7%)
$^{39}\text{K}(n,\gamma)^{40}\text{K}$	2.30E-10	1.2E+9 y	—	5.00E-1	PCB (100%)

Table 6.15: Radioactivations within the experiment materials resulting after 30 minutes of neutron irradiation. Half-life values and effective decay emission energies (E_γ and E_β) referenced from [72]. Abbreviations used in this table: ‘Tank’ (PMMA Tank), ‘XMot.’ (X-axis NEMA17 stepper motor), and ‘YMot.’ (Y-axis NEMA17 stepper motor).

The data displayed in table 6.15 has been consolidated from the activations in each component of the experimental setup. The *Components* column presents the percentage of the total activity for the particular isotope that is localised to that component. These results have been summarised for brevity, though greater detail is available about the activation of each material. The quantities of E_γ and E_β are the effective decay energies in MeV for gamma and beta emissions, respectively, as given in ICRP Publication 38 [171]. The effective values have been calculated from the summation of emission energy multiplied by emission yield for each radiation type [171]. For the purpose of a quick evaluation when reading table 6.15, the effective energy per radiation type is presented only to allow an indication to the amount of energy emitted per decay.

As shown in table 6.15, the majority of activations occur in aluminium, producing radioactive ^{28}Al , which has a moderate half-life of 2.24 min [72]. After 30 minutes of neutron irradiation, the combined activation of ^{28}Al in the whole system is $4.98\text{E}+8$ Bq. In particular, 81.3% of the ^{28}Al activations occur in the aluminium extrusion supporting frame of the system. ^{28}Al is also produced in the DIL package (2.5%) and aluminum foil (1.7%) surrounding the MicroPlus sheath, which will need to be considered. ^{15}C is produced in large quantities in the water, though it decays quickly ($t_{1/2}=2.45$ sec [72]).

^{64}Cu and ^{66}Cu are produced mainly in the MicroPlus probe (the contacts contain BeCu alloy) and also in the copper coils for the electromagnet of the NEMA stepper motors. Long lived ^{198}Au is produced in the legs and contacts of the DIL package which contains gold plated nickel. Radioisotopes of Cr, Ni and Fe are activated in stainless steel materials such as the bearings, screws and stepper motors. The die-cast aluminium box which contains the pulse shaper only has trace elements of Cu, Zn, Sn and Mn; though their neutron capture cross section is high for epithermal/thermal neutrons, allowing them to become radioactive. ^{58}Co was produced in the legs of the DIL package by the $^{58}\text{Ni}(n,p)^{58}\text{Co}$ reaction. Activations producing the ^{60}Co radioisotope were not observed in the simulation.

In terms of long half-lived radioisotopes, ^{55}Fe ($t_{1/2}=2.70$ years [72]) is produced in

components that contain stainless steel, such as bearings, screws and the outer casing of the stepper motors. ^{65}Zn ($t_{1/2}=243.9$ days [72]) is produced mainly in the μ^+ probe and shaper box. However, both of these radioisotopes are produced with low activity and low effective gamma and beta emission energies [172].

The activation of the stepper motor, which contains a significant amount of iron, was not as high as expected; with the only exotic activations being ^{149}Nd and ^{151}Nd in the permanent magnet. The boron carbide film remains relatively stable following irradiation, with only $^{27}\text{Al}(n,p)^{27}\text{Mg}$ and $^{10}\text{B}(n,p)^{10}\text{Be}$ activations observed. The activity of ^{10}Be in the boron carbide film was only $8.56\text{E-}10$ Bq, though it has a long half life of $1.5\text{E+}6$ years. The ^{27}Mg radioisotope was produced in the boron carbide film within the aluminium substrate, which can be substituted for other materials [77].

Effect of activated radioisotopes on measurements by microdosimeter

The implication of neutron activation for microdosimetry measurements was considered and is presented in these results. In this Geant4 simulation, the motion stage system is positioned against the BSA beam nozzle (figure 6.8), with the MicroPlus probe set at 50 mm depth in the water phantom. The microdosimetric response of the SOI Bridge microdosimeter is recorded during a simulated 30 minute irradiation period. The acquisition is depicted to also record for 30 minutes, in order to study both prompt and delayed reactions that are produced while beam is on.

Two cases are considered; with $^{10}\text{B}_4\text{C}$ film on SOI Bridge (figure 6.29) and bare SOI Bridge (figure 6.30).

For the case with $^{10}\text{B}_4\text{C}$ film, the products arising from ^{10}B neutron capture reactions in the boron carbide film dominates the microdosimetric spectra. As such, the bare SOI Bridge was also considered, so that the contribution of reactions with lower counts could be observed in the spectra.

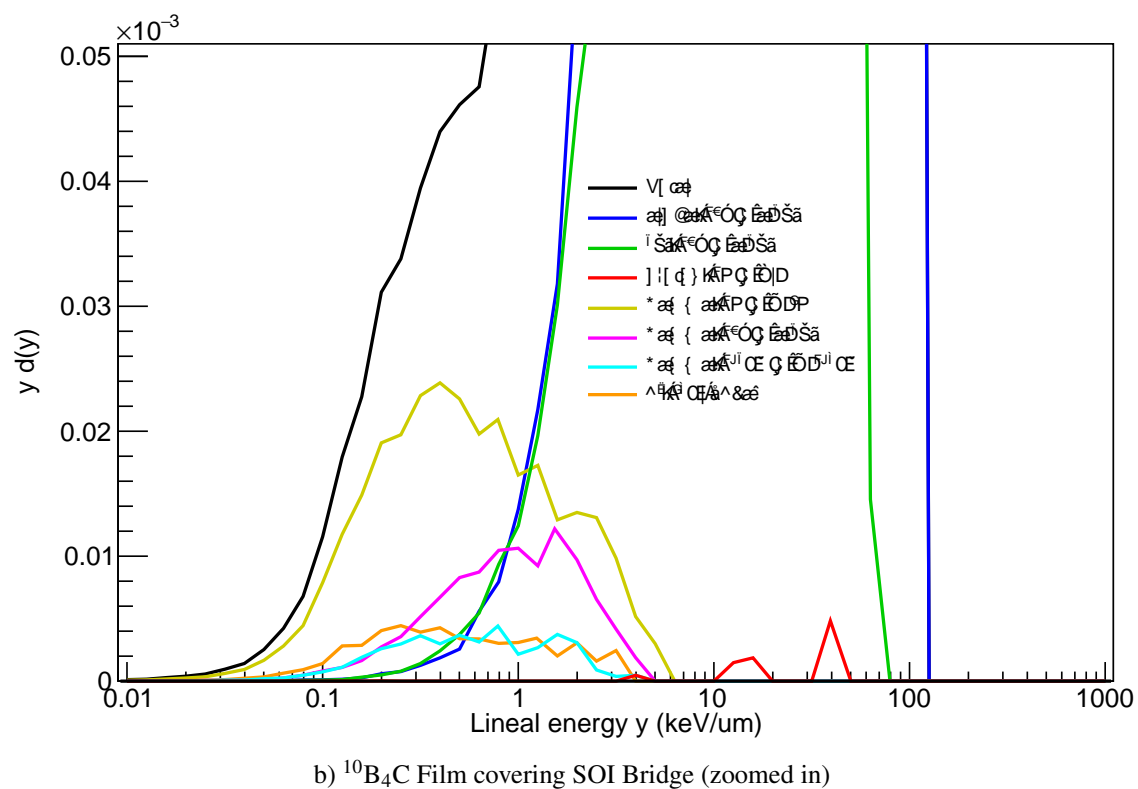
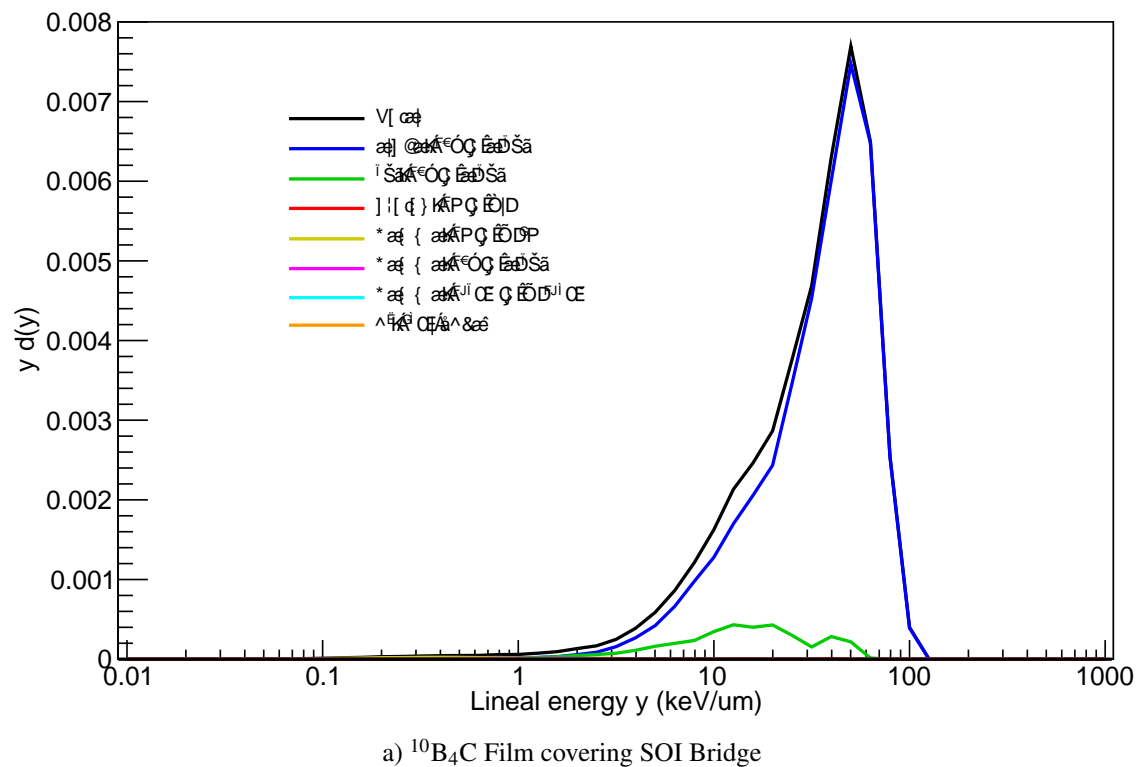


Figure 6.29: Microdosimetric spectra of the SOI Bridge during a 30 minute irradiation, with $^{10}\text{B}_4\text{C}$ Film covering the DIL package. Zoomed in y-axis range shown in b).

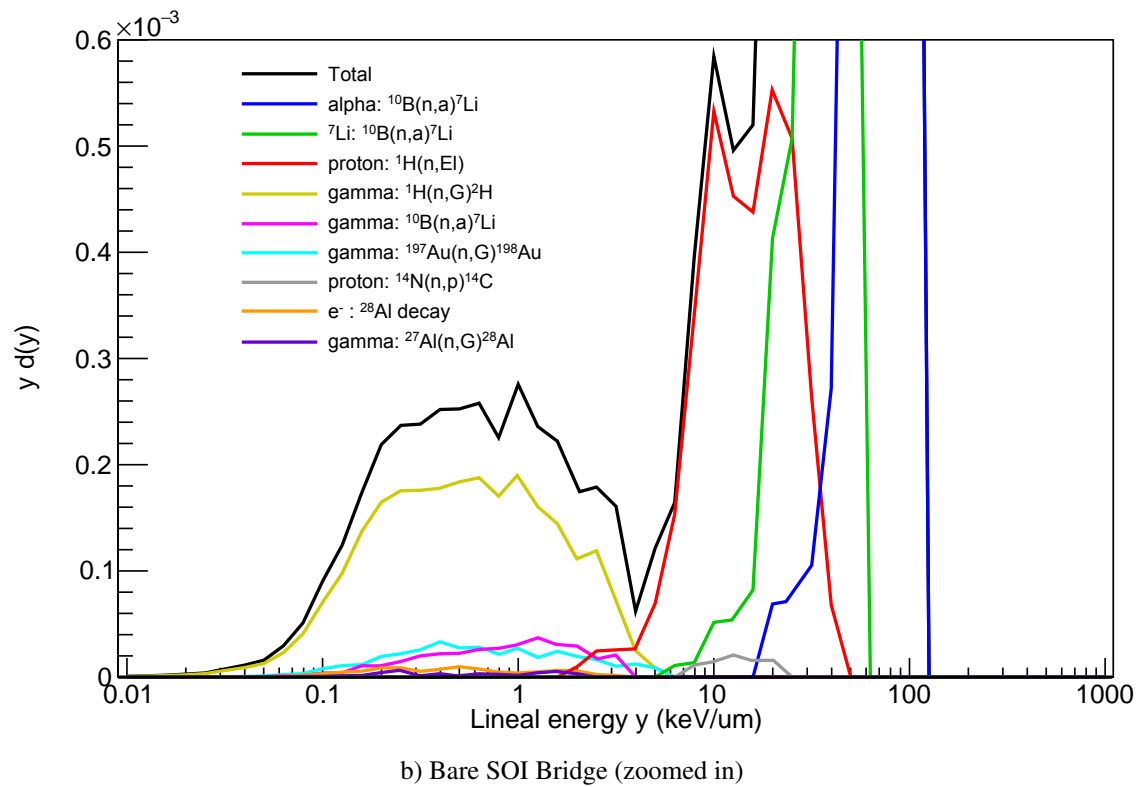
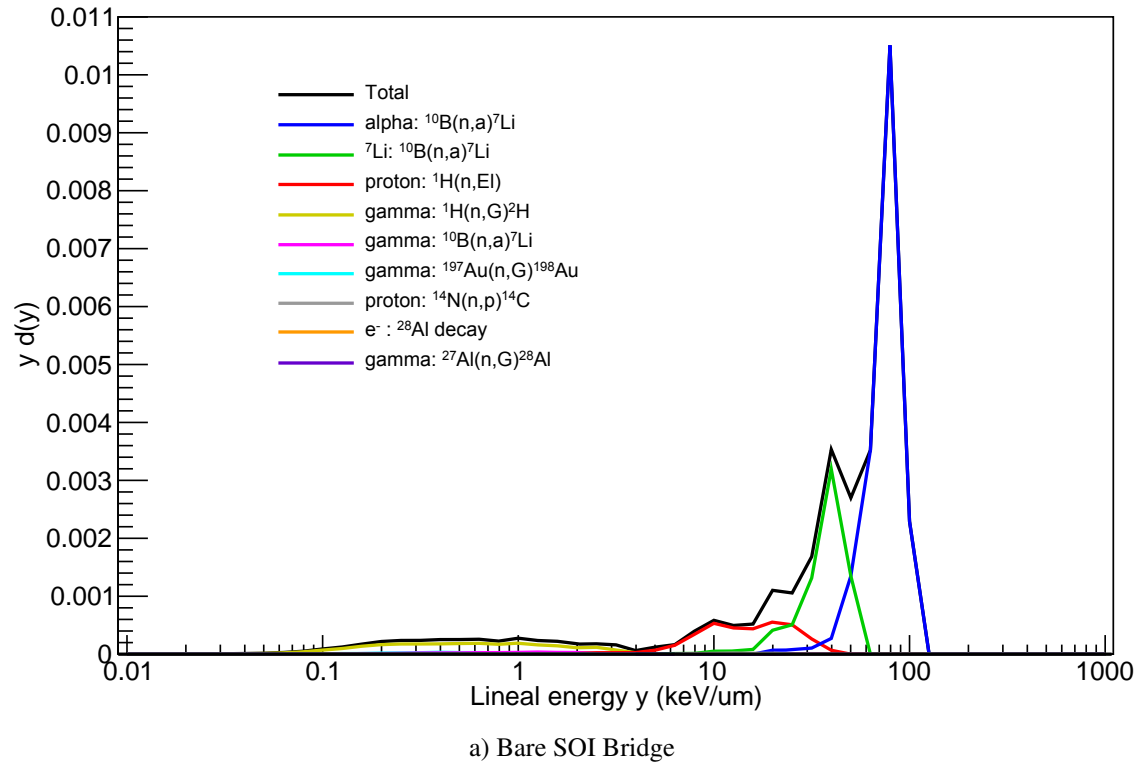


Figure 6.30: Microdosimetric spectra of the SOI Bridge during a 30 minute irradiation, with no film covering the DIL package (bare). Zoomed in y-axis range shown in b).

The main reactions observed in the microdosimetric spectra (figures 6.29 and 6.30) are described in the list below:

- **alpha:** $^{10}\text{B}(\text{n},\alpha)^7\text{Li}$, from boron carbide film and p^+ implantation region of the SVs (blue).
- **^7Li :** $^{10}\text{B}(\text{n},\alpha)^7\text{Li}$, from boron carbide film and p^+ implantation region of the SVs (green).
- **proton:** $^1\text{H}(\text{n},\text{El})$, from neutron elastic reactions with ^1H in the PMMA sheath, mainly from the water window region (red).
- **gamma:** $^1\text{H}(\text{n},\text{G})^2\text{H}$, prompt gamma from ^1H neutron capture reactions in the PMMA sheath and water phantom (olive).
- **gamma:** $^{10}\text{B}(\text{n},\alpha)^7\text{Li}$, prompt gamma from ^{10}B neutron capture reactions in the boron carbide film and p^+ implantation region of the SVs (magenta).
- **gamma:** $^{197}\text{Au}(\text{n},\text{G})^{198}\text{Au}$, prompt gamma from ^{197}Au neutron capture reactions in the gold-plated nickel DIL package leads in the MicroPlus probe (cyan).
- **e^- :** ^{28}Al decay, from β^- decay of activated ^{28}Al in the Al substrate of the boron carbide film and Al tracks on the microdosimeter (orange).
- **proton:** $^{14}\text{N}(\text{n},\text{p})^{14}\text{C}$, from neutron inelastic reactions with ^{14}N in the inner air gap of the MicroPlus probe sheath (grey).
- **gamma:** $^{27}\text{Al}(\text{n},\text{G})^{28}\text{Al}$, prompt gamma from ^{27}Al neutron capture reactions in the Al foil surrounding the MicroPlus probe sheath (purple).

For the case with $^{10}\text{B}_4\text{C}$ film, the main components in the microdosimetric spectra are products from ^{10}B neutron capture. Due to activations in the Al substrate of the film, the component of electron decay from ^{28}Al is much higher than the bare case. Protons from neutron elastic scatter with ^1H are observed in both cases, though only with lineal energies greater than 10 keV/ μm for the $^{10}\text{B}_4\text{C}$ film case.

For the bare case, products from ^{10}B neutron capture arise only by these reactions in the p^+ implantation region of the SVs. A small contribution of prompt gammas from ^{27}Al neutron capture reactions in the Al foil surrounding the MicroPlus probe sheath are observed for the bare SOI. Protons from neutron inelastic reactions with ^{14}N in air are also observed for the bare case, which were previously stopped by the film.

A similar contribution by prompt gammas from ^{197}Au neutron capture reactions is observed in both cases. These reactions occur in the gold-plated nickel DIL package leads of the MicroPlus probe. The contribution by decay products from activated ^{198}Au were very minimal and thus not visible on the microdosimetric spectra. These results shown for the simulated microdosimetric response of the SOI Bridge indicates that the neutron activation of the experimental equipment has minimal implications on microdosimetry measurements.

6.6 Dose equivalent from the activated materials

The final section of results present the dose equivalent from the activated experimental setup, calculated using Geant4, as outlined in section 6.2.4. The dose equivalent $H^*(10)$ resulting from the decay of radioisotopes after the neutrons irradiated the same point on the surface of the water tank for 30 minutes was simulated. It should be noted that the results shown here only consider dose due to decay products; not prompt neutron and gamma ray sources while the beam is on. In these results, positional references relative to the centre of the motion stage system in the scoring shell region are made in spherical coordinates. For example, '0 deg' refers to the azimuthal angle, which is normal to the previously irradiated face of the water tank.

6.6.1 $H^*(10)$ at 1 m distance - μ^+ probe in water phantom

The dose equivalent at a distance of 1 metre from the centre of the experimental system, facing the irradiated side of the water tank, was considered as shown in figure 6.31.

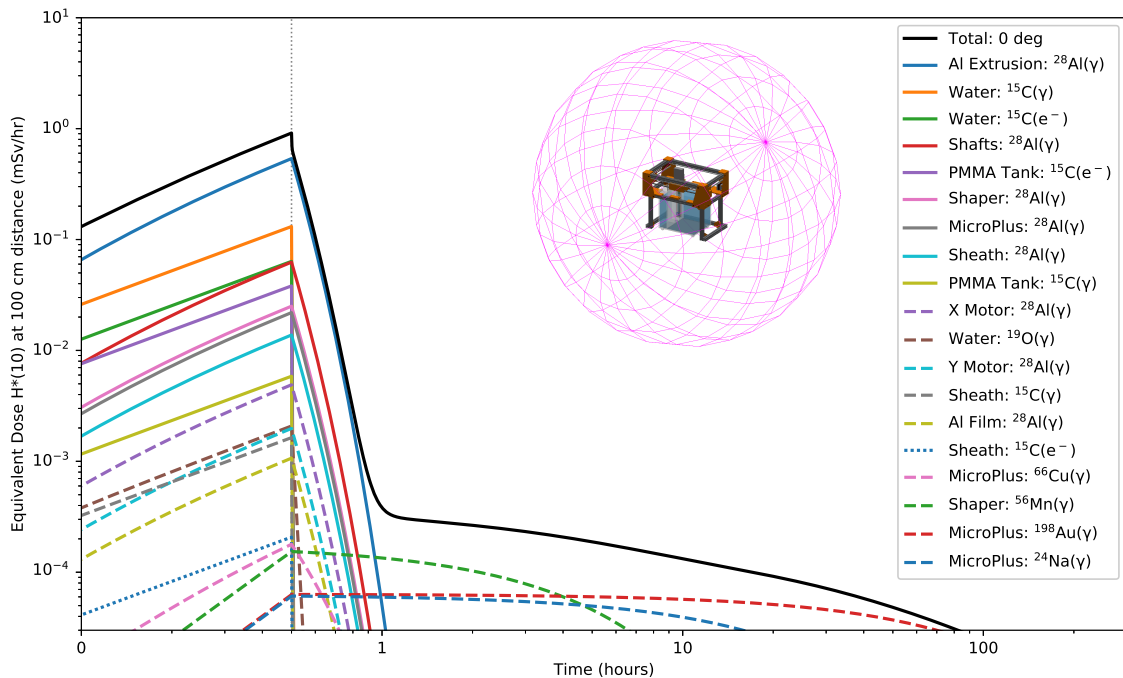


Figure 6.31: Dose equivalent $H^*(10)$ at 100 cm distance from the centre of the motion stage system, facing the side of the water tank that was irradiated by neutrons (0 deg).

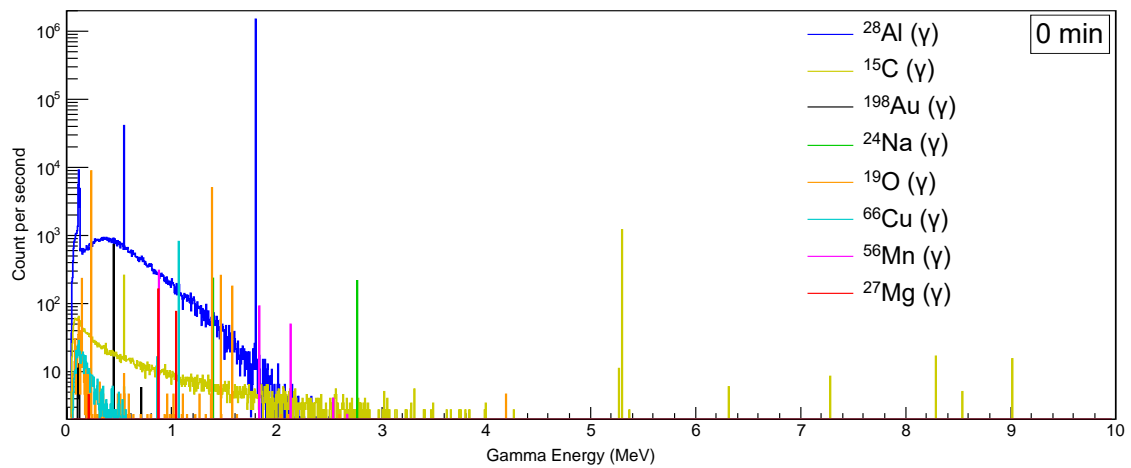
The majority of the dose is due to the Aluminium Extrusion frame, which reaches a

peak of approximately 0.5 mSv/hr after the beam is turned off after 30 minutes. ^{28}Al disintegration emits a single 1.78 MeV gamma ray [72]. ^{28}Al decays relatively quickly, falling below 0.1 $\mu\text{Sv/hr}$ after approximately 30 minutes following irradiation. ^{15}C is produced in the PMMA water tank with a large dose, and decays rapidly within a few seconds. The same for ^{19}O , which is produced in the water and PMMA tank and quickly decays.

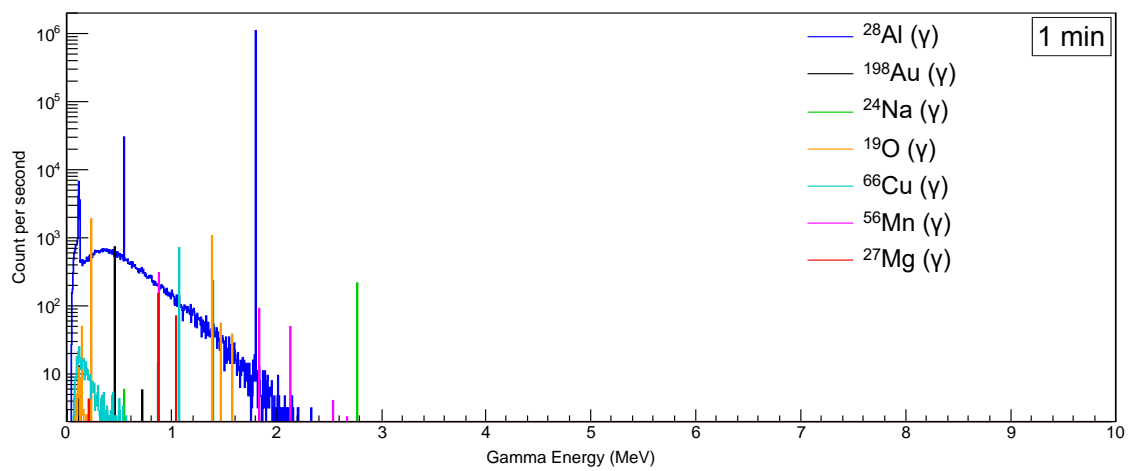
There are three long lived sources which we must consider: ^{198}Au from the DIL, ^{24}Na from the PCB and ^{56}Mn from the shaper box. ^{198}Au decays with a gamma emission with 0.41 MeV gamma energy (99%) [72]. ^{24}Na undergoes beta decay and then two gamma rays of 2.76 MeV and 1.38 MeV (99.2%) [72]. ^{56}Mn is produced by neutron capture of ^{55}Mn in the shaper box, which is a part of the MicroPlus probe. As the reaction has a high cross section for thermal neutrons [170] and this component is positioned far out-of-field of the primary beam, its activation is significant.

Following the 30 minute period after beam off, the minor concern at this distance is ^{198}Au and ^{24}Na isotopes, which are both located inside DIL package and PCB of the MicroPlus probe, respectively. However the cumulative dose delivered over the 20 hours required for the ^{198}Au in the DIL to fall below 0.1 $\mu\text{Sv/hr}$ is negligible with this configuration at 1 metre distance.

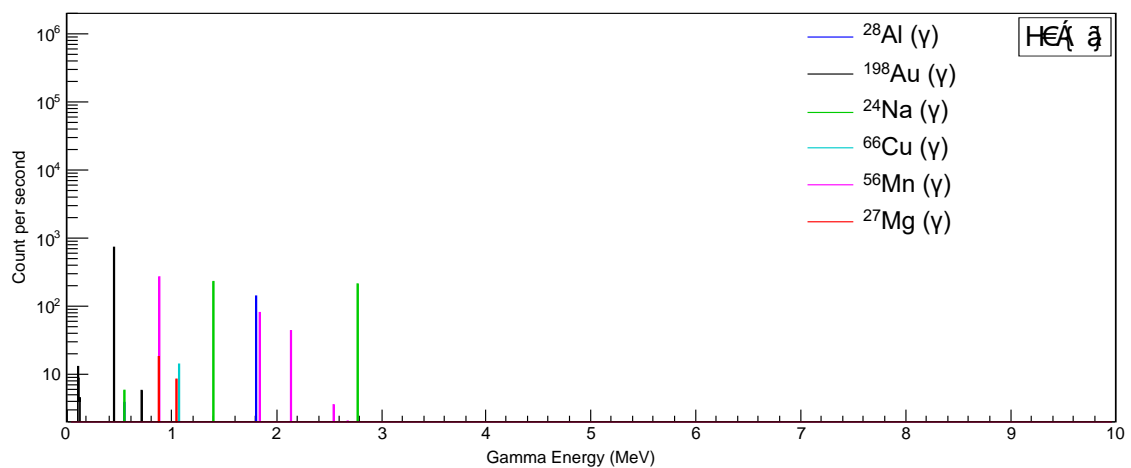
The gamma rays associated with the dose equivalent at 1 m distance are shown in figure 6.32 for increasing cool-down times following beam-off. Large counts of gamma rays from ^{28}Al , ^{19}O and ^{15}C decay are observed at initial beam off (0 min). At only 1 minute after beam off, the contribution of gamma rays from ^{19}O and ^{15}C decay have diminished, though gamma rays from ^{28}Al decay still have considerable counts. By 30 minutes after beam off, gamma rays from ^{28}Al decay are almost negligible. The main gamma rays at this time are ^{198}Au , ^{24}Na and ^{56}Mn , exhibited in figure 6.31, with their persisting dose equivalent contribution past 30 minutes after beam off.



a) 0 minutes after beam off



b) 1 minute after beam off



c) 30 minutes after beam off

Figure 6.32: Gamma ray spectra from the activated radioisotopes decay, recorded at 0 degrees azimuthal angle position, 1 m distance from the Experimental System. Gamma ray spectra for time after beam off: a) 0 minutes (initial), b) 1 minute, and c) 30 minutes.

6.6.2 $H^*(10)$ at 0.4 m distance - μ^+ probe in water phantom

The dose equivalent was simulated from the same orientation, facing the irradiated side of the tank, but at 0.4 m distance from the centre as shown in figure 6.33. Compared with the previous result, the dose is much higher with an initial peak of approximately 6 mSv/hr at beam off. Aluminium is the major source of the dose equivalent at this distance, produced mainly in the Al extrusions and shafts for the motion system. As seen before, ^{28}Al only requires 30 minutes following beam off to fall below a negligible level.

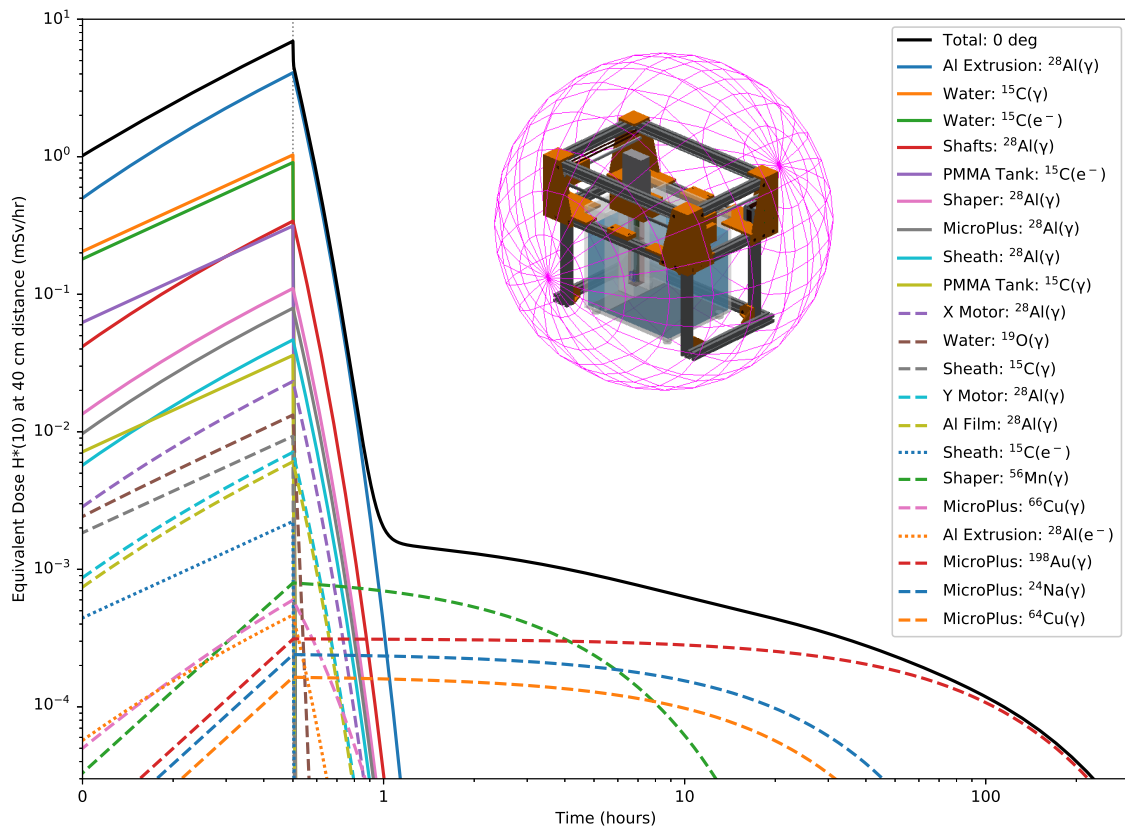


Figure 6.33: Dose equivalent $H^*(10)$ at 0.4 m distance from the centre of the motion stage system, facing the side of the water tank that was irradiated by neutrons (0 deg).

Comparison of the equivalent dose result at 1 m versus 0.4 m distance shows that the contribution from each radioisotope decay particle increases at a proportional rate. This is with the exception of ^{15}C γ rays and e^- from the water and PMMA tank, which increase at a higher rate to other decay components. This is simply due to the closer reference of these materials, which were irradiated intensely in the primary neutron field area.

The decay of ^{56}Mn produces gamma rays, mostly with energy of 0.85 MeV (98.9%)

[72] which may be impractical to shield due to weight restrictions on the motion stage carriage. The neutrons themselves should be shielded from reaching the shaper box, which can be done by a boronated or lithiated polyethylene envelope over the shaper.

The dose equivalent calculated at this distance for the entire system shows that 30 minutes following the beam off is critical. After which, the dose falls below $2 \mu\text{Sv/hr}$ with the only contribution from the activations of the detector materials. If required, the system could be safe to approach after 30 minutes. Many more factors need to be taken into consideration for a closer distance to the system, such as dose to the fingers and eyes.

Figure 6.34a shows the total dose as a function of azimuthal angular position to the motion system. The diagram in figure 6.34b shows the orientation of the motion stage system used for these results. The azimuthal angle of 0° is the side of the motion system that is facing the beam exit nozzle, which has normal incidence with the neutron beam during irradiation. The results show a higher $H^*(10)$ value at 0° (face that was irradiated) versus 180° (opposite face to that irradiated) up to 30 minutes after beam off. This is due to the high activation of ^{28}Al supports. After which, the only dose is due to the MicroPlus, shaper and DIL package.

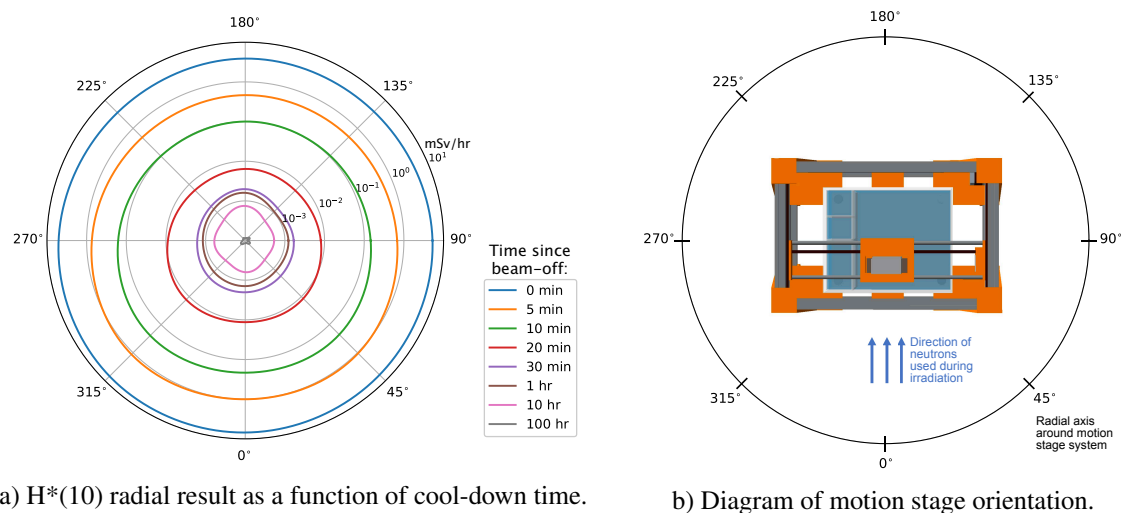


Figure 6.34: Isodose equivalent $H^*(10)$ at 0.4 m distance for all azimuthal angles around the system following beam off. Radial axis (mSv/hr) is in log scale.

6.6.3 $H^*(10)$ at 0.4 m distance - μ^+ probe including sheath and shaper in free air

This section of results is taken at the same position and distance (0.4 m) from the centre of the system except only the MicroPlus probe (with microdosimeter still inserted), PMMA sheath and shaper are present in free air. This models the scenario when the entire microdosimetry detector system is removed from the water phantom. Such is the case when the microdosimeter needs to be changed and the detector system is brought into the control room to do so. These results evaluate whether there is any risk in approaching the detector system at 0.4 m distance in free air. The dose equivalent for this simulation is shown in figure 6.35.

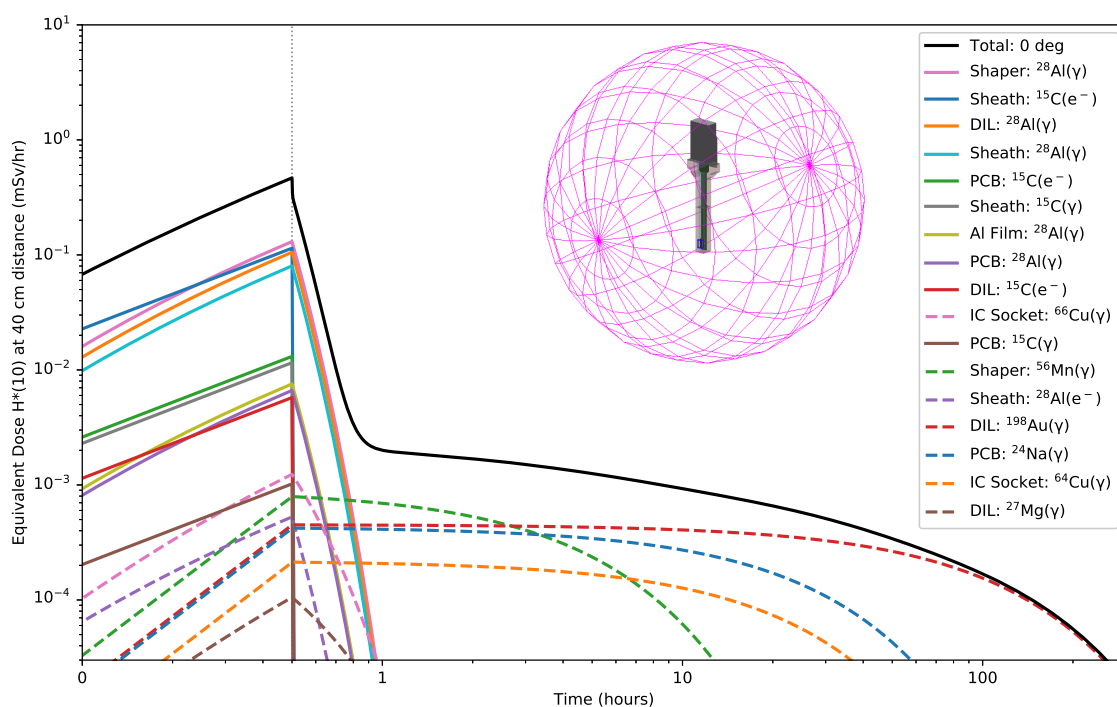


Figure 6.35: Dose equivalent $H^*(10)$ at 0.4 m distance from the MicroPlus probe including sheath and shaper in free air, facing the side that was previously irradiated by neutrons.

The overall dose is much lower as all the components of the motion stage, such as the radioactive aluminium extrusion supports, are now absent. The dose from the MicroPlus is slightly higher now as the water volume is no longer shielding most electrons and some gamma rays. The dose deriving from gamma decay remains similar, but those from elec-

trons has increased. For example, the dose from ^{15}C sheath electrons is approximately 45 times higher than before, though the ^{15}C sheath gamma rays is nearly the same. Similarly, the ^{15}C electrons from the PCB is now a major contributor, which was not seen before.

^{66}Cu is produced in the IC sockets of the MicroPlus, which has a higher dose in this scenario. It takes about 20 minutes to fall below $0.1\ \mu\text{Sv/hr}$. Overall, the resultant dose in free air is not as high as expected, with most of the high dose contributors decaying quickly within a few minutes.

The dose equivalent result shown here for the μ^+ probe including sheath and shaper in free air is a preliminary indication of the radioprotection risk without closer interaction. A more detailed study of the effects relating to an experimenter's interaction at closer proximity is necessary to make a full evaluation. This includes the dose to hands; $H'(0.07)$ and eyes; $H'(3)$, which will be completed in future work.

6.6.4 $H^*(10)$ at 0.4 m distance - μ^+ probe only in free air

This section is the same setup as the previous except only the MicroPlus probe (with microdosimeter inserted) is present in free air. The results are shown in figure 6.36.

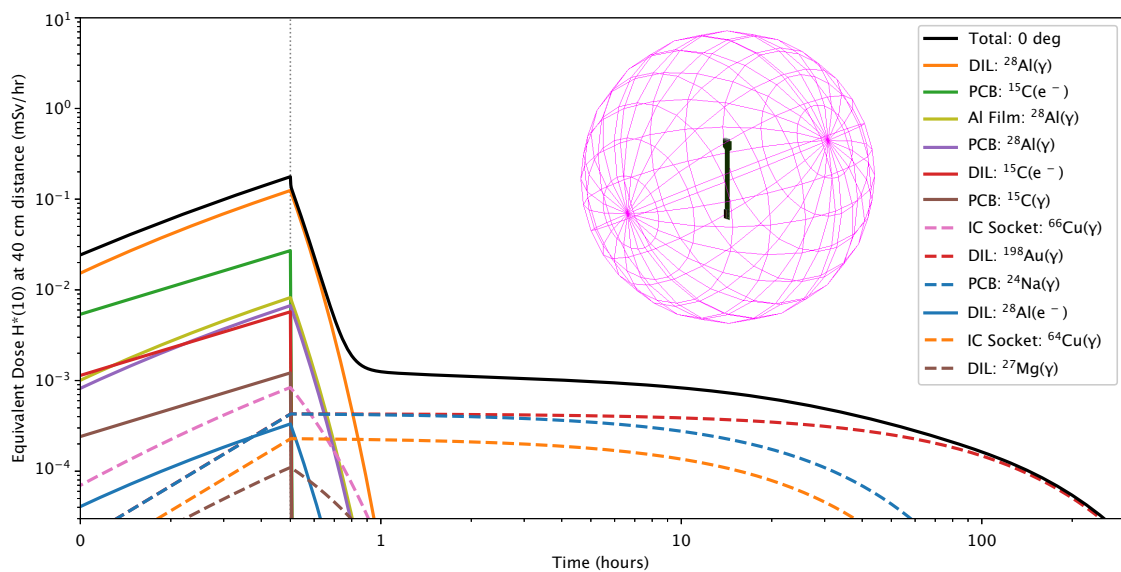


Figure 6.36: Dose equivalent $H^*(10)$ at 0.4 m distance from the MicroPlus probe only, facing the side that was previously irradiated by neutrons.

As seen in the previous section, as more components are removed, the dose due to short range particles, such as electrons increases. This is seen with the dose increase by ^{28}Al electrons created in the DIL package, which was not previously seen due to the shielding by the PMMA sheath. The 170 μm Al substrate of the boron carbide film is radioactive, given its position in the beam centre. This can be minimised by reducing the thickness of the Al substrate. The boron carbide layer itself is stable to the epithermal energies of this beam and poses no risk. The gamma dose from ^{28}Al in this film is now slightly higher than before. Consideration must be taken when handling this, as it is usually removed by hand when changing detectors. There are also now ^{27}Mg gamma rays seen in the DIL package. As stated earlier, a further study into the dose to hands and eyes is essential to make a full assessment in this scenario, which will be completed in future work.

Most importantly, we see that the ^{24}Na and ^{198}Au gamma dose remain almost the same for all results considered at this distance. Now that all components have been removed down to the bare microdosimeter and probe, we can see that there is no hidden increase in dose when dismantling the MicroPlus from the motion stage system.

Reiterating what has been concluded previously; most materials present in the detector equipment and motion stage system only require 30 minutes following beam off to fall below 2 $\mu\text{Sv/hr}$.

For perspective, the natural background dose in Australia is 1.5 mSv/year or about 0.2 $\mu\text{Sv/hr}$ [173]. The dose limit for a occupational radiation worker in Australia is defined as 20 mSv/year, (averaged over 5 years) [174]. From the results shown in this work, it would take more than 10,000 hours to reach this limit. As such, it can be considered reasonable for the researcher to interact with the equipment under these conditions, which are not significant in comparison to natural background.

Therefore, after waiting the necessary 30 minutes cooldown time, only moderate consideration must be taken and it may be possible to enter the treatment room and approach the system in order to change the experiment configuration before starting the next mea-

surement.

6.7 Discussion

This study has shown conclusively that whilst the majority of materials currently used in our motion stage and MicroPlus systems are appropriate in terms of radioprotection, results indicate the need for changes with respect to some material choices. Geant4 has been demonstrated to be an effective tool for describing the neutron fluence throughout the BSA and treatment room, with close agreement compared to PHITS.

The activation of unit samples of various materials was studied in detail to evaluate the types of reactions produced within a set of target materials during neutron irradiation using the Tokai source. The simulations demonstrated that a simplified model for target material activation analysis is possible. The use of an ancestry chain to track the parent particles and their secondary daughters enables accurate reaction scoring within the target and the identification of previously unknown sources.

The simulation here used pure aluminium, which had a relatively short half life for all radioisotopes produced. As aluminium is used as a conductive material to carry electronic signals, the additional production of low energy background electrons during operation may result in a high level of noise.

The investigation of neutron activation in PMMA is particularly important because large quantities of this material are used in phantom studies. The presence of hydrogen contributes the most to secondary production. The $^{14}\text{N}(\text{n},\text{p})^{14}\text{C}$ reaction produces a high count of protons in the sub-MeV range, such as the recoiled 0.58 MeV proton. Radioisotopes such as ^{15}C and ^{19}O were produced at a high rate but decayed below 1 μBq within 20 minutes after being irradiated for 30 minutes by the neutron source. Deuterons were created in considerable quantities through thermal capture of $^1\text{H}(\text{n},\gamma)^2\text{H}$ in PMMA at energies below 0.2 MeV, with a maximum of 1 MeV. A 0.2 MeV deuteron particle has a range in PMMA of 2.3 μm , and a 1 MeV deuteron particle has a range of 14.6 μm

[47].

Pair creation occurs as a result of the high rate of gamma photons generated in the silicon target. The inelastic scattering of silicon nuclei results in a large number of secondary neutrons with energy up to 4 MeV created in the silicon target. It was observed that these secondary neutrons caused further activations within the silicon target. This result may be undesirable in terms of microdosimetry, as more starters will be present within the sensitive volume. The $^{28}\text{Si}(n,\alpha)^{25}\text{Mg}$ and $^{29}\text{Si}(n,\alpha)^{26}\text{Mg}$ reactions produce high energy alpha particles that are absorbed by the silicon target. The average kinetic energy of the alpha particles is around 1.8 MeV, with a projected range in silicon of 6.4 μm [47]. These particles may cause background noise in the BNCT microdosimetric spectra of a silicon-based detector.

The irradiation of silicon dioxide obtains a comparable result to the silicon target. The addition of oxygen to the material resulted in a large production of high energy recoil alpha particles via $^{16}\text{O}(n,\alpha)^{13}\text{C}$ reactions. These alpha particles have an average kinetic energy of 1.9 MeV. The activation of magnesium isotopes results in a considerable contribution of alpha particles with energies ranging from 0.8 to 2.8 MeV. Due to the close proximity of silicon dioxide to the SVs in the Bridge microdosimeter, such alpha particles may produce an unwanted background signal.

The neutron activation study of water was carried out primarily to aid in the identification of reactions that may occur in the large volume of water used in the water tank. The most common interaction was the thermal capture of $^1\text{H}(n,\gamma)^2\text{H}$. The $^{17}\text{O}(n,\alpha)^{14}\text{C}$ reaction produces high rates of recoil alphas with kinetic energies of 1.5 MeV.

In terms of the activation study of the realistic experimental setup, most aluminium activations are in the Aluminium extrusion frame that support the entire motion system frame. Due to the abundance of aluminium present, this is inevitable unless a material change is made. The simulated microdosimetric response of the SOI Bridge indicated that the neutron activation of the experimental equipment has minimal implications on

BNCT microdosimetry measurements.

The enriched boron carbide film provided by the ESS remained stable during irradiation, with its only unwanted activation related to the aluminium substrate. The substrate can be replaced with different materials such as silicon wafer or Kapton foil [77].

It was observed that the 3D printed structures made from ABS plastic were stable during neutron irradiation. It should therefore be investigated in future work whether the aluminium extrusion frame can be replaced by 3D printed plastic counterparts. ABS plastic may be suitable, though more robust materials such as Nylon or Carbon Fiber should be considered. A future study on the neutron activation resistance of different 3D printer materials will be carried out using simulations and experimentally at Tokai.

Furthermore, it was seen that the pulse shaper box was activated unnecessarily. As this object is very far out-of-field, shielding should be utilised to prevent highly scattered thermal neutrons from interacting with it. Such was seen with ^{56}Mn , only a trace element in the shaper box having significant activation. Shielding of the gamma rays emitted during ^{56}Mn decay would be unsuitable as the shaper box sits on top of the MicroPlus probe in the motion stage carriage. The introduction of a shielding material such as Pb for this gamma emission would exceed the weight limit of the carriage, and may induce further activation complications. As the $^{55}\text{Mn}(n,\gamma)^{56}\text{Mn}$ cross section is most favourable for thermal neutrons, the use of a thin neutron shield for the shaper box would be more effective. A neutron shield cover made from boronated or lithiated plastic would be appropriate. An example of this would be a 3D printed cover, composed of novel boronated ABS plastic [175], that could be placed over the shaper box.

An important consideration of these results is that even though all materials have been represented as detailed as possible, some impurities may be present. This may increase the activation rate and ultimately the overall dose equivalent following beam off. It is difficult to accurately evaluate the radiation activity, therefore the results shown in this work should be taken as an indication of the dose equivalent and estimation of the adequate cooling

time.

^{198}Au and ^{66}Cu isotopes are activated in the DIL external leg leads and pin sockets of the MicroPlus probe, respectively. The actual microdosimeter device bonded to the DIL package has negligible activation. The leg leads are composed of pure gold electroplated over an electrolytic nickel underplate. Activation of the nickel was not seen in these simulations. The manufacturer has other options for the external leads such as solder dip of 60% tin, 40% lead alloy or pure tin plating.

The dose equivalent due to ^{28}Al activations is significant and restricts the experimenter to a mandatory 30 minute cool-down period before approaching the apparatus. A future study on the neutron activation resistance of different 3D printed materials that would replace key structures such as the aluminium frame will be carried out using simulations and experimentally at Tokai.

Alternative materials for use in the MicroPlus measurement system have been identified and will be evaluated in terms of its neutron activation and signal quality degradation. Future work pertaining to this context would concentrate on simulations of dose to the hands; $H'(0.07)$ and eyes; $H'(3)$. This would provide greater insight into the personal radioprotection risks involved when handling materials activated with ^{198}Au , ^{66}Cu and ^{24}Na isotopes.

This activation study has indicated that the materials associated with the MicroPlus microdosimetry probe experiment do not pose any significant concern in terms of radiation protection for use in epithermal mode BNCT, provided that a 30 minute cool down period is obeyed. This cool-down requirement should be factored into the planned experiment schedule when it is desired to change the configuration of the experiment between irradiations.

Chapter 7

Development of a Wireless Microdosimetry System ⁴

This chapter reports on the current status of the development of a wireless microdosimeter system by the Centre for Medical Radiation Physics. The CMRP Radiodosimeter is an innovative system that uses existing Silicon-On-Insulator (SOI) microdosimeters [23], however with a novel battery powered processing board consisting of a digitally adjustable shaping amplifier with wireless communication.

The system has been developed to address several issues with the current microdosimeter setup such as electronic noise from cabling, complexity of setup and required knowledge to take microdosimetric measurements. The main motivation of this project is to allow any user to take measurements using our system straight out of the box, without extensive knowledge of the electronics setup.

⁴Part of this chapter has been published in the Journal of Instrumentation: James Vohradsky, Lachlan Chartier, Linh T. Tran, Alex Pogosso, Saree Alnaghy, Jason Paino, Stefania Peracchi, Vladimir Pan, Marco Povoli, Angela Kok, Anatoly B. Rosenfeld (2022). *Introduction and Implementation of the CMRP Radiodosimeter - A Novel Wireless Microdosimetry System*. Journal of Instrumentation. DOI: 10.1088/1748-0221/17/03/P03006. (Published, 7 March 2022)

7.1 Introduction

Microdosimetry is a useful method to evaluate the relative biological effectiveness (RBE) as well as dose equivalent of any mixed radiation field without prior knowledge of type of charged particles and their spectra. The need of portable, user friendly devices for microdosimetric Quality Assurance measurements are greatly preferable to avoid sophisticated setup and time-consuming data analysis.

Currently, the ability to perform microdosimetric measurements is restricted to those with extensive prior knowledge of the electronics involved and their experimental setup.

The Centre for Medical Radiation Physics has developed a compact microdosimetric system named Radiodosimeter - a novel acquisition system that combines both wireless communication and plug-and-play design to provide a device that can be used with minimal setup. The system is compatible with current CMRP MicroPlus probe technology. The Radiodosimeter communicates with the client computer via Wi-Fi, allowing remote management and monitoring of acquisitions.

The system was bench-marked against the standard microdosimetric setup at Heavy Ion Medical Accelerator in Chiba (HIMAC), Japan and was found to have the same response. Several redundancy methods were demonstrated such as continuing an acquisition following disconnection from the client software and the ability to connect through different Wi-Fi modes (WPA2 Personal/Enterprise).

These features prove that the Radiodosimeter can operate independently of a client computer, indicating its potential to be used as a portable device for personal monitoring in mixed radiation fields, including for microdosimetric quantity verification predicted by TPS in particle therapy.

7.1.1 Description of the Radiodosimeter

The main components of the system include a digitally adjustable shaping amplifier module, Kromek K102 MCA, digital pulse generator, Raspberry Pi Zero and high capacity

lithium ion (Li-ion) batteries, enclosed in a slim 3D printed box. The dimensions of the Radiodosimeter housing box are $10 \times 15 \times 3.5 \text{ cm}^3$.

The SOI microdosimeter (silicon pixelated detector, based on 3D cylindrical sensitive volume array of micron size fabricated on $10 \mu\text{m}$ thick SOI and wire bonded in dual in-line package) is inserted into the CMRP MicroPlus probe (a charge sensitive amplifier) [23], and the probe is attached to the shaper-analyser module of the Radiodosimeter via DB9 connector. The rechargeable batteries power all electronics and provide an internal bias for the SOI microdosimeter.



Figure 7.1: Front view of the Radiodosimeter inside its housing box

The 3.7 V Li-ion batteries have a combined capacity of 5200 mAh with nominal voltage of 3.7 V. Performance of the batteries will be shown in the results. Recharging of the system requires a standard micro-USB B cable providing 5 V, 500 mA. The amplification module uses a CR-RC shaper with time constant of 1 μsec . The shaping amplifier can operate at low and high gain modes, corresponding to a maximum deposited energy of approximately 13.3 MeV and 5.3 MeV, respectively. The internal bias voltage of the Radiodosimeter provides 9.5 V with positive or negative polarity. If required, external DC bias up to $\pm 100 \text{ V}$ can be applied.

Raspberry Pi (RPi) is a microcomputer developed by the Raspberry Pi Foundation.



Figure 7.2: Back view of the Radiodosimeter inside its housing box

Kromek K102 MCA is plugged into the RPi via USB cable. Signal from the shaper amplifier is fed to the MCA via SMA coaxial analog input. The drivers and controlling software for the MCA were compiled for Raspberry Pi OS, allowing the RPi to issue commands and receive data from the MCA. After the data has been processed, it is sent to the client computer running the custom software developed by CMRP for calculating microdosimetric quantities such as RBE and dose equivalent through TCP/IP communication over Wi-Fi. The transmission request prompt rate between the Radiodosimeter and client computer is set to a 1 sec interval.

Wireless communication with the Radiodosimeter is made through the use of the RPi. The role of the RPi is to:

- a) Control the data acquisition process using the MCA,
- b) Use its GPIO pins to set shaping amplifier settings (polarity, gain, bias, calibration pulse amplitude) and read back the status of hardware (battery level, dark/leakage current of the microdosimeter, etc),
- c) Send back data when prompted by the software running on the client computer.

The anti-microphonic filter (AMF) helps remove the noise which may be caused by



Figure 7.3: Interior of the Radiodosimeter. All components except the MCA are mounted on the main PCB board.

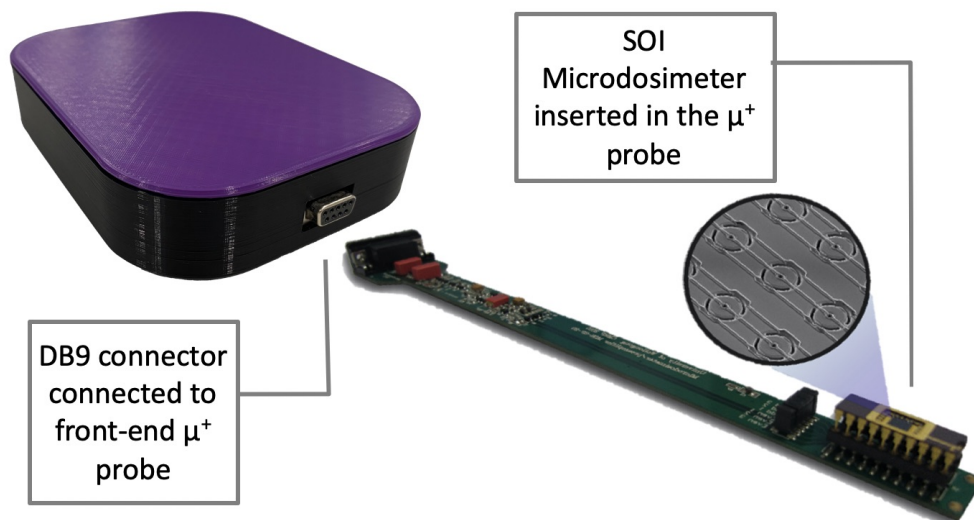


Figure 7.4: Representation of MicroPlus probe (with SOI microdosimeter on DIL package plugged in) inserted into the Radiodosimeter via DB9 connector.

mechanical vibration of the microdosimeter. The AMF is a differentiating RC circuit with time constant of $7.3 \mu\text{sec}$. When the AMF is enabled, the effective system gain reduces by approximately 8%.

The Radiodosimeter also features an internal digital pulse generator module, used for energy calibration. The calibrator can generate pulses of either of the six preset binary scaled amplitudes, corresponding to the deposited energies from approximately 258 keV

to 8256 keV. Pulse frequency is 100 Hz. The advantage of this module is that the calibration pulse amplitude can be selected remotely and no additional hardware setup (switchers or jumpers) is required.

The wireless communication is made with the system and client computer using 2.4GHz IEEE 802.11n Wi-Fi through three different methods, depending on the resources available:

- 1) **Personal method:** Both Radiodosimeter and computer are connected to a personal router, placed in an ideal position,
- 2) **Enterprise method:** Both Radiodosimeter and computer are connected to an established enterprise bridged network,
- 3) **Ad hoc method:** The Radiodosimeter is operating in broadcast mode; creating an ad hoc network that the computer can directly connect to.

In order to connect the Radiodosimeter to the computer, they must be on the same local Wi-Fi network. The client software will search for the Radiodosimeter host name on the network to resolve its IP address and then connect via TCP/IP. If the client software detects that it is connected to the ad hoc network (broadcast mode), then it will automatically connect to the gateway IP address via TCP/IP. Whilst connected to the ad hoc network, various networking settings can be configured such as adding other networks that the Radiodosimeter can connect to after reboot. The Radiodosimeter operating in broadcast mode is the preferred setting as it only requires the user to turn on the Radiodosimeter and then select the 'Radiodosimeter' Wi-Fi network on their computer. There are some concerns about reduced Wi-Fi range and increased battery usage in this mode, which will be investigated in this work.

7.1.2 Design of the Radiodosimeter GUI Software

The main screen of the GUI software suite used to interact with the Radiodosimeter is shown in figure 7.5. In this figure, the Radiodosimeter has just connected and is ready to

start acquisition.

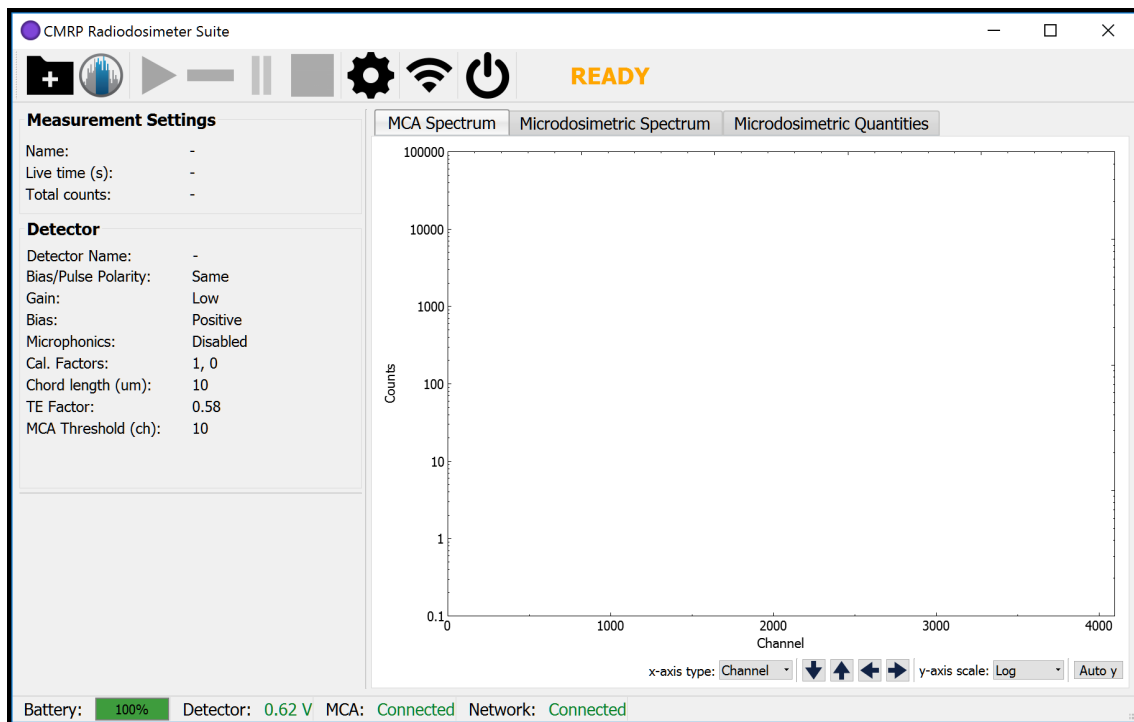


Figure 7.5: Main screen of the Radiodosimeter software suite application.

The main toolbar at the top shown in figure 7.5 has large buttons, the first two available buttons are for starting a new measurement and for calibrating the microdosimeter (detector). The last three buttons in the main toolbar are for manually setting the IP address, enabling/disabling connection and for remote reboot/shut-down of the Radiodosimeter. The tabs allow viewing of the microdosimetric spectra and a list of all previous acquisitions and their results.

Details about the remaining battery life, leakage current from the microdosimeter, MCA status and network connection status are shown in the bottom status bar. The previous configuration settings are shown on the left-hand bar, which are suggested when starting a new acquisition.

The software interface was designed to be simple and easy to use, with large buttons up the top to start different functions. Excessive menus and multiple windows were avoided to prevent confusion for the user. The software was written in Qt5 for Windows [176]. Qt has the advantage of being able to compile for other operating systems as well, making it

simple to create the software for Mac, iPhone, iPad or Android.

Figure 7.6 shows the prompt that appears when a user selects to start a new measurement. Various configurations such as acquisition length, bias polarity, gain, shaper pulse polarity, AMF and MCA threshold will be sent to the Radiodosimeter and applied before the measurement starts.

New Measurement

Acquisition Settings

Acquisition Name: 10.10am_Bridge77_test Auto Name

Detector name: Bridge77

Probe name: 10

Measurement Length (s): 300

Bias: Positive Gain: Low (max. 13.3 MeV)

Bias/Pulse Polarity: Same Microphonics: Enabled

MCA Threshold (ch): 10 Chord Length (um): 10.000 TE Factor: 0.580

A (keV/ch) = 1.000 b (ch) = 0.000

Save Cancel

Figure 7.6: Dialog that pops-up when the new measurement button is pressed.

Figure 7.7 shows the functionality when calibration is enabled. The buttons in the lower left corner allow the activation of the six discrete energy pulses which are sent into the microdosimeter. After a sufficient number of events have been collected, the user can continue to the next prompt which requires selection of the pulse centroids used for calculating the linear pulse calibration coefficients; $E = Ax + b$, where E is energy in terms of keV, x is channel number and A and b are fitting coefficients.

The Radiodosimeter system can operate independently of a client computer, performing all calculations and data storage on the RPi. In this configuration, the system will acquire data, process the microdosimetric quantities (such as RBE and dose equivalent) and store the results locally on a micro SD card. The stored data is retained on the SD card even after power off. This feature is also a redundancy method; if the connection is interrupted, the acquisition will continue remotely without loss of data. Once connection is re-established with the client computer, the user can view the acquisition status or transfer the results that have been saved on the Radiodosimeter.

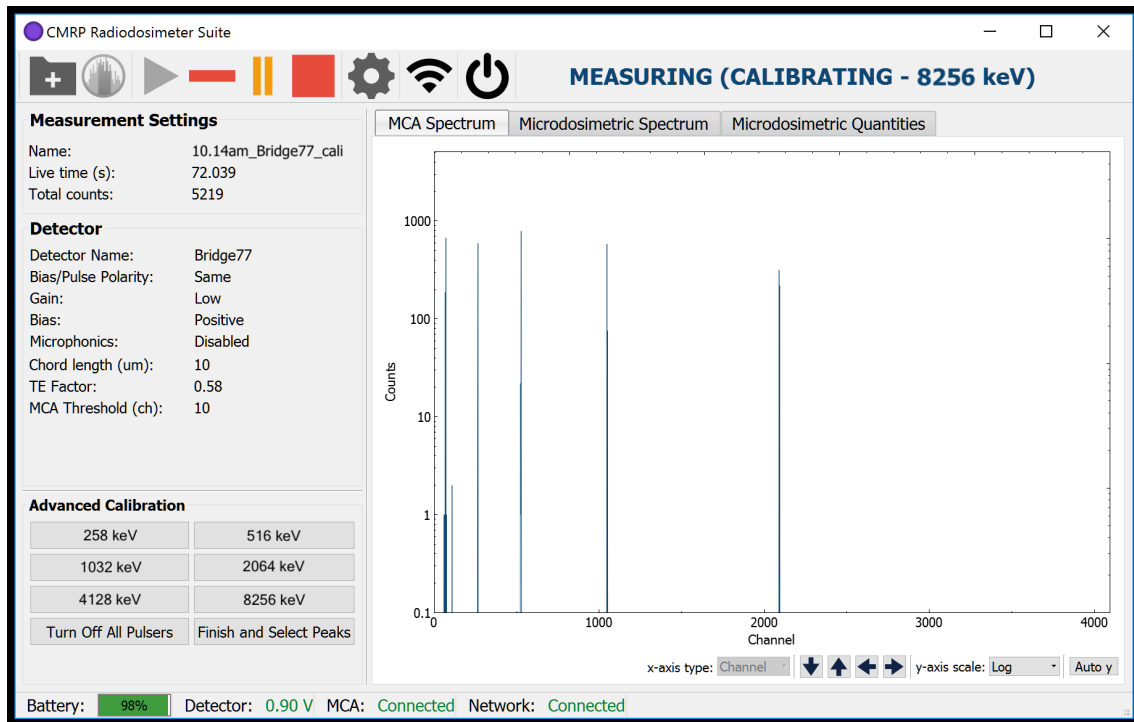


Figure 7.7: Radiodosimeter software during a calibration showing the output pulses.

7.1.3 Web interface for managing Wi-Fi settings

After successful connection has been made with the RPi, either by the ad hoc network or through an existing network, Wi-Fi settings can be managed by navigating to the web interface setup page shown in figure 7.8. This can be done on any device including mobile phone or iPad.

On this page, saved networks are shown, which can be deleted by clicking the cross symbol. The list of available networks in range to the RPi are displayed, which is shown in more detail in figure 7.9. At the bottom of the page is the form to add a new network. This can be done manually by typing in a network name or by selecting a network from the list, which applies the ideal settings for that network type (much like any other device). The form for adding a new network also handles complex networks such as WPA Enterprise, which have more settings that need to be specified, as shown in figure 7.10.

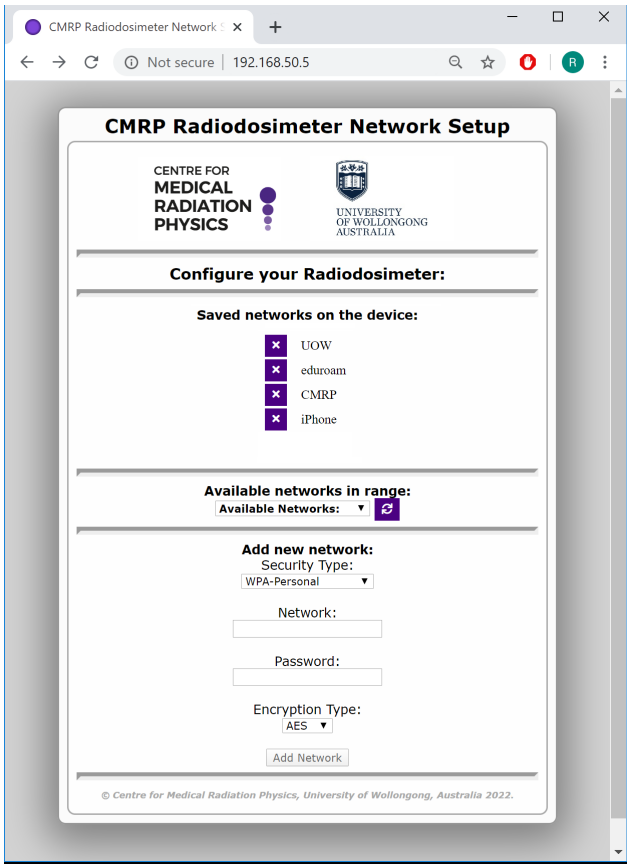


Figure 7.8: Web page interface for the RPi network management.

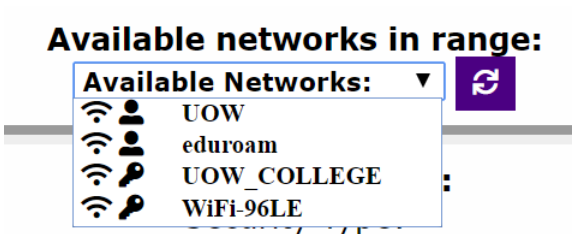


Figure 7.9: List of available networks on the web interface. The icons next to the network name indicates the signal strength and security type.

Add new network:

Security Type:

WPA-Enterprise ▼

Network:

UOW

Password:

Encryption Type:

AES ▼

Network Authentication Mode

PEAP ▼

Phase 2 Authentication Mode

None ▼

Username:

james

Password:

Add Network

Figure 7.10: Example of the new network form, adding a WPA2 Enterprise security type (such as eduroam).

7.2 Materials and Methods

7.2.1 Benchmark calibration using radioactive sources

The Radiodosimeter and standard setup were calibrated using an ^{241}Am alpha source in vacuum chamber. Firstly using a 300 μm thick planar Hamamatsu PIN diode with 100% charge collection efficiency, with an external bias of -100 V was applied to the PIN diode. The same MicroPlus probe was used for all measurements, which was connected by a cable with feed-through out of the vacuum chamber.

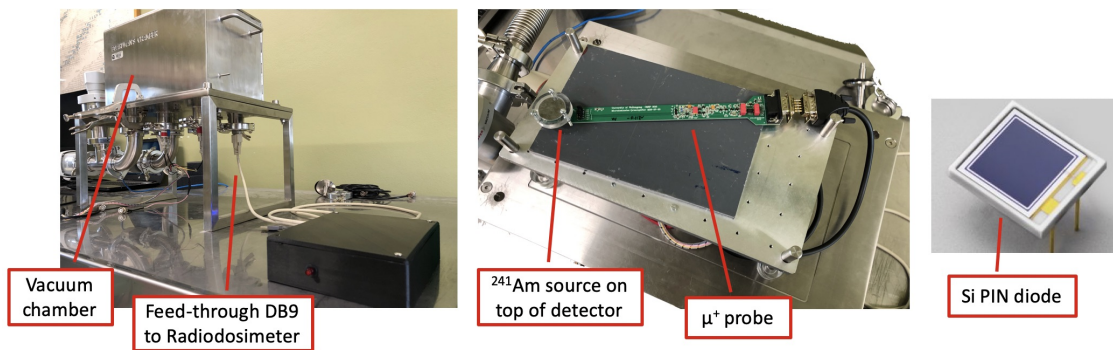


Figure 7.11: Wireless setup for radioactive source measurements using the Radiodosimeter.

For the standard setup (non-wireless), the DB9 CSA output was plugged into the external shaping amplifier. The spectral response of the detector (microdosimeter or PIN diode) was recorded using an Amptek MCA 8000A, which was processed by the computer connected with USB. Separate 12 V power supply was required for the shaping amplifier. The energy calibration of the standard measurement system was performed with an Ortec 419 precision pulse generator.

For the wireless setup, the DB9 MicroPlus probe output was plugged into the Radiodosimeter, which processed all data on-board and recorded the spectral response of the detector using its Kromek K102 MCA. The output was sent to the client computer using Wi-Fi. The in-built digital pulse generator of the Radiodosimeter was used to verify the calibration result of the wireless system.

The measurements were repeated using the 9.1 μm thick SOI Mushroom microdosime-

ter instead of PIN diode. The 9.1 μm thickness of the active layer silicon in this batch has been measured using SEM [177]. The calibration factors found using the PIN diode were used for calibrating the microdosimeter to verify the continuity between different Si devices.

A simple Monte Carlo simulation using Geant4 [127] version 10.5 was performed to measure the energy deposition in the SVs of the Mushroom model, which was positioned in a vacuum, facing a 1 cm diameter disc source of decaying ^{241}Am , with a 1.5 cm displacement between them. ROOT v6.16 was adopted as analysis tool [146]. The Geant4 result was used to compare the experimental result and confirm the calibration of the Radiodosimeter.

7.2.2 Hardware capability testing

The supply voltage of the batteries is monitored by an I2C analog-to-digital converter (ADC), connected to RPi. For different cases, after the battery was fully charged using the USB cable, an acquisition with infinite length was started. The voltage of the batteries was monitored on-board the Radiodosimeter with results saved to the SD card every 30 seconds. The battery life of the Radiodosimeter was tested under four different scenarios:

1. **Personal method mode:** Both Radiodosimeter and computer are connected using the ‘Personal method’ with a personal router.
2. **Ad hoc mode:** Computer is connected using the ‘Ad hoc method’; the Radiodosimeter broadcasts the local network, allowing direct connection.
3. **Ad hoc + abandoned mode:** Same as mode 2, except after the acquisition starts, the computer is disconnected.
4. **Standalone mode:** Radiodosimeter operates with Wi-Fi disabled.

The Radiodosimeter signal strength was evaluated outdoor in free air to provide a basic indication of the operating range when using ad hoc mode. For ad hoc mode, the Wi-Fi

network is broadcast by the RPi using its internal antenna, which is embedded on the PCB board. The range of the internal antenna was tested outdoor in free air with a clear line of sight to the Radiodosimeter system, which was placed 1 metre from the ground. The computer (2017 MacBook Pro) was positioned 1 metre from the ground and incremented distance was made away from the Radiodosimeter. The ambient temperature was 20°C. The received signal strength indicator (RSSI) measured in dBm by the computer was recorded at each position by calculating the average over 1 minute, sampling every 5 seconds. Table 7.1 provides an indication for the expected quality for different signal strengths.

Signal strength	Expected quality
-30 dBm	Maximum signal strength, right next to access point
-50 dBm	Anything down to this level is excellent signal strength
-70 dBm	Minimum signal strength for reliable packet delivery
-80 dBm	Unreliable signal strength, minimum for connection
-90 dBm	Unusable, unlikely to connect

Table 7.1: Expected quality for different wireless RSSI values.

7.2.3 Benchmark experiment with heavy ion therapy

The 3D Mushroom microdosimeter was irradiated at the Heavy Ion Medical Accelerator in Chiba (HIMAC), located at the National Institutes for Quantum Science and Technology (QST), Japan. The facility consists of ion sources, a radio frequency quadropole linear accelerator for low-speed ions and an Alvarez linear accelerator for medium-speed ions as an injector to the two synchrotrons, with maximum energy of 400 MeV/u [12].

The Radiodosimeter was benchmarked against the standard microdosimetric setup with the 9.1 μm thick SOI Mushroom microdosimeter. The same microdosimeter and probe was used. The comparison between the Radiodosimeter and standard setup was made using a 230 MeV/u ^{28}Si pristine Bragg peak heavy ion beam, delivered by the biological beamline at HIMAC. There were two setup configurations as below:

- i) **Standard operation (non-wireless):** The MicroPlus probe is connected by DB9 plug to a standard shaping amplifier, which is output through BNC cable to MCA

and computer in control room. Separate power supply box required for the shaping amplifier (figures 7.12a and 7.13a),

- ii) **Wireless operation:** The MicroPlus probe is connected by DB9 plug to the Radiodosimeter, signal is processed and sent via Wi-Fi to the computer in control room (figures 7.12b and 7.13b).

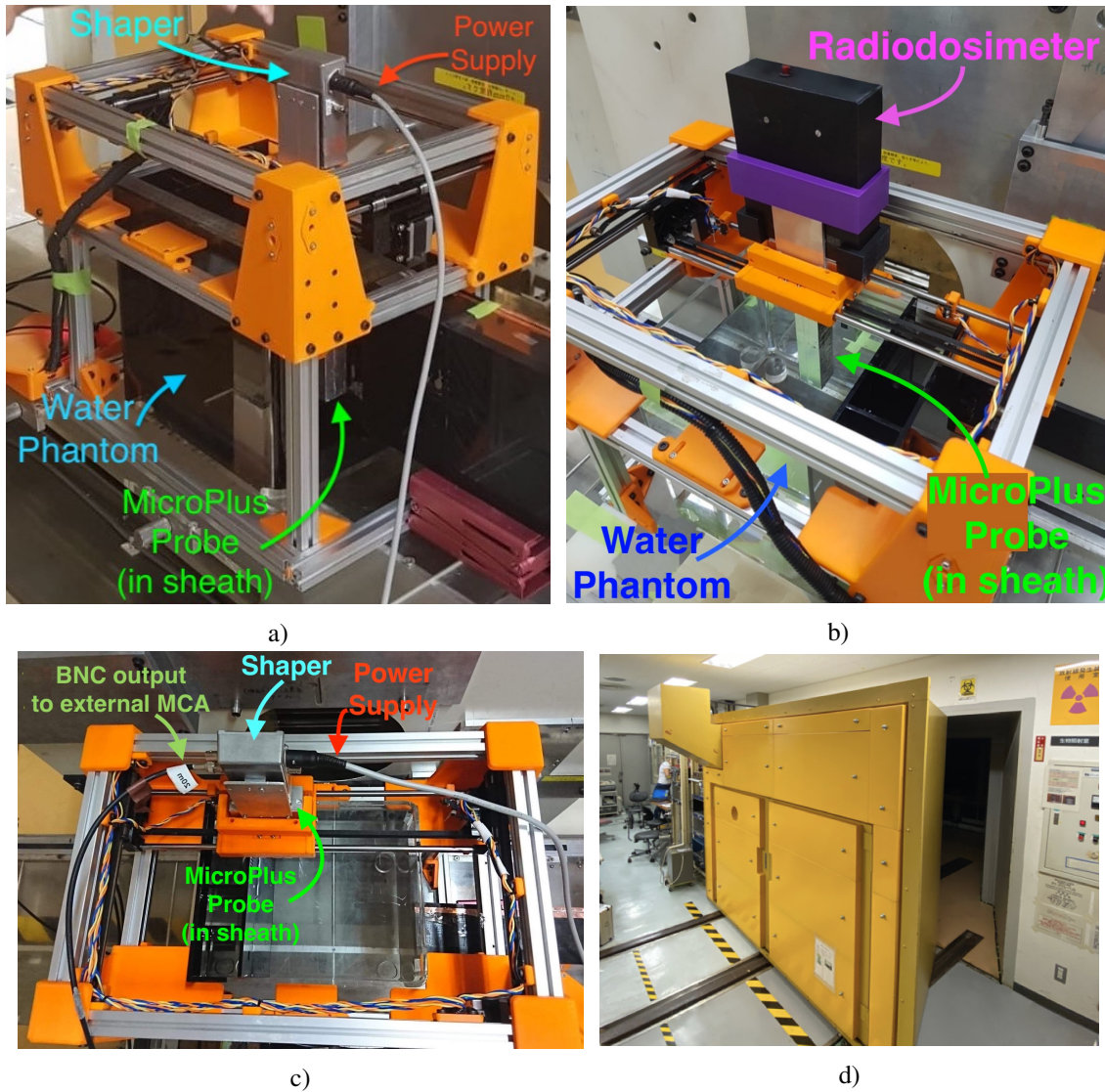


Figure 7.12: a) Standard experiment setup with wires, b) Wireless experiment setup (note: Radiodosimeter is mounted in a different 3D printed enclosure), c) Standard experiment setup shown from top-down view, d) motorised door at biological beam line at HIMAC, where cable is normally drawn through the doorway (open).

In both cases, the MicroPlus probe is covered by a waterproof PMMA sheath, which is mounted in a water phantom using an X-Y motion stage assembly to remotely control the

SOI microdosimeter location in the phantom using stepper motors. The water phantom motion stage is shown from a top down view in figure 7.12c.

In the beamline, a Ta scatterer was used upstream to broaden the ^{28}Si ion beam and improve its lateral dose uniformity. The beam was collimated to a $10 \times 10 \text{ cm}^2$ field using a brass collimator, located 16 cm upstream from the water phantom, which is visible in figure 7.12c. The physical dose of the ^{28}Si beam in water was measured using a PTW 31066 pinpoint ionisation chamber (IC).

Geant4 simulations were performed to model the HIMAC biological beamline as outlined by [178]. The residual beam exiting from the brass collimator was incident on the water phantom. The MicroPlus probe covered by PMMA sheath was modelled and placed in the water phantom. The energy deposition measured by the Mushroom microdosimeter SVs in the simulation was recorded for different depths in the water phantom.

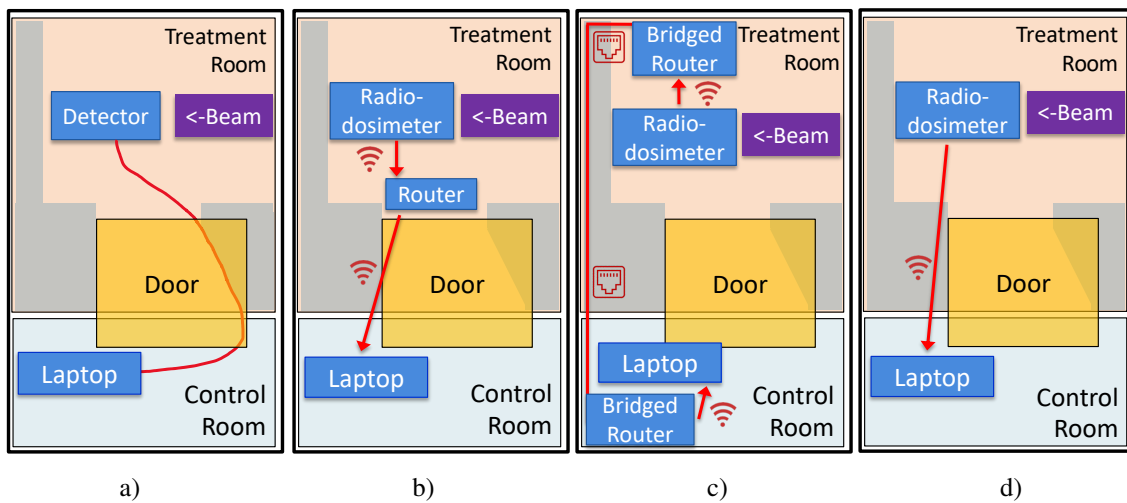


Figure 7.13: Communication methods with the treatment room with door closed: a) standard method with cables (not wireless), b) connected to personal Wi-Fi router inside treatment room, c) connected to enterprise Wi-Fi network inside treatment room, d) direct connection to Radiodosimeter’s ad hoc Wi-Fi network inside treatment room.

There are four communication methods that were tested at HIMAC; the standard method with cables and three wireless methods, as shown in figure 7.13. The standard method (a) involves running a 20 metre long BNC cable out of the treatment room into the control room where it then connects to the Amptek 8000A MCA and laptop computer. The personal method (b) requires the personal router to be placed in the treatment room, which

the client computer and Radiodosimeter connect to. The enterprise method (c) uses the established Wi-Fi network that exists at HIMAC, which has bridged routers, allowing connection from different rooms or buildings. The ad hoc method (d) only requires the Radiodosimeter, which allows direct wireless connection with the computer.

Following successful validation of these communication methods, the received signal strength from the personal method router and ad hoc Radiodosimeter to client computer was tested. The signal strength was tested at three positions at HIMAC with respect to treatment door open or closed and personal or ad hoc connection as shown in figure 7.14. The first location is inside the control room at the control room consoles, which is the longest path the signal has to travel as there is a thick wall in between. The second location is inside the control room closest to the opening of the treatment door. The third location is inside the treatment room, approximately 1 metre from the Radiodosimeter and router. The Radiodosimeter and personal router were placed at the same position in the treatment room. When testing the received signal strength from any method, the other was switched off to minimise any interference.

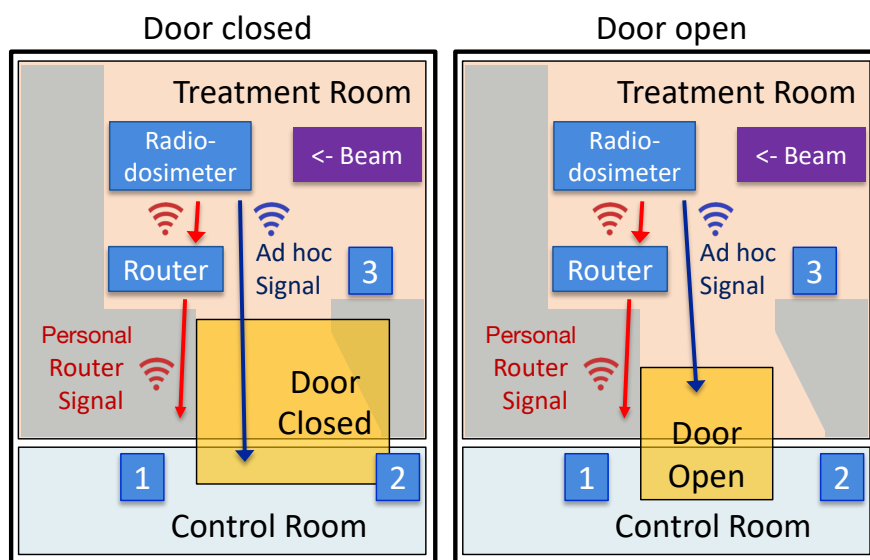


Figure 7.14: Three locations at HIMAC that the Wi-Fi signal strength was tested for personal and ad hoc methods with motorised door open or closed.

7.3 Results

7.3.1 Calibration of the Radiodosimeter

Using Si PIN diode

The calibrated MCA spectrum for ^{241}Am -emitted alpha particles measured using a 300 μm thick planar Hamamatsu Si PIN diode with -100 V external bias applied with the standard microdosimetric setup is shown in figure 7.15. The Ortec pulse generator was normalised to the 5.486 MeV alpha peak and discrete pulses with amplitudes corresponding to 1, 2, 3, 4, 5 and 5.486 MeV energy were produced (red lines) to calibrate the detector.

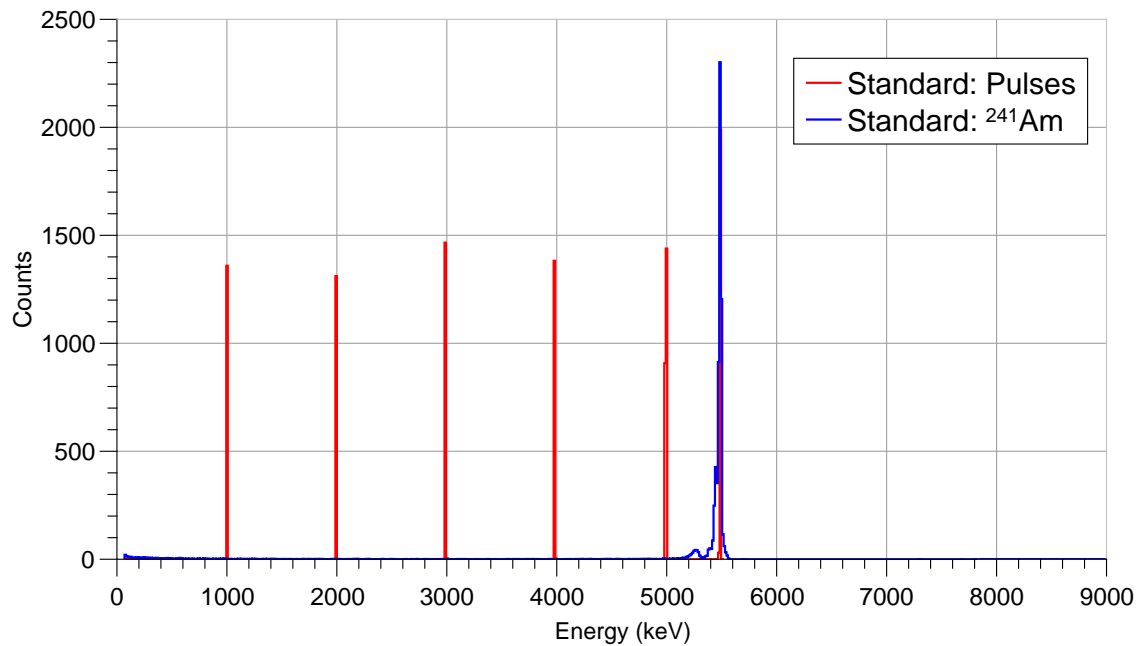


Figure 7.15: Calibrated MCA spectrum acquired with standard setup using Si PIN diode and spectrum of ^{241}Am alpha source.

The Radiodosimeter contains an internal calibration module which sends discrete pulse energies through the detector. The six discrete calibration pulse energies were defined by the capacitance measured using an original reference microdosimeter and MicroPlus probe during development of the Radiodosimeter calibration module. The different pulses are linearly defined with energies approximating to 200, 400, 800, 1600, 3200, and 6400 keV.

The un-calibrated Radiodosimeter MCA spectrum for the ^{241}Am alpha particles using the same PIN diode, -100 V external bias and MicroPlus probe is shown in figure 7.16. The six discrete calibration pulse energies were produced by the Radiodosimeter calibration module.

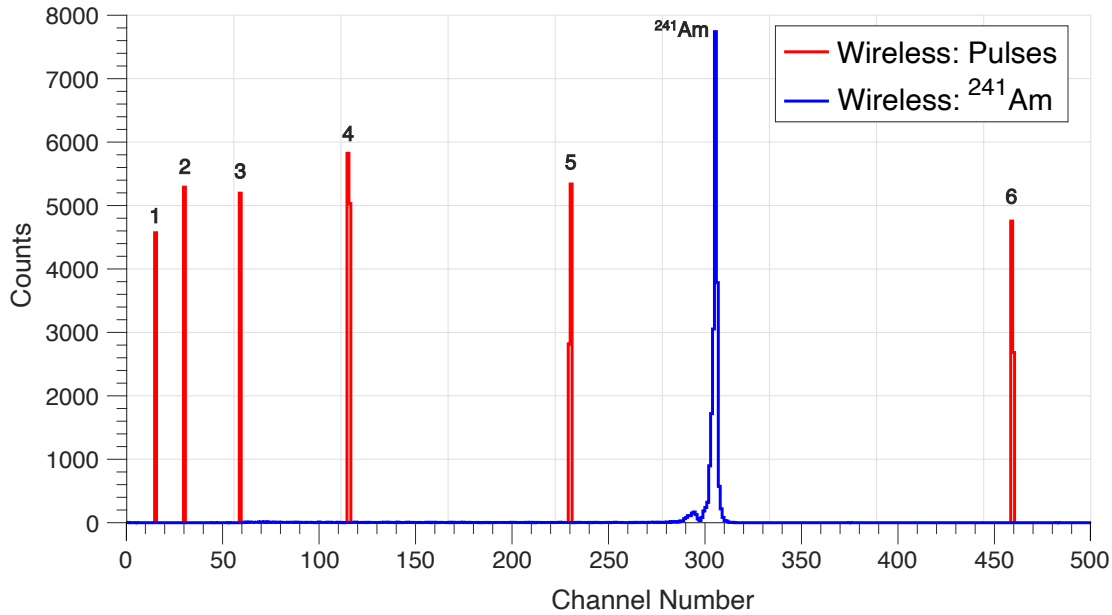


Figure 7.16: Un-calibrated MCA spectra for the six discrete pulse energies (labelled 1-6) and ^{241}Am alpha source, acquired with Radiodosimeter using Si PIN diode.

To calibrate the Radiodosimeter in this experiment, the MCA spectra of the reference wireless pulses were calibrated using the pulse definitions, along with the wireless response of the PIN diode to ^{241}Am spectral source. The calibration of the Radiodosimeter pulse energies is defined by the linear equation: $y = N(Ax + b)$. A virtual normalisation factor ($N=1.29$) was found for the wireless pulse energies such that these pulses scale relative to the 5.486 MeV ^{241}Am centroid channel in the MCA spectrum. The updated definition of the wireless pulses for this MicroPlus probe (258, 516, 1032, 2064, 4128, 8256 keV) were used to calibrate the wireless ^{241}Am MCA spectrum.

The resulting calibrated Radiodosimeter MCA spectrum for the ^{241}Am alpha particles is shown in figure 7.17. For the MCA spectra obtained in figures 7.15 and 7.17 for standard and wireless, respectively, the shape of the ^{241}Am peak is approximately the same, with no loss of resolution. Both 5.486 and 5.443 MeV ^{241}Am alpha particle peaks can be

resolved.

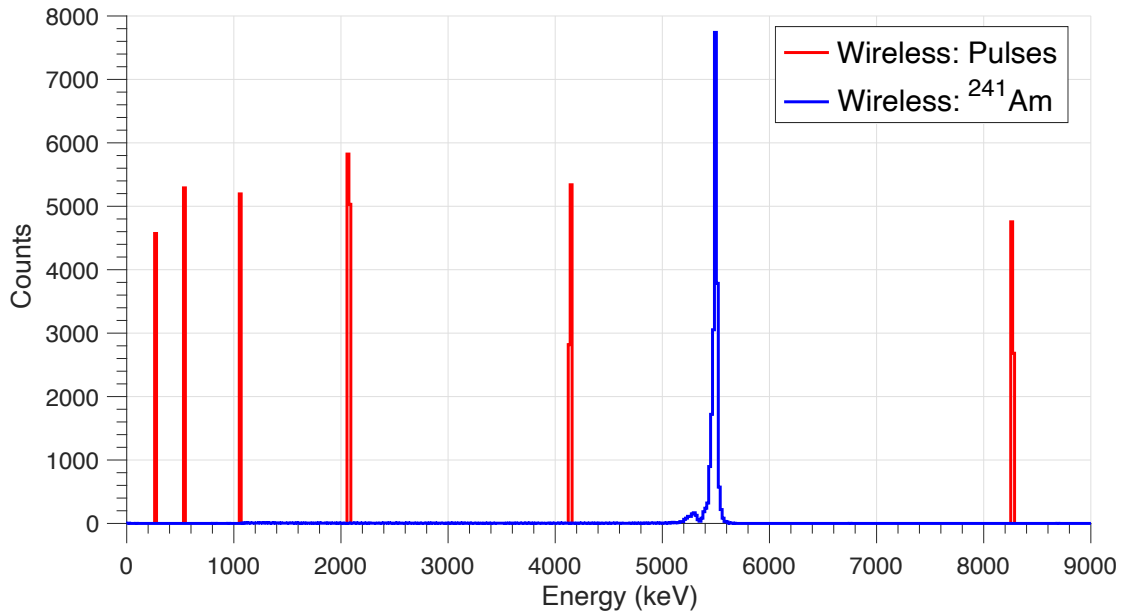


Figure 7.17: Calibrated MCA spectrum acquired with Radiodosimeter using Si PIN diode and spectrum of ^{241}Am alpha source.

Therefore, these pulses demand assessment to determine whether the difference in capacitance between the original reference and the current detector and MicroPlus probe will change their definition (ie. normalisation). The virtual normalisation value found for the PIN diode of $N=1.29$ will be confirmed using the SOI microdosimeter.

Using SOI microdosimeter

The Radiodosimeter acquisition was performed again for the ^{241}Am source using the SOI Mushroom microdosimeter with -10 V applied using the internal bias, as shown in figure 7.18. Note that the aim of this measurement is to verify the applicability of the updated pulse definitions (determined using PIN diode) for calibrating the Mushroom MCA spectra.

The calibration of the wireless MCA spectra obtained with the SOI microdosimeter was defined from the six discrete pulses of the Radiodosimeter calibration module, based on their updated definitions using the virtual normalisation factor ($N=1.29$) found from the previous PIN diode measurement. The calibrated wireless ^{241}Am MCA spectrum

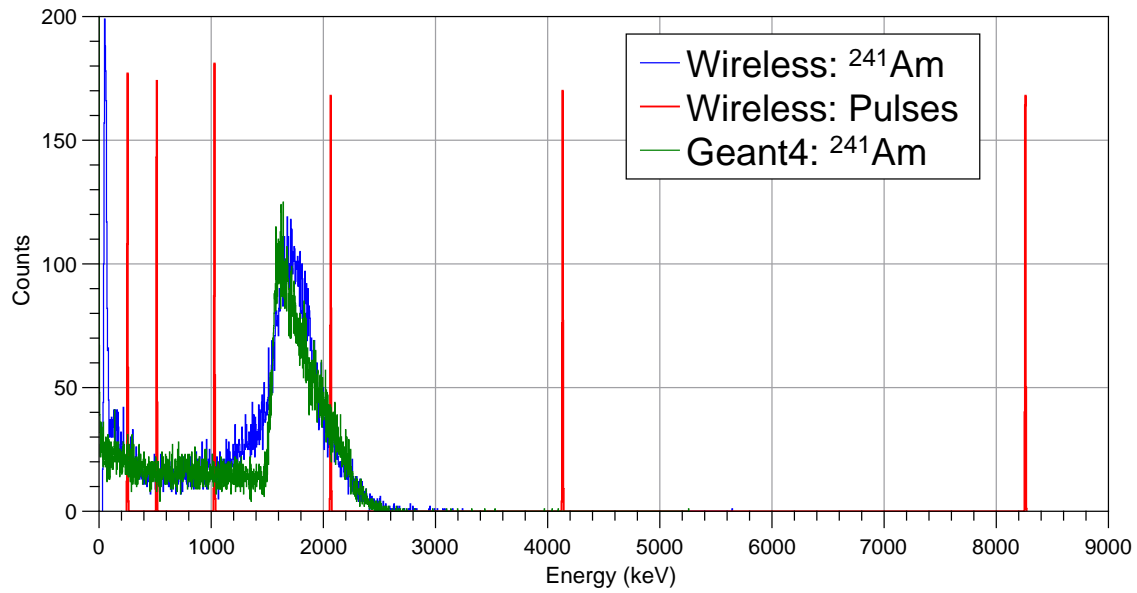


Figure 7.18: Calibrated MCA spectrum acquired with Radiodosimeter using SOI Mushroom microdosimeter and ^{241}Am alpha source.

measured with the Radiodosimeter using the virtual normalisation factor is in agreement with the Geant4 simulation result. This confirms the definition of the Radiodosimeter discrete calibration pulse energies and the continuity of energy calibration between the fully stopping 300 μm thick PIN diode and 9.1 μm thick Mushroom SV. The wireless pulses are much sharper for this measurement in comparison with previous wireless pulses using Si PIN diode, with approximately 1 to 2 channels width.

Using a basic SRIM calculation [47], the energy deposited in the SVs after passing through the overlayers is approximately 160 $\text{keV}/\mu\text{m}$. This is in agreement with the results obtained with the Radiodosimeter and Geant4.

7.3.2 Hardware capability testing

Battery stress testing

The Li-ion batteries provided power to the electronics and internal bias for the microdosimeter for over 10 hours in each scenario as shown in figure 7.19. The time elapsed and power consumption before the batteries were discharged to 3 V for the different modes is shown in table 7.2.

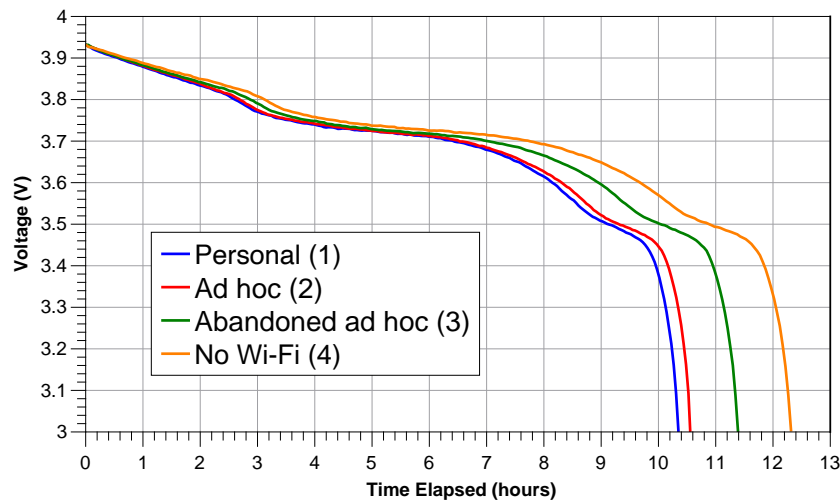


Figure 7.19: Voltage monitoring of the Radiodosimeter batteries in different scenarios for an infinite acquisition.

Mode	Battery life (hrs)	Power Consumption (W)
Personal (1)	10.35	1.85
Ad hoc (2)	10.57	1.82
Abandoned ad hoc (3)	11.40	1.69
No Wi-Fi (4)	12.32	1.56

Table 7.2: Specifics of the Radiodosimeter battery usage.

Surprisingly, the ad hoc mode (2) uses less power than connecting to the personal router (1). For the abandoned mode (3), even though the Radiodosimeter is still open for new TCP/IP connections, it uses less power again. Disabled Wi-Fi mode (4) provided the best battery life, with an additional two hours operation versus the personal mode (1). Note that this is before power consumption of the system has been optimised, such as limiting background software processes. The battery life is expected to increase with more power efficient software.

Wireless range testing in free air

The received signal strength broadcast by the Radiodosimeter in ad hoc mode was evaluated outside in free air as shown in figure 7.20. The declining signal strength has the expected relationship between RSSI and distance [179].

From the expected quality suggestions given in table 7.1, it is observed that distances up to 60 metres (> -70 dBm) are the minimum for reliable packet delivery. From 60 to 100 metres (> -80 dBm), it is an unreliable signal due to increased noise and packet loss. Beyond 100 metres would be unusable. Therefore, the Wi-Fi signal from the Radiodosimeter in ad hoc mode has a functional operating range of up to 60 metres in free air, which is acceptable.

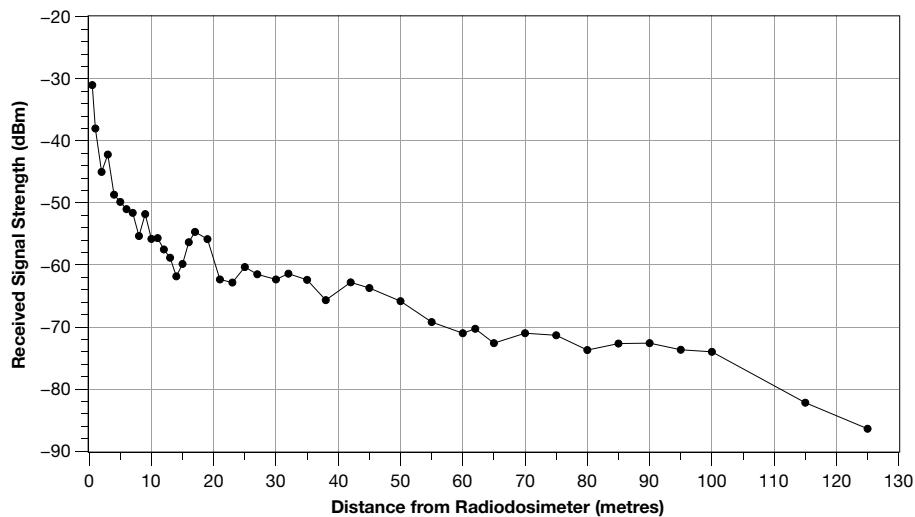


Figure 7.20: Received Wi-Fi signal strength from the Radiodosimeter operating in ad hoc mode to client computer in free air.

Wireless range testing at HIMAC

All communication methods described in figure 7.13 were tested at HIMAC. The personal router was placed inside the treatment room with Wi-Fi communication still possible while next to the closed treatment door. The use of an established Enterprise network was tested, with both Radiodosimeter and client computer connected to the established WPA2 Enterprise network at HIMAC. In this mode, it was possible to stay connected to the Radiodosimeter and monitor its status, even in different buildings as they are still on

the same bridged network. Finally, the Radiodosimeter was set to operate in ad hoc mode, broadcasting its own Wi-Fi network which was visible and connectable outside the closed treatment door.

The validity of these three different wireless communication methods has been established. The received signal strength by the client computer for personal and ad hoc connection methods with the treatment door open or closed is shown in table 7.3. The different positions as described in figure 7.14 are: 1) at control room consoles, 2) closest to the door opening in control room, and 3) inside the treatment room, approximately 1 metre from the Radiodosimeter and router.

Position		Personal method	Ad hoc method
Door Open	1	-59 dBm	-65 dBm
	2	-42 dBm	-52 dBm
	3	-37 dBm	-33 dBm
Door Closed	1	-77 dBm	-83 dBm
	2	-52 dBm	-61 dBm
	3	-35 dBm	-32 dBm

Table 7.3: Received signal strength by client computer for personal/ad hoc methods at HIMAC at different positions.

From the results in table 7.3, it can be seen that the ad hoc method has a slightly lower received signal strength compared with the personal method due to lower transmission power from the RPi's internal antenna. However the signal strength is still sufficient for reliable wireless communication, albeit poorer at the control room consoles, though the personal method also had unreliable signal here too.

The independent operation and redundancy methods of the Radiodosimeter to the client computer was tested. During an acquisition, the power of the personal router was turned off, resulting in disconnection between the RPi and client computer. The RPi server software was designed to recognise this and continue acquiring data during this time without interruption. Upon re-connection, the client computer software was able to access and download the completed acquisition file that was stored locally on the RPi, as expected.

7.3.3 Comparison with conventional microdosimetric measurements at HIMAC

The comparison of the microdosimetric spectra obtained at different depths in water phantom using the standard and wireless setup is shown in figure 7.21.

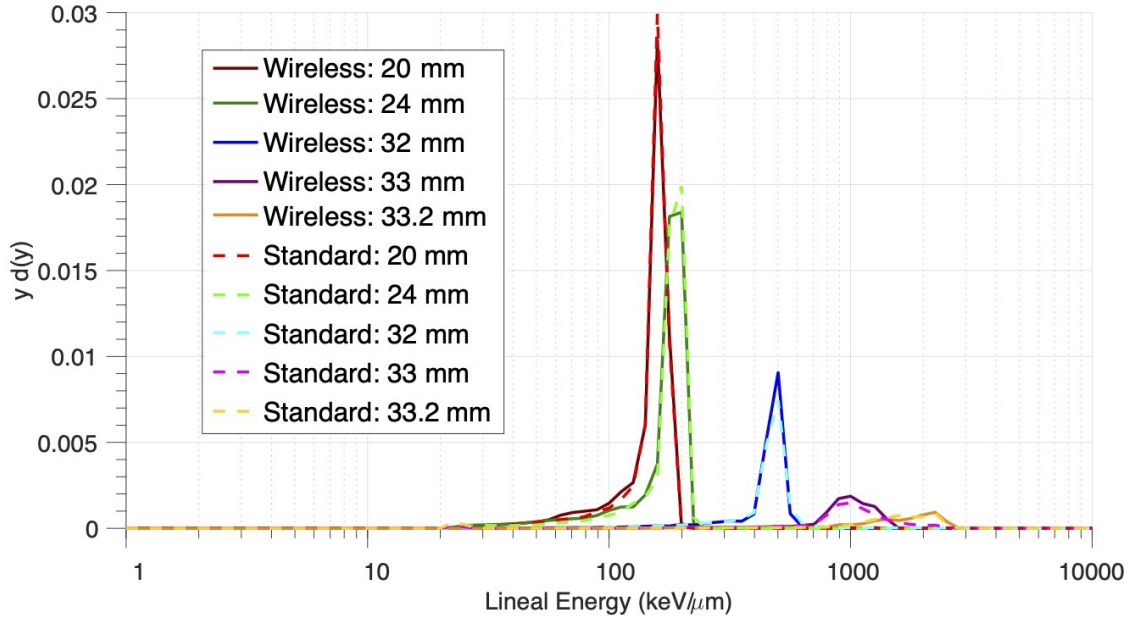


Figure 7.21: Microdosimetric spectra measured at different depths in water with SOI Mushroom microdosimeter on ^{28}Si ion 230 MeV/u beam with standard method and Radiodosimeter.

The result from the Radiodosimeter is favourable, with low noise in the measurement and good agreement with the standard setup. For these measurements with the ^{28}Si heavy ion beam, the front end electronics were set for very large LET to be able to measure higher $\overline{y_D}$ events associated with depth for ^{28}Si ion beam. Events higher than 1000 keV/μm tissue equivalent were measured with high spatial resolution, shown by the difference between 33.0 mm and 33.2 mm in figure 7.21. For this experiment, the MCA threshold was set to 20 keV/μm, resulting in fewer low energy events observed here.

The distribution of dose-mean lineal energy ($\overline{y_D}$) derived from the microdosimetric spectra as a function of depth is shown in figure 7.22. The results in the Bragg peak are consistent with that obtained using the standard setup and the verified relative dose using the PTW IC. The results obtained independently with the standard setup and Ra-

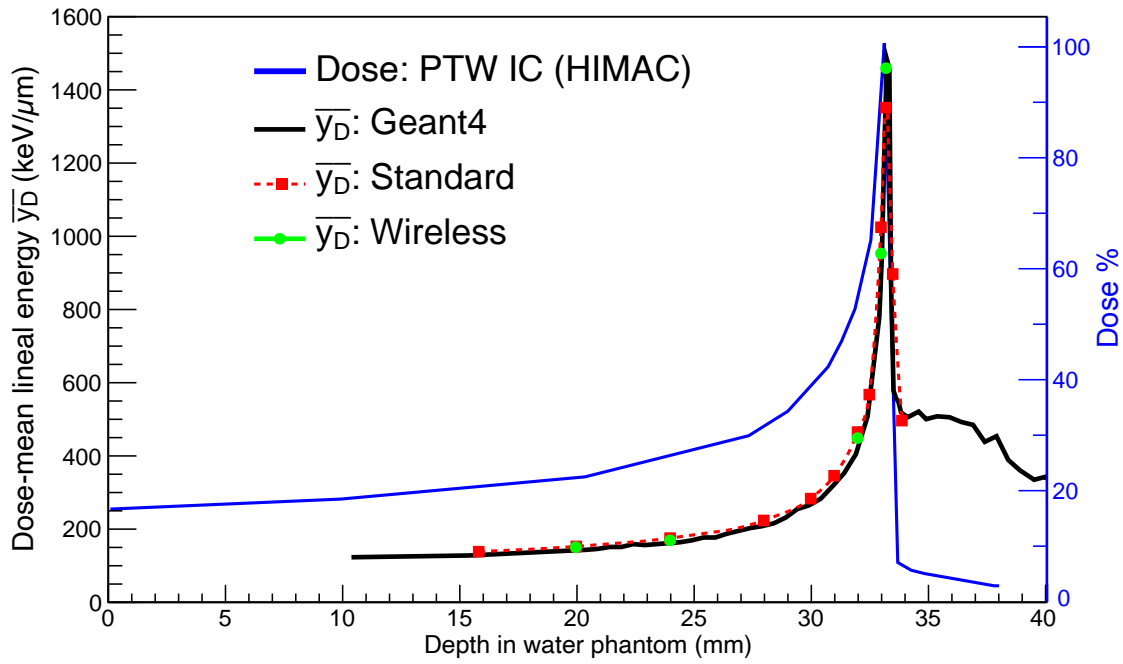


Figure 7.22: Dose-mean lineal energy (\bar{y}_D) as a function of depth in water for Mushroom and ^{28}Si 230 MeV/u. Secondary y-axis represents relative dose to Bragg peak for the PTW IC.

diodosimeter are comparable and agree well. The slightly higher \bar{y}_D measured with the Radiodosimeter is a result of a slightly different position.

Both calibration factors were validated using a Geant4 simulation [127, 131] - confirming that the energy deposition in 9.1 μm of Si supports our experimental values obtained at different depths in the water phantom.

Table 7.4 presents the \bar{y}_D percentage difference of the standard and wireless measurements compared to Geant4 as a function of depth in the water phantom. The Bragg Peak is located at about 33.2 mm depth in water. The \bar{y}_D percentage difference of the standard measurements is approximately 2.7% higher than Geant4 in the entrance BP region. For the wireless measurements in the same region, the \bar{y}_D percentage difference is approximately 1.8% higher than Geant4. It is important to note that the marginally higher measured \bar{y}_D in both cases is due to a slightly different position by the motion stage system.

Depth in water phantom (mm)	Standard: $\overline{y_D}$ percentage difference	Wireless: $\overline{y_D}$ percentage difference
15.8	+ 2.24%	-
20.0	+ 3.22%	+ 2.29%
24.0	+ 3.48%	+ 2.13%
28.0	+ 3.01%	-
30.0	+ 2.91%	-
31.0	+ 3.41%	-
32.0	+ 2.45%	+ 1.13%
32.5	+ 0.58%	-
33.0	+ 2.78%	- 0.15%
33.2	- 0.37%	+ 3.19%
33.5	+ 2.71%	-
33.9	- 1.17%	-

Table 7.4: $\overline{y_D}$ percentage difference of standard and wireless measurements compared to Geant4 as a function of depth in the water phantom.

7.4 Discussion and Future Improvements

A novel battery powered wireless microdosimetry system has been developed by CMRP that is compatible with our existing microdosimetry MicroPlus probe. The hardware and software capabilities of the Radiodosimeter have been rigorously tested as shown in this chapter in terms of detector signal response, battery life, wireless transmission methods and detector calibration.

Hardware - Microdosimetric Response and Calibration Module

The benchmarking of the Radiodosimeter has been confirmed, which performed the same as the standard setup for spectral response using ^{241}Am source in a vacuum chamber and microdosimetric measurements of ^{28}Si heavy ion beam in a water phantom. For the source calibration, the MCA spectra for standard and wireless system had the same detector resolution for the ^{241}Am peak. Similarly for the ^{28}Si heavy ion, the $\overline{y_D}$ depth distribution result is almost the same, with some small differences at the Bragg peak due to positional error in the motion stage system.

During the microdosimetric measurements at HIMAC, the microdosimeter was calibrated before and after irradiation using the Radiodosimeter's auto-calibration function.

The advantage of the Radiodosimeter is realized in this case as the digital pulse generator is built into the system, allowing auto-calibration to be performed without needing to change the setup or include bulky external electronics. However, for this version of the Radiodosimeter, the calibration pulses are discrete with fixed energy, so they cannot be adjusted. Future iterations may include digital-to-analog (DAC) converter, which would allow the pulses to be finely adjusted by a normalisation value, similar to the Ortec 419 pulse generator used in the standard setup.

Hardware - Battery

During the hardware testing of the battery life, the 5200 mAh batteries showed an operating time of up to 12.32 hours with Wi-Fi disabled. It was surprising that the Radiodosimeter had a longer battery life when utilising the ad hoc method for connection, compared with the personal method. However the current battery life is more than sufficient for purposes in our microdosimetry measurements. For future software development, the energy usage by the RPi will be optimised, limiting background processes and improving the server software.

The standard 18650 Li-ion battery type was used in the Radiodosimeter due to its high capacity and interchangeability. However, its dimensions require the Radiodosimeter enclosure box to be thicker and limit the compactness of the overall system. The use of a thinner battery cell would allow a significantly more compact system with smaller dimensions.

Hardware - Wireless Connectivity

From the evaluation of battery life and wireless range testing, it was found that the Radiodosimeter in ad hoc mode is sufficient to be used for primary operation. This result is ideal as no extra equipment is required for communicating, allowing an ‘out of the box’ operation, which decreases the complexity of setup and likelihood of technical issues. The useful range was found to be less than 60 metres in free air using the internal antenna

of the RPi board. The use of a passive external antenna connected to the RPi will be investigated to increase the range.

The ‘personal method’ of communication could be reconsidered as a range-boosted option, where the personal router is placed in between the computer and the Radiodosimeter for long distances, providing a relay for the signal. If required, an ethernet cable can be used, connecting the personal router to the computer. A standard CAT5 or CAT6 Ethernet cable can be run for 100 metres with no loss of information, while USB can only be 5 metres before requiring repeaters.

Software support for using the ‘enterprise method’ of communication is particularly useful as it enables secure connection to established networks at universities, hospitals, etc. This permits operation of multiple Radiodosimeters throughout a building or a campus, which can all be monitored remotely in real time.

When connected to the same network as the Radiodosimeter, the Wi-Fi settings can be managed through the Radiodosimeter web page interface. The decision to use a web page to access these settings was that this is accessible from any device, without needing any software. For ‘out of the box’ setup, the user will connect to the self-broadcast ad hoc network, then go to the web interface to configure the Radiodosimeter to use a different network (existing personal or enterprise network). After restarting the Radiodosimeter, it will connect to the designated network that was configured. Another scenario is if connection using the software is not possible (Radiodosimeter stuck on wrong network) and this can be managed simply through the web interface on computer or mobile phone.

Future Improvement - Decentralised Network

Figure 7.23 outlines the traditional star network architecture used in traditional Wi-Fi networking. In a star network, every device is connected to a central hub (router). The limitation of this network type is that devices can only operate within the access point range broadcast by the router.

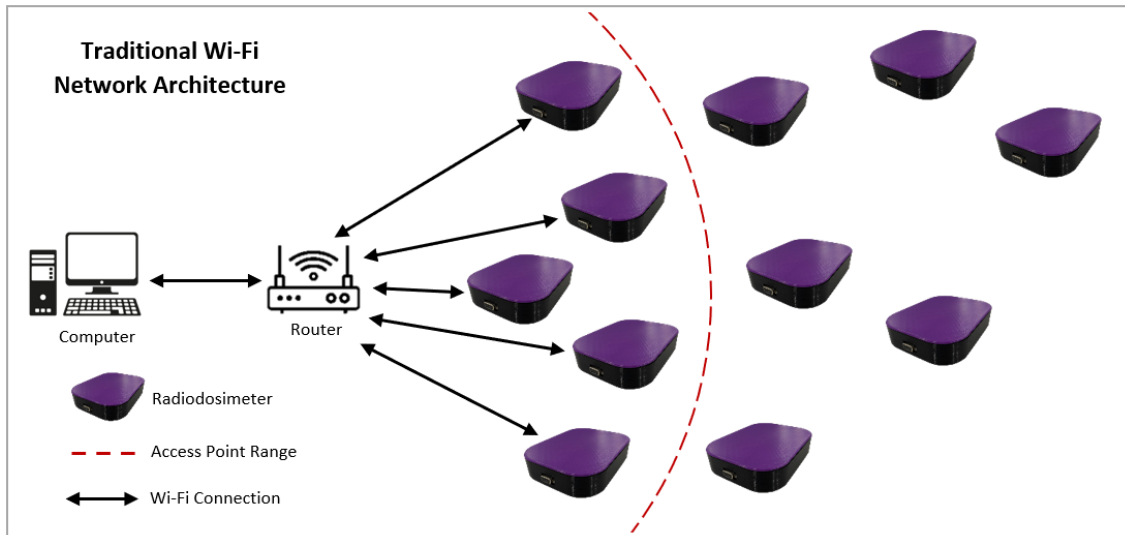


Figure 7.23: Traditional Wi-Fi Network Architecture. The single access point (router) has finite range. Radiosimulators which travel too far away result in disconnection.

The decentralised Wi-Fi mesh network shown in figure 7.24 is proposed to overcome the star network limitation, without requiring more infrastructure to be installed. In this network type, a decentralised network of Radiosimulators operating in ad hoc mode are permitted to connect to neighbouring Radiosimulators to extend the network. Radiosimulators within range still connect to the access point router, but those out of range can relay information back to the central hub along a chain of nearby Radiosimulators.

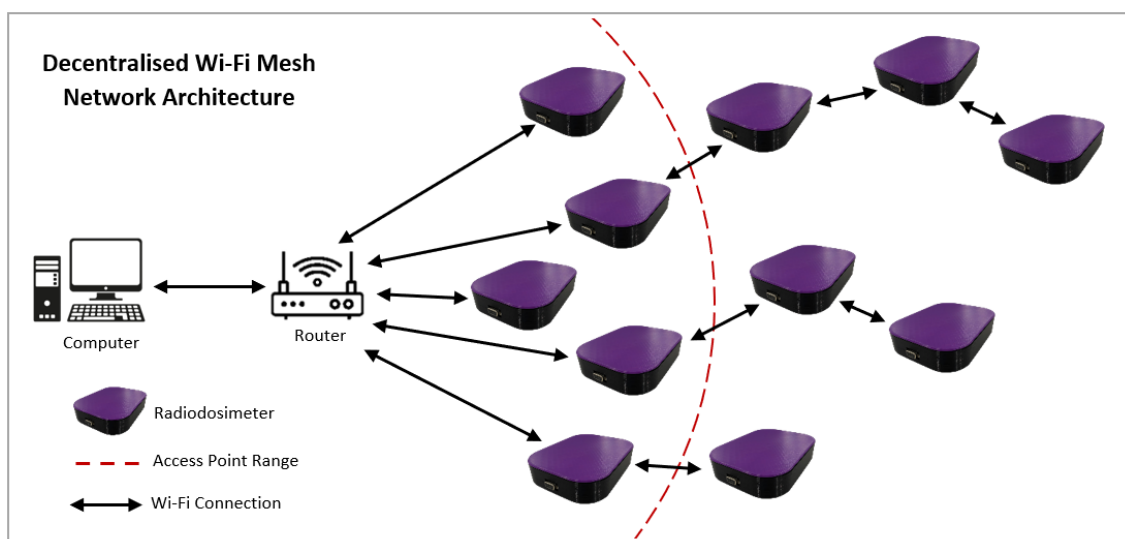


Figure 7.24: Decentralised Wi-Fi Mesh Network Architecture. The single access point (router) has finite range. Radiosimulators within range connect to the access point by default. Radiosimulators out of range are permitted to connect to the closest neighbouring Radiosimulator, extending the network mesh.

The investigation into the feasibility and application of an ad hoc decentralised Wi-Fi network of Radiodosimeters to provide communication in remote areas will be investigated in future work. The connection and monitoring of multiple devices will be developed in future versions of the software suite.

Future Improvement - External Display

An essential upgrade to the Radiodosimeter is the addition of an external display with control buttons. The status of the electronics and acquisition should be made available by inspecting the readout screen. This is especially useful for troubleshooting network connectivity issues. A small, low resolution screen would be suitable to display a few lines of text such as current Wi-Fi network and acquisition status. For the purposes of radioprotection, it could be used as an alert to indicate the detection of potentially dangerous environmental conditions.

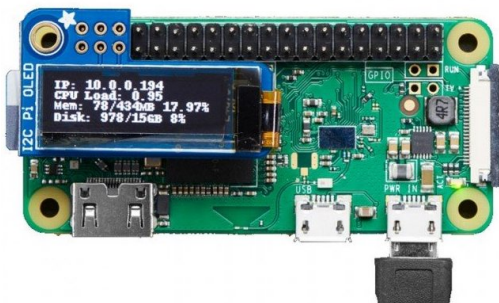


Figure 7.25: OLED display for Raspberry Pi Zero [180].



Figure 7.26: e-Ink display [181].

Two potential display types are organic-LED (OLED) and e-Ink, shown in figure 7.25 and 7.26, respectively. OLED uses a small amount of power as the backlight does not need to be on for pixels that are blank. The price of OLED is low nowadays.

e-Ink is unique as it does not require power to hold an image on the screen, only when pixels are updated. e-Ink is commonly used in Amazon Kindle reading tablet screens. Power is only required to update the image, which takes less than a second to do so. After it has updated, the image will be retained on the screen for several days until updated

again. However, the price of an e-Ink display is slightly higher than OLED.

A rotary push wheel can be employed next to the screen which can be used to navigate menus. The ability to interact directly with the Radiodosimeter is important when considering the viability of a personal wearable device (ie. handheld or badge microdosimeter).

Future Improvement - iPad application

For the purpose of demonstrating the use of this technology, presenting the software running on an iPad looks much more refined and completed. As the software is written using Qt5, which supports multi-platform applications, it is simple to implement for multiple device types. End consumer software for management of Radiodosimeters from a tablet provides a better user experience. The tablet can be used as a management console for monitoring each Radiodosimeter connected to the network.

Future Improvement - Ultra low power data transmission

Another important upgrade to consider is a solution to provide longer battery life and more functional meshed networking. Figure 7.27 displays several wireless data transmission modes in terms of bandwidth and range of different modalities. For the Radiodosimeter, Wi-Fi (802.11n) is currently used for wireless connectivity due to several factors such as cross-platform functionality on all devices. The drawback is that Wi-Fi uses a lot of power, which is one of the limiting factors in the device practicality.

Bluetooth Low-Energy (BLE) is an alternative to Wi-Fi as it uses much less power when transmitting and receiving information. However, its range is poor and requires more gateways (base stations) to maintain connectivity throughout a large area.

A new emerging wireless technology is Low-Power Wide-Area Networking (LPWAN) which provides very long range networking with very low power consumption [183]. LoRa (Long Range transmission methodology) is a type of LPWAN that uses ultra low frequencies (915 MHz), allowing transmissions up to 15km in open air [183]. The tech-

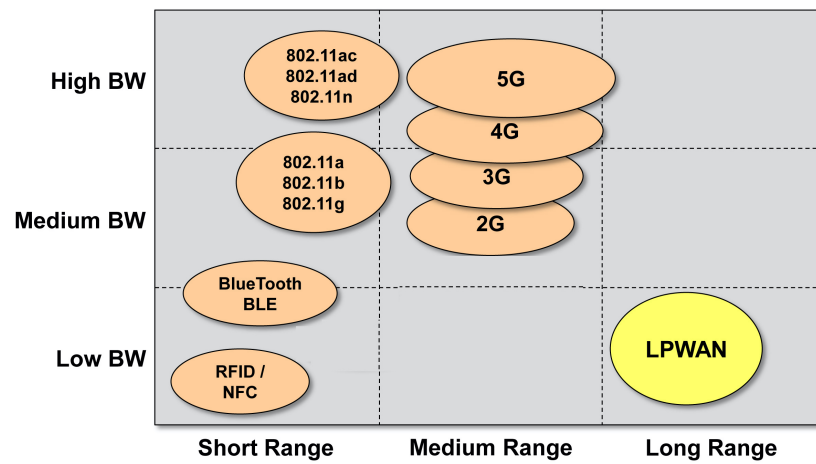


Figure 7.27: Summary of wireless data transmission modes [182]. RFID, BLE, 802.11 (Wi-Fi), 2G/3G/4G/5G (mobile phone networks) and LPWAN.

nology is designed for small devices so that they use minimal power and depending on the calculation load, the battery can last years without charging. Consumer products are available that can be plugged into a RPi. UOW SMART Infrastructure has an open source project in Wollongong for broadcasting these signals and connecting devices to it [184].

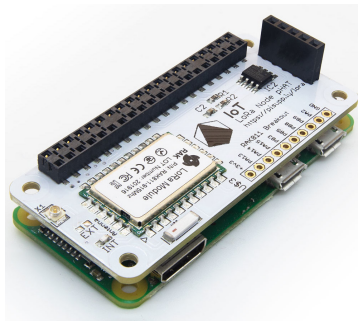


Figure 7.28: LoRa node module for Raspberry Pi Zero [185]. Note the module is as small as the RPi so its presence is negligible.



Figure 7.29: Cisco LoRa gateway host module [186]. This is a high end model used for industrial purposes.

A private LoRa network would allow meshed connectivity of Radiodosimeters in remote areas, which can be monitored on a management server console. An example of a remote location that requires long range transmission is an underground mine. The information between multiple host gateways can be relayed between each other, such as a meshed link down a mine tunnel, sending information back to the main host on the

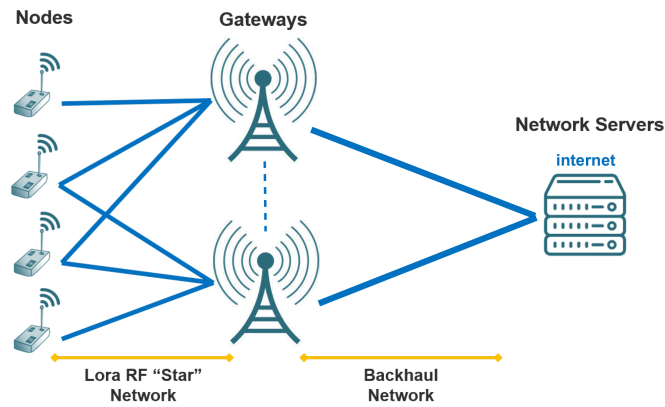


Figure 7.30: Simple LoRa network diagram showing the data transfer between nodes (Radiodosimeters) and gateways (LoRa host modules to receive and send data between the Radiodosimeter and management server). Adapted from [187].

surface. The longer wavelength of these signals would be beneficial as it can travel further through dense material. Figure 7.30 shows the data transfer between nodes and host gateway modules. In the scenario of a mine tunnel, each worker could wear their personal microdosimeter, which remains connected to host gateways positioned throughout the mine. The information would be relayed back across each gateway, reporting the readings of each microdosimeter on the management console.

The use of Low Power data transmission (ie. LoRa or BLE) addresses several limitations of the prototype Radiodosimeter system such as battery life. The application of either connectivity methods in the Radiodosimeter would be required to successfully produce wearable microdosimetry devices. With higher capacity batteries, optimised software and low power data transmission; a compact wearable microdosimeter can be produced.

The ability of the Radiodosimeter to operate independently from a client computer proves its extreme portability advantage for personal monitoring of mixed radiation fields in remote areas. The Radiodosimeter allows streamlined QA process in particle therapy that can be carried out by a technician without in-depth training, due to simplicity and automation of the microdosimeter system. The developed Radiodosimeter can be utilised in a network for radiation protections and homeland security purposes as it has selective sensitivity to different components of the mixed radiation field.

Chapter 8

Validation of different physics models in Geant4 and MCNP6 for QA in FNT and BNCT

In this chapter, the performance of Monte Carlo codes, Geant4 version 10.5.p01 and MCNP version 6.2 are benchmarked. Different physics options were used to describe the hadronic physics interactions for neutrons of various monoenergies within a water phantom.

Specific quantities simulated in the water phantom are compared such as, total depth dose, individual components contributing to total depth dose, and neutron fluence. The simulations are performed in both natural water and 50ppm ^{10}B loaded water phantoms.

The purpose of this work is to benchmark specific physics options available in the two simulation codes for QA in FNT and BNCT. The methodical presentation of the results should assist relevant users, by considering the similarities and differences that must be assessed when simulating neutrons with energies ranging from thermal to fast.

8.1 Method

Physics Options

Fourteen different physics options of Geant4 and MCNP6 were benchmarked. The different physics options used in the two codes are shown in table 8.1. A rigorous assessment on the specific processes of the different physics lists and the thermal neutron treatment is outlined in chapter 3.

#	Label for results	Physics List
<u>Geant4</u>		
1.	BICHP	QGSP_BIC_HP
2.	BERTHP	QGSP_BERT_HP
3.	INCLHP	QGSP_INCLXX_HP
4.	Shield	Shielding
5.	LEND	G4LEND
6.	BICAllHP	QGSP_BIC_AllHP
7.	BICHP/T	QGSP_BIC_HP with thermal neutron treatment enabled
8.	BERTHP/T	QGSP_BERT_HP with thermal neutron treatment enabled
9.	INCLHP/T	QGSP_INCLXX_HP with thermal neutron treatment enabled
10.	Shield/T	Shielding with thermal neutron treatment enabled
11.	LEND/T	G4LEND with thermal neutron treatment enabled
12.	BICAllHP/T	QGSP_BIC_AllHP with thermal neutron treatment enabled
<u>MCNP6</u>		
13.	MCNP	Bertini INC
14.	MCNP/T	Bertini INC with thermal neutron treatment enabled

Table 8.1: Fourteen selected physics options for the Geant4 and MCNP6 simulations performed in this chapter. Seven different hadronic physics lists for Geant4, with thermal neutron treatment disabled (no /T labelled) and enabled (labelled with /T). MCNP uses the Bertini INC hadronic physics model with with thermal neutron treatment disabled (no /T labelled) and enabled (labelled with /T).

As seen in table 8.1, seven distinct hadronic physics lists are tested in Geant4. These seven are considered with thermal neutron treatment disabled (no /T labelled) and enabled (labelled with /T). Electromagnetic standard option 4 (EMZ) was used in Geant4. All of the seven physics lists use high-precision (HP) evaluated data models, defined by G4NDL4.5. This is with the exception of ‘G4LEND’. Whilst LEND also derives from ENDF/B-VII.1 data, it uses a different physics model.

For MCNP6, the Bertini INC hadronic physics model is used, with thermal neutron treatment disabled (no /T labelled) and enabled (labelled with /T).

It is important to reiterate that the high precision neutron dataset used in Geant4 and MCNP are only valid up to their energy limit, which is usually 20 MeV. For neutrons above this energy, the inelastic interactions are defined by the particular physics model.

Simulation Geometry and Scoring Methods

A simple phantom was defined with dimensions $30 \times 30 \times 30 \text{ cm}^3$. The phantom box was segmented along the z-axis with 0.5 cm intervals to define the scoring regions. A 5 cm diameter circular plane beam of neutrons with different monoenergies was fired at the x-y plane of the phantom face (surface at $z=0$) with normal incidence. The neutron fluence and dose component contribution by different reactions was scored in the z-axis segments. These are recorded using the Sensitive Detector class in Geant4, and the PTRAC card in MCNP.

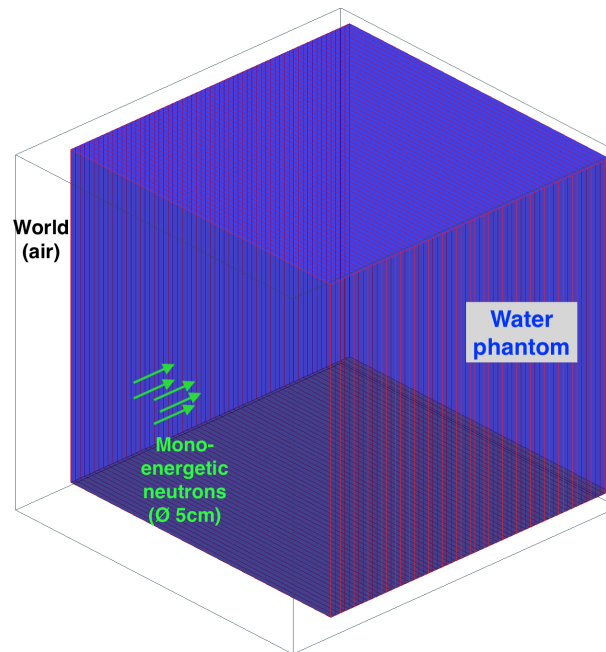


Figure 8.1: Geometry visualisation of the segmented water phantom inside the air world used in Geant4 from bird's-eye view. The water phantom has been segmented in z axis by 0.5 cm increments (shown with red lines in the phantom).

The simulations were performed in phantoms consisting of natural water (section 8.2)

and 50ppm ^{10}B loaded water (section 8.3). The ‘world’ surrounding the phantom contains air in both cases. The geometry is shown in figure 8.1.

Neutron monoenergies simulated

The eighteen different neutron monoenergies simulated are shown in table 8.2. Note that each monoenergy requires its own separate simulation.

eV range:	0.0253 eV, 0.1 eV, 1 eV, 10 eV, 100 eV,
keV range:	1 keV, 10 keV, 100 keV,
MeV range (HP):	1 MeV, 2 MeV, 5 MeV, 10 MeV, 20 MeV,
MeV range (non-HP):	30 MeV, 40 MeV, 50 MeV, 60 MeV, 70 MeV.

Table 8.2: Eighteen different neutron monoenergies simulated in this chapter.

Statistical Analysis

The two sided Kolmogorov-Smirnov (KS) test was used to quantify the agreement between distributions derived from different data sets [188]. The KS test is a goodness-of-fit statistics test, which analyses the maximum vertical distance between the cumulative frequency distribution of each data-set F_1 and F_2 , as shown in equation 8.1. The KS test output is known as a p-value, which represents the test of the null hypothesis that the two compared distributions are similar trend. The best agreement between data is established by results with a p-value closest to 1.0.

$$\max(|F_1(x) - F_2(x)|) \quad (8.1)$$

To provide a simple indication of how closely each distribution agrees with another, the percentage difference (PD) is also presented. The PD is derived from taking the mean difference of all points in the distributions being compared (F_1 and F_2), as shown in equation 8.2.

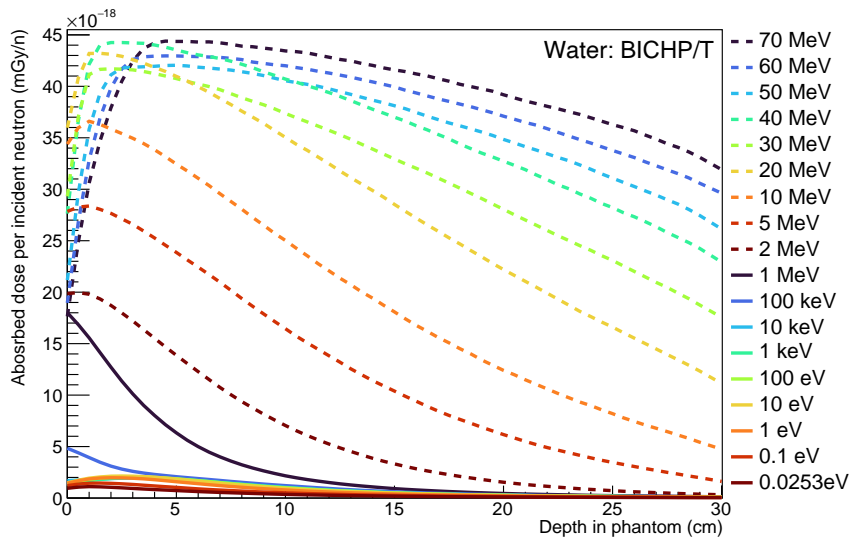
$$\langle PD \rangle = \frac{100}{n} \left(\sum_{x=1}^n \frac{F_1(x) - F_2(x)}{F_2(x)} \right) \quad (8.2)$$

8.2 Monoenergetic neutrons in water phantom

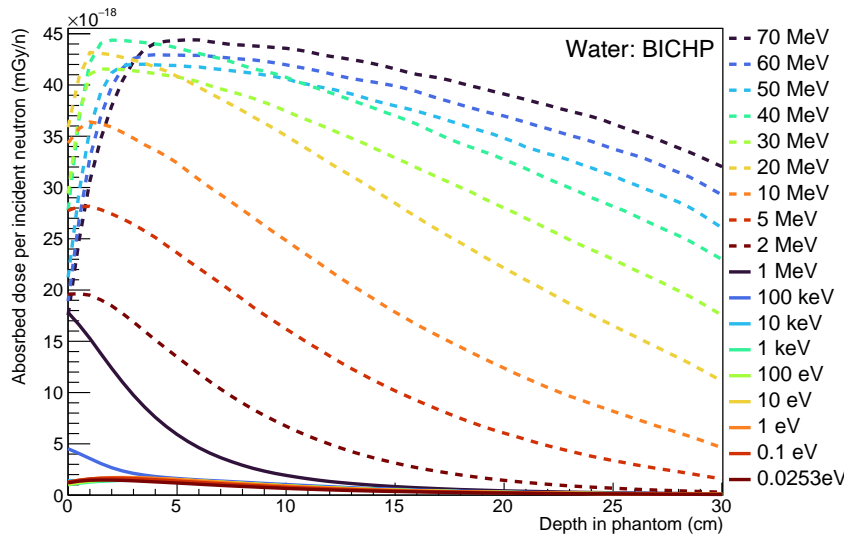
8.2.1 Comparison of BICHP with neutron thermal treatment on/off

Total depth dose in water phantom

Figures 8.2a and 8.2b present the total depth dose in the water phantom using Geant4 BICHP with the thermal neutron treatment enabled and disabled, respectively. The same data is shown zoomed on the lower monoenergies in figures 8.3a and 8.3b.



a. BICHP/T



b. BICHP

Energy	p	PD %
0.0253eV	0.002	32.43
0.1 eV	0.016	14.01
1 eV	0.079	-12.92
10 eV	0.177	-22.07
100 eV	0.258	-23.48
1 keV	0.292	-24.46
10 keV	0.122	-25.60
100 keV	0.414	-6.42
1 MeV	0.898	-1.12
2 MeV	0.973	-1.57
5 MeV	0.997	-0.75
10 MeV	1.000	-0.59
20 MeV	0.999	-0.10
30 MeV	0.998	-0.34
40 MeV	0.997	0.27
50 MeV	1.000	-0.06
60 MeV	0.999	-0.01
70 MeV	1.000	0.03

Table 8.3: Statistics tests for depth dose distribution of monoenergetic neutrons in water phantom, comparing BICHP against BICHP/T.

Figure 8.2: Absorbed dose per incident neutron as a function of depth in water phantom for monoenergetic neutrons using BICHP with thermal treatment on (a) and off (b).

Table 8.3 presents the p-value and PD statistics test results when comparing the distribution of BICHP against BICHP/T. The result indicates that only neutron energies above 5 MeV produce the same distribution (as the p-value approaches 1.0).

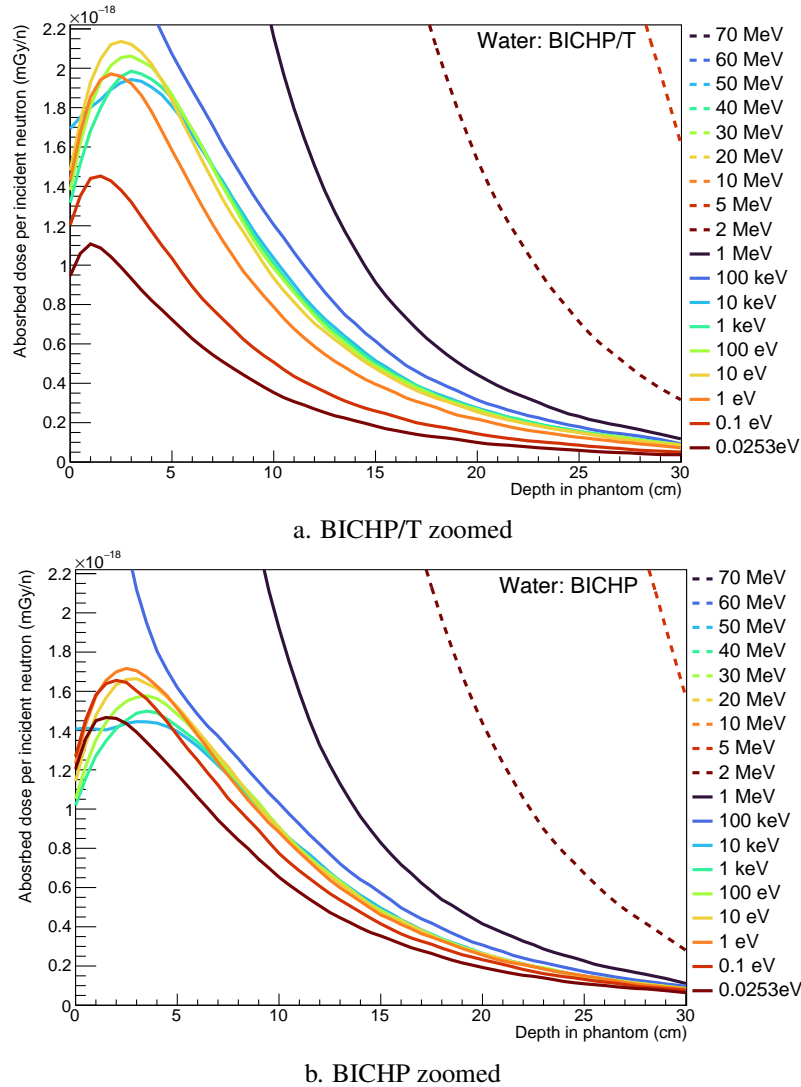
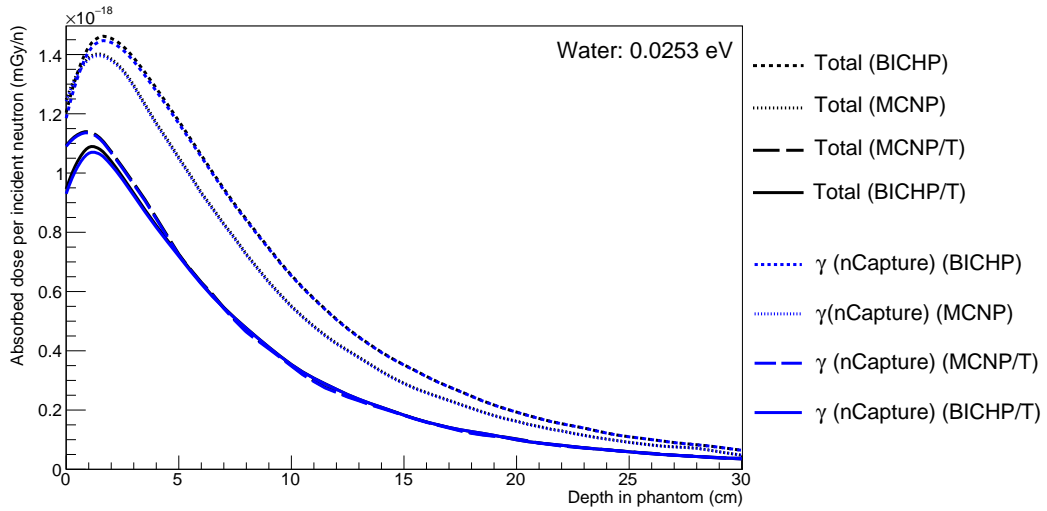


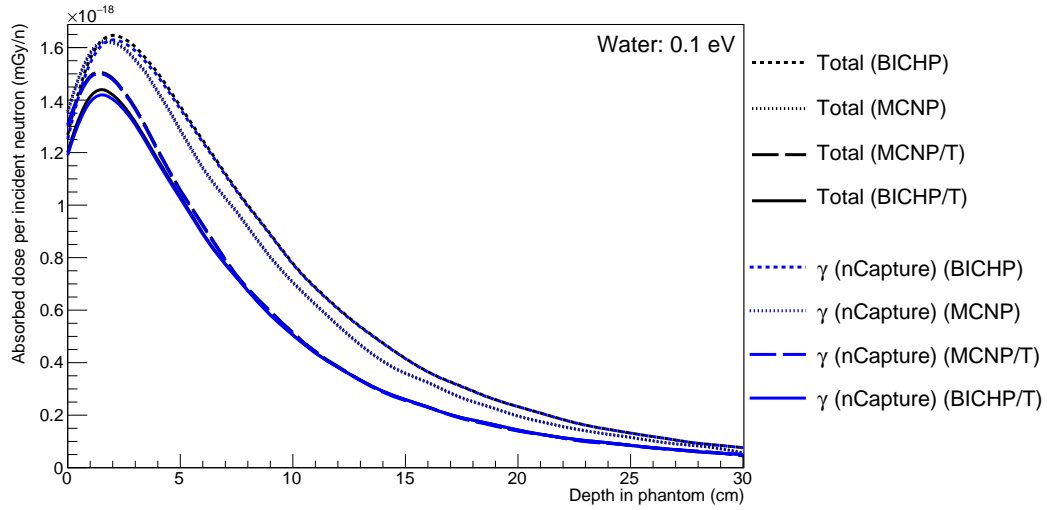
Figure 8.3: Absorbed dose per incident neutron as a function of depth in water phantom for monoenergetic neutrons using BICHP with thermal treatment on (a) and off (b). Same as Figure 8.2 but zoomed in to show lower energies.

Individual components contributing to total depth dose

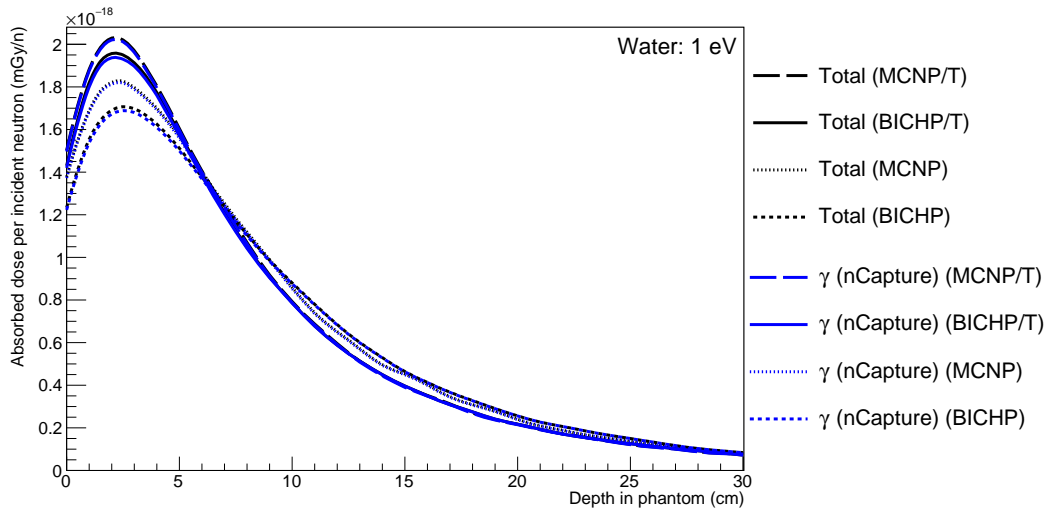
The following results present individual depth dose plots for each neutron monoenergy. The individual components that contribute to the total depth dose are shown for BICHP, BICHP/T, MCNP, and MCNP/T. Note that for 1 MeV energies onward, only BICHP and MCNP are shown, as the result for thermal neutron on/off are the same.



a. 0.0253 eV

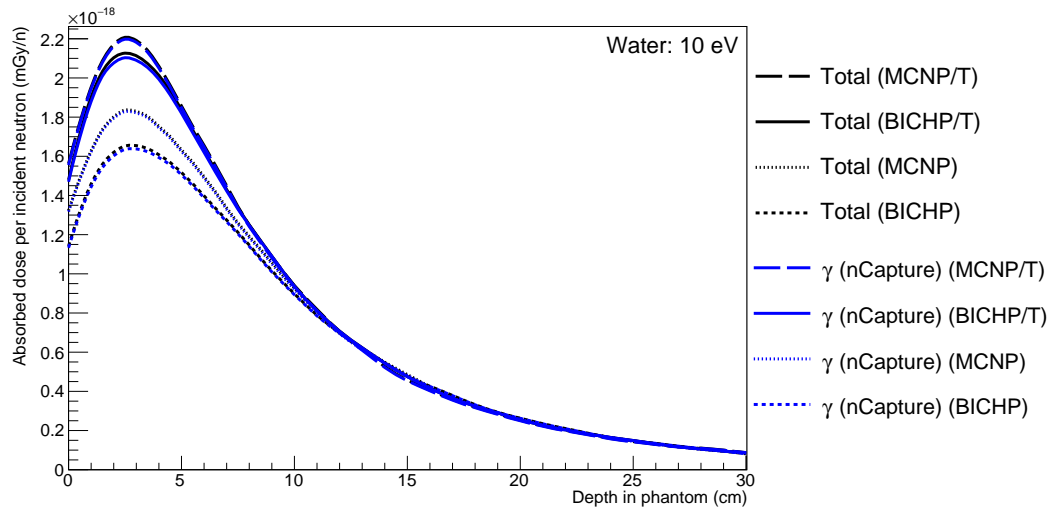


b. 0.1 eV

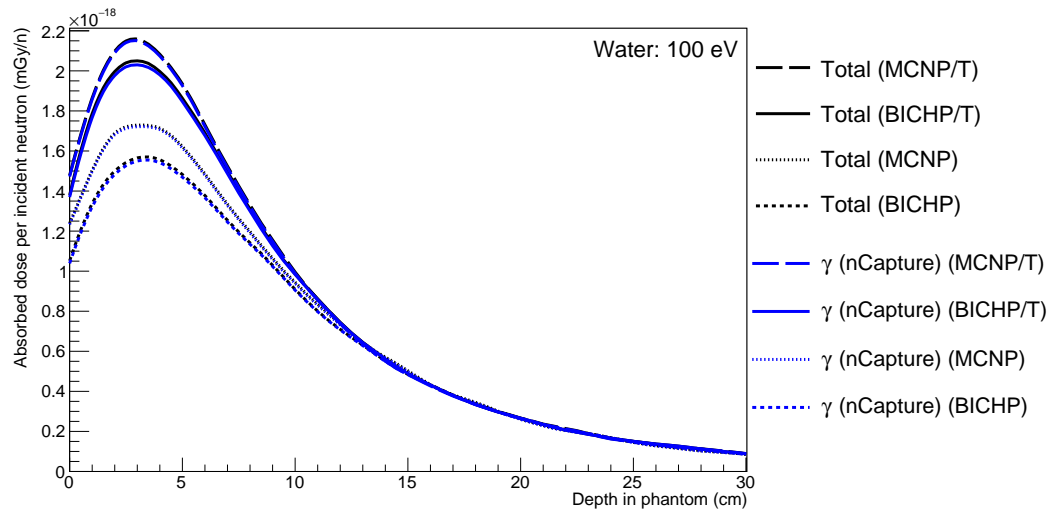


c. 1 eV

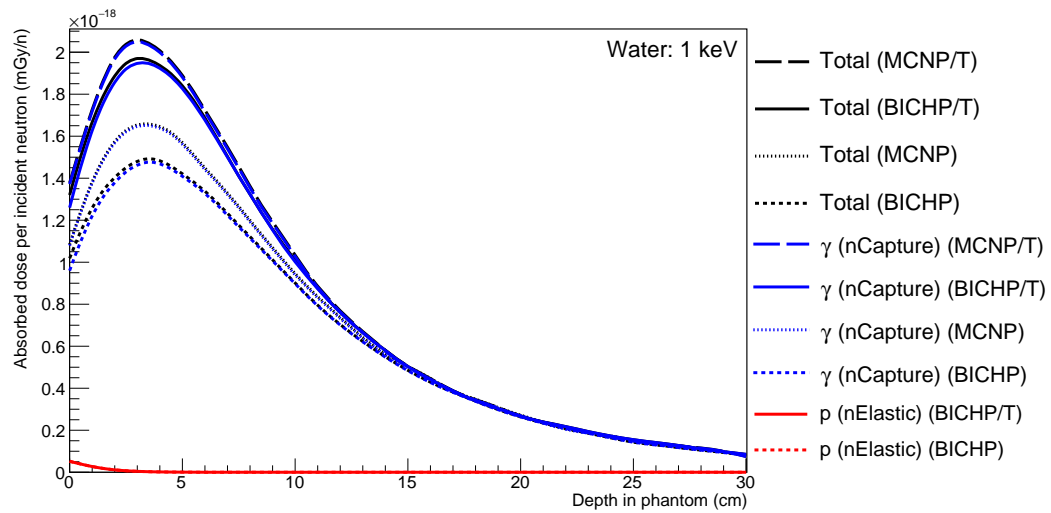
Figure 8.4: Absorbed dose per incident neutron as a function of depth in water phantom represented in terms of individual components calculated using BICHP and MCNP with T and noT; 0.0253 eV, 0.1 eV and 1 eV neutrons.



d. 10 eV

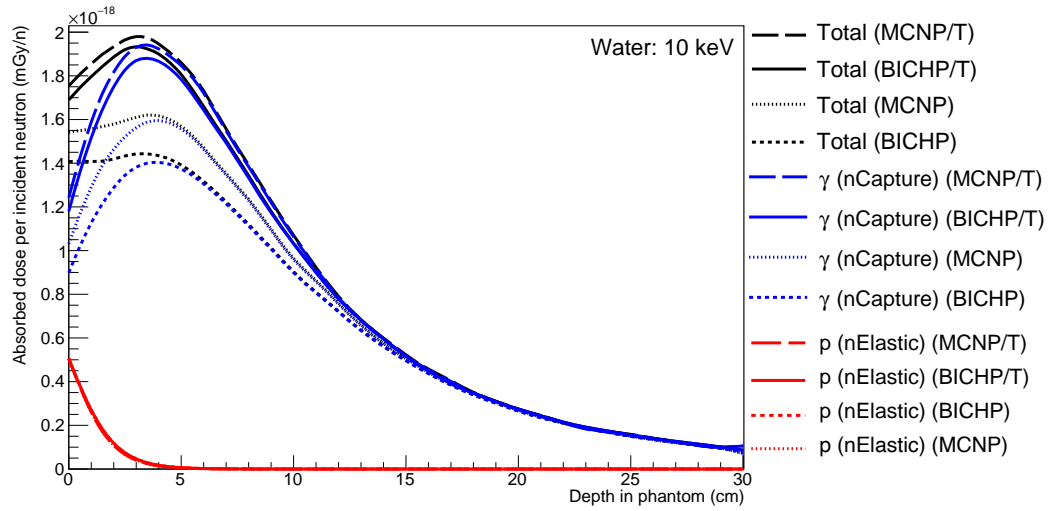


e. 100 eV

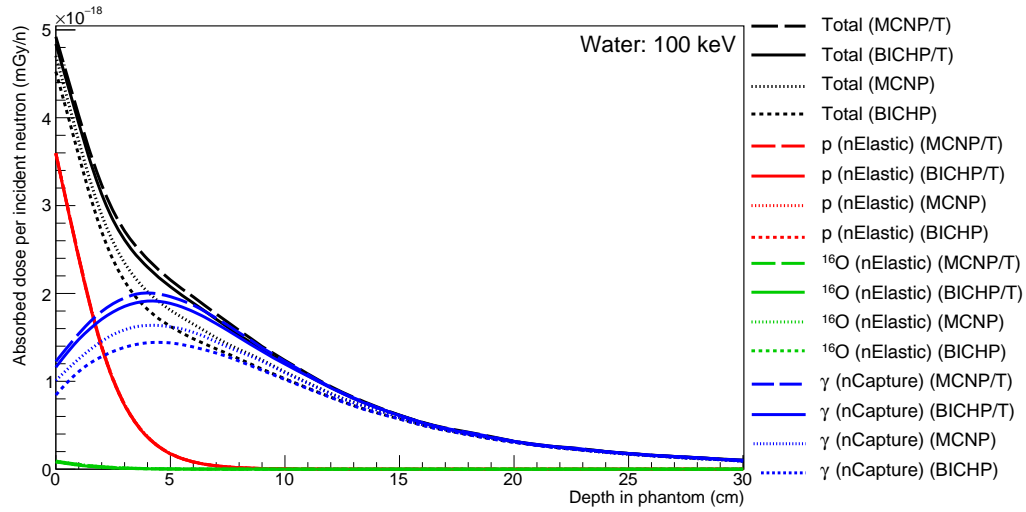


f. 1 keV

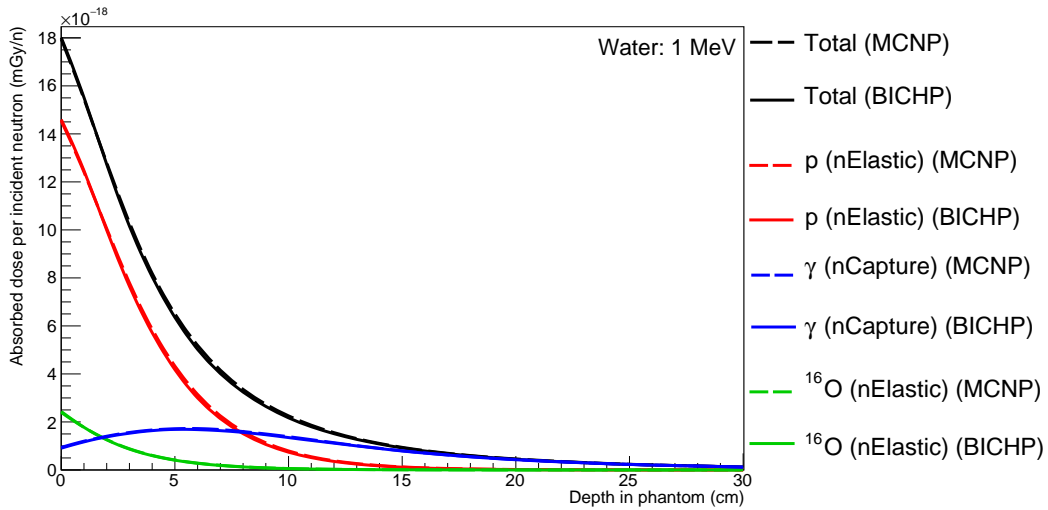
Figure 8.5: Absorbed dose per incident neutron as a function of depth in water phantom represented in terms of individual components calculated using BICHP and MCNP with T and noT; 10 eV, 100 eV and 1 keV neutrons.



g. 10 keV

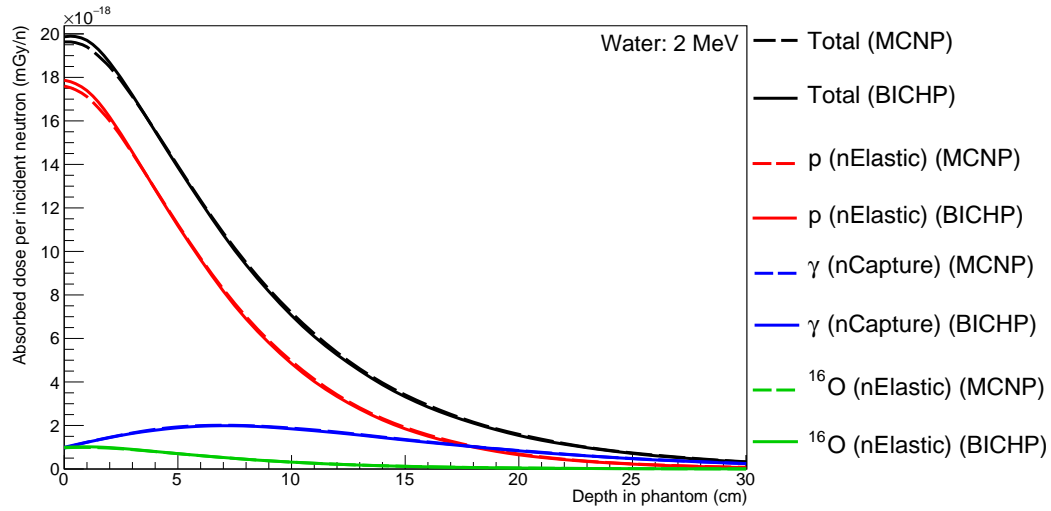


h. 100 keV

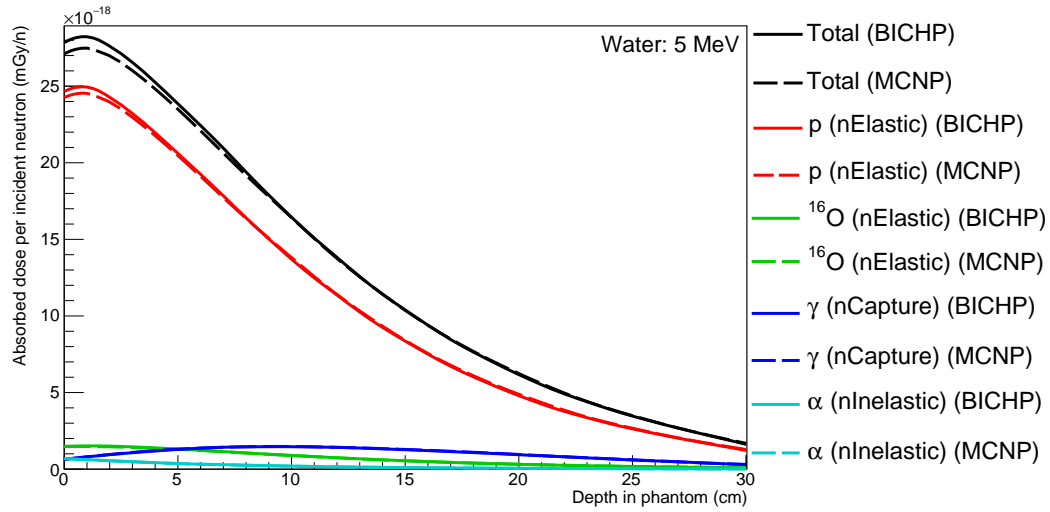


i. 1 MeV

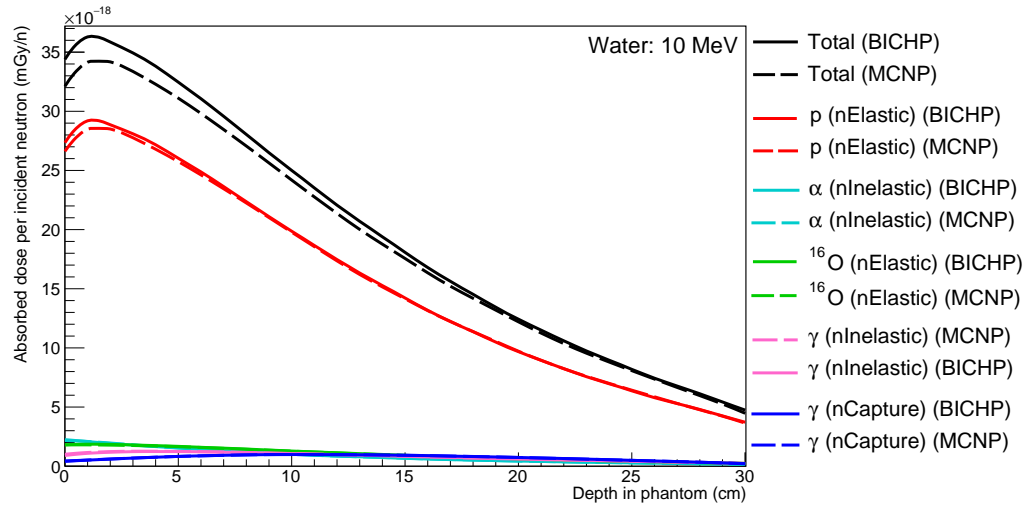
Figure 8.6: Absorbed dose per incident neutron as a function of depth in water phantom represented in terms of individual components calculated using BICHP and MCNP with T and noT; 10 keV and 100 keV. With only T; 1 MeV neutrons.



j. 2 MeV



k. 5 MeV



l. 10 MeV

Figure 8.7: Absorbed dose per incident neutron as a function of depth in water phantom represented in terms of individual components calculated using BICHP and MCNP with only T; 2 MeV, 5 MeV and 10 MeV neutrons.

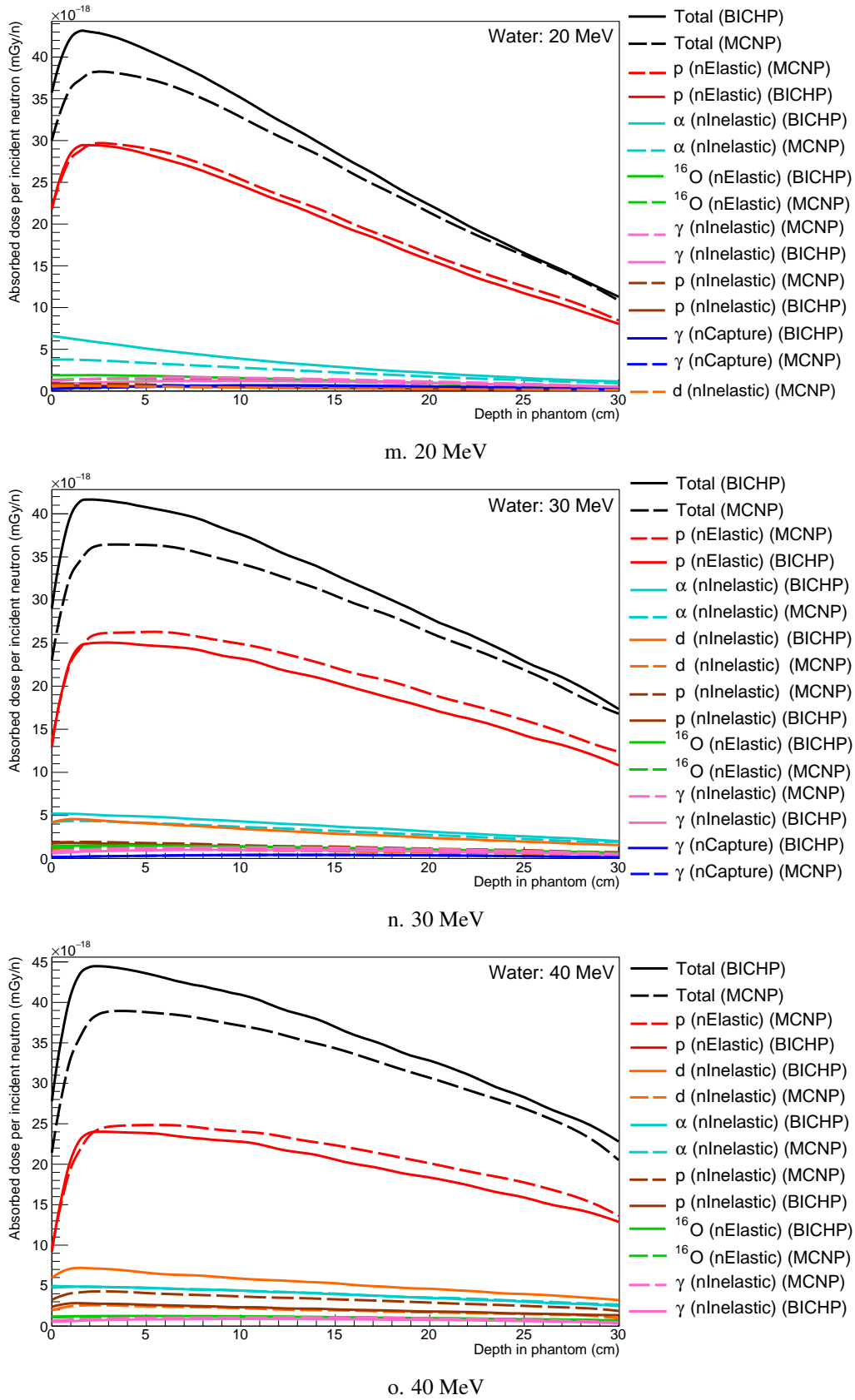
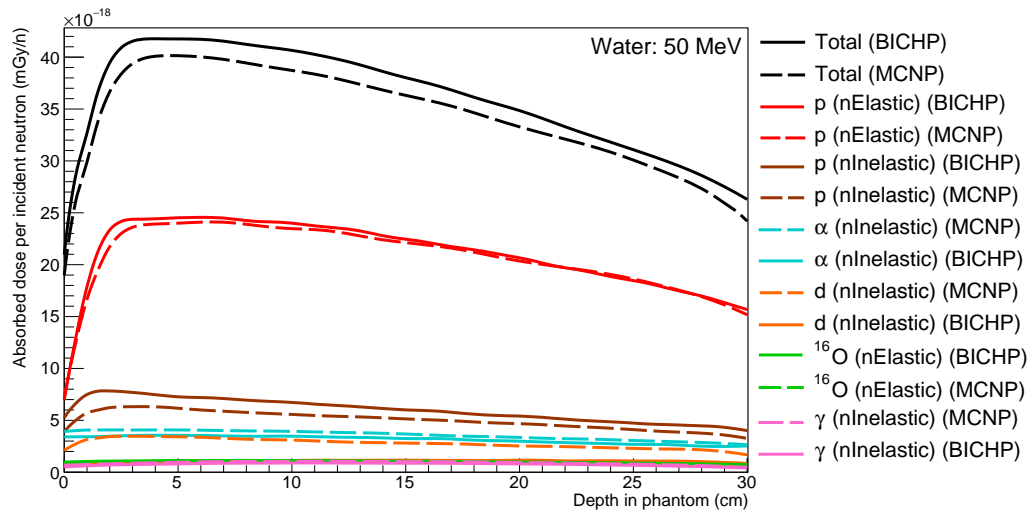
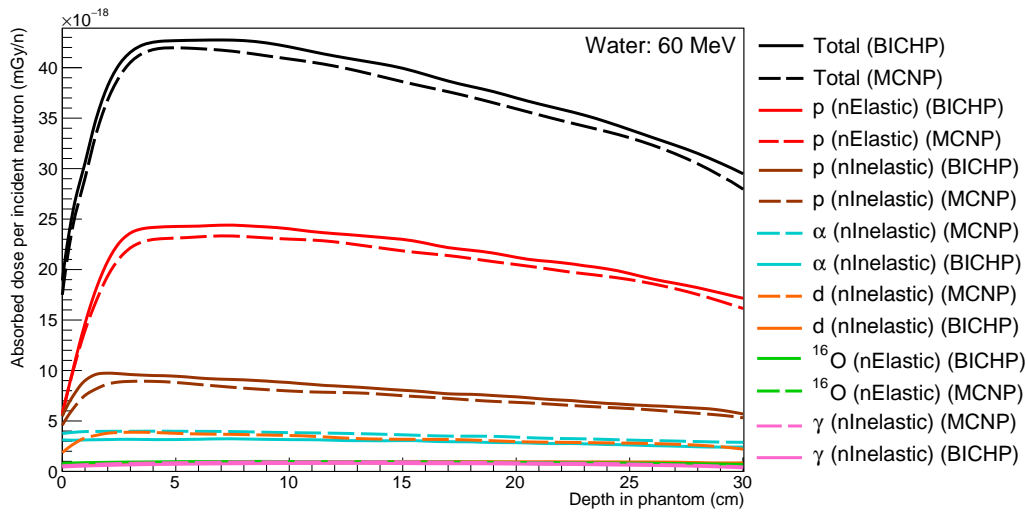


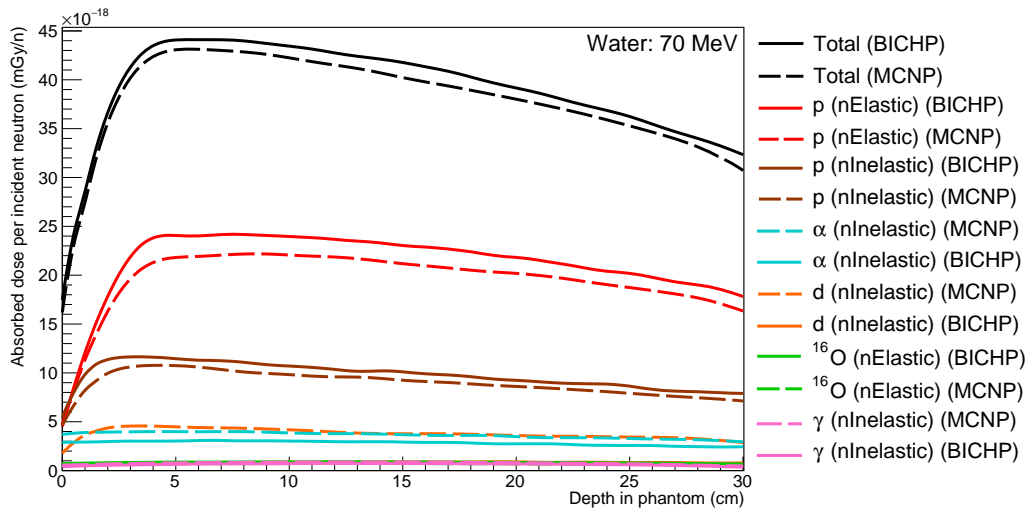
Figure 8.8: Absorbed dose per incident neutron as a function of depth in water phantom represented in terms of individual components calculated using BICHP and MCNP with only T; 20 MeV, 30 MeV and 40 MeV neutrons.



p. 50 MeV



q. 60 MeV



r. 70 MeV

Figure 8.9: Absorbed dose per incident neutron as a function of depth in water phantom represented in terms of individual components calculated using BICHP and MCNP with only T; 50 MeV, 60 MeV and 70 MeV neutrons.

From the results presented in figures 8.4 to 8.9, it is observed that Geant4 and MCNP have a similar outcome in terms of: total depth dose, and the proportion and types of reactions occurring. This is especially true for when thermal neutron treatment is applied in Geant4 and MCNP. This can be attributed to the fact that both Geant4 and MCNP use the same ENDF data to describe the inelastic neutron processes and similar thermal neutron scatter models.

However, when moving to 20 MeV energy neutrons, there are some large differences observed, as seen in figure 8.8m. Specifically, this is when evaluated datasets from ENDF are no longer used and the inelastic physics models of the two codes are applied. That being said, there appears to be conformity returning above 50 MeV neutron monoenergies.

One major difference in the individual components is observed between 30 MeV to 70 MeV, specifically relating to the proportion of deuterons vs. protons that are produced by neutron inelastic interactions. For these neutron energies, deuterons are produced mainly by $^{16}\text{O}(n,d)^{15}\text{N}$, and protons by $^{16}\text{O}(n,n+p)^{15}\text{N}$ reactions. As seen in figures 8.8n (30 MeV) to 8.9r (70 MeV), the proportion of inelastically produced protons (brown lines) and deuterons (orange lines) in Geant4 and MCNP seem to have a countered balance. It is speculated that Geant4 and MCNP favours one of these reactions over the other for non-HP energies.

8.2.2 Comparison of different physics options in water phantom

The next set of results compares the total depth dose for the fourteen different physics lists. All results are superimposed to allow a visual comparison and assess the differences between the physics options.

It is observed that enabling the thermal neutron treatment separates the total depth dose result of all physics lists into two distinct sets of distributions. This is with the exception of the MCNP physics option without thermal treatment, which presents a high deviation to the other non-thermal treatment options below 1 MeV.

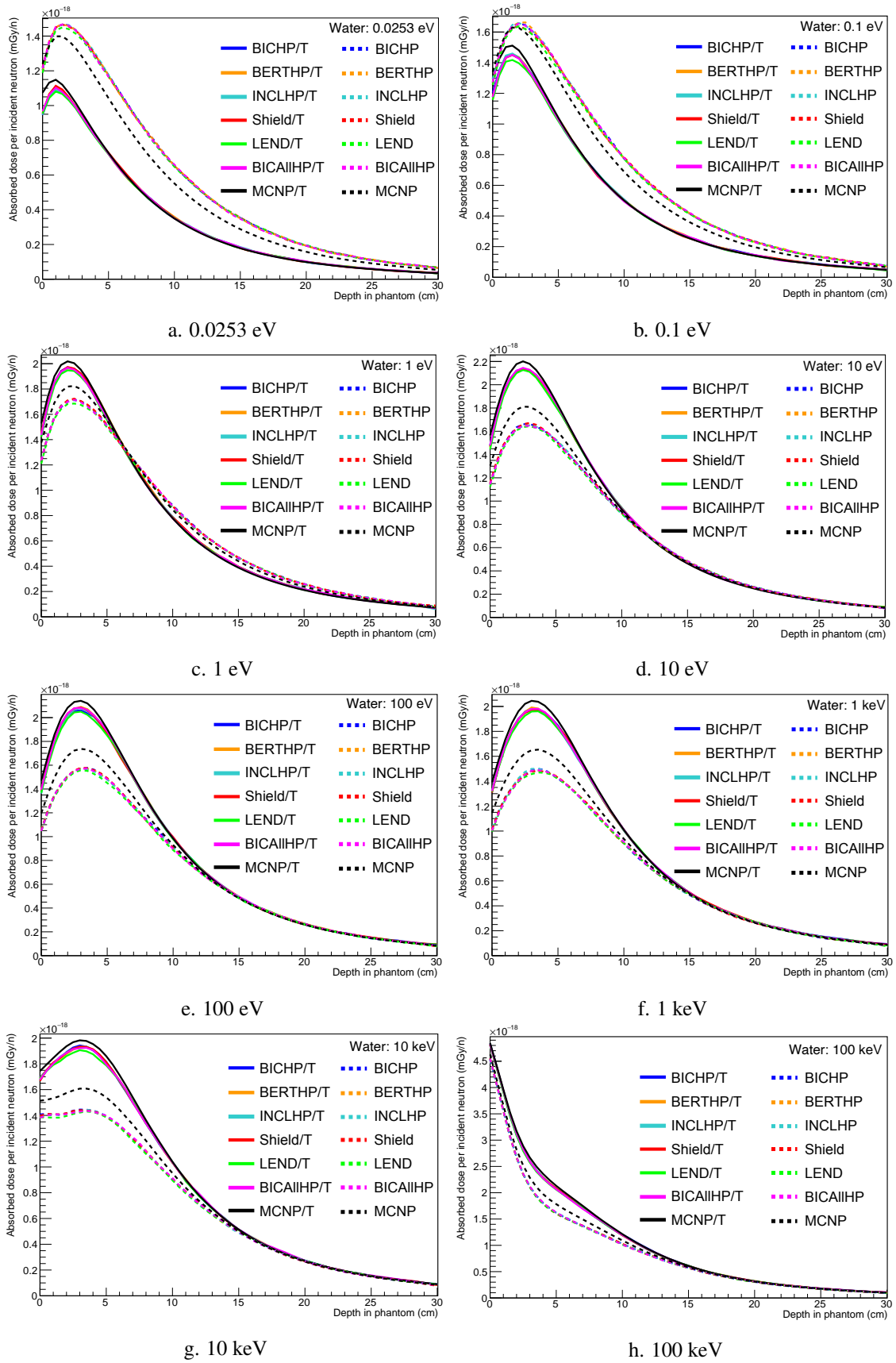


Figure 8.10: Absorbed dose per incident neutron as a function of depth in water phantom; 0.0253 eV to 100 keV.

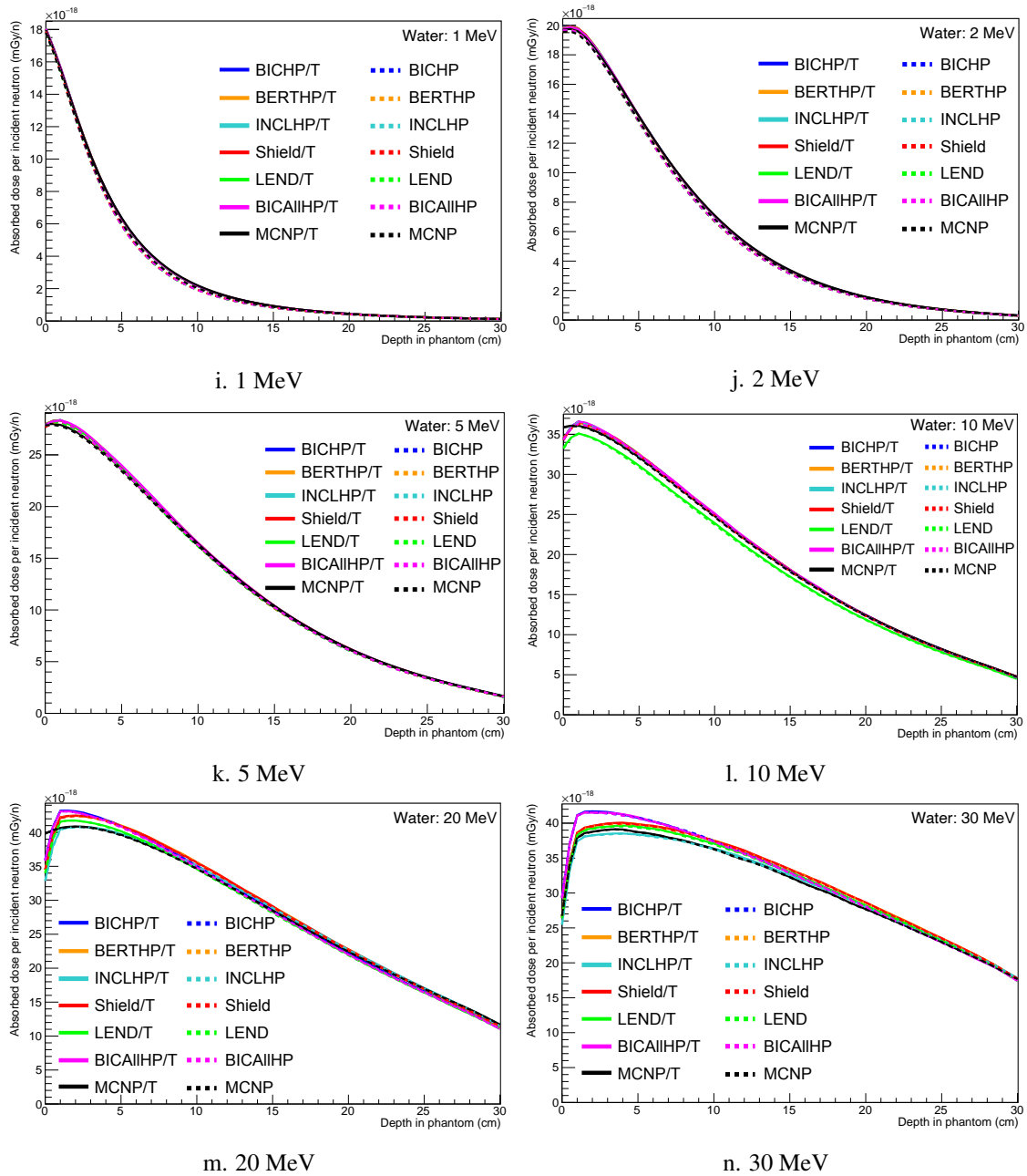


Figure 8.11: Absorbed dose per incident neutron as a function of depth in water phantom; 1 MeV to 30 MeV.

From neutron energies of 1 MeV (figure 8.11i) onward, it is observed that the use of thermal neutron treatment does not have any considerable effect. That is, the relevant physics lists for thermal neutron treatment disabled/enabled converge. The first major difference is observed for 10 MeV (figure 8.11l), with LEND reporting a lower total depth dose. From 20 MeV (figure 8.11m) to 70 MeV (figure 8.12r), the physics models are no longer based on evaluated data, and now use their own process to describe the neutron

interactions.

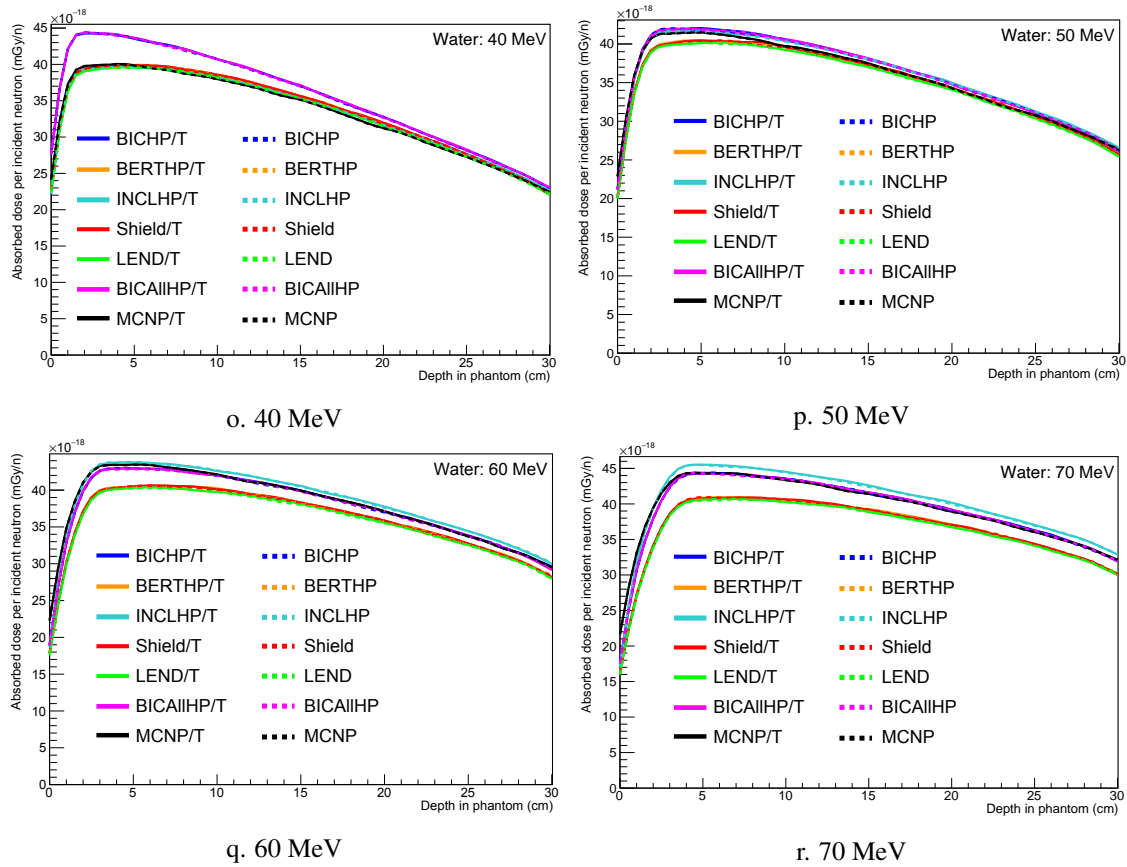


Figure 8.12: Absorbed dose per incident neutron as a function of depth in water phantom; 40 MeV to 70 MeV.

The physics models that converge to the same distributions are grouped here with their neutron process above 20 MeV listed:

1. BICHP, BICAIHP (Binary Cascade).
2. BERTHP, Shield, and LEND (Bertini Cascade).
3. INCL (INCL++),
4. MCNP (Bertini Cascade).

Note that MCNP uses Bertini Cascade in this case, but it is not always converging with BERTHP. This is observed for 20 to 30 MeV, where MCNP follows INCLHP, then BERTHP at 40 MeV, and finally follows BICHP from 30 MeV to 70 MeV. The statistics tests for p-value goodness-of-fit and PD have been graphed in figures 8.13 and 8.14, which further illustrate the trend between the relevant physics lists.

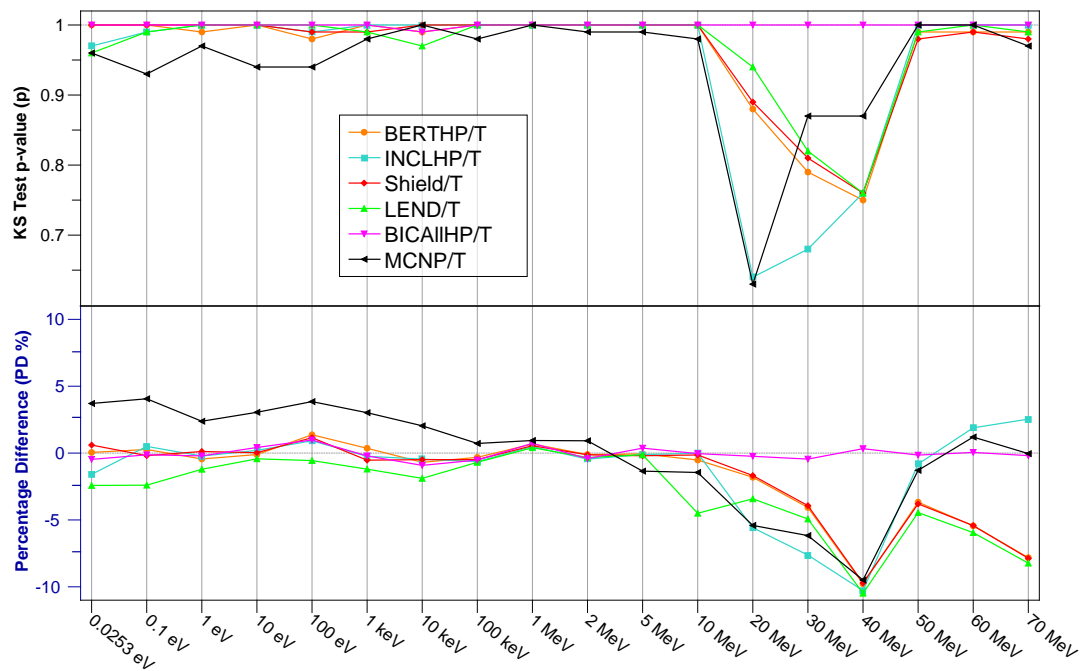


Figure 8.13: Statistics tests for depth dose distribution of monoenergetic neutrons in water phantom for the different physics lists compared against BICHP. All physics with thermal on (T) are compared against BICHP/T. Data shown in table A.1 of Appendix A.1.

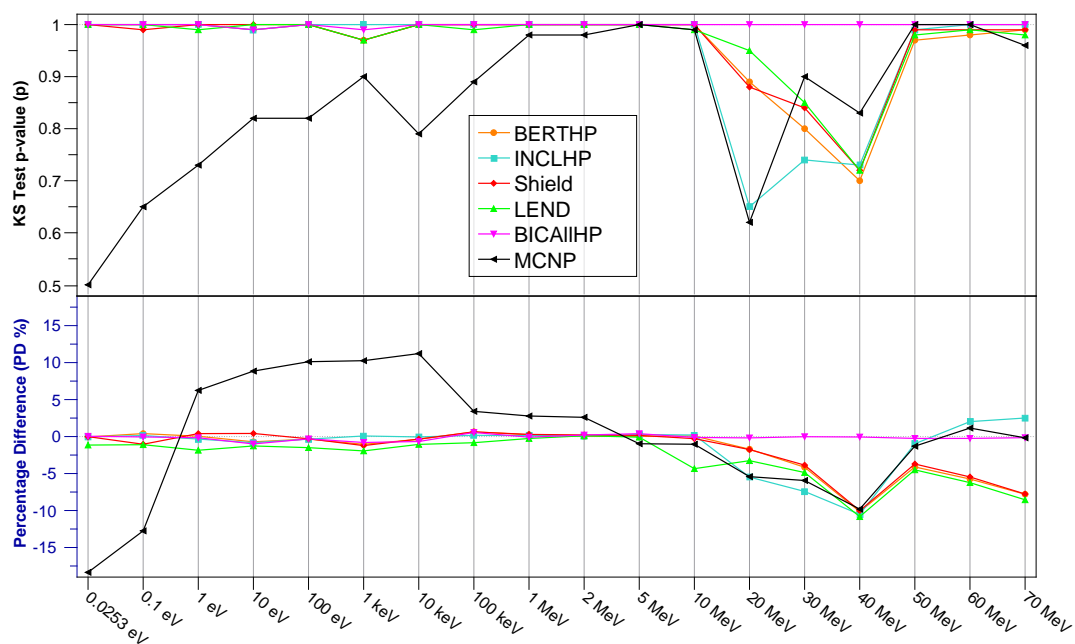


Figure 8.14: Statistics tests for depth dose distribution of monoenergetic neutrons in water phantom for the different physics lists compared against BICHP. All physics with thermal off (noT) are compared against BICHP. Data shown in table A.1 of Appendix A.1.

8.2.3 Neutron fluence in water phantom - BICHP and MCNP

The neutron fluence was calculated in the same geometry. The results shown in this section compare the neutron fluence obtained using Geant4 BICHP and MCNP, each with thermal neutron treatment enabled/disabled. The neutron fluence is recorded across the entrance surface of each z-axis segment, with the result normalised per incident neutron. For the neutron fluence presented in figures 8.15 to 8.18, the neutron energies have been categorised into total (solid line), thermal (dashed line), epithermal (dotted line), and fast (dash-dotted line).

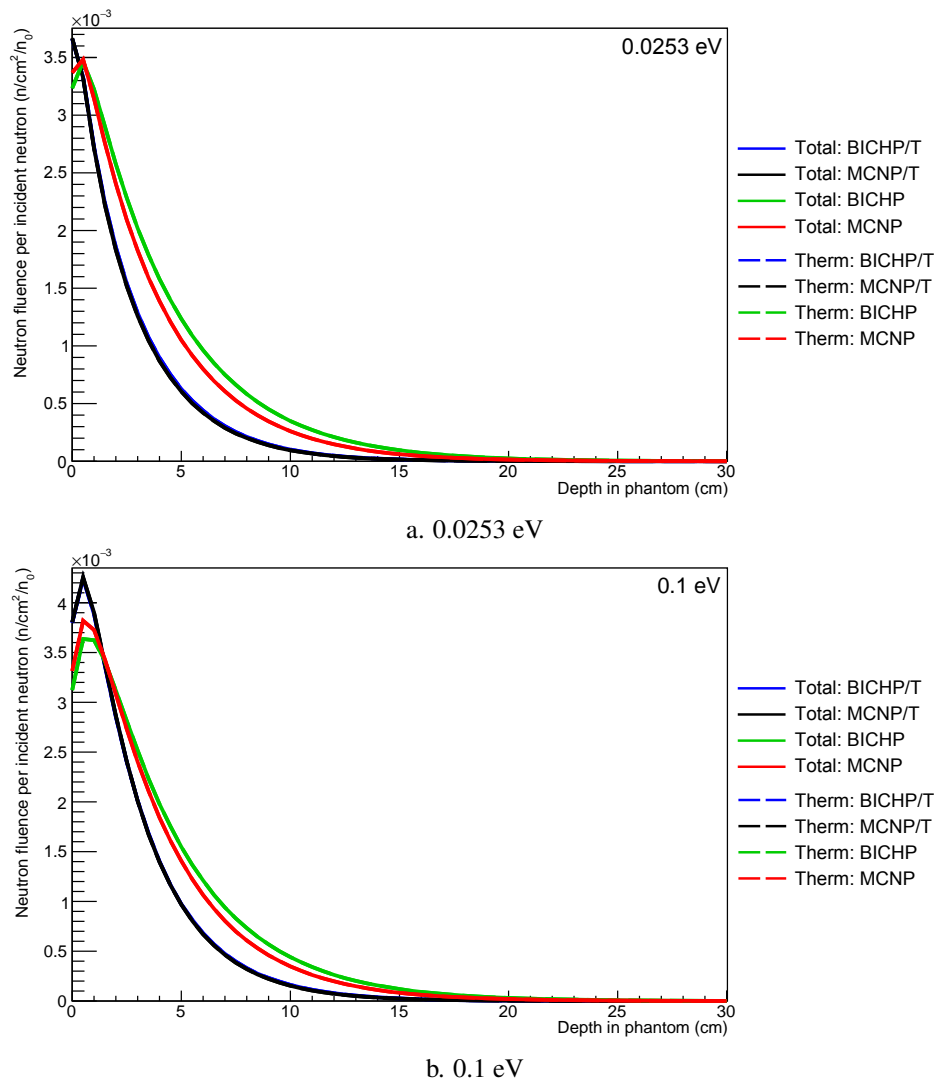


Figure 8.15: Neutron fluence per incident neutron as a function of depth in water phantom represented in terms of neutron energy: total, epithermal and thermal, calculated using BICHP and MCNP with T and noT; 0.0253 eV to 0.1 eV.

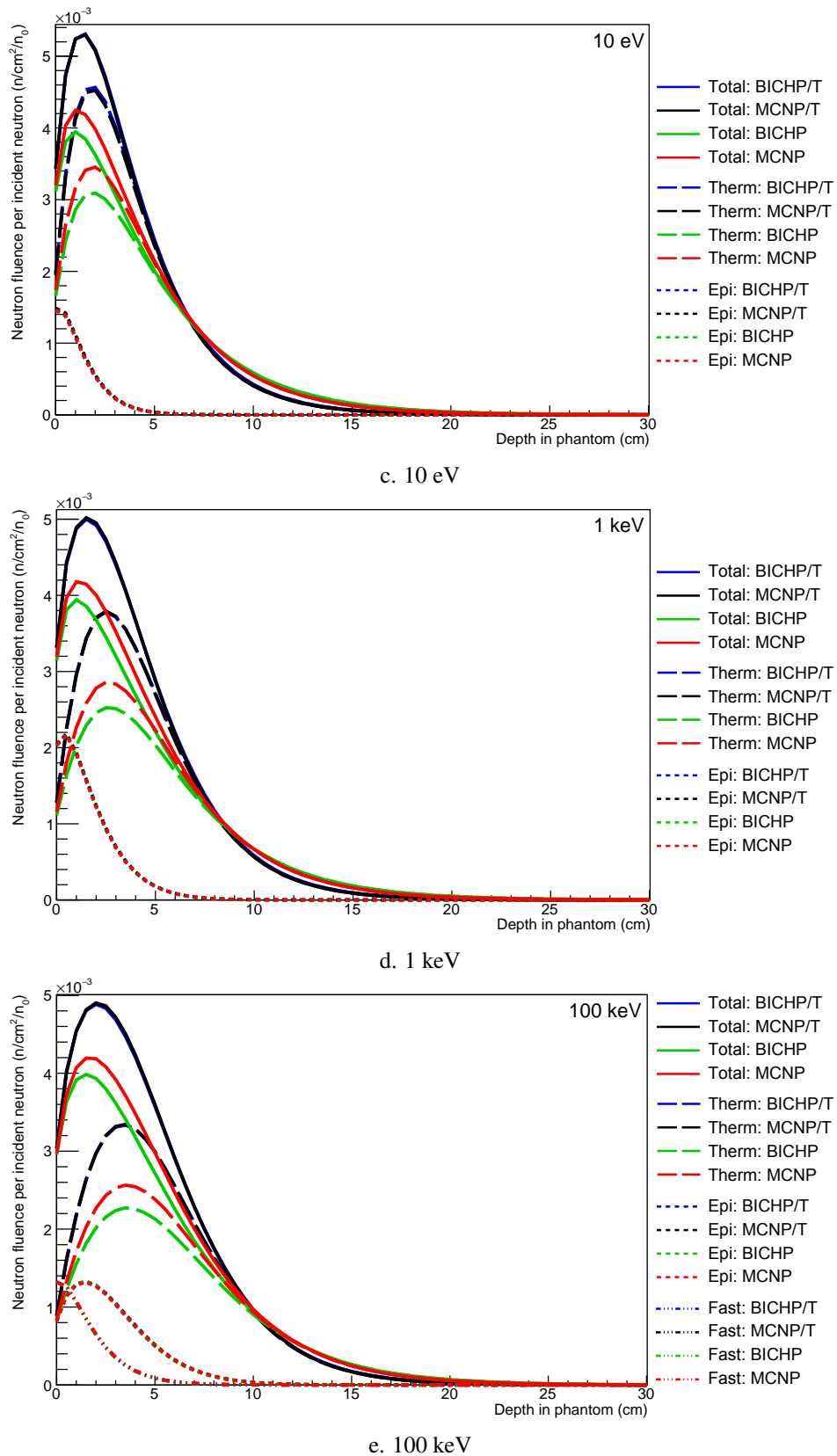


Figure 8.16: Neutron fluence per incident neutron as a function of depth in water phantom represented in terms of neutron energy: total, epithermal and thermal, calculated using BICHP and MCNP with T and noT; 10 eV to 100 keV.

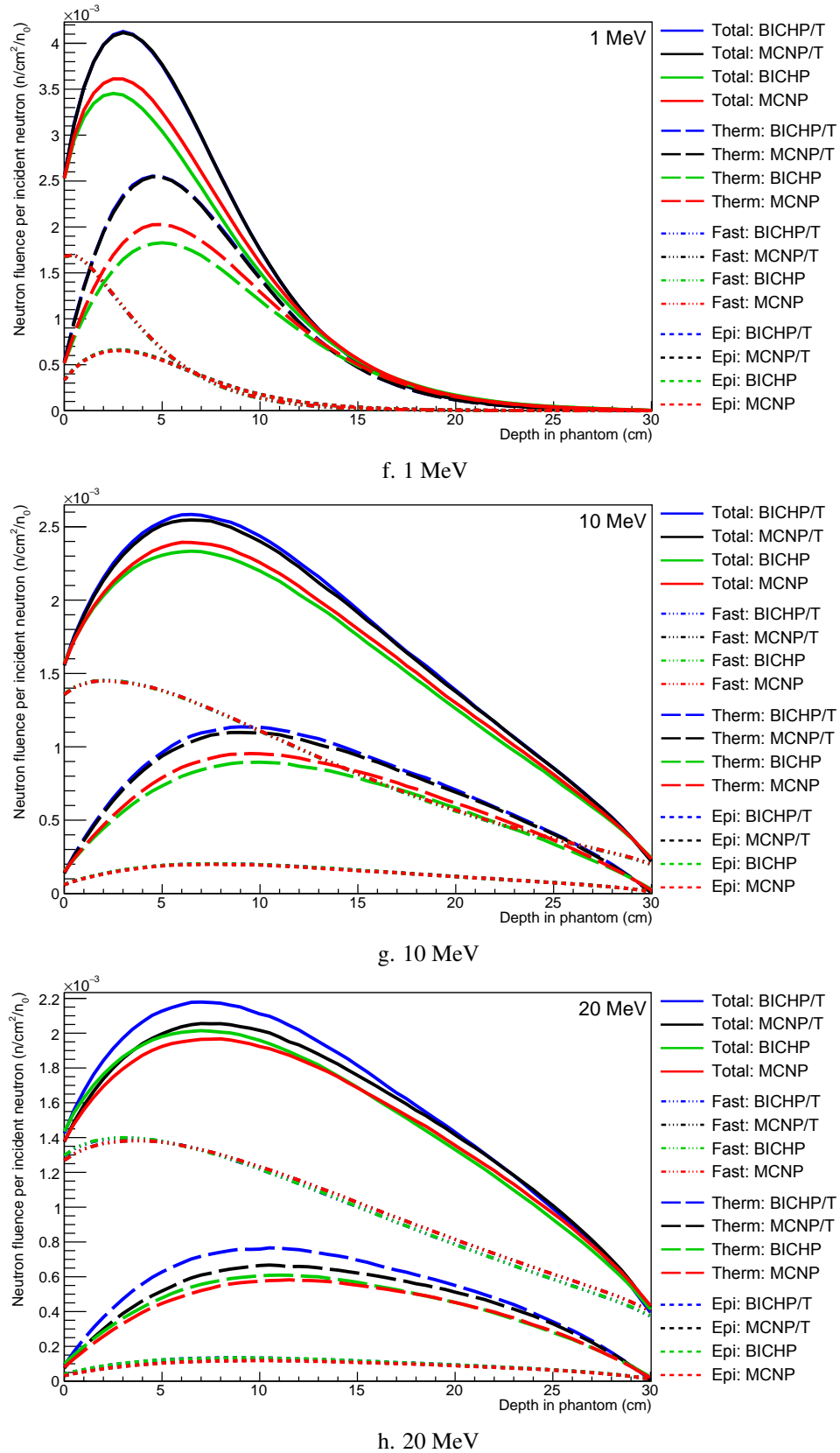


Figure 8.17: Neutron fluence per incident neutron as a function of depth in water phantom represented in terms of neutron energy: total, epithermal and thermal, calculated using BICHP and MCNP with T and noT; 1 MeV to 20 MeV.

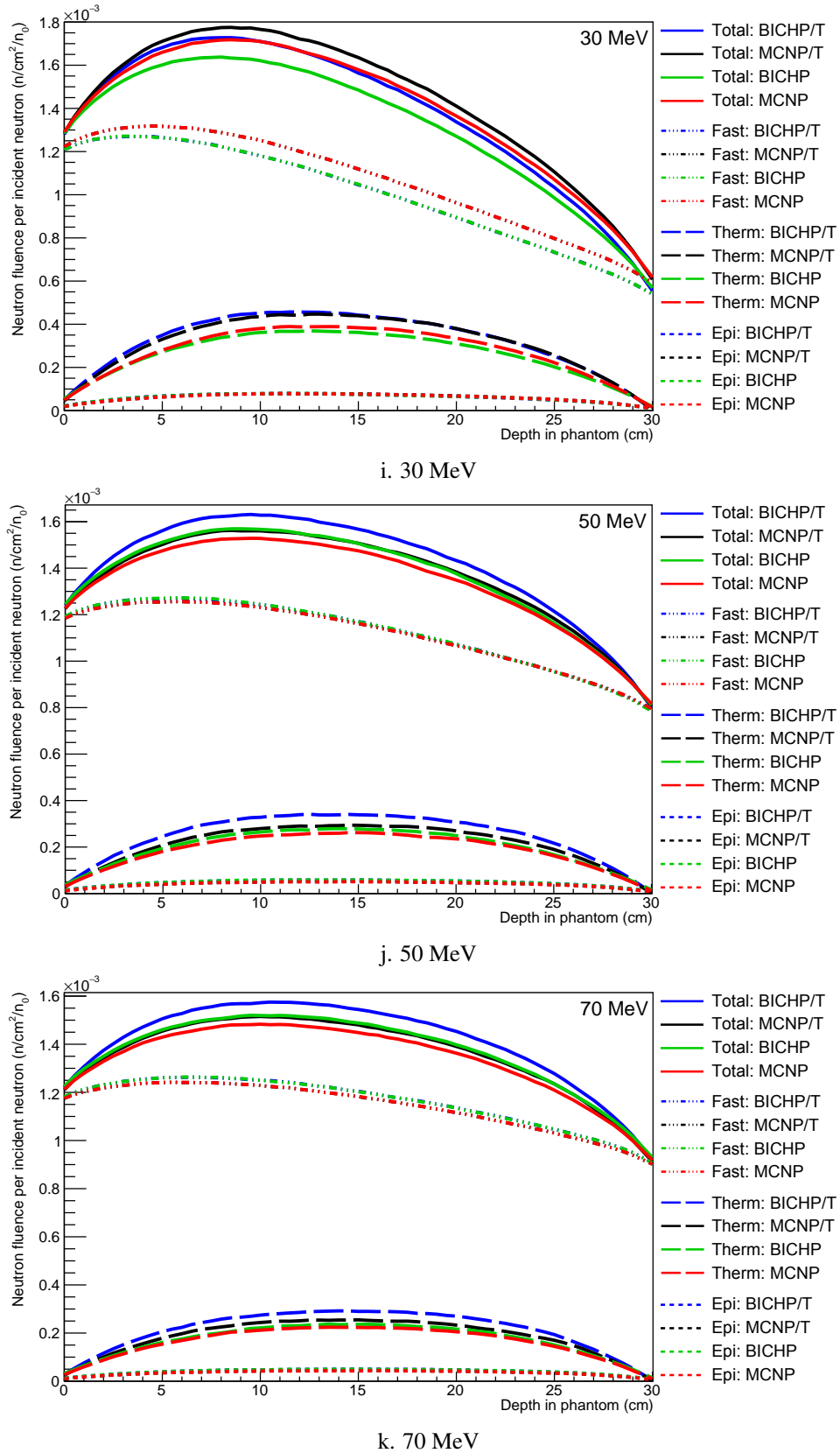


Figure 8.18: Neutron fluence per incident neutron as a function of depth in water phantom represented in terms of neutron energy: total, epithermal and thermal, calculated using BICHP and MCNP with T and noT; 30 MeV to 70 MeV.

Several key trends that were also observed for the total depth dose are seen in these results. For monoenergetic neutron ranging from 0.0253 eV (figure 8.15a) to 10 MeV (figure 8.17g), the neutron fluence calculated using Geant4 BICHP and MCNP with thermal treatment enabled yields the exact same result. This is true for fast, epithermal and thermal energies. As also seen previously, the two codes without thermal neutron treatment have very different output to each other.

For the simulations with neutron monoenergies above 10 MeV, it is observed that Geant4 BICHP produces a higher proportion of epithermal neutrons compared to MCNP. This result should be considered when simulating high energy neutrons in combination with secondary dose augmentation from epithermal energies. An example of this is fast neutron treatments with the intention of dose-enhancement modalities such as BNCT.

8.3 Monoenergetic neutrons in 50ppm B10 water phantom

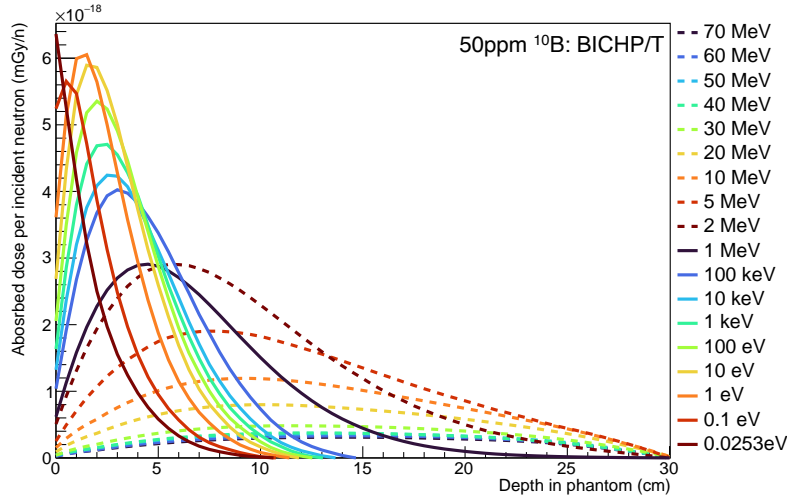
This section focuses on the depth dose characteristics of monoenergetic neutrons in a 50ppm ^{10}B loaded water phantom using Geant4 and MCNP. The method and quantities calculated is the same as the previous section, except the water phantom now has 50ppm ^{10}B included in the material.

Firstly, the total depth dose was calculated for only Geant4 BICHP with thermal neutron treatment enabled/disabled in the 50ppm ^{10}B water phantom. The individual dose components contributing to the total depth dose for the Geant4 BICHP and MCNP physics options are then studied in more detail. Finally, all of the fourteen physics list options listed in table 8.2 are compared to observe any differences in the context of total depth dose in the 50ppm ^{10}B water phantom.

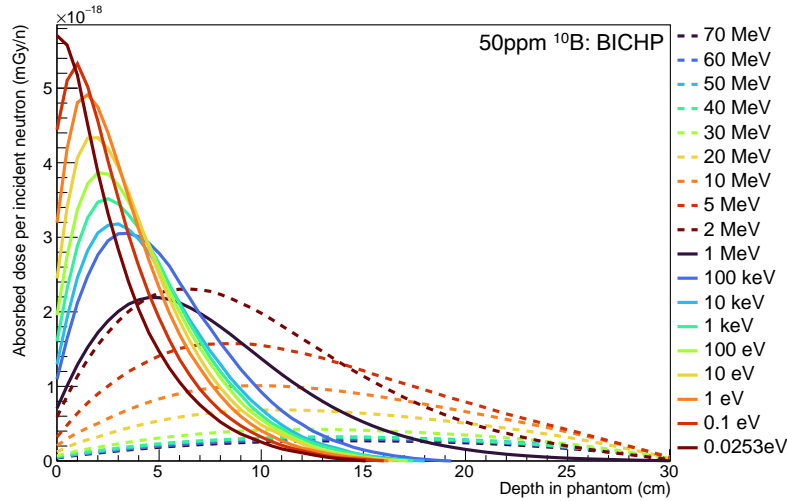
8.3.1 Comparison of BICHP with thermal treatment on/off

Total depth dose in 50ppm ^{10}B water phantom

Figures 8.19a and 8.19b present the total depth dose in the 50ppm ^{10}B water phantom using Geant4 BICHP with the thermal neutron treatment enabled and disabled, respectively. The same data is shown zoomed on the lower energies in figures 8.20a and 8.20b.



a. BICHP/T



b. BICHP

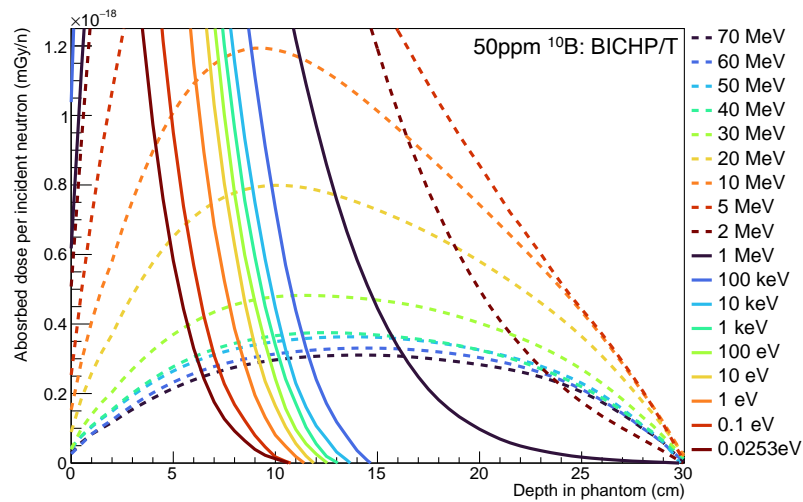
Energy	p	PD %
0.0253eV	0.000	-9.55
0.1 eV	0.000	-5.45
1 eV	0.006	-19.31
10 eV	0.012	-26.89
100 eV	0.012	-28.41
1 keV	0.028	-26.74
10 keV	0.068	-26.12
100 keV	0.081	-25.16
1 MeV	0.239	-21.65
2 MeV	0.649	-17.04
5 MeV	0.914	-14.12
10 MeV	0.985	-13.26
20 MeV	0.998	-12.01
30 MeV	0.999	-11.62
40 MeV	0.929	-10.77
50 MeV	0.994	-11.28
60 MeV	0.983	-10.21
70 MeV	0.993	-9.15

Table 8.4: Statistics tests for depth dose distribution of monoenergetic neutrons in 50ppm ^{10}B water phantom, comparing BICHP against BICHP/T.

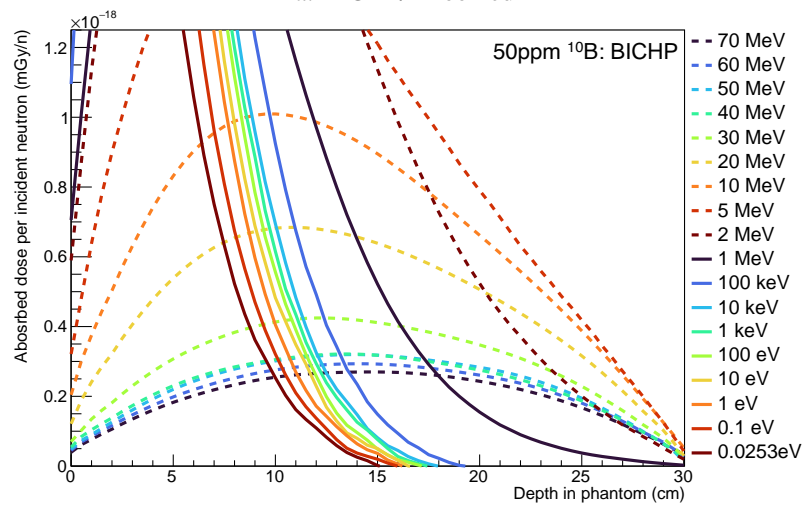
Figure 8.19: Absorbed dose per incident neutron as a function of depth in 50ppm ^{10}B water phantom for monoenergetic neutrons using BICHP with thermal treatment on (a) and off (b).

As seen previously in the calculation for the natural water phantom, the statistics tests present a close agreement between BICHP with thermal treatment enabled/disabled for

monoenergetic neutrons above 5 MeV. However, even though the p-value approaches 1.0 for higher energies, the PD is still about 10% lower for BICHP without thermal treatment. This means that the depth dose distribution is the same, but has overall lower dose throughout the phantom.



a. BICHP/T zoomed



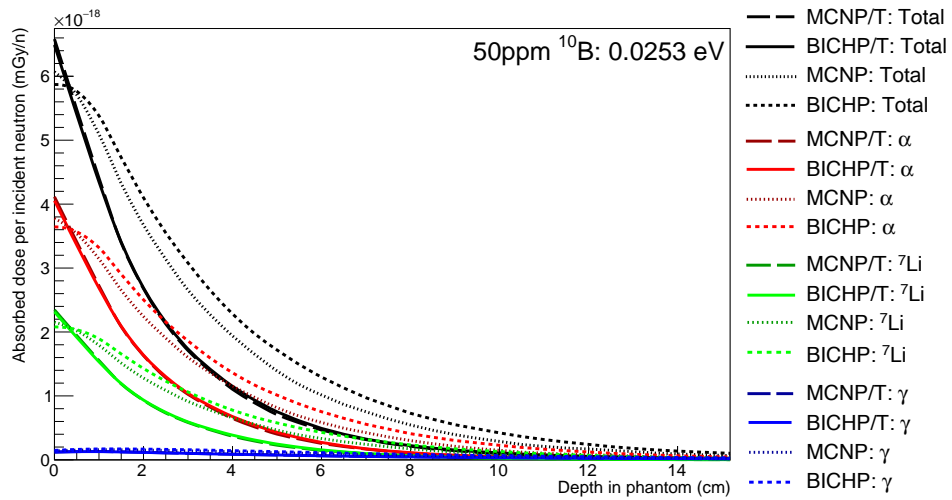
b. BICHP zoomed

Figure 8.20: Absorbed dose per incident neutron as a function of depth in 50ppm ^{10}B water phantom for monoenergetic neutrons using BICHP with thermal treatment on (a) and off (b). Same as Figure 8.19 but zoomed in to show lower energies.

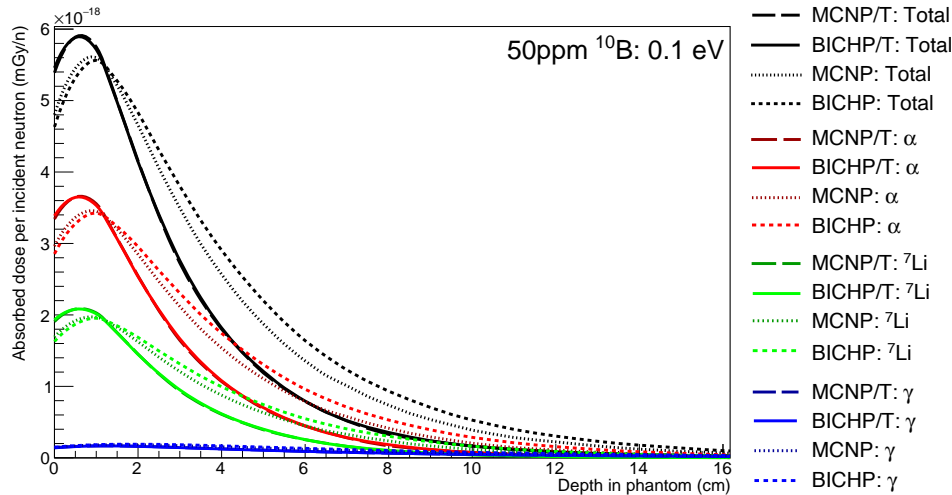
Individual components contributing to total depth dose in ^{10}B water phantom

These results present the individual depth dose plots in the 50ppm ^{10}B water phantom for each neutron monoenergy. The individual components that contribute to the total depth dose are shown for BICHP, BICHP/T, MCNP, and MCNP/T.

The results shown here for the 50ppm ^{10}B water phantom have the dose components associated with water subtracted, to allow a closer observation of only reactions arising from interactions with ^{10}B isotopes.

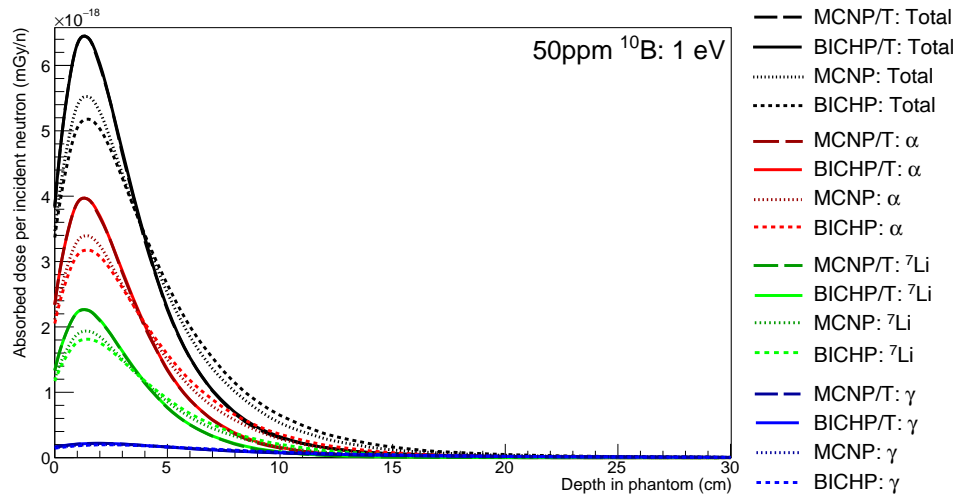


a. 0.0253 eV

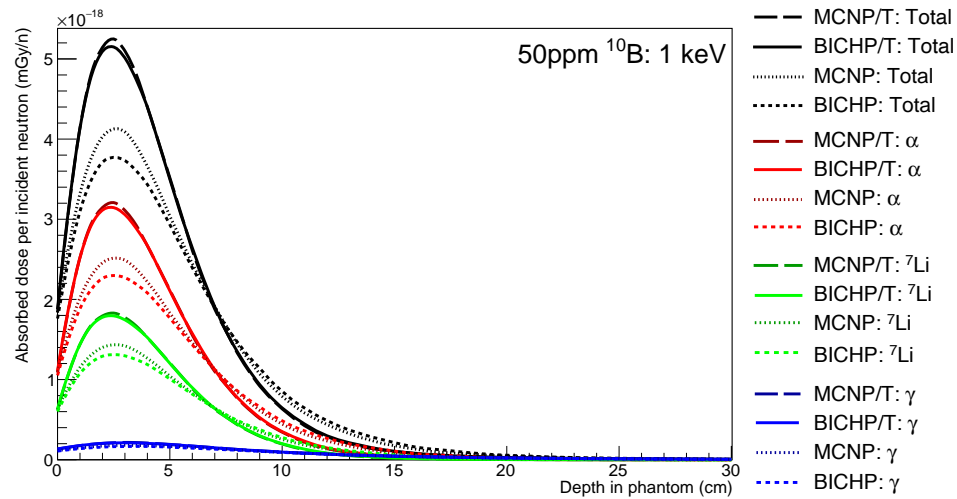


b. 0.1 eV

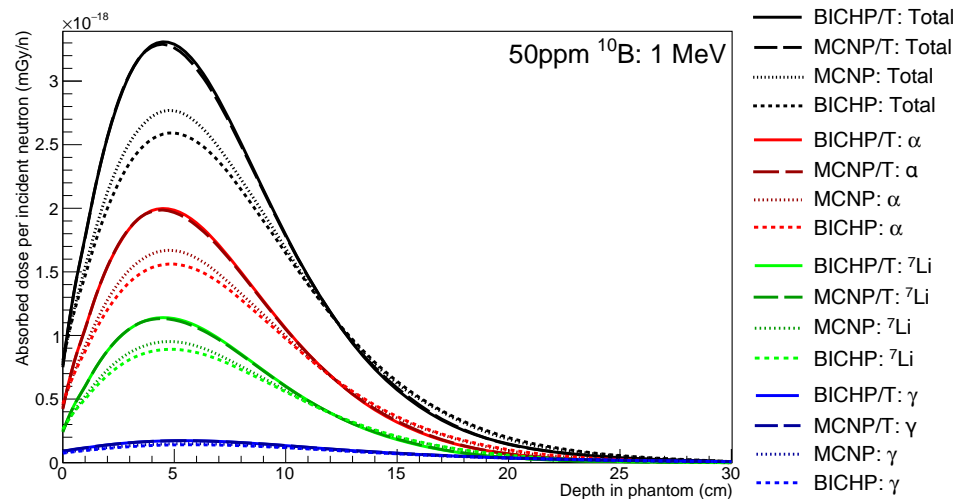
Figure 8.21: Absorbed dose per incident neutron as a function of depth in 50ppm ^{10}B water phantom represented in terms of individual components calculated using BICHP and MCNP with T and noT; 0.0253 eV and 0.1 eV.



c. 1 eV

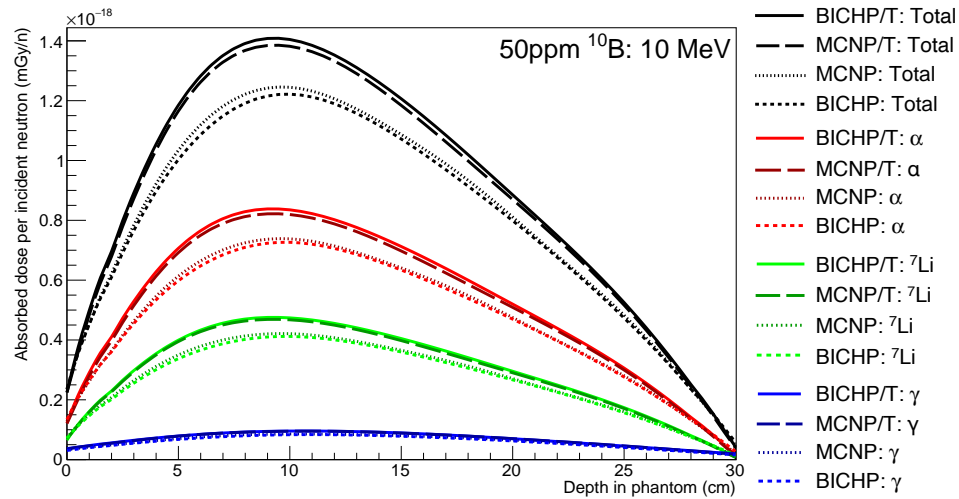


d. 1 keV

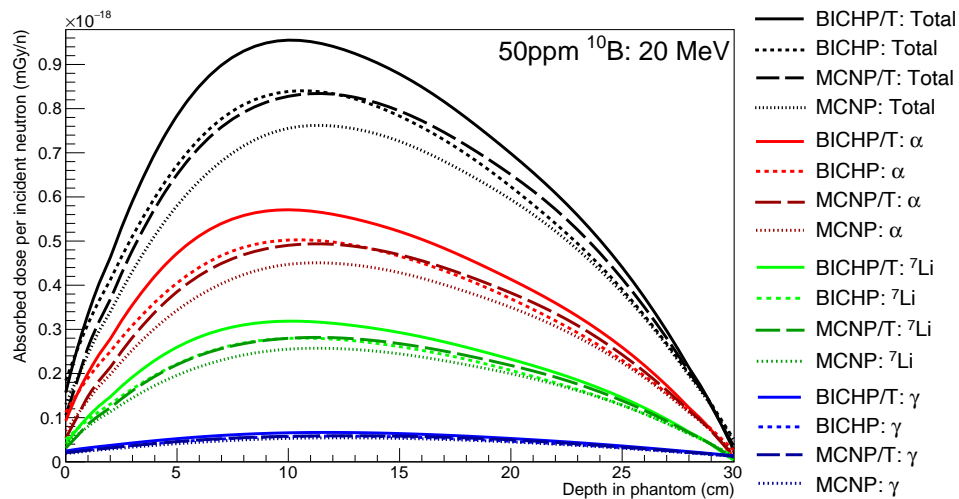


e. 1 MeV

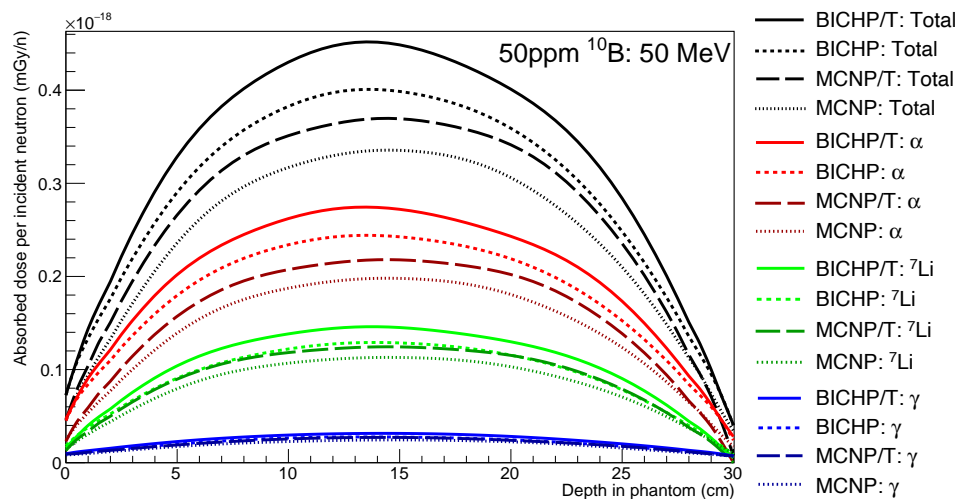
Figure 8.22: Absorbed dose per incident neutron as a function of depth in 50ppm ^{10}B water phantom represented in terms of individual components calculated using BICHP and MCNP with T and noT; 1 eV, 1 keV and 1 MeV.



f. 10 MeV



d. 20 MeV



e. 50 MeV

Figure 8.23: Absorbed dose per incident neutron as a function of depth in 50ppm ^{10}B water phantom represented in terms of individual components calculated using BICHP and MCNP with T and noT; 10 MeV, 20 MeV and 50 MeV.

The depth dose plots with individual components calculated in the ^{10}B loaded water phantom are shown above in figures 8.23 to 8.23. For the monoenergetic neutrons tested, it is observed that Geant4 BICHP and MCNP with thermal neutron treatment enabled have nearly identical results for the dose components, in terms of distribution and proportional height, up to 10 MeV.

As observed in the natural water phantom simulations, there are divergences in the physics models here for the neutrons monoenergies tested above 20 MeV (as explained earlier). In the case of the natural water phantom, the depth dose result of the same physics list with thermal neutron treatment enabled/disabled converged after 1 MeV.

However, for the depth dose calculated with the ^{10}B loaded water phantom, the physics lists of Geant4 BICHP and MCNP produce differing proportional height to their respective lists with thermal neutron treatment enabled, for all monoenergies up to 70 MeV. This result outlines the importance of considering the thermal neutron treatment model, even when simulating fast neutrons.

It is observed that the thermal neutron fluence distribution in water (figures 8.15 to 8.18 of section 8.2) is directly proportional to the relative height of the dose components shown here for ^{10}B induced reactions.

8.3.2 Comparison of different physics options in 50ppm B10 water phantom

The final set of results in this chapter compares the total depth dose calculated in the 50ppm ^{10}B water phantom for the fourteen different physics options. The results shown have the dose components that derive from water-based interactions subtracted, so only the contributions relating to ^{10}B interactions are shown. To provide a visual comparison and evaluate the variations between the physics options, the data is superimposed in the figures for each neutron monoenergy tested.

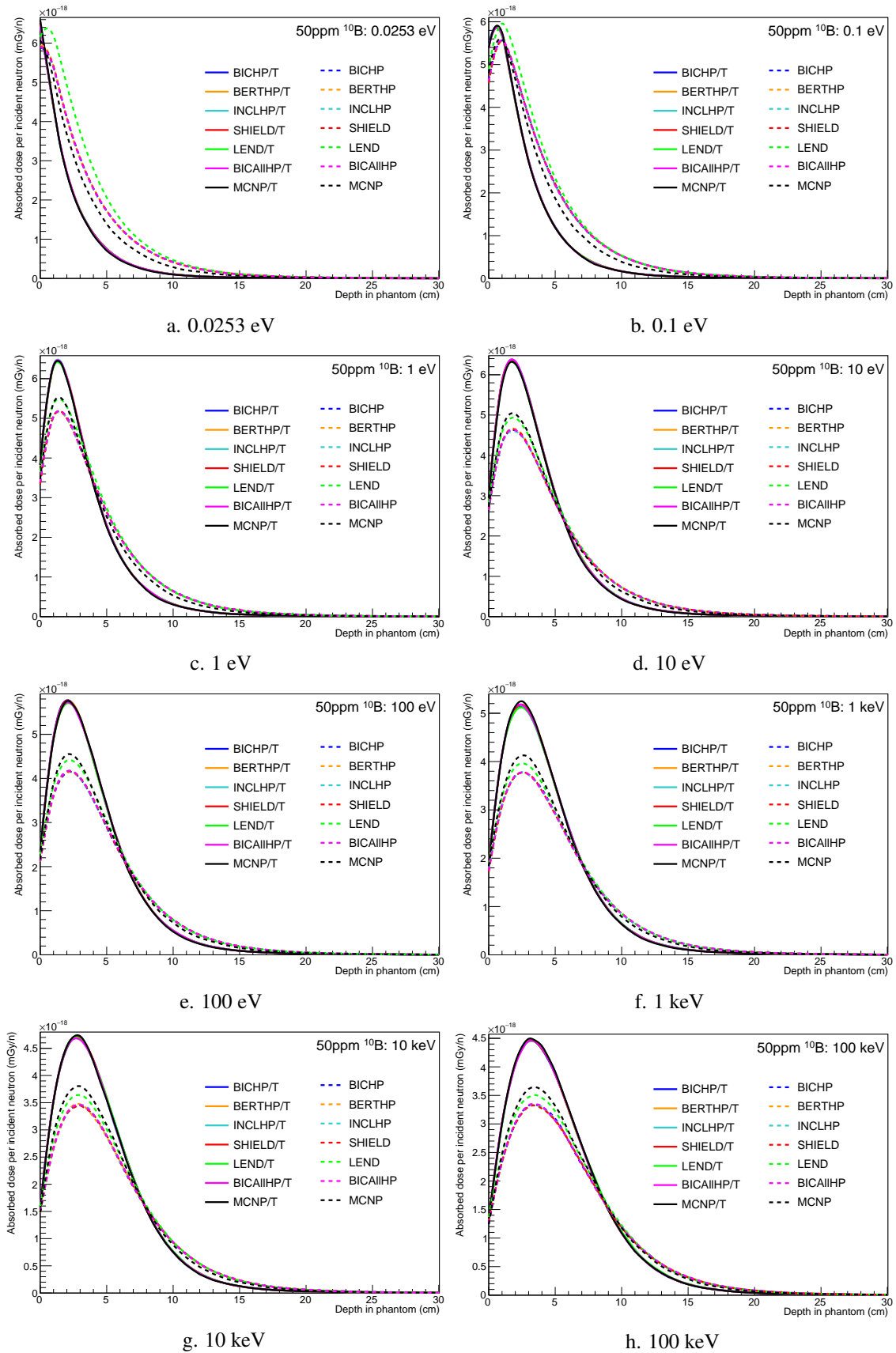


Figure 8.24: Absorbed dose per incident neutron as a function of depth in 50ppm ^{10}B water phantom; 0.0253 eV to 100 keV.

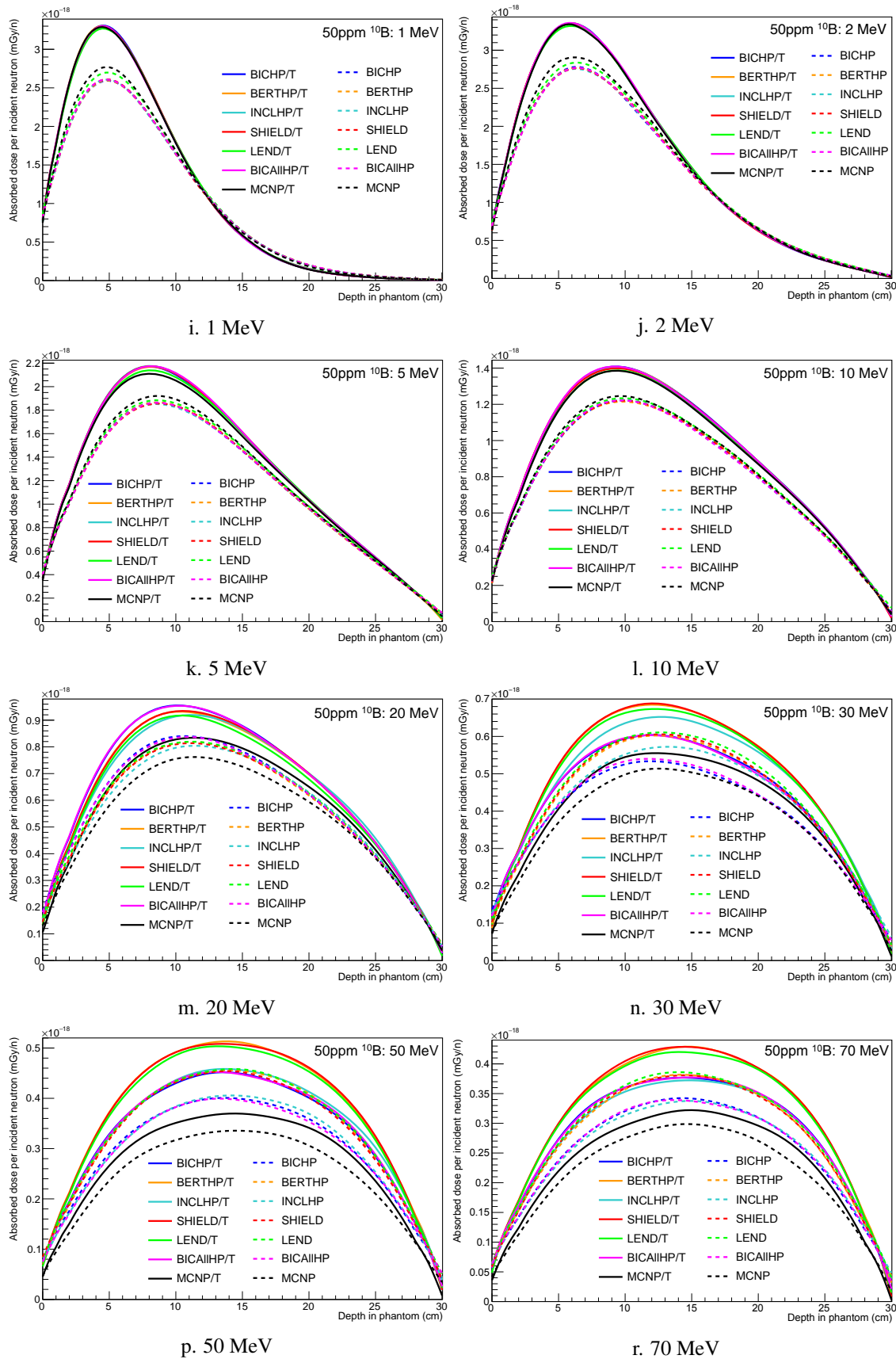


Figure 8.25: Absorbed dose per incident neutron as a function of depth in 50ppm ^{10}B water phantom; 1 MeV to 70 MeV.

As also seen in the natural water phantom, for the tested neutron monoenergies below 20 MeV, the physics models converge into two groups; relating to thermal neutron treatment enabled/disabled. This is with the exception of disabled thermal neutron treatment for LEND and MCNP, which remarkably follow a similar distribution in these neutron monoenergies.

For the neutron monoenergies tested above 20 MeV, certain physics models converge to the same distribution. These are the same groups observed for the natural water phantom. However, for the case presented here with only ^{10}B related reactions, the thermal neutron treatment enabled/disabled physics models do not converge above 20 MeV.

1. BICHP, BICAllHP (no T),
2. BERTHP, Shield, and LEND (no T),
3. INCL (no T),
4. MCNP (no T),
5. BICHP, BICAllHP (with T),
6. BERTHP, Shield, and LEND (with T),
7. INCL (with T),
8. MCNP (with T).

The statistics tests of p-value goodness-of-fit and PD for the 50ppm ^{10}B water phantom depth dose results are graphed in figures 8.26 and 8.27 for thermal neutron treatment enabled and disabled, respectively.

From results of the statistics tests, the importance of using the thermal neutron treatment is asserted. With the thermal treatment disabled, there is a very poor p-value and PD result between Geant4 BICHP and MCNP Bertini INC. However, with the treatment enabled, the two codes have excellent agreement.

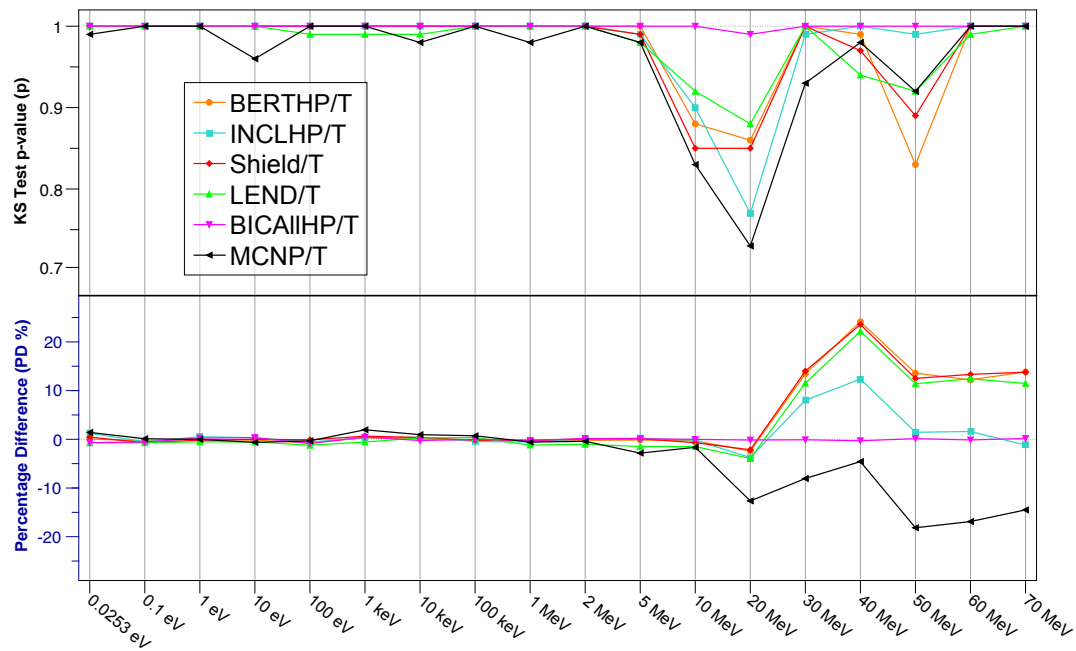


Figure 8.26: Statistics tests for depth dose distribution of monoenergetic neutrons in 50ppm ^{10}B water phantom for the different physics lists compared against BICHP. All physics with thermal on (T) are compared against BICHP/T. Data shown in table A.2 of Appendix A.2.

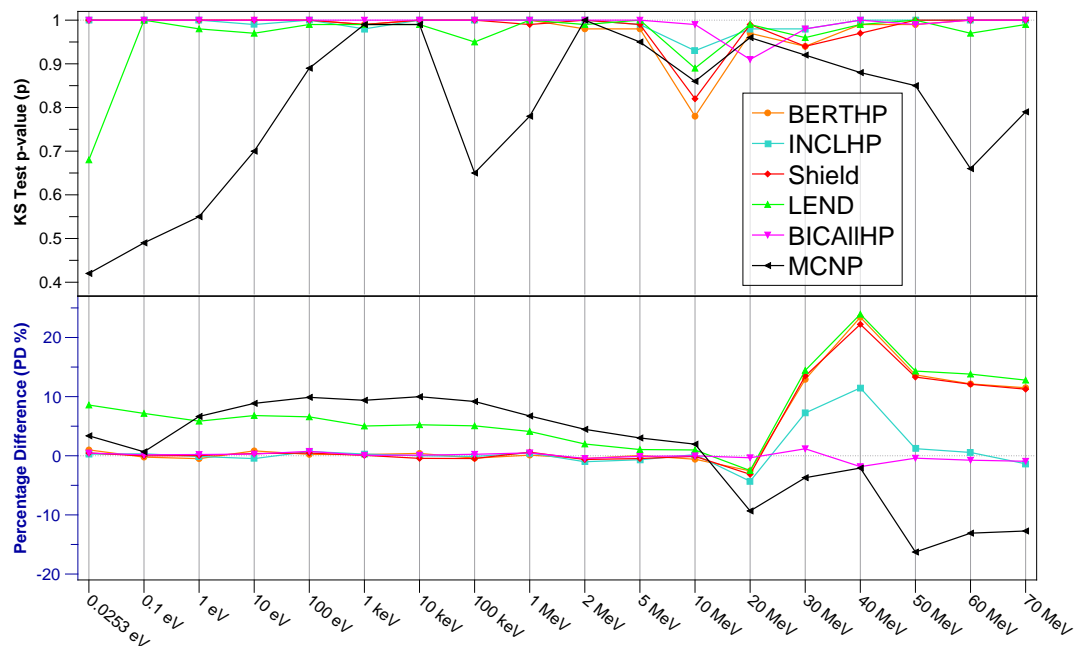


Figure 8.27: Statistics tests for depth dose distribution of monoenergetic neutrons in 50ppm ^{10}B water phantom for the different physics lists compared against BICHP. All physics with thermal off (noT) are compared against BICHP. Data shown in table A.2 of Appendix A.2.

8.4 Discussion

In this chapter, fourteen different physics models were benchmarked using various monoenergetic neutrons for the two Monte Carlo codes. The results show that certain options enable MCNP capabilities to produce close agreement with Geant4. This relates specifically to whether the thermal neutron treatment is included in the model.

When the thermal neutron treatment is enabled, the total overall dose is higher for each physics model. This is due to a higher amount of elastic collisions occurring in water with ^1H , thus higher neutron moderation and differences in neutron energy fluence.

The best agreement was found between the MCNP Bertini INC model and the Geant4 QGSP_BIC_AllHP physics list, with thermal neutron treatment enabled in both codes. The Geant4 QGSP_BIC_AllHP physics list uses the same neutron process model as QGSP_BIC_HP, with the added exception of the high-precision TENDL evaluated datasets. The TENDL data is also available in MCNP, which provides detailed descriptions of the interactions of charged particles such as proton, deuteron, triton and alpha particles up to 200 MeV. As such, the Geant4 QGSP_BIC_AllHP physics list (with thermal neutron treatment enabled) was selected for all simulations performed in this thesis. This is particularly important for the work presented in the chapters 5 and 6, that focus on neutron accelerators which utilise the $^9\text{Be}(p,n)$ inelastic collision to produce neutrons.

Similar relevant work has been published by Enger et al. (2006) [134], Geng et al. (2016) [189] and Tran et al. (2018) [190]. These publications compare the effect of thermal neutron treatment activation in Geant4 and MCNP for water, which agree with the results shown in this chapter. They show that the use of thermal neutron treatment is required to provide the same result for neutron fluence and depth dose in Geant4 and MCNP, with agreement to their experimental measurements [134]. Similarly, they also show that neutron fluence and dose is underestimated by both codes when the thermal neutron treatment is neglected [134][190].

The thermal neutron fluence distribution in natural water (figures 8.15 to 8.18) was

observed as directly proportional to the relative height of the component depth dose produced by ^{10}B in the 50ppm ^{10}B water phantom. It may be thought as intuitive to apply this fact and infer that a relevant fluence distribution will always equal the same dose, but this approach is fundamentally inaccurate - particularly in a clinical setting. The behaviour of all radiation particles, especially neutrons, are stochastic in nature and cannot be predicted in such a manner. This is the very principle and foundational purpose of employing Monte Carlo simulations for radiation particle transport, based upon using a random probability distribution to describe these interactions.

Chapter 9

Conclusions and Future Work

This thesis has presented the research and implementation of new microdosimetric instrumentation for use with solid-state microdosimeters in radioprotection purposes and QA of various hadron therapy modalities. The main components of this work included design optimisation of the existing SOI Bridge V2 microdosimeter for BNCT QA, experimental characterisation of the iThemba LABS fast neutron facility with Monte Carlo verification, investigation of radioprotection risks at the Tokai iBNCT facility during microdosimetry experiments and the development of a novel wireless microdosimeter.

Optimisation of the SOI Bridge microdosimeter for BNCT QA

In the design optimisation study of the SOI Bridge V2 microdosimeter in BNCT QA, Geant4 was used to model and provide recommendations for improvements in the geometry and detector packaging. This study concluded that the current materials used in the SOI microdosimeters pose no radioprotection risk, though the SVs should be made thinner to increase the interactions by ‘crossers’. Thinner $^{10}\text{B}_4\text{C}$ films should also be used to decrease energy loss before reaching the microdosimeter. SVs with thickness of 1 μm or less were shown to be best suited for BNCT microdosimetry. However, the Bridge microdosimeter with 2 μm SV thickness and $30 \times 30 \mu\text{m}^2$ SV lateral area is the most feasible design for BNCT QA using the current fabrication technology. The production of BNC

reactions in the boron doped p^+ implantation region of the Bridge microdosimeter SVs was also investigated. For the alpha particles produced in this region, the rate of crossers is much higher than that from the $^{10}\text{B}_4\text{C}$ film, due to lower energy loss before reaching the SVs. This result validates the feasibility of applying the boron doped p^+ region in SOI microdosimeters for dedicated BNCT microdosimetry.

Model of the South Africa iThemba Fast Neutron Beamline

In the study to characterise the fast neutron therapeutic beam produced at iThemba LABS in South Africa, Geant4 and MCNP6 were utilised and successfully modelled the neutron gantry and treatment room of the facility. The SOI Bridge V2 microdosimeter was used in the simulation and experiments at the facility to obtain the microdosimetric response in the mixed radiation field. The neutron beam characterised in Monte Carlo simulations from the accelerator model was then simulated in a water phantom and its characteristics recorded by the silicon microdosimeters; bare and covered by a ^{10}B enriched boron carbide converter, at different positions. The microdosimetric quantities calculated using Geant4 and MCNP6 are in agreement with experimental measurements. Different physics options for Geant4 and MCNP6 were evaluated based on their neutron energy yield from the $^9\text{Be}(p,n)$ inelastic reaction by 66 MeV protons. It was found that with the thermal neutron scattering treatment enabled for both Geant4 using QGSP_BIC_AllHP and MCNP6 using Bertini INC produced the best agreement. The performance of the custom developed post-simulation analysis application for MCNP's PTRAC output is demonstrated in these results. The ability to describe all reactions and their associated particles in MCNP is not usually possible with the standard scoring method cards.

The thermal neutron sensitivity and production of ^{10}B capture products in the p^+ boron-implanted dopant regions of the Bridge microdosimeter was also investigated. The BNC products, ^{10}B and ^7Li were produced in the Geant4 and MCNP6 simulations, validating the same reactions observed in the experimental measurements for the expected energy region. The obtained results provides a benchmark comparison of Geant4 and MCNP6

capabilities for further applications of these codes for neutron microdosimetry and the future development of dedicated SOI microdosimeters for BNCT.

Model of the Tokai iBNCT Epithermal Neutron Beamline

The study relating to the characterisation of the Tokai iBNCT epithermal neutron beamline was performed to investigate the rate of unwanted neutron activation in the equipment used by CMRP for BNCT QA measurements in view of future experiments at the iBNCT facility.

The beamline was simulated in Geant4, successfully modelling the beam shaping assembly and production of epithermal neutrons with close agreement with PHITS. This information was used in further simulations to model and optimise the geometry of materials which would be used in the experimental setup. The ambient dose equivalent $H^*(10)$ as a function of time was calculated for different positions in the treatment room, indicating that a 30 minute cool down period should be obeyed before interacting with the equipment. This cool-down requirement should be factored into the planned experiment schedule when it is desired to change the configuration of the experiment between irradiations. The SOI Bridge microdosimeter had negligible activation, even though it was directly in the central beam axis. The Geant4 results indicate that the majority of materials used in the experimental measurement system are appropriate in terms of radio-protection. However, there are some material changes, which should be considered for future work.

The dose equivalent due to ^{28}Al activations in the structural frame of the motion stage system is significant. ^{28}Al has a short half-life, so it will not be prevented from leaving the facility, but restricts a mandatory 30 minute cool-down period before approaching the apparatus, slowing down the experiment, when squandered beam time is a critical issue. Therefore future work should be carried out to develop a substitution for the aluminium extrusion frame, possibly replaced by 3D printed plastic options. ABS plastic may be suitable, though more robust materials such as Nylon or Carbon Fiber should be consid-

ered. A future study on the neutron activation resistance of different 3D printed materials will be carried out using simulations and experimentally at Tokai.

The pulse shaper box was also activated unnecessarily. As this object is very far out-of-field, shielding should be utilised to prevent highly scattered thermal neutrons from interacting with it. The addition of a thin cover for the shaper box made from boronated or lithiated plastic would be appropriate. An example is the novel boronated ABS plastic [175], that can be 3D printed.

^{198}Au and ^{66}Cu isotopes were activated in the DIL external leg leads and pin sockets of the MicroPlus probe, respectively. The DIL leg leads are composed of pure gold electroplated over an electrolytic nickel underplate. Nickel activation was not observed in the simulations. Other options for the external leads are available such as solder dip of 60% tin, 40% lead alloy or pure tin plating.

Validation of different physics models in Geant4 and MCNP6 for QA in FNT and BNCT

For the work completed in this satellite chapter, fourteen different physics models were benchmarked using various monoenergetic neutrons for Geant4 and MCNP. The results show that certain options enable MCNP capabilities to produce close agreement with Geant4. The best agreement was found between the MCNP Bertini INC model and the Geant4 QGSP_BIC_AllHP physics list, with thermal neutron treatment enabled in both codes. These two physics options were selected for all Geant4 and MCNP6 simulations performed in this thesis. Future work for this work would consider more intranuclear cascade physics models in MCNP6 and applications to more complex tests than a simple box phantom.

Development of a Wireless Microdosimetry System

The study involving the development of the Radiodosimeter wireless microdosimetry system was one of the most important achievements in this thesis. The Radiodosimeter was

addresses several issues with the current setup such as electronic noise from cabling and complexity of setup. The main motivation of this project is to allow any user to take measurements using our system straight out of the box, without extensive knowledge of the electronics setup.

The Radiodosimeter was benchmarked against the standard setup, for spectral response using ^{241}Am source in a vacuum chamber and microdosimetric measurements of ^{28}Si heavy ion beam in a water phantom, both with excellent agreement. In relation to the digital pulse generator, used for auto-calibration, future iterations should include digital-to-analog converter, allowing pulses to be finely adjusted by a normalisation value

Several future recommendations are outlined in the discussion of chapter 7, with the key points summarised here, such as the addition of a screen for basic output, the development of an ad hoc decentralised Wi-Fi network of Radiodosimeters to provide communication in remote areas, and the investigation into low power transmission modes like LoRa [183] and Low Energy Bluetooth.

The use of Low Power data transmission (i.e. LoRa or BLE) addresses several limitations of the prototype Radiodosimeter system such as battery life. The application of either connectivity methods in the Radiodosimeter would be required to successfully produce wearable microdosimetry devices. With higher capacity batteries, optimised software and low power data transmission; a compact wearable microdosimeter can be produced.

The ability of the Radiodosimeter to operate independently from a client computer proves its extreme portability advantage for personal monitoring of mixed radiation fields in remote areas. The Radiodosimeter allows streamlined QA process in particle therapy that can be carried out by a technician without in-depth training, due to simplicity and automation of the microdosimeter system. The developed Radiodosimeter can be utilised in a network for radiation protections and homeland security purposes as it has selective sensitivity to different components of the mixed radiation field.

Bibliography

- (1) V. L. Pisacane, J. F. Ziegler, M. E. Nelson, M. Caylor, D. Flake, L. Heyen, E. Youngborg, A. B. Rosenfeld, F. Cucinotta, M. Zaider and J. F. Dicello, “MIDN: a spacecraft microdosimeter mission”, *Radiation Protection Dosimetry*, 2006, **120**, 421–426.
- (2) P. D. Bradley, A. B. Rosenfeld, B. Allen, J. Coderre and J. Capala, “Performance of Silicon Microdosimetry Detectors in Boron Neutron Capture Therapy”, *Radiation Research*, 1999, **151**, 235–243.
- (3) International Commission on Radiation Units and Measurements, *ICRU Report 36: Microdosimetry*, tech. rep., Bethesda, 1983.
- (4) P. D. Bradley, Ph.D. Thesis, University of Wollongong, 2000, pp. 220–261.
- (5) D. Bolst, S. Guatelli, L. T. Tran, L. Chartier, M. L. F. Lerch, N. Matsufuji and A. B. Rosenfeld, “Correction factors to convert microdosimetry measurements in silicon to tissue in ^{12}C ion therapy”, *Physics in Medicine and Biology*, 2017, **62**, 2055–2069.
- (6) M. Zaider and H. H. Rossi, *Microdosimetry and Its Applications*, Springer, 1996, pp. 1–57.
- (7) D. Prokopovich, Ph.D. Thesis, University of Wollongong, 2010, pp. 1–26, 195–199.
- (8) A. M. Kellerer and H. H. Rossi, “The theory of dual radiation action”, *Current Topics in Radiation Research Quarterly*, 1972, **8**, 73.

- (9) R. B. Hawkins, “A Statistical Theory of Cell Killing by Radiation of Varying Linear Energy Transfer”, *Radiation Research*, 1994, **140**, 366–374.
- (10) R. B. Hawkins, “A microdosimetric-kinetic model of cell death from exposure to ionizing radiation of any LET, with experimental and clinical applications”, *International Journal of Radiation Biology*, 1996, **69**, 739–755.
- (11) R. B. Hawkins, “A microdosimetric-kinetic theory of the dependence of the RBE for cell death on LET”, *Medical Physics*, 1998, **25**, 1157–1170.
- (12) Y. Kase, T. Kanai, M. Sakama, Y. Tameshige, T. Himukai, H. Nose and N. Matsu-fuji, “Microdosimetric Approach to NIRS-defined Biological Dose Measurement for Carbon-ion Treatment Beam”, *Journal of Radiation Research*, 2011, **52**, 59–68.
- (13) Y. Kase, T. Kanai, Y. Matsumoto, Y. Furusawa, H. Okamoto, T. Asaba, M. Sakama and H. Shinoda, “Microdosimetric measurements and estimation of human cell survival for heavy-ion beams”, *Radiation Research*, 2006, **166**, 629–638.
- (14) M. Scholz and G. Kraft, “Track structure and the calculation of biological effects of heavy charged particles”, *Advances in Space Research*, 1996, **18**, 5–14.
- (15) R. Katz, 1988, pp. 57–83.
- (16) A. B. Rosenfeld, T. Kron, F. D’Errico and M. Moscovitch, “Advanced Semi-conductor Dosimetry in Radiation Therapy”, *AIP Conference Proceedings*, 2011, **1345**, 48–74.
- (17) H. H. Rossi, “Specification of Radiation Quality”, *Radiation Research*, 1959, **10**, 522–531.
- (18) D. Srdoc, “Experimental technique of measurement of microscopic energy distribution in irradiated matter using Rossi counters”, *Radiation Research*, 1970, **43**, 302–319.
- (19) V. Conte, A. Bianchi, A. Selva, G. Petringa, G. A. Cirrone, A. Parisi, F. Vanhavere and P. Colautti, “Microdosimetry at the CATANA 62 MeV proton beam with a sealed miniaturized TEPC”, *Physica Medica*, 2019, **64**, 114–122.

- (20) A. B. Rosenfeld, G. I. Kaplan, M. G. Carolan, B. J. Allen, R. Maughan, M. Yudelev, C. Kota and J. Coderre, "Simultaneous macro and micro dosimetry with MOSFETs", *IEEE Transactions on Nuclear Science*, 1996, **43**, 2693–2700.
- (21) L. T. Tran, L. Chartier, D. Bolst, D. A. Prokopovich, S. Guatelli, M. Nancarrow, M. I. Reinhard, M. Petasecca, M. L. Lerch, V. L. Pereverlaylo, N. Matsufuji, D. Hinde, M. Dasgupta, A. Stuchbery, M. Jackson and A. B. Rosenfeld, "3D Silicon Microdosimetry and RBE Study Using ¹²C Ion of Different Energies", *IEEE Transactions on Nuclear Science*, 2015, **62**, 3027–3033.
- (22) P. D. Bradley and A. B. Rosenfeld, "Tissue equivalence correction for silicon microdosimetry detectors in boron neutron capture therapy", *Medical Physics*, 1998, **25**, 2220–2225.
- (23) A. B. Rosenfeld, "Novel detectors for silicon based microdosimetry, their concepts and applications", *Nuclear Instruments and Methods in Physics Research Section A: Accelerators, Spectrometers, Detectors and Associated Equipment*, 2016, **809**, 156–170.
- (24) I. M. Cornelius and A. B. Rosenfeld, "Verification of Monte Carlo Calculations in Fast Neutron Therapy Using Silicon Microdosimetry", *IEEE Transactions on Nuclear Science*, 2004, **51**, 873–877.
- (25) D. A. Prokopovich, M. I. Reinhard, I. M. Cornelius and A. B. Rosenfeld, "SOI microdosimetry for mixed field radiation protection", *Radiation Measurements*, 2008, **43**, 1054–1058.
- (26) S. Guatelli, M. I. Reinhard, B. Mascialino, D. A. Prokopovich, A. S. Dzurak, M. Zaider and A. B. Rosenfeld, "Tissue Equivalence Correction in Silicon Microdosimetry for Protons Characteristic of the LEO Space Environment", *IEEE Transactions on Nuclear Science*, 2008, **55**, 3407–3413.
- (27) N. S. Lai, W. H. Lim, A. L. Ziebell, M. I. Reinhard, A. B. Rosenfeld and A. S. Dzurak, "Development and Fabrication of Cylindrical Silicon-on-Insulator Microdosimeter Arrays", *IEEE Nuclear Science Symposium Conference Record*, 2008, 1044–1049.

- (28) J. Livingstone, D. A. Prokopovich, M. L. F. Lerch, M. Petasecca, M. I. Reinhard, H. Yasuda, M. Zaider, J. F. Ziegler, V. L. Pisacane, J. F. Dicello, V. L. Perevertaylo and A. B. Rosenfeld, “Large area silicon microdosimeter for dosimetry in high LET space radiation fields: Charge collection study”, *IEEE Transactions on Nuclear Science*, 2012, **59**, 3126–3132.
- (29) L. T. Tran, Ph.D. Thesis, University of Wollongong, 2014, pp. 43–114.
- (30) L. T. Tran, L. Chartier, D. A. Prokopovich, M. I. Reinhard, M. Petasecca, S. Guatelli, M. L. F. Lerch, V. L. Perevertaylo, M. Zaider, N. Matsufuji, M. Jackson, M. Nancarrow and A. B. Rosenfeld, “3D-mesa ‘Bridge’ Silicon Microdosimeter: Charge Collection Study and Application to RBE Studies in 12C radiation therapy”, *IEEE Transactions on Nuclear Science*, 2015, **62**, 504–511.
- (31) L. T. Tran, S. Guatelli, D. A. Prokopovich, M. Petasecca, M. L. F. Lerch, M. I. Reinhard, J. F. Ziegler, M. Zaider and A. B. Rosenfeld, “A novel silicon microdosimeter using 3D sensitive volumes: Modeling the response in neutron fields typical of aviation”, *IEEE Transactions on Nuclear Science*, 2014, **61**, 1552–1557.
- (32) L. T. Tran, D. Bolst, B. James, V. Pan, J. Vohradsky, S. Peracchi, L. Chartier, E. Debrot, S. Guatelli, M. Petasecca, M. Lerch, D. Prokopovich, Ž. Pastuović, M. Povoli, A. Kok, T. Inaniwa, S. H. Lee, N. Matsufuji and A. B. Rosenfeld, “Silicon 3D Microdosimeters for Advanced Quality Assurance in Particle Therapy”, *Applied Sciences*, 2022, **12**, DOI: 10.3390/app12010328.
- (33) L. T. Tran, D. Bolst, S. Guatelli, A. Pogosso, M. Petasecca, M. L. Lerch, L. Chartier, D. A. Prokopovich, M. I. Reinhard, M. Povoli, A. Kok, V. L. Perevertaylo, N. Matsufuji, T. Kanai, M. Jackson and A. B. Rosenfeld, “The relative biological effectiveness for carbon, nitrogen, and oxygen ion beams using passive and scanning techniques evaluated with fully 3D silicon microdosimeters”, *Medical Physics*, 2018, **45**, 2299–2308.
- (34) L. T. Tran, L. Chartier, D. A. Prokopovich, D. Bolst, M. Povoli, A. Summanwar, A. Kok, A. Pogosso, M. Petasecca, S. Guatelli, M. I. Reinhard, M. Lerch, M.

- Nancarrow, N. Matsufuji, M. Jackson and A. B. Rosenfeld, “Thin Silicon Microdosimeter Utilizing 3-D MEMS Fabrication Technology: Charge Collection Study and Its Application in Mixed Radiation Fields”, *IEEE Transactions on Nuclear Science*, 2018, **65**, 467–472.
- (35) J. A. Davis, K. Ganesan, A. D. C. Alves, S. Guatelli, M. Petasecca, J. Livingstone, M. L. F. Lerch, D. A. Prokopovich, M. I. Reinhard, R. N. Siegle, S. Prawer, D. Jamieson, Z. Kuncic, V. L. Pisacane, J. F. Dicello, J. Ziegler, M. Zaider and A. B. Rosenfeld, “Characterization of a novel diamond-based microdosimeter prototype for radioprotection applications in space environments”, *IEEE Transactions on Nuclear Science*, 2012, **59**, 3110–3116.
- (36) J. A. Davis, K. Ganesan, D. A. Prokopovich, M. Petasecca, M. L. F. Lerch, D. N. Jamieson and A. B. Rosenfeld, “A 3D lateral electrode structure for diamond based microdosimetry”, *Applied Physics Letters*, 2017, **110**, 013503.
- (37) J. A. Davis, K. Ganesan, A. D. C. Alves, D. A. Prokopovich, S. Guatelli, M. Petasecca, M. L. F. Lerch, D. N. Jamieson and A. B. Rosenfeld, “Characterization of an Alternative Diamond Based Microdosimeter Prototype”, *IEEE Transactions on Nuclear Science*, 2014, **61**, 3479–3484.
- (38) F. García, G. Pelligrini, J. Balbuena, M. Lozano, R. Orava and M. Ullan, “A novel ultra-thin 3D detector-For plasma diagnostics at JET and ITER tokamaks”, *Nuclear Instruments and Methods in Physics Research, Section A: Accelerators, Spectrometers, Detectors and Associated Equipment*, 2009, **607**, 57–60.
- (39) L. T. Tran, D. A. Prokopovich, M. Petasecca, M. L. F. Lerch, C. Fleta, G. Pellegrini, C. Guardiola, M. I. Reinhard and A. B. Rosenfeld, “Ultra-thin 3-D detector: Charge collection characterization and application for microdosimetry”, *IEEE Transactions on Nuclear Science*, 2014, **61**, 3472–3478.
- (40) D. Bolst, L. T. Tran, L. Chartier, D. A. Prokopovich, A. Pogosso, S. Guatelli, M. I. Reinhard, M. Petasecca, M. L. F. Lerch, N. Matsufuji, V. L. Perevertaylo, C. Fleta, G. Pellegrini, M. Jackson and A. B. Rosenfeld, “RBE study using solid

- state microdosimetry in heavy ion therapy”, *Radiation Measurements*, 2017, **106**, 512–518.
- (41) C. Guardiola, C. Fleta, G. Pellegrini, F. García, D. Quirion, J. Rodríguez and M. Lozano, “Ultra-thin 3D silicon sensors for neutron detection”, *Journal of Instrumentation*, 2012, **7**, DOI: 10.1088/1748-0221/7/03/P03006.
- (42) C. Guardiola, F. Gómez, C. Fleta, J. Rodríguez, D. Quirion, G. Pellegrini, A. Lousa, L. Martínez-De-Olcoz, M. Pombar and M. Lozano, “Neutron measurements with ultra-thin 3D silicon sensors in a radiotherapy treatment room using a Siemens PRIMUS linac”, *Physics in Medicine and Biology*, 2013, **58**, 3227–3242.
- (43) D. Pennicard, G. Pellegrini, M. Lozano, C. Fleta, R. Bates and C. Parkes, “Design, simulation, production and initial characterisation of 3D silicon detectors”, *Nuclear Instruments and Methods in Physics Research, Section A: Accelerators, Spectrometers, Detectors and Associated Equipment*, 2009, **598**, 67–70.
- (44) C. Guardiola, A. Carabe, F. Gómez, G. Pellegrini, C. Fleta, S. Esteban, D. Quirion and M. Lozano, “First Silicon Microdosimeters Based on Cylindrical Diodes”, *Sensors & Transducers*, 2014, **183**, 129–133.
- (45) C. Fleta, S. Esteban, M. Baselga, D. Quirion, G. Pellegrini, C. Guardiola, M. A. Cortés-Giraldo, J. García López, M. C. Jiménez Ramos, F. Gómez and M. Lozano, “3D cylindrical silicon microdosimeters: Fabrication, simulation and charge collection study”, *Journal of Instrumentation*, 2015, **10**, DOI: 10.1088/1748-0221/10/10/P10001.
- (46) J. A. Davis, S. Guatelli, M. Petasecca, M. L. F. Lerch, M. I. Reinhard, M. Zaider, J. Ziegler and A. B. Rosenfeld, “Tissue Equivalence Study of a Novel Diamond-Based Microdosimeter for Galactic Cosmic Rays and Solar Particle Events”, *IEEE Transactions on Nuclear Science*, 2014, **61**, 1544–1551.
- (47) J. F. Ziegler, M. D. Ziegler and J. P. Biersack, “SRIM – The stopping and range of ions in matter (2010)”, *Nuclear Instruments and Methods in Physics Research Section B: Beam Interactions with Materials and Atoms*, 2010, **268**, 1818–1823.

- (48) Spectrum Semiconductor Materials, *Side-Brazed Dual In-Line Ceramic Package (DIP)* - Spectrum Semiconductor Materials website, 2022.
- (49) L. Chartier, L. Tran, D. Bolst, A. Pogossoy, S. Guatelli, M. Petasecca, M. Lerch, D. Prokopovich, M. Reinhard, V. Perevertaylo, M. Jackson, N. Matsufuji and A. Rosenfeld, “New silicon microdosimetry probes for RBE and biological dose studies using stationary and movable targets in ^{12}C ion therapy”, *Journal of Physics: Conference Series Micro-Mini Nano-Dosimetry Innovative Technologies in Radiation Therapy (MMND-ITRO2016)*, 2016, **777**, 26–28.
- (50) L. Chartier, Doctor of Philosophy Thesis, University of Wollongong, 2020.
- (51) A. B. Rosenfeld, L. T. Tran, S. Guatelli, D. Bolst, E. Debrot, S. Peracchi, B. James, V. Pan, J. Vohradsky, M. Petasecca, M. Lerch, D. Prokopovich, Z. Pastuovic, M. Povoli, A. Kok, T. Inaniwa and N. Matsufuji, Asian Forum for Accelerators and Detectors, Novosibirsk, Russia, 2021.
- (52) D. Rorer and G. Wambersie, *Current Status of neutron capture therapy*, tech. rep. May, 2001.
- (53) E. Brunckhorst, Ph.D. Thesis, University of Hamburg, 2009, pp. 11–28.
- (54) M. B. Chadwick, M. Herman, P. Obložinský, M. E. Dunn, Y. Danon, A. C. Kahler, D. L. Smith, B. Pritychenko, G. Arbanas, R. Arcilla, R. Brewer, D. A. Brown, R. Capote, A. D. Carlson, Y. S. Cho, H. Derrien, K. Guber, G. M. Hale, S. Hoblit, S. Holloway, T. D. Johnson, T. Kawano, B. C. Kiedrowski, H. Kim, S. Kunieda, N. M. Larson, L. Leal, J. P. Lestone, R. C. Little, E. A. McCutchan, R. E. MacFarlane, M. MacInnes, C. M. Mattoon, R. D. McKnight, S. F. Mughabghab, G. P. Nobre, G. Palmiotti, A. Palumbo, M. T. Pigni, V. G. Pronyaev, R. O. Sayer, A. A. Sonzogni, N. C. Summers, P. Talou, I. J. Thompson, A. Trkov, R. L. Vogt, S. C. van der Marck, A. Wallner, M. C. White, D. Wiarda and P. G. Young, “ENDF/B-VII.1 Nuclear data for science and technology: Cross sections, covariances, fission product yields and decay data”, *Nuclear Data Sheets*, 2011, **112**, 2887–2996.

- (55) N. S. Hosmane, J. A. Maguire, Y. Zhu and M. Takagaki, *Boron and gadolinium neutron capture therapy for cancer treatment*, World Scientific Publishing Co., Singapore, 2012, pp. 5–71.
- (56) G. L. Brownell and R. J. Shalek, *Nuclear Physics in Medicine*, tech. rep., 2013, pp. 2–68.
- (57) R. F. Barth, M. G. H. Vicente, O. K. Harling, W. Kiger, K. J. Riley, P. J. Binns, F. M. Wagner, M. Suzuki, T. Aihara, I. Kato and S. Kawabata, “Current status of boron neutron capture therapy of high grade gliomas and recurrent head and neck cancer”, *Radiation Oncology*, 2012, **7**, 146–189.
- (58) T. Yamamoto, K. Tsuboi, K. Nakai, H. Kumada, H. Sakurai and A. Matsumura, “Boron neutron capture therapy for brain tumors”, *Translational Cancer Research*, 2013, **2**, 80–86.
- (59) M. Kortensniemi, *Solutions for clinical implementation of boron neutron capture therapy in Finland*, tech. rep., 2002.
- (60) D. Nigg, C. Wemple, D. E. Wessol, F. J. Wheeler, C. Albright, M. Cohen, M. Frandsen, G. Harkin and M. Rossmeier, “SERA - An advanced treatment planning system for neutron therapy and BNCT”, *Transactions of the American Nuclear Society*, 1999, **80**.
- (61) H. Kumada, A. Matsumura, H. Sakurai, T. Sakae, M. Yoshioka, H. Kobayashi, H. Matsumoto, Y. Kiyanagi, T. Shibata and H. Nakashima, “Project for the development of the linac based NCT facility in University of Tsukuba”, *Applied Radiation and Isotopes*, 2014, **88**, 211–215.
- (62) T. Y. Lin and Y. W. H. Liu, “Development and verification of THORplan - A BNCT treatment planning system for THOR”, *Applied Radiation and Isotopes*, 2011, **69**, 1878–1881.
- (63) M. Kortensniemi, *Solutions for clinical implementation of boron neutron capture therapy in Finland*, tech. rep., 2002.
- (64) Y. Sakurai, H. Tanaka, T. Takata, N. Fujimoto, M. Suzuki, S. Masunaga, Y. Kinashi, N. Kondo, M. Narabayashi, Y. Nakagawa, T. Watanabe, R. Ono and A.

- Maruhashi, “Advances in boron neutron capture therapy (BNCT) at Kyoto university - From reactor-based BNCT to accelerator-based BNCT”, *Journal of the Korean Physical Society*, 2015, **67**, 76–81.
- (65) KURNS, *Institute for Integrated Radiation and Nuclear Science, Kyoto University website - Kyoto University Research Reactor*, 2022.
- (66) R. F. Barth, A. H. Fairchild and R. G. Soloway, “Boron neutron capture therapy for cancer”, *Cancer Research*, 1990, **50**, 1061–1070.
- (67) S. Green, “Recent developments in boron neutron capture therapy”, *Radiation Physics and Chemistry*, 1998, **8**, 545–551.
- (68) H. Kobayashi, M. Yoshioka, T. Kurihara, H. Kumada, A. Matsumura, H. Sakurai and F. Hiraga, ABNP14, INFN, 2014.
- (69) H. Tanaka, Y. Sakurai, M. Suzuki, S. Masunaga, T. Mitsumoto, S. Yajima, H. Tsutsui, T. Sato, T. Asano, G. Kashino, Y. Kinashi, Y. Liu, K. Ono and A. Maruhashi, “Measurement of the thermal neutron distribution in a water phantom using a cyclotron based neutron source for boron neutron capture therapy”, *IEEE Nuclear Science Symposium Conference Record (NSS/MIC)*, 2009, 2355–2357.
- (70) T. Hiroshimoto, Kyoto University: Radiation Medical Physics, 2013.
- (71) T. Nakamoto, UCANS V @ INFN LNL, Italy, 2015.
- (72) ENSDF, *ENSDF Database, Version 2019-01*, 2019.
- (73) H. Kobayashi, T. Kurihara and H. Matsumoto, Proceedings of IPAC 2012, 2012, pp. 4083–4085.
- (74) G. Busetto, *Boron Neutron Capture Therapy*, 2016.
- (75) C. Guardiola, C. Fleta, C. Guardiola, C. Fleta, C. Guardiola and C. Fleta, “Geant4 and MCNPX simulations of thermal neutron detection with planar silicon detectors”, 2011, DOI: 10.1088/1748-0221/6/09/T09001.
- (76) M. Lemke, D. L. Lambert, B. Edvardsson and C. Diode, “Related content Plasma CVD-Grown 10 B-Enriched Boron Films for Si Neutron Detectors”, 1990.
- (77) C. Höglund, J. Birch, K. Andersen, T. Bigault, J.-C. Buffet, J. Correa, P. van Esch, B. Guerard, R. Hall-Wilton, J. Jensen, A. Khaplanov, F. Piscitelli, C. Vettier, W.

- Vollenberg and L. Hultman, “B4C thin films for neutron detection”, *Journal of Applied Physics*, 2012, **111**, 104908.
- (78) F. Ghanbari and A. H. Mohagheghi, “resemble an AmLi source, with the average and maximum neutron energies of 545 keV and 1.5 MeV, respectively. 2”, 2001, **248**, 413–416.
- (79) G. I. Kaplan, “Integral and pulse mode silicon dosimetry for dose verification on radiation oncology modalities”, *University of Wollongong*, 2001.
- (80) A. Yutaka, M. Takai, I. Ogawa and T. Kishimoto, “Experimental Investigation of Thermal Neutron- Induced Single Event Upset in Static Random Access Memories”, *The Japan Society of Applied Physics*, 2001, **40**, 151–153.
- (81) B. Guerard, R. Hall-Wilton and F. Murtas, Academia-Industry Matching Event, CERN October, 2013.
- (82) F. Piscitelli, A. Khaplanov, A. Devishvili, S. Schmidt, C. Höglund, J. Birch, A. J. C. Dennison, P. Gutfreund and P. V. Esch, *Proceedings A: Royal Society Publishing* 472, 2016, p. 20150711.
- (83) R. August, H. Hughes, P. McMarr and R. Whitlock, *Neutron detection device and method of manufacture - WO Patent App. PCT/US2004/033,686*, 2005.
- (84) A. Winkler, H. Koivunoro, V. Reijonen, I. Auterinen and S. Savolainen, “Prompt gamma and neutron detection in BNCT utilizing a CdTe detector”, *Applied Radiation and Isotopes*, 2015, **106**, 139–144.
- (85) T. Kobayashi, Y. Sakurai and M. Ishikawa, “A non-invasive dose estimation system for clinical BNCT based on PG-SPECT - Conceptual study and fundamental experiments using HPGe and CdTe semiconductor detectors”, *Medical Physics*, 2000, **27**, 2124–2132.
- (86) D. K. Yoon, J. Y. Jung, K. Jo Hong, K. Sil Lee and T. Suk Suh, “GPU-based prompt gamma ray imaging from boron neutron capture therapy”, *Medical Physics*, 2015, **42**, 165–169.

- (87) B. Hales, T. Katabuchi, N. Hayashizaki, K. Terada, M. Igashira and T. Kobayashi, “Feasibility study of SPECT system for online dosimetry imaging in boron neutron capture therapy”, *Applied Radiation and Isotopes*, 2014, **88**, 167–170.
- (88) H. Lylia, H. Slamene, T. Akhal and B. Zouranen, *Concepts, Instrumentation and Techniques of Neutron Activation Analysis*, 2013, pp. 142–178.
- (89) I. C. on Radiation Units and Measurements, *ICRU Report 16: Linear Energy Transfer*, tech. rep., ICRU, 1970.
- (90) P. Georg, “Particle therapy in head and neck cancer—expanding therapeutic options”, *Magazine of European Medical Oncology*, 2020, **13**, 389–394.
- (91) J. Alonso and T. Antaya, in *Reviews of Accelerator Science and Technology*, 2012, vol. 5, pp. 227–263.
- (92) J. D. Grant and J. Y. Chang, “Proton-Based Stereotactic Ablative Radiotherapy in Early-Stage Non-Small-Cell Lung Cancer”, *BioMed Research International*, 2014, DOI: 10.1155/2014/389048.
- (93) T. Ohno, “Particle radiotherapy with carbon ion beams”, *EPMA Journal*, 2013, **4**, DOI: 10.1186/1878-5085-4-9.
- (94) R. R. Wilson, “Radiological Use of Fast Protons”, *Radiology*, 1946, **47**, 487–491.
- (95) D. Schardt, T. Elsässer and D. Schulz-Ertner, “Heavy-ion tumor therapy: Physical and radiobiological benefits”, *Reviews of Modern Physics*, 2010, **82**, 383–425.
- (96) J. R. Castro, W. M. Saunders, C. A. Tobias, G. T. Chen, S. Curtis, J. T. Lyman, J. Michael Collier, S. Pitluck, K. A. Woodruff, E. A. Blakely, T. Tenforde, D. Char, T. L. Phillips and E. L. Alpen, “Treatment of cancer with heavy charged particles”, *International Journal of Radiation Oncology, Biology, Physics*, 1982, **8**, 2191–2198.
- (97) D. E. Linstadt, J. R. Castro and T. L. Phillips, “Neon ion radiotherapy: Results of the phase I/II clinical trial”, *International Journal of Radiation Oncology, Biology, Physics*, 1991, **20**, 761–769.
- (98) J. R. Castro, D. E. Linstadt, J. P. Bahary, P. L. Petti, I. Daftari, J. M. Collier, P. H. Gutin, G. Gauger and T. L. Phillips, “Experience in charged particle irradiation of

- tumors of the skull base: 1977-1992”, *International Journal of Radiation Oncology, Biology, Physics*, 1994, **29**, 647–655.
- (99) T. Kamada, H. Tsujii, E. A. Blakely, J. Debus, W. De Neve, M. Durante, O. Jäkel, R. Mayer, R. Orecchia, R. Pötter, S. Vatnitsky and W. T. Chu, “Carbon ion radiotherapy in Japan: An assessment of 20 years of clinical experience”, *The Lancet Oncology*, 2015, **16**, 93–100.
- (100) O. Mohamad, H. Makishima and T. Kamada, “Evolution of carbon ion radiotherapy at the national institute of radiological sciences in Japan”, *Cancers*, 2018, **10**, DOI: 10.3390/cancers10030066.
- (101) B. James, M. Povoli, A. Kok, M. J. Goethem, M. Nancarrow, N. Matsufuji, M. Jackson, A. B. Rosenfeld, L. T. Tran, D. Bolst, S. Peracchi, J. A. Davis, D. A. Prokopovich, S. Guatelli, M. Petasecca and M. Lerch, “SOI Thin Microdosimeters for High LET Single-Event Upset Studies in Fe, O, Xe, and Cocktail Ion Beam Fields”, *IEEE Transactions on Nuclear Science*, 2019, **67**, 146–153.
- (102) C. Stannard, F. Vernimmen, H. Carrara, D. Jones, S. Fredericks, J. Hille and E. De Kock, “Malignant salivary gland tumours: Can fast neutron therapy results point the way to carbon ion therapy?”, *Radiotherapy and Oncology*, 2013, **109**, 262–268.
- (103) S. B. Field, “An historical survey of radiobiology and radiotherapy with fast neutrons.”, *Current topics in radiation research quarterly*, 1976, **11**, 1–86.
- (104) J. Gueulette, H. G. Menzel, P. Pihet and A. Wambersie, Fast Neutrons and High-LET Particles in Cancer Therapy, ed. R. Engenhart-Cabillic and A. Wambersie, Springer Berlin Heidelberg, Berlin, Heidelberg, 1998, pp. 31–53.
- (105) G. Coutrakon, J. Cortese, A. Ghebremedhin, J. Hubbard, J. Johanning, P. Koss, G. Maudsley, C. R. Slater, C. Zuccarelli and J. Robertson, “Microdosimetry spectra of the Loma Linda proton beam and relative biological effectiveness comparisons”, *Medical Physics*, 1997, **24**, 1499–1506.
- (106) R. S. Stone, “Neutron therapy and specific ionization”, *The American Journal of Roentgenology and Radium Therapy*, 1948, **59**, 771–785.

- (107) F. N. D. Kurie, "Present-day design and technique of the cyclotron: A description of the methods and application of the cyclotron as developed by Ernest O. Lawrence and his associates at the radiation laboratory, Berkeley", *Journal of Applied Physics*, 1938, **9**, 691–701.
- (108) J. Chadwick, "Possible Existence of a Neutron", *Nature*, 1932, **129**, 312.
- (109) H. Svensson and T. Landberg, "Neutron therapy-the historical background", *Acta Oncologica*, 1994, **33**, 227–231.
- (110) J. F. Fowler, R. L. Morgan and C. A. P. Wood, "I. The Biological and Physical Advantages and Problems of Neutron Therapy", *The British Journal of Radiology*, 1963, **36**, 77–80.
- (111) L. H. Gray, A. D. Conger, M. Ebert, S. Hornsey and O. C. A. Scott, "The Concentration of Oxygen Dissolved in Tissues at the Time of Irradiation as a Factor in Radiotherapy", *The British Journal of Radiology*, 1953, **26**, 638–648.
- (112) M. Catterall, D. K. Bewley and I. Sutherland, "Second report on results of a randomised clinical trial of fast neutrons compared with x or gamma rays in treatment of advanced tumours of head and neck", *British Medical Journal*, 1977, **1**, 1642.
- (113) D. T. L. Jones and A. Wambersie, Workshop on Nuclear Data for Science and Technology: Medical Applications ICTP, Trieste, Italy, Trieste, Italy, 2007.
- (114) H. M. Specht, T. Neff, W. Reuschel, F. M. Wagner, S. Kampfer, J. J. Wilkens, W. Petry and S. E. Combs, "Paving the road for modern particle therapy - What can we learn from the experience gained with fast neutron therapy in Munich?", *Frontiers in Oncology*, 2015, **5**, 1–7.
- (115) D. T. L. Jones and S. J. Mills, "The South African National Accelerator Centre: Particle therapy and isotope production programmes", *Radiation Physics and Chemistry*, 1998, **51**, 571–578.
- (116) D. T. L. Jones, J. E. Symons, T. J. Fulcher, F. D. Brooks, M. R. Nchodu, M. S. Allie, A. Buffler and M. J. Oliver, "Neutron fluence and kerma spectra of a p(66)/Be(40) clinical source", *Medical Physics*, 1992, **19**, 1285–1292.
- (117) D. T. L. Jones, International Workshop on Fast Neutron Therapy, 2006, pp. 1–14.

- (118) D. T. L. Jones, “Present status and future trends of heavy particle radiotherapy”, *Proceedings of the 15th International Conference on Cyclotrons and their Applications, Caen, France*, 1998, 13–20.
- (119) M. A. Ross, P. M. DeLuca Jr., D. T. L. Jones, A. Lennox and R. L. Maughan, “Calculated Fluence Spectra at Neutron Therapy Facilities”, *Radiation Protection Dosimetry*, 1997, **70**, 481–484.
- (120) J. F. Briesmeister, *MCNP - A General Monte Carlo N-Particle Transport Code, Version 4A: LA- 12625-M*, tech. rep., Los Alamos National Laboratory, 1993.
- (121) R. E. Prael and H. Lichtenstein, *User Guide to LCS: The LAHET Code System: LA-UR-89-3074*, tech. rep., Los Alamos National Laboratory, 1989.
- (122) T. D. Bohm, P. M. Deluca, L. J. Cox, R. L. Maughan, D. T. Jones and A. Lennox, “Monte Carlo calculations to characterize the source for neutron therapy facilities”, *Medical Physics*, 1999, **26**, 783–792.
- (123) K. Ono, “Prospects for the new era of boron neutron capture therapy and subjects for the future”, *Therapeutic Radiology and Oncology*, 2018, **2**, DOI: 10.21037/tro.2018.09.04.
- (124) T. Sato, S. I. Masunaga, H. Kumada and N. Hamada, “Microdosimetric Modeling of Biological Effectiveness for Boron Neutron Capture Therapy Considering Intra- and Intercellular Heterogeneity in ^{10}B Distribution”, *Scientific Reports*, 2018, **8**, DOI: 10.1038/s41598-017-18871-0.
- (125) K. Gordon, I. Gulidov, T. Fatkhudinov, S. Koryakin and A. Kaprin, “Fast and Furious: Fast Neutron Therapy in Cancer Treatment”, *International Journal of Particle Therapy*, 2022, **9**, 59–69.
- (126) T. D. Malouff, A. Mahajan, S. Krishnan, C. Beltran, D. S. Seneviratne and D. M. Trifiletti, “Carbon Ion Therapy: A Modern Review of an Emerging Technology”, *Frontiers in Oncology*, 2020, **10**, DOI: 10.3389/fonc.2020.00082.
- (127) S. Agostinelli, “GEANT4 - A simulation toolkit”, *Nuclear Instruments and Methods in Physics Research A*, 2003, **506**, 250–303.

- (128) J. Vohradsky, S. Guatelli, J. A. Davis, L. T. Tran and A. B. Rosenfeld, “Evaluation of silicon based microdosimetry for Boron Neutron Capture Therapy Quality Assurance”, *Physica Medica*, 2019, **66**, 8–14.
- (129) J. Vohradsky, L. T. Tran, S. Guatelli, L. Chartier, C. Vandevorode, E. A. de Kock, J. Nieto-Camero, D. Bolst, S. Peracchi, C. Höglund and A. B. Rosenfeld, “Response of SOI microdosimeter in fast neutron beams: experiment and Monte Carlo simulations”, *Physica Medica*, 2021, **90**, 176–187.
- (130) S. Guatelli, D. Cutajar, B. Oborn and A. B. Rosenfeld, AIP Conference Proceedings, Vol. 1345, 2011, pp. 303–322.
- (131) J. Allison, K. Amako, J. Apostolakis, H. Araujo and P. Dubois, “Geant4 developments and applications”, *IEEE Transactions on Nuclear Science*, 2006, **53**, 270–278.
- (132) D. Wight, Centre for Medical Radiation Physics, University of Wollongong, 2013.
- (133) A. J. Koning, D. Rochman, J.-C. Sublet, N. Dzysiuk, M. Fleming and S. van der Marck, “TENDL: Complete Nuclear Data Library for Innovative Nuclear Science and Technology”, *Nuclear Data Sheets*, 2019, **155**, 1–55.
- (134) S. A. Enger, P. Munck Af Rosenschöld, A. Rezaei and H. Lundqvist, “Monte Carlo calculations of thermal neutron capture in gadolinium: A comparison of GEANT4 and MCNP with measurements”, *Medical Physics*, 2006, **33**, 337–341.
- (135) C. J. Werner, *MCNP6.2 Release Notes: LA-UR-18-20808*, tech. rep., Los Alamos National Laboratory, 2018.
- (136) B. M. Van Der Ende, J. Atanackovic, A. Erlandson and G. Bentoumi, “Use of GEANT4 vs. MCNPX for the characterization of a boron-lined neutron detector”, *Nuclear Instruments and Methods in Physics Research, Section A: Accelerators, Spectrometers, Detectors and Associated Equipment*, 2016, **820**, 40–47.
- (137) S. Garny, V. Mares and W. Rühm, “Response functions of a Bonner sphere spectrometer calculated with GEANT4”, *Nuclear Instruments and Methods in Physics Research, Section A: Accelerators, Spectrometers, Detectors and Associated Equipment*, 2009, **604**, 612–617.

- (138) R. Lemrani, M. Robinson, V. A. Kudryavtsev, M. De Jesus, G. Gerbier and N. J. C. Spooner, “Low-energy neutron propagation in MCNPX and GEANT4”, *Nuclear Instruments and Methods in Physics Research, Section A: Accelerators, Spectrometers, Detectors and Associated Equipment*, 2006, **560**, 454–459.
- (139) S. Garny, G. Leuthold, V. Mares, H. G. Paretzke and W. Ruhm, “GEANT4 transport calculations for neutrons and photons below 15 MeV”, *IEEE Transactions on Nuclear Science*, 2009, **56**, 2392–2396.
- (140) K. Hartling, B. Ciungu, G. Li, G. Bentoumi and B. Sur, “The effects of nuclear data library processing on Geant4 and MCNP simulations of the thermal neutron scattering law”, *Nuclear Instruments and Methods in Physics Research, Section A: Accelerators, Spectrometers, Detectors and Associated Equipment*, 2018, **891**, 25–31.
- (141) R. A. I. Forster, M. E. Rising and A. Sood, *The History of Monte Carlo and MCNP at Los Alamos: LA-UR-21-26274*, tech. rep., Los Alamos National Laboratory, Los Alamos, 2021.
- (142) S. Jeffrey, H. Grady, E. Richard, J. Arnold, S. G. Mashnik, J. S. Bull, H. G. Hughes, R. E. Prael and A. J. Sierk, “Current status of MCNP6 as a simulation tool useful for space and accelerator applications”, 2012.
- (143) J. C. Adams, W. S. Brainerd, R. A. Hendrickson, R. E. Maine, J. T. Martin and B. T. Smith, *The Fortran 2003 Handbook: The Complete Syntax, Features and Procedures*, Springer, 1st edn., 2008.
- (144) J. Lloyd, K. Donald, D. K. Parsons and J. L. Conlin, *Release of Continuous Representation for $S(\alpha, \beta)$ ACE Data: LA-UR-12-00800*, tech. rep., Los Alamos National Laboratory, 2014.
- (145) J. L. Conlin, D. K. Parsons, S. J. Gardiner, A. C. I. Kahler, M. B. Lee, M. C. White, M. G. Gray, D. K. Parsons, M. Gray, A. C. Kahler and M. B. Lee, *Continuous Energy Neutron Cross Section Data Tables Based upon ENDF/B-VII.1*, tech. rep., 2013.

- (146) R. Brun and F. Rademakers, “ROOT - An object oriented data analysis framework”, *Nuclear Instruments and Methods in Physics Research Section A: Accelerators, Spectrometers, Detectors and Associated Equipment*, 1997, **389**, 81–86.
- (147) D. W. Siderius, *NIST Standard Reference Simulation Website - National Institute of Standards and Technology*, tech. rep., 2017.
- (148) P. Arce, D. Bolst, D. Cutajar, S. Guatelli, A. Le, A. B. Rosenfeld, D. Sakata, M.-C. Bordage, J. M. C. Brown, P. Cirrone, G. Cuttone, L. Pandola, G. Petringa, M. A. Cortes-Giraldo, J. M. Quesada, L. Desorgher, P. Dondero, A. Mantero, A. Dotti, D. H. Wright, B. Faddegon, J. Ramos-Mendez, C. Fedon, S. Incerti, V. Ivanchenko, D. Konstantinov, G. Latyshev, I. Kyriakou, C. Mancini-Terracciano, M. Maire, M. Novak, C. Omachi, T. Toshito, A. Perales, Y. Perrot, F. Romano, L. G. Sarmiento, T. Sasaki, I. Sechopoulos and E. C. Simpson, “Report on G4-Med, a Geant4 benchmarking system for medical physics applications developed by the Geant4 Medical Simulation Benchmarking Group”, *Medical Physics*, 2021, **48**, 19–56.
- (149) A. R. García and E. Mendoza, G4 Hadronic group meeting, Ciemat, Gobierno de Espana, 2013.
- (150) C. Anderson, G. McKinney, J. Tutt and M. James, “Delta-ray Production in MCNP 6.2.0”, *Physics Procedia*, 2017, **90**, 229–236.
- (151) G. Van Rossum and F. L. Drake, *Python 3 Reference Manual*, CreateSpace, Scotts Valley, CA, 2009.
- (152) C. J. Solomon, C. Bates and J. Kulesza, *The MCNPTools Package: Installation and Use: LA-UR-17-21779*, tech. rep., Los Alamos National Laboratory, Los Alamos, 2017.
- (153) H. Baba, Y. Onizuka, M. Nakao, M. Fukahori, T. Sato, Y. Sakurai, H. Tanaka and S. Endo, “Microdosimetric evaluation of the neutron field for BNCT at Kyoto University reactor by using the PHITS code”, *Radiation Protection Dosimetry*, 2011, **143**, 528–532.

- (154) Y. Onizuka, Proceeding of the Scientific Meeting 2002 on ‘Advancement of the System for Neutron Capture Therapy’, KURRI-KR-95, Research Reactor Institute Kyoto University, 2003, pp. 53–58.
- (155) IAEA, *Radiation Protection and Safety of Radiation Sources: International Basic Safety Standards*, tech. rep., 2011.
- (156) J. P. Pignol, J. Slabbert and P. Binns, “Monte Carlo simulation of fast neutron spectra: Mean lineal energy estimation with an effectiveness function and correlation to RBE”, *International Journal of Radiation Oncology Biology Physics*, 2001, **49**, 251–260.
- (157) B. J. Mijneer, L. J. Goodman, E. J. Hall, H. G. Menzel, C. J. Parnell, J. Rassow and P. Wootton, *ICRU Report 45. Clinical neutron dosimetry. Part 1: Determination of absorbed dose in a patient treated by external beams of fast neutrons*, tech. rep. 2, Bethesda, 1989.
- (158) M. Safavi-Naeini, A. Chacon, S. Guatelli, D. R. Franklin, K. Bamberg, M. C. Gregoire and A. Rosenfeld, “Opportunistic dose amplification for proton and carbon ion therapy via capture of internally generated thermal neutrons”, *Scientific Reports*, 2018, **8**, 1–14.
- (159) R. L. Maughan, C. Kota and M. Yudelev, “A microdosimetric study of the dose enhancement in a fast neutron beam due to boron neutron capture”, *Physics in Medicine and Biology*, 1993, **38**, 1957–1961.
- (160) S. Agosteo, P. Colautti, A. Fazzi, D. Moro and A. Pola, “A solid state microdosimeter based on a monolithic silicon telescope”, *Radiation protection dosimetry*, 2006, **122**, 382–386.
- (161) N. Hu, R. Uchida, L. T. Tran, A. Rosenfeld and Y. Sakurai, “Feasibility study on the use of 3D silicon microdosimeter detectors for microdosimetric analysis in boron neutron capture therapy”, *Applied Radiation and Isotopes*, 2018, **140**, 109–114.
- (162) A. Parisi, E. Boogers, L. Struelens and F. Vanhavere, “Uncertainty budget assessment for the calibration of a silicon microdosimeter using the proton edge

- technique”, *Nuclear Instruments and Methods in Physics Research A*, 2020, **978**, 164449.
- (163) S. Agosteo, G. Fallica, A. Fazzi, M. Introini, A. Pola and G. Valvo, “A pixelated silicon telescope for solid state microdosimetry”, *Radiation Measurements*, 2008, **43**, 585–589.
- (164) H. Kumada, K. Takada, F. Naito, T. Kurihara, T. Sugimura, Y. Matsumoto, H. Sakurai, A. Matsumura and T. Sakae, AIP Conference Proceedings, 2019, vol. 2160.
- (165) S. Peracchi, N. Matsufuji, A. Kok, M. Povoli, M. Jackson, A. B. Rosenfeld, L. T. Tran, B. James, D. Bolst, D. A. Prokopovich, J. A. Davis, S. Guatelli, M. Petasecca and M. L. Lerch, “A Solid-State Microdosimeter for Dose and Radiation Quality Monitoring for Astronauts in Space”, *IEEE Transactions on Nuclear Science*, 2020, **67**, 169–174.
- (166) H. Kumada and K. Takada, “Treatment planning system and patient positioning for boron neutron capture therapy”, *Therapeutic Radiology and Oncology*, 2018, **2**, 50.
- (167) ICRP, *ICRP Publication 103: The 2007 Recommendations of the International Commission on Radiological Protection*, tech. rep. 37, 2007.
- (168) T. Sato, Y. Iwamoto, S. Hashimoto, T. Ogawa, T. Furuta, S. ichiro Abe, T. Kai, P. E. Tsai, N. Matsuda, H. Iwase, N. Shigyo, L. Sihver and K. Niita, “Features of Particle and Heavy Ion Transport code System (PHITS) version 3.02”, *Journal of Nuclear Science and Technology*, 2018, **55**, 684–690.
- (169) K. Shibata, O. Iwamoto, T. Nakagawa, N. Iwamoto, A. Ichihara, S. Kunieda and S. Chiba, “JENDL-4.0: A New Library for Nuclear Science and Engineering”, *Journal of Nuclear Science and Technology*, 2011, **48**, 1–30.
- (170) ENDF, *Evaluated Nuclear Data File (ENDF), Version 2020-07-07*, 2020.
- (171) ICRP, *ICRP Publication 38: Radionuclide Transformations - Energy and Intensity of Emissions*, tech. rep. 10, 1983.
- (172) ICRP, *ICRP Publication 60: 1990 Recommendations of the International Commission on Radiological Protection*. Tech. rep., 1991.

- (173) D. V. Webb, S. B. Solomon and J. E. M. Thomson, “Background radiation levels and medical exposure levels in Australia”, *Radiation Protection in Australia*, 1999, **16**, 25–32.
- (174) ARPANSA, *Radiation Protection Series: Code for Radiation Protection in Planned Exposure Situations*, tech. rep. C-1 (Rev. 1), ARPANSA, 2020.
- (175) A. Olsson, M. S. Hellsing and A. R. Rennie, *New possibilities using additive manufacturing with materials that are difficult to process and with complex structures*, 2017.
- (176) Qt Group, *Qt Software Version 5*, 2022.
- (177) B. James, L. T. Tran, J. Vohradsky, D. Bolst, V. Pan, M. Carr, S. Guatelli, A. Pogosso, M. Petasecca, M. Lerch, D. A. Prokopovich, M. I. Reinhard, M. Povoli, A. Kok, D. Hinde, M. Dasgupta, A. Stuchbery, V. Perevertaylo and A. B. Rosenfeld, “SOI Thin Microdosimeter Detectors for Low-Energy Ions and Radiation Damage Studies”, *IEEE Transactions on Nuclear Science*, 2019, **66**, 320–326.
- (178) D. Bolst, L. T. Tran, S. Guatelli, N. Matsufuji and A. B. Rosenfeld, “Modelling the Biological Beamline at HIMAC using Geant4”, *Journal of Physics: Conference Series*, 2019, **1154**, DOI: 10.1088/1742-6596/1154/1/012003.
- (179) M. Bullmann, T. Fetzner, F. Ebner, M. Ebner, F. Deinzer and M. Grzegorzec, “Comparison of 2.4 GHz WiFi FTM- and RSSI-Based Indoor Positioning Methods in Realistic Scenarios”, *Sensors*, 2020, **20**, 1–26.
- (180) Adafruit, *Adafruit Website - Adafruit PiOLED - 128x32 Monochrome OLED Add-on for Raspberry Pi Product 3527*, 2022.
- (181) Waveshare, *Waveshare Website - 2.13inch e-Paper HAT*, 2022.
- (182) T. A. Vázquez, S. Barrachina-Muñoz, B. Bellalta and A. Bel, “HARE: Supporting efficient uplink multi-hop communications in self-organizing LPWANs”, *Sensors*, 2018, **18**, DOI: 10.3390/s18010115.
- (183) LoRA Alliance, *LoRaWAN 1.1 Specification*, tech. rep., 2017.

- (184) A. Drenoyanis, R. Raad, I. Wady and C. Krogh, “Implementation of an IoT based radar sensor network for wastewater management”, *Sensors*, 2019, **19**, DOI: 10.3390/s19020254.
- (185) Pi Supply, *Pi Supply Website - LoRa Gateway HAT for Raspberry Pi*, 2022.
- (186) Cisco Systems Inc., *Cisco Wireless Gateway for LoRaWAN Data Sheet*, tech. rep., 2021, pp. 1–19.
- (187) I. Butun, N. Pereira and M. Gidlund, “Security risk analysis of LoRaWAN and future directions”, *Future Internet*, 2019, **11**, 1–22.
- (188) N. V. Smirnov, “Tables for estimating the goodness of fit of empirical distribution”, *Annals of Mathematical Statistics*, 1948, **19**.
- (189) C. Geng, X. Tang, F. Guan, J. Johns, L. Vasudevan, C. Gong, D. Shu and D. Chen, “GEANT4 calculations of neutron dose in radiation protection using a homogeneous phantom and a Chinese hybrid male phantom”, *Radiation Protection Dosimetry*, 2016, **168**, 433–440.
- (190) H. N. Tran, A. Marchix, A. Letourneau, J. Darpentigny, A. Menelle, F. Ott, J. Schwindling and N. Chauvin, “Comparison of the thermal neutron scattering treatment in MCNP6 and GEANT4 codes”, *Nuclear Instruments and Methods in Physics Research, Section A: Accelerators, Spectrometers, Detectors and Associated Equipment*, 2018, **893**, 84–94.

Appendix A

Statistics test data for different physics options

A.1 Comparison of different physics options in water phantom

		BERT HP/T	INCL HP/T	Shield /T	LEND /T	BICAll HP/T	MCNP /T	BERT HP	INCL HP	Shield	LEND	BICAll HP	MCNP
0.0253 eV	p	1.00	0.97	1.00	0.96	1.00	0.96	1.00	1.00	1.00	1.00	1.00	0.50
	PD	0.05	-1.59	0.60	-2.42	-0.47	3.71	-0.05	-0.05	-0.01	-1.15	0.04	-18.36
0.1 eV	p	1.00	0.99	1.00	0.99	1.00	0.93	1.00	1.00	0.99	1.00	1.00	0.65
	PD	0.27	0.50	-0.19	-2.40	-0.13	4.06	0.40	0.14	-1.04	-1.10	-0.05	-12.75
1 eV	p	0.99	1.00	1.00	1.00	1.00	0.97	1.00	1.00	1.00	0.99	1.00	0.73
	PD	-0.44	-0.22	0.12	-1.21	-0.21	2.38	0.04	-0.34	0.40	-1.85	-0.16	6.24
10 eV	p	1.00	1.00	1.00	1.00	1.00	0.94	0.99	0.99	1.00	1.00	0.99	0.82
	PD	-0.11	0.20	0.03	-0.43	0.42	3.05	-0.71	-0.83	0.42	-1.27	-1.00	8.85
100 eV	p	0.98	0.99	0.99	1.00	1.00	0.94	1.00	1.00	1.00	1.00	1.00	0.82
	PD	1.37	0.92	1.15	-0.56	0.98	3.85	-0.34	-0.35	-0.30	-1.50	-0.31	10.12
1 keV	p	1.00	1.00	0.99	0.99	1.00	0.98	0.97	1.00	0.97	0.97	0.99	0.90
	PD	0.36	-0.24	-0.53	-1.20	-0.21	3.02	-1.05	0.08	-1.22	-1.94	-0.80	10.26
10 keV	p	0.99	1.00	1.00	0.97	0.99	1.00	1.00	1.00	1.00	1.00	1.00	0.79
	PD	-0.69	-0.45	-0.49	-1.89	-0.92	2.04	-0.37	-0.05	-0.34	-1.06	-0.67	11.22
100 keV	p	1.00	1.00	1.00	1.00	1.00	0.98	1.00	1.00	1.00	0.99	1.00	0.89
	PD	-0.32	-0.64	-0.49	-0.69	-0.52	0.72	0.64	0.17	0.63	-0.83	0.55	3.41
1 MeV	p	1.00	1.00	1.00	1.00	1.00	1.00	1.00	1.00	1.00	1.00	1.00	0.98
	PD	0.68	0.49	0.55	0.40	0.73	0.94	0.25	0.13	0.29	-0.26	-0.08	2.78
2 MeV	p	1.00	1.00	1.00	1.00	1.00	0.99	1.00	1.00	1.00	1.00	1.00	0.98
	PD	-0.11	-0.45	-0.13	-0.33	-0.41	0.92	0.02	0.09	0.22	0.11	0.21	2.60
5 MeV	p	1.00	1.00	1.00	1.00	1.00	0.99	1.00	1.00	1.00	1.00	1.00	1.00
	PD	-0.06	-0.11	-0.20	-0.13	0.37	-1.35	0.03	0.27	0.16	-0.08	0.39	-0.97
10 MeV	p	1.00	1.00	1.00	1.00	1.00	0.98	1.00	1.00	1.00	0.99	1.00	0.99
	PD	-0.52	-0.01	-0.14	-4.50	-0.04	-1.45	0.08	0.21	-0.28	-4.34	-0.12	-1.04
20 MeV	p	0.88	0.64	0.89	0.94	1.00	0.63	0.89	0.65	0.88	0.95	1.00	0.62
	PD	-1.81	-5.58	-1.68	-3.42	-0.24	-5.41	-1.71	-5.48	-1.76	-3.26	-0.18	-5.42
30 MeV	p	0.79	0.68	0.81	0.82	1.00	0.87	0.80	0.74	0.84	0.85	1.00	0.90
	PD	-4.07	-7.63	-3.93	-4.93	-0.45	-6.17	-4.15	-7.42	-3.86	-4.86	-0.02	-5.94
40 MeV	p	0.75	0.76	0.76	0.76	1.00	0.87	0.70	0.73	0.72	0.72	1.00	0.83
	PD	-9.78	-10.28	-9.71	-10.48	0.33	-9.49	-10.15	-10.52	-10.02	-10.83	-0.06	-9.81
50 MeV	p	0.99	1.00	0.98	0.99	1.00	1.00	0.97	0.99	0.99	0.98	1.00	1.00
	PD	-3.67	-0.82	-3.80	-4.45	-0.15	-1.29	-4.11	-0.97	-3.71	-4.50	-0.25	-1.30
60 MeV	p	0.99	1.00	0.99	1.00	1.00	1.00	0.98	1.00	0.99	0.99	1.00	1.00
	PD	-5.44	1.89	-5.42	-5.95	0.05	1.20	-5.74	2.02	-5.46	-6.23	-0.25	1.15
70 MeV	p	0.99	1.00	0.98	0.99	1.00	0.97	0.99	1.00	0.99	0.98	1.00	0.96
	PD	-7.82	2.54	-7.87	-8.23	-0.19	-0.04	-7.80	2.51	-7.77	-8.55	-0.15	-0.17

Table A.1: Statistics tests for depth dose distribution of monoenergetic neutrons in water phantom for the different physics lists compared against BICHP. All physics with thermal on (T) are compared against BICHP/T, and physics with thermal off (no T) are compared against BICHP.

A.2 Comparison of different physics options in 50ppm

^{10}B water phantom

		BERT HP/T	INCL HP/T	Shield /T	LEND /T	BICAll HP/T	MCNP /T	BERT HP	INCL HP	Shield	LEND	BICAll HP	MCNP
0.0253 eV	p	1.00	1.00	1.00	1.00	1.00	0.99	1.00	1.00	1.00	0.68	1.00	0.42
	PD	0.05	1.24	0.45	-0.72	-0.68	1.41	0.99	0.27	0.46	8.58	0.46	3.37
0.1 eV	p	1.00	1.00	1.00	1.00	1.00	1.00	1.00	1.00	1.00	1.00	1.00	0.49
	PD	-0.32	-0.50	-0.71	-0.71	-0.57	0.11	-0.23	0.33	-0.01	7.16	0.16	0.67
1 eV	p	1.00	1.00	1.00	1.00	1.00	1.00	1.00	1.00	1.00	0.98	1.00	0.55
	PD	0.01	0.53	-0.17	-0.52	0.25	-0.02	-0.49	-0.12	0.03	5.85	0.21	6.65
10 eV	p	1.00	1.00	1.00	1.00	1.00	1.00	1.00	1.00	1.00	0.95	1.00	0.70
	PD	-0.19	0.33	-0.01	-0.54	0.34	-0.63	0.83	-0.48	0.38	6.80	0.29	8.86
100 eV	p	1.00	1.00	1.00	0.99	1.00	1.00	1.00	1.00	1.00	0.97	1.00	0.89
	PD	-0.73	-0.57	-0.10	-1.22	-0.87	-0.32	0.23	0.72	0.45	6.58	0.75	9.88
1 keV	p	1.00	1.00	1.00	1.00	1.00	0.96	1.00	0.99	1.00	0.97	1.00	0.99
	PD	0.31	0.32	0.64	-0.56	0.46	1.95	0.21	0.29	0.07	5.03	0.08	9.38
10 keV	p	1.00	1.00	1.00	1.00	1.00	0.98	1.00	1.00	0.99	1.00	1.00	0.99
	PD	0.09	0.42	0.37	0.28	-0.26	0.95	0.40	0.00	-0.44	5.24	0.10	9.99
100 keV	p	1.00	1.00	1.00	1.00	1.00	1.00	1.00	1.00	1.00	0.99	1.00	0.65
	PD	-0.21	-0.44	-0.17	0.35	-0.02	0.72	-0.40	-0.11	-0.47	5.06	0.25	9.18
1 MeV	p	1.00	1.00	1.00	0.99	1.00	1.00	1.00	1.00	1.00	0.99	1.00	0.78
	PD	-0.17	-0.57	-0.23	-1.18	-0.23	-0.57	0.11	0.48	0.61	4.11	0.49	6.73
2 MeV	p	1.00	1.00	1.00	0.99	1.00	1.00	0.99	0.98	0.99	0.99	1.00	1.00
	PD	-0.21	0.07	0.08	-1.02	0.14	-0.41	-0.46	-1.01	-0.63	1.99	-0.45	4.47
5 MeV	p	1.00	1.00	1.00	0.99	1.00	0.98	1.00	1.00	1.00	0.99	1.00	0.95
	PD	-0.15	0.23	0.12	-1.48	0.10	-2.84	0.04	-0.67	-0.47	1.05	-0.10	3.01
10 MeV	p	1.00	1.00	1.00	1.00	1.00	0.83	0.98	1.00	1.00	0.99	1.00	0.86
	PD	-0.30	-0.21	-0.70	-1.51	-0.02	-1.65	-0.59	0.19	-0.10	0.98	-0.01	1.96
20 MeV	p	1.00	0.99	0.99	0.98	1.00	0.73	0.98	0.99	0.99	1.00	1.00	0.96
	PD	-2.43	-3.74	-2.16	-3.94	-0.15	-12.66	-2.56	-4.31	-3.14	-2.50	-0.34	-9.33
30 MeV	p	0.88	0.90	0.85	0.92	1.00	0.93	0.78	0.93	0.82	0.89	0.99	0.92
	PD	13.45	8.02	14.01	11.53	-0.10	-8.05	12.92	7.23	13.49	14.43	1.18	-3.71
40 MeV	p	0.86	0.77	0.85	0.88	0.99	0.98	0.97	0.98	0.99	0.99	0.91	0.88
	PD	24.13	12.37	23.58	22.17	-0.30	-4.58	23.42	11.47	22.23	23.94	-1.84	-2.08
50 MeV	p	1.00	0.99	1.00	1.00	1.00	0.92	0.94	0.98	0.94	0.96	0.98	0.85
	PD	13.58	1.44	12.50	11.42	0.13	-18.17	13.68	1.20	13.31	14.32	-0.41	-16.28
60 MeV	p	0.99	1.00	0.97	0.94	1.00	0.99	0.99	1.00	0.97	0.99	1.00	0.66
	PD	12.21	1.60	13.33	12.42	-0.13	-16.89	12.15	0.56	12.09	13.81	-0.75	-13.09
70 MeV	p	0.83	0.99	0.89	0.92	1.00	0.99	0.99	1.00	1.00	1.00	0.99	0.79
	PD	13.84	-1.19	13.78	11.47	0.16	-14.50	11.50	-1.36	11.26	12.79	-0.93	-12.72

Table A.2: Statistics tests for depth dose distribution of monoenergetic neutrons in 50ppm ^{10}B water phantom for the different physics lists compared against BICHP. All physics with thermal on (T) are compared against BICHP/T, and physics with thermal off (no T) are compared against BICHP.